CALIFORNIA DEPARTMENT OF RESOURCES RECYCLING AND RECOVERY

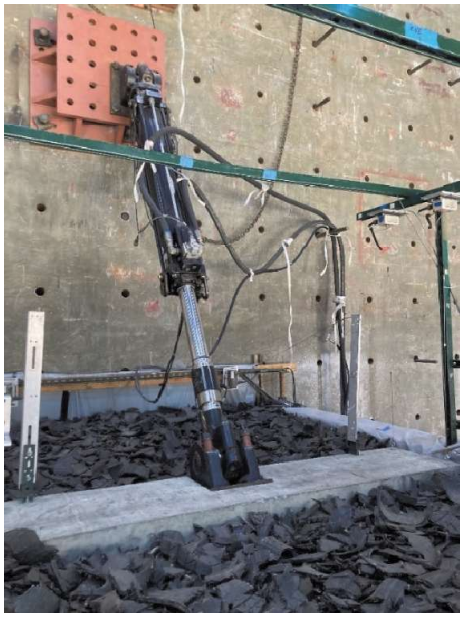

Engineering Assessment Report

ASSESSMENT OF THE BEARING STRENGTH AND SEISMIC RESPONSE OF SHALLOW FOUNDATIONS IN TIRE-DERIVED AGGREGATE (TDA)

OCTOBER 2023

Prepared by
Axel Arnold Yarahuaman Chamorro, M.S., S.M.ASCE,
John S. McCartney, Ph.D., P.E., F.ASCE,
University of California San Diego (UCSD)
Department of Structural Engineering

CalRecycle Agreement No. DRR20081

TABLE OF CONTENTS

EXECUTIVE SUMMARY v
1. INTRODUCTION 1
2. LITERATURE REVIEW 4
2.1 Footing Response in TDA 4
2.2 TDA Dynamic Response 5
3. MATERIAL DESCRIPTION 8
4. ONE-DIMENSIONAL COMPRESSION RESPONSE 8
4.1 Experimental design 8
4.2 Instrumentation 10
4.3 Experimental results 11
4.3.1 One-dimensional compression 11
4.3.2 Use of a hyperbolic on-dimensional stress-strain model 13
4.3.3 Short-term creep characterization 15
5. QUASI-STATIC TESTING PROGRAM 16
5.1 Testing Program Scope 16
5.2 Experimental setup 17
5.3 Experimental procedures 28
5.4 Experimental results 29
5.5 Closing Remarks on Quasi-Static Bearing Capacity Testing Program 42
6. DYNAMIC TESTING PROGRAM 43
6.1 Testing program scope 43
6.2 Experimental setup 43
6.2.1 Shake table description. 43
6.2.2 Laminar shear box description 45
6.2.3 Specimen configuration 46
6.2.4 Construction techniques 50
6.2.5 Instrumentation 55
6.3 Experimental procedure 59
6.3.1 Testing protocol 59

6.4 Experimental results 65
6.4.1 System identification 65
6.4.2 Moment-rocking response 69
6.4.3 Settlement-rocking response 72
6.4.4 Recentering response 78
6.5 Final Comments from Seismic Testing Program 79
7. CONCLUSIONS 80
7.1 One-dimensional compression conclusions 80
7.2 Quasi-static testing program conclusions 80
7.3 Dynamic testing program conclusions 81
8. REFERENCES 81

Appendix A: Quasi-static testing specimen No 01

- Sub Appendix A.1 Instrumentation plans

Appendix B: Quasi-static testing specimen No 02

- Sub Appendix B.1 Instrumentation plans

Appendix C: Quasi-static testing specimen No 03

- Sub Appendix C.1 Instrumentation plans

Appendix D: Quasi-static testing specimen No 04

- Sub Appendix D.1 Instrumentation plans

Appendix E: Quasi-static testing specimen No 05

- Sub Appendix E.1 Instrumentation plans

Appendix F: Quasi-static testing specimen No 06

- Sub Appendix F.1 Instrumentation plans

Appendix G: Quasi-static testing specimen No 07

- Sub Appendix G.1 Instrumentation plans

Appendix H: Quasi-static testing specimen No 08

- Sub Appendix H.1 Instrumentation plans

Appendix I: Dynamic testing specimen No 01

- Sub Appendix I.1 Instrumentation plans
- Sub Appendix I.2 - Time history records for DT01-SS150-F01F10
- Sub Appendix I.3 - Time history records for DT01-SS300-F01F10
- Sub Appendix I.4 - Time history records for DT01-SS450-F01F10
- Sub Appendix I.5 - Time history records for DT01-SS525-F01F10
- Sub Appendix I.6 - Time history records for DT01-NOR-050P
- Sub Appendix I.7 - Time history records for DT01-NOR-075P
- Sub Appendix I.8 - Time history records for DT01-NOR-100P
- Sub Appendix I.9 - Time history records for DT01-MAU-100P

Appendix J: Dynamic testing specimen No 02

- Sub Appendix J.1 Instrumentation plans
- Sub Appendix J.2 - Time history records for DT02-SS08-F04F10
- Sub Appendix J.3 - Time history records for DT02-SS12-F04F10
- Sub Appendix J.4 - Time history records for DT02-SS16-F04F10
- Sub Appendix J.5 - Time history records for DT02-SS20-F04F10
- Sub Appendix J.6 - Time history records for DT02-NOR-050P
- Sub Appendix J.7 - Time history records for DT02-NOR-075P
- Sub Appendix J.8 - Time history records for DT02-NOR-100P
- Sub Appendix J.9 - Time history records for DT02-MAU-100P

Appendix K: Dynamic testing specimen No 03

- Sub Appendix K.1 Instrumentation plans.
- Sub Appendix K.2 - Time history records for DT03-SS08-F04F10
- Sub Appendix K.3 - Time history records for DT03-SS12-F04F10
- Sub Appendix K.4 - Time history records for DT03-SS16-F04F10
- Sub Appendix K.5 - Time history records for DT03-SS20-F04F10
- Sub Appendix K.6 - Time history records for DT03-SS24-F04F10
- Sub Appendix K.7 - Time history records for DT03-NOR-050P
- Sub Appendix K.8 - Time history records for DT03-NOR-075P
- Sub Appendix K.9 - Time history records for DT03-NOR-100P
- Sub Appendix K.10 - Time history records DT03-MAU-100P

EXECUTIVE SUMMARY

Tire-derived aggregate (TDA) is an alternative lightweight backfill material for civil engineering applications that is formed by shredding end-of-life tires into shreds with a specified particle size range. TDA with larger particle sizes up to 300 mm, referred to as Type B TDA, represents the most economical and sustainable form of TDA due to its lower cost of processing and the smaller amount of exposed steel wire. Several studies have characterized the mechanical properties of TDA governing their shearing response under monotonic and cyclic loading and have found that TDA has similar shear strength to granular backfill soils, albeit with a lower shear modulus, a higher damping ratio, and a larger deformation at peak shear strength. Further, field demonstration studies have shown that TDA can be used as a backfill that generates lower vertical stresses on the underlying subgrade and lower horizontal stresses on retaining structures.

A remaining research question is the mechanical bearing response of inclusions embedded in TDA, which may range from foundations or footings that support structures, signposts, or guard rails to pipelines or utilities that cross through the backfill. While theories have been developed for the bearing capacity of footings on soils, their applicability to TDA has not been studied. Further, the response of shallow foundations on TDA to earthquake shaking is another related subject that has not been studied, even though TDA has the potential to provide a flexible buffer between the ground and a structure or reduced lateral seismic pressures. To address these issues, this report presents the results from an experimental testing program with three phases aimed at characterizing the one-dimensional compression response of Type B TDA, the quasi-static load-settlement response of footings in Type B TDA, and the dynamic lateral response of shallow foundations resting on Type B TDA during earthquake shaking.

The first phase of the study evaluated the one-dimensional compression response of Type B TDA under a constant rate of strain test up to a vertical effective stress of 20.4 kPa, which was then maintained for 1 hour to evaluate the creep response. A bi-log-linear compression curve fitted to the nonlinear compression curve for Type B TDA had compression and recompression indices of 0.32 and 0.04, respectively, which are greater than those of most soils. However, the bi-log-linear model was not practical for fitting the compression curve data as the definition of a preconsolidation or yield stress for compacted TDA is vague. Instead, a hyperbolic model was

found to provide a good fit to the compression curve, which is recommended for compression analyses with Type B TDA. A secondary compression index of 0.0029 was observed during creep testing, which is within the range of values obtained from studies on TDA with smaller particle sizes. The main conclusion from these tests is that Type B TDA is expected to deform more than granular soils during compressive loading.

In the second phase of the study, the ultimate bearing capacity of Type B TDA was evaluated through eight quasi-static tests on large-scale concrete footings. Various factors such as footing dimensions, footing embedment, inclination angle, and footing roughness (precast vs. cast-in-place) were considered in the tests to analyze their effects on the bearing capacity/settlement of shallow footings in Type B TDA. Comparison of the compression curves indicates that embedment of strip footings leads to a stiffer bearing response, and that a strip footing with a greater width will have a stiffer bearing response. Repeat tests on strip footings under load control and displacement control show similar load-settlement curves. Further, reloading of a footing after a bearing test led to a similar response to the first loading cycle. The bearing responses of circular footings were stiffer than a strip footing, with a stiffer response for a circular footing with a greater diameter, but the circular footings tended to show a clear bearing capacity failure while the strip footing did not. Loading of a strip footing under inclined loading of 30 and 60 degrees from vertical led to a clearer bearing capacity failure compared to vertically loaded strip footings. The strip footing loaded under 60 degrees had a stiffer response than the vertically loaded footing, likely due to the mobilization of horizontal passive resistance in the TDA. In tests performed in load control conditions, bearing capacity failure occurred primarily due to excess tilting of the footing. The predicted bearing capacity from the Brinch-Hansen model using the friction angle obtained from shear strength tests on Type B TDA was generally consistent with the ultimate bearing capacity at the point of tilting. However, like results from shear strength tests on Type B TDA, bearing capacity failure of footings in TDA occurred at relatively large footing settlements (more than 20 to 70% of the footing width) compared to that expected for footings in soils (usually less than 10% of the footing width). Accordingly, the bearing capacity of footings in TDA was interpreted using both the ultimate bearing capacity at the point of tilting and the bearing stress at a settlement-based failure criterion of 10% of the footing width. Engineers may prefer to use the latter settlement-based bearing stress in design to minimize settlements, so a correlation equation was proposed between this value and the ultimate bearing capacity predicted from the Brinch-

Hansen model. Overall, the quasi-static bearing capacity tests provide useful observations for understanding the bearing capacity of footings or thrust blocks for water pipelines in Type B TDA and validated quantitative relationships for prediction of the bearing capacity. A major take-away is that TDA has a high bearing capacity and can effectively resist footing loads, but that associated settlements should be considered in design.

The third phase of the study evaluated the dynamic response of flexible-base footing-structure specimens on top of three different Type B TDA thicknesses by using the shake table at the University of California San Diego Powell Laboratory. Multiple white noise motions, sine sweep motions, and the 1994 Northridge and the 2010 Maule earthquake records were applied to each specimen. The fundamental period of the flexible base structure using Type B TDA was underestimated by 40% using the model of Pais and Kausel, and the period lengthening of the footing-structure system was independent of TDA thickness. The Type B TDA provided the footing with moderate transient settlement and uplift but significantly low residual settlement and an almost perfect re-centering system, with an average re-centering ratio of 0.97. The moment-rocking response of the footing with Type B TDA exhibited substantial nonlinearity, with rocking stiffness softening at moment demands slightly below the moment capacity. Overall, the shake table testing on footings in Type B TDA indicates that TDA can provide a low-cost seismic isolation material for structures supported by shallow footings.

1. INTRODUCTION

The United States has experienced an exponential increase in the number of end-of-life waste tires (CalRecycle 2016; Edeskar 2004). Studies have found that waste tires can be recycled and used for civil engineering projects in the form of tire-derived aggregate (TDA) as an alternative backfill material. Multiple studies have been conducted to assess the feasibility and measure the engineering properties of TDA as a lightweight fill material in embankments or backfill behind retaining walls (Drescher and Newcomb 1994; Hoppe 1994; Tweedie et al. 1998; Humphrey 2008a; Mills and McGinn 2010; Tandon et al. 2007; Meles et al. 2014). Several studies concluded that TDA has a similar or better performance than conventional fill soils in terms of shear strength (Humphrey et al. 1992, Bosscher et al. 1993; Hoppe 1998; Dickson et al. 2001, El Naggar 2016). An advantage of using TDA over soils as a backfill is that its unit weight is as low as 4-7 kN/m^3, which is about 33-50% of most granular backfill soils (Ghaaowd et al. 2017). However, concerns identified with TDA is that they are more deformable than soils and are susceptible to creep, although these concerns can be mitigated in design using an overbuild strategy (Humphrey 2008b).

The two main categories of TDA described by ASTM D6270 and used in practice are Type A TDA, with particle sizes ranging from 75-100 mm, and Type B TDA, with particle sizes ranging from 150-300 mm. Type B TDA is more cost-effective because it requires less processing than Type A TDA. According to ASTM D6270, Type B TDA layers can be up to 300 mm-thick while Type A TDA layers are limited to 100 mm (ASTM 2012). Although Type B TDA has advantages for use in practice, the impacts of the large particles on the behavior of Type B TDA have not been studied due to limitations in the size, load, and displacement capability of testing devices. This study focuses on the one-dimensional compression response, the quasi-static load-settlement response, and dynamic lateral response of concrete footings embedded in Type B TDA.

The one-dimensional compression program aims to characterize the axial deformation response induced by axial stresses applied to Type B TDA in a large-scale container which interior dimensions are at least 7.3 larger than the largest TDA particle. The quasi-static bearing capacity program has the objective of investigating the effects of footing dimensions, footing embedment, inclination angle, and footing roughness (precast vs. cast-in-place) on the bearing capacity/settlement of shallow footings in Type B TDA in quasi-static loading tests, compare experimental results with predictions from soil-based theories, and provide necessary modifications specific to TDA standards. A cast-in-place footing can be simulated by placing a

layer of TDA within a form for the footing then placing concrete. This footing along with bonded TDA particles can be transferred to the container for testing. Raw data from the experimental program will consist of stress vs. displacement for each test specimen, which will be used to determine the bearing capacity. The bearing capacity values will be compared with various theories available in the literature (Terzaghi 1943, Hansen 1970, Vesic 1963), with shear strength parameters obtained from the tests of Ghaaowd et al. (2017). Bearing capacity factors will be adjusted for TDA based on analysis. The dynamic testing program includes shaking table tests were performed to understand the cyclic TDA-foundation interaction mechanisms. The modulus reduction properties from McCartney et al. (2017) will be used. Placement of TDA beneath a footing during construction of a new structure may not only provide insulation benefits but may also provide seismic isolation to the overlying structure. Specifically, the high damping ratio of the TDA identified by McCartney et al. (2017) may mean that the TDA will dissipate the shear stresses and transmit smaller shear stresses to an overlying structure. Because of the efforts required to mobilize the large laminar container at UCSD, this provides an opportunity to gain useful information that may promote the further use of TDA in new building construction. The general testing program includes a single large-scale one-dimensional compression test, eight quasi-static foundation bearing capacity tests, and three shake table tests. The details of the testing program are presented in Table 1.1.

Table 1.1 Overview of general testing program (B = Weight, D = Embedment)

Test type	Specimen	Loading	Test Parameters
One-dimensional compression	OT01	Vertical	Oedometer parameters
Quasi-static bearing capacity	QT01	Vertical	Precast strip footing, B = 0.46 m, D = 0.0 m
	QT02	Vertical	Precast strip footing, B = 0.46 m, D = 0.46 m
	QT03	Vertical	Precast strip footing, B = 0.91 m, D = 0.91 m
	QT04	Vertical	Precast strip footing, B = 0.46 m, D = 0.46 m
	QT05	Vertical	Cast-in-place circular footing, Diameter = 0.46 m, D = 0.30 m
	QT06	Vertical	Cast-in-place circular footing, Diameter = 0.30 m, D = 0.30 m
	QT07	Inclined (30°)	Precast strip footing, B = 0.46 m, D = 0.46 m
	QT08	Inclined (60°)	Precast strip footing, B = 0.46 m, D = 0.46 m
Dynamic testing	DT01	Base displacement	Precast strip footing, B = 0.46 m, D = 0.46 m, TDA thickness = 1.14 m.
	DT02	Base displacement	Precast strip footing, B = 0.46 m, D = 0.46 m, TDA thickness = 1.40 m.
	DT03	Base displacement	Precast strip footing, B = 0.46 m, D = 0.46 m, TDA thickness = 1.89 m

2. LITERATURE REVIEW

2.1 Footing Response in TDA

There have not been studies in the past focused on the bearing capacity of concrete footings in Type B TDA, although there have been a few studies focused on the bearing capacities of footings on granular soil layers overlying TDA. Mahgoub and El Naggar (2020) studied the performance of rigid footings resting on a surface of conventional backfill soil on top of a TDA layer. The study considered three full-scale field tests with different thicknesses of TDA. A 3D finite element numerical model was developed using the results of the field tests to evaluate the failure mechanism of shallow foundations overlaying a layer of TDA. The study found that the implementation of the TDA layer generated the improvement of the stress transferring and the reduction of the stress influence zone underneath the footing. The results were further studied by Mahgoub and El Naggar (2022) to implement a simplified design method that estimates the ultimate bearing capacity of shallow foundations built on top of TDA while considering into account the granular layer thickness, TDA layer thickness, footing width, footing shape, footing depth, and allowable settlement. It is important to remark that the design method depends on an initially defined allowable settlement because the TDA is highly compressible. Therefore, if it is considered with the typical settlement limits of conventional soils, the bearing capacity would automatically be much lower than conventional soils.

There have also been studies focused on the compression response of TDA mixed with soils, which is not a recommended reuse option for TDA due to the additional labor required for mixing and because it does not maximize the reuse of TDA. For example, Chenari et al. (2017) conducted a series of large-scale oedometer tests to characterize the settlement response of sand reinforced with TDA. The study considered five different ratios of TDA-sand, three aspect ratios and relative skeletal densities, and seven overburden pressures. The experimental results were used to develop a 2D linear elastic finite element model that assumes plane-strain conditions to estimate the settlement of shallow rigid foundations on coarse-grained soil combined with TDA. The numerical model was coupled with Monte Carlo simulations to perform the parametric study. The results indicated that the TDA-sand ratio is the main parameter that controls the settlement of the footing. The overburden pressure and relative skeletal density moderately controlled the response as well. Arefnia et al. (2021) studied the bearing capacity of strip footings on a layer of kaolin mixed with TDA. Their study considered thirteen 1-g experimental tests prepared on a rigid box

0.6 m by 0.9 m in plan and 0.6 m in height. The TDA-kaolin mixtures were composed of a range of 0% to 60% TDA to kaolin by weight. The strip footing was placed on top of the stabilized TDA-kaolin and was subjected to load-control conditions until reaching the ultimate bearing capacity. The results show that the added TDA generated an increase in the bearing capacity, except for the 20% TDA-kaolin mixture. The experimental results were used to develop a finite element model which overestimated the experimental bearing capacity by 9% on average.

2.2 TDA Dynamic Response

Several studies have established the dynamic material properties of TDA. Feng and Sutterer (2000) performed resonant column tests to measure the shear modulus and damping ratio of granulated rubber (particle size = 2.00 to 4.76 mm) mixed with Ottawa sand. This study found that the addition of sand produced an increase in shear modulus and reduction in damping ratio. They also tested pure granulated rubber and measured shear modulus values ranging from 1100 to 2800 kPa for effective stresses ranging from 69 to 483 kPa and shear strains ranging from 0.003 to 0.1%. This range of effective stress is much greater than expected for many TDA construction applications, such as retaining walls or embankments, and thus additional work is needed to understand variations in shear modulus at lower effective stress levels. Feng and Sutterer (2000) also observed that damping ratio of granulated rubber was not particularly sensitive to effective stress and had an initially high value of 4.5 to 6.0%. In most of their tests, the damping ratio increased with increasing shear strain amplitude, while in one test a small decrease was observed initially followed by an increase at higher shear strain amplitudes.

Kaneko et al. (2003) performed cyclic shear strain tests on saturated specimens of TDA in the form of tire chips having a maximum particle size of 1.1 mm. The measured hysteresis loops have shapes like those of granular soils, with a clear peak value at the point of strain reversal. Kaneko et al. (2003) also found that, because the particles are deformable, shear strains can be accommodated with less particle sliding and rearrangement. This feature, combined with the high hydraulic conductivity, suggests that tire chips will not experience generation of excess pore water pressures during cyclic loading that may lead to liquefaction.

McCartney et al. (2017) performed multiple quasi-static cyclic simple shear tests to characterize the cyclic properties and response of Type B TDA. The cyclic simple shear tests reached vertical stress with a range of 19.3 to 76.6 kPa and shear strain amplitudes from 0.1 to 10%. The generated stress-shear strain hysteresis loops were similar to granular soil hysteresis

loops in shape, but with lower shear modulus and larger damping ratio for comparable strain ranges. Their study found that the shear modulus of Type B TDA has a maximum value of 2,386 kPa which decreases with larger shear strains. It was also observed that the shear modulus nonlinearly increased with larger applied vertical stresses. The damping ratio of Type B TDA was found to be 21-26.8% at low shear strain amplitude (0.1 %) and decreases with the increase of shear strain amplitudes. Null dependency was found between the damping ratio and the vertical stress level.

Besides the previously mentioned studies, other multiple studies also investigated the shear modulus and damping ratio of soil-TDA mixtures (Anastasiadis et al. 2012a, 2012b; Senetakis et al. 2012a, 2012b, Nakhei et al. 2012; Mashiri et al. 2013). These studies generally observed that the shear modulus decreased, and the damping ratio increased with the percentage of TDA in the soil-TDA mixture. For example, Anastasiadis et al. (2012a) found that the shear modulus decreased from 45 to 10 MPa and the damping ratio increased from 0.68 to 0.40% when adding 35% TDA to the soil at a confining stress of 30 kPa.

The seismic response of TDA has also been studied for more specific purposes such as backfill material in gravity retaining walls (Ahn and Cheng 2014) and geosynthetic-reinforced retaining walls (Xiao et al. 2012). Ahn and Cheng (2014) performed a shake table test on a large-scale (2 m high) cantilever retaining structure constructed from a layer of Type B TDA and an overlying layer of sand. This study found that the dynamic pressure exerted on the wall was smaller in the TDA layer. Further, the TDA experienced relatively large residual shear deformations of up to 50 mm without catastrophic failure. Xiao et al. (2012) performed a shake table test on a reduced-scale (1.6 m high) geosynthetic-reinforced retaining structure constructed from TDA with a maximum particle size of 150 mm and compared the results with a similarly constructed wall using only sand. The wall constructed with TDA backfill had less lateral displacement, less vertical settlement, apparent acceleration attenuation toward the top of the wall, and lower static and dynamic lateral stresses on the wall. These studies indicate that TDA backfill for retaining walls offers several advantages in comparison to natural backfill soils.

In addition, it is known that materials that experience stiffness degradation could attenuate accelerations transmitted to the superstructure when used as base isolation (Madhusudhan et al. 2017). TDA and TDA mixtures satisfy this requirement, therefore, multiple studies experimentally and numerically evaluated their implementation as seismic isolation approach for structures.

Regarding experimental studies, Tsang et al. (2020) performed the first centrifuge testing on rubber-soil mixtures (RSM) as an engineered low-modulus foundation material as an earthquake protection system. They found that the implementation of an RSM foundation layer can generate energy radiation by sliding and rocking of the foundation which reduces the total dissipated energy of the isolated structure by over 60%. It was observed that the elasticity of the RMS avoided soil yielding and failure and significantly reduced residual ground deformation. Nikitas and Bhattacharya (2023) studied the addition of tire chips as a settlement and liquefaction mitigation strategy by conducting 1-g shake table experiments on six different configurations of the tire-base. A rigid square foundation was placed on top of the finished soil surface as a base for the model house to stand. Besides the effective mitigation of liquefaction, it was found that the tire-base reduces the displacements and tilting of the low-weight superstructure. It was also observed that the tire-subbase led to a lengthening of the foundational fundamental period of the system which could potentially help against high-frequency demands. Regarding numerical studies, Tsang et al. (2012) developed a finite element program to study the response of soil-foundation-structure systems. The superstructure was modeled following two-dimensional frame elements assembled. The foundation and subsoil materials were modeled using four-node quadrilateral plane-strain elements. The study found that implementation of RSM generates a reduced response of 40-60% on average. These results were highly dependent on the thickness of the RSM layer. They also developed and explored the correlation between the generated lengthening of the fundamental period and the reduction of effectiveness of RSM. Pistolas et al. (2020) developed a numerical model with a flexible Single-Degree-Of-Freedom (SDOF) oscillator on top of an RSM foundation material. The interface between the foundation and the RSM material allows for separation and sliding. The RSM was modeled by introducing a material with shear modulus degradation bounded by a Drucker-Prager yield surface with isotropic hardening and non-associative plastic flow rule, which was derived from experimental monotonic triaxial tests. This study concluded that the implementation of an RSM layer can effectively mitigate most of the seismic motion transferred to the soil-structure system. For far-field motions, the base shear and drifts were reduced to 80% and 50%, respectively. For near-field motions, the rocking is amplified but the base shear and drift are reduced by 60% and 20%, respectively. It was also observed that the RSM drastically amplifies the fundamental period of the SDOF even at relatively small depths.

3. MATERIAL DESCRIPTION

Type B TDA is composed of recycled waste tires shredded to a size ranging from 150 to 300 mm (Ghaaowd et al. 2017). The particles are flat and irregular with one plan dimension being greater than the other. Twelve randomly selected Type B TDA particles are presented in Figure 3.1 as a representative set of Type B particle shapes. The particle size distribution conducted by manual sorting is shown in Figure 3.1. An important advantage of TDA it is lower specific gravity (1.15) compared to conventional soils (approximately 2.65) (Ghaaowd and McCartney 2020). After compaction, the Type B TDA dry unit weight reaches 4 to 7 kN/m^3 (Ghaaowd et al. 2017; McCartney et al. 2017) which is equivalent less than one-half of most backfill soils (Ghaaowd and McCartney 2020).

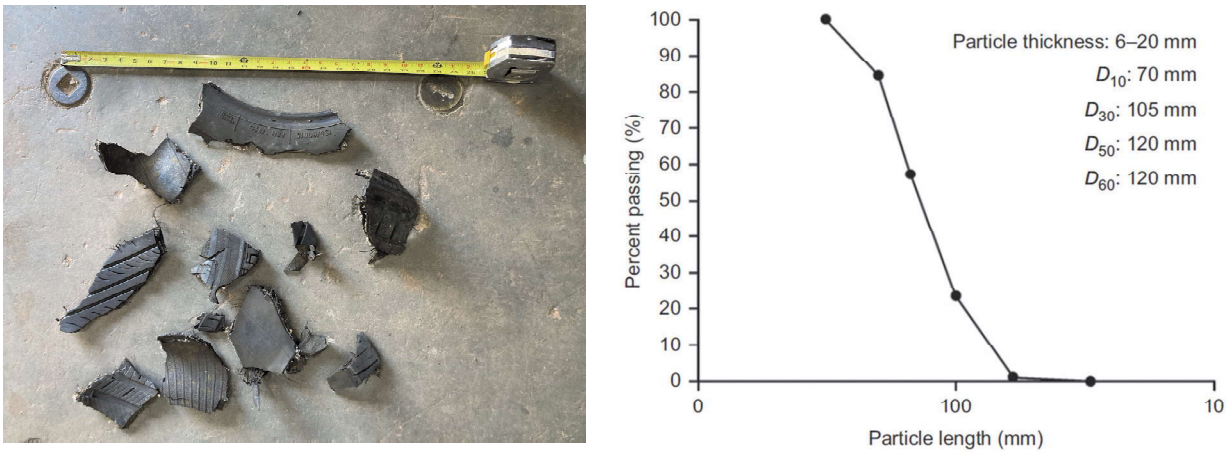

(a) **(b)**

Figure 3.1 Type B particle size: (a) Example of Type B TDA particles, and (b) Particle size distribution (Ghaaowd and McCartney 2020).

4. ONE-DIMENSIONAL COMPRESSION RESPONSE

4.1 Experimental design

A preliminary experimental program was designed as part of this project to assess the one-dimensional compression behavior of an 0.810 m-thick layer of Type B TDA. A compression test was conducted on a large-scale 1-dimensional compression device built at the UCSD Powell Lab using 4 blocks of reinforced concrete walls 254 mm thick as well as one side of the existing strong wall of the lab as shown in Figure 4.1. Two 5.029 m long, and 3.048 m high blocks compose the east and west sides of the container. One 0.350 m × 1.575 m block composes the bottom of the north side of the container. One 6.350 m × 1.473 m block composes the top of the north side of the container. The south side of the container consists of a portion of the existing 1.000 m-thick

strong wall of the lab. All reinforced concrete blocks were anchored to the strong floor and wall using high tension bolts and steel chains. The resulting large-scale 1-dimensional compression device has inside dimensions of 5.029 m × 2.184 m in plan and 3.048 m in height, with adequate capacity to restrain the lateral displacement of the TDA to measure one-dimensional compression as shown in Figure 4.1(d).

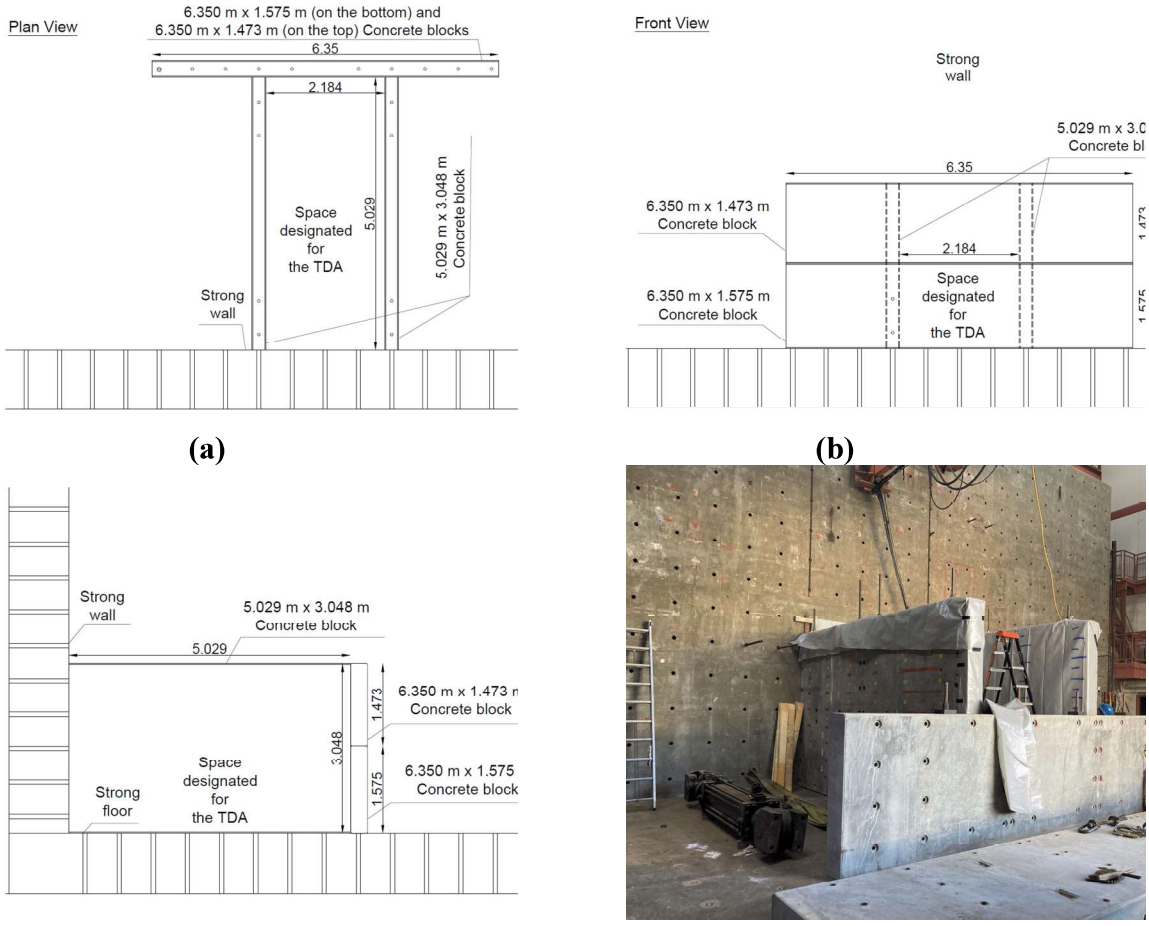

Figure 4.1 TDA container (units in m): (a) Plan view, (b) Front view, (c) Side view, (f) Picture of container under construction.

One-dimensional compression tests require minimizing the friction between the TDA particles and the inner surface of container so that the externally applied stress is uniform across the depth of the TDA layer. This study followed the approach considered by Yarahuaman and McCartney (2022) and Yarahuaman and McCartney (2023) and implemented two layers of thin polyethylene sheet having a thickness of 60 mils (on each side) to cover the inner walls to represent a low-friction interface. The Type B TDA specimen was placed inside the container and compacted

uniformly to a dry unit weight of 4.71 kN/m^3. The loading system was then set on top of the TDA specimen. The loading system consists of a steel diagonal braced reaction frame, a hydraulic actuator, an actuator mounting plate, and a reinforced concrete platen, as shown in Figure 4.2. The hydraulic actuator has a static capacity of 222 kN. The platen has dimensions of 5.395 m × 2.130 m and a thickness of 285 mm. The diagonal braced reaction frame is fixed to the strong wall as a support for the actuator. One end of the actuator is attached to the reaction frame by four bolts. The other end of the actuator is fixed to the actuator mounting plate. The mounting plate allows the connection between the actuator and the platen. The objective of the platen is to distribute the vertical load uniformly on the TDA.

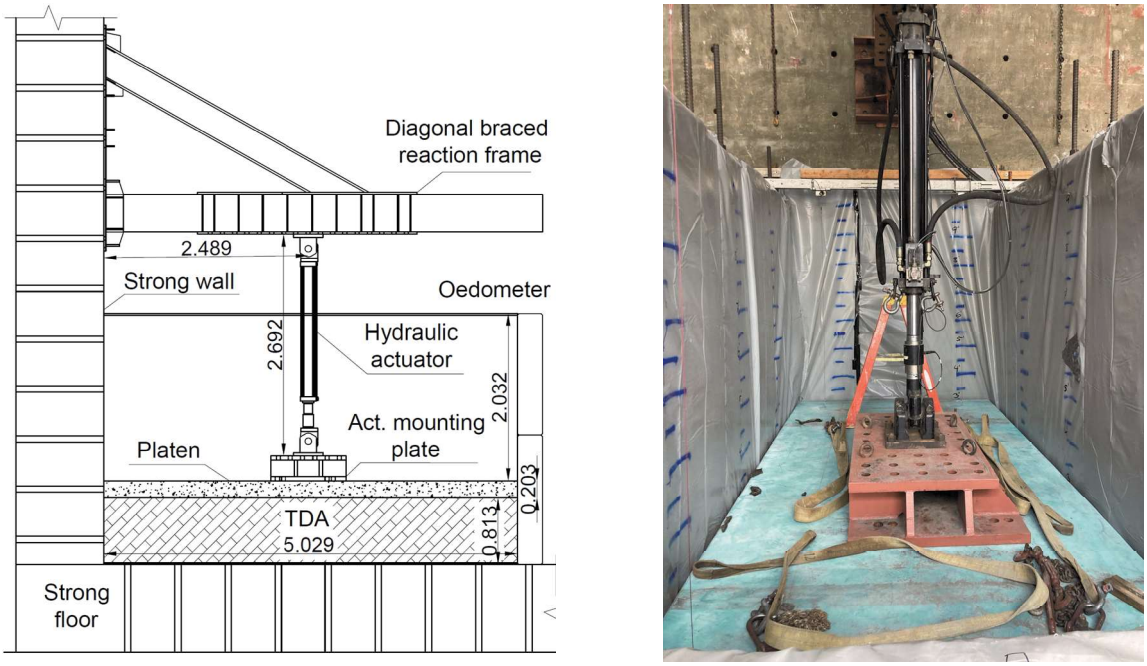

(a) **(b)**

Figure 4.2 Loading system (units in m): (a) Elevation section view, and (b) Picture of hydraulic loading system.

4.2 Instrumentation

A schematic showing instrumentation in the TDA specimen is shown in Figure 4.3. Spring-loaded linear potentiometers were placed vertically near to the corners of the platen to measure the TDA settlements. Potentiometers P01, P02, P03, and P04 shown in Figure 4.3 are used to monitor the north-east, north-west, south-east, and south-west locations, respectively. Aluminum rails were mounted across the top of the container to mount instrumentation.

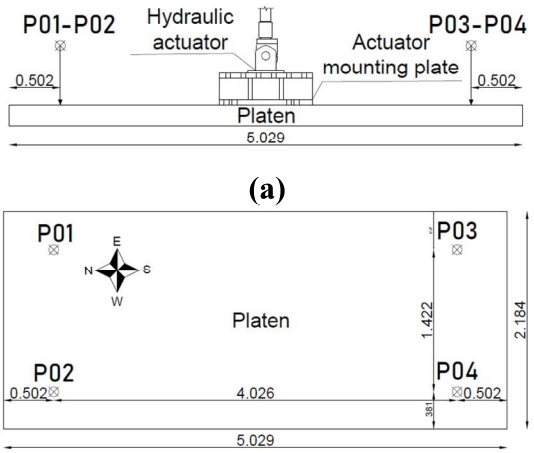

Figure 4. 3 Instrumentation layout (units in m): (a) Side view, and (b) Plan view

4.3 Experimental results

4.3.1 One-dimensional compression

This paper reports results from a single experiment performed to study the 1-dimensional compression behavior of Type B TDA compacted to an initial dry unit weight of 4.71 kN/m^3. The test protocol consisted of the load-control application of a vertical monotonic load up to 222 kN at a load rate of 222 kN/hr. When the load reached its maximum value, the load was held constant for 1 hr. After that, the specimen was unloaded following a rate of -222 kN/hr down to 5 kN. The results indicate that the maximum vertical effective stress reached was 20.4 kPa. The potentiometer time-history records indicate that the displacement of the platen is uniform and remains level which indicates that the TDA settled uniformly around the entire plan area of the container. Figure 4.4(a) also shows that that creep occurs during the constant load stage. The one-dimensional compression response of the TDA is plotted in terms of vertical strain versus vertical stress on a natural scale in Figure 4.4(a) and in terms of void ratio versus vertical stress on a log scale in Figure 4.4(b) for better comparison with the compression curves of soils. Assuming a bi-log-linear model for the TDA, Casagrande's method was used in Figure 4.4(b) to obtain the compression index C_C and recompression index C_r.

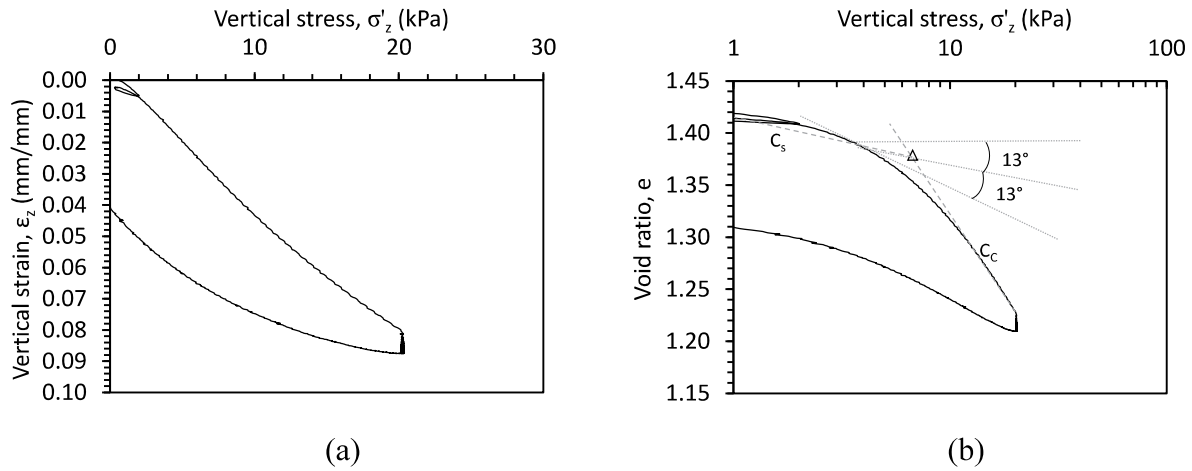

Figure 4. 4 Type B TDA response: (a) Stress-strain curve, and (b) Stress-void ratio curve

The results in Figure 4.4 reveal a non-linear compression response of Type B TDA during loading and unloading that is similar in some ways to that of soils. The compression during loading is attributed to the void volume reduction and not to the compressibility of the TDA particles themselves due to the relatively low normal stresses and low volume compressibility of rubber as indicated by a Poisson's ratio of approximately 0.5 (Feng and Sutterer 2000). The compression curve (i.e., void ratio versus log of vertical stress) indicates a nonlinear behavior with an apparent yield stress that can be found from the maximum curvature when the stress is plotted on a log scale. The obtained apparent yield stress σ'_c, compression index C_c, and apparent "recompression" index C_r obtained from the compression curve in Figure 5(b) were 6.80 kPa, 0.32 and 0.04, respectively. The compression response of the TDA is compared to other similar studies on Type A and Type B TDA as shown in Figure 6. Ghaaowd et al. (2017) proposed a log-linear Type B TDA compression curve with C_c = 0.80 and C_r = 0.03 for TDA with an initial unit weight of 6.00 kN/m^3 under vertical effective stresses up to nearly 80 kPa. Humphrey et al. (2008b) found a log-linear compression curve with C_c = 0.45 and C_r = 0.10 for Type A TDA with an initial unit weight of 5.04 kN/m^3 under vertical effective stress up to nearly 27 kPa. This comparison confirms that the compression curve of TDA is generally nonlinear with less compression up to a certain point after which the compression curve steepens. The initial stage of compression is similar for the two studies on Type B TDA with similar recompression indices. Nonetheless, the C_c computed by Ghaaowd et al. (2017) is 150% larger than the C_c obtained for Type B TDA in Figure 4.5. This difference could be due to the greater vertical stress range applied by Ghaoowd et al. (2017) but

also could be due to the way the compression curve of Ghaaowd et al. (2017) was defined. The apparent yield stress used by Ghaaowd et al. (2017) indicates a sharp break, while the compression data in this study indicates a smoother nonlinear response. This comparison indicates that a bi-log-linear model may not be appropriate for Type B TDA. Overall, the results indicate that Type B TDA is less compressive than Type A TDA but much more compressive than conventional soils for the studied vertical stresses. These findings suggest that Type B TDA could be more beneficial than Type A TDA and less beneficial than conventional soils when settlements are limited.

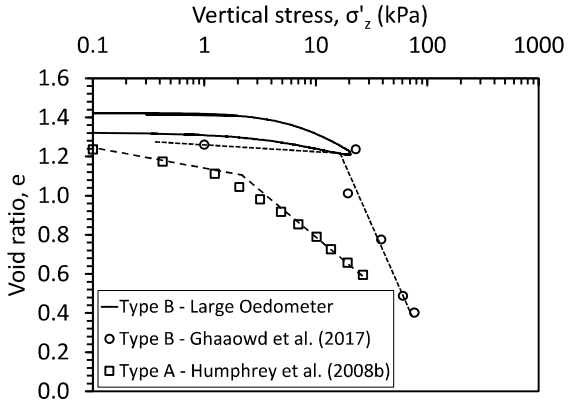

Figure 4.5 Comparison of one dimensional stress-strain curves of Type A and Type B TDA

4.3.2 Use of a hyperbolic on-dimensional stress-strain model

Due to the nonlinear compression response of Type B TDA that may not be well represented with a bi-log-linear model, it may be advantageous to represent the compression curve of TDA with a hyperbolic model as proposed by Meles et al. (2014). The one-dimensional compressional model from their study follows a form of the hyperbolic model proposed by Drnevich (1975), given as follows:

$$\sigma'_z = \frac{D_i \varepsilon_z}{1 - {\varepsilon_z}/{\varepsilon_m}} \qquad \textbf{Eq. 4.1}$$

where $\sigma'_z$is the vertical stress, D_i represents the initial tangent modulus, ε_z is the vertical axial strain and, ε_m is the strain at which the strain-stress curve becomes asymptotic. One method to determine the parameters in Eq. 4.1 is by using experimental data from a one-dimensional compression test and by transforming Eq. 4.1 to obtain a linearized version as follows:

$$\frac{\sigma'_z}{\varepsilon_z} = D_i + \frac{\sigma'_z}{\varepsilon_m} \qquad \textbf{Eq. 4.2}$$

which represents a linear relationship with slope $\frac{\sigma}{\varepsilon_m}$ and intercept D_i. The fitting parameters for the data set of Meles et al. (2014) are given in Table 4.1 along with those for the experimental data for Type B TDA from Figure 6. The calibration process on the transformed coordinates is shown in Figure 4.6(a) for Type B TDA. The fitted hyperbolic compression curves from both studies are shown and compared in Figure 4.6(b). The model parameters for both data sets are consistent.

Table 4.1 One-dimensional hyperbolic model parameters for Type B TDA compression

Calibrated dataset	D_i	$1/\varepsilon_m$
Meles et al. (2014)	134	2.65
Data in Figure 6	205	2.41

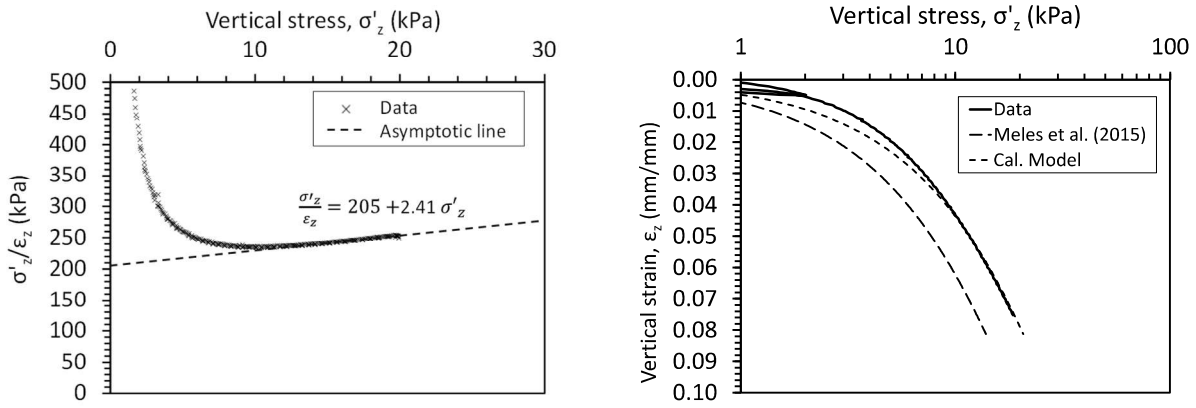

(a) **(b)**

Figure 4.6 One-dimensional compression model for Type B TDA: (a) Calibration of model with experimental data, and (b) Comparison of data with hyperbolic models.

The hyperbolic model has a good fit to the one-dimensional compression curve for Type B TDA used in the project at large stresses, with a slight underestimation at low stresses potentially because of the experimental unloading/reloading path, as shown in Figure 4.6(b). The compression curve for Type B TDA measured in this study indicates a similar slope to that of the curve fit to the data of Meles et al. (2014), but with a shift to the right indicating less change in void ratio for a given vertical stress. This difference could be due to the initial densities of the TDA in this study and that of Meles et al. (2014). It is important to note that the compression curve of Type B TDA on a natural scale in Figure 4.4(a) is not completely linear but does not show a clear point of yielding, so the nonlinear shape in Figure 4.6(b) can partly be attributed to the log scale. Beyond

the apparent yield stress, the calibrated model predicts the one-dimensional compression with considerable accuracy until the end of the compression stage. Overall, the hyperbolic compression curve model proposed by Meles et al. (2014) calibrated with experimental data represents the one-dimensional compression well for Type B TDA at the initial unit weight evaluated in this study. As TDA is a compact material, it is advantageous to use a hyperbolic model instead of a bi-log-linear model that requires definition of an apparent yield stress.

4.3.3 Short-term creep characterization

Short-term time dependent creep deformation was investigated for the Type B TDA subjected to a constant vertical effective stress of 20.4 kPa over a period of 1 hour. Although previous studies recommend evaluation of creep for minimum periods of time ranging from 5 days (Wartman et al. 2007), 30 days (Adesokan et al. 2020), or 50 days (Tweedie et al. 1997), this study evaluated time-dependent compression as a complement to the one-dimensional compression characteristics, and the loading time was limited due to the use of hydraulic actuators for load application. Once the one-dimensional compression test reached the peak vertical load, the load was maintained constant for 1 hour before unloading. The time-strain curve for the constant load stage is shown in Figure 4.7. A parameter used to characterize the creep behavior of soils in is the secondary compression index $C_{\alpha\varepsilon}$, which is defined as follows (Wartman et al. 2007):

$$C_{\alpha\varepsilon} = \frac{\Delta\varepsilon_v}{\log\left({}^{t_2}/_{t_1}\right)} \qquad \textbf{Eq. 4.3}$$

where $\Delta\varepsilon_v$ is the change in time-dependent volumetric strain, t_1 is the time when time-dependent compression begins, t_2 and is the time at which the magnitude of the time-dependent compression is to be estimated. The results shown in Figure 4.7 indicate that the volume of the Type B TDA specimen decreases non-linearly over time, with the largest volume change occurring during the first minutes of the constant load. The TDA material seems to be stabilizing over time. The modified secondary compression index $C_{\alpha\varepsilon}$ computed in this study is 0.0029. In practice, creep or time-dependent compression is typically addressed by waiting eight weeks after the TDA placement before the placement of the settlement-sensitive components (Wartman et al. 2007). The computed value of $C_{\alpha\varepsilon}$ suggests that this approach could be satisfactory for typical Type B TDA embankments but further studies on creep over longer periods and at different vertical effective stresses is needed to complement the information from this study.

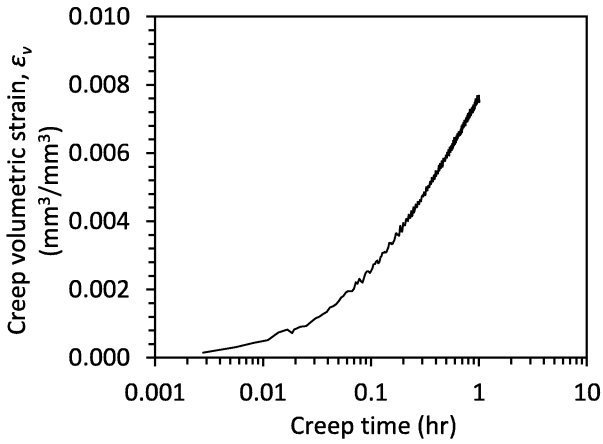

Figure 4.7 Creep volumetric strain versus time for Type B TDA under $\sigma' = 20.4$ kPa.

The secondary compression index can be translated to a modified secondary compression ratio of 0.009 (following Eq. 4.4), which indicates that most of the TDA B TDA settlement occurs during the initial settlement and less during time-dependent settlement.

$$Modified\ secondary\ compression\ ratio = \frac{C_{\alpha\varepsilon}}{C_c} \qquad \textbf{Eq. 4.4}$$

Salgado (2022) found that the secondary compression ratio for conventional soils cush clay, slits, mudstone, and peat ranges between 0.02 and 0.07. The results suggest that Type B TDA experiences less time-dependent settlement than conventional soils which could be beneficial. However, it should be noted this study conducted time-dependent settlement for only one hour, therefore, further testing at longer periods of time is required to apply these results to practice.

5. QUASI-STATIC TESTING PROGRAM

5.1 Testing Program Scope

The container used for the large-scale one-dimensional compression tests on Type B TDA was adapted to perform a total of eight quasi-static tests on footings embedded in Type B TDA. A summary of the testing specimen's configuration is shown in Table 5.1. The specimens were tested in numerical order starting from QT-01 and finishing at QT-08. During this process, the TDA was not fully removed and replaced again after each test because that approach would take significant labor and time due to the size of the specimens. It was expected that the stresses and settlement generated by each test modified the initial parameters of the TDA. As a solution to this problem, the volume of initial and added TDA, compaction methods, and settlement after each test were monitored to objective equivalent TDA parameters which are shown in Table 5.1.

Table 5.1 Summary of quasi-static testing specimen's configuration

Specimen	Thickness of TDA layer [m]	Average TDA layer unit weight [kN/m^3]	Footing width or diameter, B [m]	Footing length, L [m]	Footing embedment, D [m]	Inclination of loading with vertical plane, i [°]
QT-01	3.00	6.25	0.46	2.13	0.00	0
QT-02	3.00	6.77	0.46	2.13	0.46	0
QT-03	3.00	7.10	0.91	2.13	0.91	0
QT-04	3.00	7.40	0.46	2.13	0.46	0
QT-05	3.00	7.85	0.46	---	0.30	0
QT-06	3.00	8.02	0.30	---	0.30	0
QT-07	3.00	8.10	0.46	2.13	0.46	30
QT-08	3.00	8.18	0.46	2.13	0.46	60

5.2 Experimental setup

The experimental program was designed to assess the bearing strength of a 3.0 m-thick layer of Type B TDA subjected to loaded shallow foundations. Multiple bearing strength tests were conducted using the same large-scale compression device as the one-dimensional testing program. The Type B TDA specimen was placed inside the container and compacted uniformly using a vibrating bobcat. The unit weights attained for the TDA layers were summarized in Table 5.1. The loading system was then set on top of the TDA specimen. The loading system consists of a steel diagonal braced reaction frame, one or two hydraulic actuators, an actuator mounting plate, and a two-to-one actuator head adapter for some cases. Each hydraulic actuator has a static capacity of 222 kN. The diagonally braced reaction frame is fixed to the strong wall as a support for the actuator. One end of the actuators is attached to the reaction frame by four bolts. The other end of the actuators is fixed to the top of the footing. When 2 actuators were used, both were placed in a north-south parallel orientation, so a two-to-one actuator head adapter was required to transfer the two actuator loads to a single point on top of the footing. To apply inclined loads, the top head of the actuator was directly attached to the strong wall using an actuator mounting plate, instead of attaching it to the reaction frame.

The quasi-static specimens consist of two precast strip footings and two cylindrical cast-in-place footings to evaluate the bearing strength of TDA. Strip footings No 01 and 02 consist of reinforced concrete rectangular prisms, as shown in Figures 5.1 to 5.2. Strip footing No 02 is twice

as wide and high as strip footing No 01. Both strip footings were pre-cast before placing them on the TDA, thus, all sides of both footings had a flat and smooth surface. Further, additional connectors were cast into two bevels on the top surface to accommodate connections to an inclined actuator having angles from vertical of 30 or 60°. The footing also has four 100 mm-diameter through holes near the edges to accommodate tell-tales for settlement plates embedded in the TDA layer. Cylindrical footings No 01 and 02 consist of reinforced concrete cylinders, as shown in Figures 5.3 and 5.4. Cylindric footing No 02 has a 50% larger diameter than cylindrical footing No 01. Both cylindrical footings were "cast-in-place" in a different smaller container before being placed in the actual testing container. Following this approach, both cylindrical footings were provided with a rough and irregular surface on the bottom side and lower half-contour which attempts to simulate actual cast-in-place conditions. It is important to mention that a low-permeable synthetic geomembrane was used as a base to diminish the quantity of concrete water migrating outside of the cylinder form.

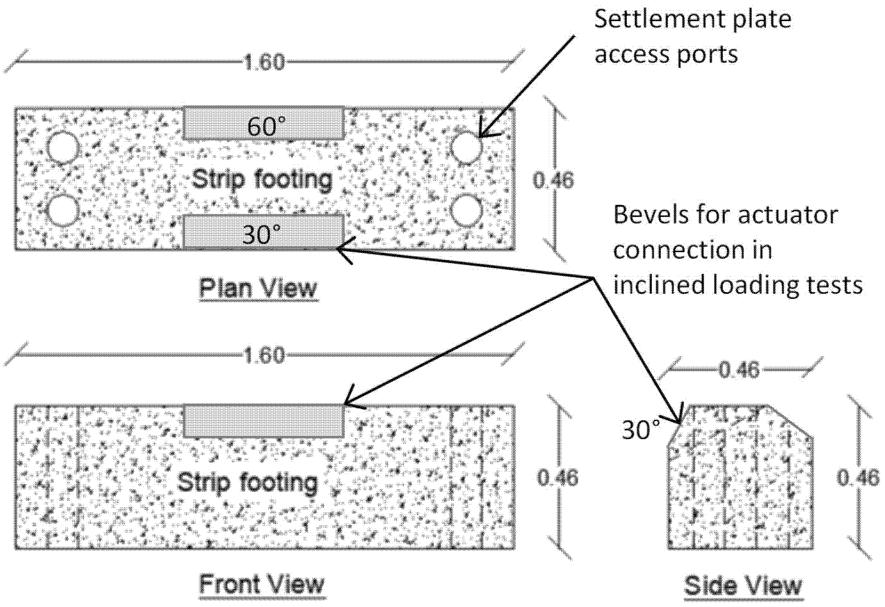

Figure 5.1 Strip footing No 01.

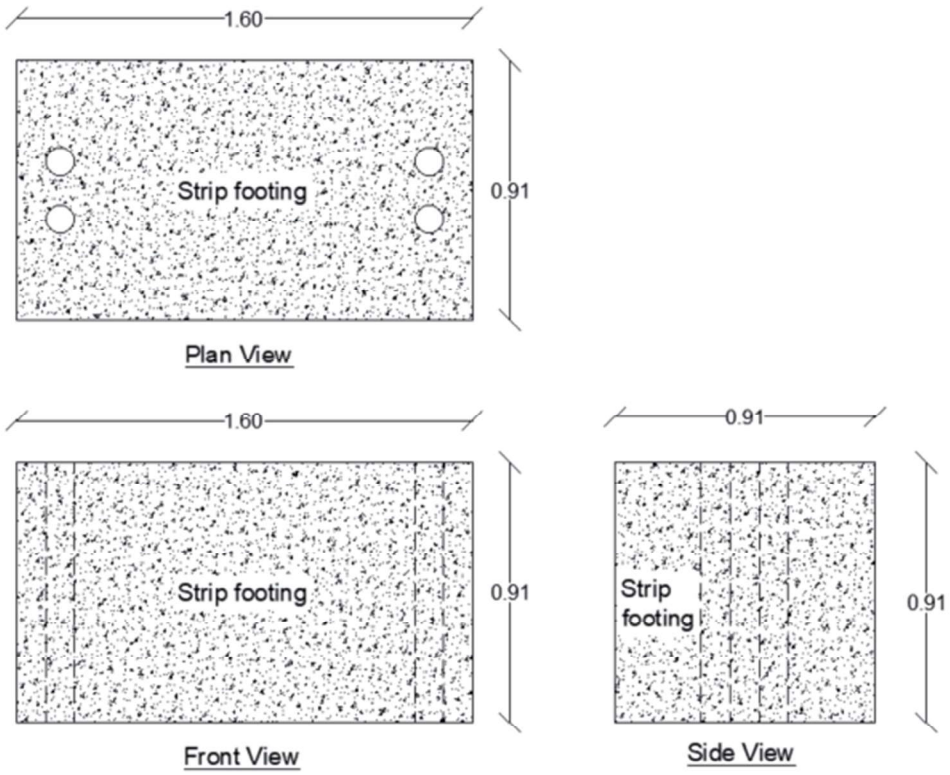

Figure 5.2 Strip footing No 02.

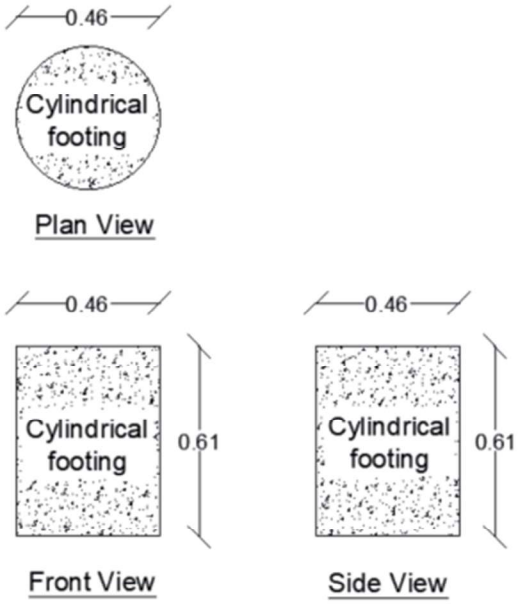

Figure 5.3 Cylindrical footing No 01 (cast into a Sonotube within a TDA layer).

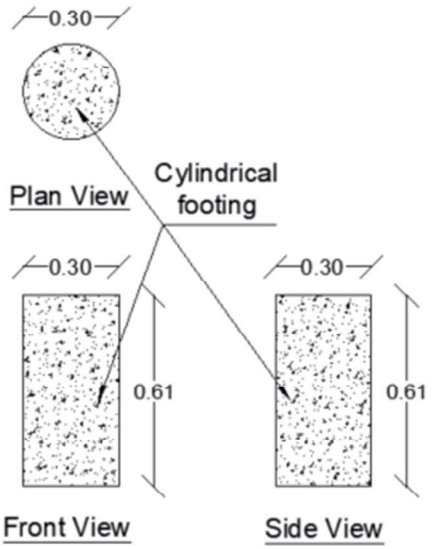

Figure 5.4 Cylindrical footing No 02 (cast into a Sonotube within a TDA layer).

This study considered eight quasi-static specimens which used the four types of footings previously described. The weight specimens were configurated to evaluate the stress-settlement response of Type B TDA beneath shallow foundations of different widths, embedment, shape, and load inclination as shown in Figures 5.5 to 5.12. Specimen QT-01 represents a typical surface strip footing placed on the TDA layer subjected to a fully vertical load. Specimens QT-02, QT-03, and QT04 represent a typical fully embedded strip footing placed on the TDA layer subjected to a fully vertical load. Specimens QT-05 and QT-06 represent a partially embedded cylindrical footing placed on the TDA layer subjected to a fully vertical load. Specimens QT-07, and QT-08 represent a typical fully embedded strip footing placed on the TDA layer subjected to an inclined load.

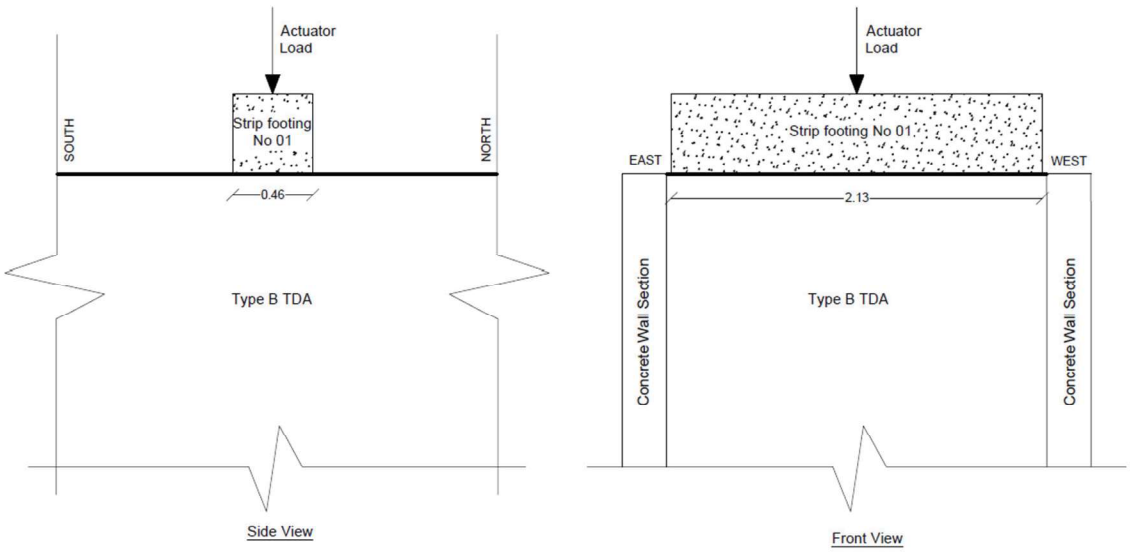

(a)

(b)

Figure 5.5 Specimen QT-01 configuration: (a) Conceptual drawing, and (b) Picture.

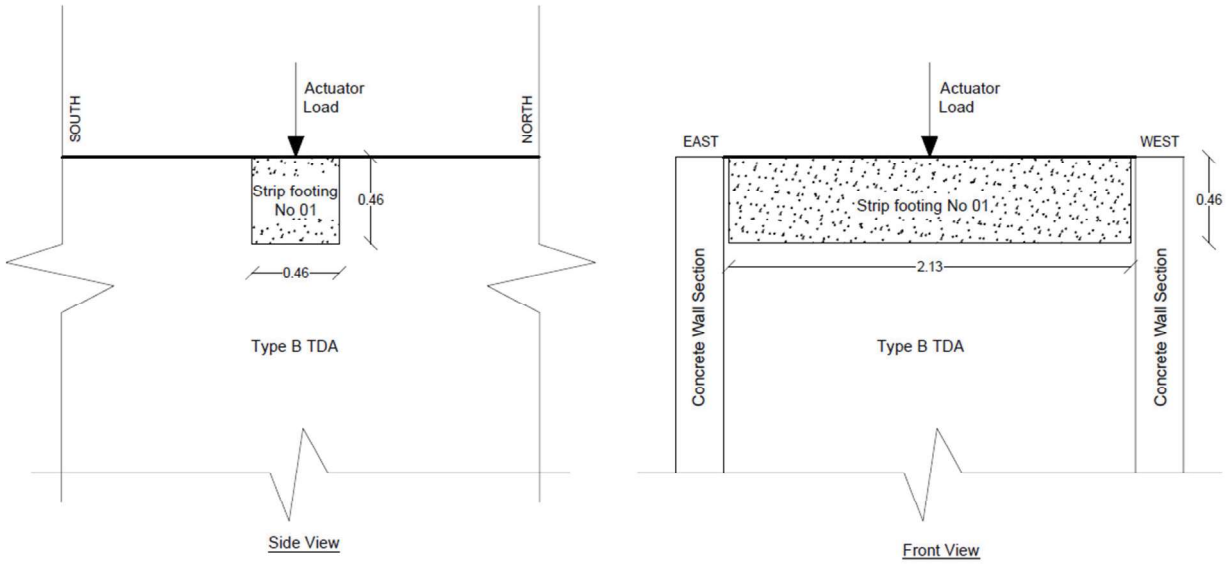

(a)

(b)

Figure 5.6 Specimen QT- 02 configuration: (a) Conceptual drawing, and (b) Picture.

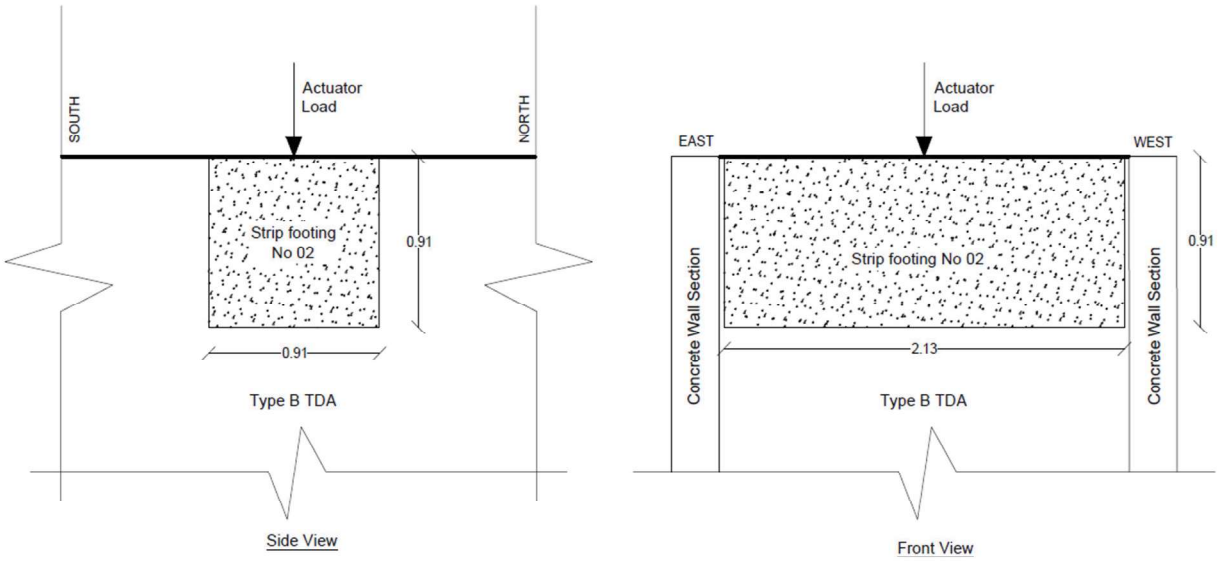

(a)

(b)

Figure 5.7 Specimen QT-03 configuration: (a) Conceptual drawing, and (b) Picture.

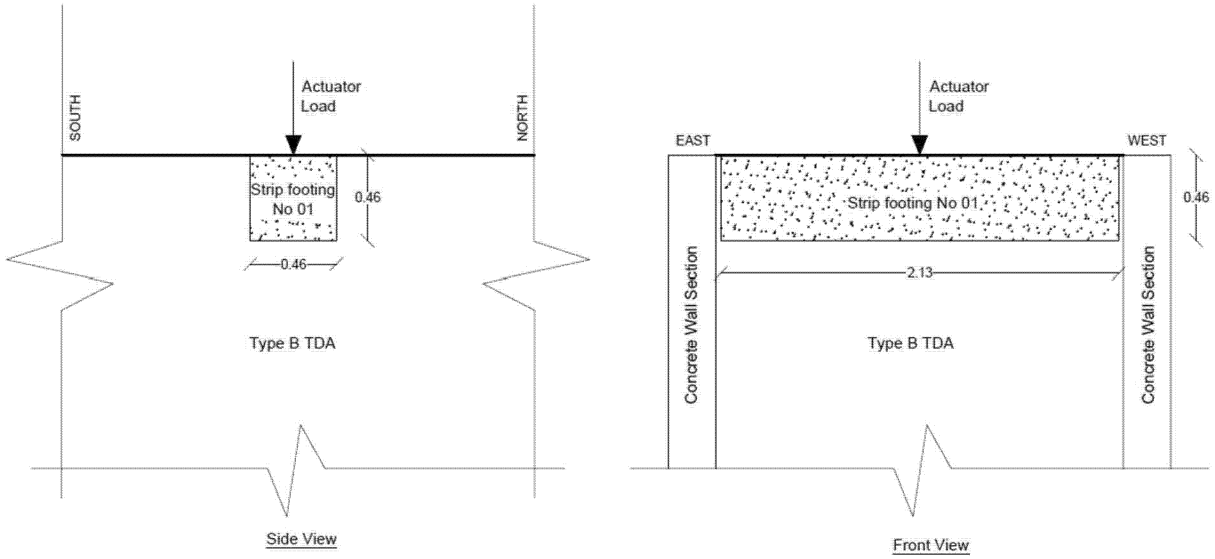

(a)

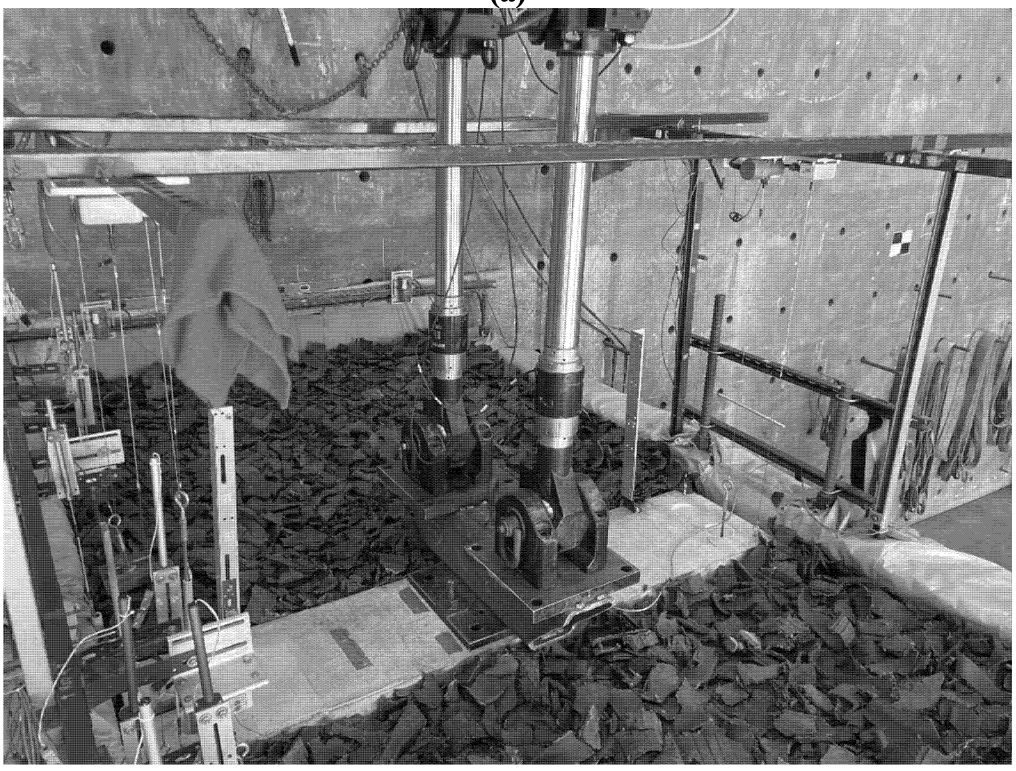

(b)

Figure 5.8 Specimen QT-04 configuration: (a) Conceptual drawing, and (b) Picture.

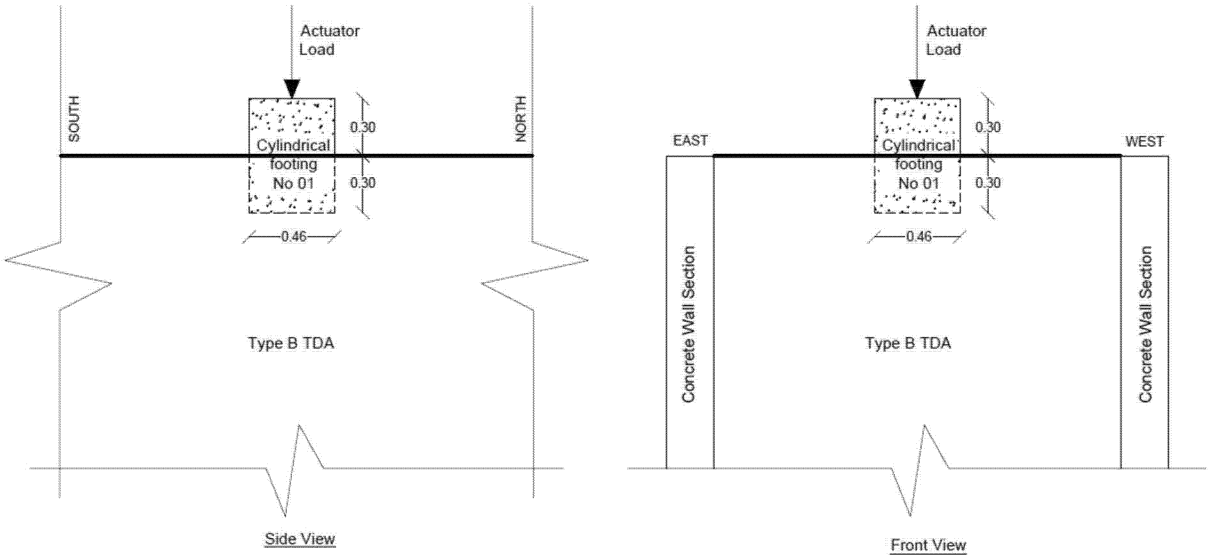

(a)

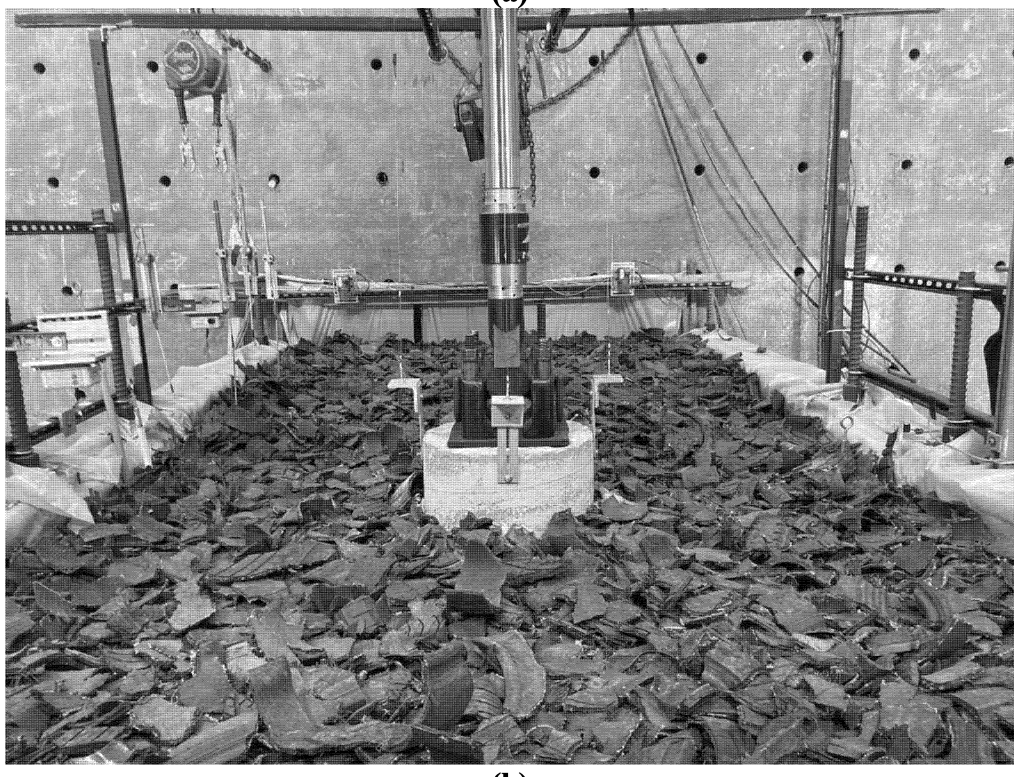

(b)

Figure 5.9 Specimen QT-05 configuration: (a) Conceptual drawing, and (b) Picture.

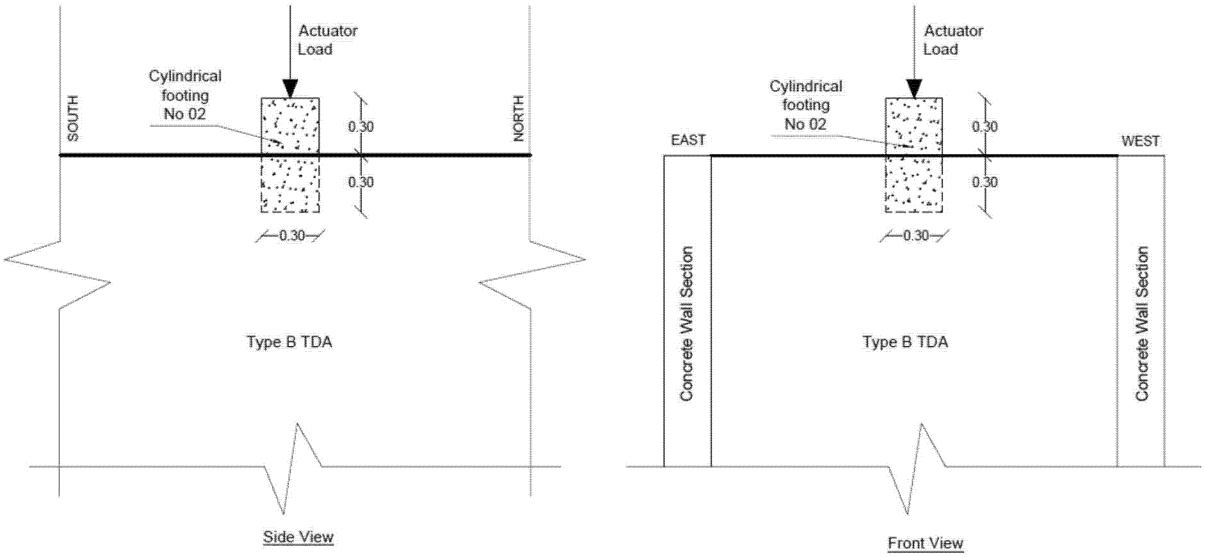

(a)

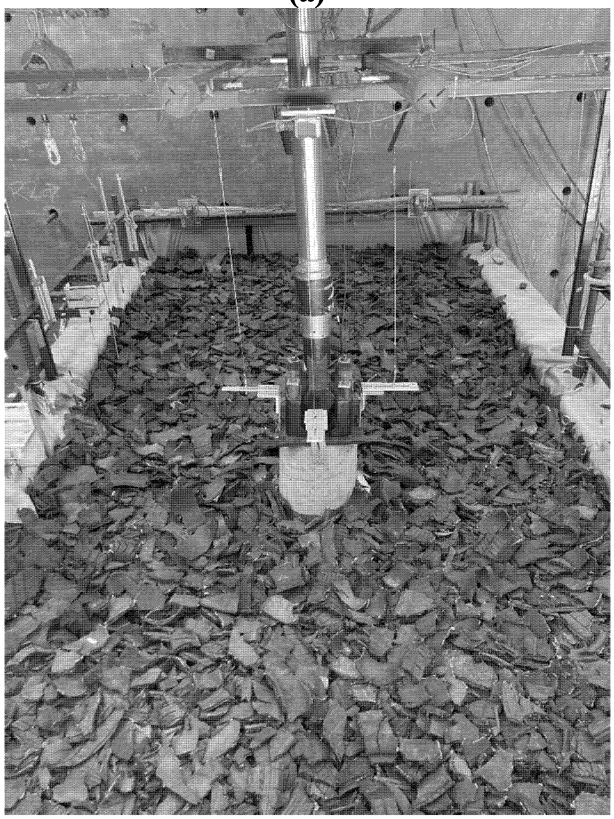

(b)

Figure 5.10 Specimen QT-06 configuration: (a) Conceptual drawing, and (b) Picture.

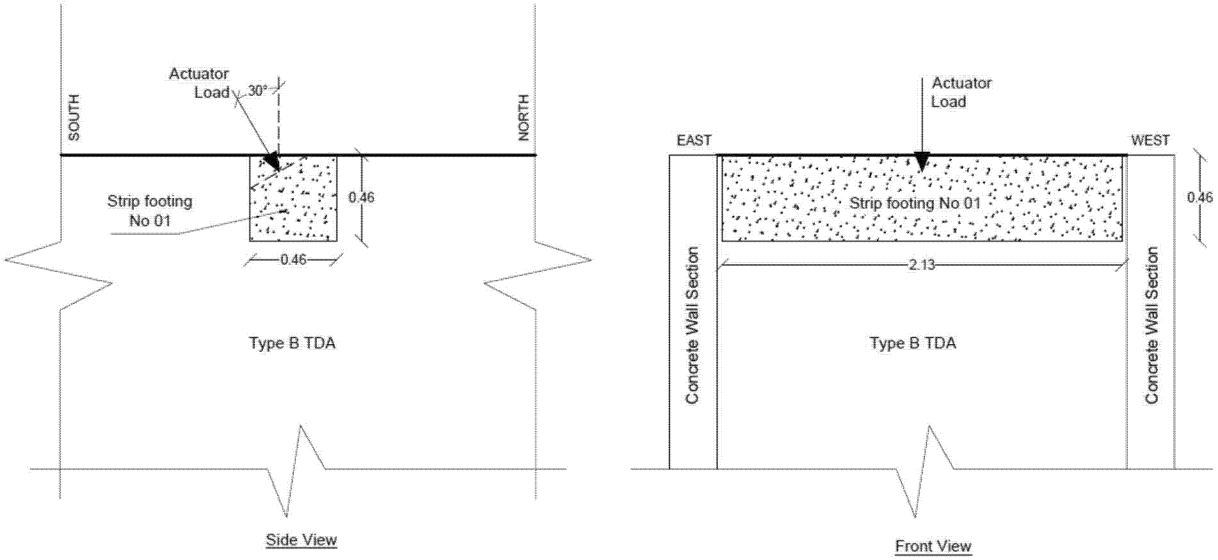

(a)

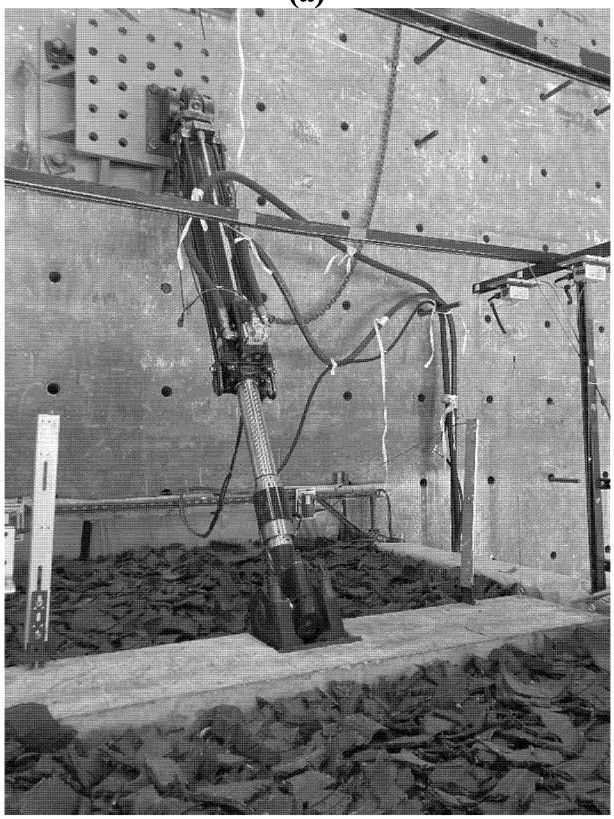

(b)

Figure 5.11 Specimen QT-07 configuration: (a) Conceptual drawing, and (b) Picture.

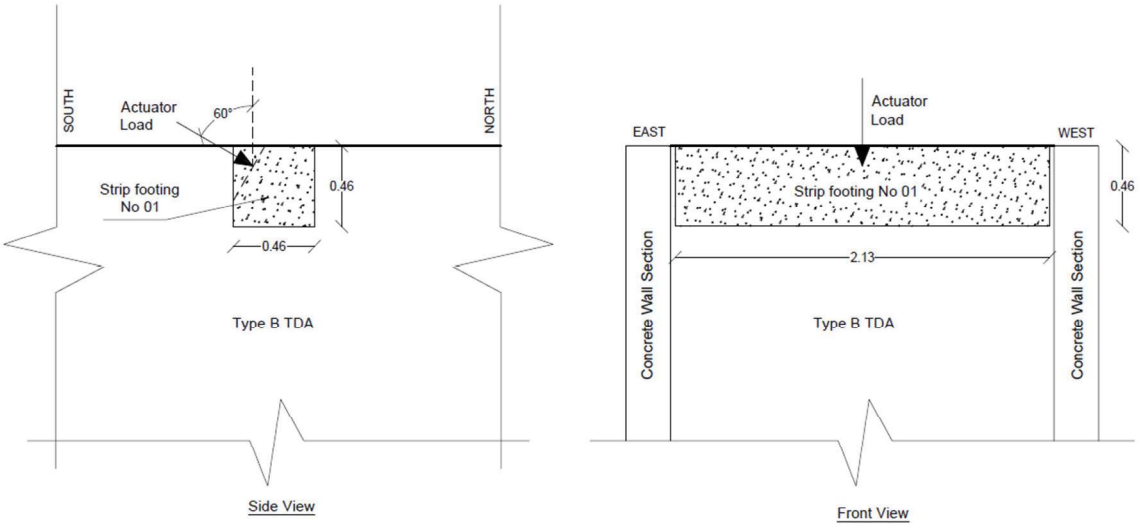

(a)

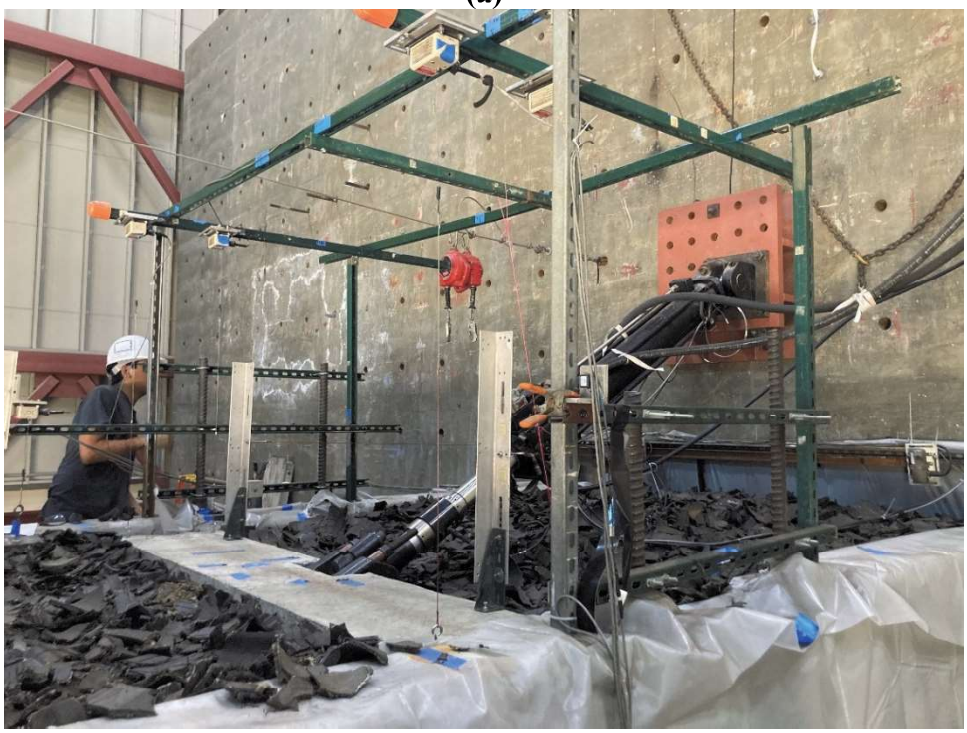

(b)

Figure 5.12 Specimen QT-08 configuration: (a) Conceptual drawing, and (b) Picture.

5.3 Experimental procedures

The focus of the testing protocol is to apply a quasi-static inclined or vertical loading on top of the footing enough to reach bearing strength failure. The load is applied following load-control and displacement-control approaches using 1 or 2 hydraulic actuators of 220 kN capacity and max stroke of 0.45 m each. The load and unloading rates were slow enough to avoid inertial effects. The testing protocol details of each specimen are shown in Table 5.2.

Table 5.2 Summary of experimental protocol

Specimen	Testing control type	Load Inclination with the vertical [°]	Number of actuators	N-S rocking restrained	Loading rate	Unloading rate
QT-01	Load-control	0	1	No	8.89 kN/min	8.89 kN/min
QT-02	Displacement-control	0	2	Yes	12.7 mm/min	12.7 mm/min
QT-03	Load-control	0	2	No	8.89 kN/min	17.79 kN/min
QT-04	Load-control	0	2	No	8.89 kN/min	17.79 kN/min
QT-05	Displacement-control	0	1	No	12.7 mm/min	12.7 mm/min
QT-06	Displacement-control	0	1	No	12.7 mm/min	12.7 mm/min
QT-07	Displacement-control	30	1	No	12.7 mm/min	12.7 mm/min
QT-08	Displacement-control	60	1	No	12.7 mm/min	12.7 mm/min

Specimen QT-01 followed a load-control approach and used only one actuator to enable the footing to experience rocking or sliding along the TDA surface. It was observed that only one actuator did not generate enough load to produce a clear failure. Accordingly, specimen QT-02 followed a displacement-control approach and used two actuators. This configuration was used to apply greater loads to the footing, and the switch to displacement-control was proposed to capture any induced softening behavior. However, an unintended limitation of this approach was that it restricted the rocking of the foundation. Accordingly, Specimens QT-03 and QT-04 followed a load-control approach and used 2 actuators to reach larger loads and not restrict rocking or sliding of the footing. Because of the specific footing configurations where the lower bearing capacity was expected, QT-04 and QT-05, QT-06, and QT-07 only one actuator was used, and followed a displacement-control approach to capture any possible softening behavior.

5.4 Experimental results

This section presents the results from quasi-static testing of specimens No QT-01 to QT-08. The results consist of bearing pressure-normalized settlement curves for each specimen at each key location of the footing to reflect any tilting, along with the average settlement. The bearing pressure is obtained by dividing the single or double actuator load over the area of the bottom face

of the footings. The normalized settlement is computed by dividing the settlement over the width of the footing. Monitored locations of strip footings No 01 and 02 are the north and south edges of the top of the footing, and monitored locations of cylindrical footings No 01 and 02 are the north, east, south, and west edges of the top of the footing. The load-settlement curves for these tests are shown in Figures 5.13 to 5.20, and the key results are listed in Table 5.3. These include the ultimate bearing capacity at the point of tilting (if any), the bearing stress at a settlement-failure criterion of 10% of the footing width (also noted as a square in Figs. 5.13 to 5.20).

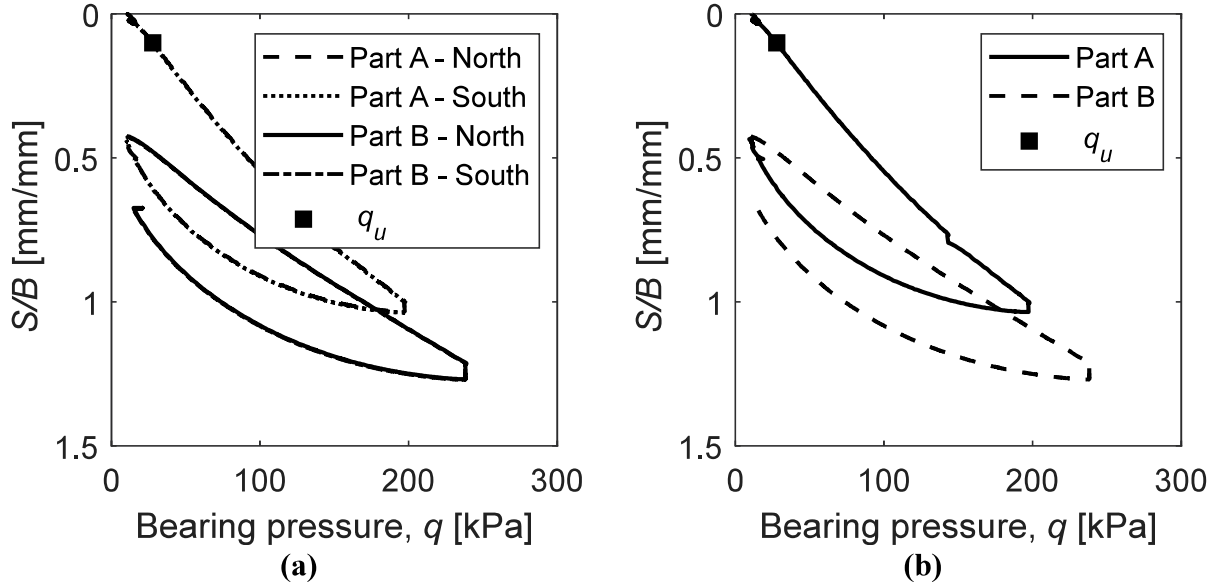

(a) **(b)**

Figure 5.13 Settlement-stress response during QT-01: (a) Per footing location, and (b) Footing average.

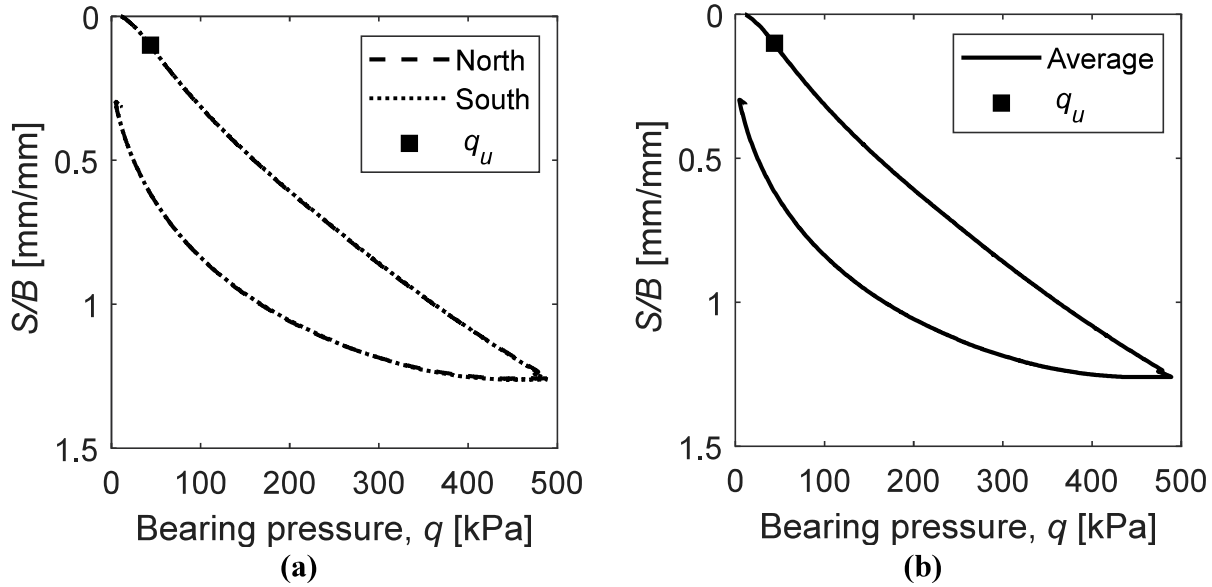

(a) **(b)**

Figure 5.14 Settlement-stress response during QT-02: (a) Per footing location, and (b) Footing average.

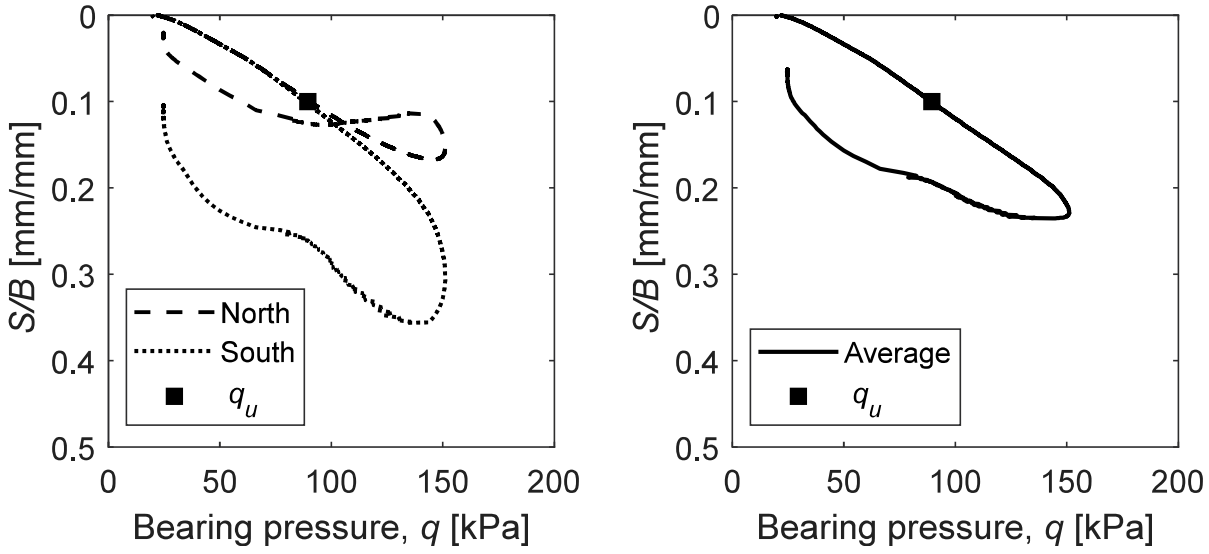

(a) **(b)**

Figure 5.15 Settlement-stress response during QT-03: (a) Per footing location, and (b) Footing average.

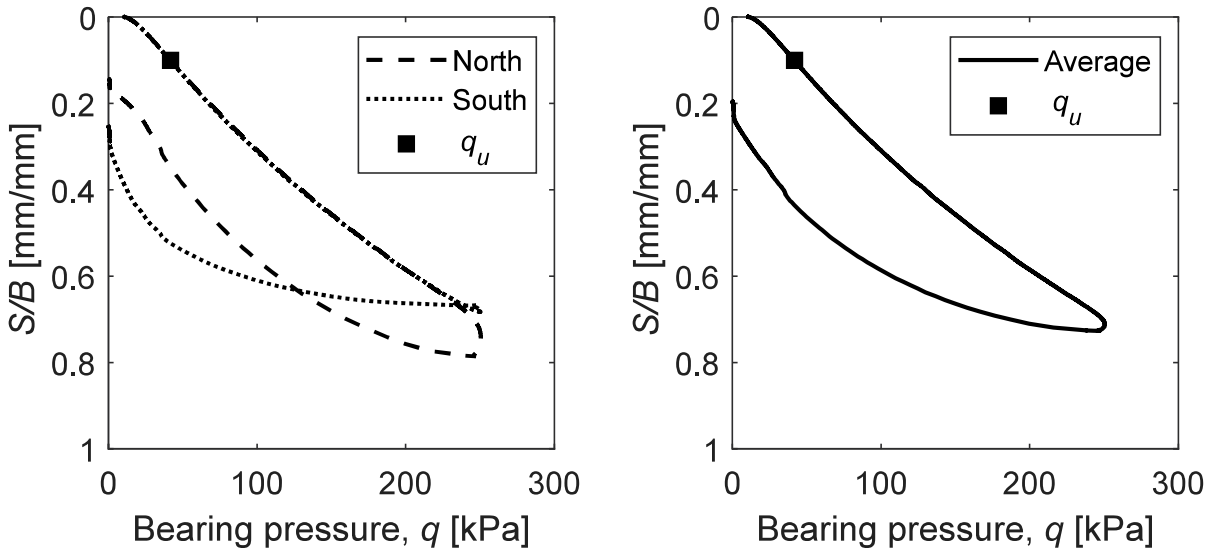

(a) **(b)**

Figure 5.16 Settlement-stress response during QT-04: (a) Per footing location, and (b) Footing average.

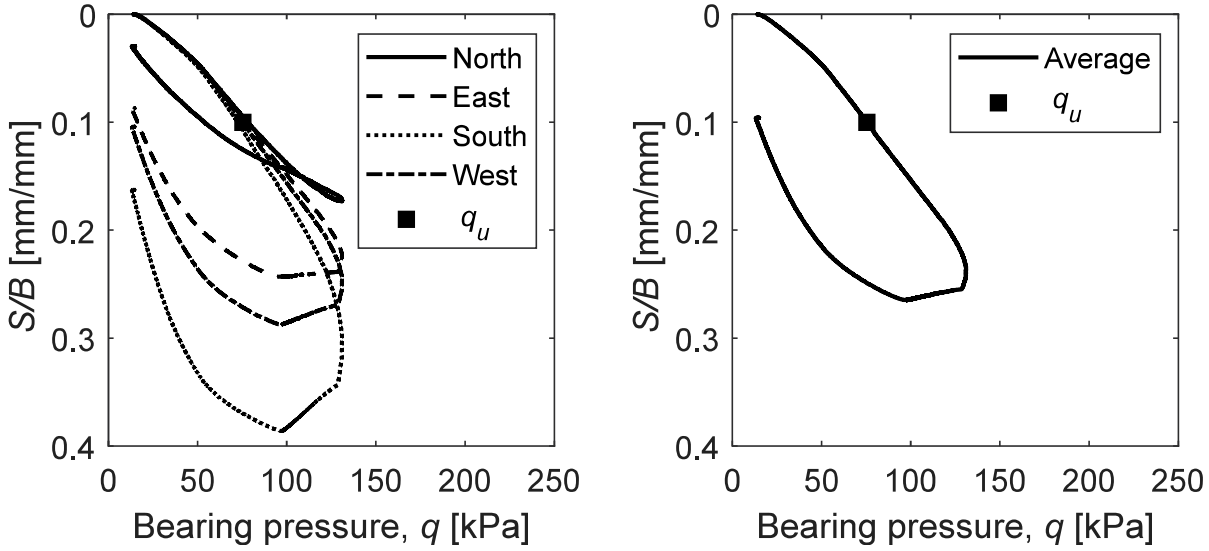

(a) **(b)**

Figure 5.17 Settlement-stress response during QT05: (a) Per footing location, and (b) Footing average.

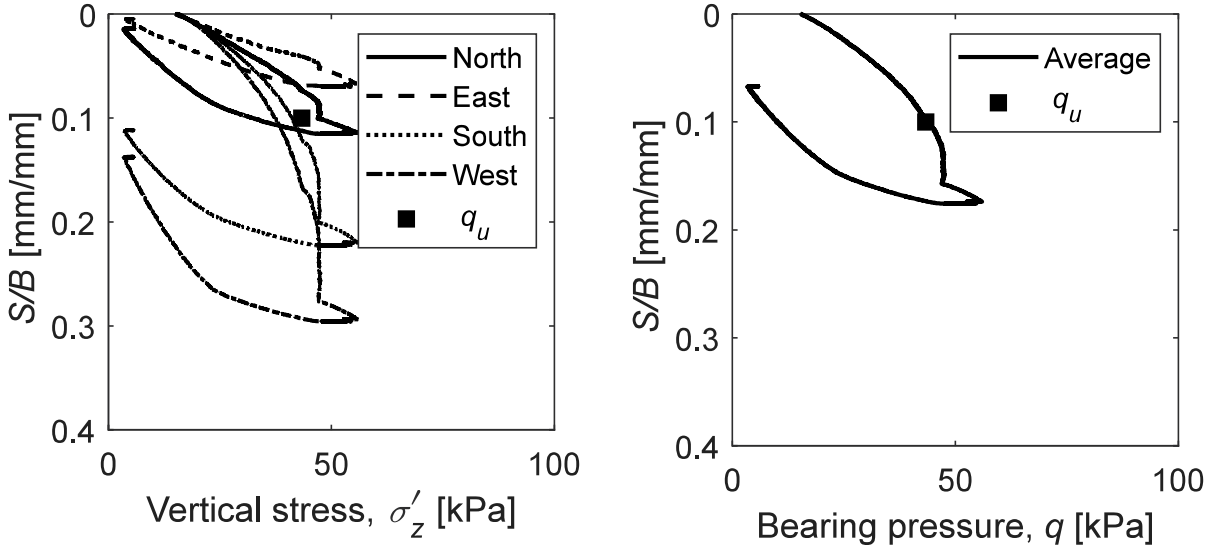

(a) **(b)**

Figure 5.18 Settlement-stress response during QT06: (a) Per footing location, and (b) Footing average.

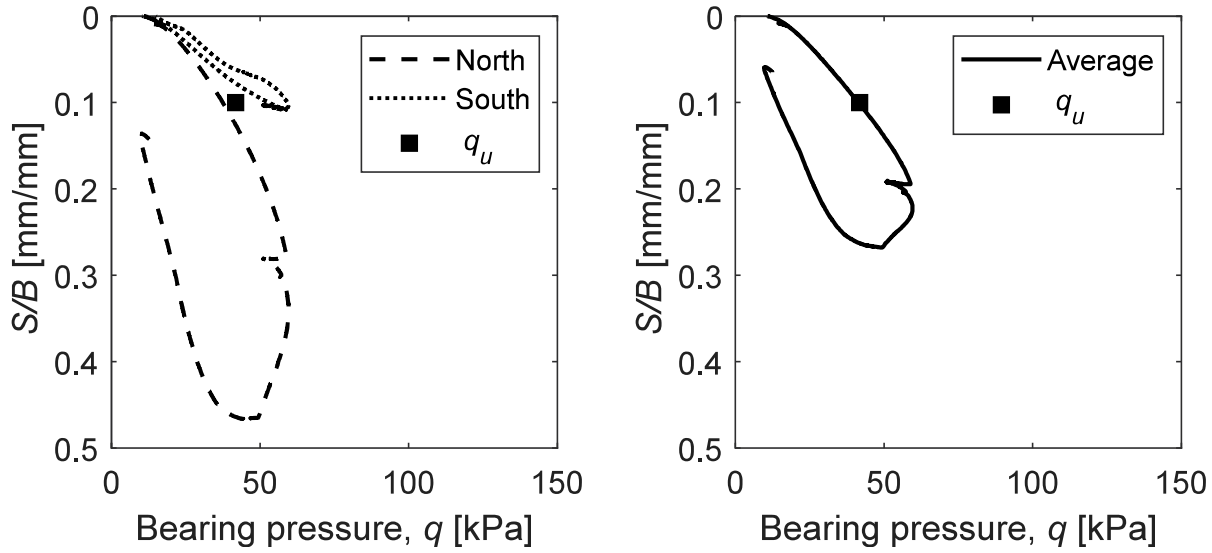

(a) **(b)**

Figure 5.19 Settlement-stress response during QT07: (a) Per footing location, and (b) Footing average.

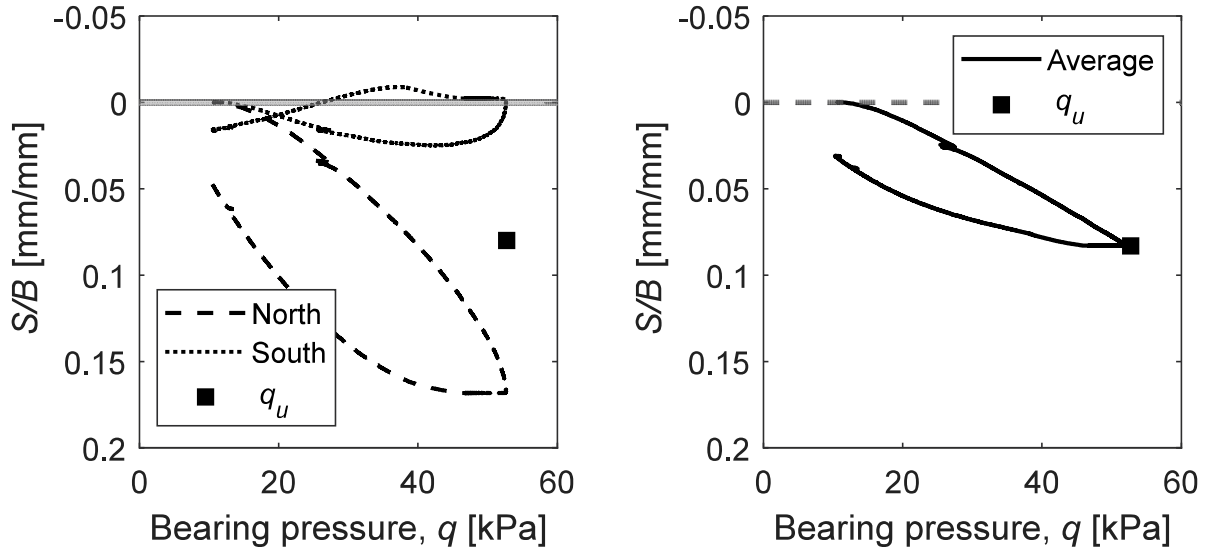

(a) **(b)**

Figure 5.20 Settlement-stress response during QT08: (a) Per footing location, and (b) Footing average.

Table 5.3 Summary of quasi-static test results on footings in Type B TDA

Specimen	Average TDA layer unit weight [kN/m^3]	Estimated TDA layer friction angle, ϕ [°]	Reason to stop loading	Failure mode	Bulging of adjacent TDA	Ultimate bearing pressure, q_{ult} [kPa]	Bearing pressure at settlement criterion, $q_{S=0.1B}$ [kPa]	Predicted ultimate bearing pressure, $q_{u,pred}$ [kPa]
QT-01	6.25	38.0	Max. load of actuator	Punching shear	No	N/A	28	74
QT-02	6.77	39.0	Max. load of actuators	Punching shear	No	N/A	44	320
QT-03	7.10	35.0	Rocking of footing	Punching shear	No	153	90	398
QT-04	7.40	35.0	Rocking of footing	Punching shear	No	238	42	195
QT-05	7.85	33.0	Rocking of footing	Punching shear	No	130	75	133
QT-06	8.02	31.0	Rocking of footing	Punching shear	No	64	48	100
QT-07	8.10	30.0	Rocking of footing	Punching shear	No	48	24	38
QT-08	8.18	30.0	Rocking of footing	Punching shear	No	27	18	35

Assessment of the individual load-settlement curves indicates that Type B TDA shows a punching shear failure mode when induced to bearing pressure of shallow foundations. This behavior is consistent with the findings of Vesic (1973) which state that high-compressible soils typically experience punching shear failure rather than general shear failure or local shear failure. An issue is that punching shear failure is characterized by an unclear and hard-to-establish point of failure. Multiple methods exist to determine that point of punching shear failure for conventional soils such as: (1) the ultimate load as the point at which the slope of the load-settlement curve is zero or steady low value (Vesic 1963), (2) the ultimate load as the breakpoint of the load-settlement curve in log scale for both axes, and (3) the ultimate load as the point at which the strain is twice

the strain for a 10% variation of the attained load (Hansen 1970). These methods are designed for load-settlement curves that show a strain-softening trend when the load is increased beyond a peak value which is typical of dense granular soils or overconsolidated clays. The footings in Type B TDA results show a continuously strain-hardening load-settlement curve which complicates the identification of a clear point of bearing capacity failure.

An alternative solution exists and comes from a practical point of view. This approach considers excessive settlement as foundation failure which is clearly justified by the philosophy of foundation design (Vesic 1973). This method is also consistent with the simplified design procedure proposed by Maghoub and El Naggar (2022) for Type A TDA which depends on an initially proposed settlement limit. The key challenge is then to establish the magnitude of settlement needed to mobilize the ultimate load of the footing. Skempton (1951) observed that that required settlement ranges between 3 to 7% of the footing width for surface footings, and up to 15% for deep footings built on saturated clay. De Beer (1958), De Beer (1958), Meyerhof (1948), Muhs and Kahl (1961), and Vesic (1963) observed that that required settlement ranges between 5 to 15% of the footing width for surface footings, and up to 25% for deep footings built on sand. Moreover, a failure criterion of 10% of the footing depth is widely used for piles (Vesic 1973). Most specimens tested in this study consider footings that have zero depth or the magnitude of the depth as the same as the width. Consequently, the bearing stress at a settlement equal to 10% of the footing width is proposed as an alternate bearing stress to use in design, and these values are summarized in Table 5.3.

The ultimate bearing capacity values at the point of tilting and the bearing stress at a settlement equal to 10% of the footing width were compared in Table 5.3 with those predicted from the generalized bearing capacity equation of Brinch Hansen (Hansen 1970) using the estimated friction angles and unit weights for each layer of TDA summarized in Table 5.3. Brinch Hansen's generalized bearing capacity equation for a drained frictional material like TDA is given as follows:

$$q_{ult,pred} = c'N_c s_c d_c i_c e_c + \sigma_{zD}{}'N_q s_q d_q i_q e_q + \frac{1}{2}\gamma' B N_\gamma s_\gamma d_\gamma i_\gamma e_\gamma \qquad \textbf{Eq. 5.1}$$

where c' is the drained cohesion of the TDA (equal to zero), σ_{zD}' is the surcharge stress above the base of the footing, γ' is the unit weight of the TDA, and B is the footing width. The bearing capacity factors can be determined as follows:

$$N_c = \frac{(N_q - 1)}{\tan\phi'}$$

$$N_q = e^{\pi\tan\phi'}\tan^2\left(45 + \frac{\phi'}{2}\right) \qquad \textbf{Eq. 5.2}$$

$$N_\gamma = 1.5(N_q - 1)\tan\phi'$$

where ϕ' is the secant friction angle of the TDA for the mean effective stress under the footing. The shape factors are determined as follows:

$$s_c = 1 + (B/L)(N_q/N_c)$$

$$s_q = 1 + (B/L)\tan\phi' \qquad \textbf{Eq. 5.3}$$

$$s_\gamma = 1 - 0.4(B/L)$$

where L is the length of the footing. The depth factors are determined as follows:

$$d_c = (d_q s_q N_q - 1)/[(N_q - 1)s_c]$$

$$d_q = 1 + 0.1(D_f/B) \qquad \textbf{Eq. 5.4}$$

$$d_\gamma = 1$$

where D_f is the embedment depth. The inclination factors are determined as follows:

$$i_c = (1 - \lambda/90)^2$$

$$i_q = (1 - \lambda/90)^2 \qquad \textbf{Eq. 5.5}$$

$$i_\gamma = (1 - \lambda/\phi')^2$$

where λ is the inclination of the applied load. Finally, the eccentricity factors are determined as follows:

$$e_c = 1 - 2(e/B)$$

$$e_q = 1 - 2(e/B) \qquad \textbf{Eq. 5.6}$$

$$e_\gamma = 1 - 3.5(e/B) + 3(e/B)^2$$

The predictions from the bearing capacity equation are summarized in Table 5.3, and a comparison between the measured and predicted ultimate bearing capacity values is shown in Figure 5.21. Except for the footing with a larger width in Specimen QT-03, the predictions from the Brinch Hansen bearing capacity equation were consistent with the ultimate bearing capacity at the point of tilting. The footing in Specimen QT-03 may have failed prematurely due to a nonuniform distribution in TDA density below the footing, but the bearing stiffness from this test was greater than in all of the other tests indicating that it is indeed trending toward a higher

capacity. The predicted bearing capacity values were very sensitive to the estimated friction angle and unit weight, which emphasizes the importance of having good estimates of these values when predicting the bearing capacity of TDA in the field. The results in Figure 5.21 indicate that use of conventional bearing capacity equations developed for soils with an equivalent friction angle to TDA can be used to estimate the bearing capacity of footings in TDA. However, the stress-settlement curves in Figures 5.13 to 5.20 indicate that the ultimate bearing capacity at the point of tilting may occur at settlements ranging from 20% to 70% of the footing width, which is much greater than that expected for footings in stiff soils (Skempton 1951). Engineers may prefer to use the bearing stress at a settlement failure criterion of 10% of the footing width instead. Accordingly, a correction equation is proposed in Figure 5.21 that can be used to correlate the ultimate bearing capacity from Eq. 5.1 (after considering the different geometric variables for the particular footing) with the bearing stress of the footing in TDA at a settlement failure criterion of S=0.1B.

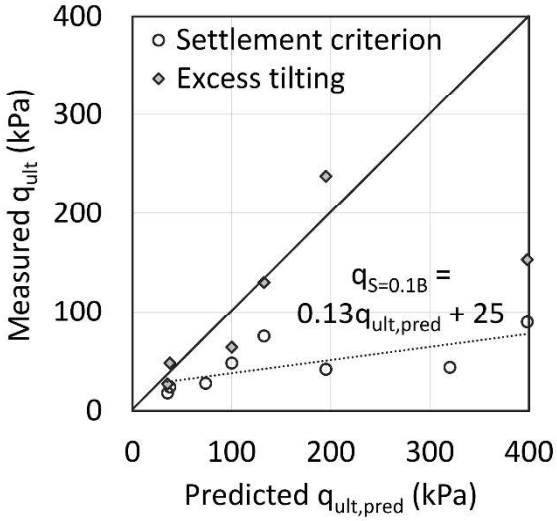

Figure 5.21 Measured vs. predicted ultimate bearing capacity for the different footings.

To better understand the roles of variables like the footing width, embedment depth, footing shape, and load inclinations, comparisons can be made between the different load settlement curves. The curves in Figure 5.22 show comparisons of the load settlement curves for strip footings in TDA having different embedment depths D and footing widths B. The points of failure according to the settlement failure criterion are also shown on each load-settlement curve for reference. The stiffest load-settlement response was noted for the footing with the largest value of B. Two tests were performed on footings with the same embedment depth of 0.46 but with load

control and displacement control conditions. The test performed in load control conditions in test QT4 reached failure due to tilting at a bearing stress of approximately 250 kPa, while the test performed in displacement control continued to a large bearing stress of nearly 500 kPa as tilting was prohibited. Despite these differences, the stiffnesses of the load settlement curves in these repeat tests were very similar. The test with no embedment (QT1) showed the lowest stiffness for the load displacement curve. The foundation in this test was loaded for a second cycle, and a similar stiffness was observed when loading beyond the maximum value. The footing in test QT1 exhibited some creep displacement when the load was held at the largest stresses on the first and second cycles. Overall, when comparing the stiffnesses of the load-settlement curves, the roles of embedment and footing width expected from the bearing capacity formula in Eq. 5.1 are observed.

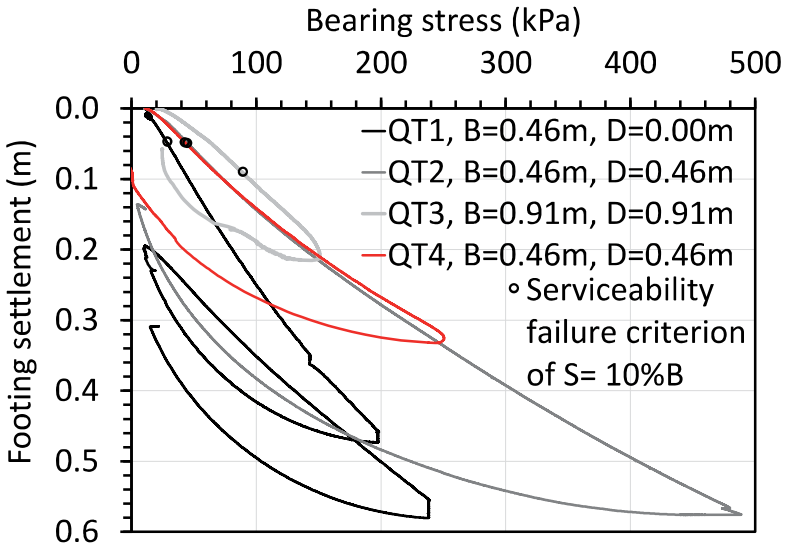

Figure 5.22 Impact of embedment and footing width on the stress-settlement curves of strip footings in Type B TDA.

The impact of footing shape on the load-settlement curve is shown in Figure 5.23. The strip footing with embedment has the softest load settlement curve of the three tests. The cast-in-place footing with a greater diameter has a greater stiffness than the cast-in-place footing with a smaller diameter, as expected. A clear bearing capacity failure was noted for the two circular foundations, which represents the behavior of a footing for a signpost or guardrail embedded in Type B TDA.

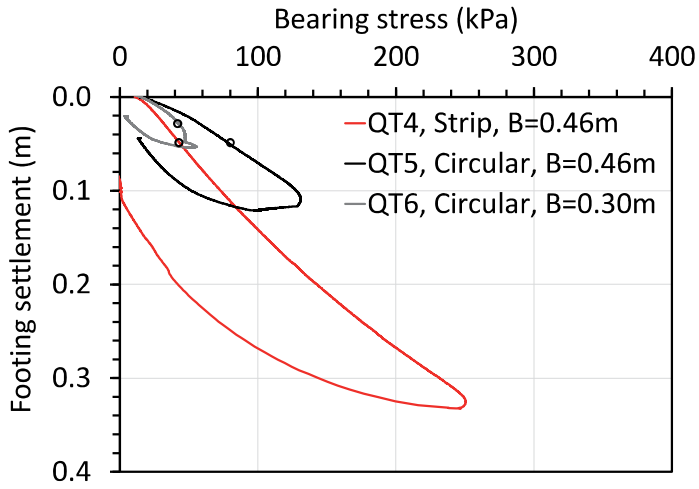

Figure 5.23 Impact of footing shape on the stress-settlement of footings in Type B TDA.

The impact of loading inclination is shown in Figure 5.24. In both tests on a footing with an inclined load, tilting of the footing was observed at a relatively low bearing stress, which was assumed to correspond to failure. An interesting observation is that the stiffness of the load-settlement curve of the strip footing with a load inclination of 30 degrees was very similar to the load-settlement curve of the strip footing with a vertical load inclination. However, the stiffness of the load-settlement curve of the strip footing with a greater load inclination of 60 degrees was greater than the two other tests. This may be because a greater zone of TDA was mobilized during compression, or that the shear strength on horizontally-oriented TDA particles was mobilized instead of primarily compression of the void space like in the vertically-loaded strip footing.

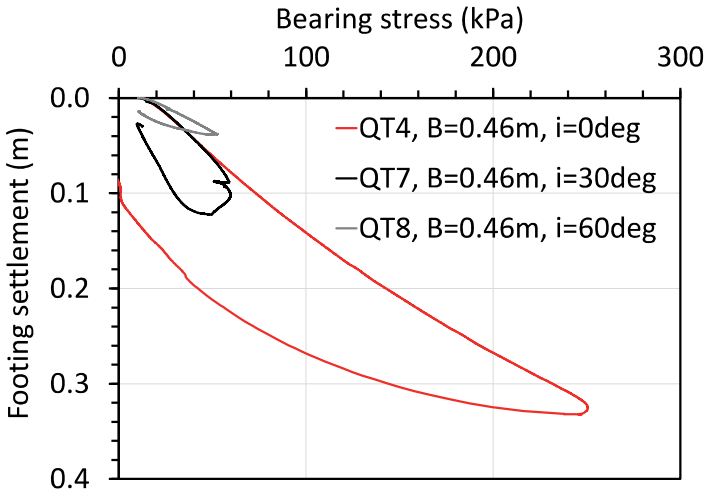

Figure 5.24 Impact of load inclination angle on the stress-settlement curve of strip footings in Type B TDA.

Additional insights can be gained by inspecting the deformation of the surface of the TDA during loading and the internal deformations of the TDA obtained using settlement plates. Test QT4 was used as a baseline test to show the typical surface deformations of the TDA during vertical foundation loading. To make these comparisons, time series of the loading and surface deformations are shown in Figure 5.25(a) and 5.25(b), respectively. Then, profiles of surface settlement at different moments in time during loading and unloading of the footing are shown in Figures 5.26(a) and 5.26(b), respectively. Loading of the footing causes a dragdown of the TDA surface during loading, and that unloading leads to permanent deformations of the TDA surface.

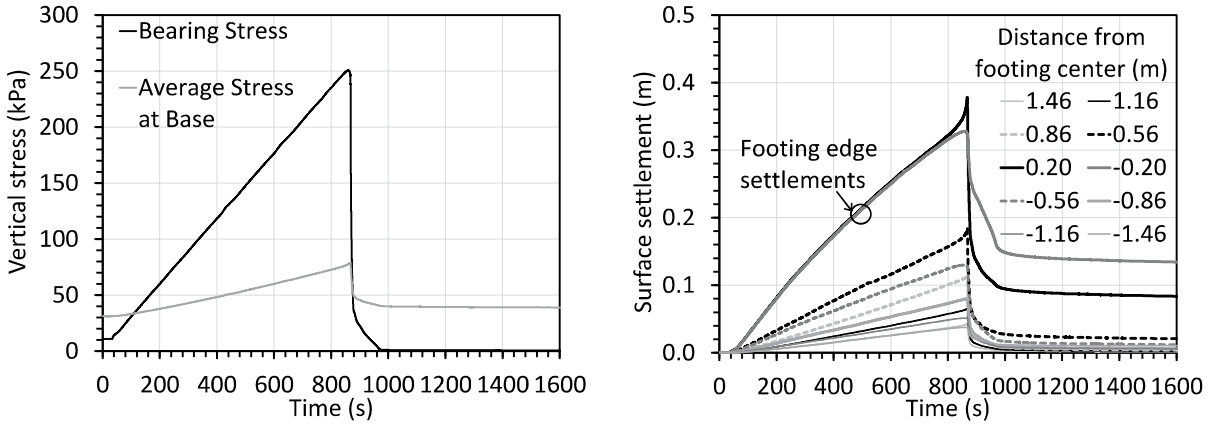

(a) (b)

Figure 5.25 Time series from test QT4: (a) Foundation loading versus time along with earth pressure cell measurements at the base of the TDA layer; (b) Surface settlements at different locations from the footing center

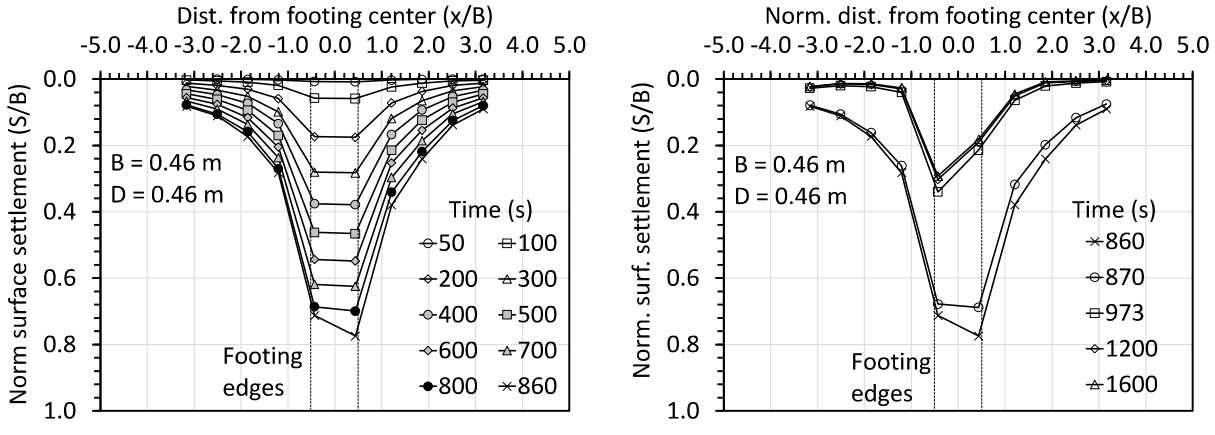

(a) (b)

Figure 5.26 Surface deformations as a function of distance from the center of the footing in test QT4 (footing width of B=0.46m): (a) Loading; (b) Unloading.

Time series of the settlement plate measurements under the footing at different depths are shown in Figure 5.27(a) and at a depth of 0.46 m from the surface at different horizontal distances from the center of the footing are shown in Figure 5.27(b). The vertical settlement profiles as a function of depth at different times during loading are shown in Figure 5.28(a) and at different times during unloading are shown in Figure 5.28(b). Settlements are observed at a depth more than 4 times the width of the footing (B=0.46m) during loading, and that permanent settlements are observed to this depth during unloading. The subsurface settlements at a depth of 0.46 m from the TDA surface at different distances from the center of the footing in Figure 5.29(a) mirror the trends in the surface settlements at different distances from the center of the footing shown in Figure 5.26. However, there seems to be an inversion in the trend after 700 s of loading where some of the locations further from the footing start to heave upward. This may reflect the plastic flow of TDA upward and away from the footing, even though this is not exhibited on the TDA surface. During unloading a heave is noted in the TDA at this depth. Overall, the trends in the settlement response of the TDA layer are consistent with those expected for a punching bearing capacity, albeit with large displacement magnitudes due to the lower stiffness of the TDA.

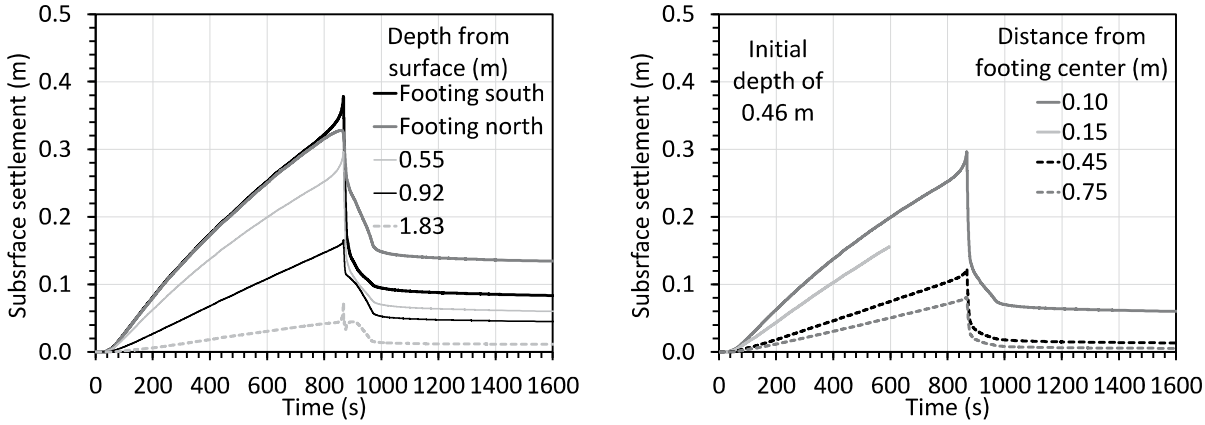

Figure 5.27 Time series from test QT4: (a) Subsurface settlements below the footing; (b) Subsurface settlements at a depth of 0.46 m below the TDA surface but at different distances from the center of the footing

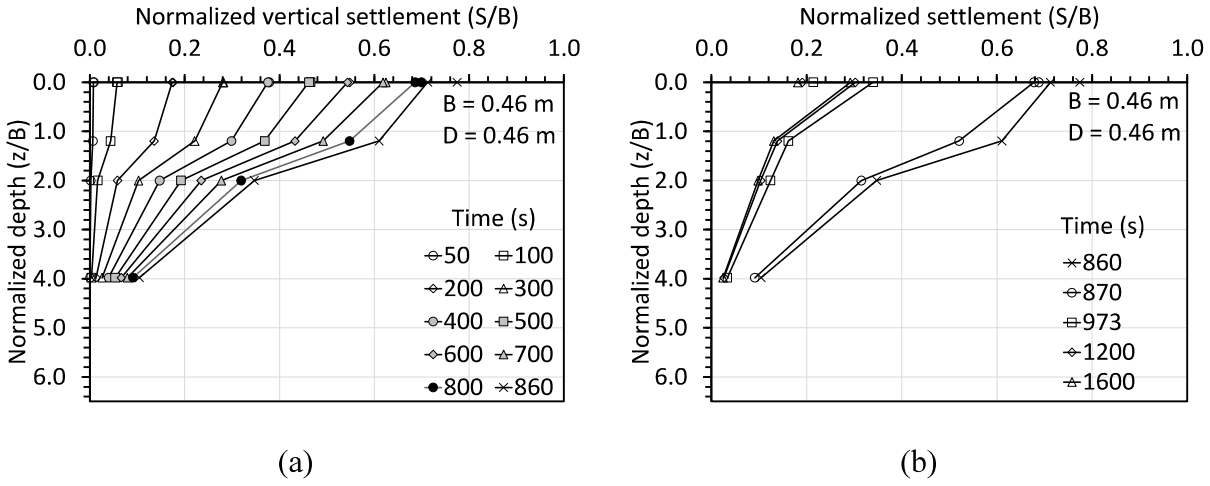

(a) (b)

Figure 5.28 Subsurface deformations as a function of depth from the TDA surface in test QT4 (footing width of B=0.46m): (a) Loading; (b) Unloading.

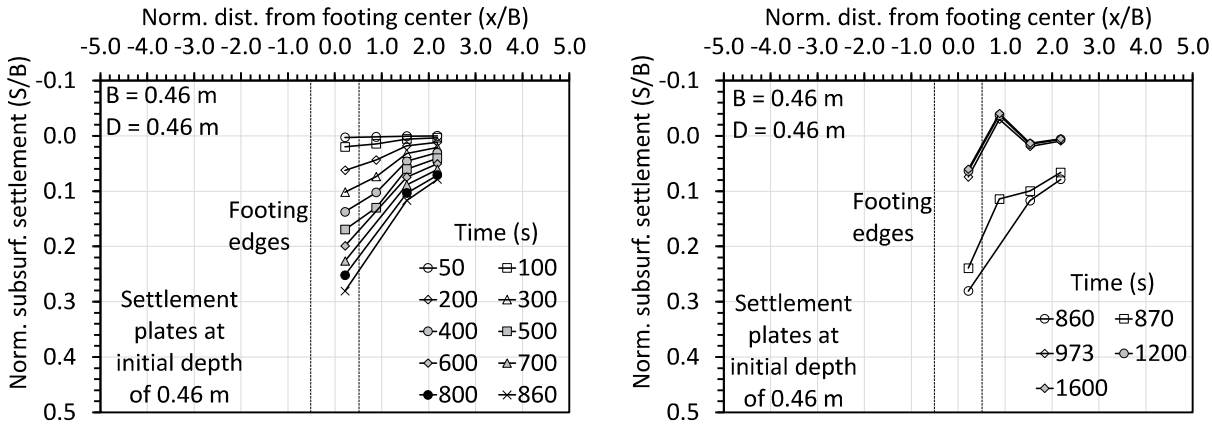

(a) (b)

Figure 5.29 Subsurface deformations as a function of distance from the center of the footing in test QT4 (footing width of B=0.46m): (a) Loading; (b) Unloading.

5.5 Closing Remarks on Quasi-Static Bearing Capacity Testing Program

This study presented an evaluation of the bearing capacity of shallow footings in TDA to both provide a better insight into the roles of different variables like footing width, embedment depth, footing shape, and loading inclination, and to evaluate the role of predictions from bearing capacity equations using shear strength parameters from direct shear tests on TDA. The trends in the bearing stress-settlement curves with the footing width, embedment depth, footing shape, and loading inclination were consistent with expectations from past studies on footings in soils. Further, the ultimate bearing capacity was well predicted using a generalized bearing capacity equation with the average secant friction angle for the TDA layer beneath the footing. However,

the footing settlements at bearing capacity were much larger than expected for footings in soils. A correlation was developed to provide practitioners guidance on the expected bearing stresses that could be mobilized at a serviceability limit state corresponding to normalized settlements of 10% of the footing width. The TDA layer was also observed to deform slightly differently from granular soils around footings, with a drag-down effect in the TDA near the footing edges. The TDA was also observed to absorb large surficial settlements across its depth, confirming its suitability for use as a bridging material for pipelines or utilities.

6. DYNAMIC TESTING PROGRAM

6.1 Testing program scope

A total of three dynamic tests were performed using the uniaxial shake table in the University of California San Diego (UCSD) South Powell Laboratory. The specimens were tested in numerical order starting from DT-01 and finishing in DT-03. During this process, the TDA was not fully removed and replaced again after each test because that approach would take significant labor and time due to the size of the specimens. The average TDA unit weight was controlled by measuring the top surface level of TDA after each test, weighing each amount of TDA added, and using consistent compaction methods. The general test specimen consists of a strip or cylindrical footing non-, partially, or fully embedded into Type B TDA, as substructure, which is attached to a Single-Degree-Of-Freedom (SDOF) lumped mass system as superstructure. The main variations among specimens consisted in the thickness of the Type B TDA layer and the A/Ac value, as summarized in Table 6.1.

Table 6.1 Summary of dynamic testing specimen's configuration

Specimen	Thickness of TDA layer [m]	Average γ_{TDA} [kN/m]	*A/Ac*	Footing Width, *B* [m]	Footing Length, *L* [m]	Footing Embedment, *D* [m]
DT-01	0.69	5.85	> 100	0.46	41.60	0.46
DT-02	0.93	6.29	27.0	0.46	41.60	0.46
DT-03	1.43	5.79	19.0	0.46	41.60	0.46

6.2 Experimental setup

6.2.1 Shake table description.

As mentioned, this study uses the uniaxial shake table in the University of California San Diego (UCSD) South Powell Laboratory to apply earthquake motions to Type B TDA-structure

specimens. The table consists of a 16 mm-thick (5/8 in-thick) steel plate having a length of 4.88 m (16.1 ft) in the direction of shaking and a width of 3.05 m (10.2 ft), as shown in Figure 6.1.

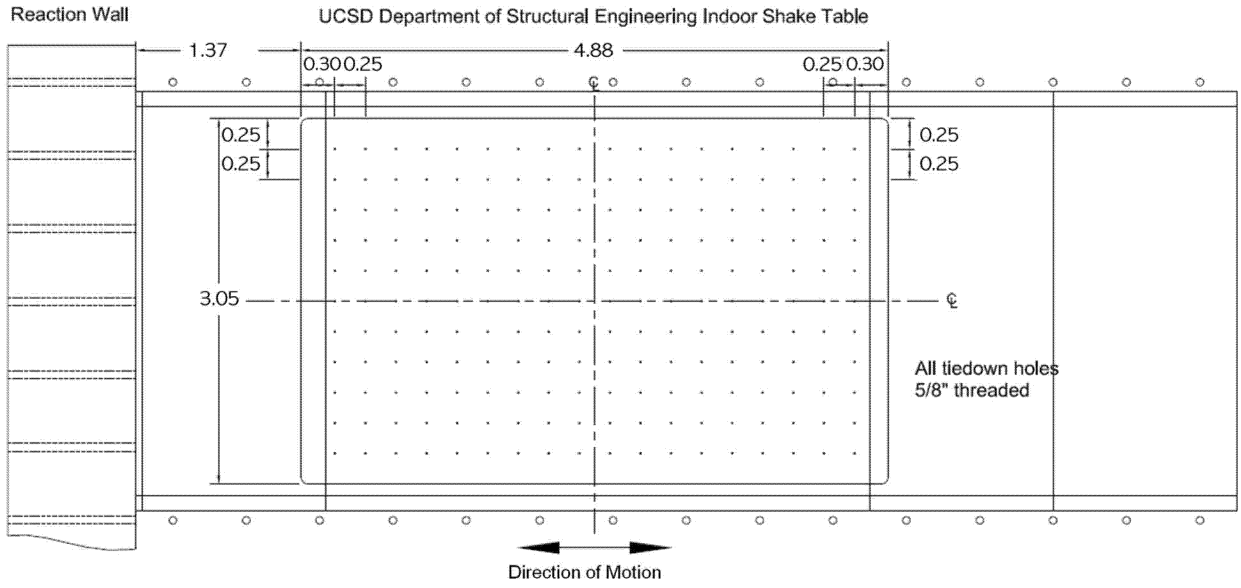

Figure 6.1 Plan view of the UCSD Powell Laboratory shake table.

The shake table has a design rated payload capacity of 350 kM (79 kips) and a moment capacity of 420 kN-m (310 kips-ft). The table rests on lead jacket bearings supported by two stationary steel shafts and is driven by a fatigue-rated double 05 mm), with a static capacity of 490 kN (110 kips) and a dynamic capacity of 405 kN (91 kips). The actuator can induce peak horizontal accelerations over 9 g on the acting hydraulic actuator, as shown in Figure 6.2. The actuator has a total dynamic stroke of 11 in (bare table) and can reach 1 g under the maximum payload (Trautner et al. 2017). The shake table uses a digital controller which can control and measure (for feedback) the table displacement, velocity, and acceleration, which are accentuated in low-frequency, middle-frequency, and high-frequency domains to improve system performance (Trautner et al. 2017). Greater payloads than the capacity have been tested on the table (e.g., Zheng et al. 2018, 1999; Zayed et al. 2020; Yarahuaman and McCartney 2022), but this may lead to a reduction in table performance.

Figure 6.2 Photo of the bottom of the UCSD Powell Laboratory shake table from Trautner et al. (2017).

6.2.2 Laminar shear box description

The UCSD Powell Laboratory is equipped with a large laminar shear box with internal dimensions of 3.90 × 1.75 × 2.90 m (12 ft - 9.5 inch × 5 ft - 9 inch × 9 ft - 6.25 inch) [length × width × height] as shown in Figure 6.3. The laminar shear box is composed of 44 laminar frames, each one 64-mm height. The lowest frame is fixed to the bottom of the laminar box hence its motion is restricted. The rest of the frames are supported by rollers and are allowed to move up to 0.30 m (1 ft) in the north-south direction only. The laminar frames are supported by collar W-section beams at the top and bottom, as well as by six W-section columns on the longest sides.

Figure 6.3 Laminar shear box on top of the shake table in the UCSD Powell Laboratory.

6.2.3 Specimen configuration

The general test specimen consists of a strip footing fully embedded into Type B TDA, as substructure, which is attached to an SDOF superstructure placed inside the laminar shear box as shown in Figure 6.4. This study considers three specimens with a 0.45 m-thick concrete strip footing fully embedded in TDA layers of different initial thicknesses and unit weights. Additionally, the SDOF structure presents different masses to reach different A/Ac values. The rest of the parameters, such as the length and width of the TDA layer, and the dimensions and the embedment of the footing, remain constant. The specific specimens' parameters are listed in Table 6.2. A friction angle of 33° was considered for all specimens, which is reasonable for the vertical stress ranges beneath the footings in these tests.

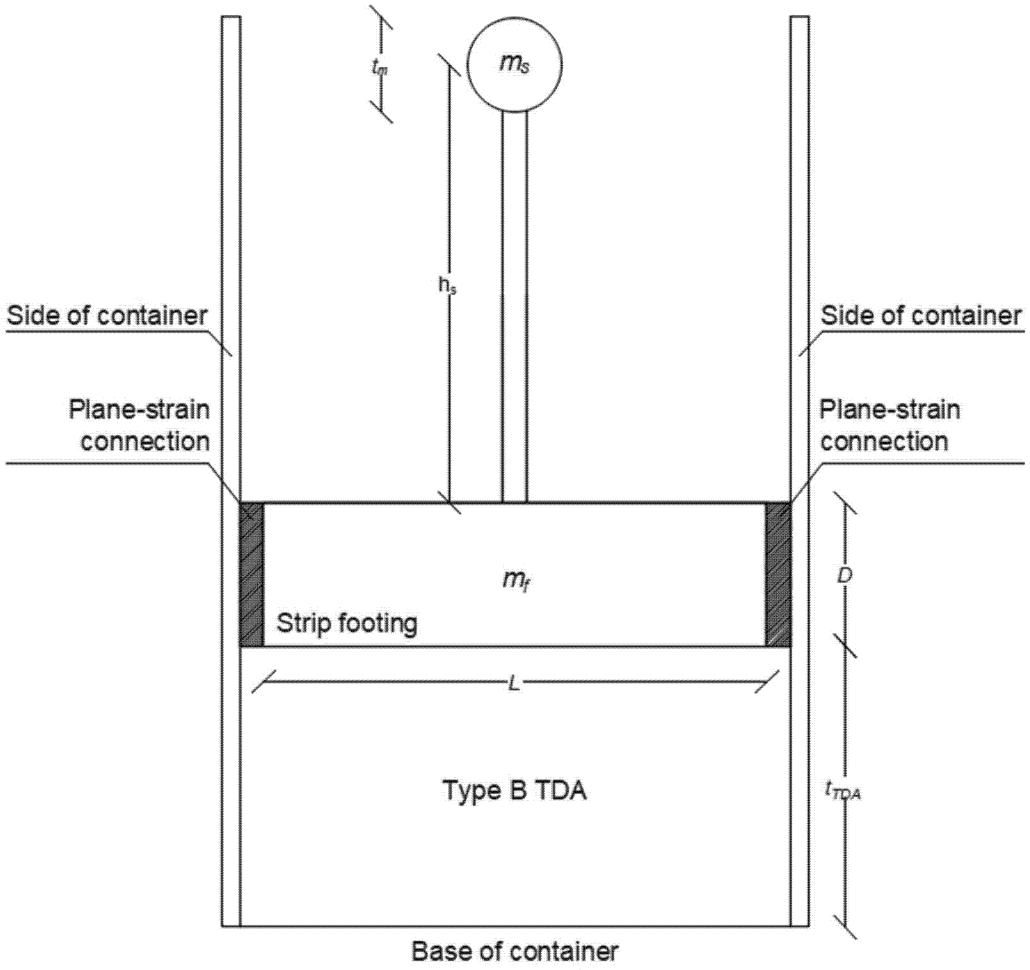

Figure 6.4 General conceptual configuration of specimens.

Table 6.2 Specific dynamic specimen parameters

Specimen	t_{TDA} [m]	γ_{TDA} [kN/m^3]	A/Ac	B [m]	L [m]	D [m]	m_f [kg]	m_s [kg]	t_m [m]	h_s [m]	k_s [kN/m]
DT-01	0.69	5.85	> 100	0.46	1.60	0.46	802.78	114.00	0.29	1.48	187.25
DT-02	0.93	6.29	27.0	0.46	1.60	0.46	802.78	456.00	0.31	1.51	187.25
DT-03	1.43	5.79	19.0	0.46	1.60	0.46	802.78	456.00	0.31	1.51	187.25

The superstructure consists of an SDOF system composed of a lumped mass, m_f, attached to an HSS 3 x 3 x 3/16-inch column element. The HSS section is fully fixed to the strip footing to provide a shear and moment connection. The reasoning behind this configuration is two reasons. First, this study is focused on the effect of the TDA on the foundation and superstructure, therefore, an SDOF system is selected because it is one of the simplest structures to evaluate. Second, the height and mass of the structure of the SDOF system were strategically designed to generate a large natural period for the flexible base system (a system that considers the flexibility of the soil), which could demonstrate that TDA could work as a geotechnical seismic isolation approach. The description and discussion of the flexible base system can be found in the next paragraph.

Within the soil-structure interaction field, a rigid base represents a soil that has infinite stiffness and does not deform. A rigid foundation represents a foundation element with infinite stiffness and no deformation (NIST 2012). Therefore, a fixed base system represents the combination of a rigid foundation resting or embedded on a rigid base. On the other hand, NIST (2012) states that a flexible base system considers the deformability or compliance of both the foundation elements and the soil. This study considers the evaluation of both cases, the fixed base and the flexible base systems, considering the Type B TDA instead of the soil. The characteristics of the flexible base system are determined by performing a TDA-structure interaction study following NIST (2015) guidelines for soil-structure interaction.

The fixed base system depends only on the strength of the vertical element and the mass applied to the top. The stiffness of the vertical element k is 225 kN/m (15,439 lb/ft). Thus, the natural period of the fixed base system T is computed using Eq. 6.1:

$$T = 2\pi\sqrt{\frac{m}{k}} \qquad \textbf{Eq. 6. 1}$$

The TDA-structure interaction analysis considers the solutions of Pais and Kausel (1988) as impedance function solutions because they are the most used approach in practice (NIST 2012). The approach of Pais and Kausel (1988) considers a rigid rectangular foundation resting embedded

on a half-space with a given shear wave velocity. Pais and Kausel (1988) solutions use the shear modulus G because it is closely related to the shear wave velocity V_s and material unit weight γ as shown in Equation 6.2. The Type B TDA shear modulus at 1% shear strain is obtained from McCartney et al. (2017), as shown in Figure 6.5.

$$V_s = \sqrt{\frac{G}{\gamma/g}} \qquad \textbf{Eq. 6. 2}$$

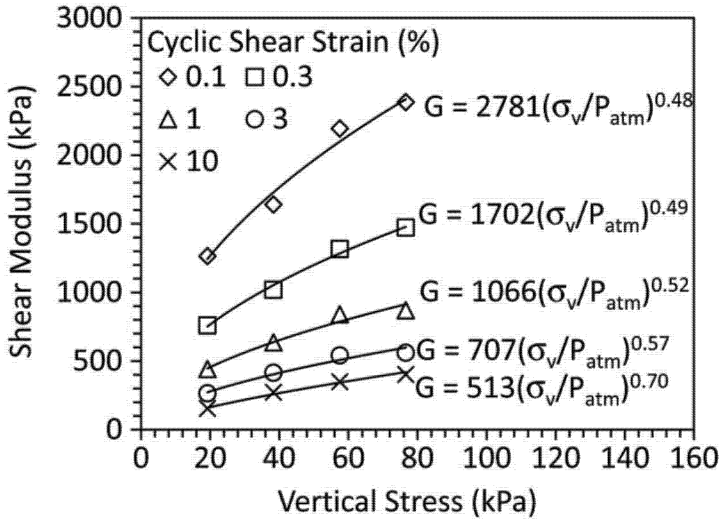

Figure 6.5 Effect of vertical stress and cyclic shear strain amplitude on shear modulus of Type B TDA (McCartney et al. 2017)

The power relationship proposed by McCartney et al. (2017) provides the Type B TDA shear modulus at 1% shear strain at a specific vertical stress. This study evaluates the flexible base system using the period lengthening factor (shown in Equation 6.3) suggested by NIST (2012), which considers the stiffness of the fixed base system, the effective height of the structure, the translation stiffness along the x-axis, and the rocking stiffness along the y-axis as illustrated in Figure 6.6.

$$\frac{\tilde{T}}{T} = \sqrt{1 + \frac{k}{k_x} + \frac{kh^2}{k_{yy}}} \qquad \textbf{Eq. 6. 3}$$

Pais and Kausel (1988) solutions consider stiffness and damping in the six degrees of freedom as shown in Figure 6.6. The stiffness is denoted as k_j, the static foundation stiffness at zero frequency for mode j is denoted as K_j, the dynamic stiffness modifier is denoted as α_j, and the embedment modifier is denoted as η_j as presented in Equation 3. As previously mentioned,

this study considers translation along the x-axis and rocking about the y-axis. Therefore, the solutions considered are presented in Equations 6.4 to 6.12.

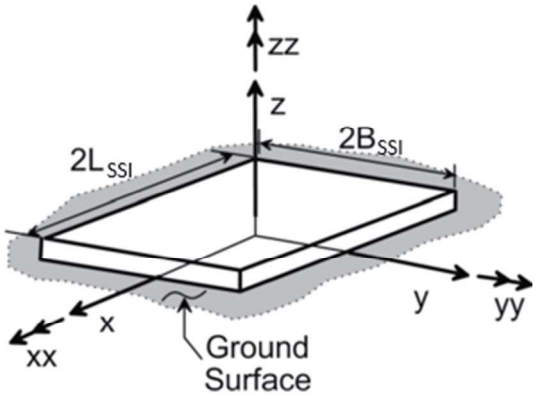

Figure 6.6 Translation and rotational axis of rigid footings at the ground surface (NIST 2012)

$$k_j = K_j \times \alpha_j \times \eta_j \qquad \textbf{Eq. 6. 4}$$

$$K_{x,sur} = \frac{GB_{SSI}}{2-\nu}\left[6.8\left(\frac{L_{SSI}}{B_{SSI}}\right)^{0.65} + 2.4\right] \qquad \textbf{Eq. 6. 5}$$

$$K_{yy,sur} = \frac{GB_{SSI}^{\ 3}}{1-\nu}\left[3.73\left(\frac{L_{SSI}}{B_{SSI}}\right)^{2.4} + 0.27\right] \qquad \textbf{Eq. 6. 6}$$

$$\alpha_x = 1.0 \qquad \textbf{Eq. 6. 7}$$

$$\alpha_{yy} = 1.0 - \left[\frac{0.55a_0^2}{\left(0.6 + \frac{1.4}{\left(\frac{L_{SSI}}{B_{SSI}}\right)^3}\right) + a_0^2}\right] \qquad \textbf{Eq. 6. 8}$$

$$\eta_x = \left[1.0 + \left(0.33 + \frac{1.34}{1 + B_{SSI}/L_{SSI}}\right)\left(\frac{D}{L_{SSI}}\right)^{0.8}\right] \qquad \textbf{Eq. 6. 9}$$

$$\eta_{yy} = \left[1.0 + \frac{D}{B_{SSI}} + \left(\frac{1.6}{0.35 + \left(\frac{L_{SSI}}{B_{SSI}}\right)^4}\right)\left(\frac{D}{B_{SSI}}\right)^2\right] \qquad \textbf{Eq. 6. 10}$$

$$k_x = K_{x,sur} \times \alpha_x \times \eta_x \qquad \textbf{Eq. 6. 11}$$

$$k_{yy} = K_{yy,sur} \times \alpha_y \times \eta_{yy} \qquad \textbf{Eq. 6. 12}$$

where G is the TDA shear modulus, ν is the Poisson's ratio of the soil, L_{SSI} is the half-length of the footing along x-axis as shown in Figure 6.6, B_{SSI} is the half-width of the footing along the y-axis as shown in Figure 6.6, D is the embedment of the footing, and $a_0 = \omega B_{SSI}/V_s$ is the dimensionless frequency. It is important to mention that L_{SSI} and B_{SSI} follow the same orientation as B and L, respectively. The TDA and SDOF properties are presented in Table 6.7.

Figure 6.7 TDA-footing-structure system parameters

Specimen	G_{TDA} [kPa]	$V_{S\text{-}TDA}$ [m/s]	ν_{TDA}	L_{SSI} [m]	B_{SSI} [m]	D [m]	ω [rad/s]	T [s]	$\bar{T}$ [s]	$\frac{\tilde{T}}{\bar{T}}$
DT-01	321	23.2	0.3	0.23	0.46	0.46	39.3	0.16	0.24	1.56
DT-02	355	23.5	0.3	0.23	0.80	0.46	20.3	0.31	0.47	1.51
DT-03	329	23.6	0.3	0.23	0.80	0.46	20.3	0.31	0.48	1.54

6.2.4 Construction techniques

This section describes the materials and construction procedures used to set up the test specimen at the UCSD South Powell Laboratory. As previously described, the specimens were placed inside the laminar shear box positioned on top of the shake table. The interior base of the laminar box was irregular, as shown in Figure 6.8, therefore, a concrete platen of 3.65 m by 1.61 m and thickness of 0.15 m. was added and fixed as a base, as shown in Figure 6.9. The concrete platen covered 88% of the inside base area and the remaining was filled by TDA. The concrete platen was coupled with a set of lifting slings and cargo nets to remove the TDA after testing, as shown in Figure 6.9. The lifting slings and cargo nets were attached to the base of the concrete platen and surrounded the sides of the TDA specimen. At the same time, the interior sidewalls of the box were covered by two thin polyethylene layers (on each side) to represent a low-friction interface between the sidewalls and the TDA as shown in Figure 6.10. This sort of interface is required to simulate in plane-strain conditions.

The construction of the TDA specimen was performed by placing lifts of TDA of 5.5 inches after compaction. Each lift was compacted using a vibratory rammer tamper applied twice to the entire TDA area. As it was not possible to perform field density tests on the TDA, the actual unit weight of the TDA layer was estimated from the weight of TDA placed on each lift and the height achieved for the lift, as shown in Figure 6.11. Once the TDA layer reached the target level of the base of the footing, the footing was placed and leveled on top of the TDA, as illustrated in Figure

6.12. The sides of the footings were filled by compacted TDA following the approach mentioned before. The SDOF system was attached to the footing, as shown in Figure 6.13. Once the specimen was built, a steel frame was attached to the top collar beam of the laminar box to provide support for the instrumentation.

An example of a fully dynamic testing specimen is shown in Figure 6.14. It should be noted that the extremes of the strip footing have a plane-strain or free-displacement connection in the North-South direction but a restrained-displacement connection in the East-West direction (i.e., a plane-strain boundary condition perpendicular to the direction of train travel along the rails). The free-displacement connection was ensured using a boundary connection at the ends of the footing. The 2-D plane-strain connections consist of two 3.0 × 2.5 × 18-inch lumber fixed to the four borders of the end of the footing. One side of the lumber elements is attached to the footing, and the other end is covered by Teflon to provide minimum friction. This end connection for the rails is shown in Figure 6.15.

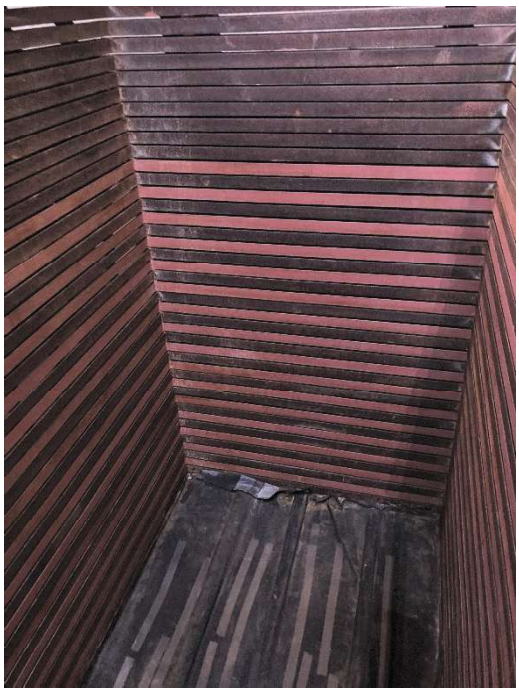

Figure 6.8 Interior of laminar shear container without TDA.

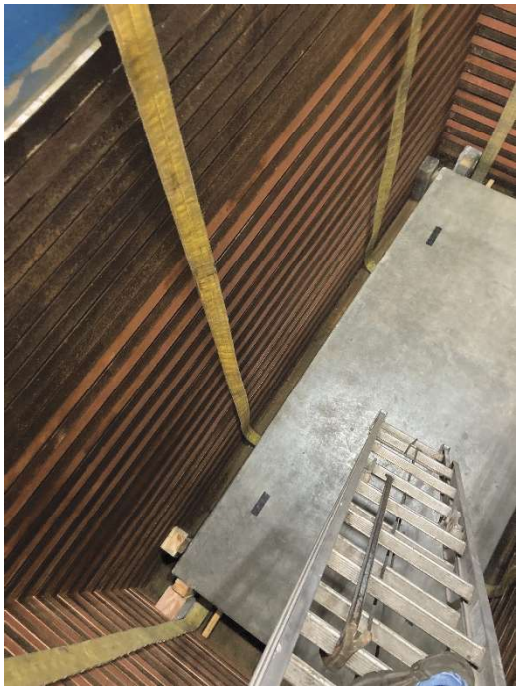

Figure 6.9 Placement of concrete platen.

Figure 6.10 Installation of cargo nets and visqueen plastic.

Figure 6.11 Placement of TDA.

Figure 6.12 Placement of footing on top of TDA.

Figure 6.13 Placement of footing, SDOF system and surrounding TDA.

Figure 6.14 Top view of test specimen built on shake table after placement of steel frames for instrumentation support.

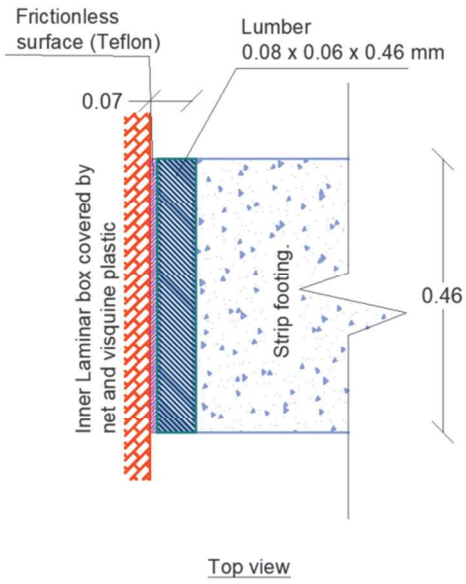

(a)

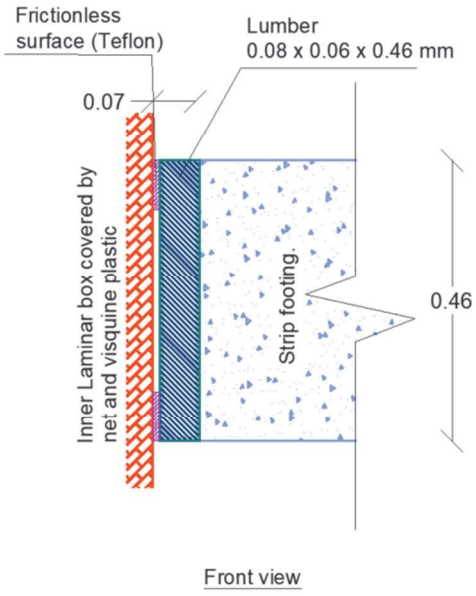

(b) **(c)**

Figure 6.15 2-D Plane-strain connection detailing: (a) Top view, (b) Front view, and (c) Actual picture.

6.2.5 Instrumentation

Instrumentation is included within the testing specimen and on the laminar container to characterize the deformation response of the system during the application of earthquake motions. An example cross-sectional and plan instrumentation layout of the testing specimen DT-03 is

shown in Figures 6.16 to 6.18. Test specimens DT-01 and DT-02 follow the same instrumentation layout as test specimen DT03 with the only difference being that the position of the footing and superstructure is lower due to the smaller thickness of the TDA layer.

The vertical and horizontal displacements and rocking of the footing are measured by eight spring potentiometers. The horizontal acceleration of the footing is monitored by one accelerometer placed on top of the footing. The footing rocking pre- and post-shaking event is measured by two static inclinometers. The horizontal and vertical stress induced by the TDA on the footing is monitored by four pressure cells. The vertical and horizontal displacement of the lumped mass is measured by two string potentiometers. The horizontal acceleration of the lumped mass is monitored by a single three-dimensional accelerometer. The TDA layer is monitored by two embedded one-dimensional accelerometers positioned to measure horizontal shaking. The horizontal acceleration of the concrete platen is measured by a one-dimensional accelerometer. The horizontal acceleration of the laminar box is monitored at the base by a one-dimensional accelerometer. Finally, a profile of string potentiometers is used to control the deformation response of the laminar frames.

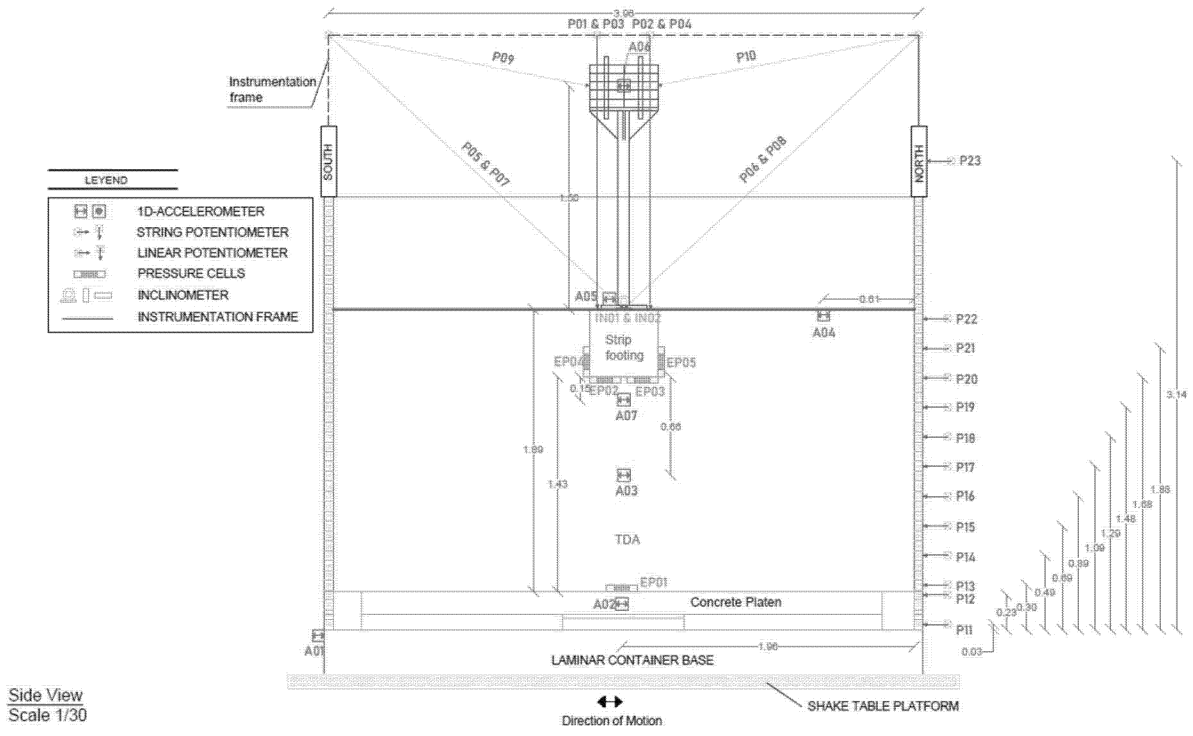

Figure 6.16 Typical sensor and measurement device locations shown in side view within a testing specimen (Note: See appendices for actual instrumentation layouts).

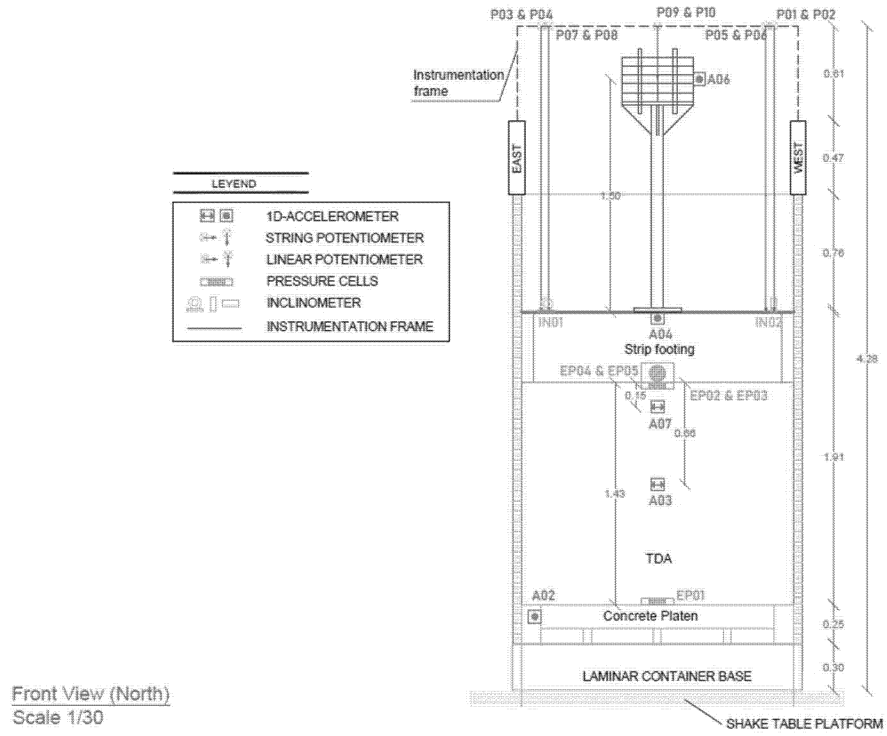

Figure 6.17. Typical sensor and measurement device locations shown in front view within a testing specimen (Note: See appendices for actual instrumentation layouts).

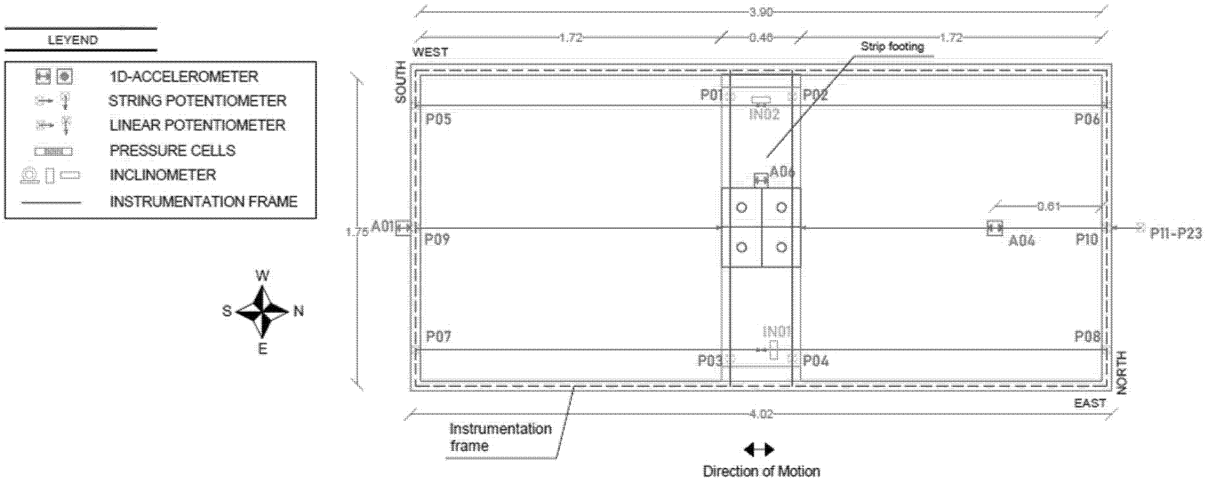

Figure 6.18. Typical sensor and measurement device locations shown in plan view within a testing specimen (Note: See appendices for actual instrumentation layouts).

Pictures of the sensors included in the testing specimens are shown in Figure 6.19 and include string potentiometers (Model P- 5A/15A/25A/30A/40A from Rayelco, PATRIOT Sensors and Controls Corp.), accelerometers (Model CXL02LF1 from Crossbow), earth pressure cells

(Model SPT-3K/6K from AFB Engineered Test System), and inclinometers (Model EA-2016 from AccuStar). The data acquisition hardware used in this study is a National Instruments (NI) PXI-1052 system that works as a processer. All sensors were connected to NI-SCXI-1520 signal conditioners via NI-SCXI-1314 terminal blocks. Data from all sensors was collected at a simultaneous sampling rate of 512 Hz during shaking.

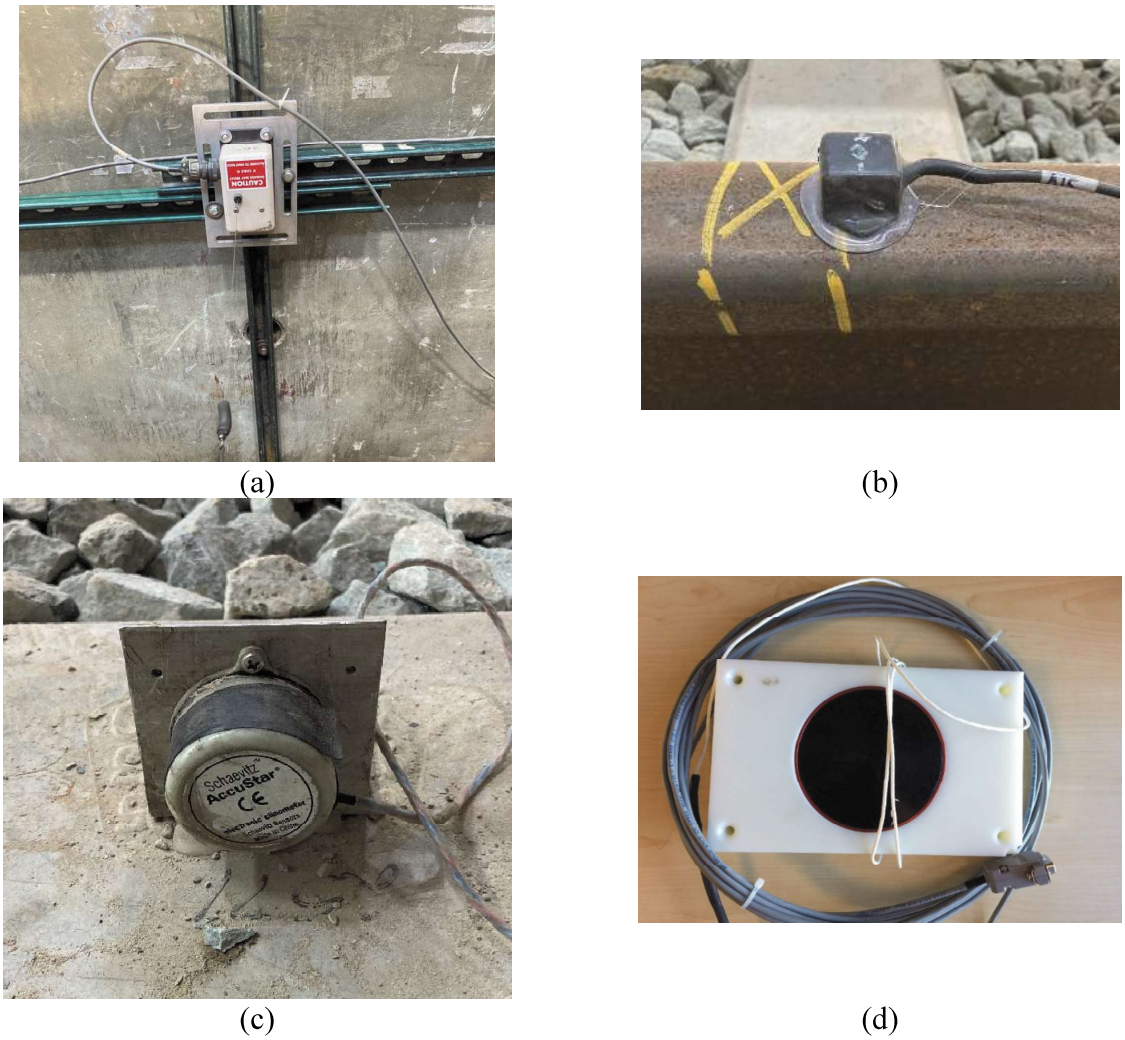

(a) (b)

(c) (d)

Figure 6.19 Sensors included in the testing specimen: (a) String potentiometer, (b) Accelerometer, (c) Inclinometer, and (d) Earth pressure cell (adapted from Yarahuaman and McCartney 2020).

6.3 Experimental procedure

6.3.1 Testing protocol

The sequence of motions applied during shake table testing was defined based on the capability of the shake table as recommended by Trautner et al. (2017). For each of the testing specimens, the series of motions include white noise motions, sine sweep motions, and earthquake motions applied to the specimen in sequence. The testing protocol for the seismic evaluation of each one of the testing specimens is shown in Tables 6.3 to 6.5.

Table 6.3. Testing protocol for specimen DT01

Order	Motion (Scaled)	Code Name	Control	Peak Ground Acceleration (PGA) [g]	Max. Amplitude	Dominant Frequency [Hz]	Duration [s]
1	White Noise 01	DT01-WN01-01	Acceleration				120
2	Sine Sweep Max. Amp. = 1.50 mm	DT01-SS150-F01F10	Displacement	0.08	1.0 mm	1.0 - 10.0	20
3	Sine Sweep Max. Amp. = 3.00 mm	DT01-SS300-F01F10	Displacement	0.16	3.00 mm	1.0 - 10.0	20
4	Sine Sweep Max. Amp. = 4.50 mm	DT01-SS450-F01F10	Displacement	0.24	4.50 mm	1.0 - 10.0	20
5	Sine Sweep Max. Amp. = 5.25 mm	DT01-SS525-F01F10	Displacement	0.28	5.25 mm	1.0 - 10.0	20
6	White Noise 02	DT01-WN01-02	Acceleration				120
7	1994 Northridge (50% Disp.)	DT01-NOR-050P	Displacement	0.16	50%	0.34	45
8	1994 Northridge (75% Disp.)	DT01-NOR-075P	Displacement	0.24	75%	0.34	45
9	White Noise 03	DT01-WN01-03	Acceleration				120
10	1994 Northridge (100% Disp.)	DT01-NOR-100P	Displacement	0.33	100%	0.34	45
11	White Noise 04	DT01-WN01-04	Acceleration				120
12	2010 Maule (100% Disp.)	DT01-MAU-100P	Displacement	0.44	100%	0.16	160
13	White Noise 05	DT01-WN01-05	Acceleration				120

Table 6.4. Testing protocol for specimen DT02

Order	Motion (Scaled)	Code Name	Control	PGA [g]	Max. Amplitude	Dominant Frequency [Hz]	Duration [s]
1	White Noise 01	DT02-WN01-01	Acceleration				120
2	White Noise 02	DT02-WN02-01	Acceleration				120
3	White Noise 03	DT02-WN03-01	Acceleration				120
4	Sine Sweep Max. Amp. = 8.0 mm	DT02-SS08-F04F10	Displacement	0.08	8.0 mm	0.4 - 10.0	20
5	Sine Sweep Max. Amp. = 12.0 mm	DT02-SS12-F04F10	Displacement	0.16	12.0 mm	0.4 - 10.0	20
6	Sine Sweep Max. Amp. = 16.0 mm	DT02-SS16-F04F10	Displacement	0.24	16.0 mm	0.4 - 10.0	20
7	Sine Sweep Max. Amp. = 20.0 mm	DT02-SS20-F04F10	Displacement	0.28	20.0 mm	0.4 - 10.0	20
8	White Noise 04	DT02-WN01-02	Acceleration				120
9	1994 Northridge (50% Disp.)	DT02-NOR-050P	Displacement	0.16	0.50	0.34	45
10	White Noise 05	DT02-WN01-03	Acceleration				120
11	1994 Northridge (75% Disp.)	DT02-NOR-075P	Displacement	0.24	75%	0.34	45
12	White Noise 06	DT02-WN01-04	Acceleration				120
13	1994 Northridge (100% Disp.)	DT02-NOR-100P	Displacement	0.33	100%	0.34	45
14	White Noise 07	DT02-WN01-05	Acceleration				120
15	2010 Maule (100% Disp.)	DT02-MAU-100P	Displacement	0.44	100%	0.16	160
16	White Noise 08	DT02-WN01-06	Acceleration				120

Table 6.5. Testing protocol for specimen DT03

Order	Motion (Scaled)	Code name	Control	PGA [g]	Max. amplitude	Dominant frequency [Hz]	Duration [s]
1	White Noise 01	DT03-WN01-01	Acceleration				120
2	White Noise 02	DT03-WN02-01	Acceleration				120
3	White Noise 03	DT03-WN03-01	Acceleration				120
4	Sine Sweep Max. Amp. = 8.0 mm	DT03-SS08-F04F10	Displacement	0.08	8.0 mm	0.4 - 10.0	20
5	Sine Sweep Max. Amp. = 12.0 mm	DT03-SS12-F04F10	Displacement	0.16	12.0 mm	0.4 - 10.0	20
6	Sine Sweep Max. Amp. = 16.0 mm	DT03-SS16-F04F10	Displacement	0.24	16.0 mm	0.4 - 10.0	20
7	Sine Sweep Max. Amp. = 20.0 mm	DT03-SS20-F04F10	Displacement	0.28	20.0 mm	0.4 - 10.0	20
8	Sine Sweep Max. Amp. = 24.0 mm	DT03-SS24-F04F10	Displacement	0.32	24.0 mm	0.4 - 10.0	20
9	White Noise 04	DT03-WN01-02	Acceleration				120
10	1994 Northridge (50% Disp.)	DT03-NOR-050P	Displacement	0.16	50%	0.34	45
11	White Noise 05	DT03-WN01-03	Displacement				120
12	1994 Northridge (75% Disp.)	DT03-NOR-075P	Displacement	0.24	75%	0.34	45
13	White Noise 06	DT03-WN01-04	Acceleration				120
14	1994 Northridge (100% Disp.)	DT03-NOR-100P	Displacement	0.33	100%	0.34	45
15	White Noise 07	DT03-WN01-05	Acceleration				120
16	2010 Maule (100% Disp.)	DT03-MAU-100P	Displacement	0.44	100%	0.16	160
17	White Noise 08	DT03-WN01-06	Acceleration				120

The first portion of the testing protocol consist of a system identification program and focuses on determining the natural period and frequency of the Type B TDA layer as well as the flexible base system for each testing specimen. The system identification sequence is composed

of one or three white noise motions at different amplitudes applied to the specimen before any other motion. The white noise motions consist of low-intensity clipped-band, flat, and acceleration-control white noise from 0.50 to 0.30 Hz as recommended by FEMA 461 (2007). An example of the white noise motion is illustrated in Figure 6.20. In addition to the three initial white noise motions, a white nose motion is applied to the specimen after each sine sweep and earthquake motion to evaluate the evolution of the specimen.

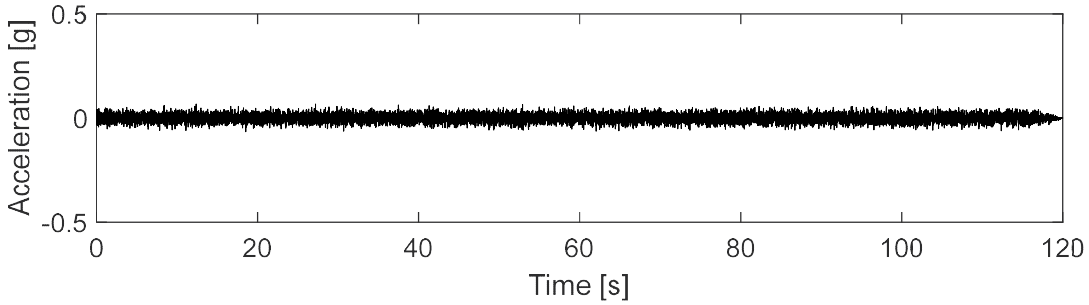

Figure 6.20 Example of the acceleration time-history record for white noise (DT01-WN01-01).

The second portion of the testing protocol includes multiple sines sweep motions. The sine sweep motions consist of sine waves with varying frequencies instead of a fixed frequency. These types of motions facilitate the characterization of the specimen while exposing the specimen to higher demands than the white noise motions. This study considers two types of sine sweep motions designed to excite the specimen at their resonant frequency and different amplitudes, as shown in Figures 6.21 and 6.22. The sine sweeps are applied continuously using displacement-control mode.

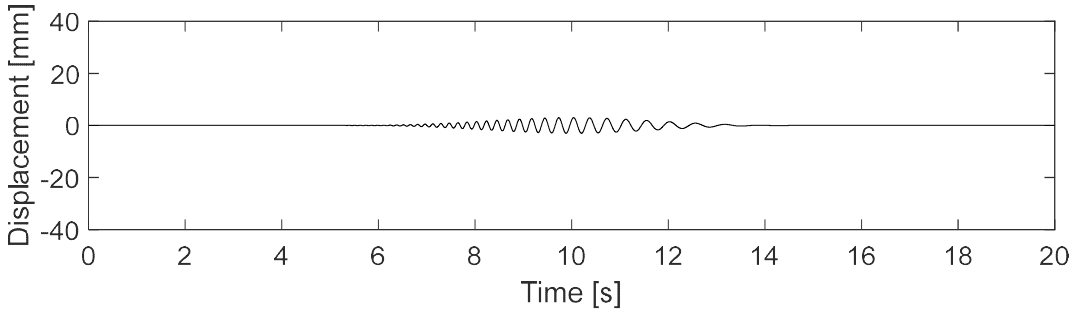

Figure 6.21 Example of sine sweep DT01 displacement time-history records (DT01-SS300-F01F10)

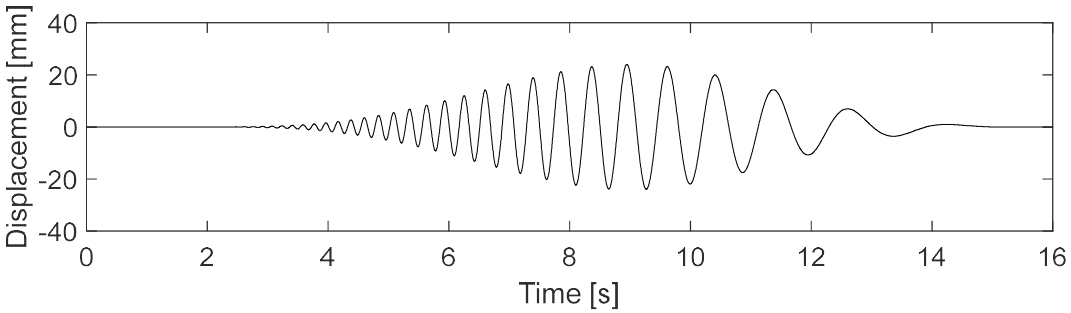

Figure 6.22 Example of sine sweep DT02 displacement time-history records (DT03-SS24-F04F10).

The final portion of the testing protocol consists of selected earthquake motions that belong to the time-history records from the 1994 Northridge earthquake and the 2010 Maule earthquake. The motions were selected because of their broad-frequency content. The characteristics of these earthquake motions are listed in Table 6.6. The earthquake motions were applied in displacement-control mode. The displacement and acceleration time records are shown in Figures 6.23 to 6.24.

Table 6.6 Earthquake motions characteristics

Item	Motion – Station (Direction)	Abbreviation	PGA [g]	Pred. period (s)	Duration (s)
1	Northridge 1994 - 17645 Saticoy (090°)	NR	0.33	0.33	60
2	Maule 2010 – Curico S/N 499 (NS)	ML	0.48	0.16	180

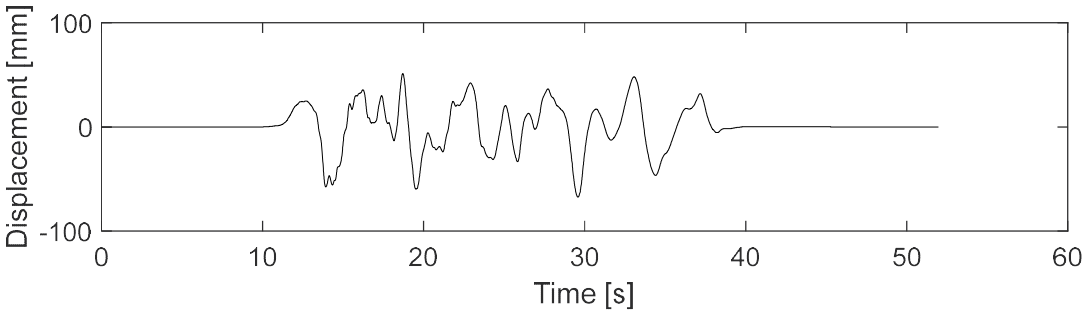

(a)

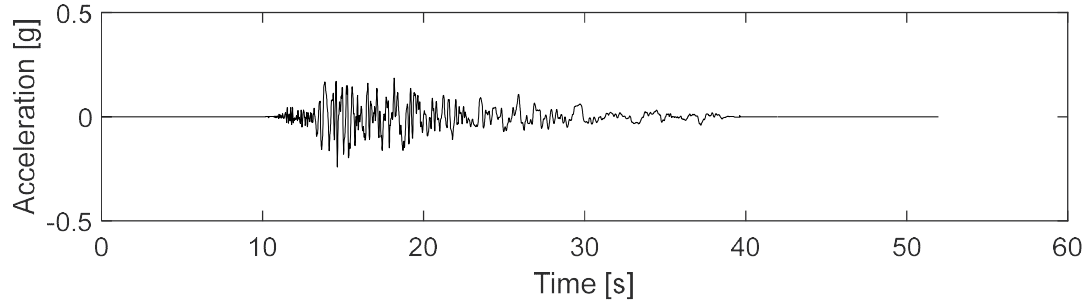

(b)

Figure 6.23 1994 Northridge earthquake: (a) Displacement time-history record, and (b) Acceleration time-history record.

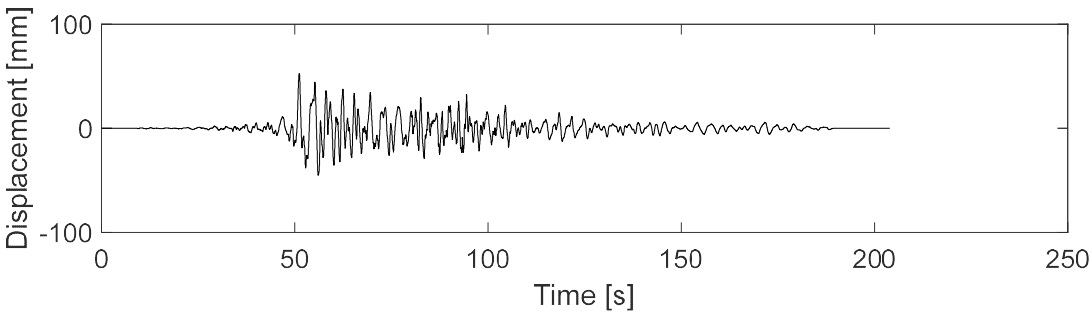

(a)

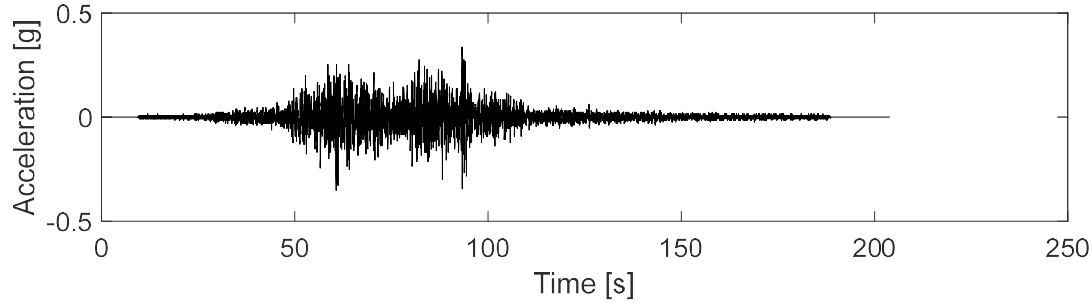

(b)

Figure 6.24 2010 Maule earthquake: (a) Displacement time-history record, and (b) Acceleration time-history record.

6.4 Experimental results

6.4.1 System identification

This section describes the system identification results applied to each specimen. As shown in the testing protocols, the specimen DT01 considered one white noise motion at the beginning of the testing program. The specimens DT02 and DT03 considered three white noise motions at the beginning of the program. The first, second, and third white noise motions had a PGA of 0.05g, 0.08g, and 0.11 g, respectively. The results shown in this section consider the Fourier spectrum for (1) the horizontal acceleration of the lumped mass as a control point for the TDA-footing-superstructure system, and (2) the horizontal acceleration of the top of the TDA layer as a control point for the TDA free field behavior. The results for specimen DT01 can be found in Figures 6.25 and 6.26. The results for specimen DT02 are shown in Figures 6.27 and 6.28. The results for specimen DT01 are shown in Figures 6.29 and 6.30.

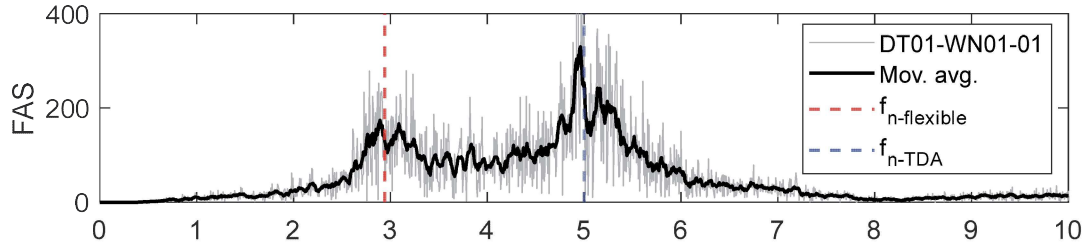

Figure 6.25 Fourier spectrum of the horizontal acceleration of the lumped mass during initial white noise motions applied to specimen DT01

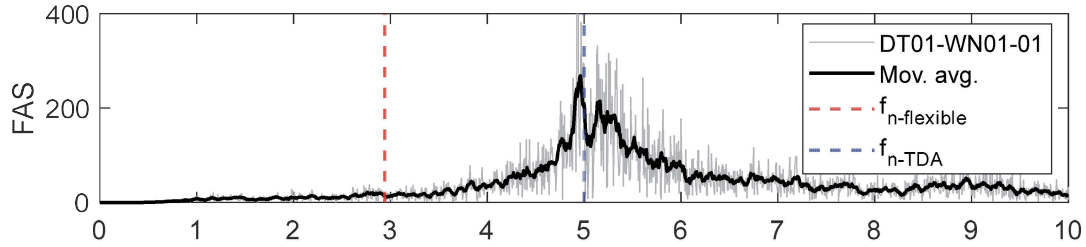

Figure 6.26 Fourier spectrum of the horizontal acceleration of TDA top free field during initial white noise motions applied to specimen DT01

The computed Fourier spectrums are overall very noisy. Although peaks are still noticeable, moving average curves are implemented for a clearer view of peaks. Regarding specimen DT01, the Fourier spectrum that belongs to the lumped mass shows two clear peaks, as shown in Figure 6.25. The Fourier spectrum that belongs to the free field case shows one clear peak, as shown in Figure 6.26. Both Fourier spectrums indicate that the fundamental frequency of the TDA-structure specimen is 3.30 Hz which is equivalent to a period of 0.30 s. Both Fourier

spectrums indicate that the fundamental frequency of the TDA specimen is 5.00 Hz which is equivalent to a period of 0.20 s.

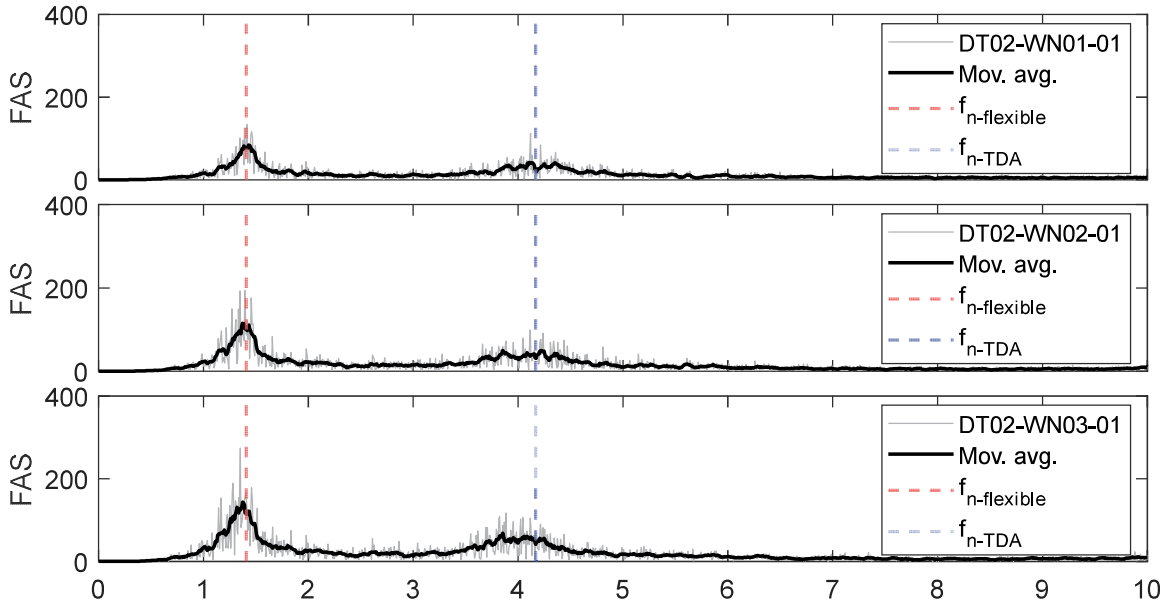

Figure 6.27 Fourier spectrum of the horizontal acceleration of the lumped mass during initial white noise motions applied to specimen DT02

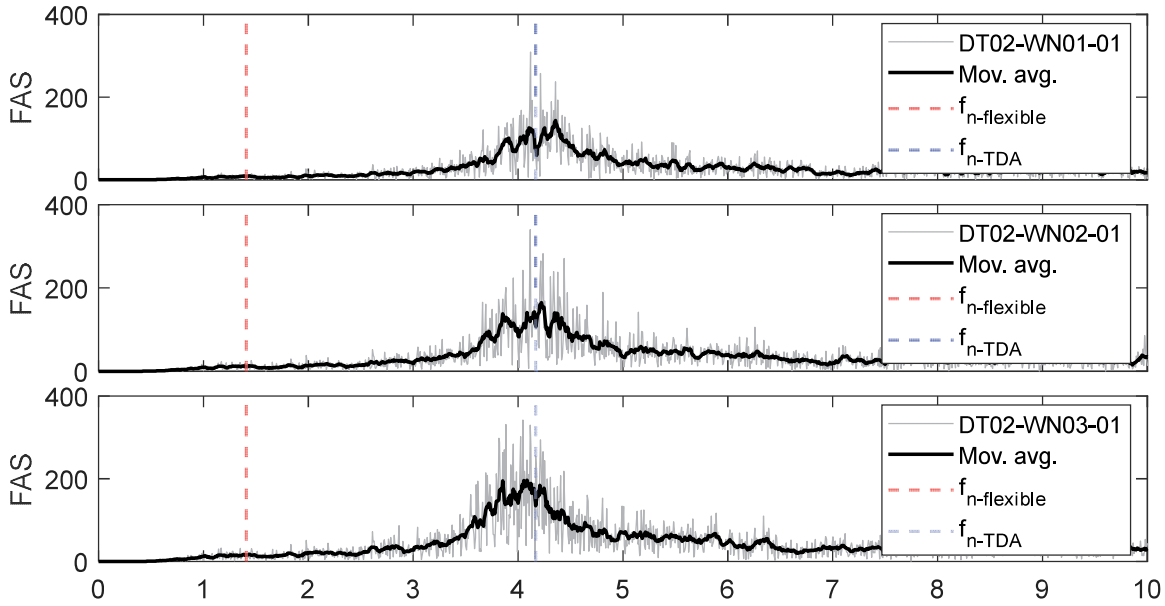

Figure 6.28 Fourier spectrum of the horizontal acceleration of TDA top free field during initial white noise motions applied to specimen DT02

Regarding specimen DT02, the Fourier spectrum that belongs to the lumped mass also shows two clear peaks, as shown in Figure 6.27. The Fourier spectrum that belongs to the free field

case also shows one clear peak, as shown in Figure 6.28. Both Fourier spectrums indicate that the fundamental frequency of the TDA-structure specimen is 1.41 Hz which is equivalent to a period of 0.71 s. Both Fourier spectrums indicate that the fundamental frequency of the TDA specimen is 4.17 Hz which is equivalent to a period of 0.24 s.

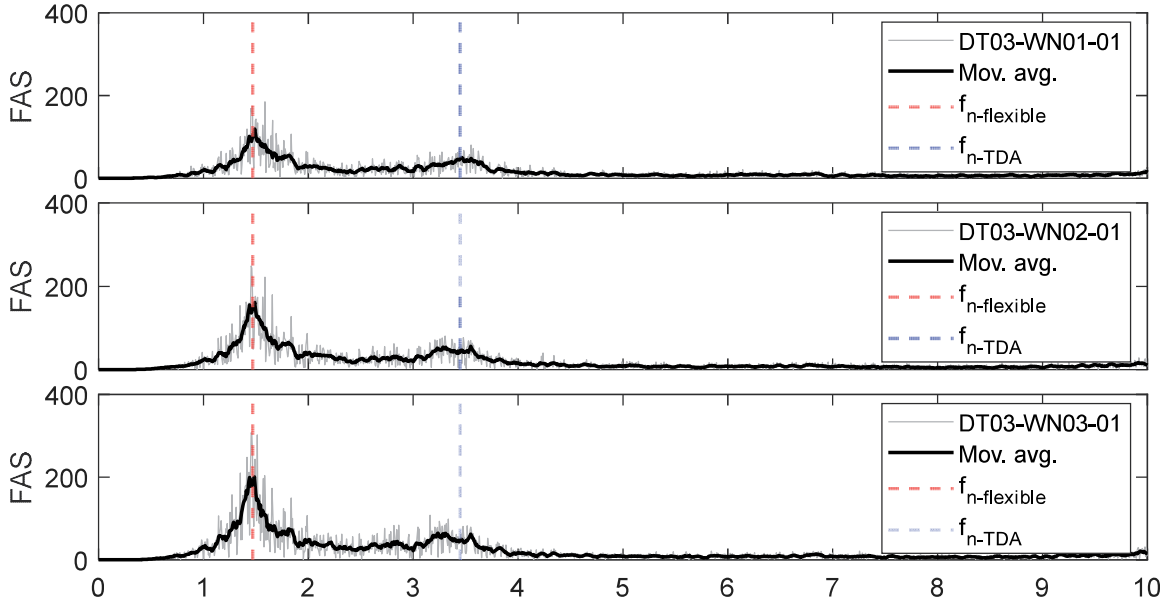

Figure 6.29 Fourier spectrum of the horizontal acceleration of the lumped mass during initial white noise motions applied to specimen DT03

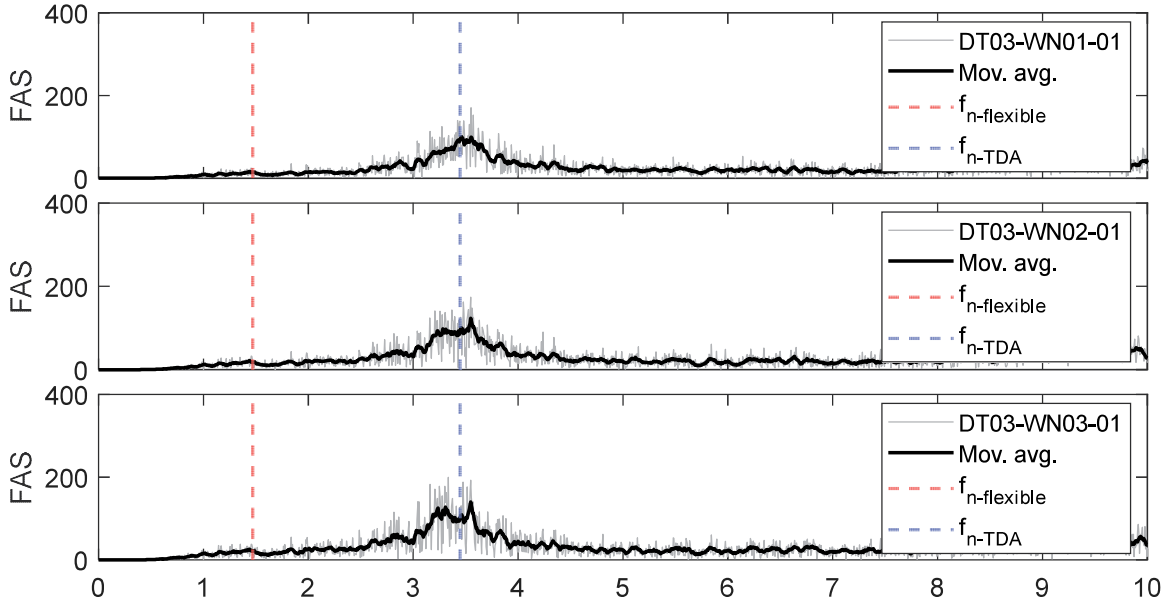

Figure 6.30 Fourier spectrum of the horizontal acceleration of TDA top free field during initial white noise motions applied to specimen DT03

Regarding specimen DT03, the Fourier spectrum that belongs to the lumped mass shows two clear peaks, as shown in Figure 6.29. The Fourier spectrum that belongs to the free field case also shows one clear peak, as shown in Figure 6.30. Both Fourier spectrums indicate that the fundamental frequency of the TDA-structure specimen is 1.47 Hz which is equivalent to a period of 0.68 s. Both Fourier spectrums indicate that the fundamental frequency of the TDA specimen is 3.45 Hz which is equivalent to a period of 0.29 s. Table 6.7 and Figures 6.31 to 6.32 show the summary of system identification results. The measured fundamental period of each specimen is compared to the estimated fundamental period using Pais and Kausel (1988), as shown in Figure 6.31. The period of the free field TDA is related to its thickness, as shown in Figure 6.32.

Table 6. 7. Summary of system identification results

Specimen	T [s]	$\overline{T}_{predicted}$ [s]	$\overline{T}_{measured}$ [s]	t_{TDA} [m]	T_{TDA} [s]
DT01	0.16	0.24	0.30	1.14	0.20
DT02	0.31	0.47	0.71	1.38	0.24
DT03	0.31	0.48	0.68	1.89	0.29

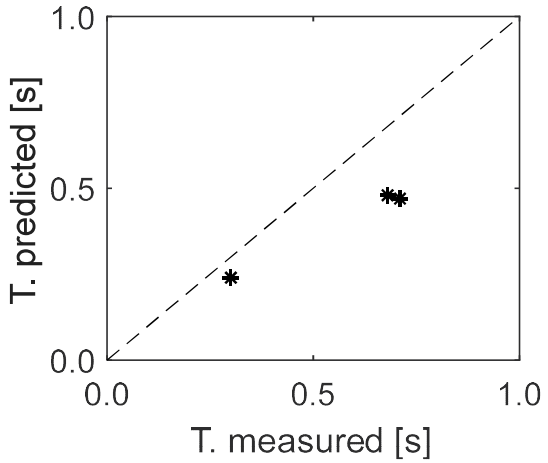

Figure 6.31 Comparison of predicted and measured fundamental period of the specimens

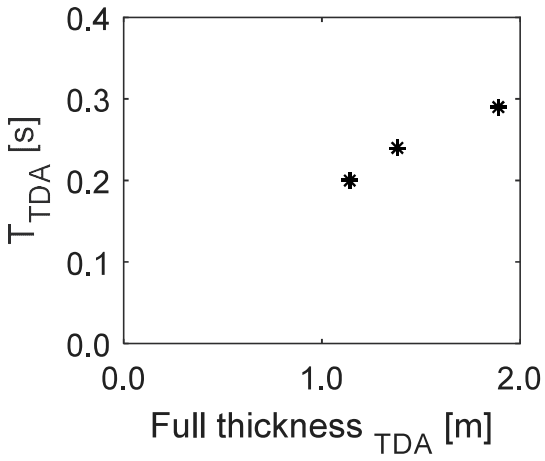

Figure 6.32 Relationship between the full thickness of TDA and its fundamental period.

According to the testing results and the estimated TDA properties, it is observed that the Pais and Kausel (1988) approach underestimates the period of the specimens by an average of 40%, as shown in Figure 6.31. Regarding the free field conditions of the TDA, it is observed that the fundamental period of the TDA increases with the TDA layer thickness, as shown in Figure 6.32. The period of a soil stratum is directly proportional to its height hence this response is expected.

6.4.2 Moment-rocking response

This subsection describes the moment-rocking response of the most demanding motions considered in the testing protocol of each question, which are sine sweep motion with the largest amplitude, the 1994 Northridge earthquake 100% displacement-based scaled, and the 2010 Maule earthquake 100% displacement-based scaled. The results for the rest of the motions can be found in the Appendix section. Results for specimen DT01 are shown in Figure 6.33, results for specimen DT02 are shown in Figure 6.34, and results for specimen DT03 are shown in Figure 6.35.

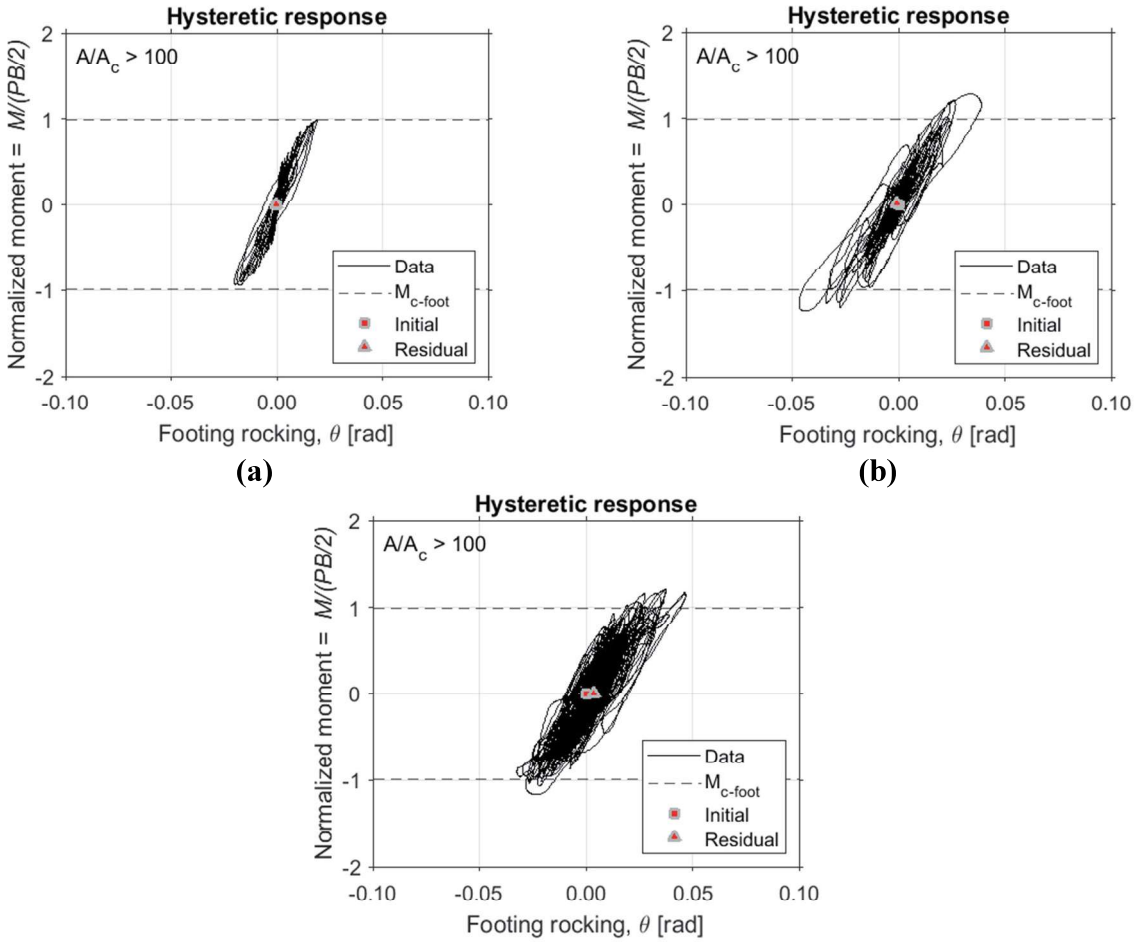

Figure 6.33 Moment-rocking response during (a) DT01-SS525-F01F10, (b) DT01-NOR-100P; (c) DT01-MAU-100P.

The experimental results indicate that the overall moment-rocking response of TDA is nonlinear, as shown in Figure 6.33. The moment-rocking response under the sine sweep motion DT01-SS525-F01F10 is mainly linear with small nonlinearity starting to form when the moment gets closer to the moment capacity. The moment-rocking response under motions the earthquake

motions DT01-NOR-100P and DT01-MAU-100P experience stiffness softening and follows an "S" shape. Specimen DT01 experienced significantly small residual rocking in all motions.

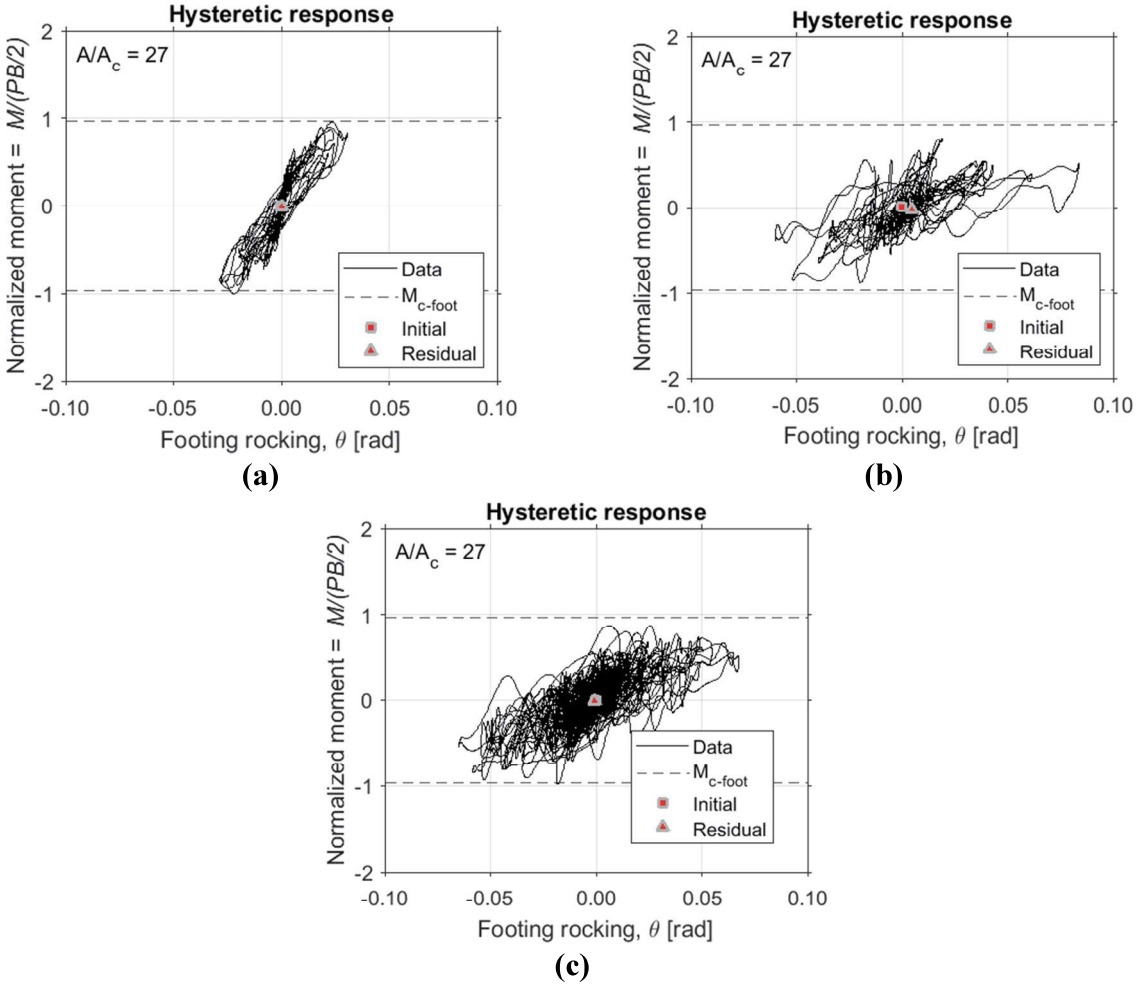

Figure 6.34 Moment-rocking response during (a) DT02-SS20-F04F10, (b) DT02-NOR-100P; (c) DT02-MAU-100P.

Overall, it is observed that specimen DT02 experiences a more nonlinear moment-rocking response than specimen DT01, as shown in Figure 6.34. The moment-rocking response under the sine sweep motion DT02-SS20-F04F10 shows stiffness softening even before the moment capacity is reached. The same trend is observed for the specimen induced by the earthquake motions DT02-NOR-100P and DT02-MAU-100P. Although the specimen DT02 is subjected to high nonlinear response, it should be noted that the specimen experienced significantly small residual rocking in all motions.

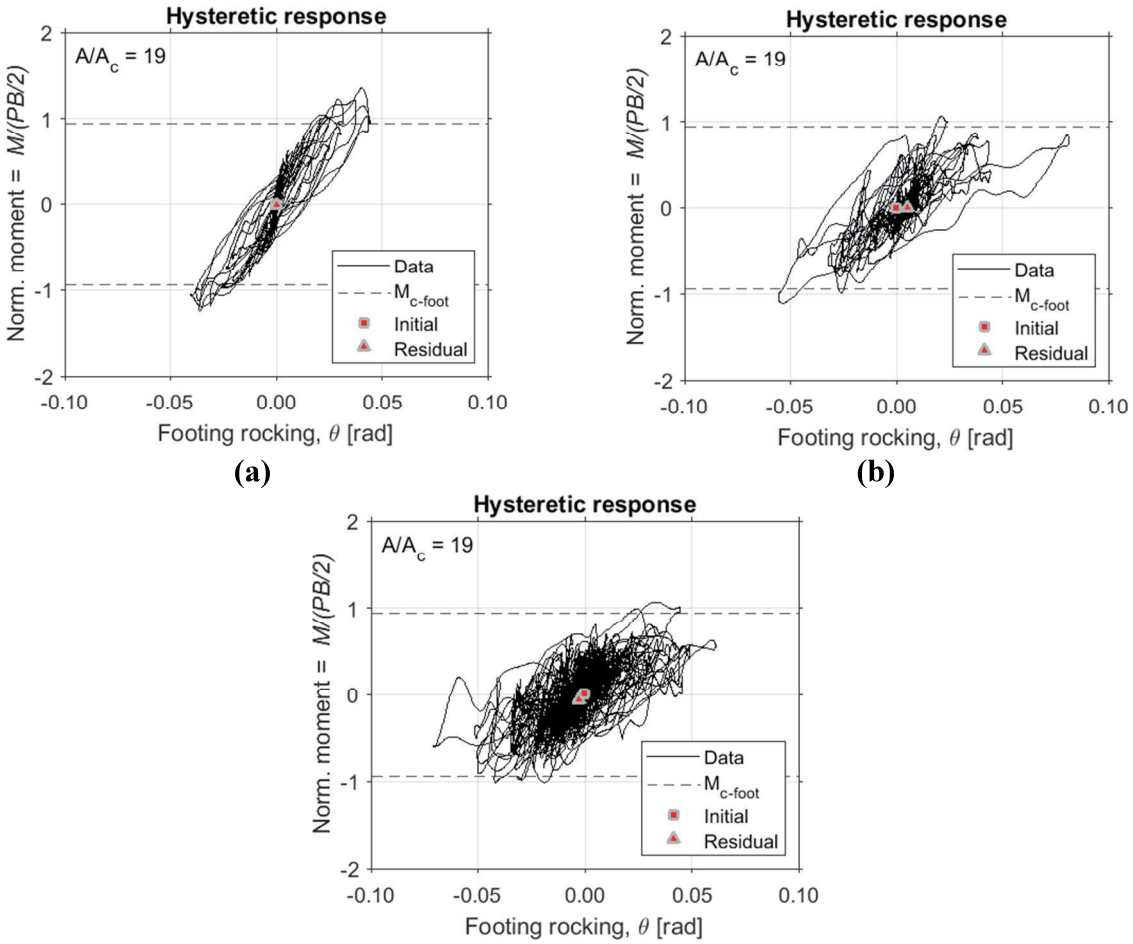

Figure 6.35 Moment-rocking response during (a) DT03-SS24-F04F10, (b) DT03-NOR-100P, and (c) DT03-MAU-100P.

Overall, it is observed that specimen DT03 experiences higher nonlinear moment-rocking response than specimen DT01, and higher moment demand than DT02 as shown in Figure 6.35. The moment-rocking response under the sine sweep motion DT03-SS24-F04F10 is nonlinear following an "S" shape. Softening can be observed before and past the moment capacity limit. The moment-rocking response from earthquake motions DT03-NOR-100P and DT03-MAU-100P also shows stiffness softening even when the moment capacity was not reached in some cycles. In the same way as specimens DT01 and DT02, DT 03 experienced significantly small residual rocking in all motions. The moment-rocking results overall indicate that the testing specimens experienced high nonlinearity with stiffness softening even before reaching their corresponding moment capacity. However, even with a nonlinear response, the resulting residual rocking was significantly small for all motions.

6.4.3 Settlement-rocking response

This subsection describes the settlement-rocking response of the most demanding motions considered in the testing protocol of each question, which are sine sweep motion with the largest amplitude, the 1994 Northridge earthquake 100% displacement-based scaled, and the 2010 Maule earthquake 100% displacement-based scaled. The results for the rest of the motions can be found in the Appendix section. Results for specimen DT01 are shown in Figure 6.36, results for specimen DT02 are shown in Figure 6.37, and results for specimen DT03 are shown in Figure 6.38.

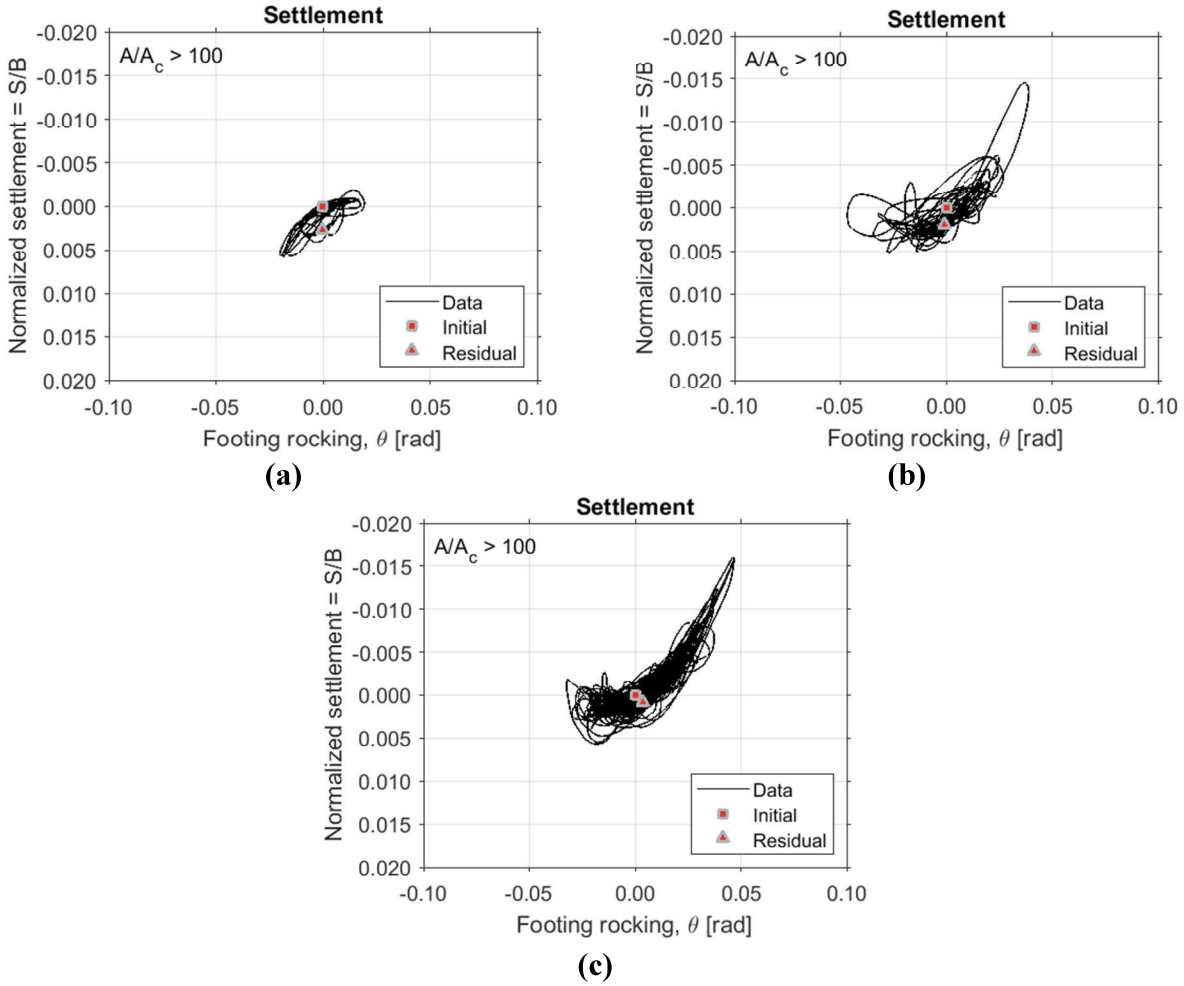

Figure 6.36 Settlement-rocking response during (a) DT01-SS525-F01F10; (b) DT01-NOR-100P; (c) DT01-MAU-100P.

The transient experimental results show that the specimen DT01 experiences temporary settlement and uplift when oscillating. Settlement is observed when the specimen oscillates south, and uplift when it oscillates north. Once the base excitation has ended, the generated residual settlement is significantly small, as shown in Figure 6.36. It is also observed that the sine sweep

motion DT01-SS525-F01F10 generates more settlement than both earthquake motions. No residual uplift is observed.

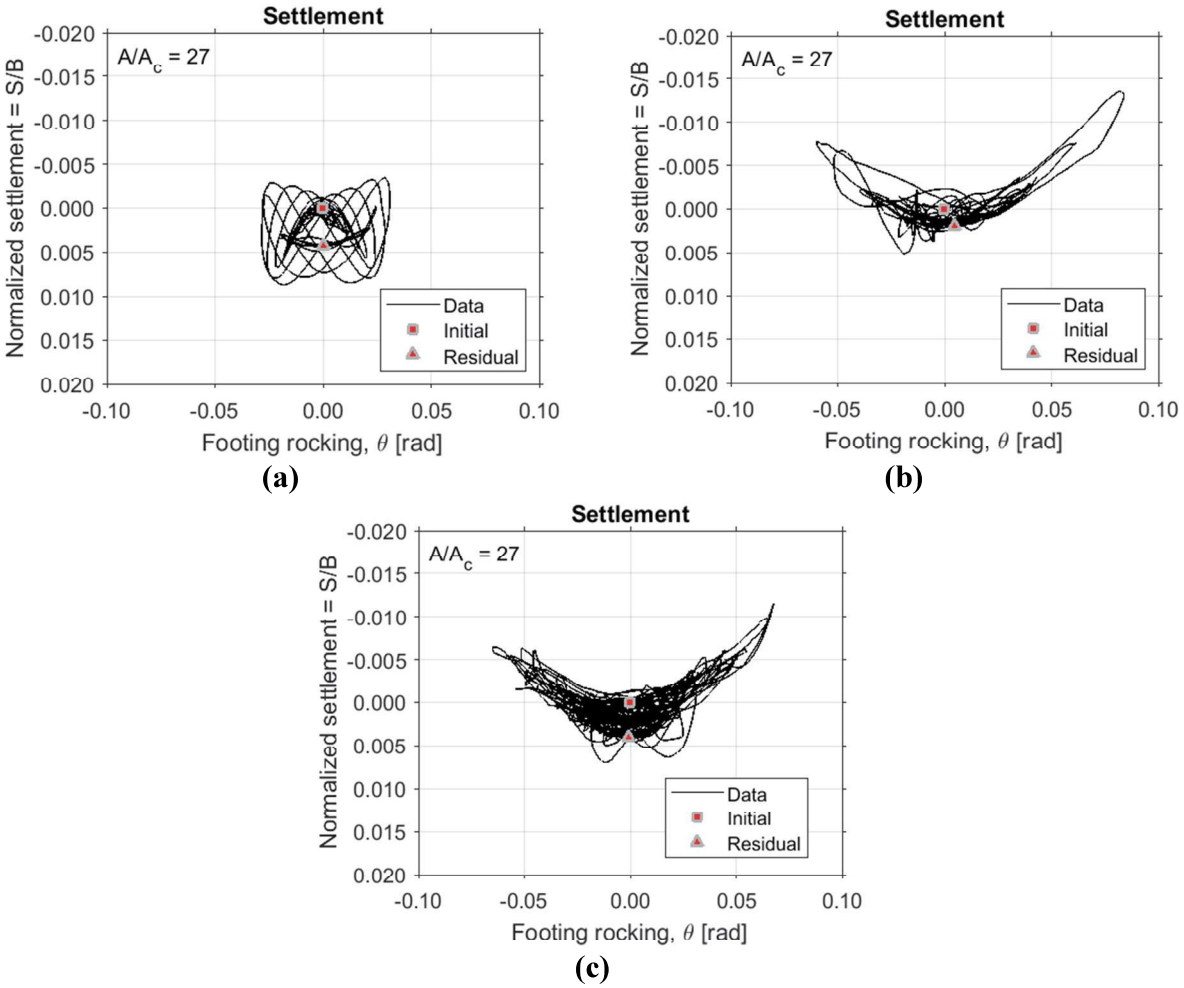

Figure 6.37 Settlement-rocking response during (a) DT02-SS20-F04F10; (b) DT02-NOR-100P; (c) DT02-MAU-100P.

The transient experimental results show that the specimen DT02 experiences temporary settlement and uplift when oscillating. Temporary settlement is observed when the specimen is in a centered position while temporary uplift is experienced when the specimen has its peak oscillations to the north and south. Once the base excitation has ended, the generated residual settlement is small, as shown in Figure 6.37. It is also observed that the sine sweep motion DT02-SS20-F04F10 generates as much settlement than earthquake motion DT02-MAU-100P. No residual uplift is observed.

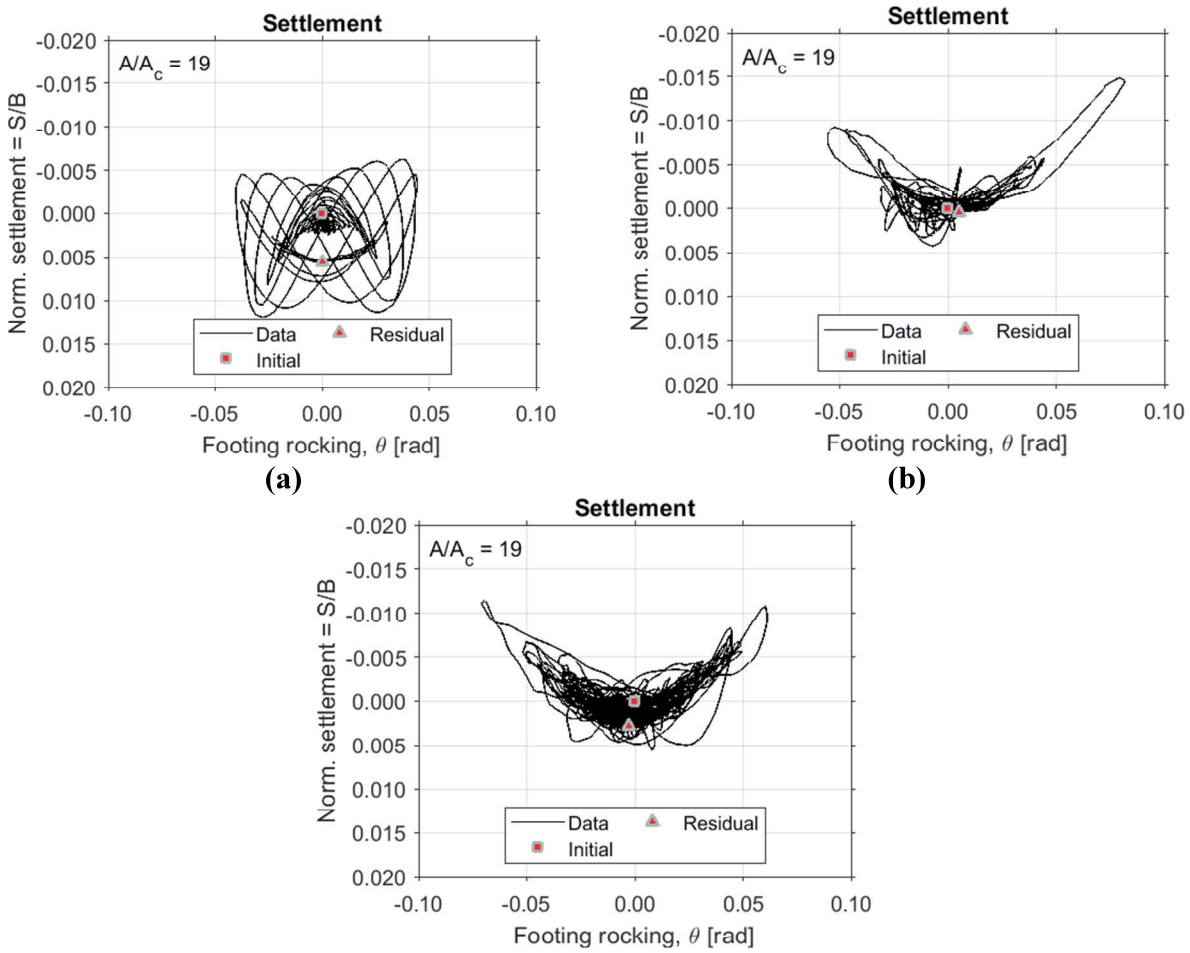

Figure 6.38 Settlement-rocking response during (a) DT03-SS24-F04F10, (b) DT03-NOR-100P; (c) DT03-MAU-100P.

The transient experimental results show that specimen DT03 is similar to specimen DT01 and DT02 because it experiences temporary settlement and uplift when oscillating. Temporary settlement is observed when the specimen is in a centered position while temporary uplift is experienced when the specimen has its peak oscillations to the north and south. Once the base excitation has ended, the generated residual settlement is small, as shown in Figure 6.38. It is also observed that the sine sweep motion DT03-SS24-F04F10 generates more settlement than both earthquake motions. No residual uplift is observed. Overall, the settlement-rocking response for all studied specimens in this project indicates moderate transient settlement and uplift but significantly small residual settlement after each motion. The relationship between normalized settlement and rocking response during the entire testing protocol of each testing is shown in Figure 6.39.

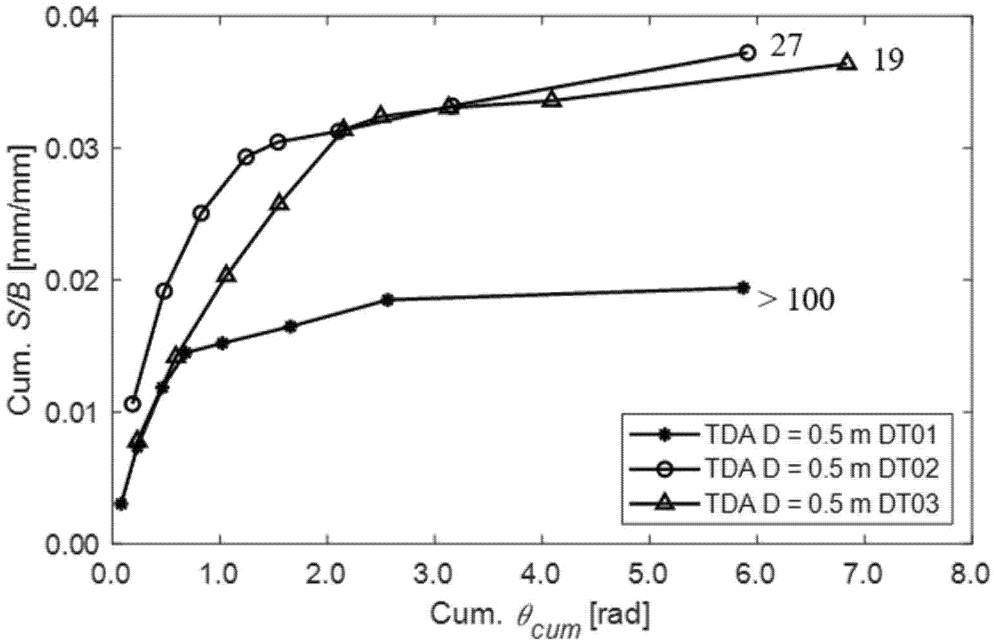

Figure 6.39 Progression of normalized settlement – cumulative rocking response for each dynamic test. The labels correspond to the A/A_c values.

The relationship between normalized settlement and rocking response indicates that even at higher rocking demands of 6.8 rad, the cumulative settlement is still small. The results indicate that the footing settles more during the first motions, which are the sine sweep motions. The studied earthquake motions, which are the last four data points of each specimen, show overall less settlement than the sweep motions. These results could be produced for a couple of reasons. The first reason is that the sine-sweep motions overall generate slightly larger rocking moments than the earthquake motions, as shown in Figures 6.33 – 6.35. The second reason is that shaking and the applied stress induce densification of the TDA layer during each motions which generates a stiffer bearing material hence lower settlement. Multiple studies evaluate the settlement rocking response in terms of the incremental settlement and rocking induced by each motion (Deng et al. 2012, Hakhamaneshi 2014, and Sharma and Deng 2018). Therefore, this study follows the same approach considering only the earthquake motions with the purpose of decreasing the effect of densification of the TDA layer after each motion, as shown in Figure 6.40. A regression best-to-fit linear trend is fitted to each specimen. The slope of the line is known as the dynamic coefficient of settlement.

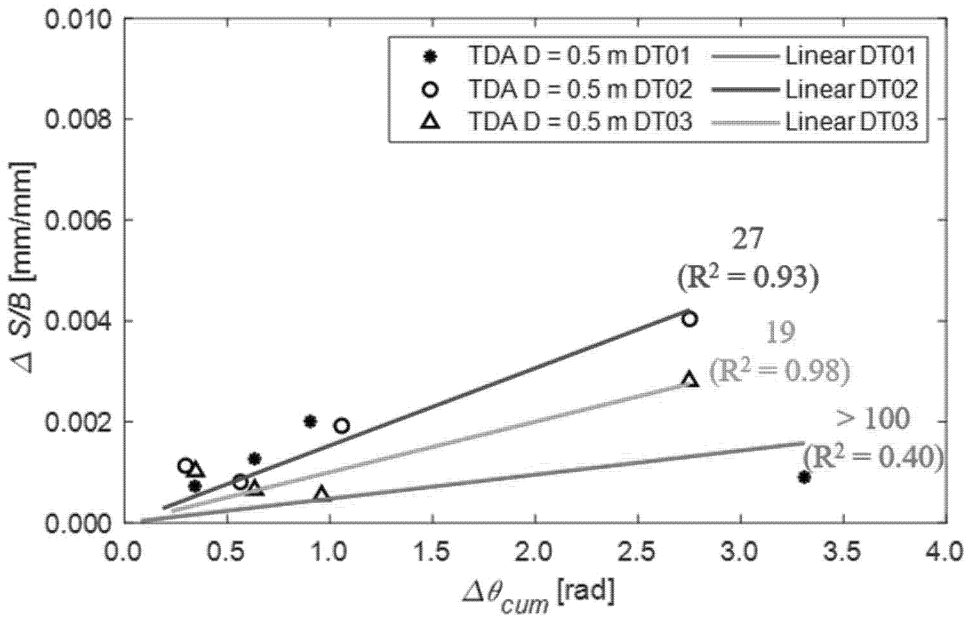

Figure 6.40 Incremental normalized settlement – cumulative rocking response for each dynamic test. The labels correspond to the A/A_c values.

Overall, specimen DT02 exhibited the highest settlement, while specimen DT01 had the lowest settlement, as depicted in Figure 6.40. The R^2 values for all specimens displayed satisfactory correlation, except for DT01. Surprisingly, DT02 experienced slightly more settlement than DT03, contrary to what was expected. According to Deng et al. (2012), the lower the A/Ac value, the more settlement is expected. This unusual trend may be attributed to the fact that the A/Ac values were calculated based on estimated TDA properties specific to this study. In other words, the A/Ac values depend on the weight of the footing-structure specimen and the strength properties of the bearing material. Although DT02 and DT03 had similar footing-structure weights, they differed slightly in their estimated TDA properties, which could explain this unexpected pattern. It is also important to highlight that the settlement difference between DT02 and DT03 under the maximum rocking demand is extremely minimal, measuring only 0.5 mm. Conducting further testing and investigation could provide more clarity on these results. The dynamic coefficients of settlement for specimens DT01, DT02, and DT03 are 0.0005, 0.0015, and 0.010, respectively. The experimental results of this study are compared to published studies developed in conventional soils in non-embedded conditions, as shown in Figure 6.41, and embedded conditions, as shown in Figure 6.42. This study evaluates specimens with A/Ac in the high range (19, 27, and >100) but the comparison is still conducted as a reference baseline.

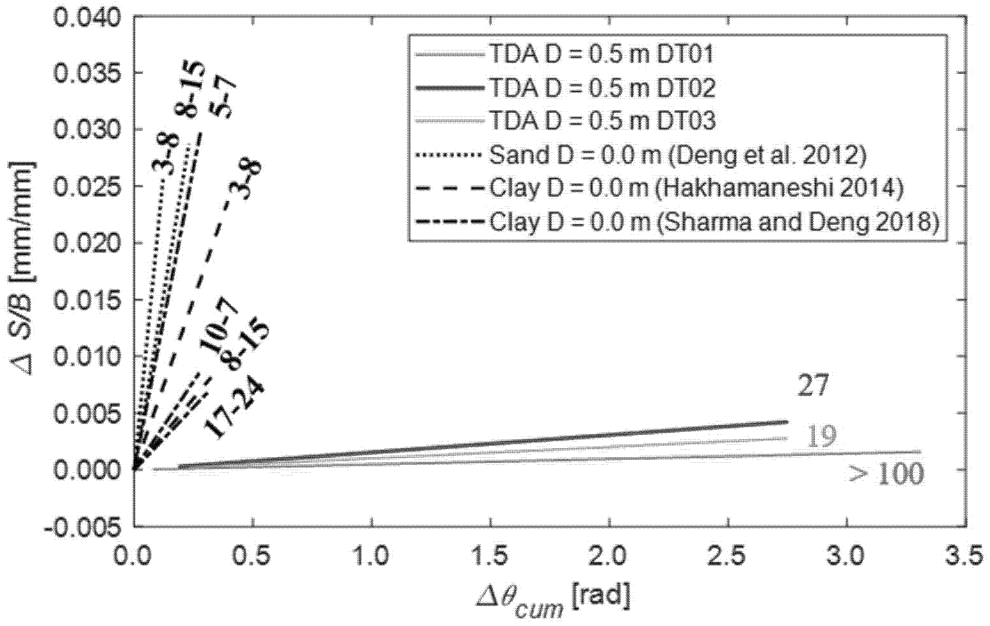

Figure 6.41 Comparison of the incremental normalized settlement – cumulative rocking response of the footing on top of Type B TDA versus published literature of conventional soils with zero embedment. The labels correspond to the A/A_c values.

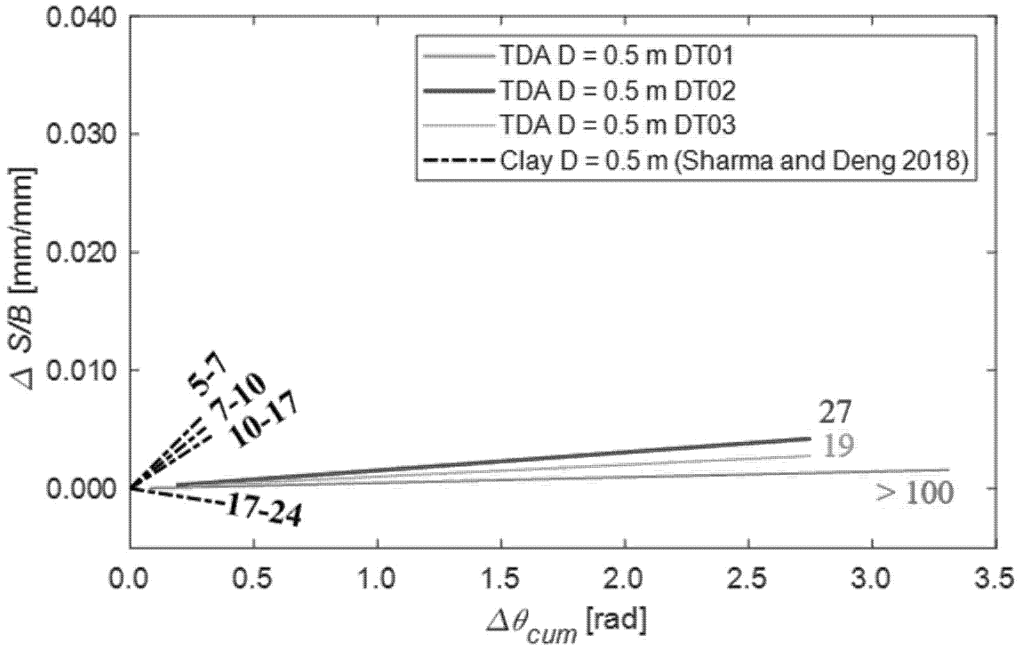

Figure 6.42 Comparison of the incremental normalized settlement – cumulative rocking response of the footing on top of Type B TDA versus published literature of conventional soils with similar embedment. The labels correspond to the A/A_c values.

The comparison of the experimental results with published studies for embedded footings indicates that the embedded footing on TDA still settles drastically less than clay and sand even at larger rocking demands, as illustrated in Figures 6.41 and 6.42. Another interesting observation is that none of the TDA specimens experienced uplift, even in cases where specimens with similar A/A_c values would typically exhibit uplift in clay material. Sharma and Deng (2018) stated that the uplift is generated by collapsing soil from the side of the footing into the base of the footing when oscillating. During testing, it was observed that the TDA particles do not collapse even when the footing was induced to maximum rocking. This mechanism alleviated the uplift that affected the specimen in clay from Sharma and Deng (2018).

6.4.4 Recentering response

As previously shown in the moment-rocking results subsection, the residual footing rocking after each motion was significantly small. These results can be translated to a variable defined by Deng et al. (2014) and known as re-centering ratio R_d , which is calculated following Eq 6.13.

$$R_d = 1 - \frac{\theta_{res}}{\theta_{cum}} \qquad \textbf{Eq. 6. 13}$$

where θ_{res} is the residual footing rocking, and θ_{cum} is the cumulative footing rocking. The re-centering mechanism is attributed to the gap closure when the moment demand has ended. A R_d value of 1.0 indicates null residual rocking, thus, a perfect re-centering system. Deng et al. (2014) proposed an empirical equation to estimate R_d based on the A/Ac value. The results from this study are compared with the estimated R_d, as shown in Figure 6.43, using the empirical Deng et al. (2014) equation (Eq. 6.14):

$$R_d = \frac{1}{2.055\frac{A_c}{A} + 1.015} \qquad \textbf{Eq. 6. 14}$$

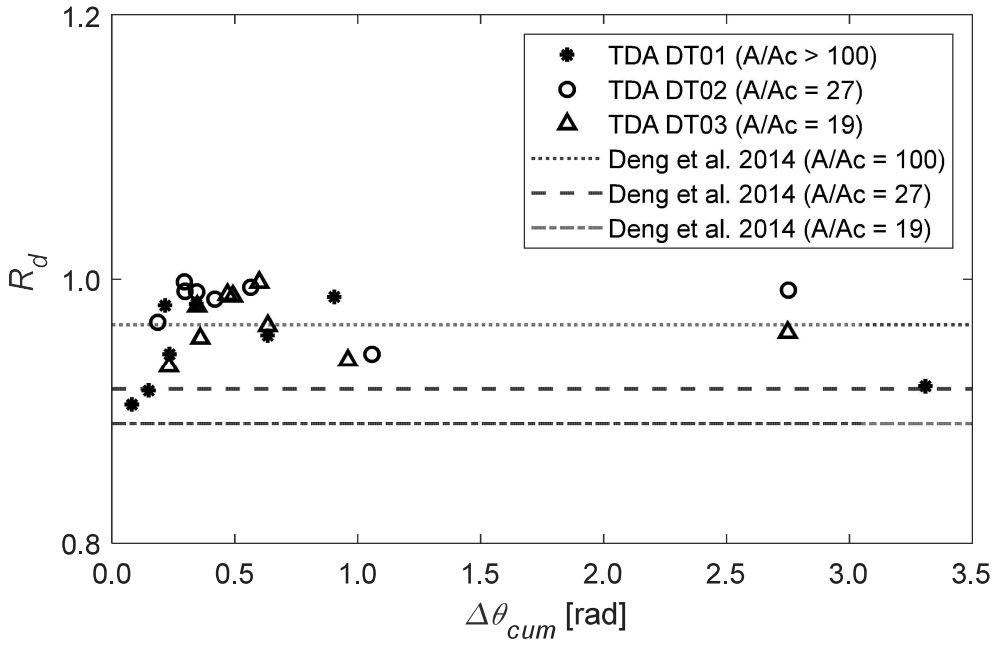

Figure 6.43 Comparison of re-centering rations with empirical equation proposed by Deng et al. (2014)

The re-centering ratios obtained from the study demonstrate that the use of TDA resulted in an impressive average re-centering ratio of 0.97, indicating a near-perfect re-centering mechanism for shallow footings, as shown in Figure 6.43. When compared to conventional soils, TDA exhibits superior re-centering capacity for A/Ac values of 19 and 27. However, for A/Ac values larger than 100, the re-centering capacity of TDA is relatively lower. These findings suggest that a heavier footing-structure specimen on TDA is less prone to overturning than a lighter footing-structure specimen.

6.5 Final Comments from Seismic Testing Program

In summary, Type B TDA provides enhanced performance for shallow foundations under seismic conditions, surpassing conventional soil alternatives. Its notable advantages include reduced residual settlement and superior re-centering capabilities. The results from these experiments indicate that Type B TDA shows promise to serve well as a low-cost geotechnical seismic isolation system for structures.

7. CONCLUSIONS

7.1 One-dimensional compression conclusions

The one-dimensional compression behavior of the Type B TDA yields a non-linear stress-strain relationship during loading and unloading. The computed compression and recompression indices for a fitted bi-log-linear compression curve are 0.32 and 0.04, respectively, but the bi-log-linear model was found to have a shortcoming in the need to define an apparent yield stress. Alternatively, a hyperbolic model was fitted to the compression curve, which was found to provide a good match with the data. The hyperbolic model parameters correspond well with those obtained from compression tests on Type B TDA performed in smaller containers. Overall, the results suggest that Type B TDA may be less beneficial than conventional soils in scenarios where settlements need to be limited, unless an overbuild strategy is used. The investigation of the short-term creep behavior of Type B TDA indicated that the volume of the material decreases over time with the highest volumetric strain change occurring during the first minutes of constant load application. The results allowed the computation of the secondary compression index as 0.0029, which is consistent with that measured for Type A TDA in previous studies. Overall, the findings suggest that Type B TDA experiences less time-dependent settlement compared to conventional soils. However, it is important to note that the time-dependent settlement testing was limited to one hour, and further investigation is required to apply these findings in practical applications.

7.2 Quasi-static testing program conclusions

When subjected to quasi-static vertical or inclined footing stresses, the Type B TDA exhibited a punching shear failure mechanism typical of high-compressibility soils. It is known that the ultimate bearing capacity of materials with a punching shear failure mechanism is challenging to characterize because the bearing stress continues to increase with continued footing settlements. This study found that the ultimate bearing capacity from the experiments at the point of excess tilting correlates well with the predicted bearing capacity from an equation that considers the effects of embedment, size, shape, and loading inclination. In addition, this study provides a correlation equation to predict the bearing stress at a settlement corresponding to 10% of the width of the footing, which may be more practical for engineering designs. TDA has high bearing capacity in general compared to granular soils, but it also has much higher ductility, indicating its potential usefulness in situations where larger settlements are permitted.

7.3 Dynamic testing program conclusions

The system identification results indicated that Pais and Kausel (1988) model underestimates the fundamental period of the flexible base structure by 40% when using Type B TDA. It was also observed that the period lengthening of the footing-structure system is independent of the TDA thickness. The fundamental period of Type B TDA under free field conditions increases with the thickness of the layer, following the same mechanism as conventional soils. Type B TDA introduces substantial nonlinearity into the moment-rocking response of the footing. The system experiences rocking stiffness softening at moment demands that are slightly below its moment capacity. Nonetheless, the findings suggest that estimating the moment capacity using the weight of the footing and superstructure, as well as the A/A_c value, can still serve as a useful baseline reference when employing a Type B TDA. Type B TDA exhibits moderate transient settlement and uplift of the footing during dynamic oscillation. However, it demonstrates remarkably low residual settlement after each motion. Type B TDA further mitigates residual uplift due to the absence of collapse in the TDA adjacent to the sides of the footing during rocking. Moreover, Type B TDA offers the footing an exceptionally effective re-centering system, as evidenced by an average re-centering ratio of 0.97. surpassing the typical ratios observed in conventional soils for the studied A/Ac values. In summary, Type B TDA offers improved performance, in terms of reduced residual settlement and effective re-centering capabilities, for shallow foundations subjected to seismic demands compared to conventional soils.

8. REFERENCES

Adesokan, D., Fleming, I., and Hammerlindl, A. (2020). "One-dimensional (1D) immediate compression and creep in large particle-sized tire-derived aggregate (TDA) for leachate collection and removal systems (LCRSs)". *Can. Geotech. J.* 58: 982-994.

Ahn, I.-S., and Cheng, L. (2014). "Tire derived aggregate for retaining wall backfill under earthquake loading." *Construction and Building Materials*. 57, 105-116.

Anastasiadis, A., Senetakis, K., and Pitilakis, K. (2012a). "Small strain shear modulus and damping ratio of sand/rubber and gravel/rubber mixtures." *J. Geotech. Geol. Eng.*, 30(2), 363–382.

Anastasiadis, A., Senetakis, K., Pitilakis, K., Gargala, C., and Karakasi, I. (2012b). "Dynamic behavior of sand/rubber mixtures. 1: Effect of rubber content and duration of confinement on small-strain shear modulus and damping ratio." *J. ASTM Int.*, 9(2), 1–19.

Arefnia, A., Dehghanbanadaki, A., and Kassim, K.A. (2021). “Ultimate bearing capacity of strip footing resting on clay soils mixed with tire-derived aggregates”. *Front. Struct. Civ. Eng*. 15(4): 1016-1024.

CalRecycle (California Department of Resources Recycling and Recovery) (2016). “California waste tire market report: 2015.” *DRRR 2016-01567*, Sacramento, CA.

Chenari, J. R., Fatahi, B., Akhavan Maroufi, M.A., and Alaie, R. (2017). “An experimental and numerical investigation into the compressibility and settlement of sand mixed with TDA”. *Geotech. Geol. Eng*. 35: 2401-2420.

Deng, L., Kutter, B.L., Kunnath, S.K. (2014). “Seismic design of rocking shallow foundations: a displacement-based methodology”. *Journal of Bridge Engineering*, 19(11): 1-11.

Drescher, A., and Newcomb, D.E. (1994). “Development of design guidelines for use of shredded tires as a lightweight fill in road subgrade and retaining walls.” *Report No. MN/RC-94/04*, Dept. of Civil and Mineral Engineering, Univ. of Minnesota, Minneapolis.

Drnevich, V. (1975). “Constrained and shear moduli for finite elements.” *Journal of the Geotechnical Engineering Division*, 101, (5), 459–473.

Edeskar, T. (2004) “Technical and environmental properties of tire shreds focusing on ground engineering applications.” *Report SE-971 87*. Lulea, Dept. of Civil and Mining Engineering, Lulea University., Lulea, Sweden.

El Naggar, H., Soleimani, P., and Fakhroo, A. (2016). “Strength and stiffness properties of green lightweight fill mixtures”. *Geotech. Geol. Eng*. 34, 867–876.

Federal Emergency Management Agency (FEMA) (2007). FEMA 461: Interim testing protocols for determining the seismic performance characteristics of structural and nonstructural components. Prepared by the Applied Technology Council in cooperation with the Mid-America Earthquake Center, the Multidisciplinary center for earthquake engineering research, and the Pacific Earthquake Engineering Research Center.

Feng, Z.Y., and Sutterer, K.G. (2000). “Dynamic properties of granulated rubber/sand mixtures.” Geotechnical Testing Journal. 23(3), 338–344.

Fox, P.J., Thielmann, S.S., Sanders, M.J., Latham, C., Ghaaowd, I., and McCartney, J.S. (2018). “Large-scale combination direct shear/simple shear device for tire-derived aggregate.” *ASTM Geotechnical Testing Journal*. 41(2), 340-353. DOI: 10.1520/GTJ20160245.

Fukuwa, W., Ali Gahnnad, M., Tobita, J., and Nishizaka, R. (1998). "Analytical and experimental studies in effect of soil-structure interaction on damping, natural frequency, and effective input motion of buildings". *UNJR Workshop on Soil-Structure Interaction*, Menlo Park, CA. 14-1-14-5.

Ghaaowd, I. and McCartney, J.S. (2020). "Pullout of geogrids from tire derived aggregate with large particle size." *Geosynthetics International*. 27(6): 671-684. 10.1680/jgein.20.00009.

Ghaaowd, I. Fox, P.J. and McCartney, J.S. (2020). "Shearing behavior of the interfaces between tire derived aggregate and three soil materials." 32(6): 04020120 *Journal of Materials in Civil Engineering*. 10.1061/(ASCE)MT.1943-5533.0003213.

Ghaaowd, I., McCartney, J.S., Thielmann, S., Sanders, M. and Fox, P.J. (2017). "Shearing behavior of tire derived aggregate with large particle sizes. I: Internal and concrete interface direct shear behavior." *ASCE Journal of Geotechnical and Geoenvironmental Engineering*. 143(10), 04017078. DOI: 10.1061/(ASCE)GT.1943-5606.0001775.

Hansen, J. B. (1970). "A revised and extended formula for bearing capacity". *Danish Geotechnical Institute*, 28: 5-11.

Hoppe, E.J. (1994). "Field study of shredded-tire embankment." *Report No. FHWA/VA-94-IR1*, Virginia Dept. of Transportation, Richmond, VA.

Humphrey, D.N. (2008). *Civil Engineering Application of Tire Derived Aggregate*. Alberta Recycling Management Authority, Edmonton, AB, Canada.

Humphrey, D.N. (2008b). "Tire derived aggregate as lightweight fill for embankments and retaining walls." *Scrap Tire Derived Geomaterials – Opportunities and Challenges*. Hazarika and Yasuhara (eds). Taylor and Francis, London. 59-81.

Madhusudhan, B. R., Boominathan, A., and Banerjee, S. (2017). "Static and large-strain dynamic properties of sand-rubber tire shred mixtures". *J. Mater. Civ. Eng.*, 29(10): 04017165.

Mahgoub, A., and El Naggar, H., (2020). "Shallow foundation on lightweight TDA backfill: Field tests and 3D numerical modelling". *Computers and Geotechnics* 126 - 103761

Mahgoub, A., and El Naggar, H., (2022). "Using TDA underneath shallow foundations: simplified design procedure". *International Journal of Geotechnical Engineering*, 16(7): 787-801.

Mashiri, M. S., Sheikh, M., Neaz, V. J., and Tsang, H. (2013). "Dynamic properties of sand-tire chip mixtures." *Australian Earthquake Engineering Society Conf., S. Anderson, ed., Australian Earthquake Engineering Society*, Mckinnon, VIC, Australia, 1–8.

McCartney, J.S., Ghaaowd, I., Fox, P.J., Sanders, M., Thielmann, S., and Sander, A. (2017). "Shearing behavior of tire derived aggregate with large particle sizes. II: Cyclic simple shear behavior." *ASCE Journal of Geotechnical and Geoenvironmental Engineering*. 143(10): 04017079. DOI: 10.1061/(ASCE)GT.1943-5606.0001781.

Meles, D., Bayat, A., and Chan, D. (2014). "One-dimensional compression model for tire-derived aggregate using large-scale testing apparatus." *International Journal of Geotechnical Engineering*, 8:2, 197-204, DOI: 10.1179/1939787913Y.0000000019.

Mills, B., and McGinn, J. (2010). "Design, construction, and performance of highway embankment failure repair with tire-derived aggregate." *Transportation Research Record 1345,* Transportation Research Board, Washington, DC, 90–99.

Nakhaei, A., Marandi, S.M., Sani Kermani, S., and Bagheripour, M.H. (2012). "Dynamic properties of granular soil mixed with granulated rubber." *Soil Dyn. Earthquake Eng*., 43: 124–132.

National Institute of Standards and Technology (NIST) (2012). *Soil-Structure Interaction of Building Structures*. NIST GCR 12-917-21, developed by NEHRP Consultants Joint Venture.

Nikitas, G., and Bhattacharya, S. (2023) "Experimental study on sand-tire chip mixture foundations acting as a soil liquefaction countermeasure". *Bulletin of Earthquake Engineering.*

Orang, M. J., Motamed, R., Prabhakaran, A., and Elgamal, A. (2021). "Large-scale shake table tests on a shallow foundation in liquefiable soils." *Journal of Geotechnical and Geoenvironmental Engineering* 147(1): 04020152.

Pais, A., and Kausel, E. (1988). "Approximate formulas for dynamic stiffness of rigid foundations". *Soil Dynamics and Earthquake Engineering*, 7(4): 213-227.

Pistolas, G. A., Pitilakis, K., and Anastasiadis, A. (2020). "A numerical investigation on the seismic isolation potential of rubber/soil mixtures." *Earthquake Eng. And Eng. Vibr.* 19: 683-704.

Salgado, R. (2022). *The Engineering of Foundations, Slopes and Retaining Structures* (2nd ed.). CRC Press. https://doi.org/10.1201/b22079

Senetakis, K., Anastasiadis, A., and Pitilakis, K. (2012a). "Dynamic properties of dry sand/rubber (SRM) and gravel/rubber (GRM) mixtures in a wide range of shearing strain amplitudes." *Soil Dyn. Earthquake Eng*., 33(1): 38–53.

Senetakis, K., Anastasiadis, A., Pitilakis, K., and Souli, A. (2012b). "Dynamic behavior of sand/rubber mixtures. II: Effect of rubber content on G=GO-γ-DT curves and volumetric threshold strain." *J. ASTM Int*., 9(2), 1–12.

Skempton, A.W. (1951). "The bearing capacity of clays." *Proc. Bldg. Res. Conf*., 1: 180-189.

Tandon, V., Velazco, D.A., Nazarian, S., and Picornell, M. (2007). "Performance monitoring of embankment containing tire chips: Case study." *J. Perform. Const. Fac.*, 21(3): 207–214.

Terzaghi, K. (1943). *Theoretical Soil Mechanics*. Wiley, New York. http://dx.doi.org/10.1002/9780470172766.

Trautner, C., Zheng, Y., McCartney, J.S., and Hutchinson, T. (2017). "An approach for shake table performance evaluation during repair and retrofit actions." *Earthquake Eng. Struct. Dyn*. 47: 131-146. https://doi.org/10.1002/eqe.2942.

Tsang, H., Lo, S. H., Xu, X., and Neaz Sheikh, M. (2012). "Seismic isolation for low-to-medium-rise buildings using granulated rubber-soil mixtures: numerical study." *Earthquake Eng. Struct. Dyn.* 41: 2009-2024.

Tsang, H., Tran, D., Hung, W., Pitilakis, K., and Gad, E.F. (2020). "Performance of geotechnical seismic isolation system using rubber-soil mixtures in centrifuge testing". *Earthquake Engineering & Structural Dynamics* 50: 1271-1289.

Tweedie, J.J., Humphrey, D.N., and Sandford, T.C. (1998). "Full scale field trials of tire shreds as lightweight retaining wall backfill, at-rest condition." *Proc. Transportation Research Board, Washington, DC.*

Vesic, A.S. (1963). "Bearing capacity of deep foundations in sand". *Highway Research Board*, 39: 112-153.

Vesic, A.S. (1973). "Analysis of ultimate loads on shallow foundations". *Journal of the Soil Mechanics and Foundation Division*, 99(1): 45-73.

Wartman, J., Natale, M. F., and Strenk, P.M. (2007). "Immediate and time-dependent compression of tire derived aggregate." *Journal of Geotechnical and Geoenvironmental Engineering* 133(3): 245–56. DOI: 10.1061/(ASCE)1090-0241(2007)133:3(245).

Xiao, M., Bowen, J., Graham, M., and Larralde, J. (2012). "Comparison of seismic responses of geosynthetically-reinforced walls with tire-derived aggregates and granular backfills." *J. Mater. Civil Eng.*, 24(11): 1368–1377. 10.1061/(ASCE)MT.1943-5533.0000514

Yarahuaman, A. and McCartney, J.S. (2022). "Seismic response of rail embankments." *Proc. GeoCongress 2022*. Charlotte. Mar. 20-23. GSP 336, ASCE, Reston, VA. 300-310. https://doi.org/10.1061/9780784484067.031.

Yarahuaman, A., and McCartney, J.S. (2023). "Large-scale testing of the static one-Dimensional Compression Response of Tire-Derived Aggregate." *Proc. Geo-Congress 2023*, 593–603. Los Angeles, California. ASCE. https://doi.org/10.1061/9780784484685.060.

Zayed, M., Ebeido, A., Prabhakaran, A., Qiu, Z., and Elgamal, A. (2020). "Asymmetric input motion for accumulation of lateral ground deformation in laminar container shake table testing". *Canadian Geotechnical Journal*. 58(2): 210-223. https://doi.org/10.1139/cgj-2018-0647.

Zheng, Y., Sander, A.C., Rong, W., Fox, P.J., Shing, P.B., and McCartney, J.S. (2017). "Shaking table test of a half-scale geosynthetic-reinforced soil bridge abutment." *ASTM Geotechnical Testing Journal*. 41(1): 171-192. DOI: 10.1520/GTJ20160268.

APPENDIX A – Quasi-static testing specimen No 01

A.1 - Instrumentation Layout for Quasi-static testing specimen No 01.

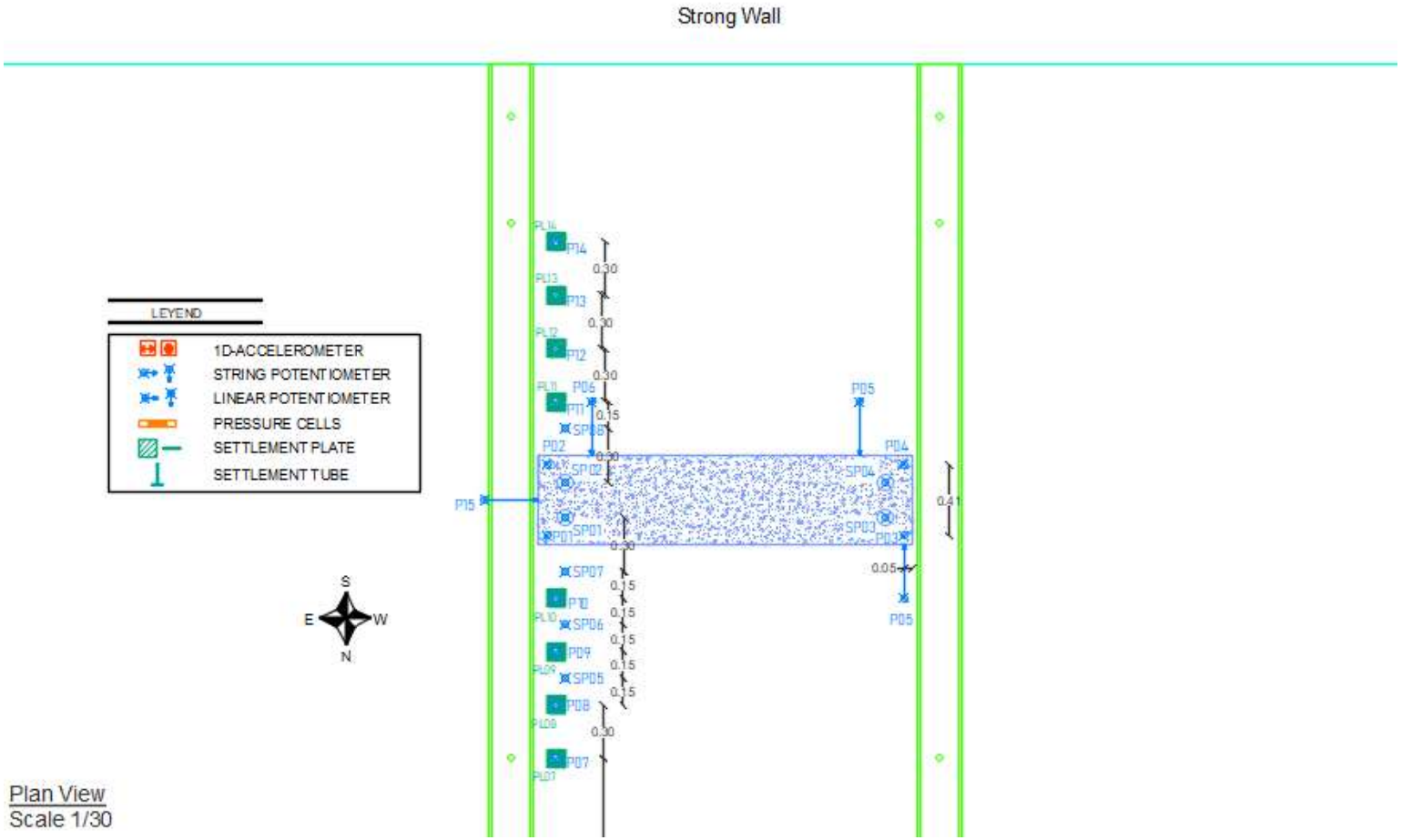

Figure A.1-1. Instrumentation Layout – Plan View.

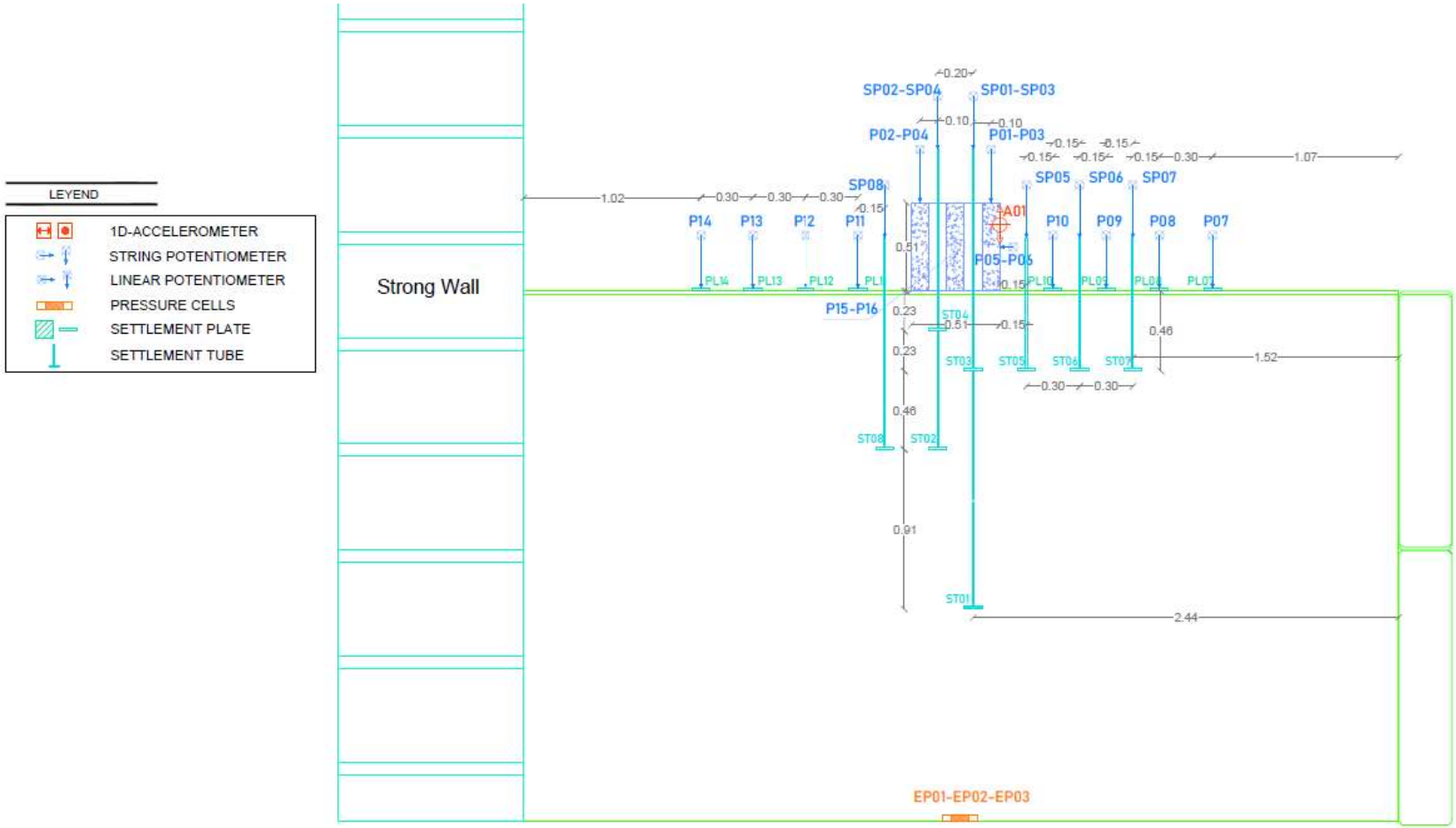

Figure A.1-2. Instrumentation Layout – Side View.

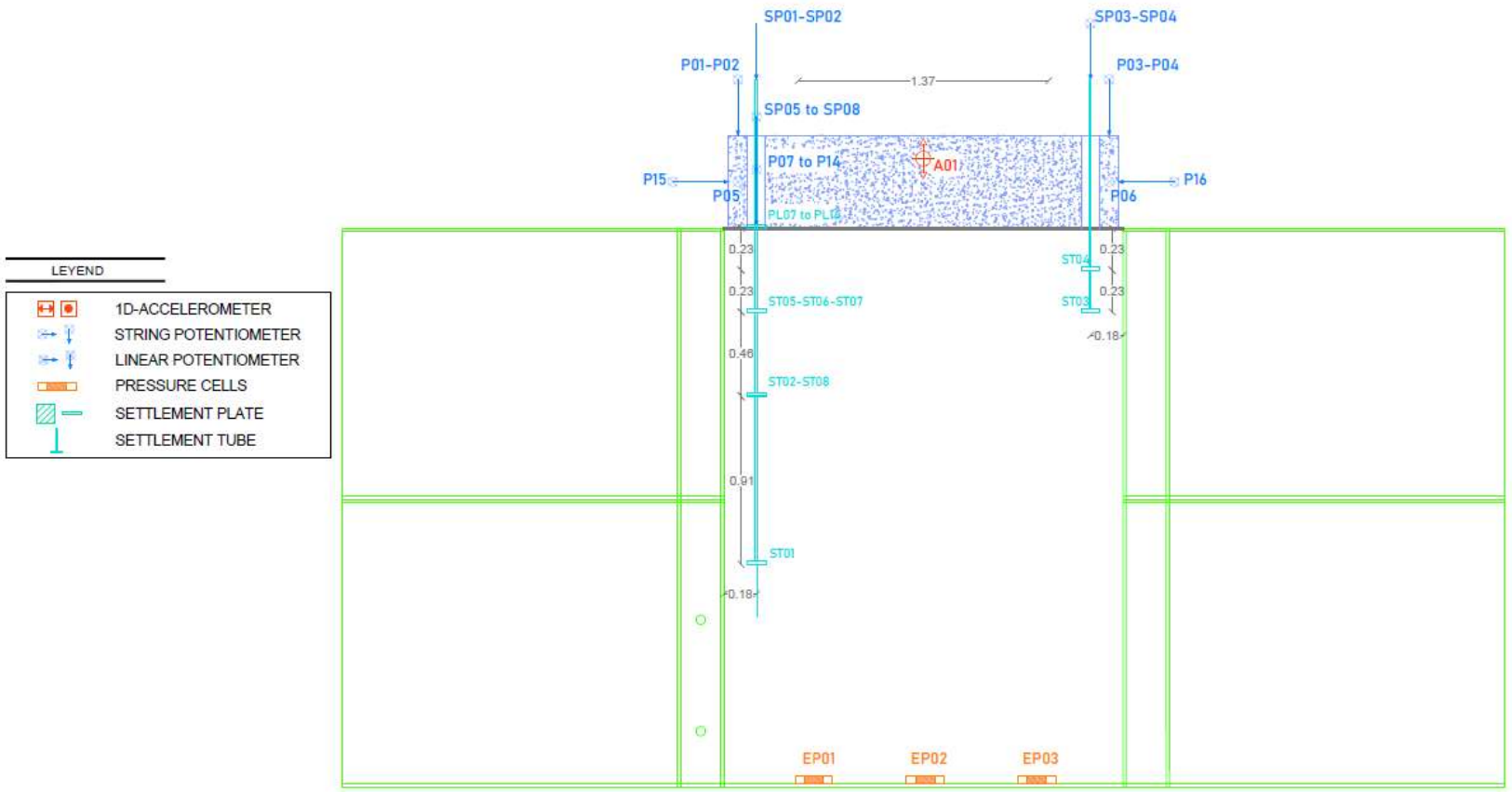

Figure A.1-3. Instrumentation Layout – Front View.

APPENDIX B – Quasi-static testing specimen No 02

B.1 - Instrumentation Layout for Quasi-static testing specimen No 02.

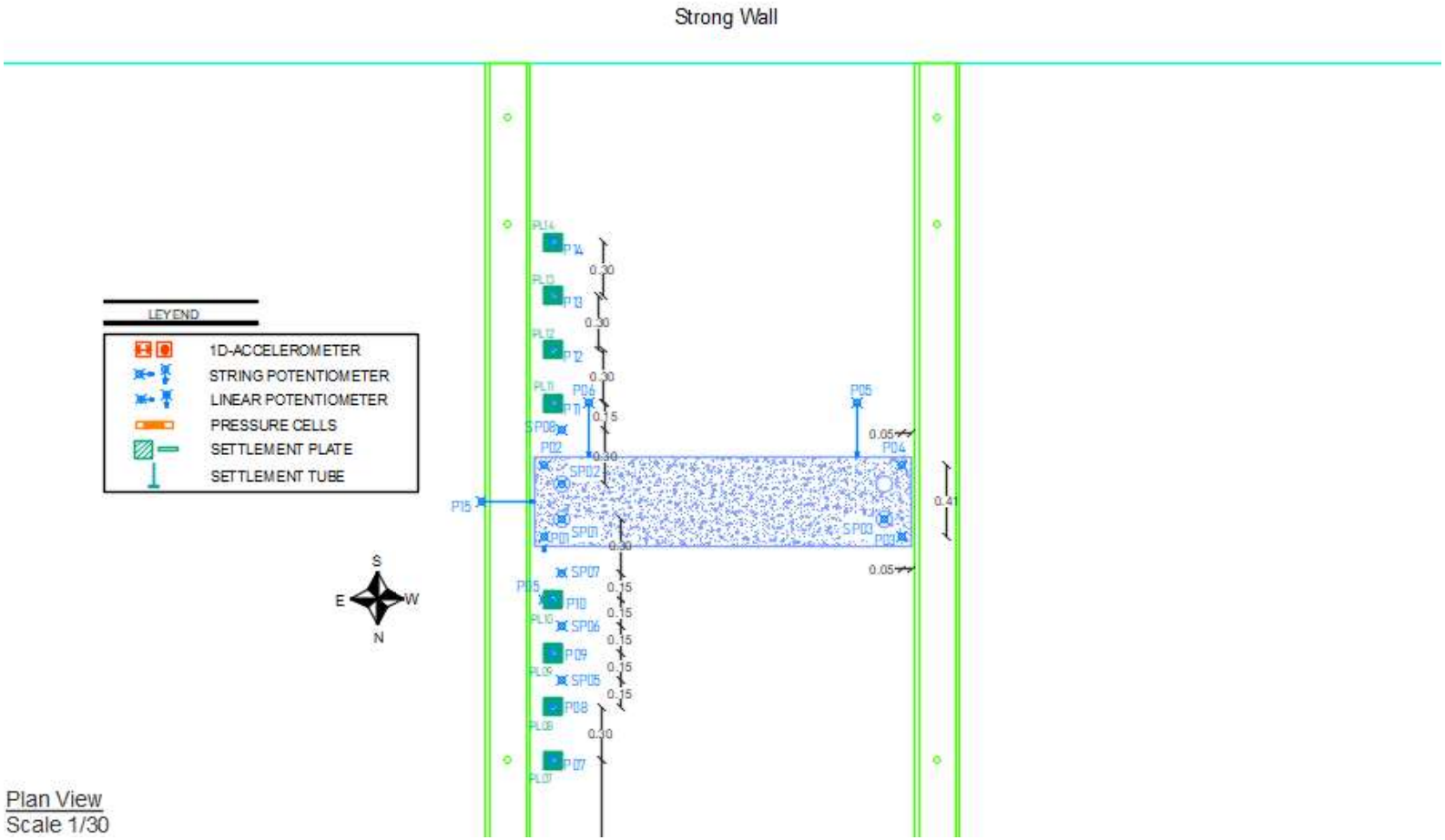

Figure B.1-1. Instrumentation Layout – Plan View.

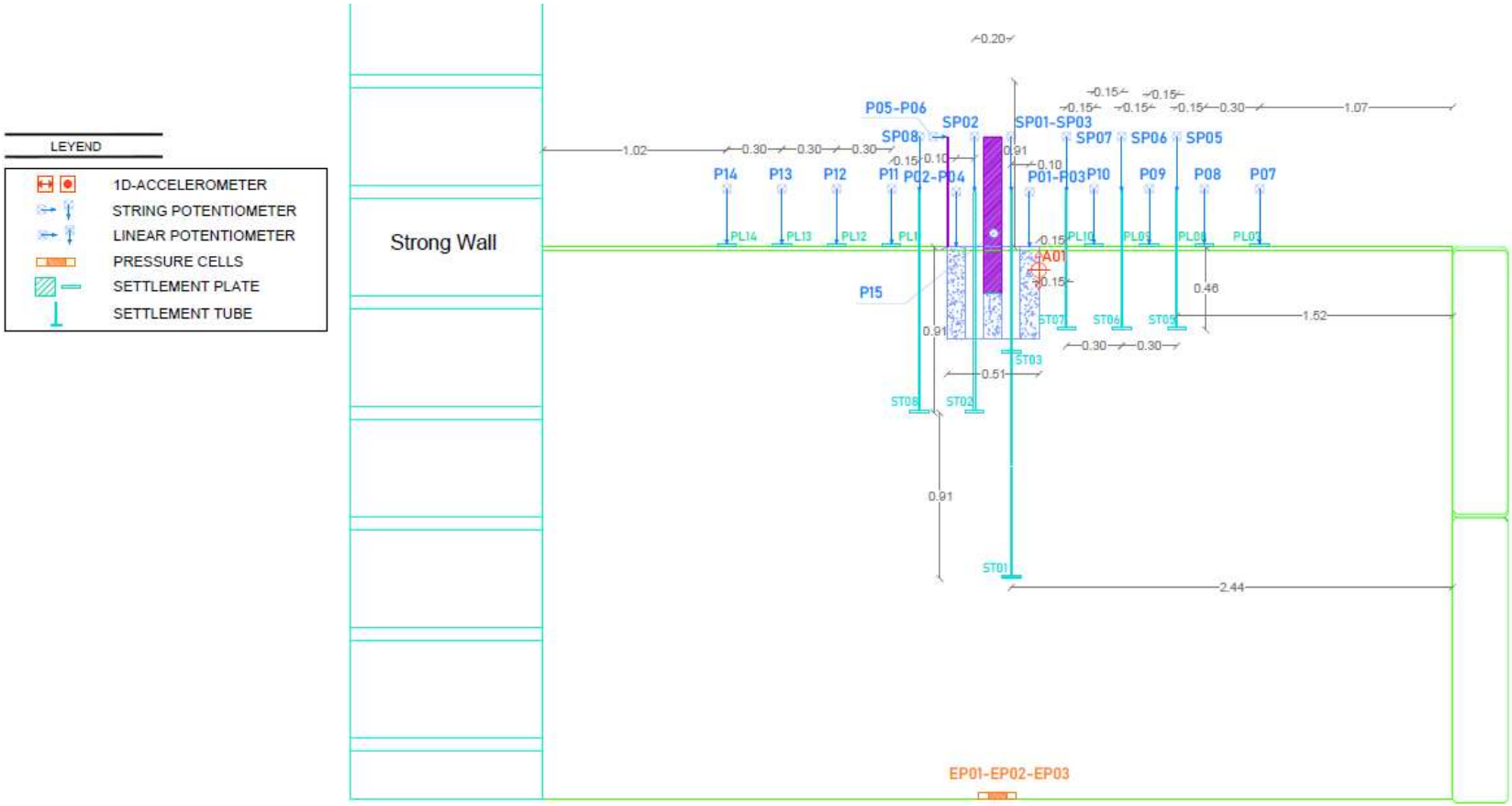

Figure B.1-2. Instrumentation Layout – Side View.

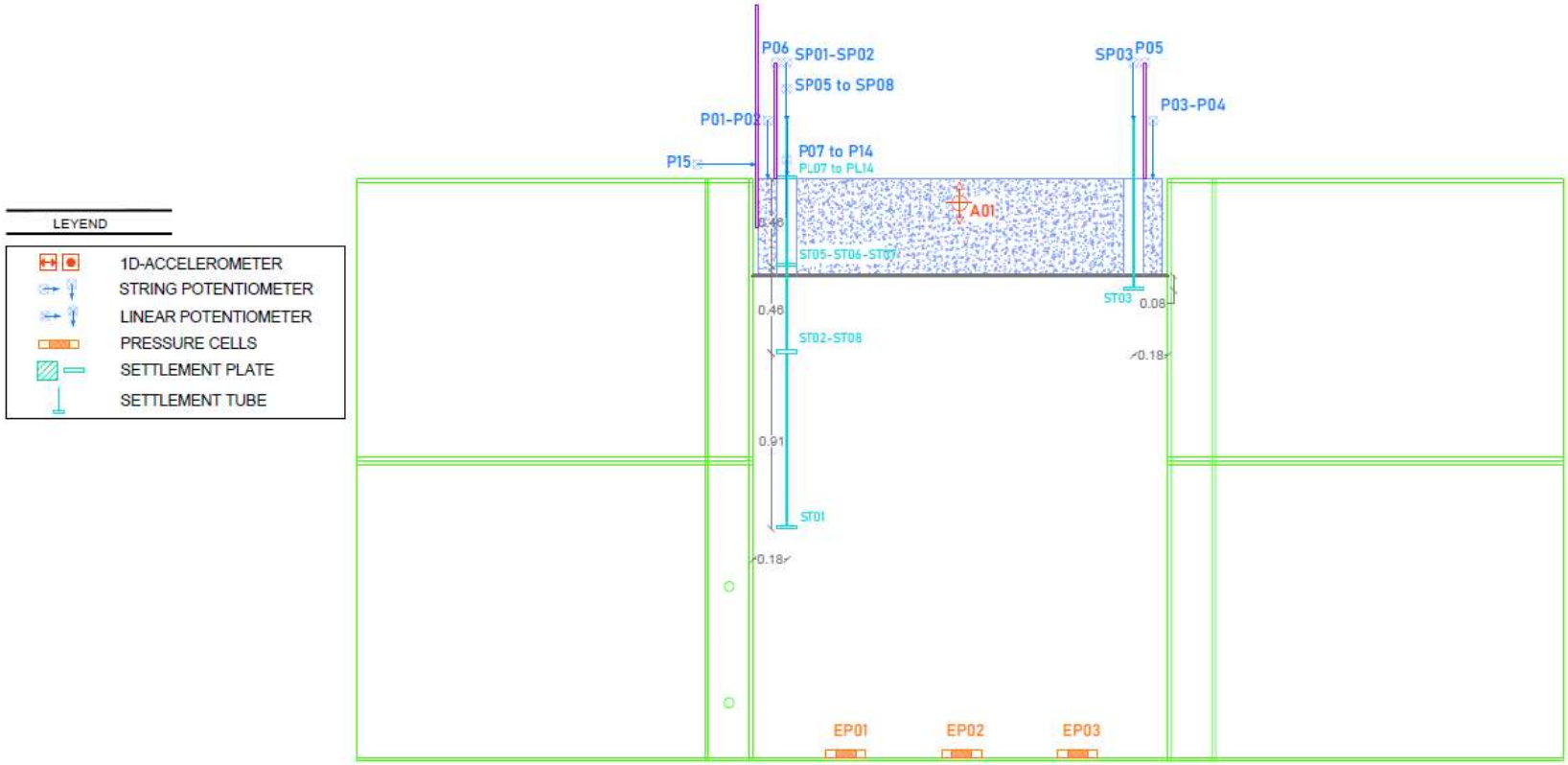

Figure B.1-3. Instrumentation Layout – Front View.

APPENDIX C – Quasi-static testing specimen No 03

C.1 - Instrumentation Layout for Quasi-static testing specimen No 03.

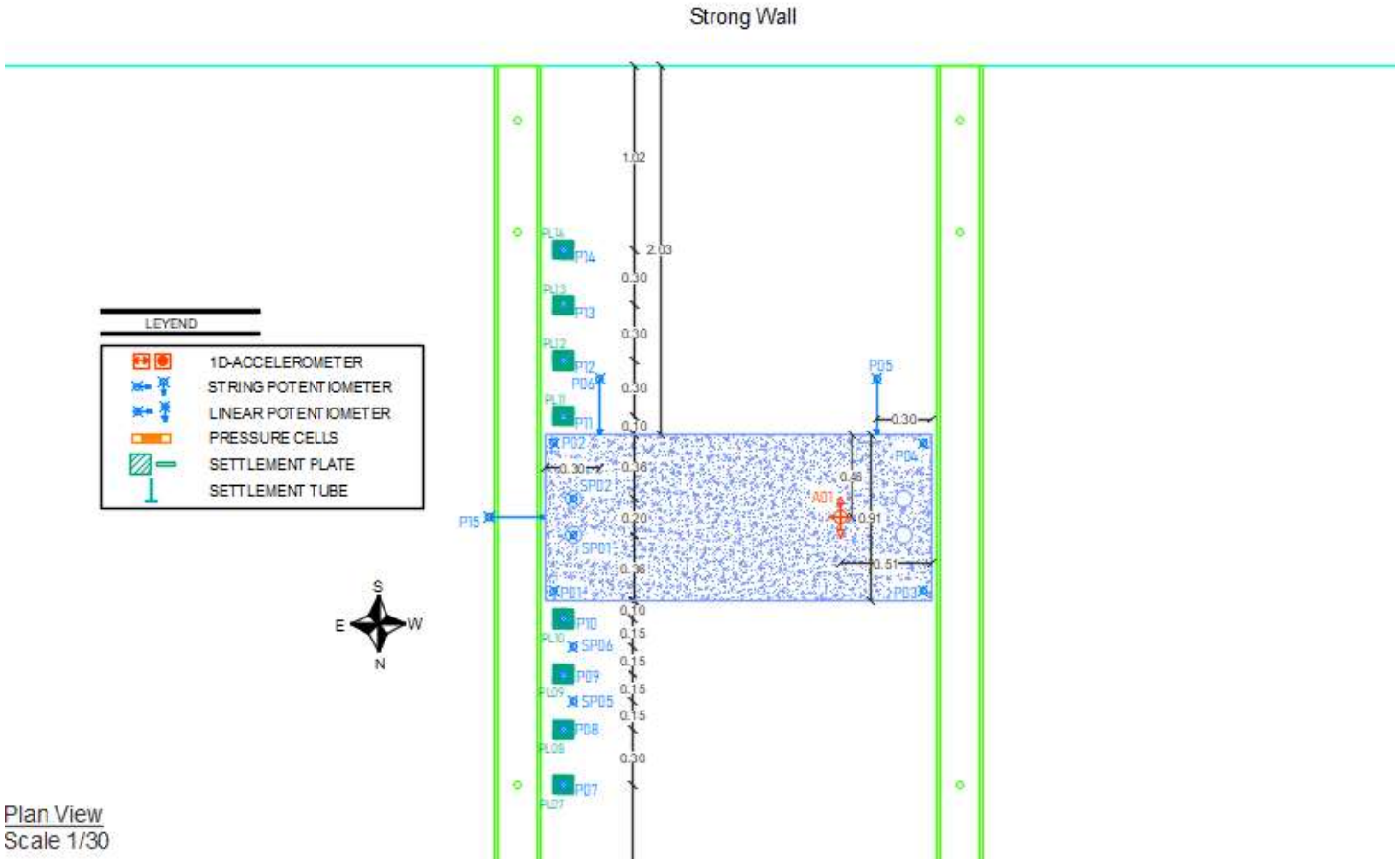

Figure C.1-1. Instrumentation Layout – Plan View.

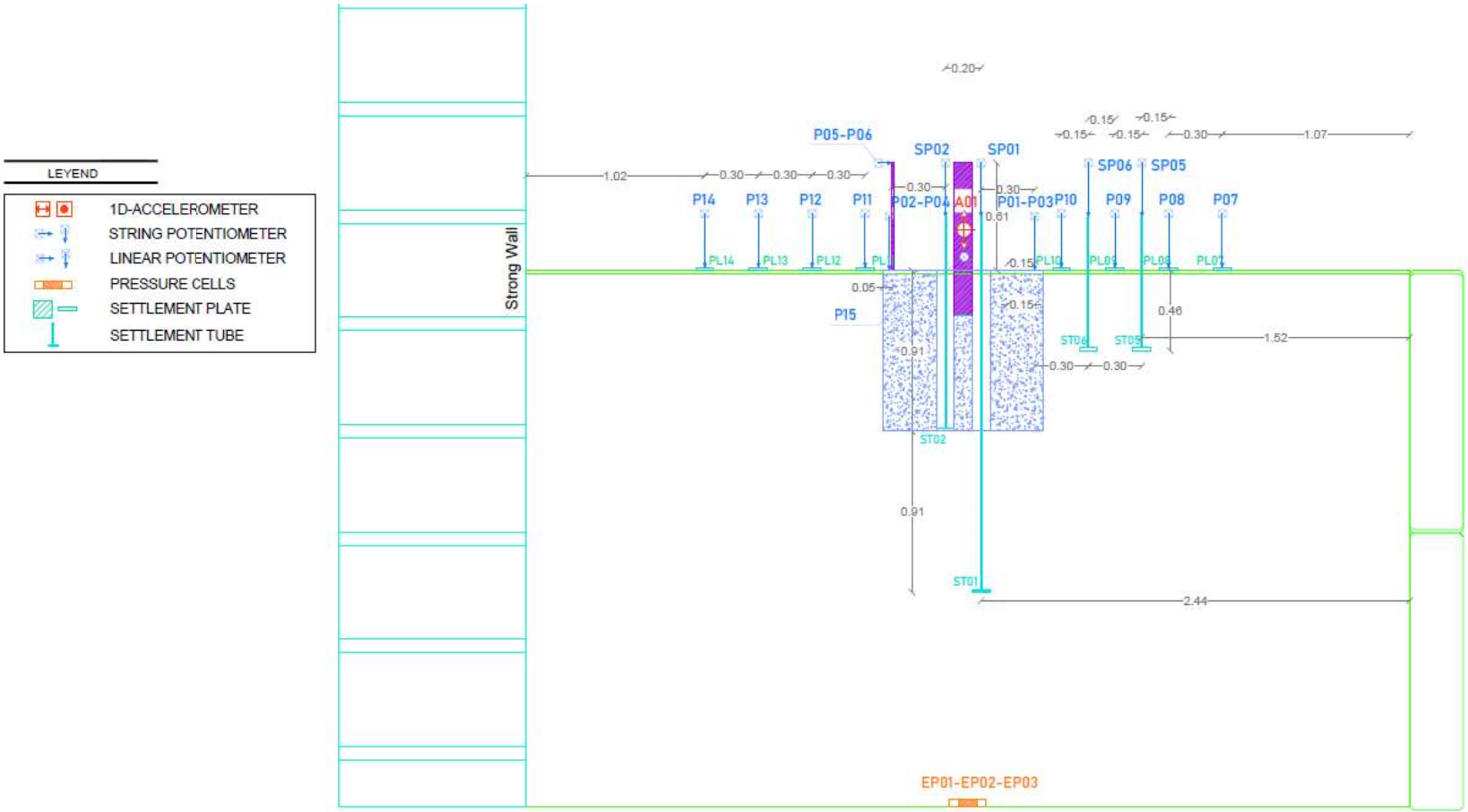

Figure C.1-2. Instrumentation Layout – Side View.

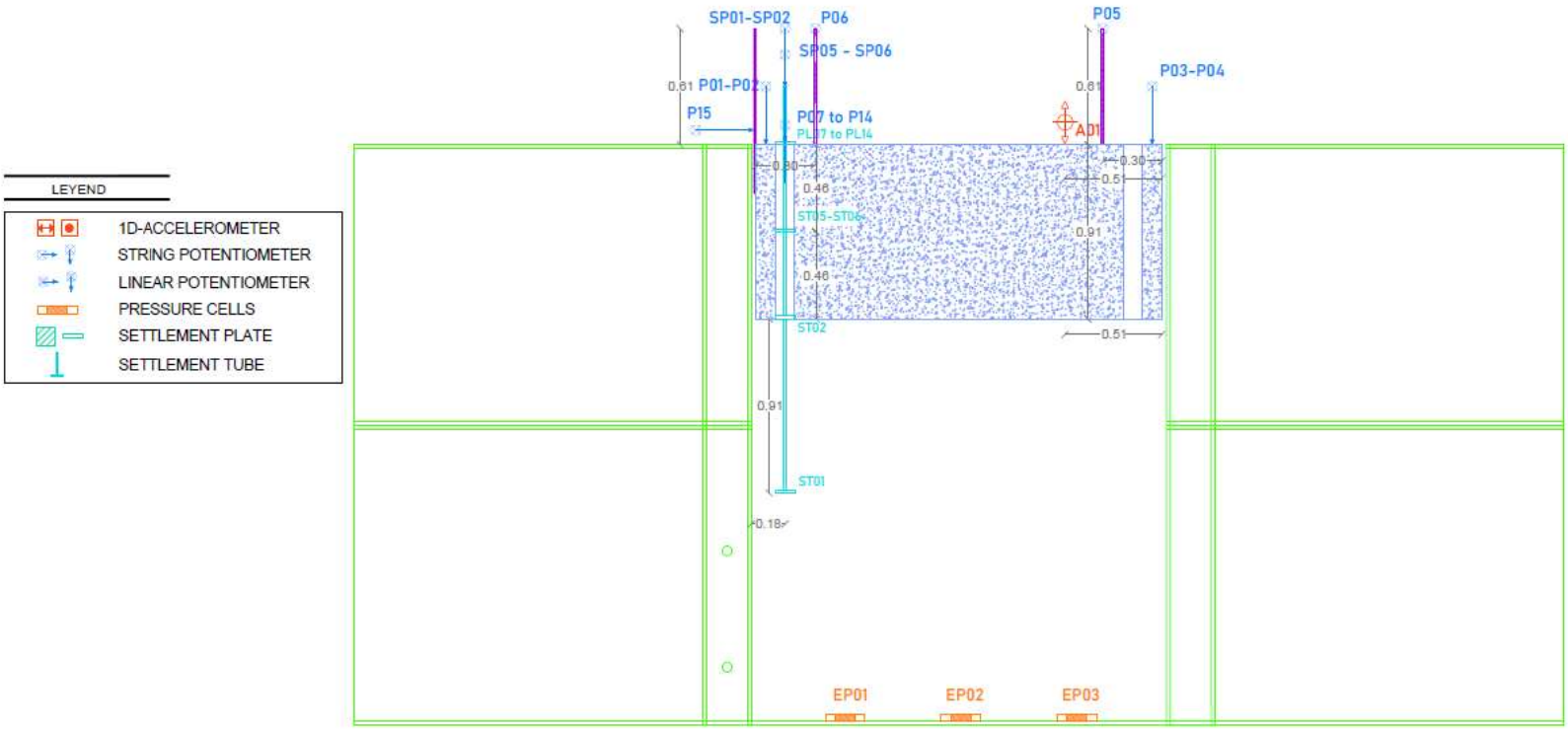

Figure C.1-3. Instrumentation Layout – Front View.

APPENDIX D – Quasi-static testing specimen No 04

D.1 - Instrumentation Layout for Quasi-static testing specimen No 04.

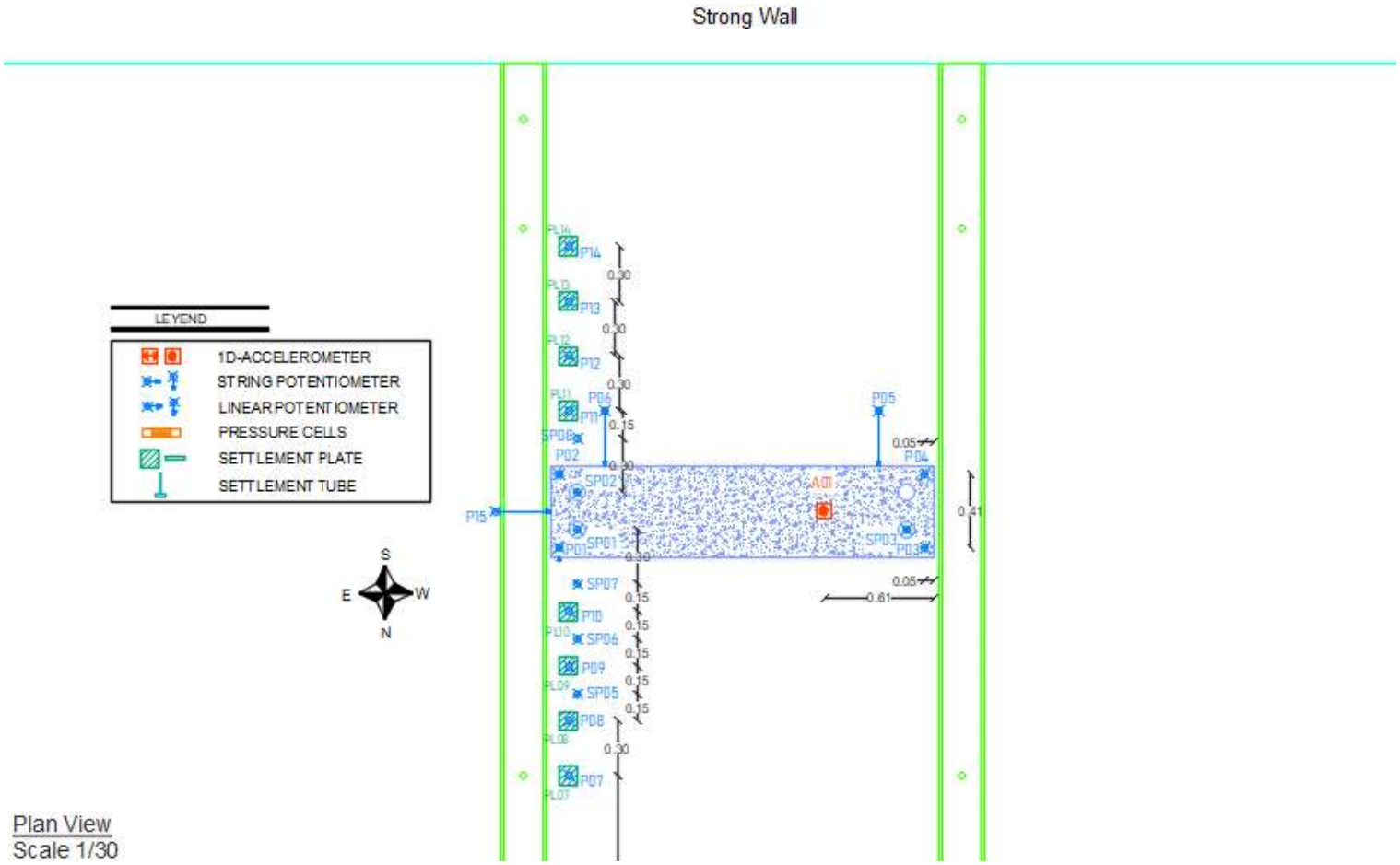

Figure D.1-1. Instrumentation Layout – Plan View.

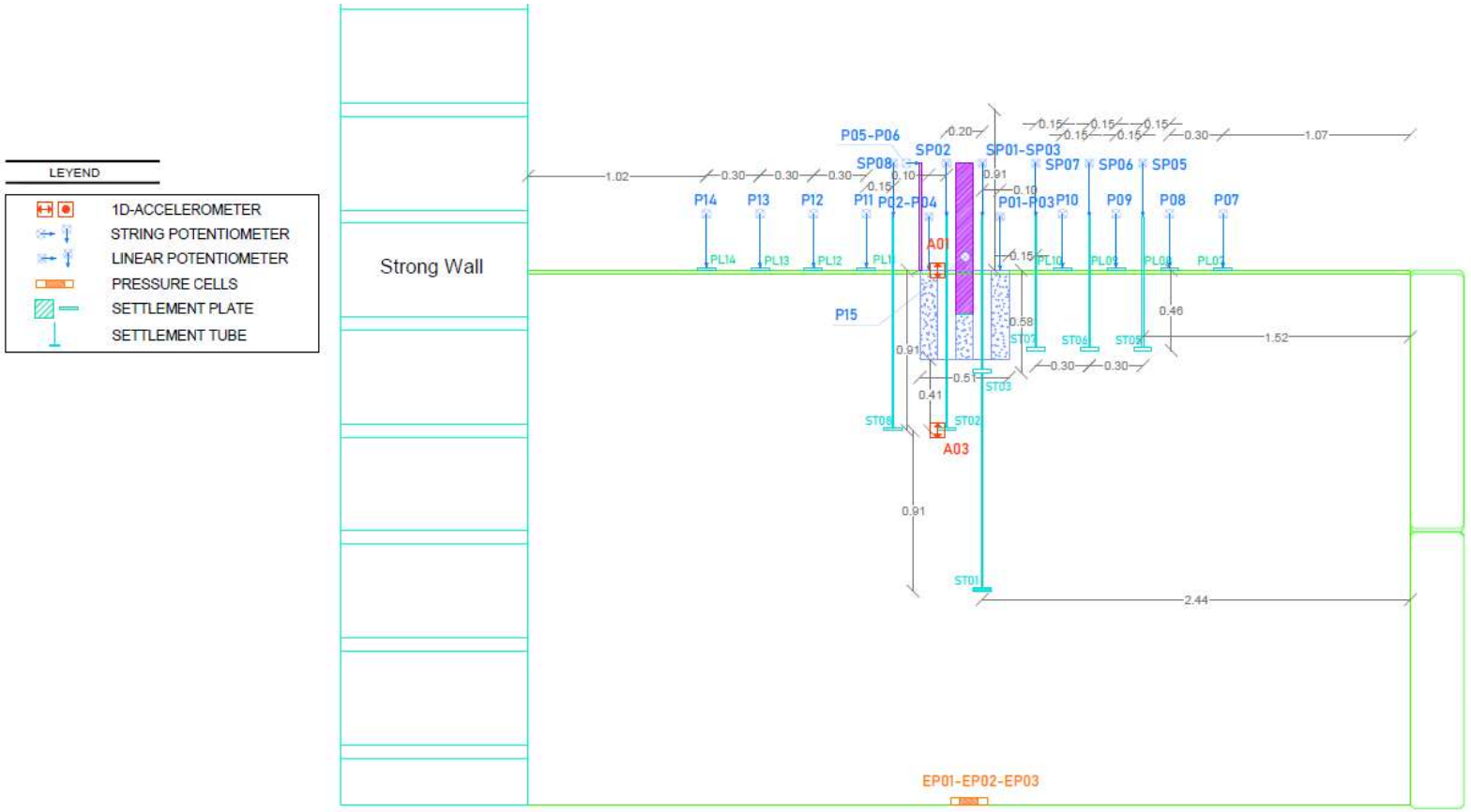

Figure D.1-2. Instrumentation Layout – Side View.

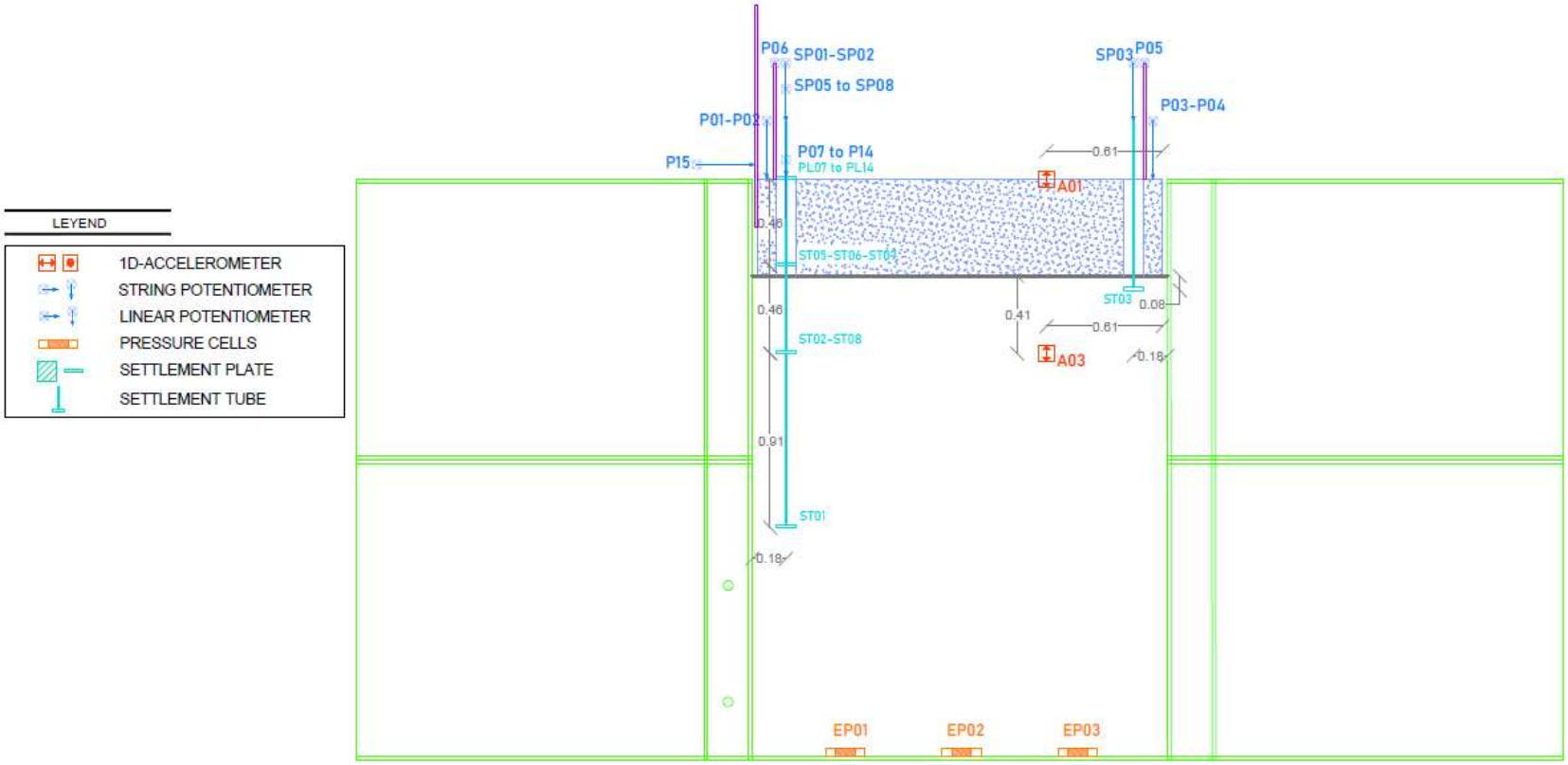

Figure D.1-3. Instrumentation Layout – Front View.

APPENDIX E – Quasi-static testing specimen No 05

E.1 - Instrumentation Layout for Quasi-static testing specimen No 05.

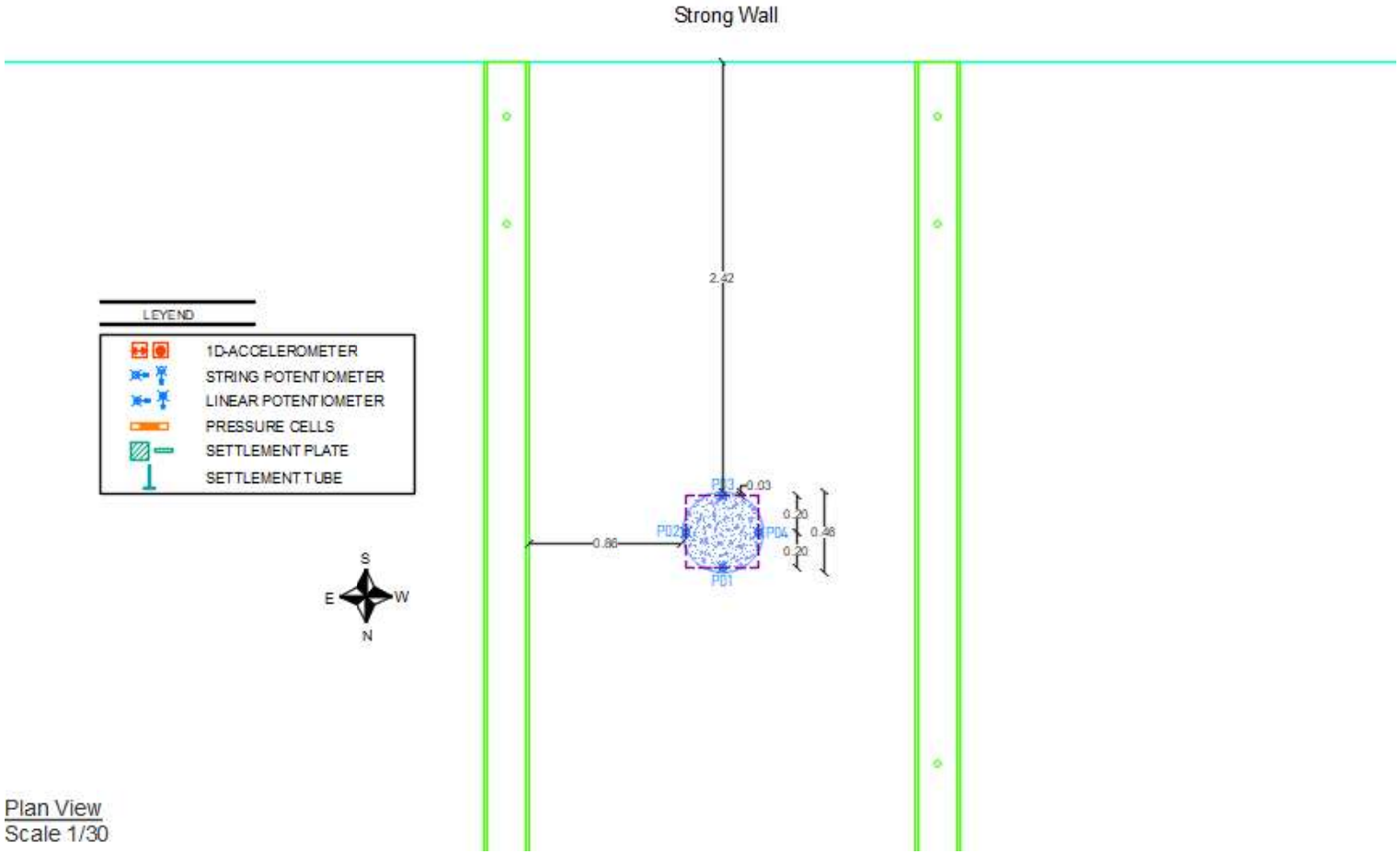

Figure E.1-1. Instrumentation Layout – Plan View.

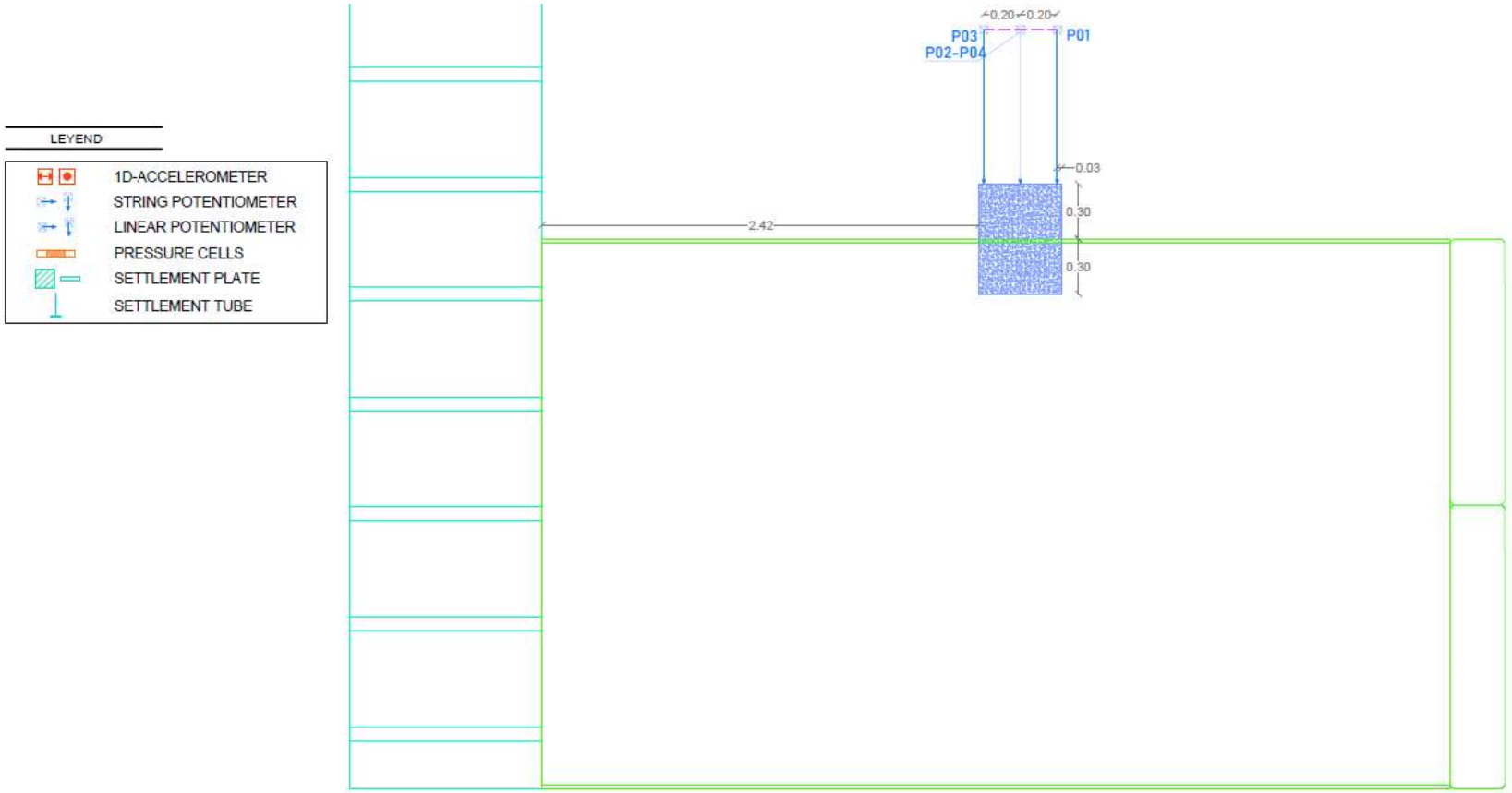

Figure E.1-2. Instrumentation Layout – Side View.

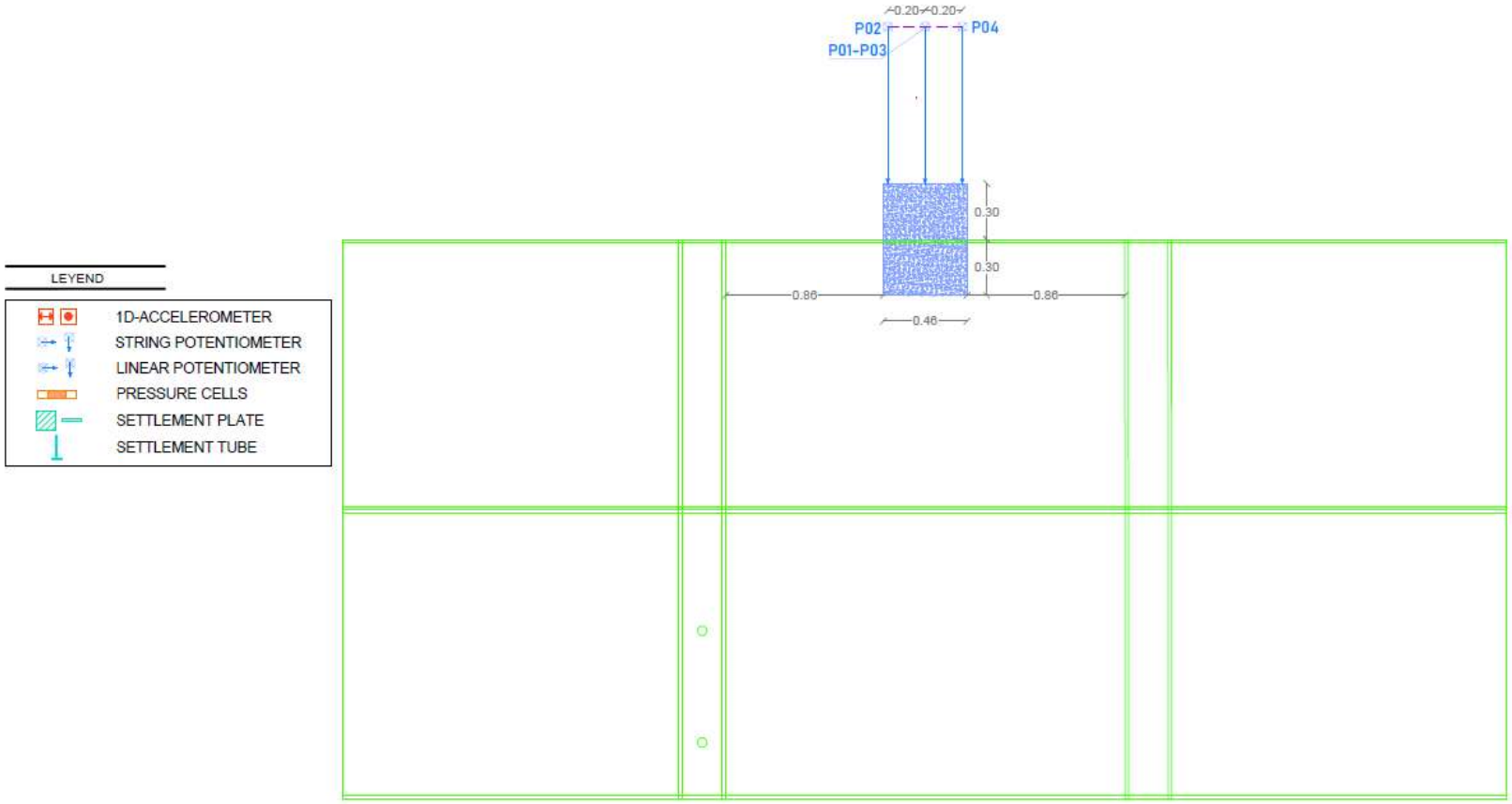

Figure E.1-3. Instrumentation Layout – Front View.

APPENDIX F – Quasi-static testing specimen No 06

F.1 - Instrumentation Layout for Quasi-static testing specimen No 06.

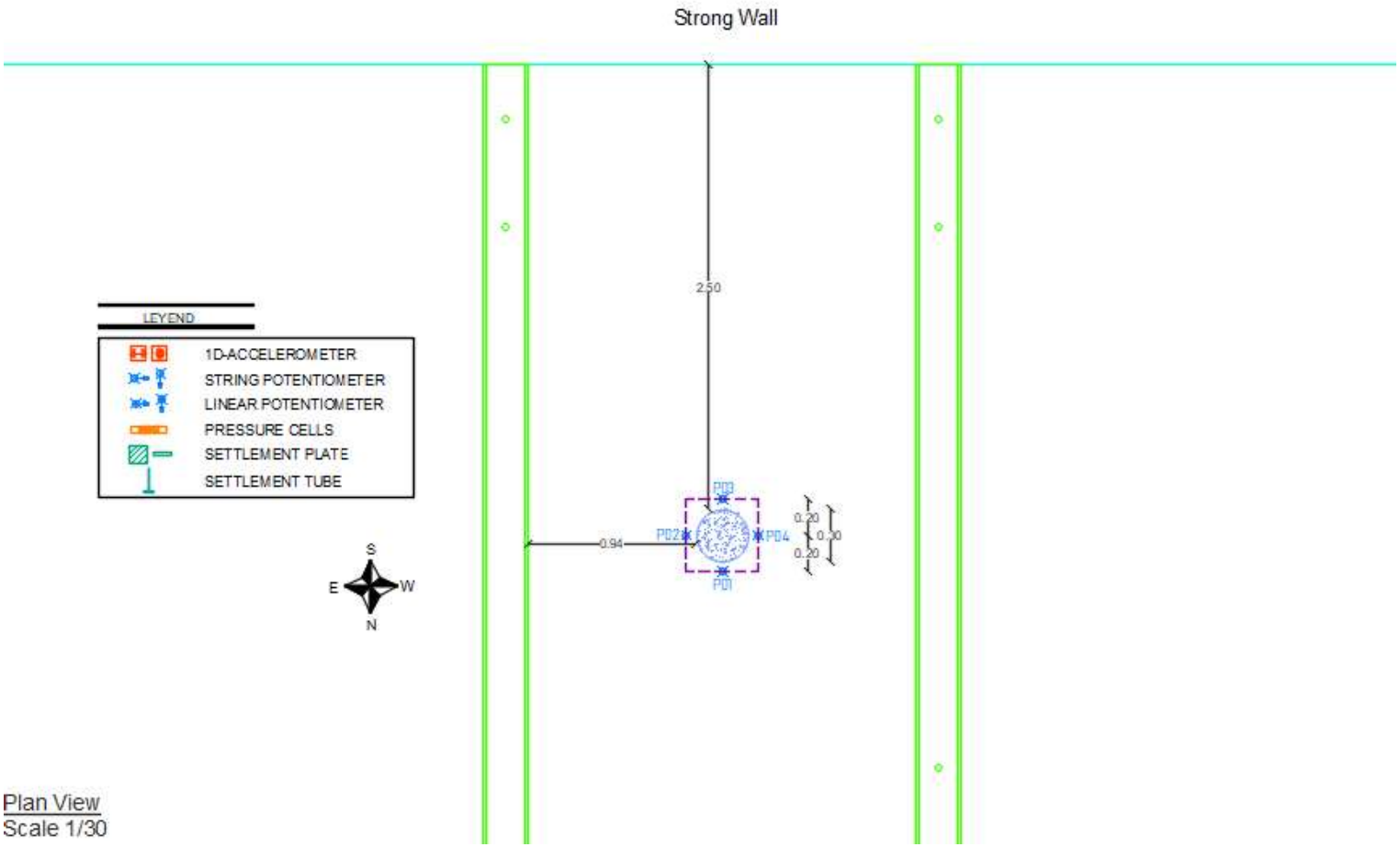

Figure F.1-1. Instrumentation Layout – Plan View.

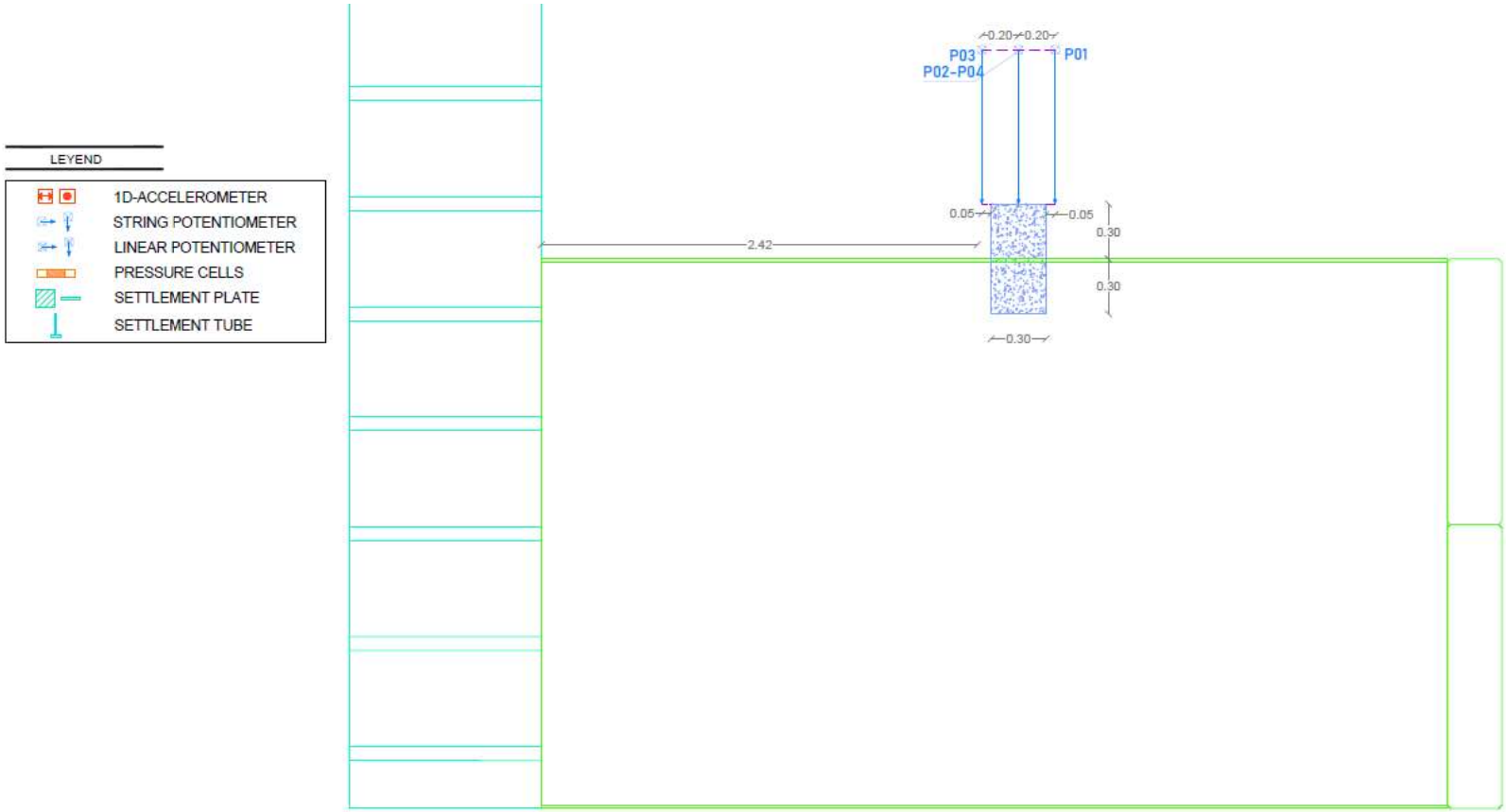

Figure F.1-2. Instrumentation Layout – Side View.

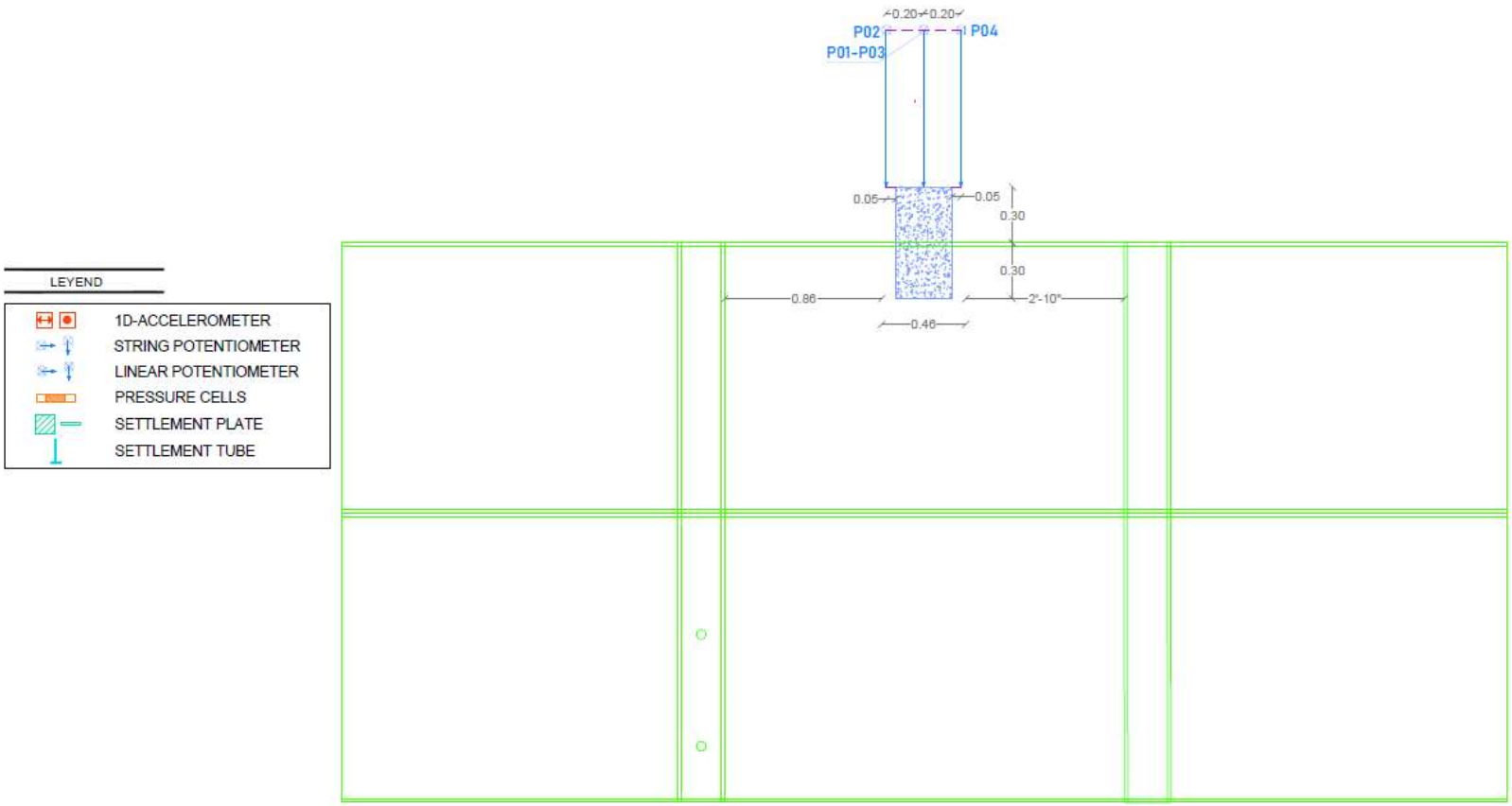

Figure F.1-3. Instrumentation Layout – Front View.

APPENDIX G – Quasi-static testing specimen No 07

G.1 - Instrumentation Layout for Quasi-static testing specimen No 07.

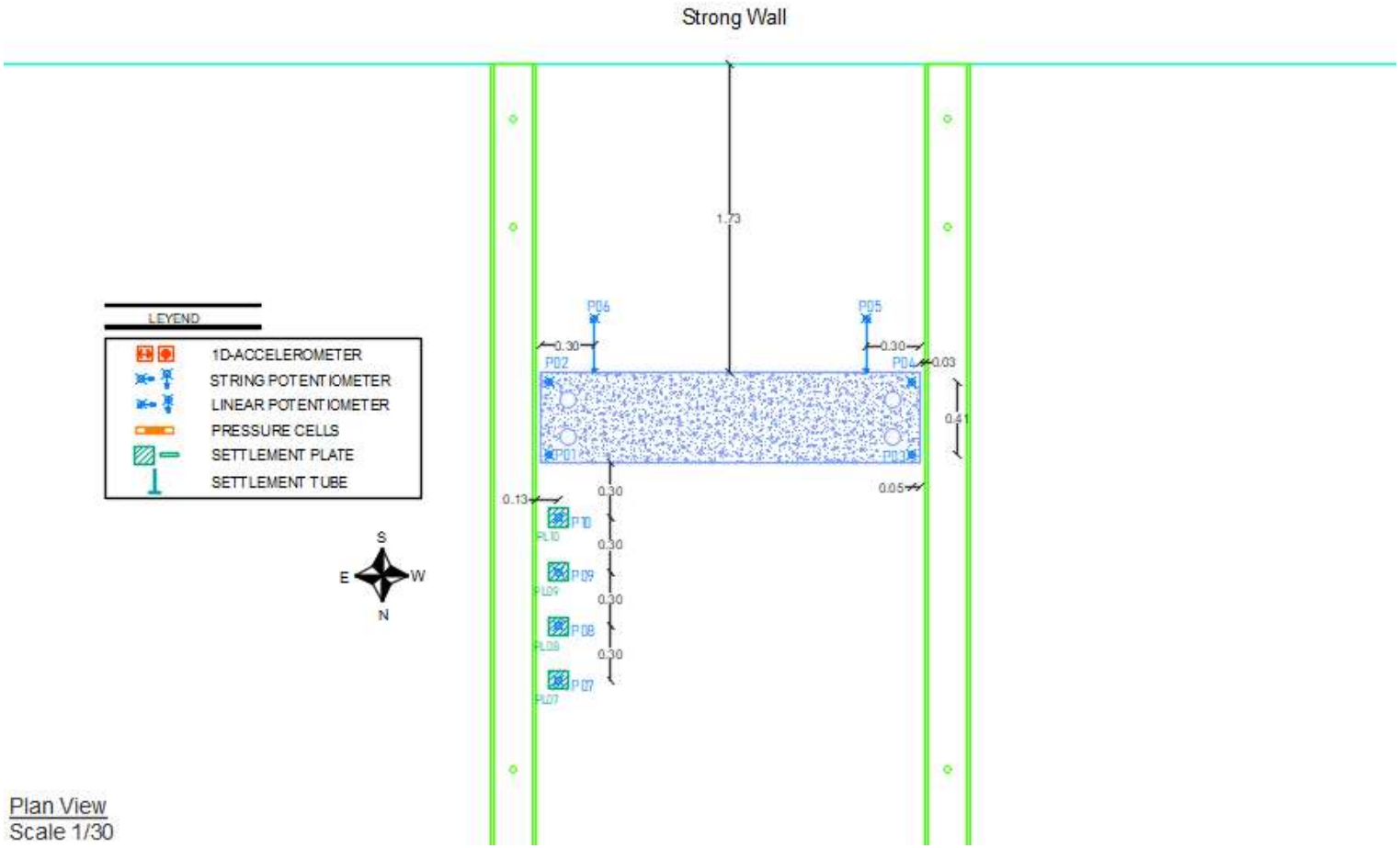

Figure G.1-1. Instrumentation Layout – Plan View.

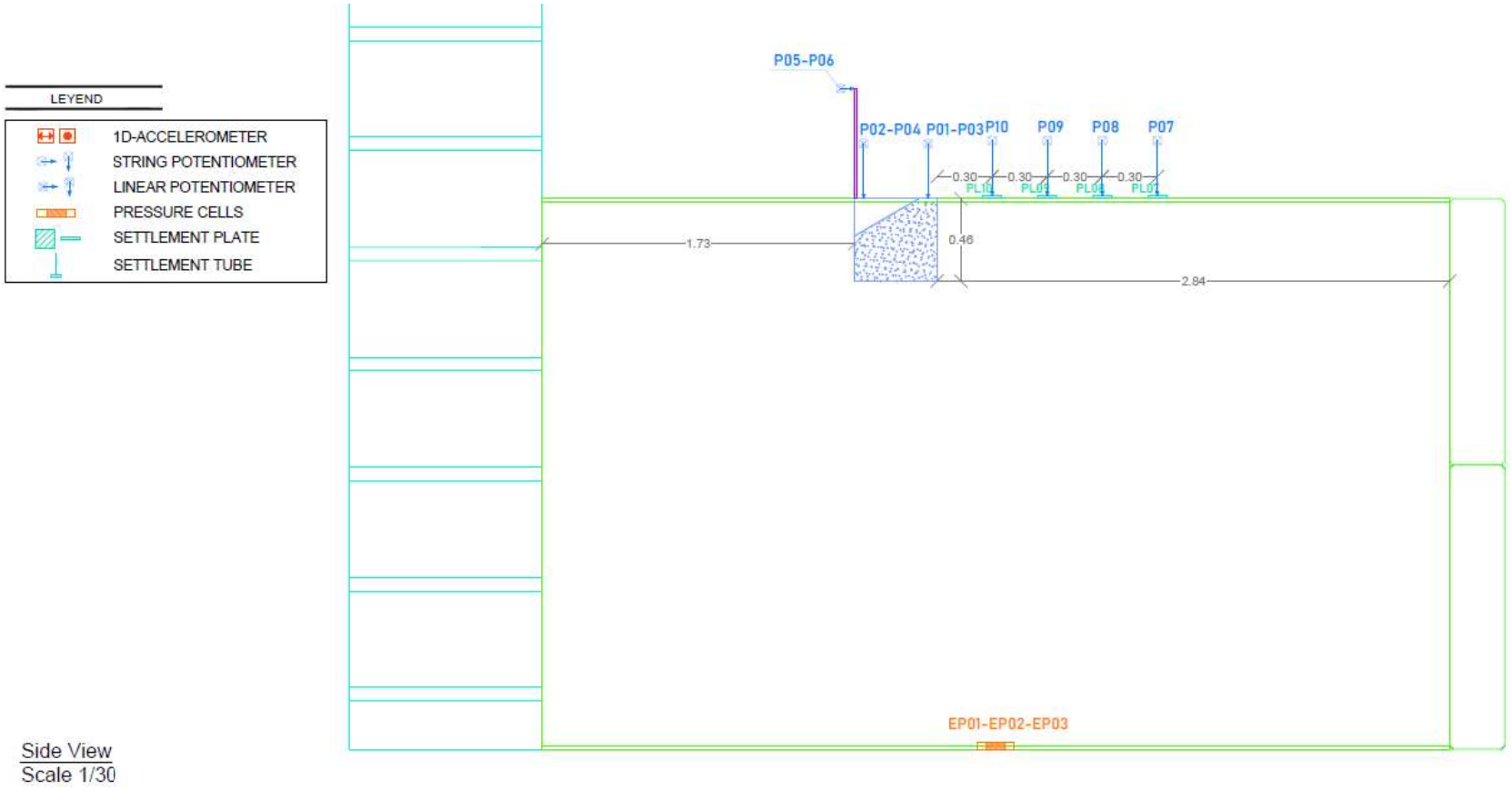

Figure G.1-2. Instrumentation Layout – Side View.

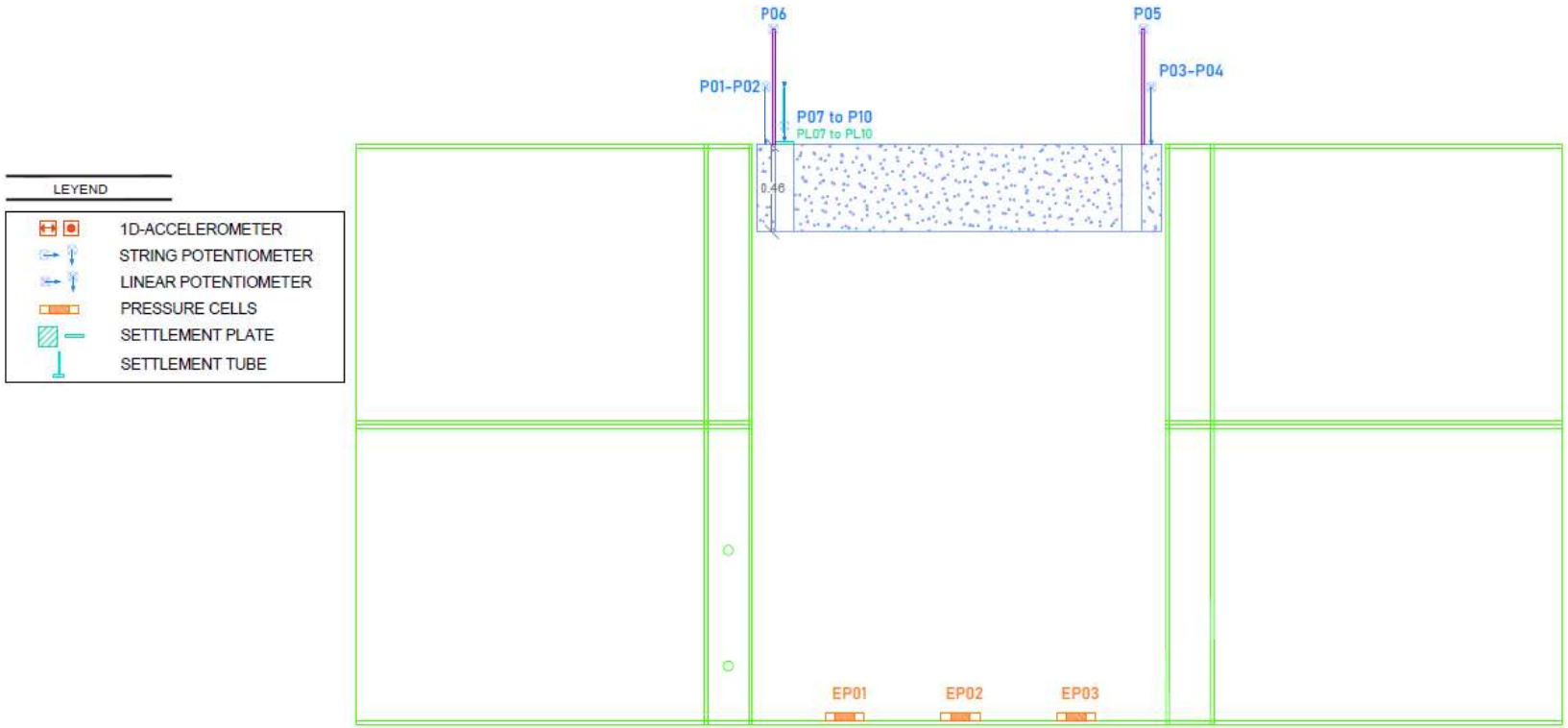

Figure G.1-3. Instrumentation Layout – Front View.

APPENDIX H – Quasi-static testing specimen No 08

H.1 - Instrumentation Layout for Quasi-static testing specimen No 08.

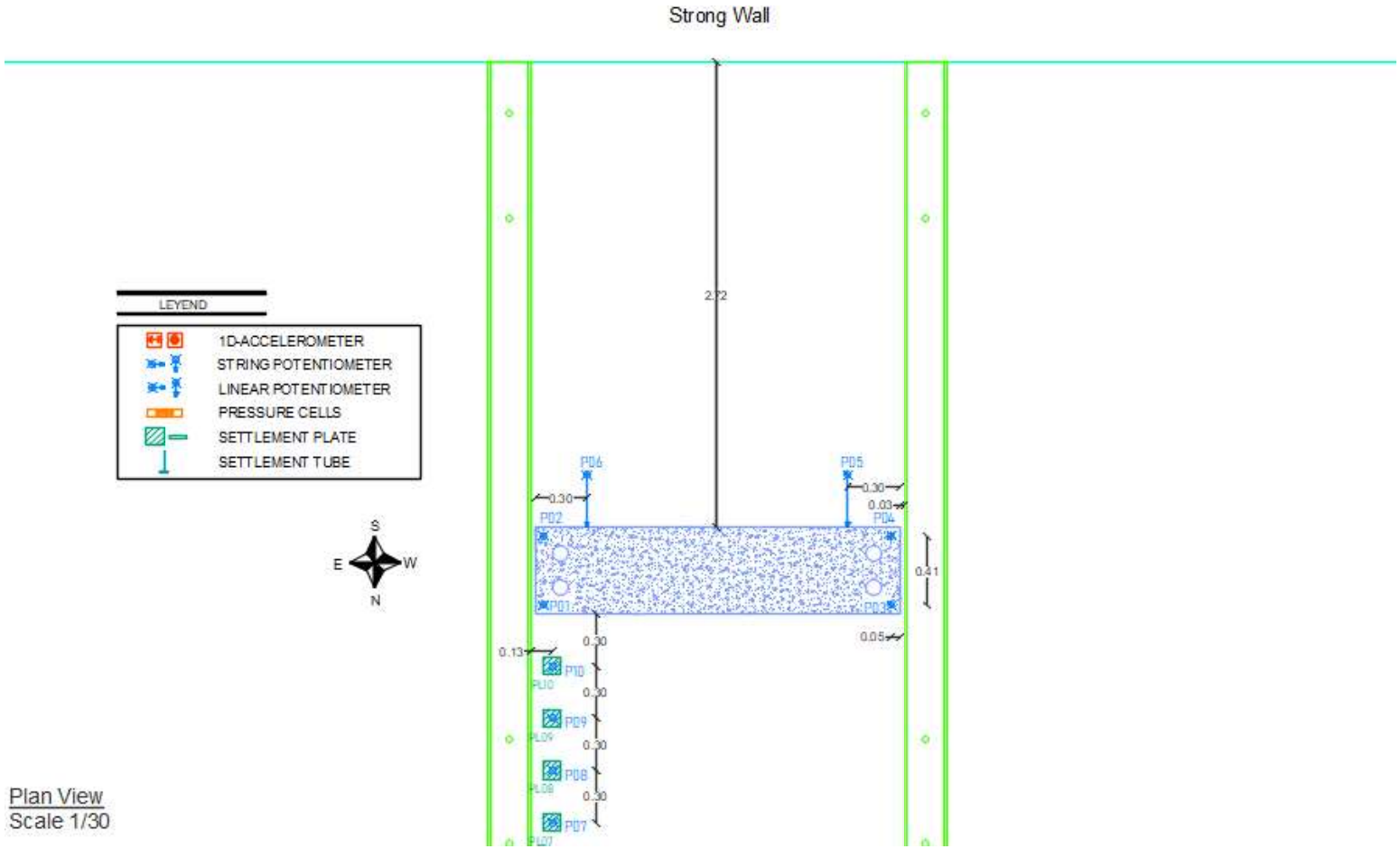

Figure H.1-1. Instrumentation Layout – Plan View.

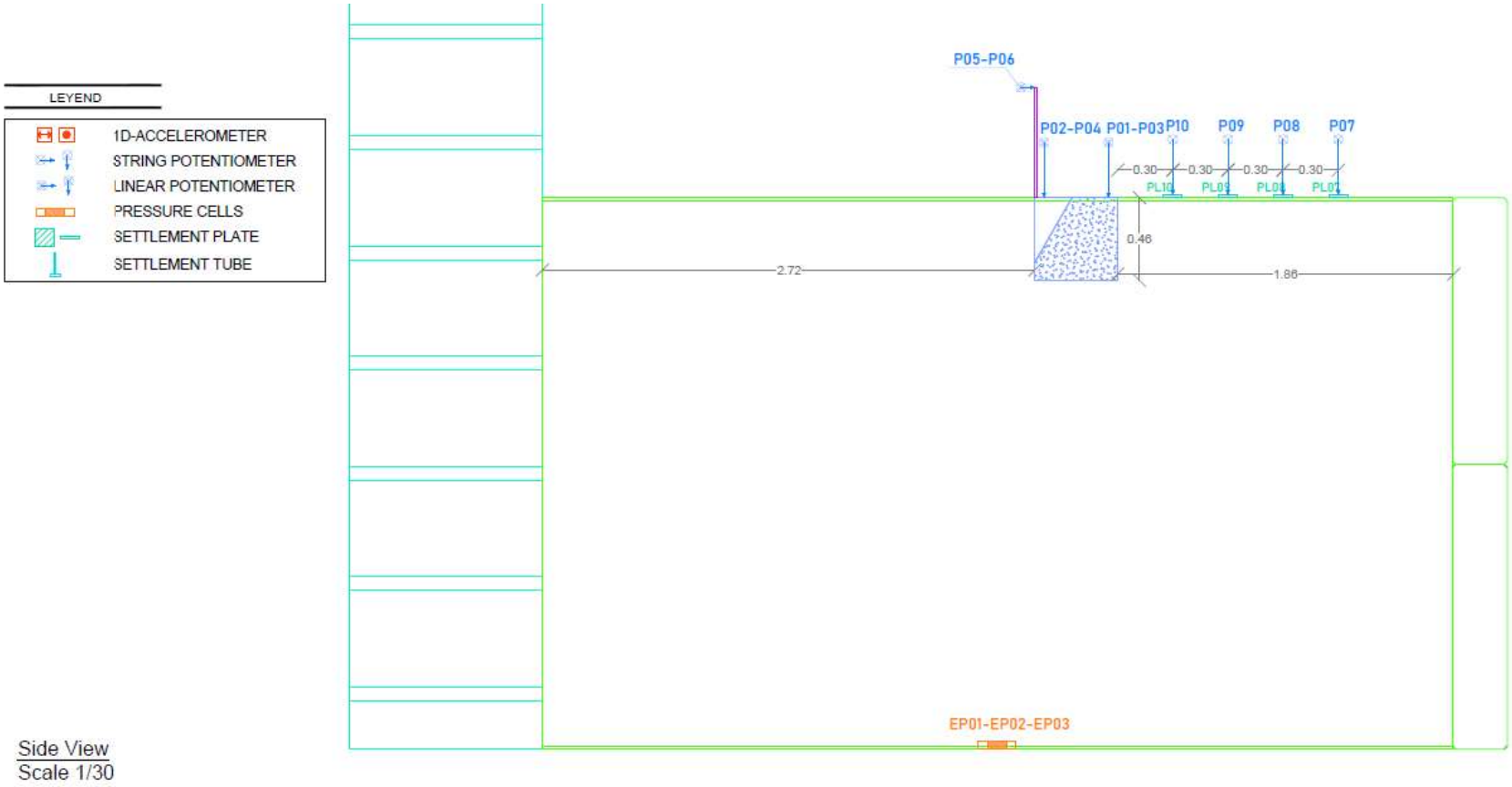

Figure H.1-2. Instrumentation Layout – Side View.

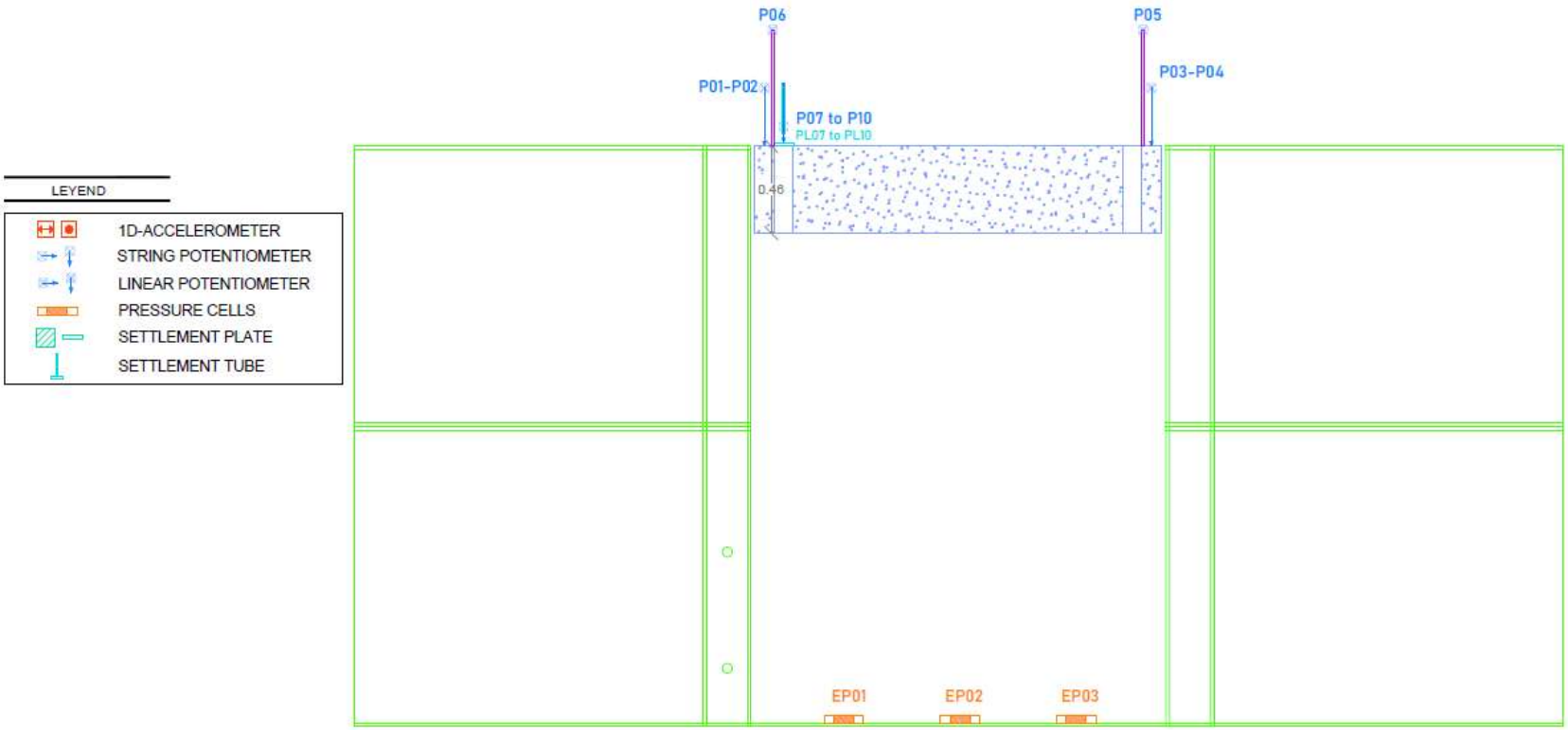

Figure H.1-3. Instrumentation Layout – Front View.

I.8. Time-history Records for DT01-NOR-100P motion.

I.8.1 Input Motion

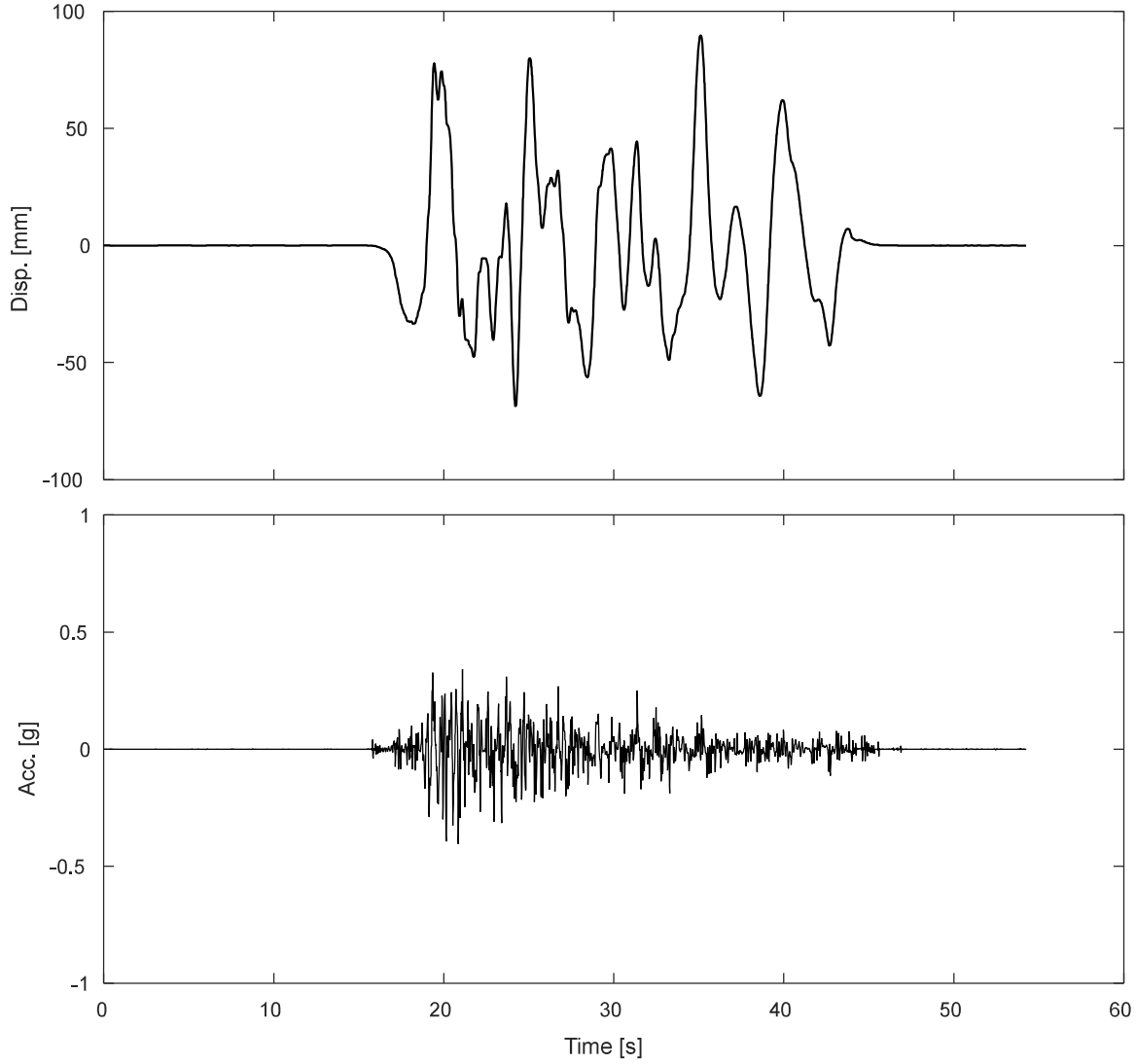

Figure I.8-1. Measured input displacement and acceleration at the base of the specimen during DT01-NOR-100P motion

I.8.1 Accelerometers.

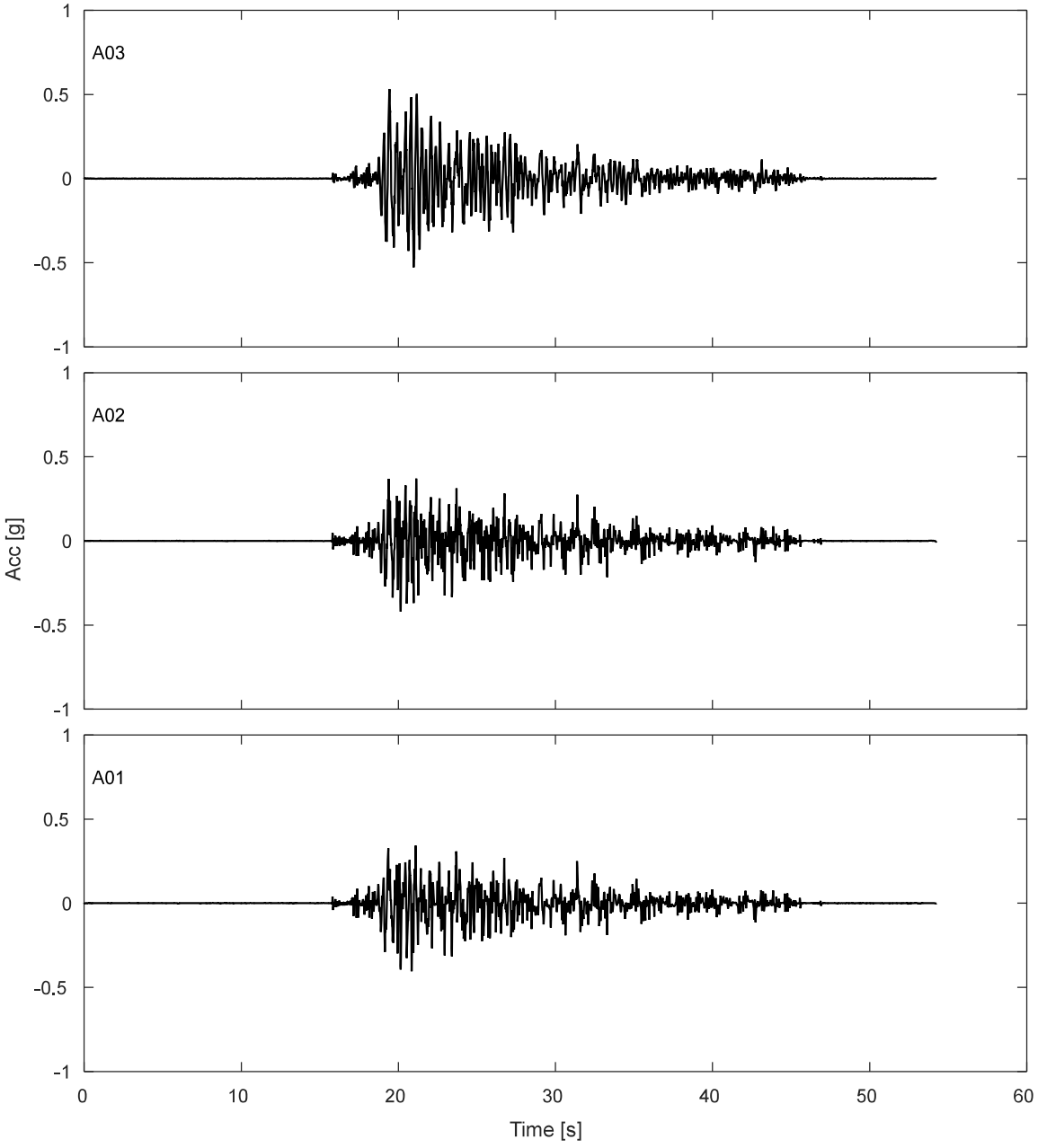

Figure I.8-2. Accelerations results along TDA during DT01-NOR-100P motion.

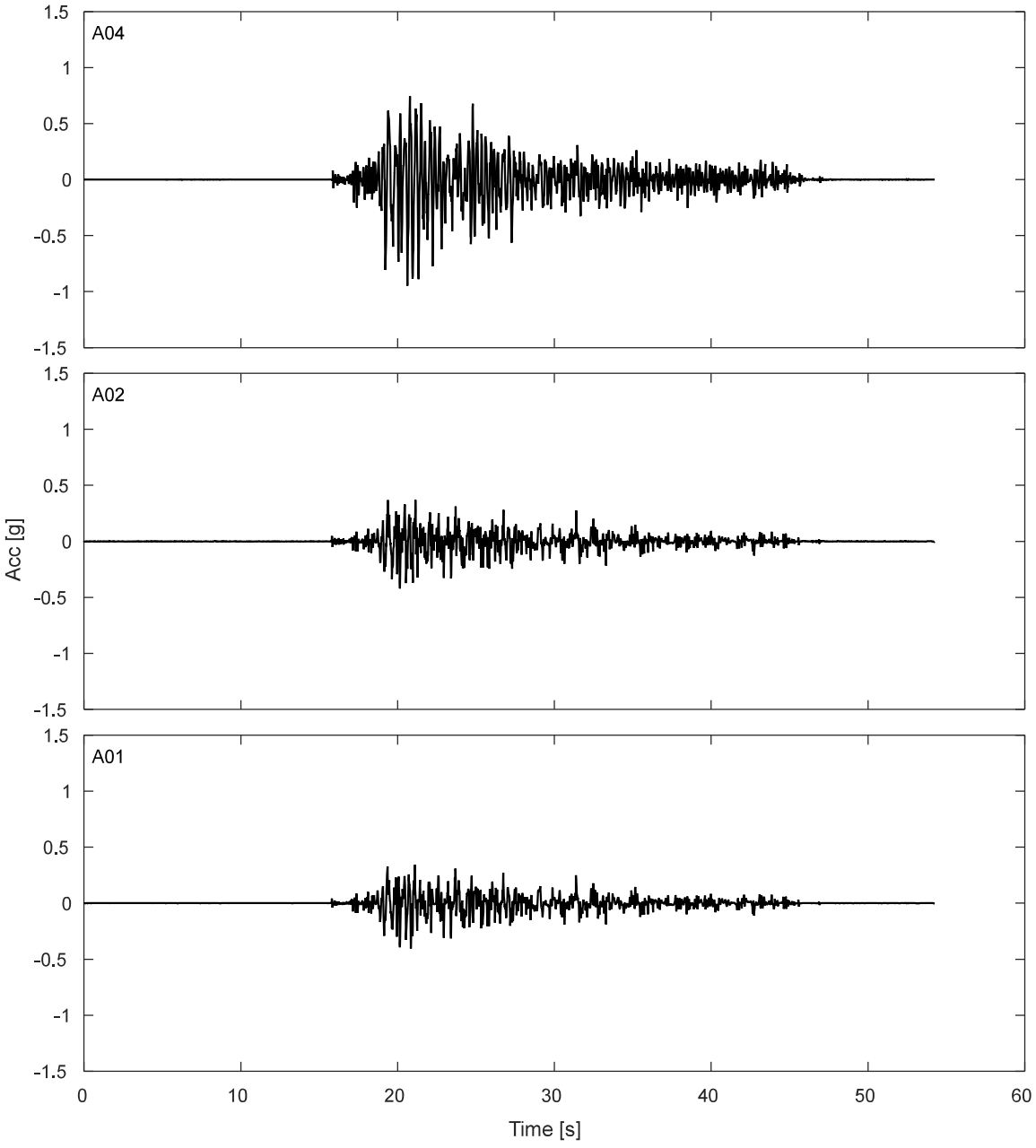

Figure I.8-3. Free field accelerations results for TDA during DT01-NOR-100P motion.

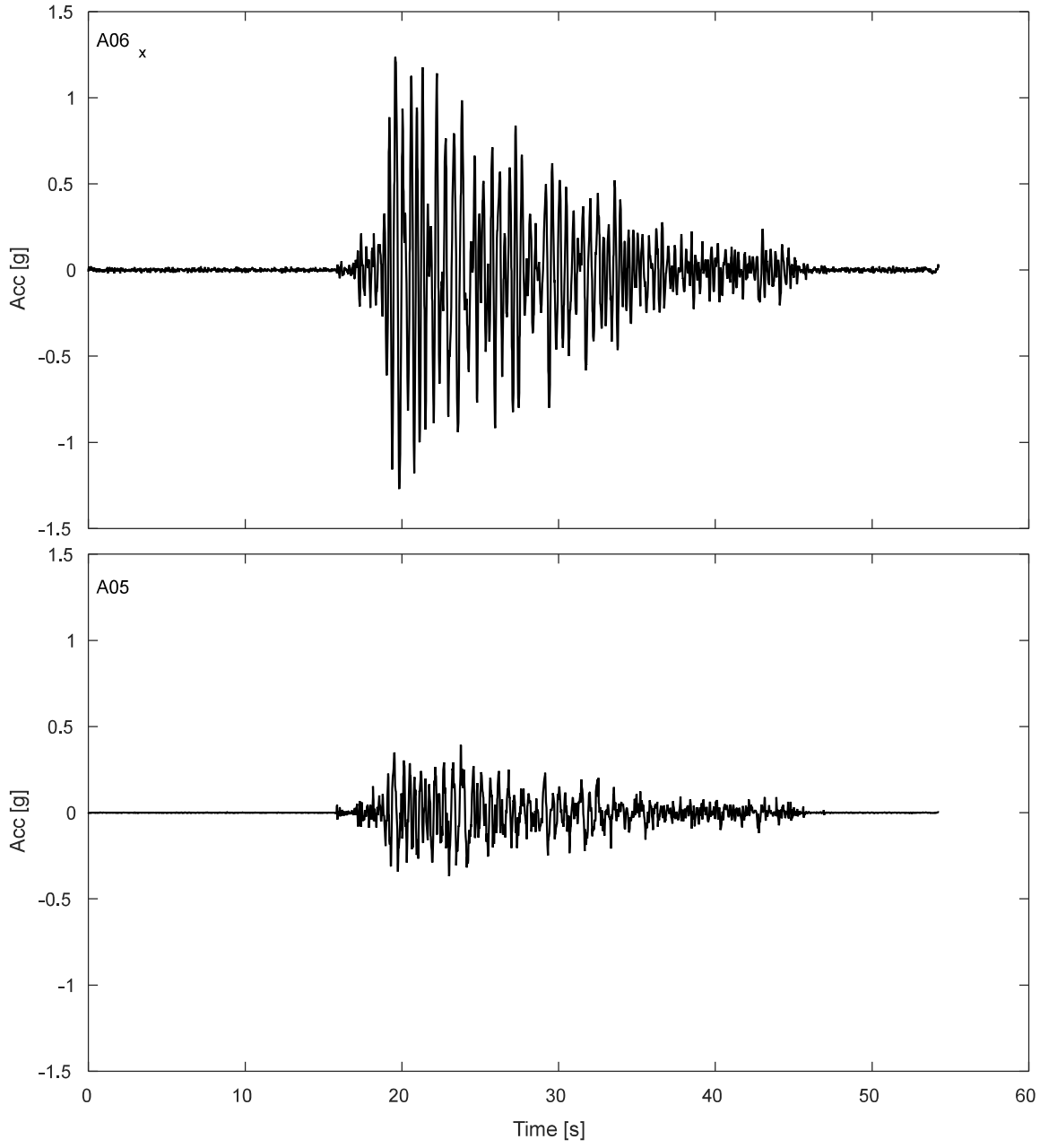

Figure I.8-4. Accelerations results SDOF structure during DT01-NOR-100P motion.

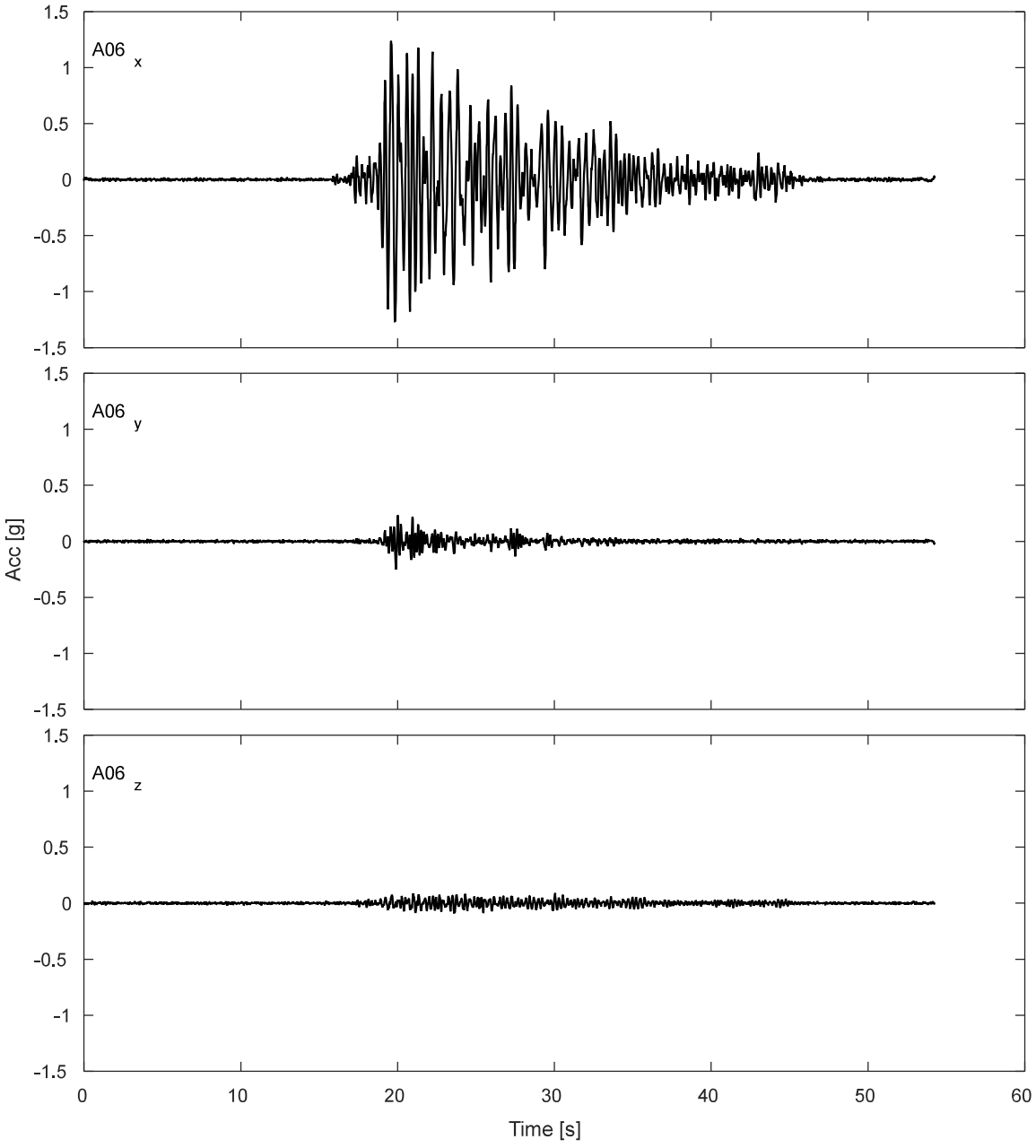

Figure I.8-5. Accelerations results for lumped mass of SDOF structure during DT01-NOR-100P motion.

I.8.2 Potentiometers.

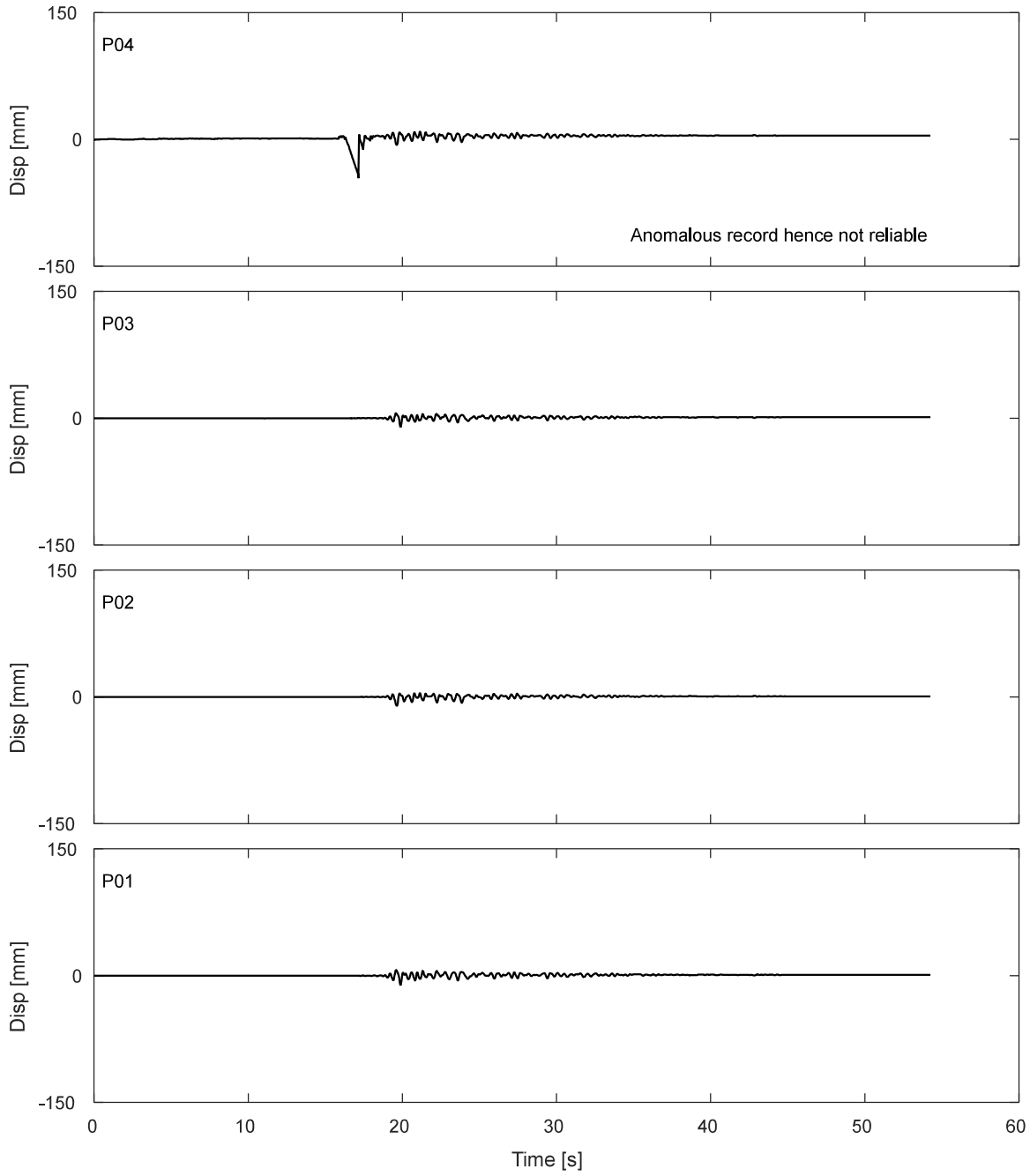

Figure I.8-6. Results of fully vertical potentiometers attached to corners of top of strip footing during DT01-NOR-100P motion.

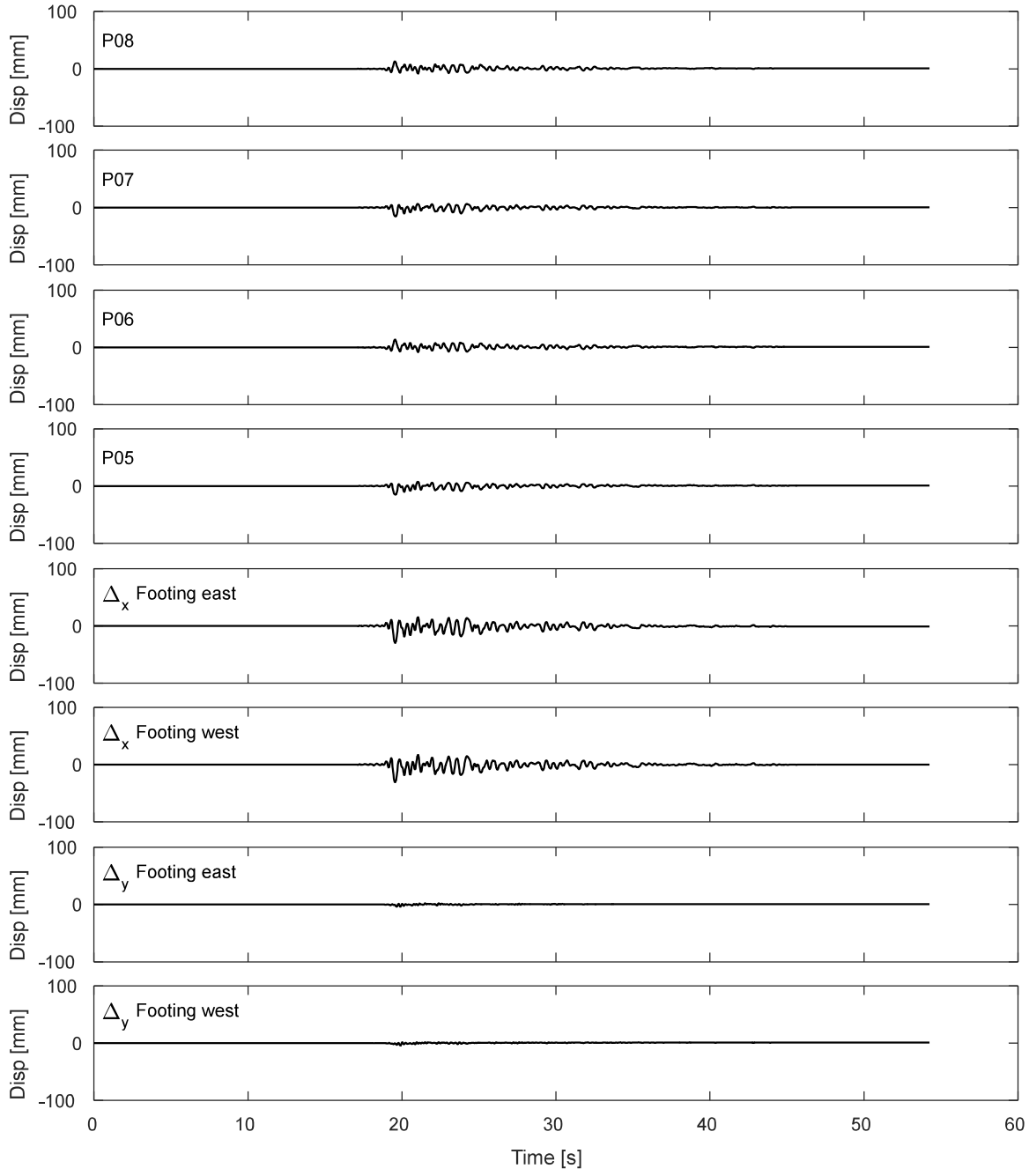

Figure I.8-7. Results of inclined potentiometers attached to top of strip footing during DT01-NOR-100P motion.

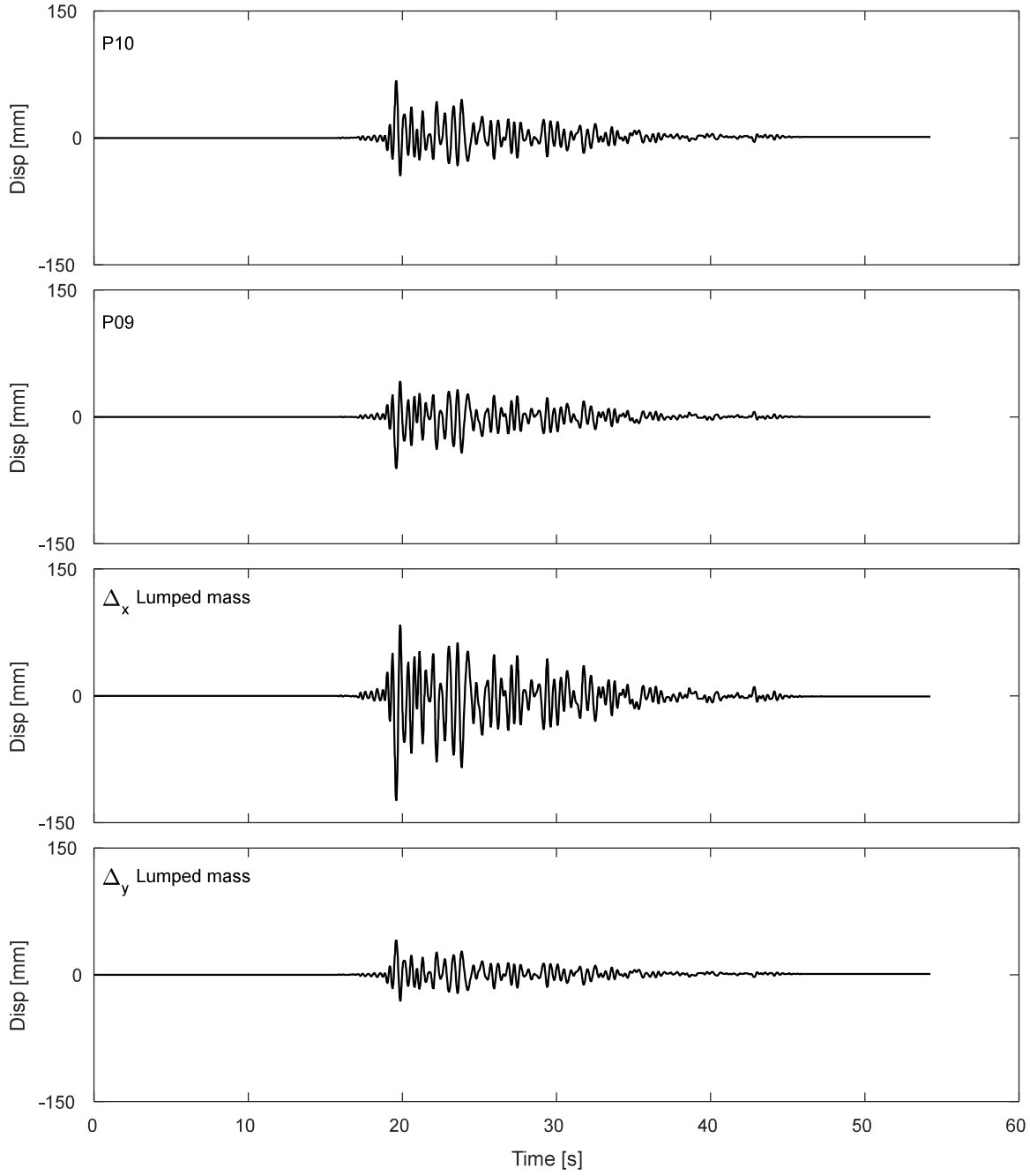

Figure I.8-8. Results of inclined potentiometers attached to lumped mass during DT01-NOR-100P motion.

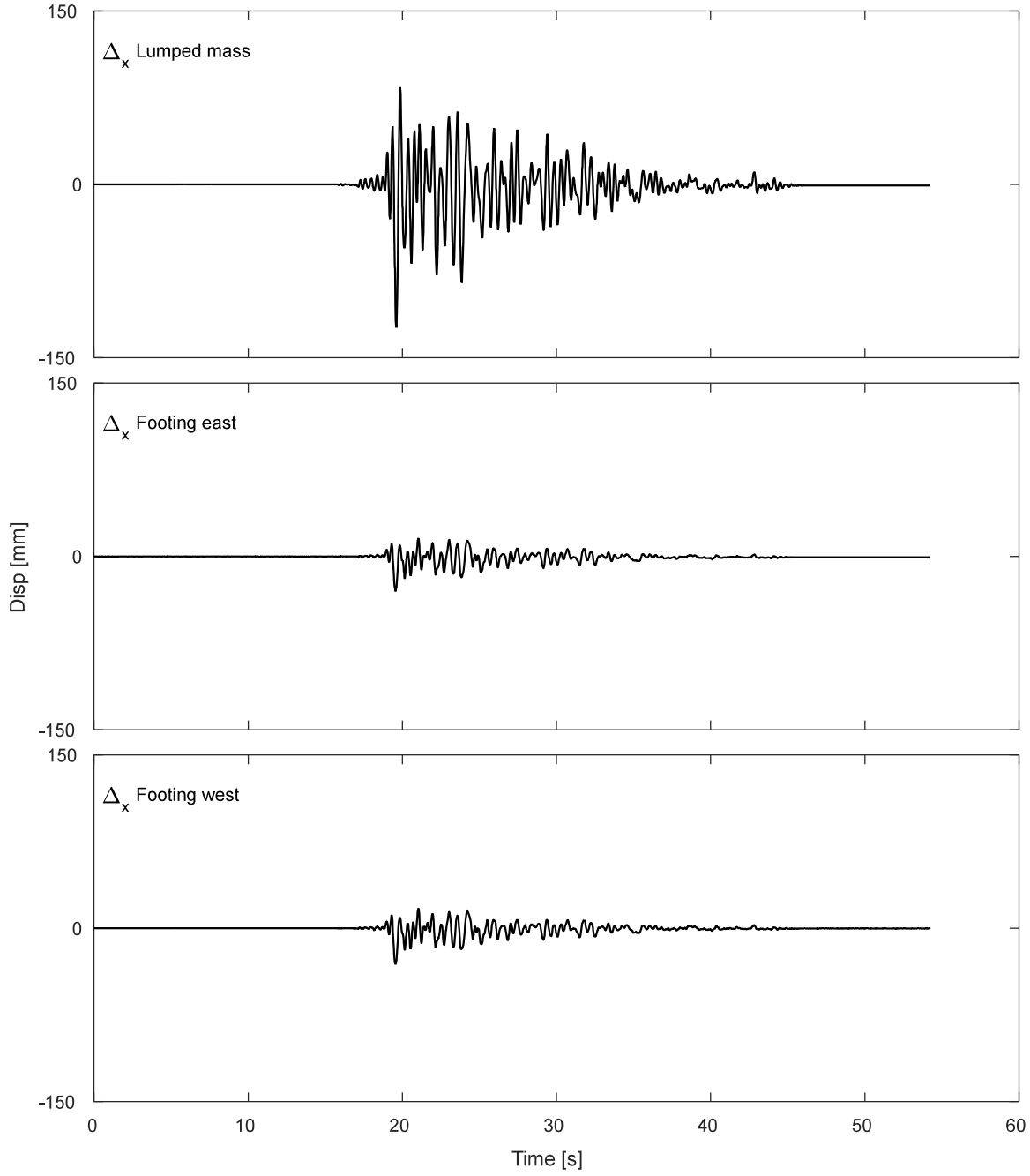

Figure I.8-9. Results of horizontal displacement of lumped mass and footing during DT01-NOR-100P motion.

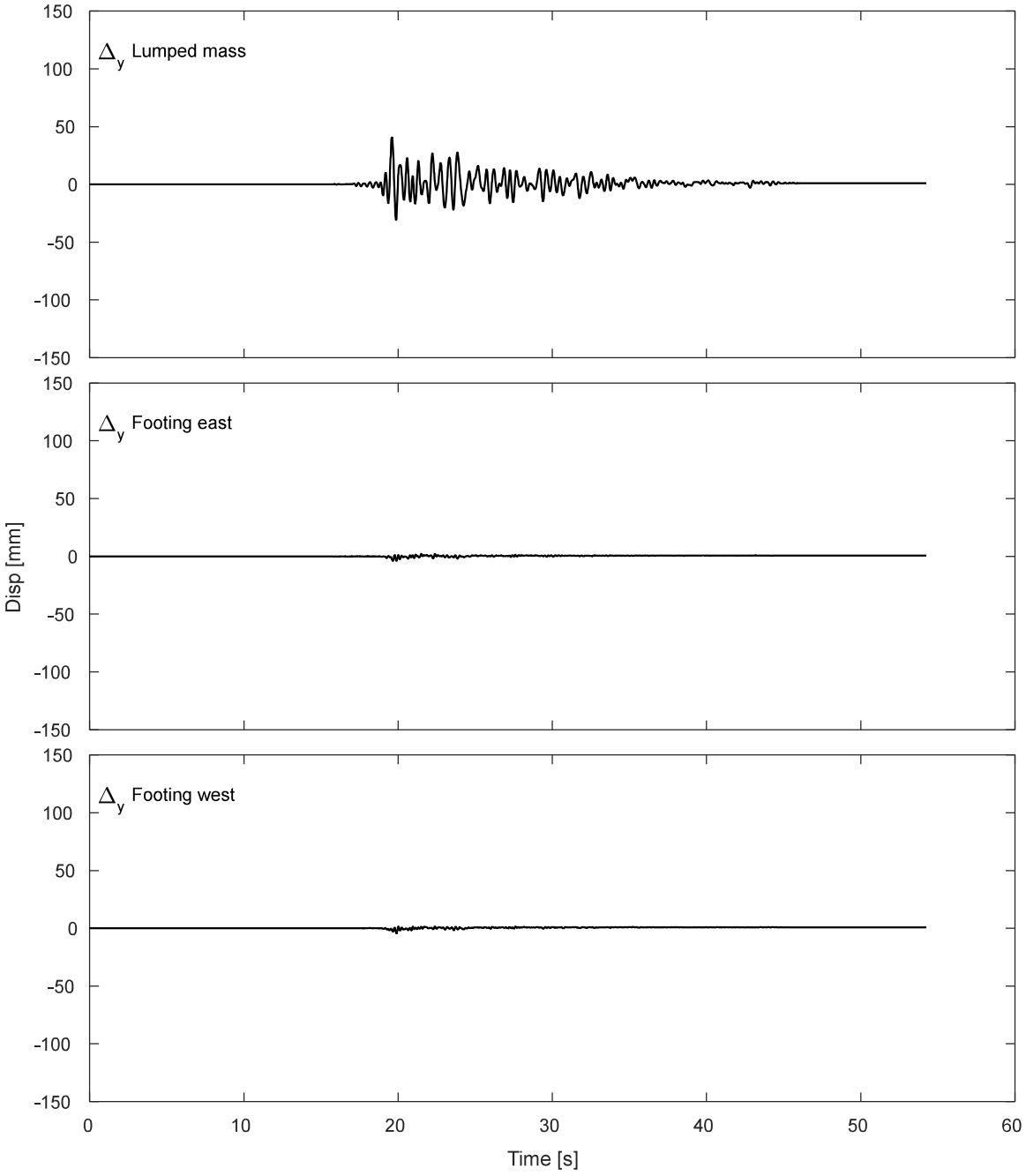

Figure I.8-10. Results of vertical displacement of lumped mass and footing during DT01-NOR-100P motion.

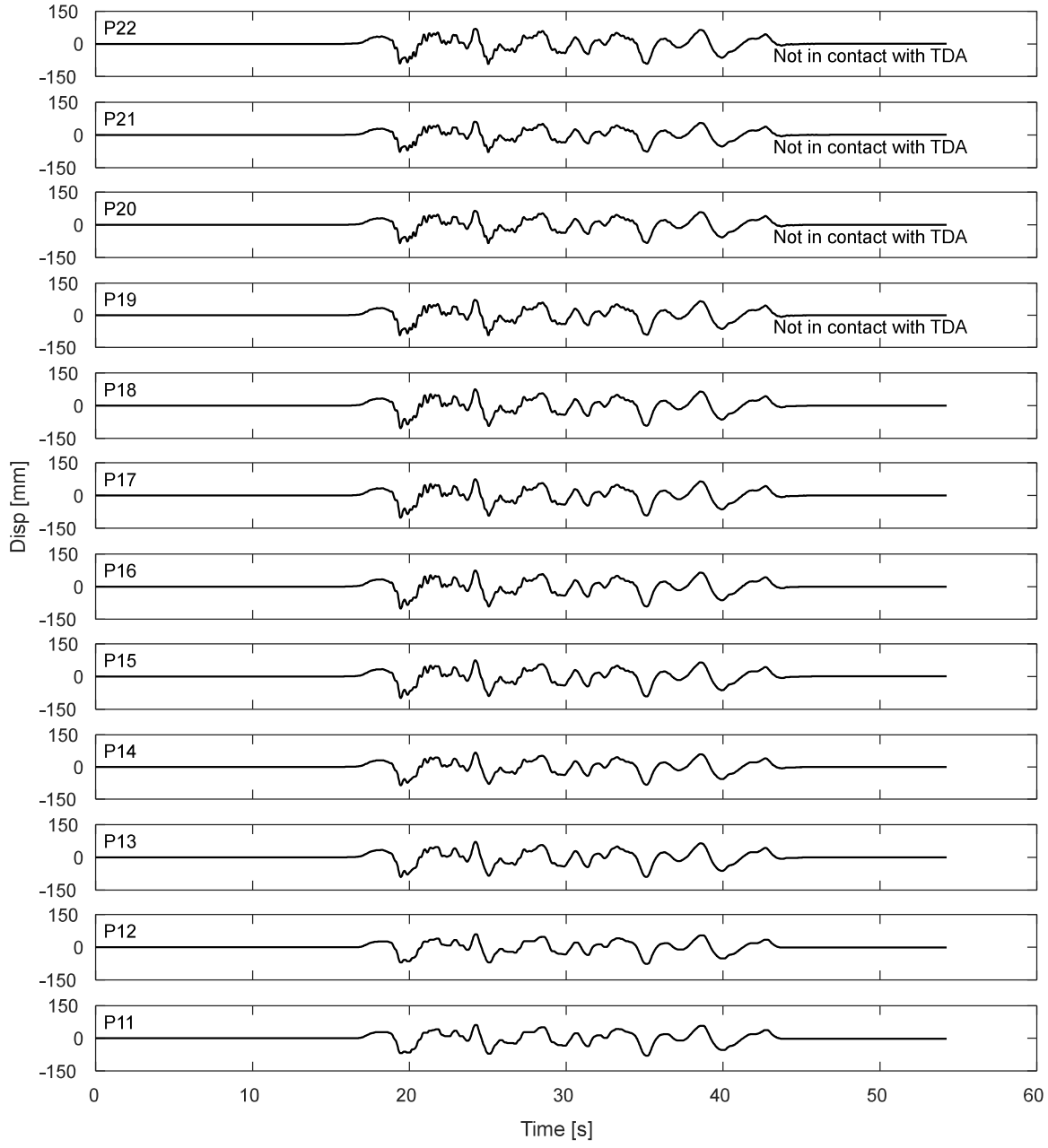

Figure I.8-11. Potentiometers results for the laminar box during DT01-NOR-100P motion.

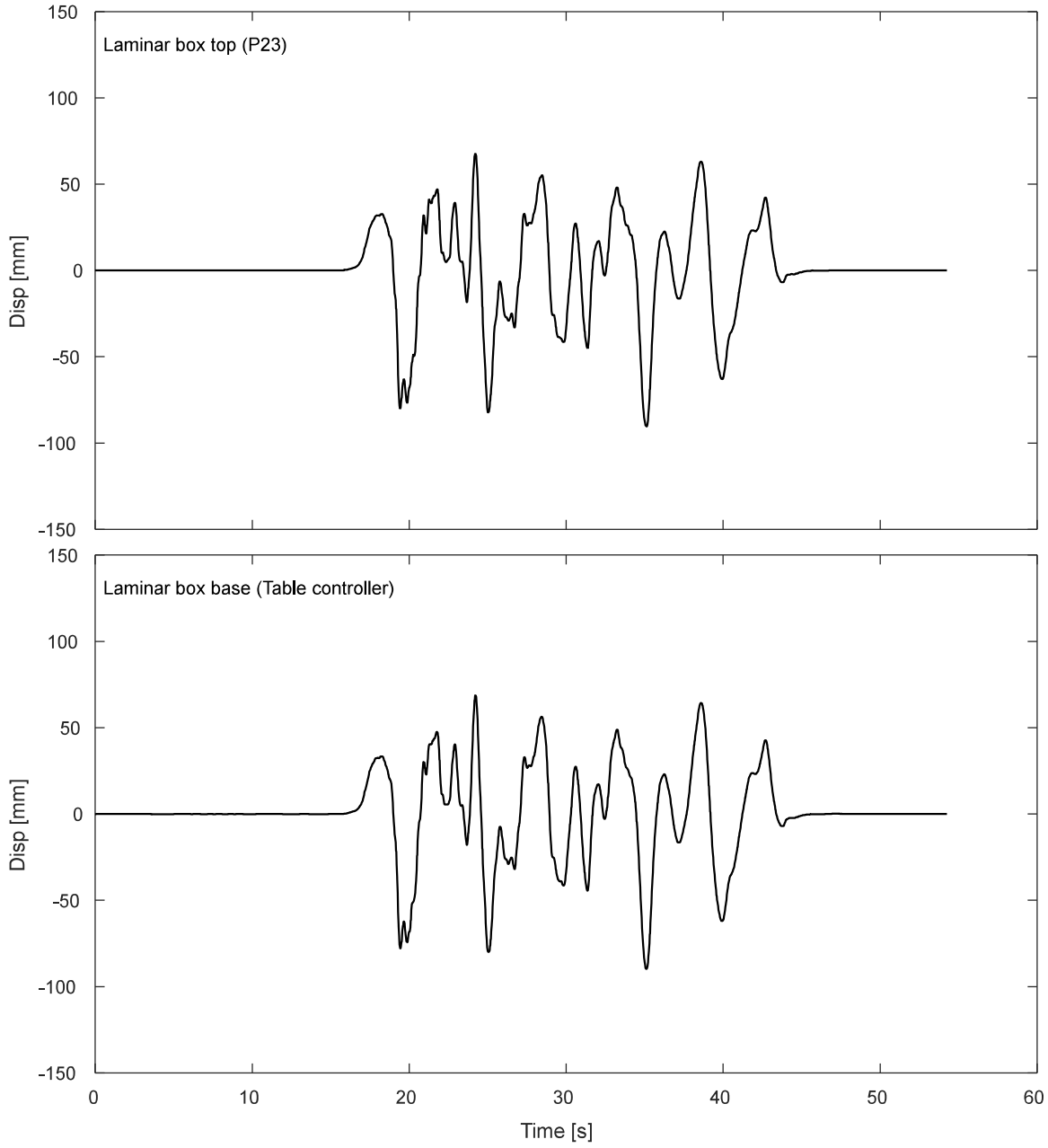

Figure I.8-12. Displacement response of top and base of laminar box during DT01-NOR-100P motion.

I.8.3. Inclinometers.

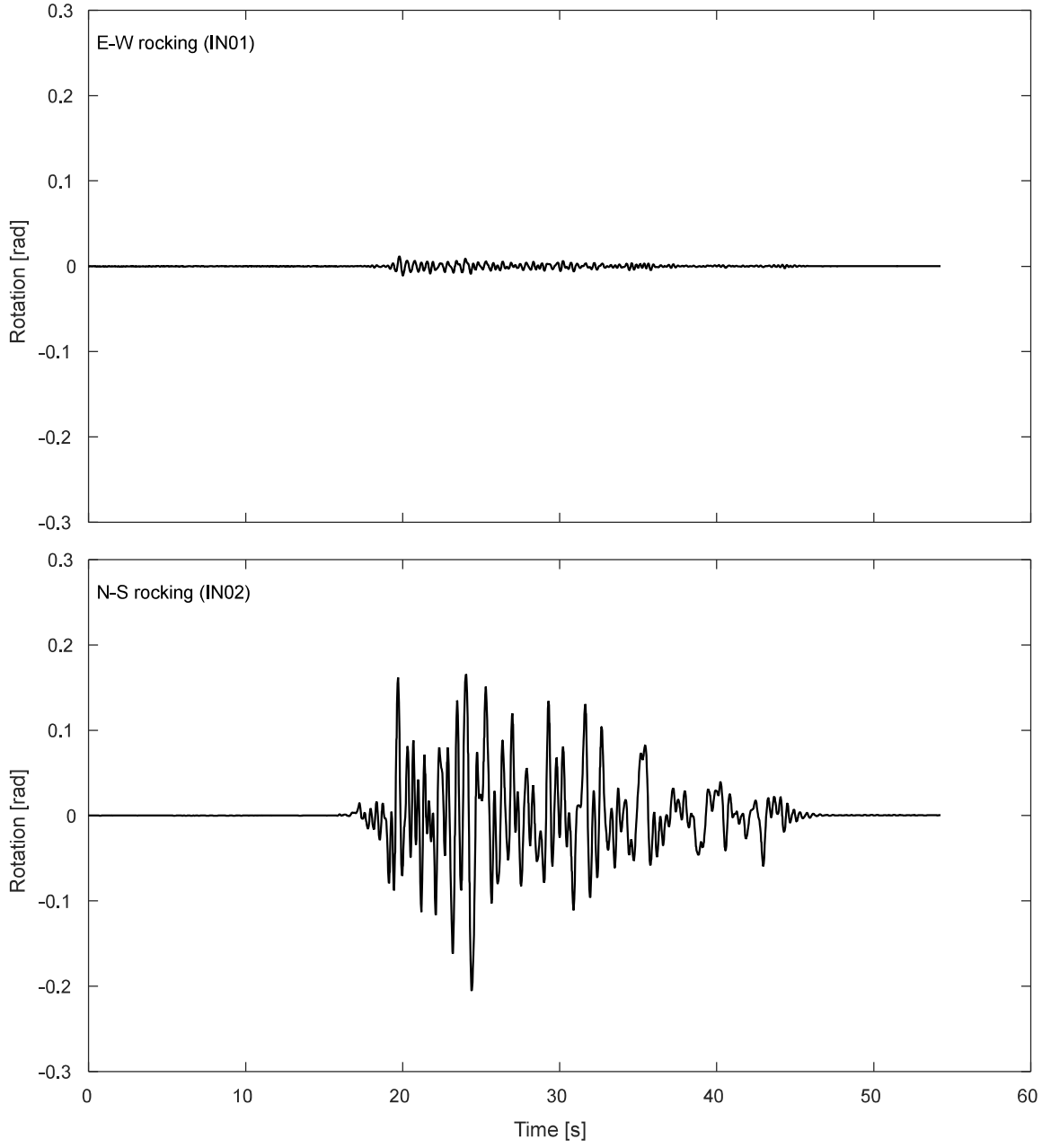

Figure I.8-13. Inclinometer results for the footing during DT01-NOR-100P motion.

I.8.4. Pressure cells.

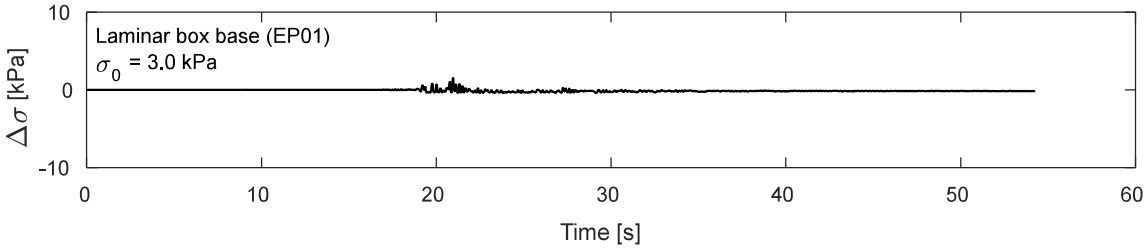

Figure I.8-14. Pressure cells results at laminar box base during DT01-NOR-100P motion.

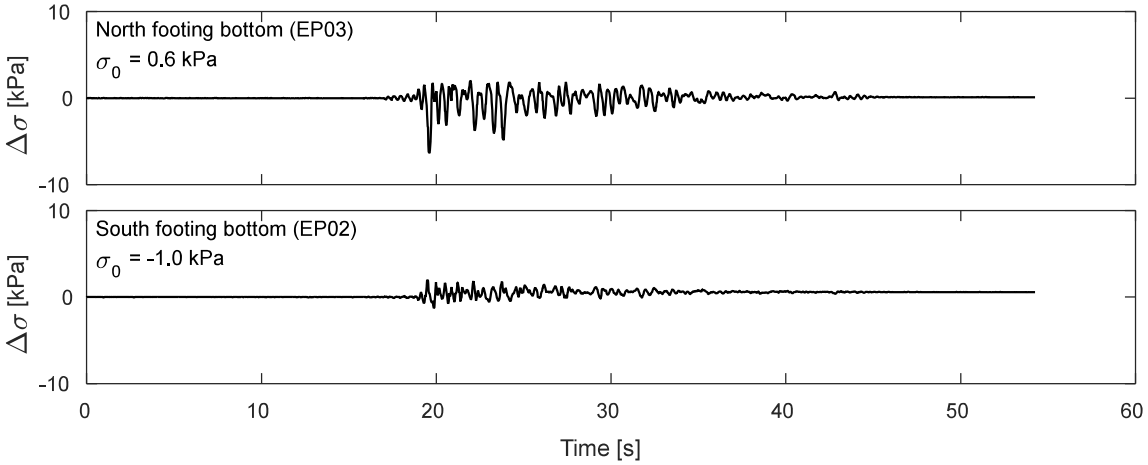

Figure I.8-15. Pressure cells results at footing bottom during DT01-NOR-100P motion.

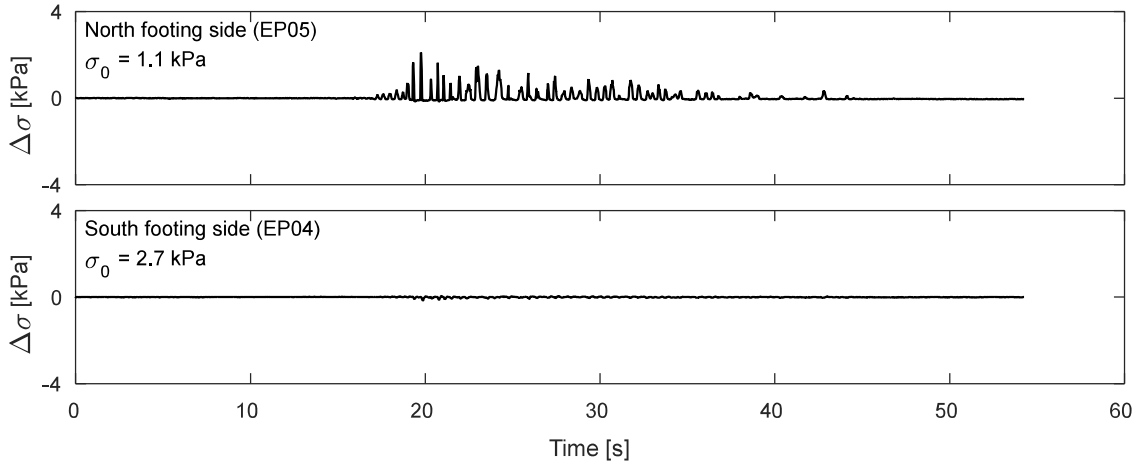

Figure I.8-16. Pressure cells results at footing sides during DT01-NOR-100P motion.

I.9. Time-history Records for DT01-MAU-100P motion.

I.9.1 Input Motion

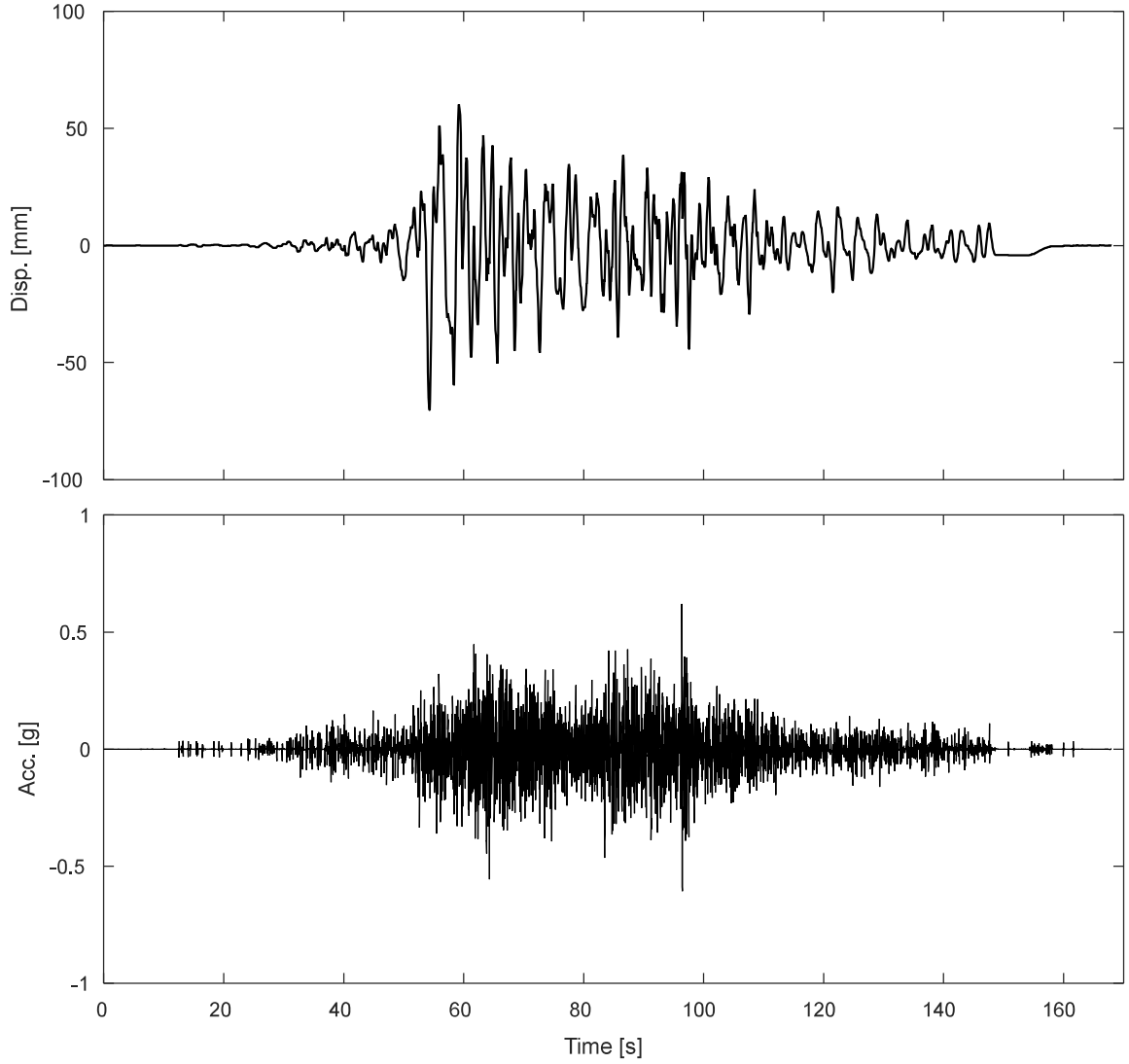

Figure I.9-1. Measured input displacement and acceleration at the base of the specimen during DT01-MAU-100P motion

I.9.1 Accelerometers.

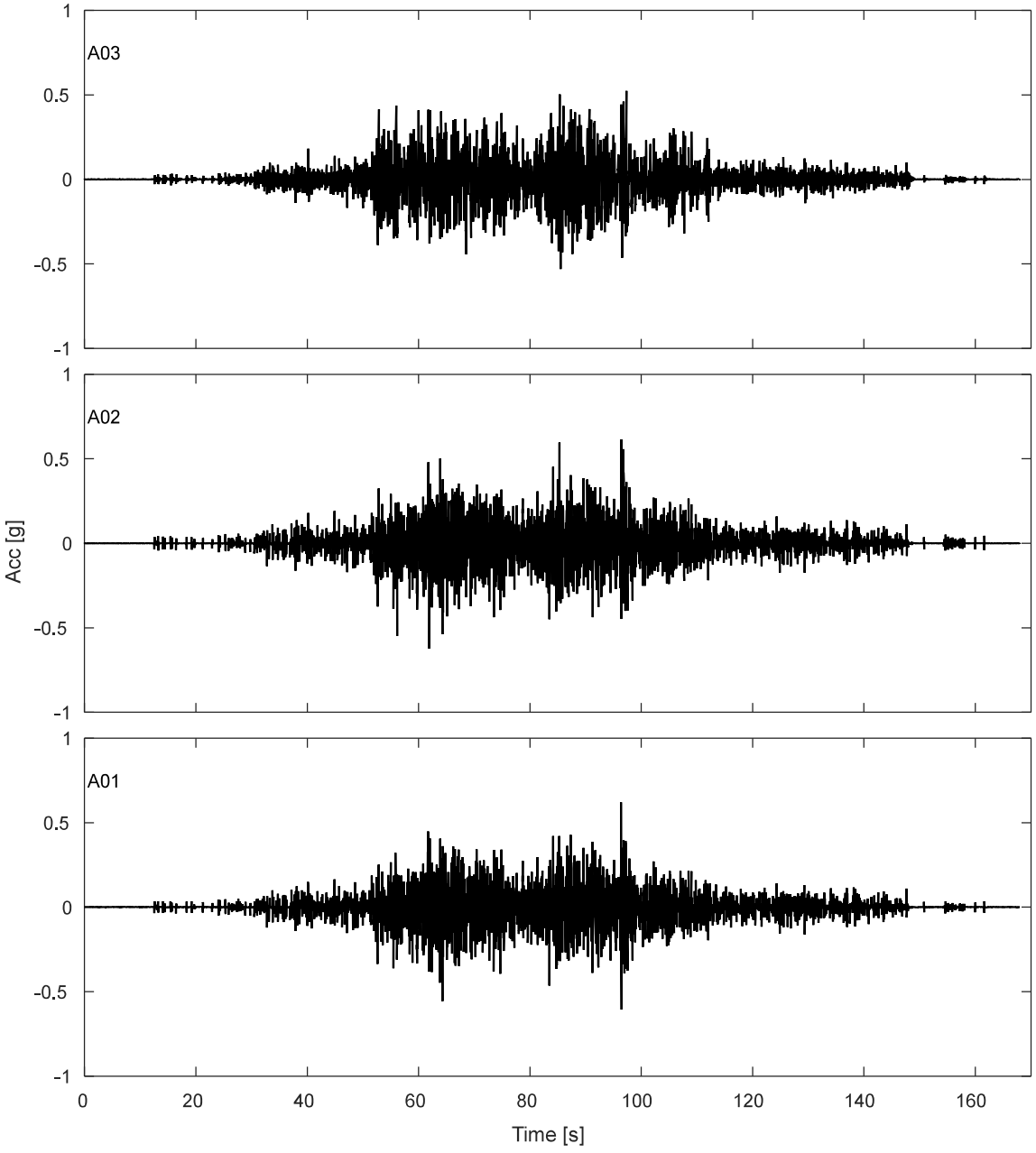

Figure I.9-2. Accelerations results along TDA during DT01-MAU-100P motion.

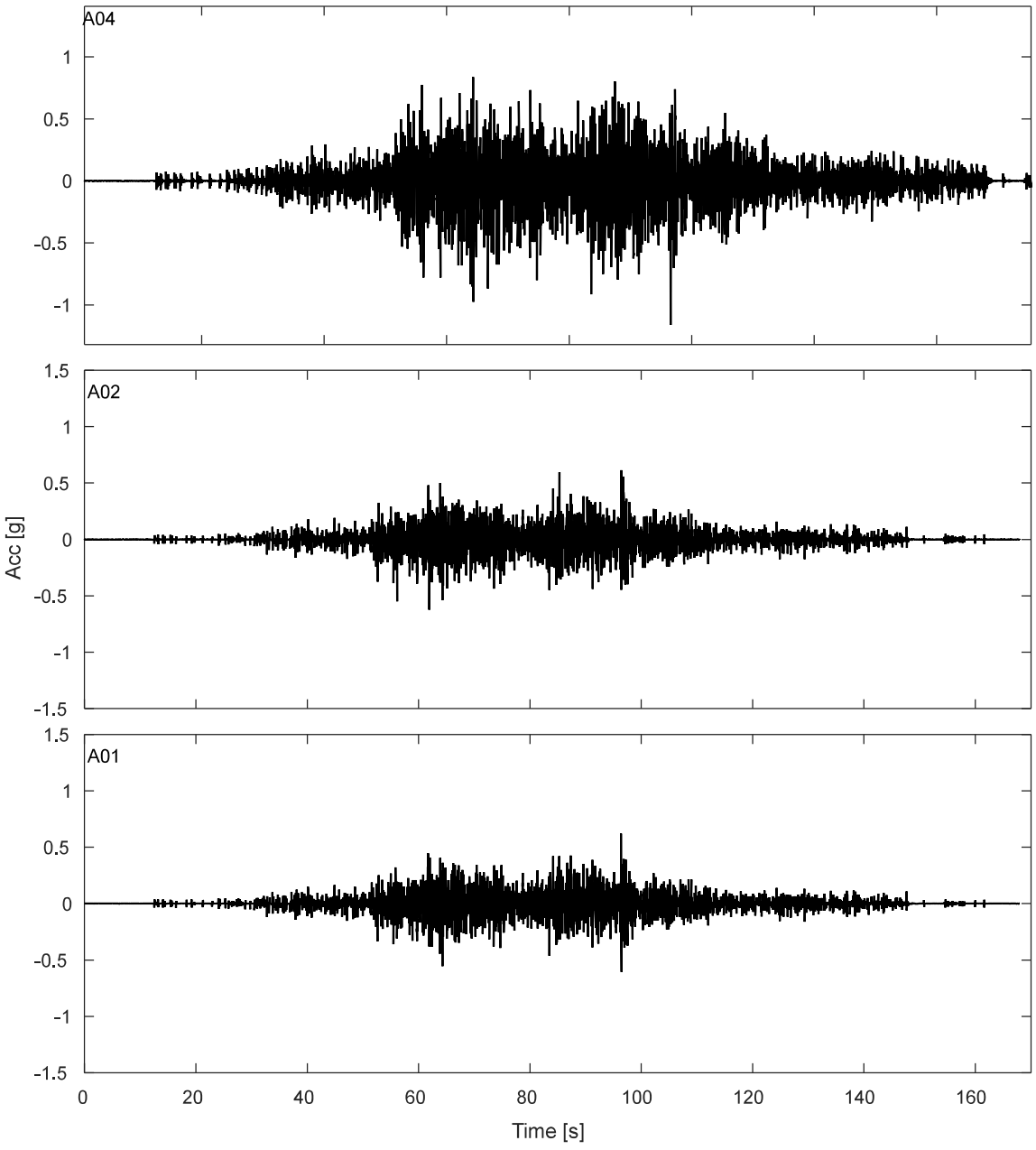

Figure I.9-3. Free field accelerations results for TDA during DT01-MAU-100P motion.

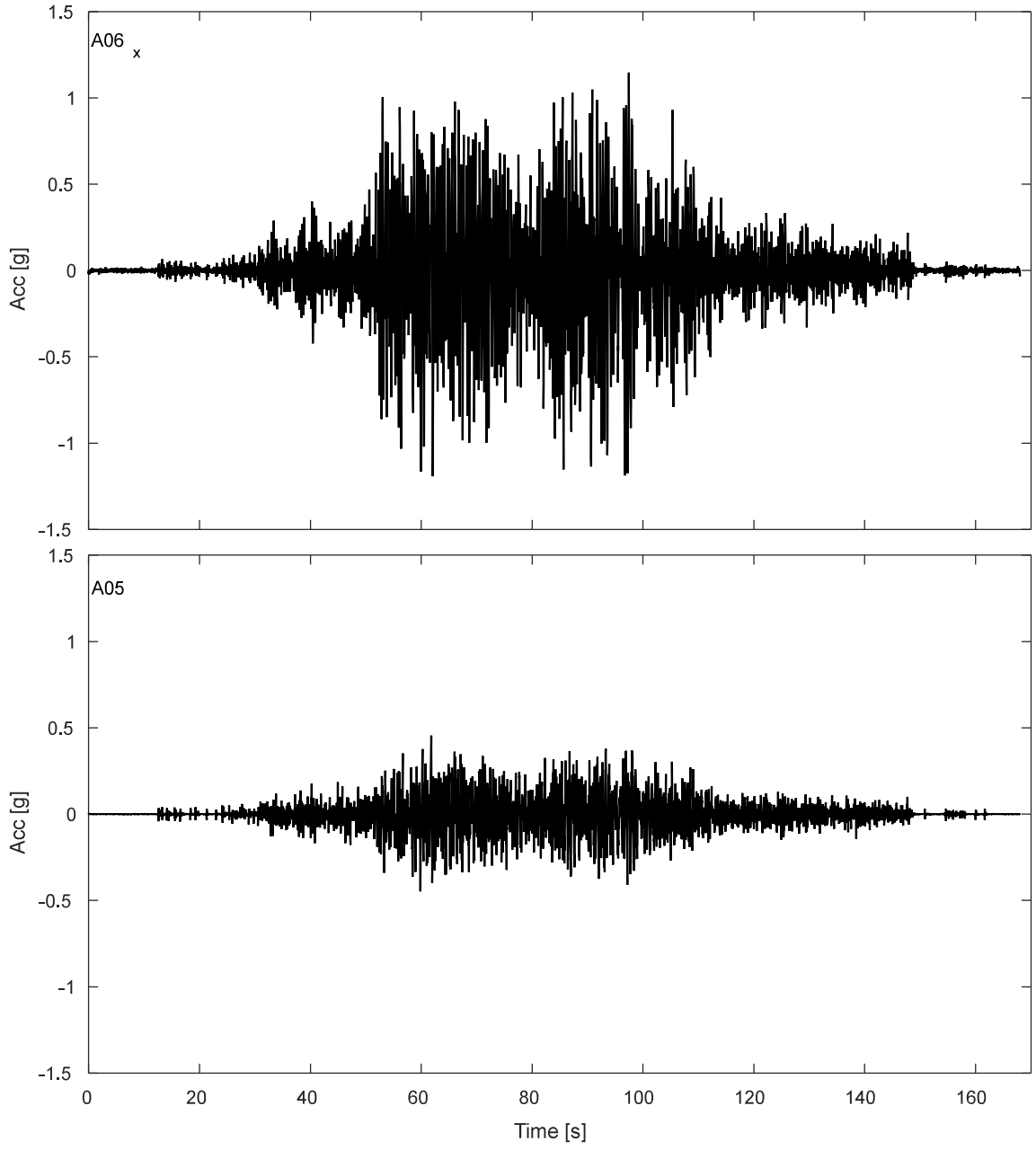

Figure I.9-4. Accelerations results SDOF structure during DT01-MAU-100P motion.

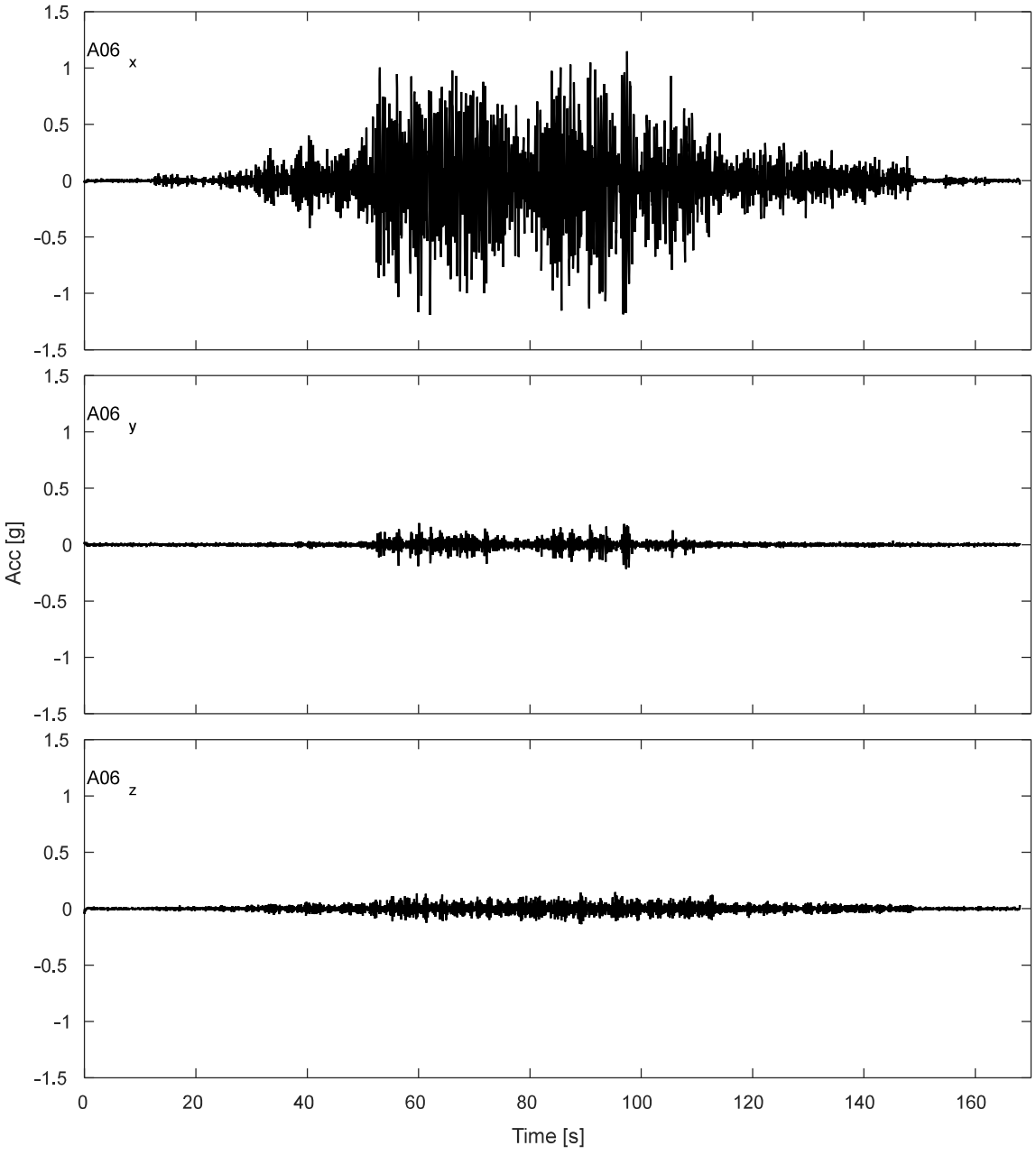

Figure I.9-5. Accelerations results for lumped mass of SDOF structure during DT01-MAU-100P motion.

I.9.2 Potentiometers.

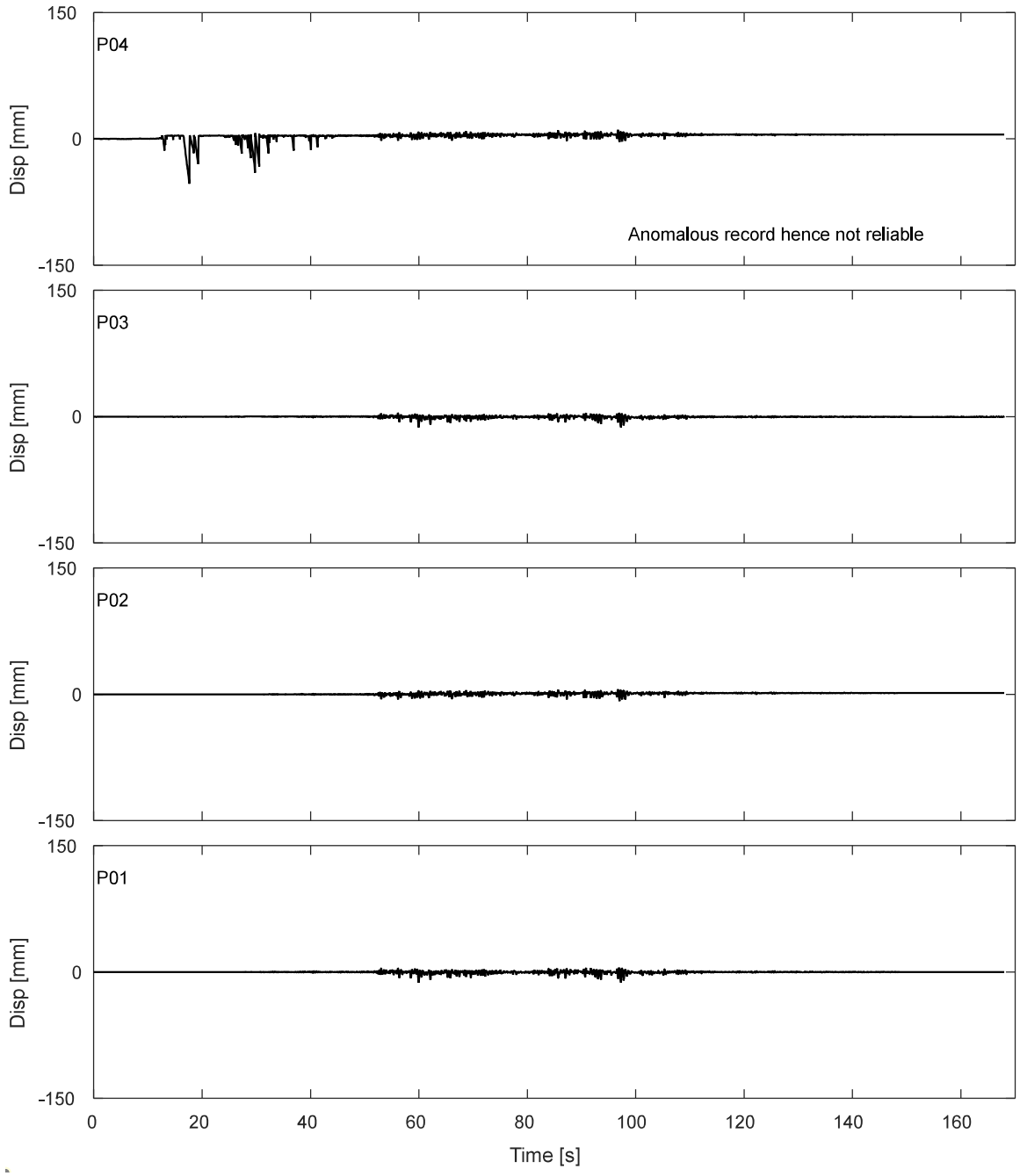

Figure I.9-6. Results of fully vertical potentiometers attached to corners of top of strip footing during DT01-MAU-100P motion.

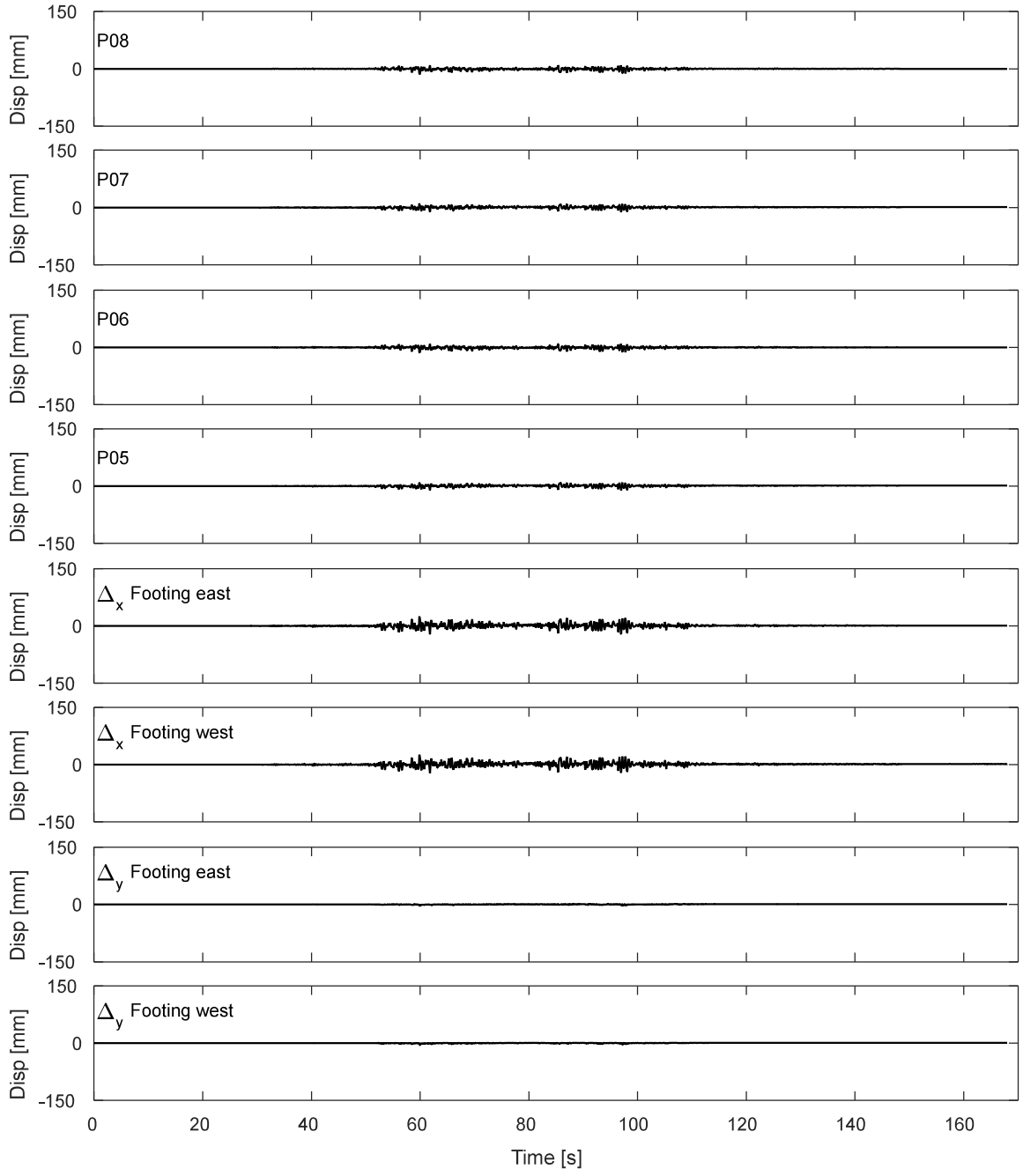

Figure I.9-7. Results of inclined potentiometers attached to top of strip footing during DT01-MAU-100P motion.

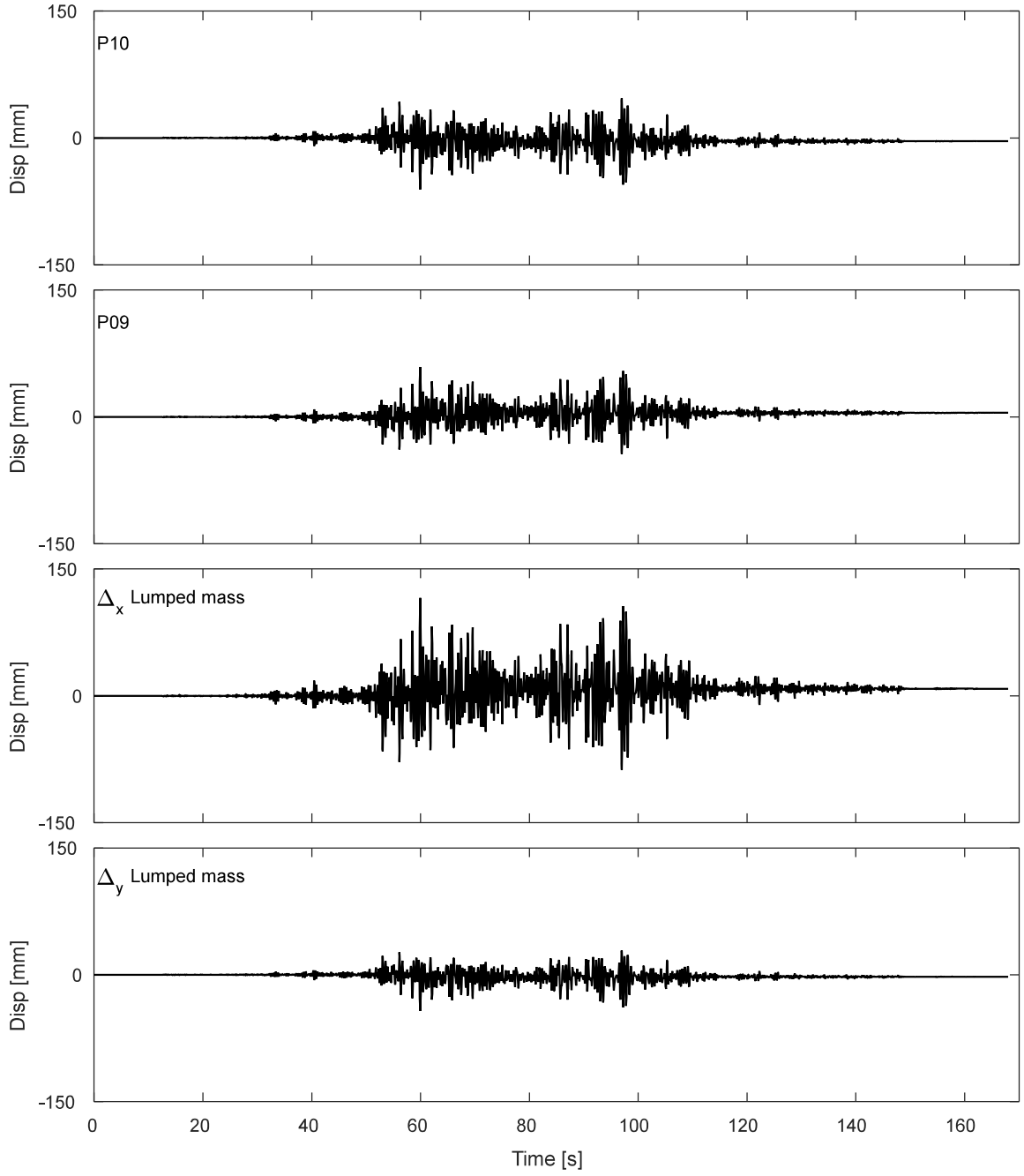

Figure I.9-8. Results of inclined potentiometers attached to lumped mass during DT01-MAU-100P motion.

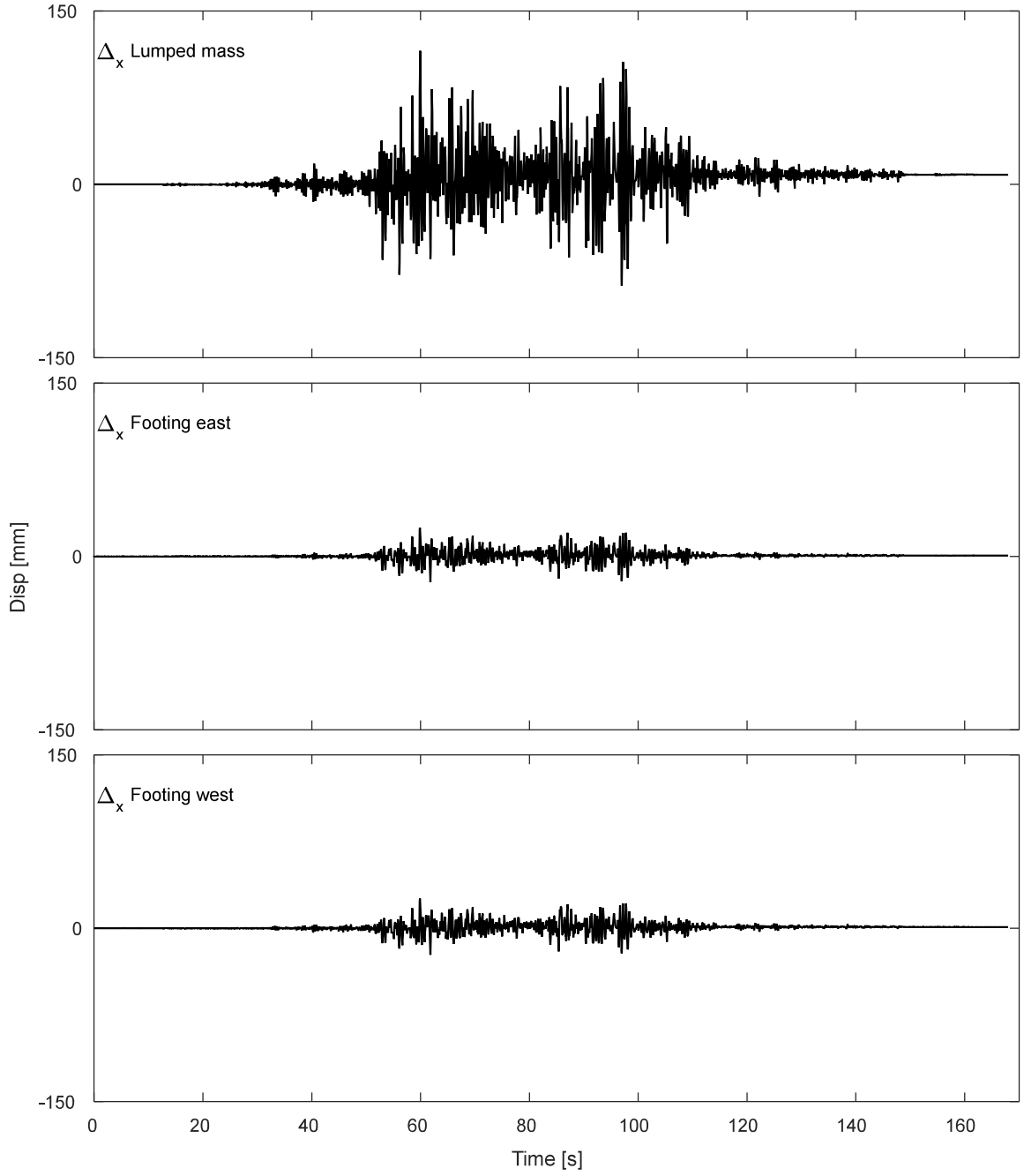

Figure I.9-9. Results of horizontal displacement of lumped mass and footing during DT01-MAU-100P motion.

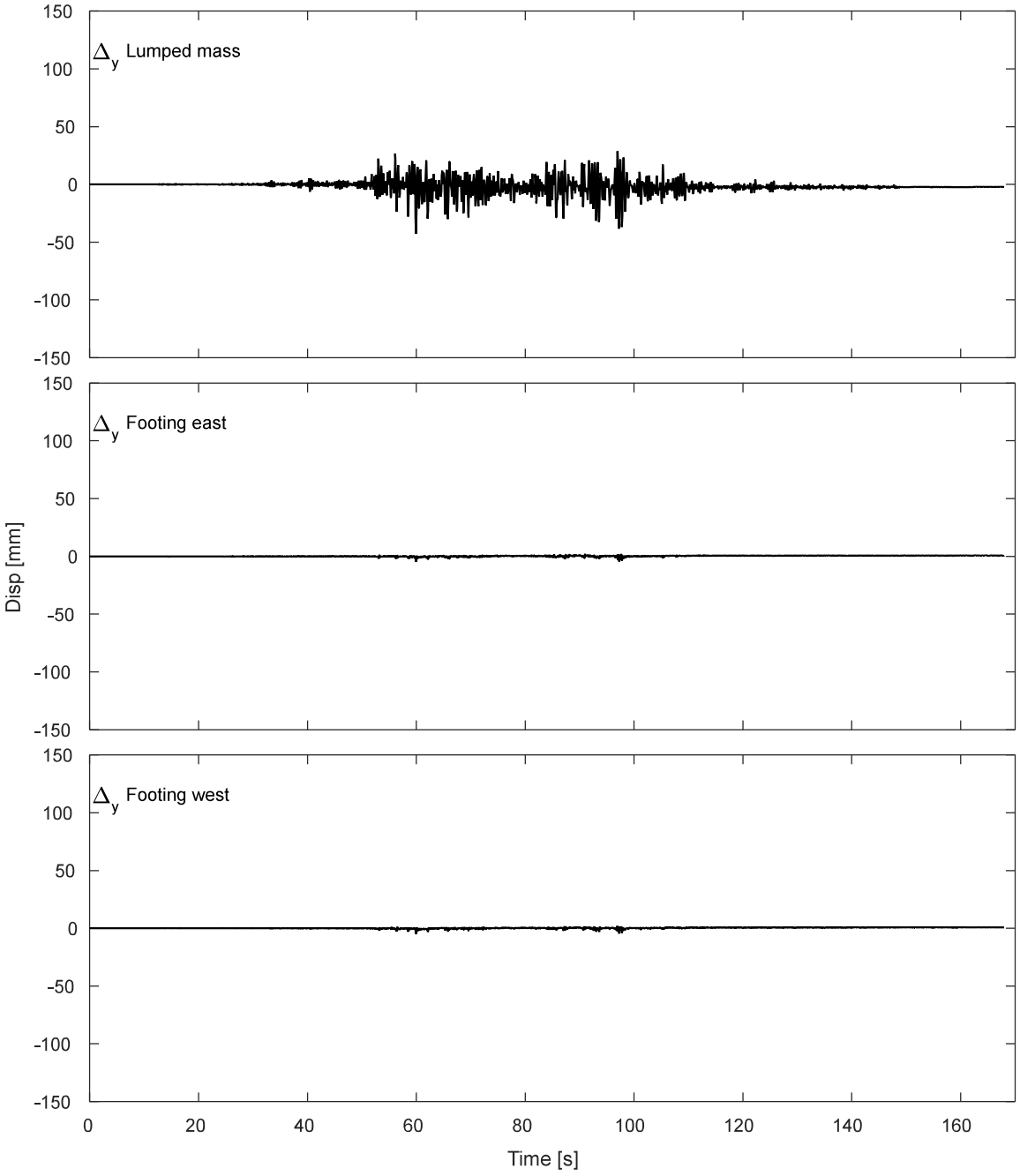

Figure I.9-10. Results of vertical displacement of lumped mass and footing during DT01-MAU-100P motion.

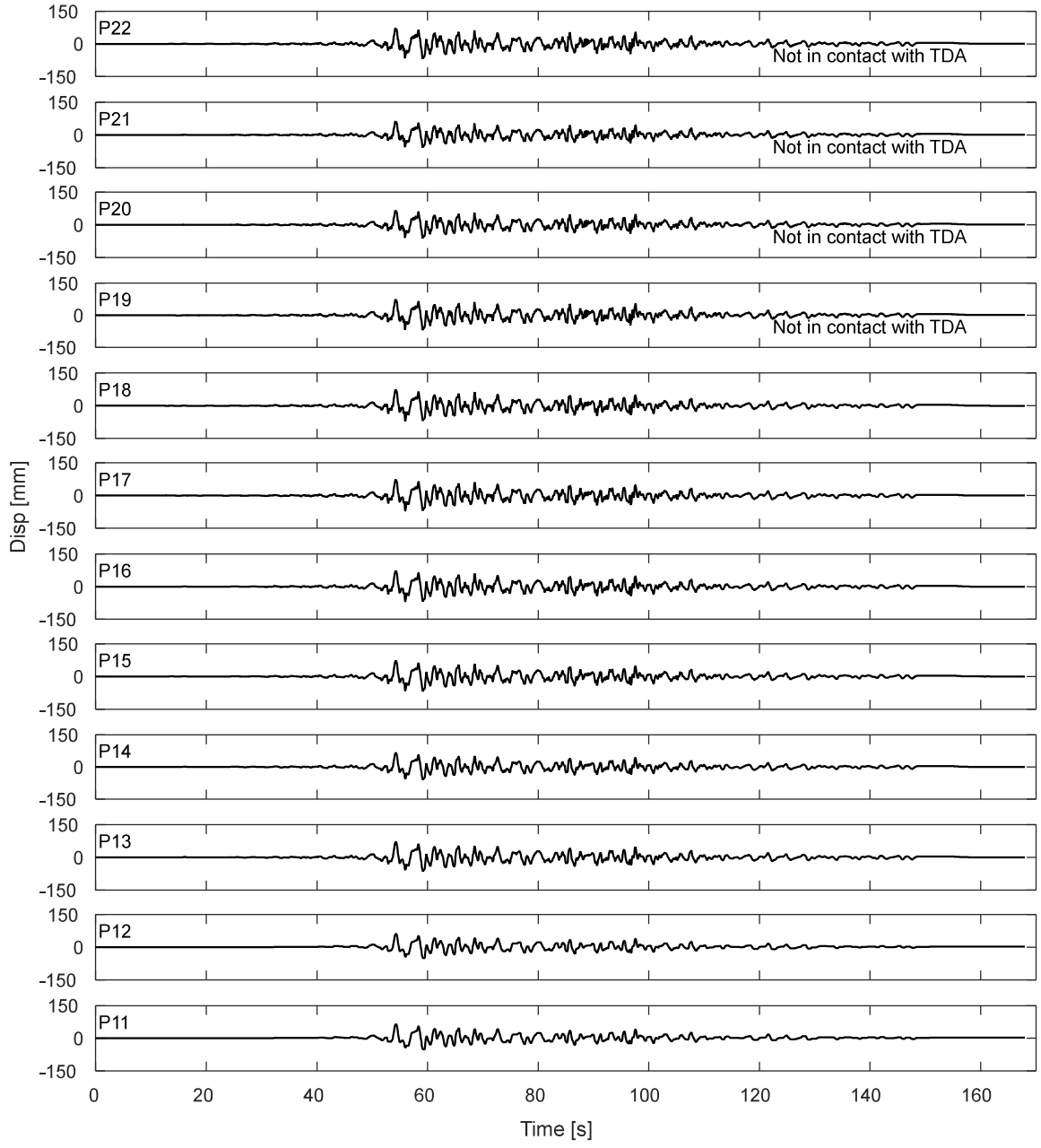

Figure I.9-11. Potentiometers results for the laminar box during DT01-MAU-100P motion.

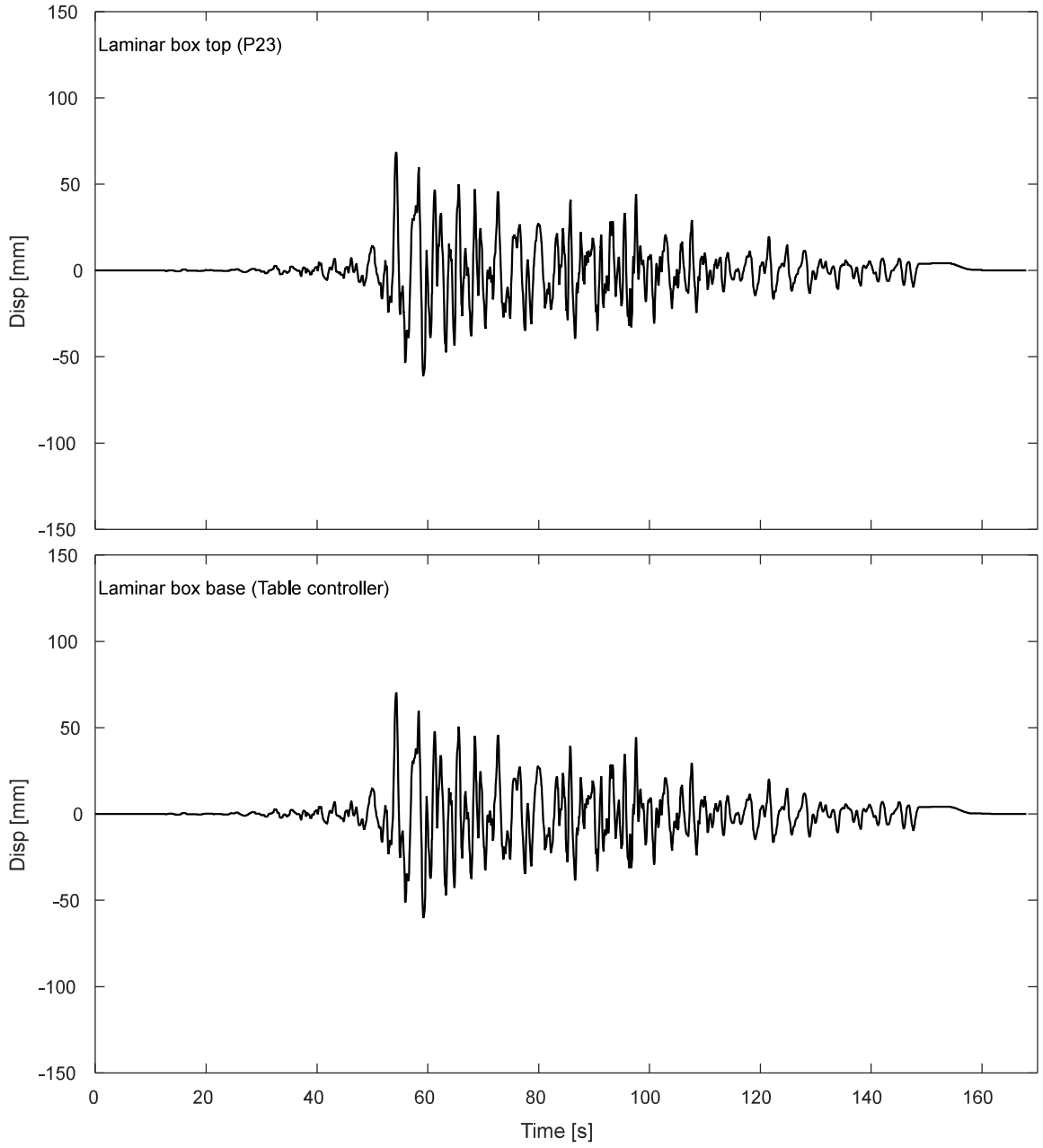

Figure I.9-12. Displacement response of top and base of laminar box during DT01-MAU-100P motion.

I.9.3. Inclinometers.

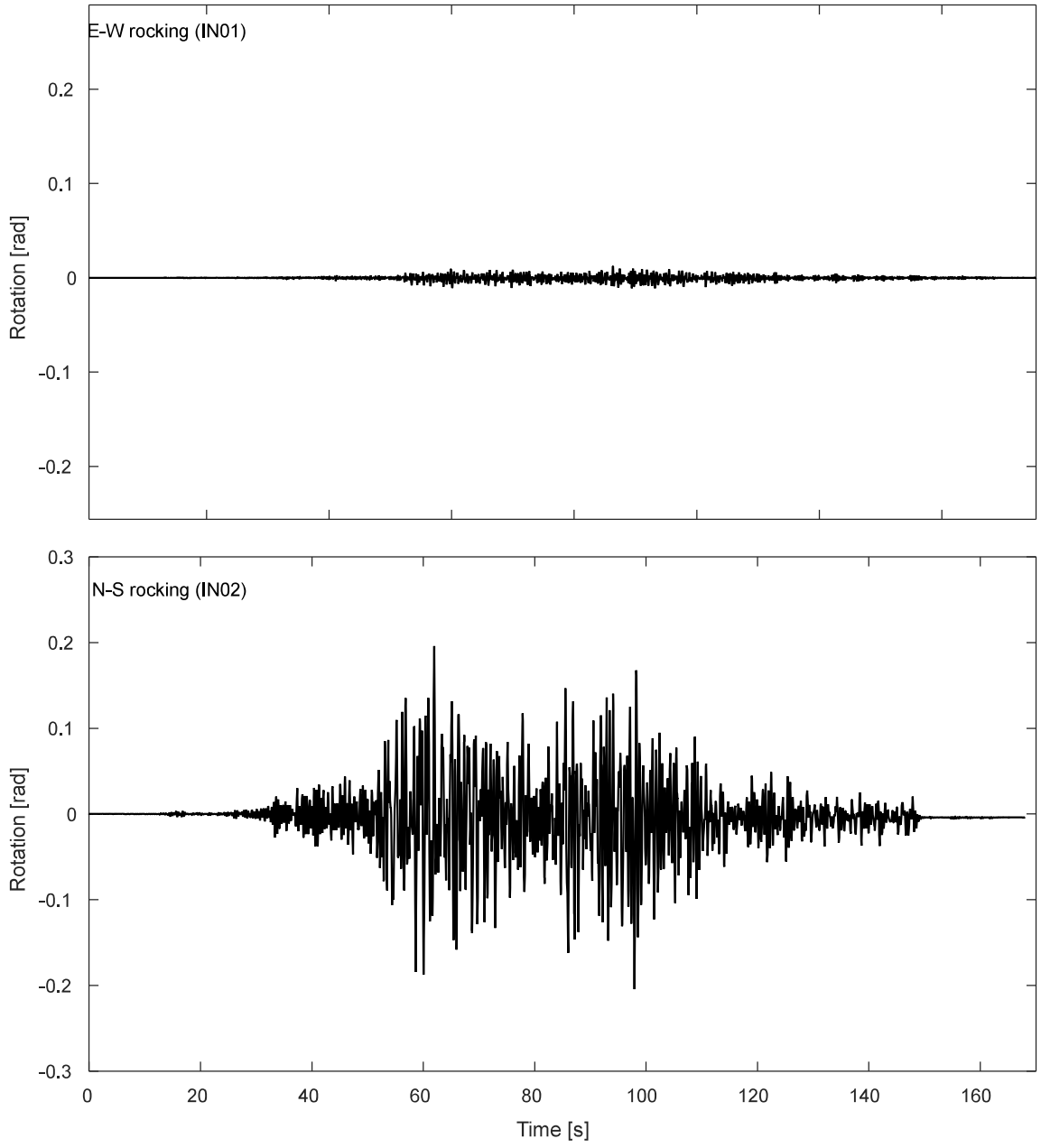

Figure I.9-13. Inclinometer results for the footing during DT01-MAU-100P motion.

I.9.4. Pressure cells.

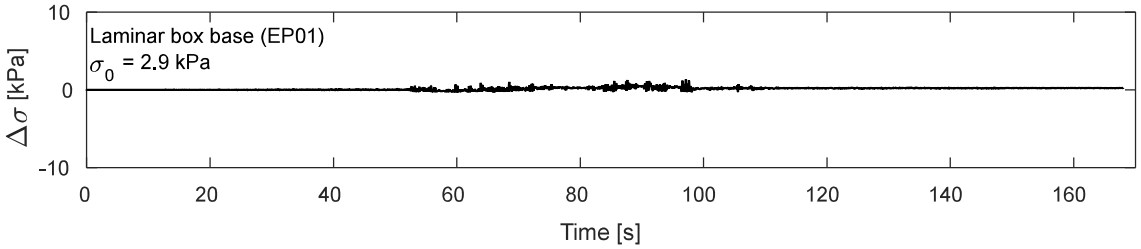

Figure I.9-14. Pressure cells results at laminar box base during DT01-MAU-100P motion.

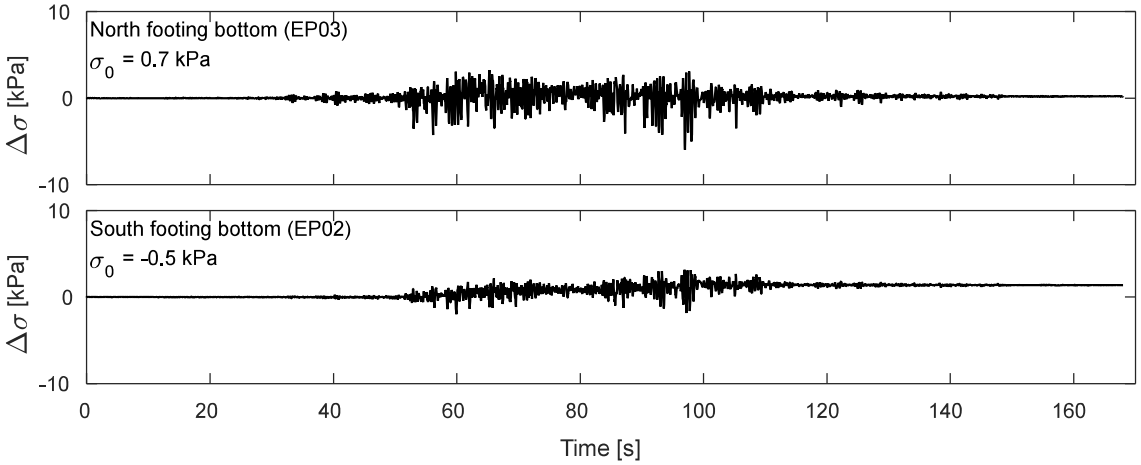

Figure I.9-15. Pressure cells results at footing bottom during DT01-MAU-100P motion.

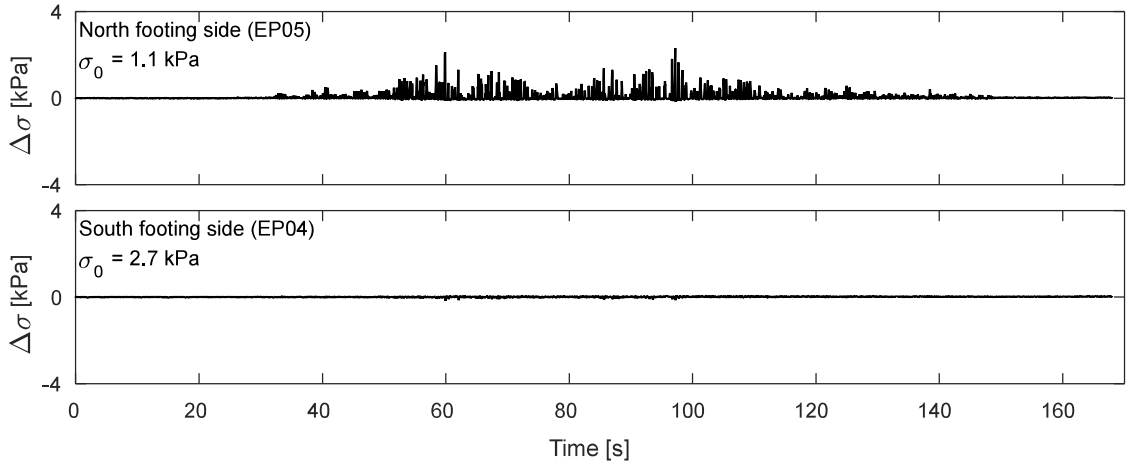

Figure I.9-16. Pressure cells results at footing sides during DT01-MAU-100P motion.

APPENDIX I – Dynamic testing specimen No 02 (DT01)

I.1 - Instrumentation Layout for Dynamic Test No 02.

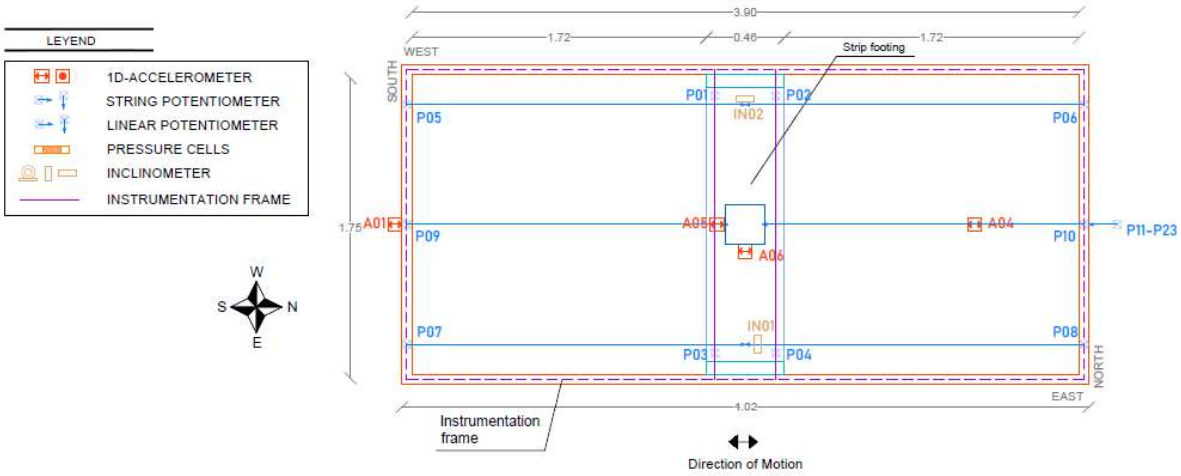

Figure K.1-1. Instrumentation Layout – Plan View.

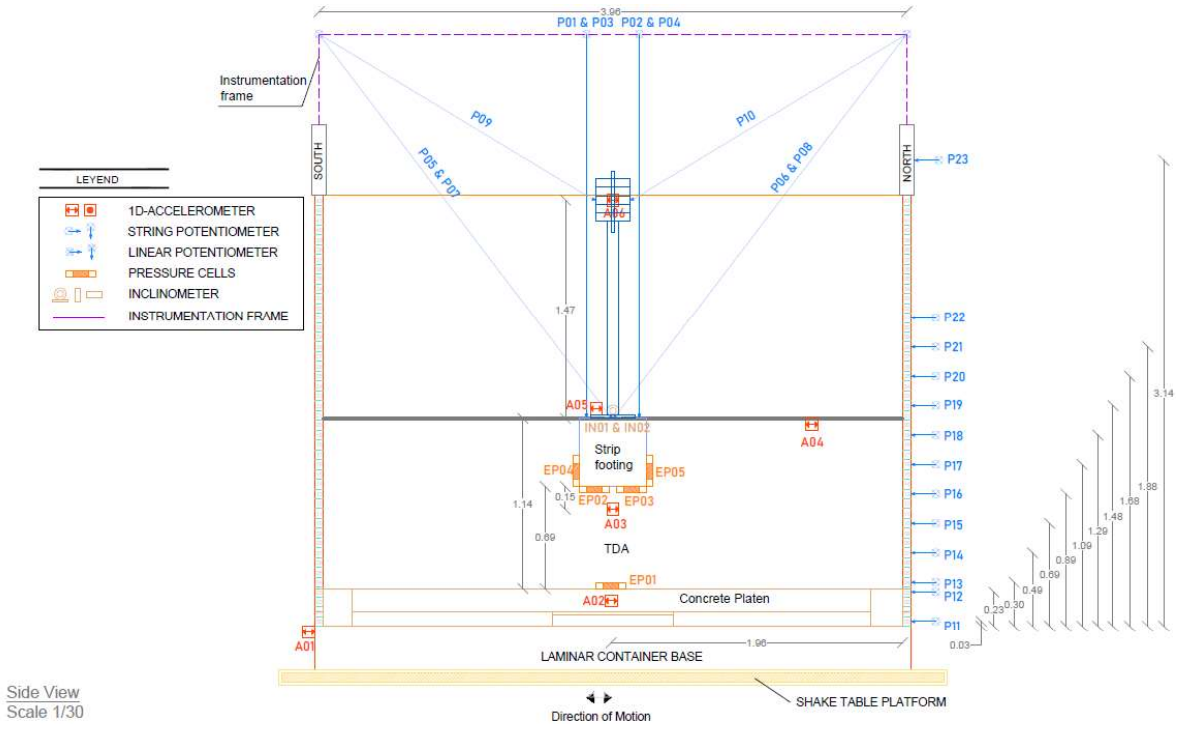

Figure I.1-2. Instrumentation Layout – Side View.

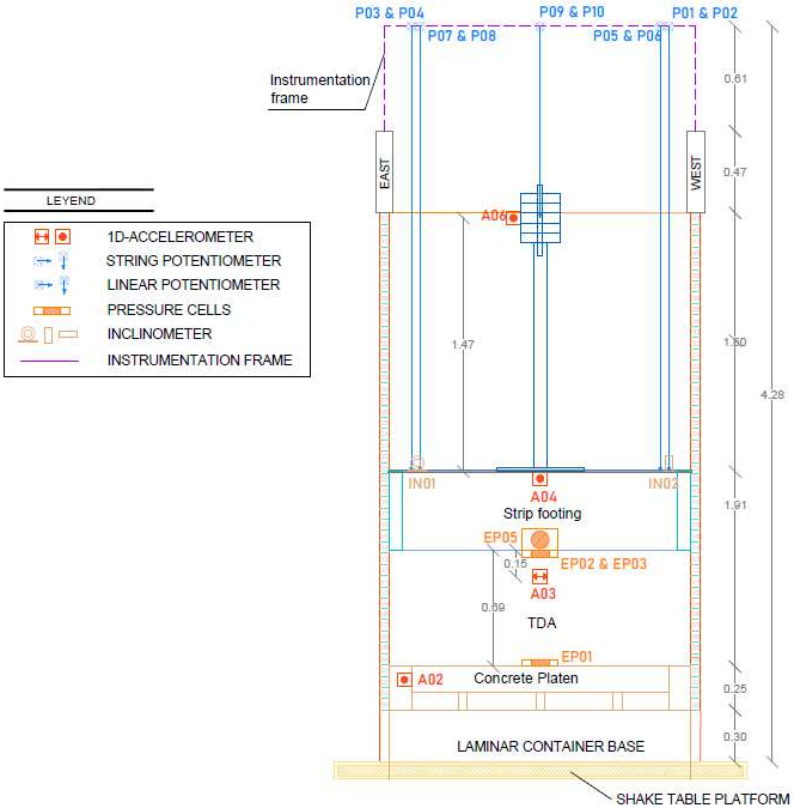

Figure I.1-3. Instrumentation Layout – Front View.

I.2. Time-history Records for DT01-SS150-F01F10 motion.

I.2.1 Input Motion

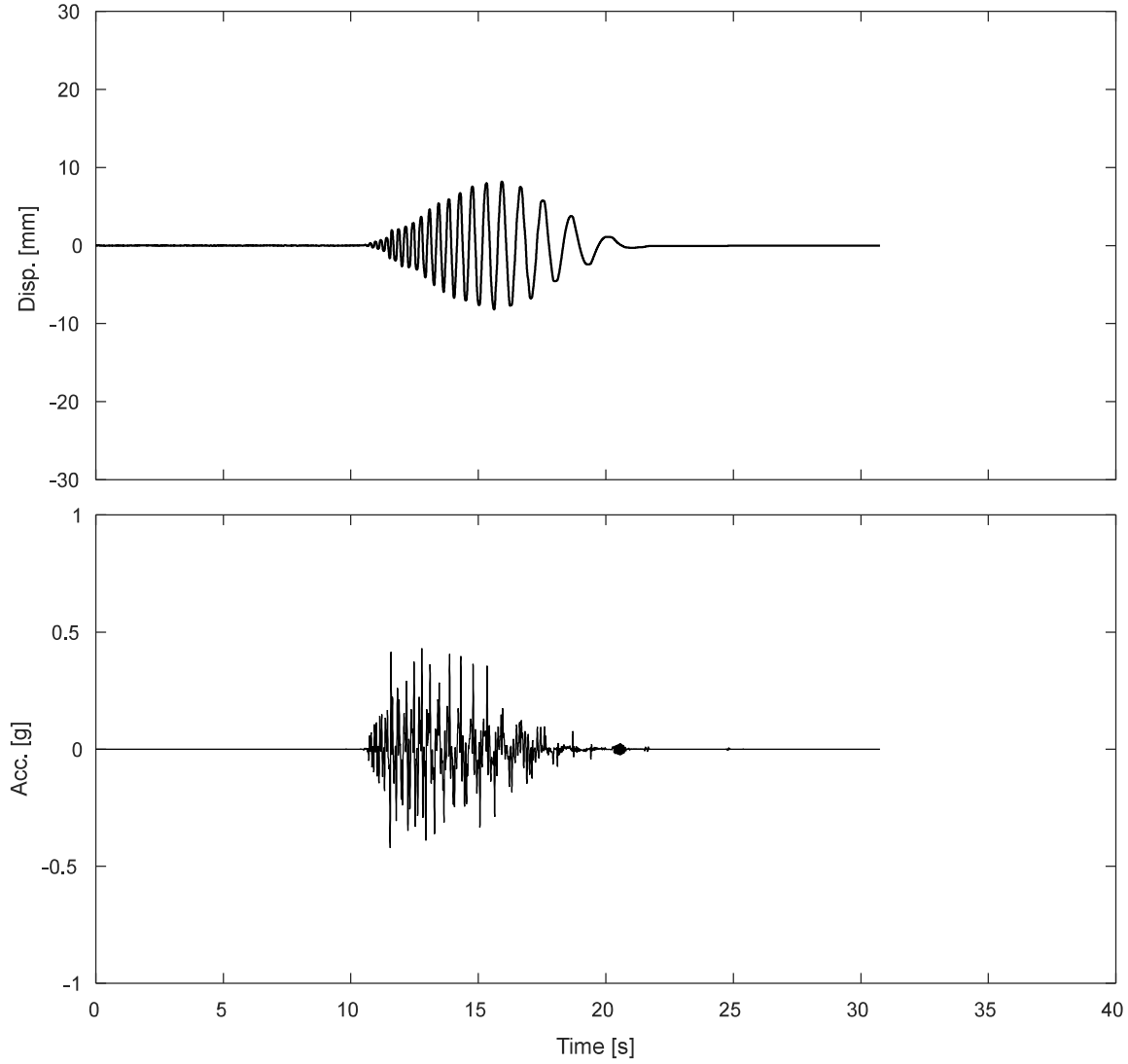

Figure I.2-1. Measured input displacement and acceleration at the base of the specimen during DT01-SS150-F01F10 motion

I.2.1 Accelerometers.

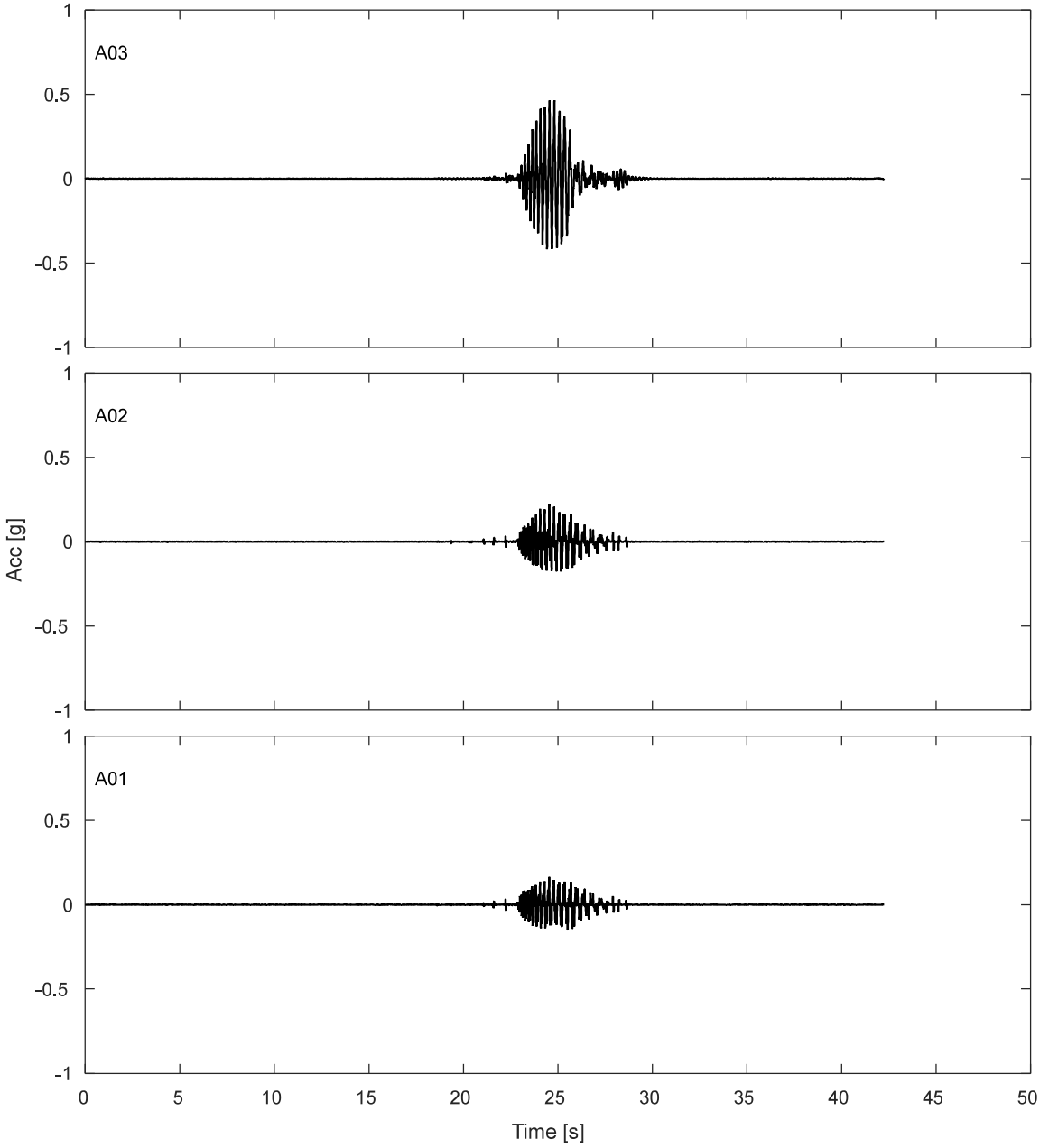

Figure I.2-2. Accelerations results along TDA during DT01-SS150-F01F10 motion.

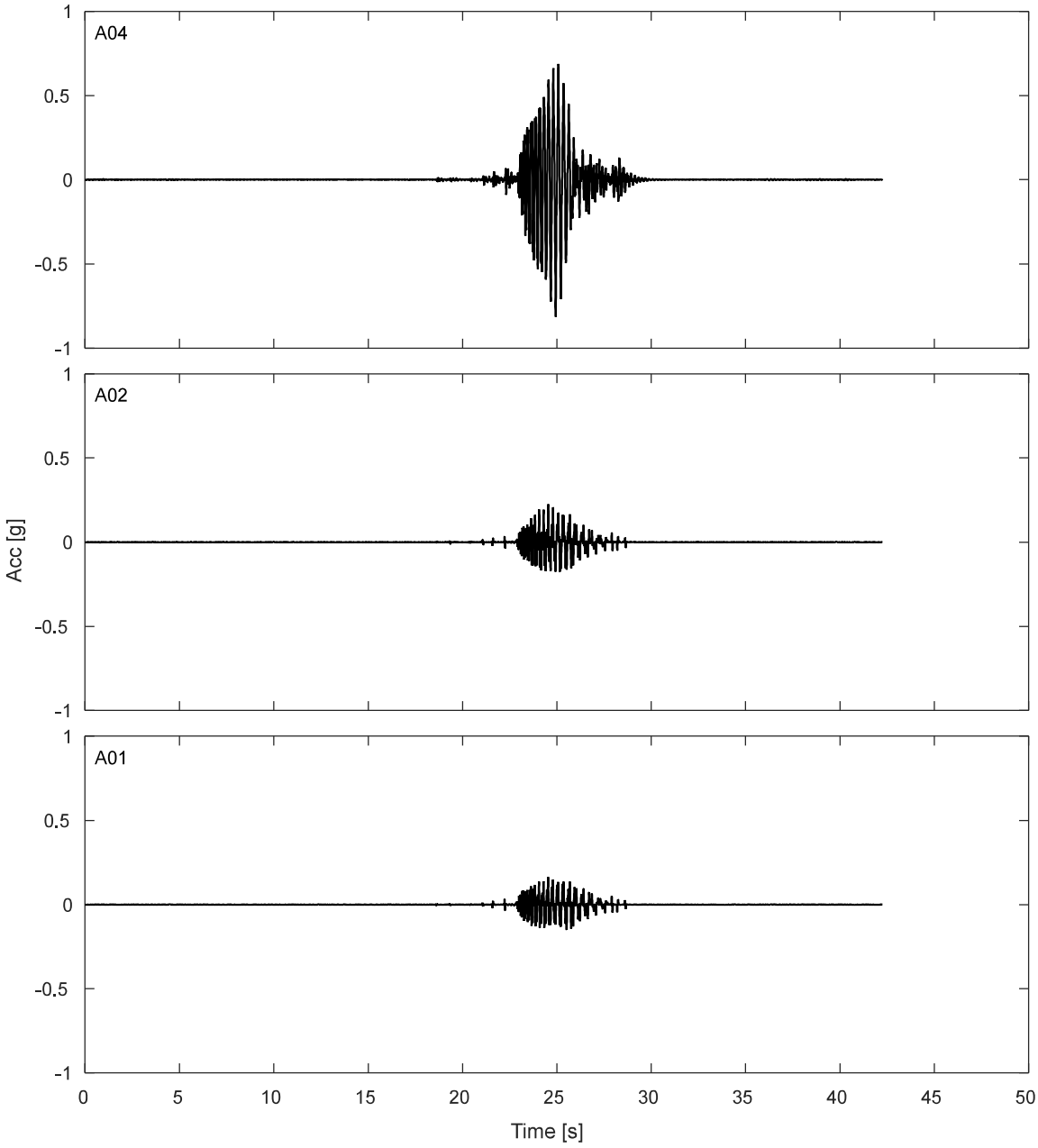

Figure I.2-3. Free field accelerations results for TDA during DT01-SS150-F01F10 motion.

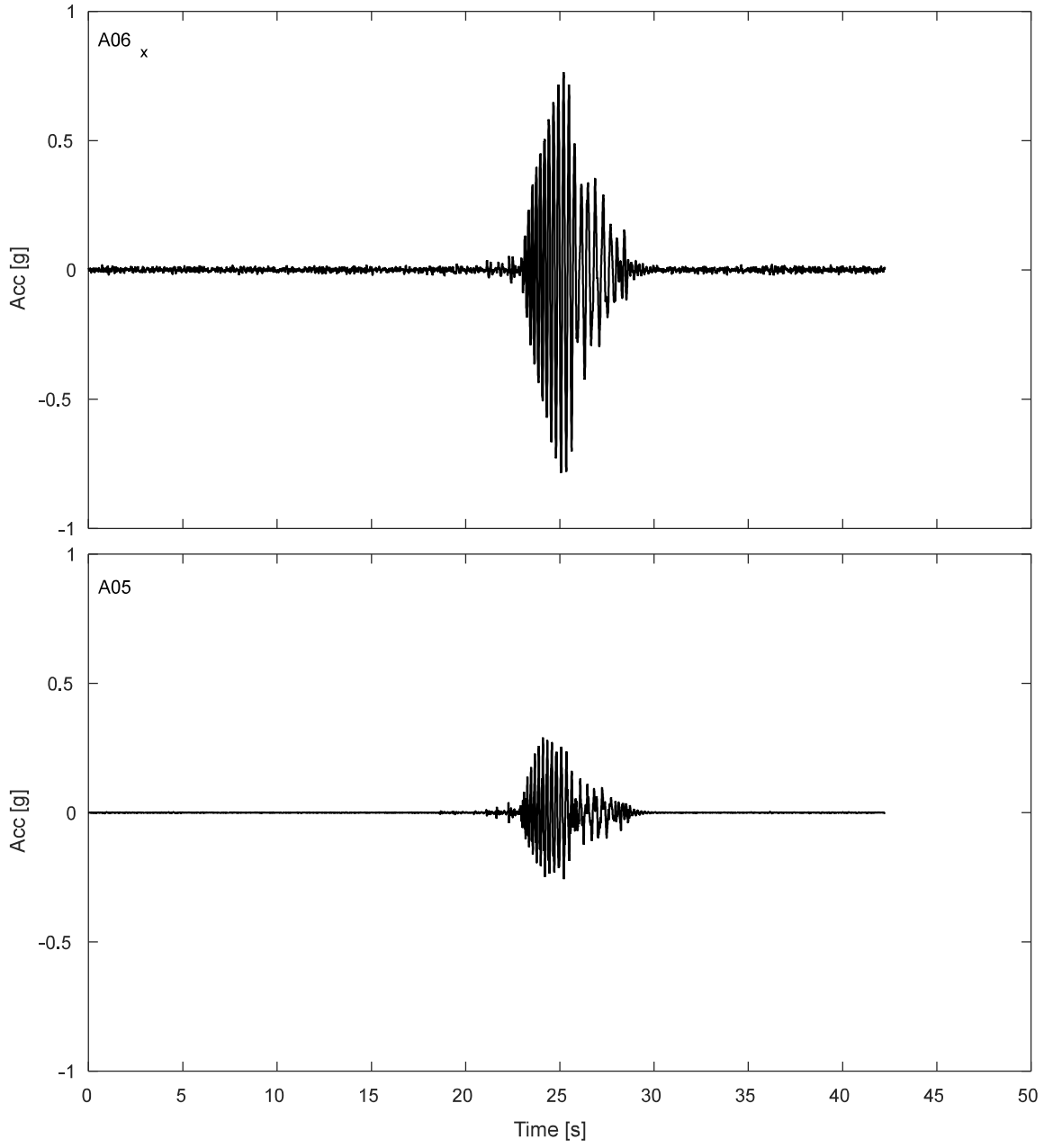

Figure I.2-4. Accelerations results SDOF structure during DT01-SS150-F01F10 motion.

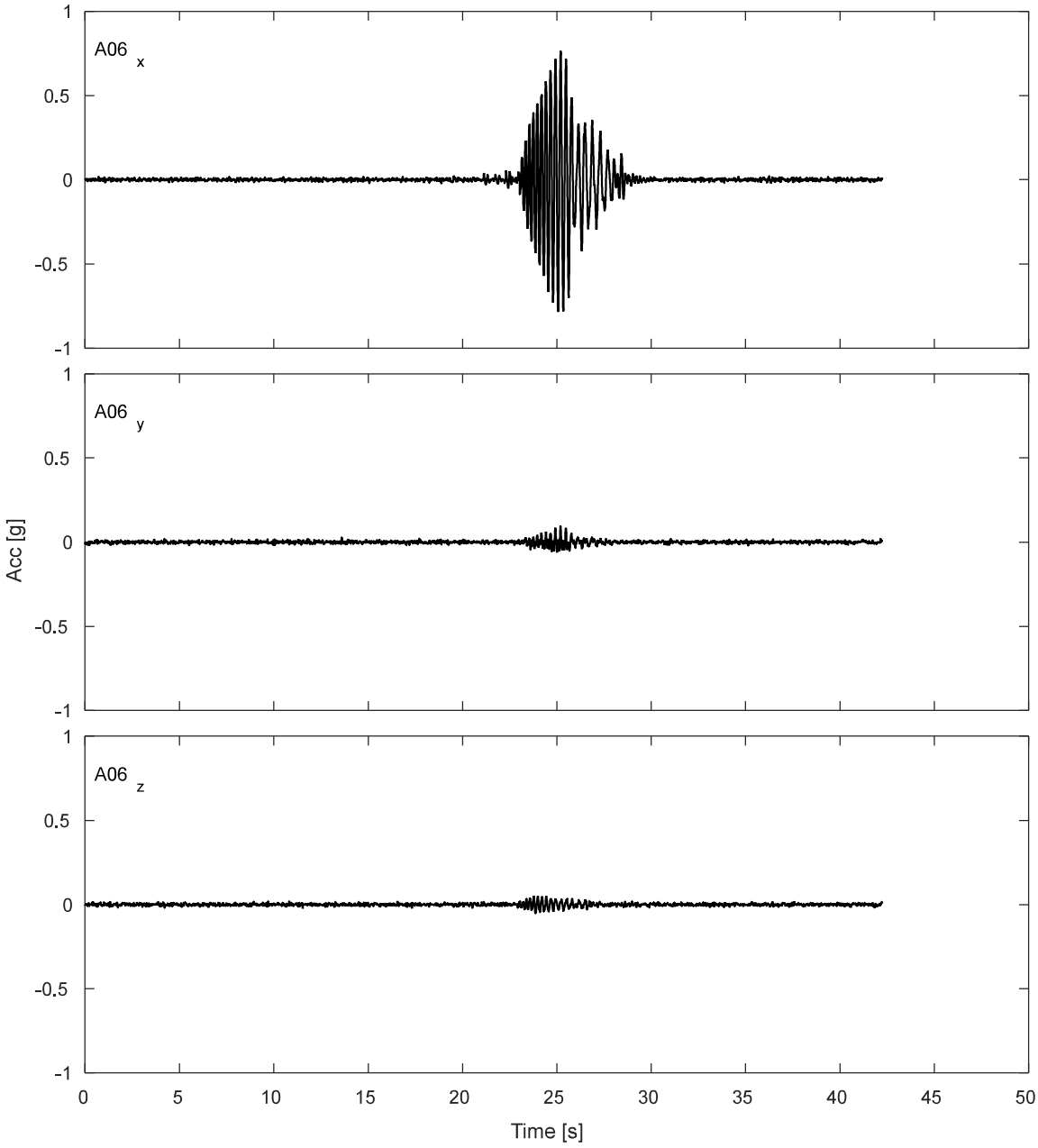

Figure I.2-5. Accelerations results for lumped mass of SDOF structure during DT01-SS150-F01F10 motion.

I.2.2 Potentiometers.

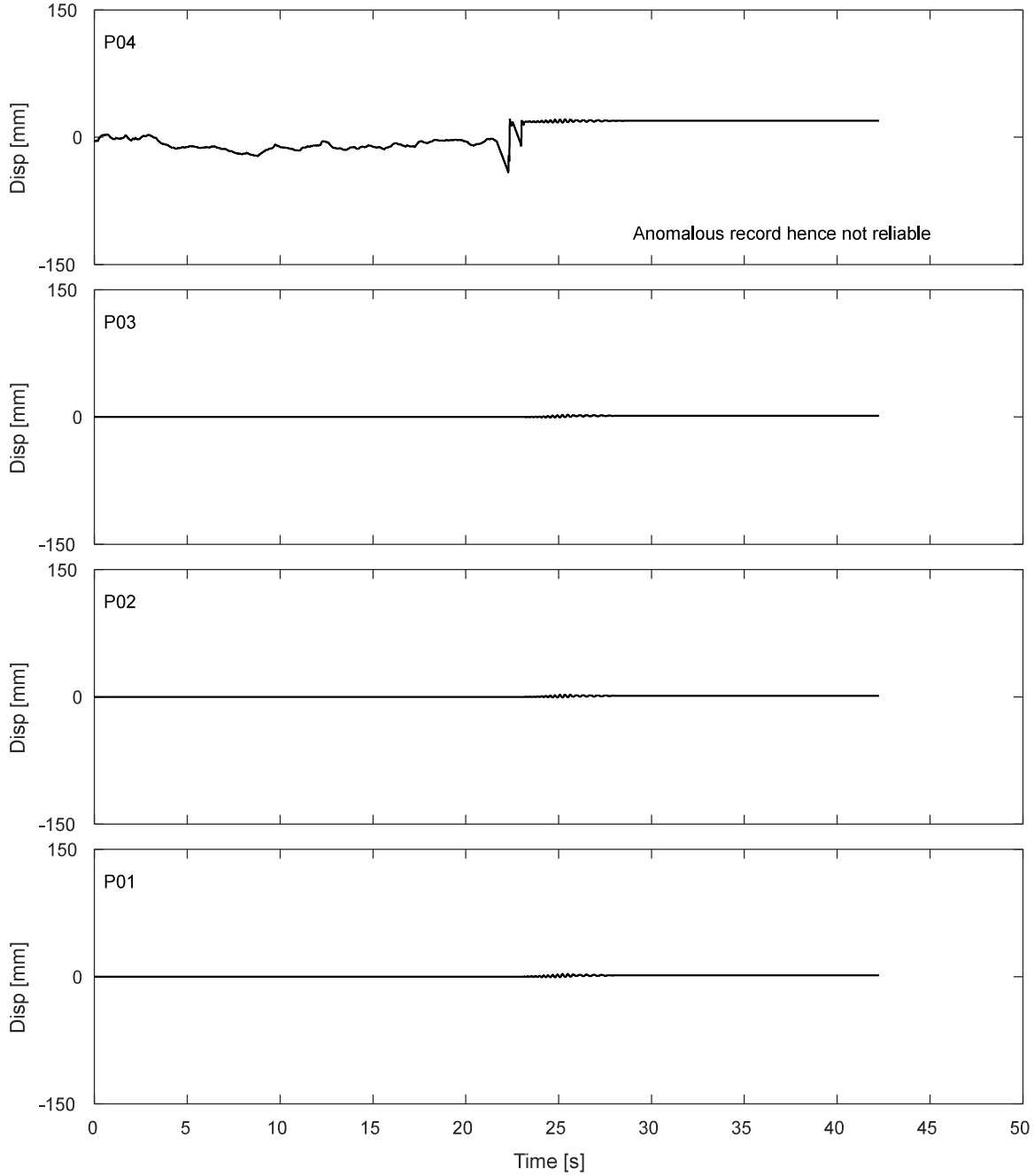

Figure I.2-6. Results of fully vertical potentiometers attached to Corners of top of strip footing during DT01-SS150-F01F10 motion.

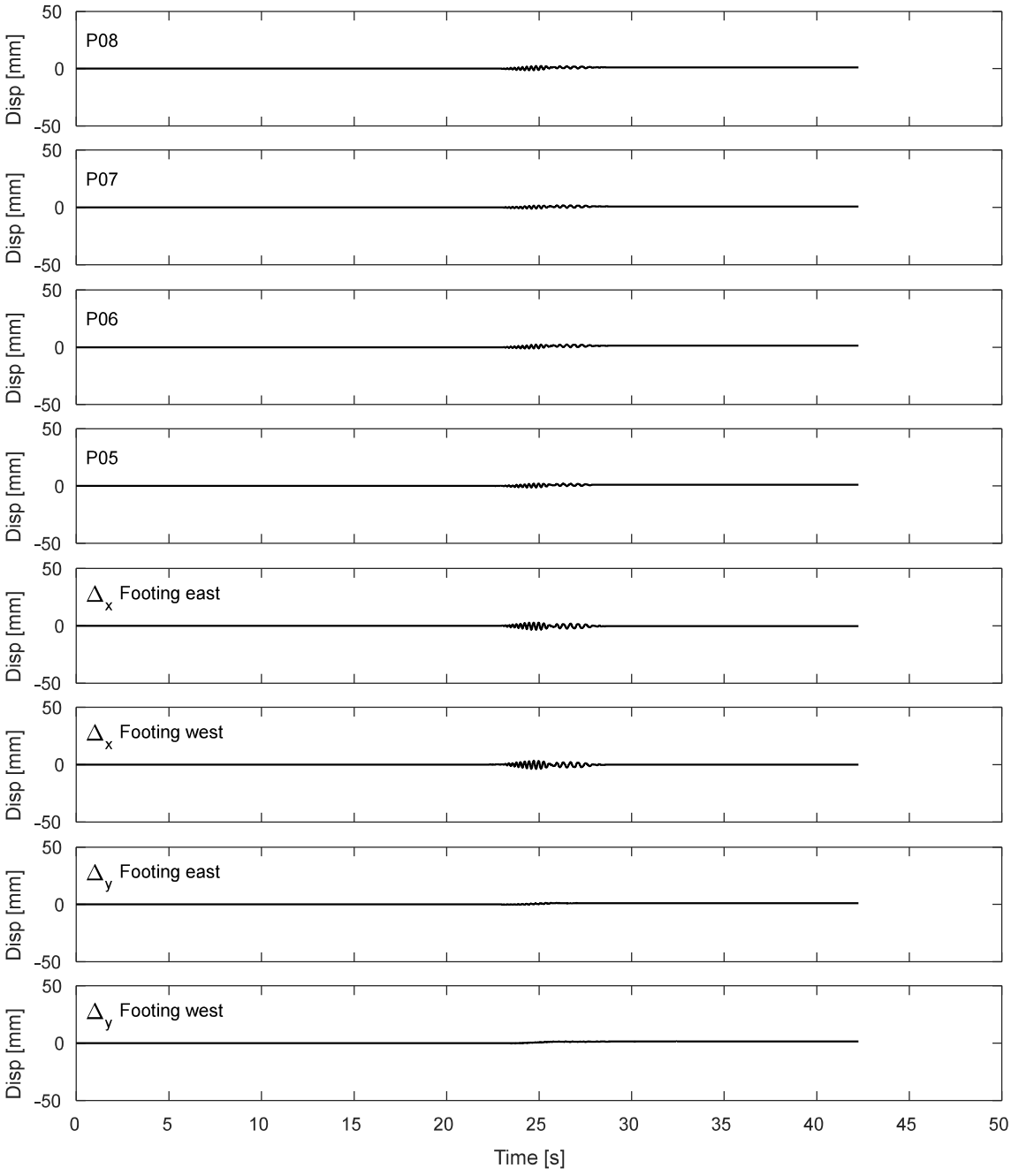

Figure I.2-7. Results of inclined potentiometers attached to top of strip footing during DT01-SS150-F01F10 motion.

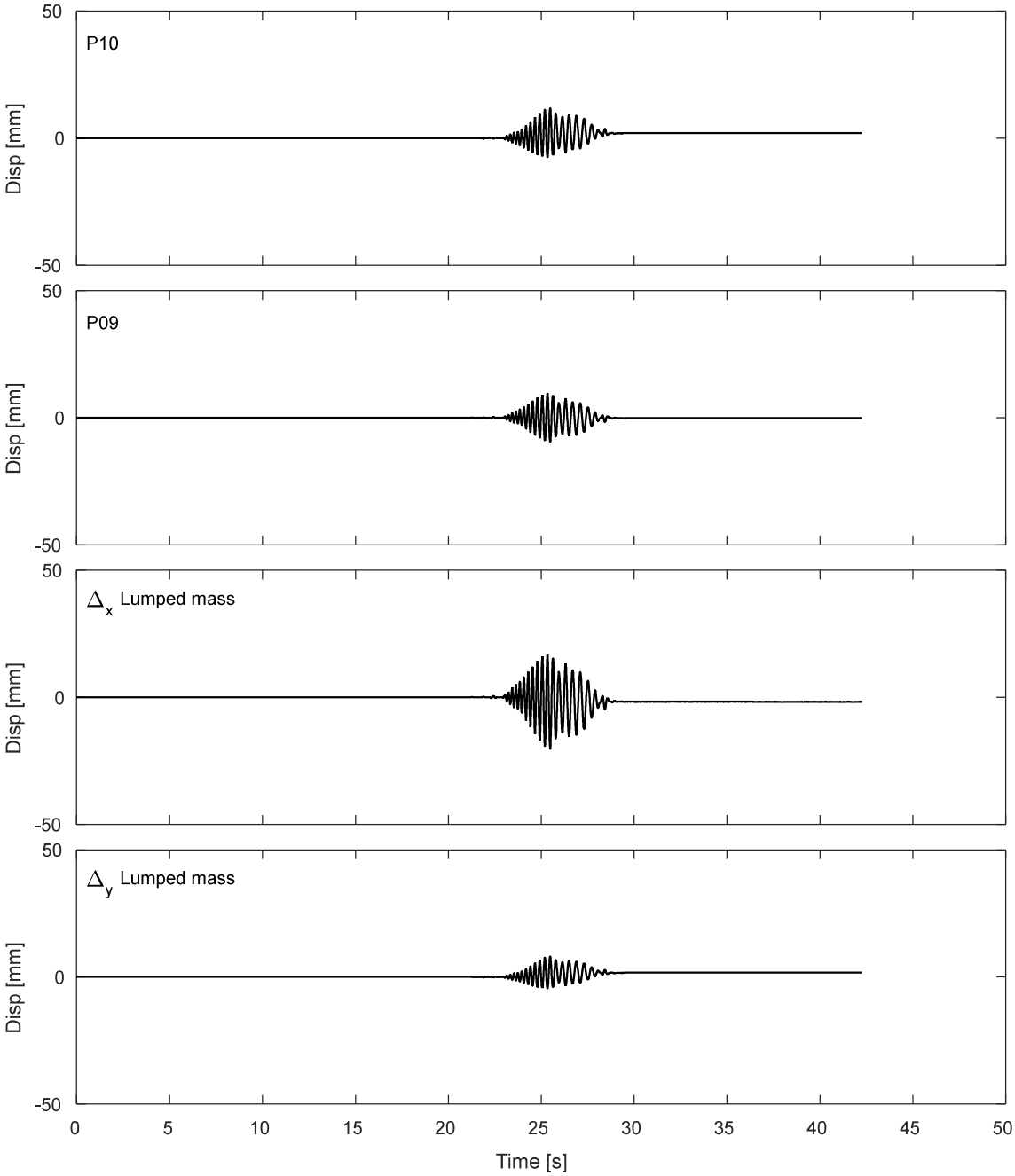

Figure I.2-8. Results of inclined potentiometers attached to lumped mass during DT01-SS150-F01F10 motion.

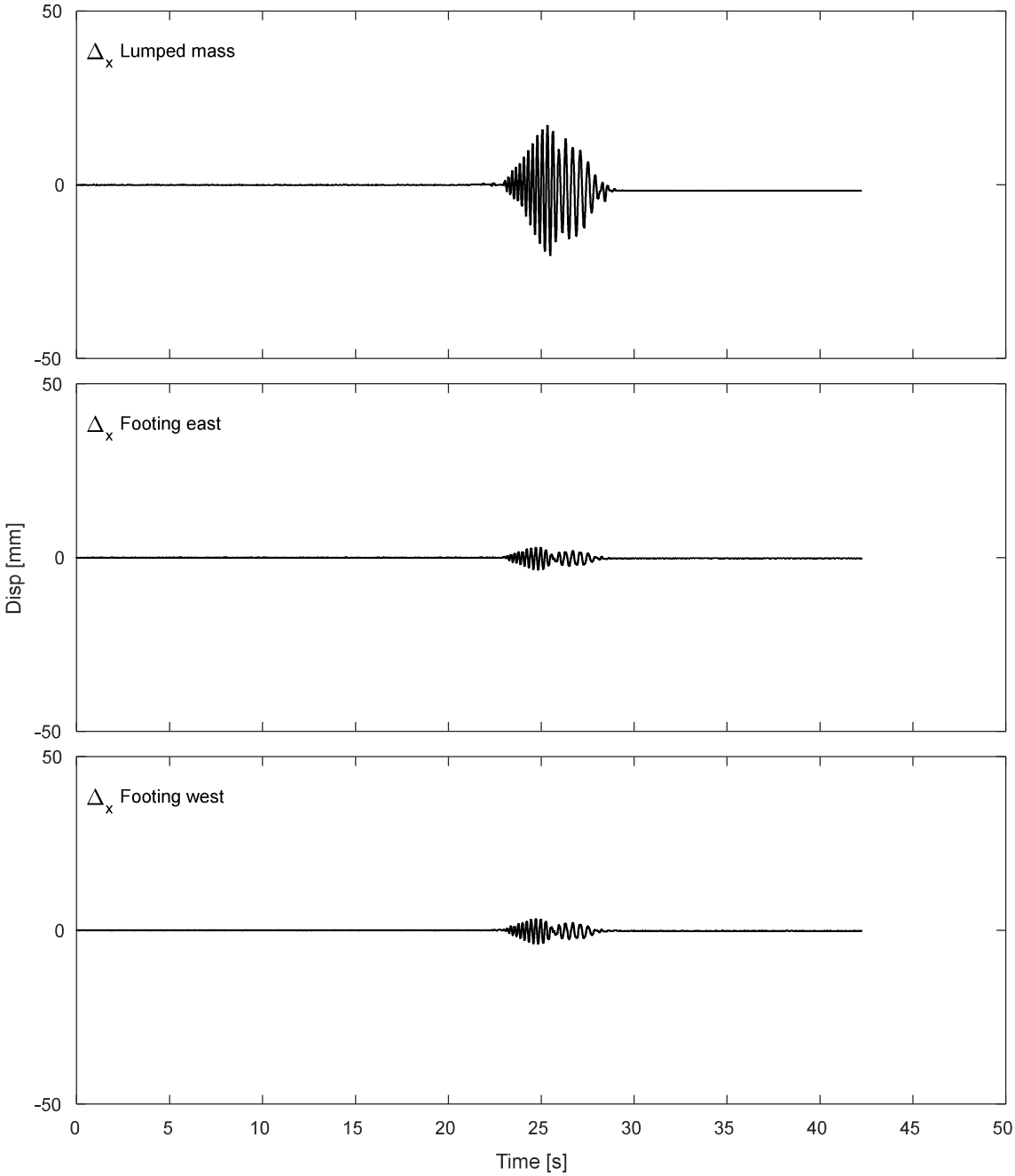

Figure I.2-9. Results of horizontal displacement of lumped mass and footing during DT01-SS150-F01F10 motion.

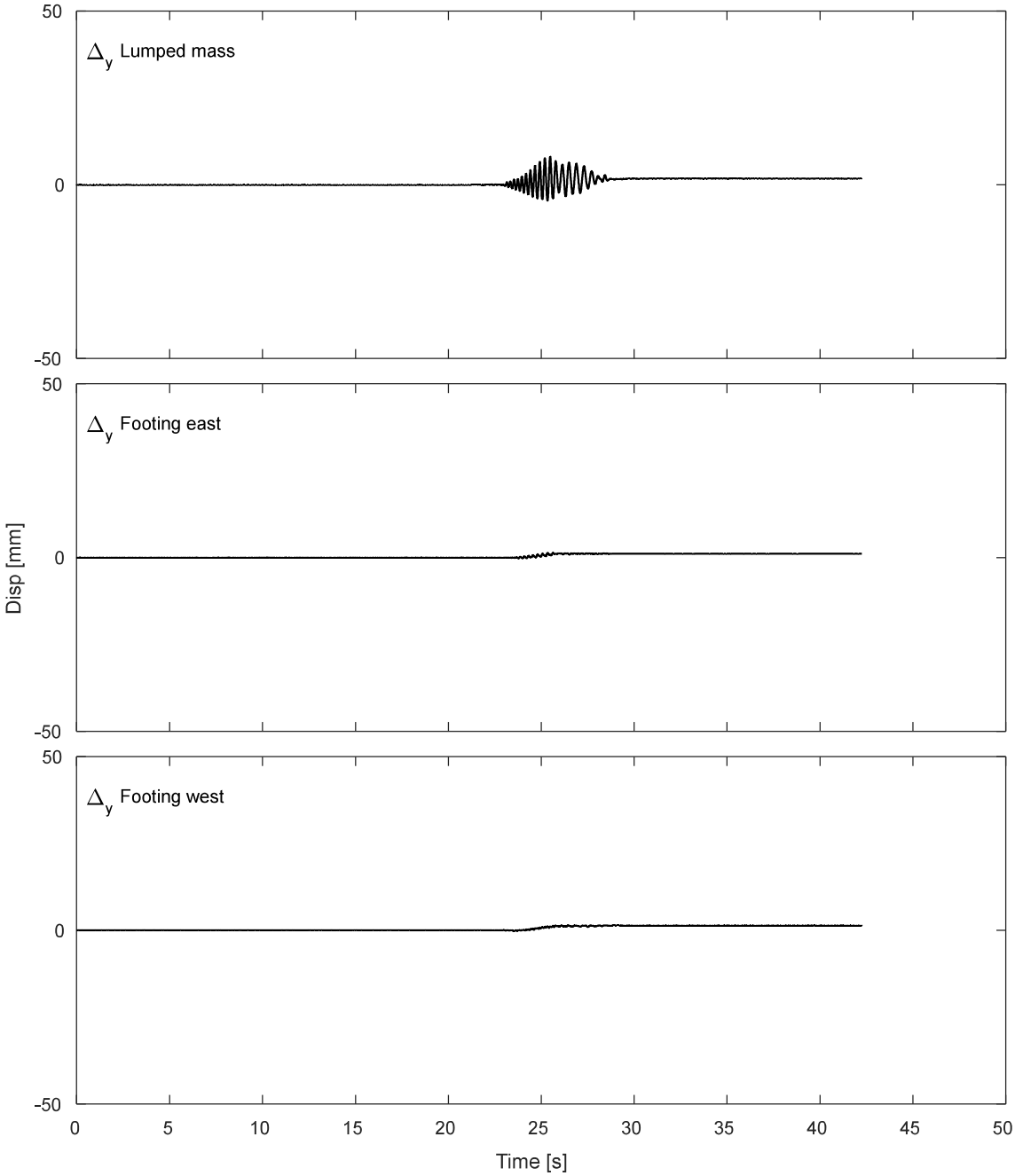

Figure I.2-10. Results of vertical displacement of lumped mass and footing during DT01-SS150-F01F10 motion.

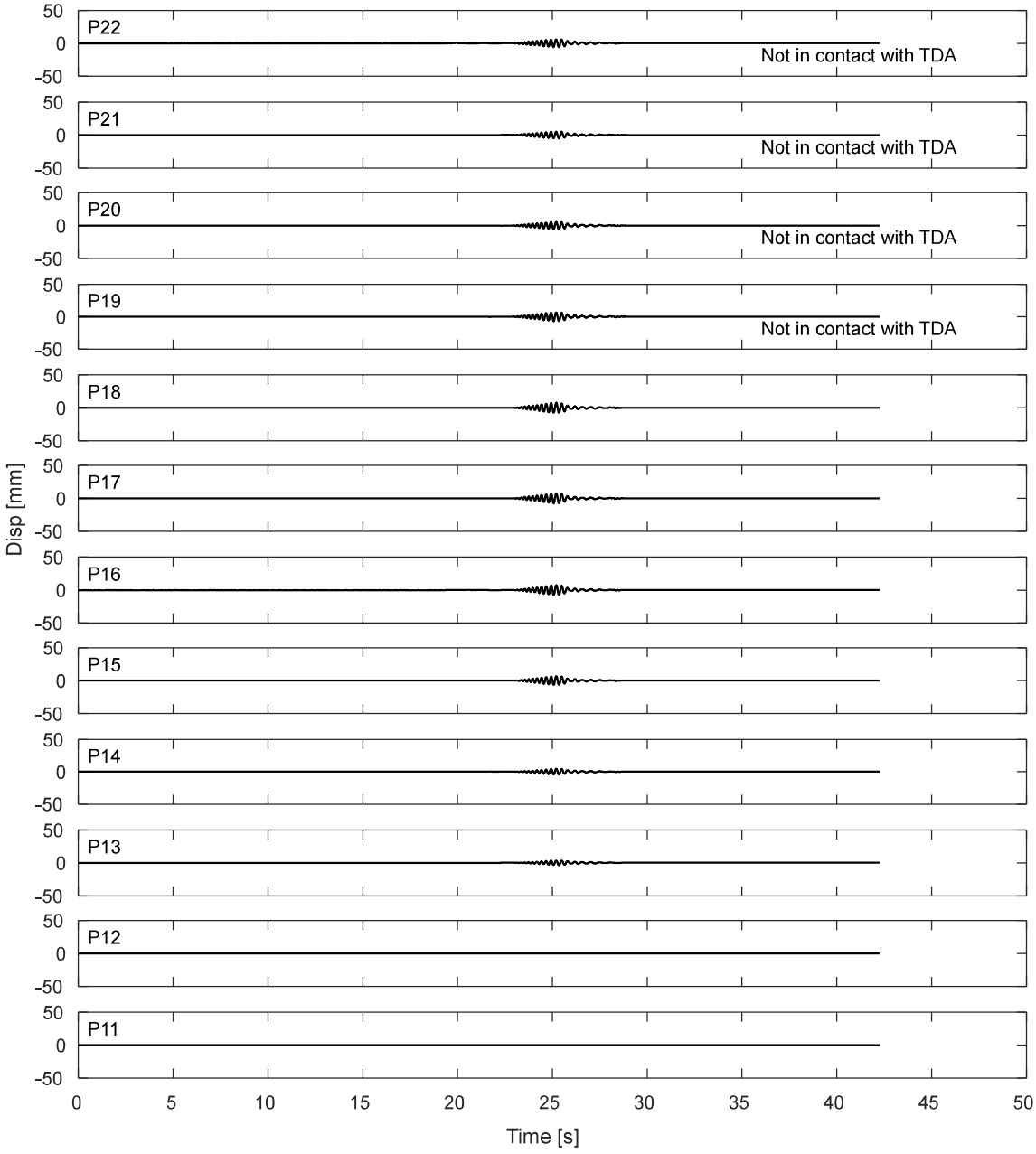

Figure I.2-11. Potentiometers results for the laminar box during DT01-SS150-F01F10 motion.

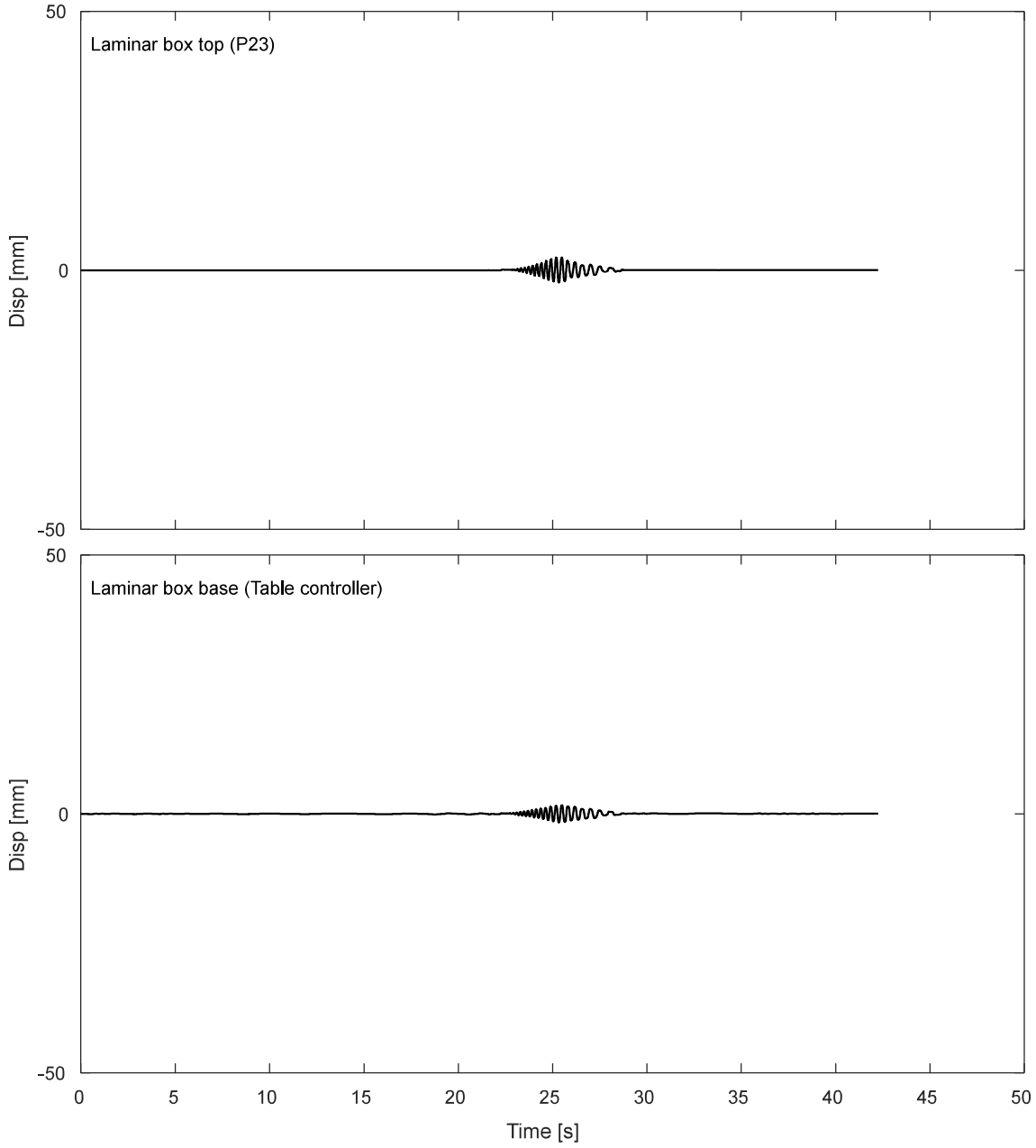

Figure I.2-12. Displacement response of top and base of laminar box during DT01-SS150-F01F10 motion.

I.2.3. Inclinometers.

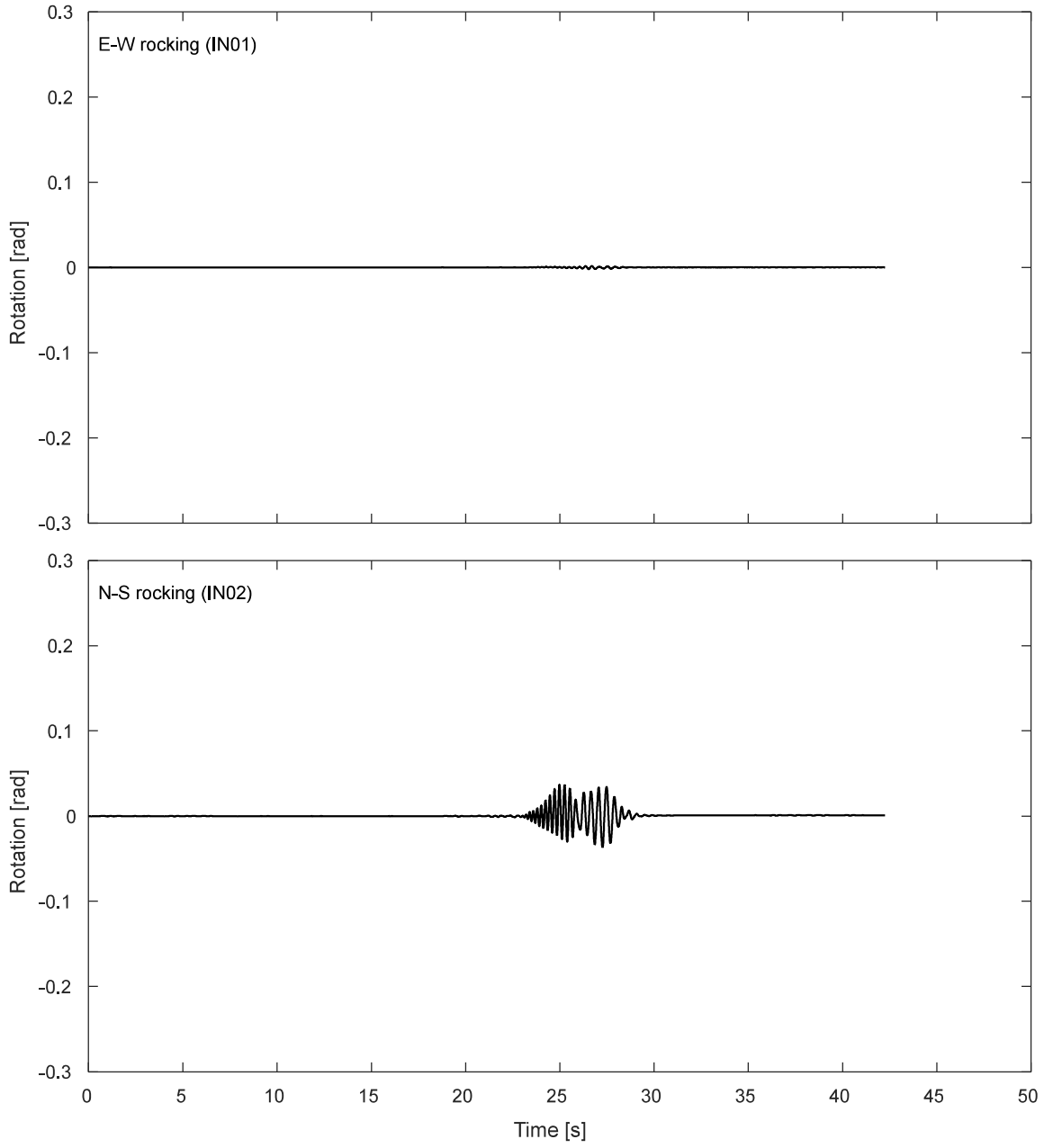

Figure I.2-13. Inclinometer results for the footing during DT01-SS150-F01F10 motion.

I.2.4. Pressure cells.

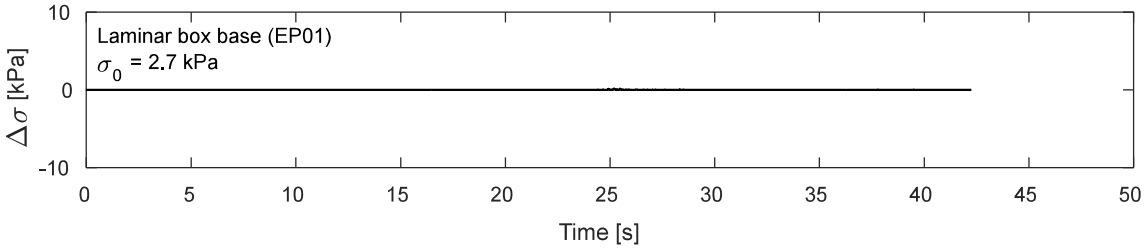

Figure I.2-14. Pressure cells results at laminar box base during DT01-SS150-F01F10 motion.

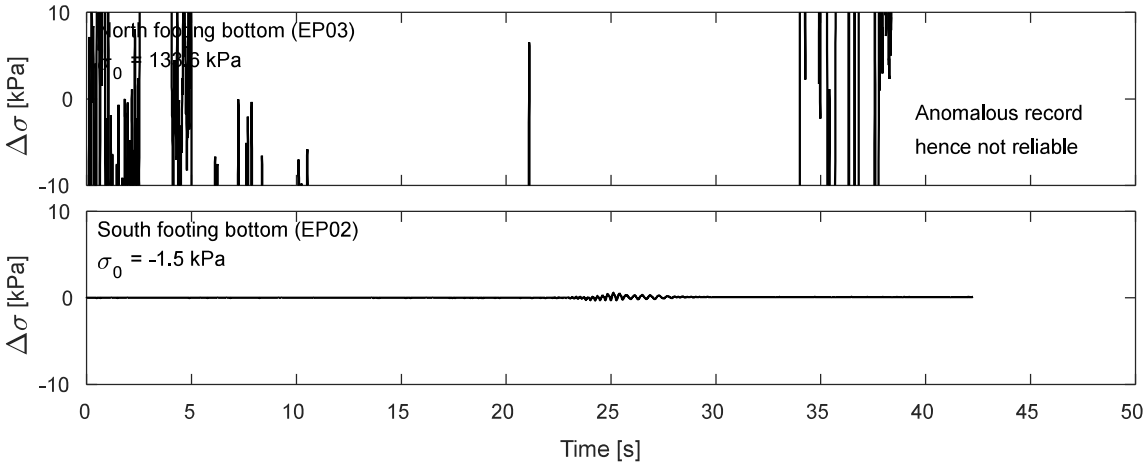

Figure I.2-15. Pressure cells results at footing bottom during DT01-SS150-F01F10 motion

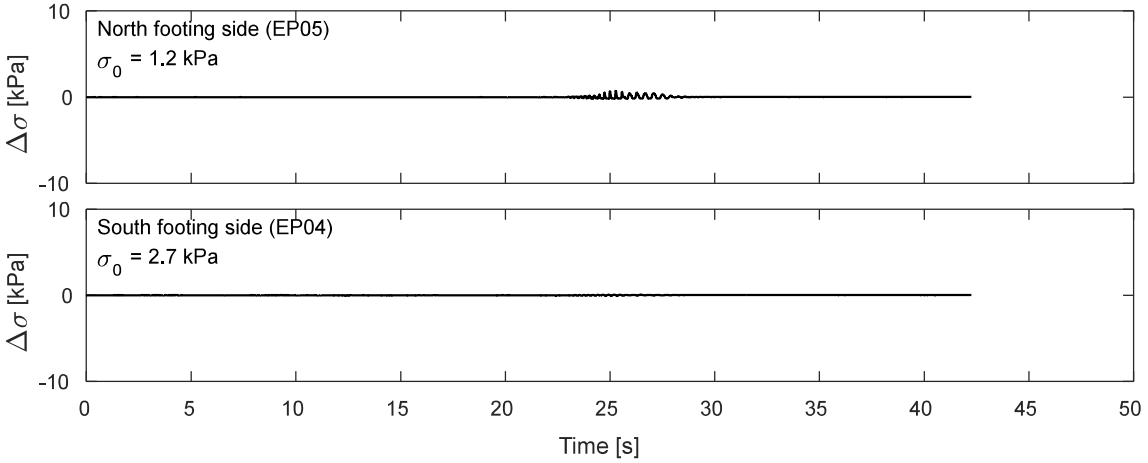

Figure I.2-16. Pressure cells results at footing sides during DT01-SS150-F01F10 motion.

I.3. Time-history Records for DT01-SS300-F01F10 motion.

I.3.1 Input Motion

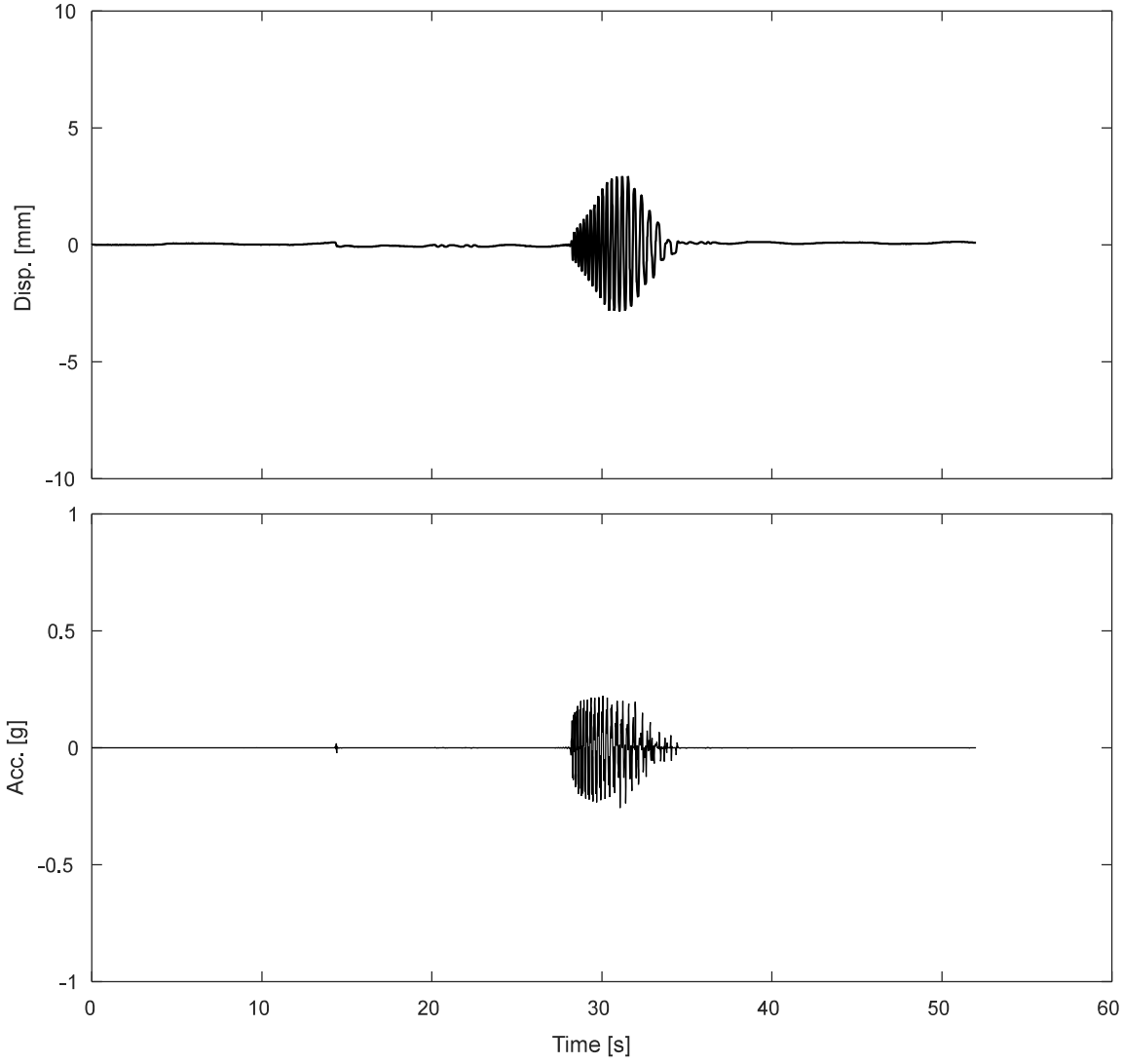

Figure I.3-1. Measured input displacement and acceleration at the base of the specimen during DT01-SS300-F01F10 motion

I.3.1 Accelerometers.

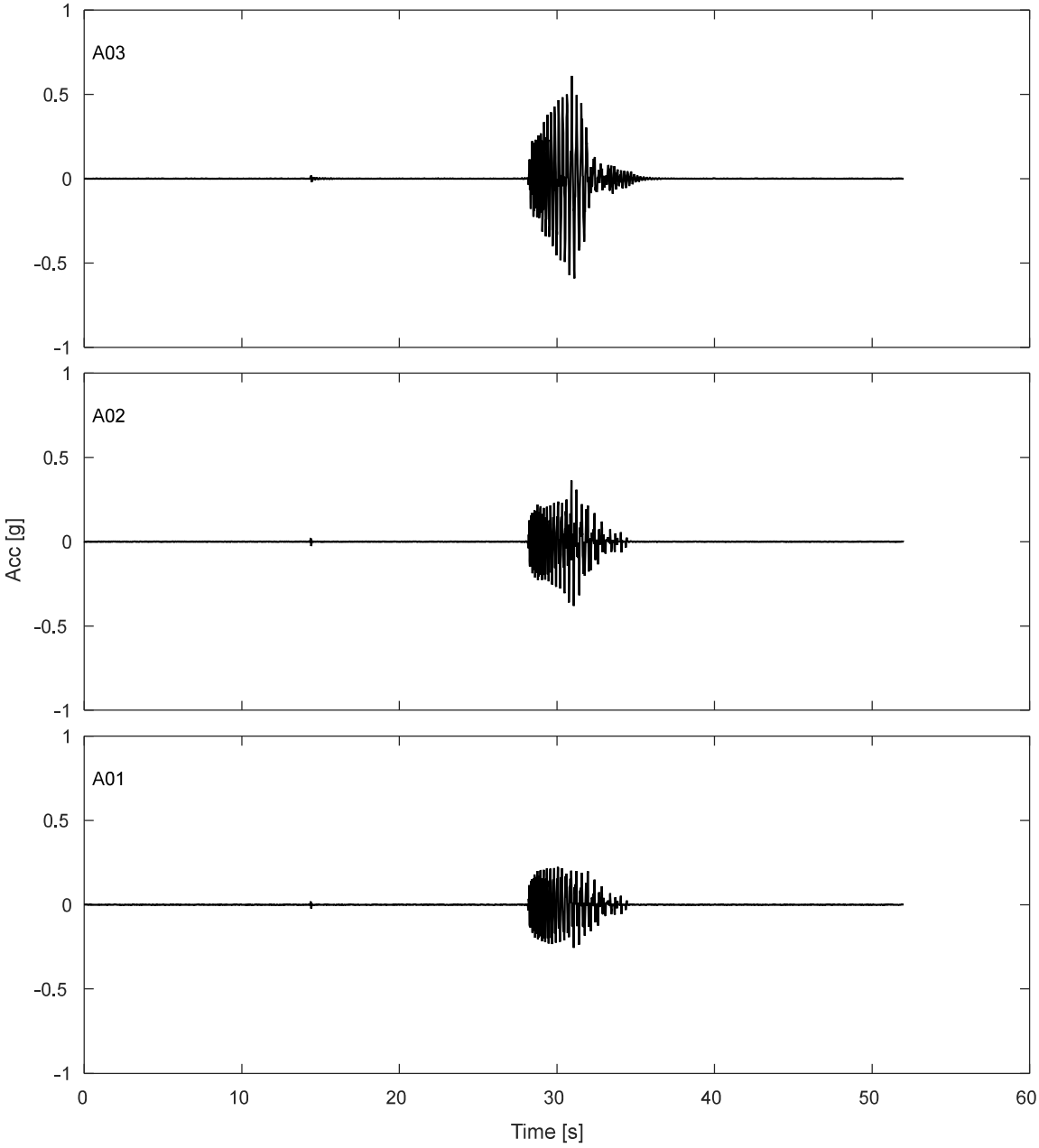

Figure I.3-2. Accelerations results along TDA during DT01-SS300-F01F10 motion.

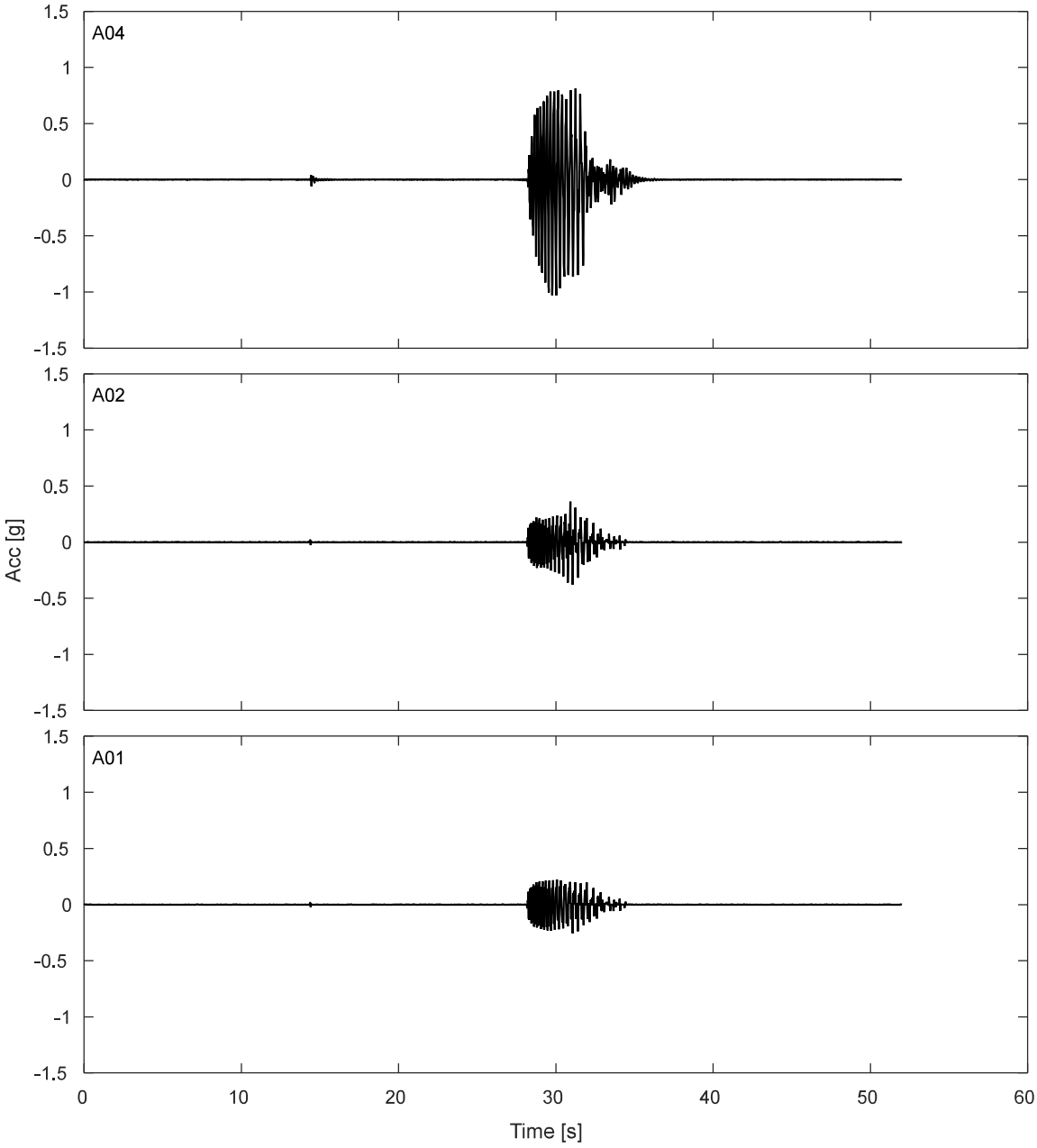

Figure I.3-3. Free field accelerations results for TDA during DT01-SS300-F01F10 motion.

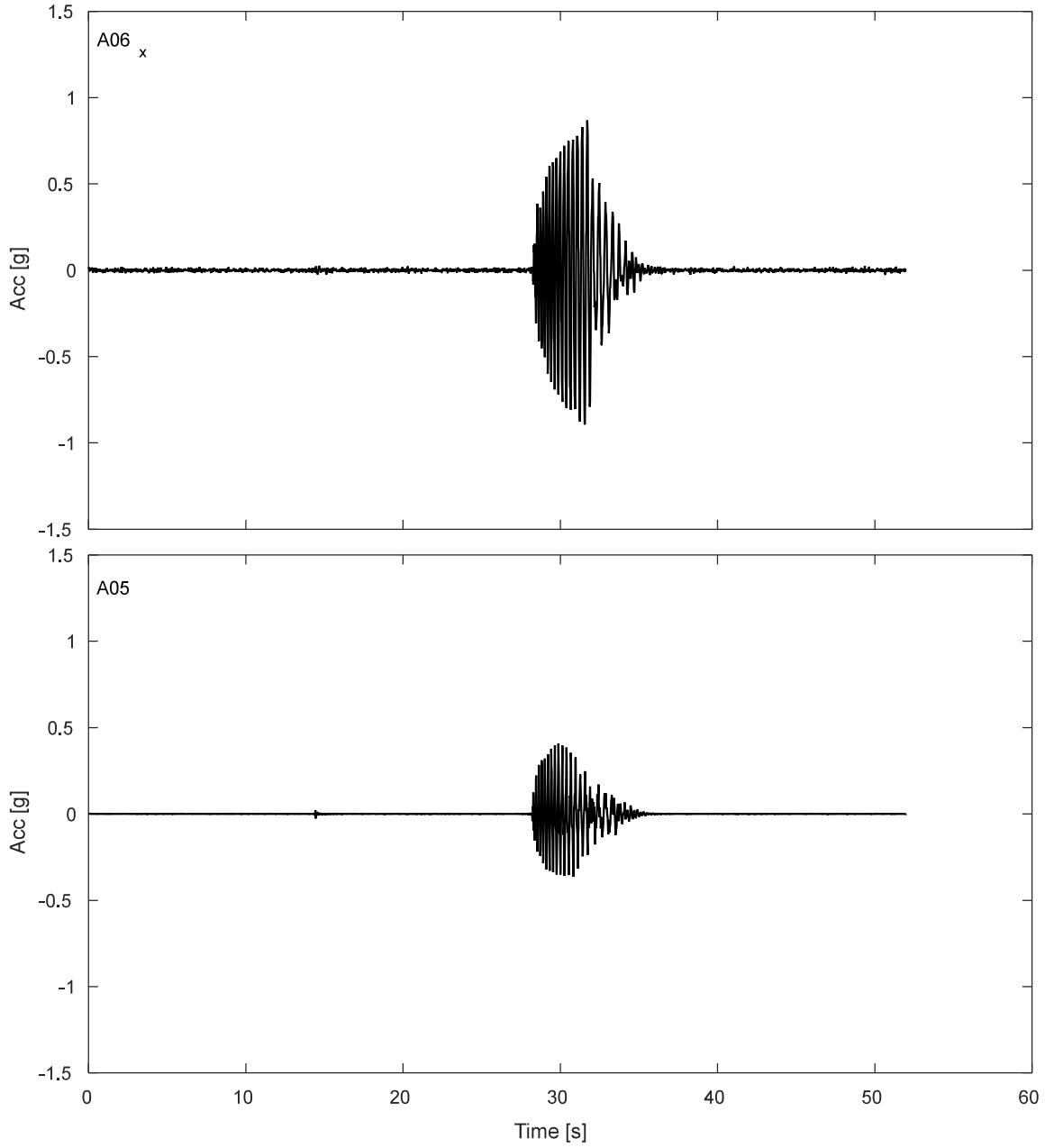

Figure I.3-4. Accelerations results SDOF structure during DT01-SS300-F01F10 motion.

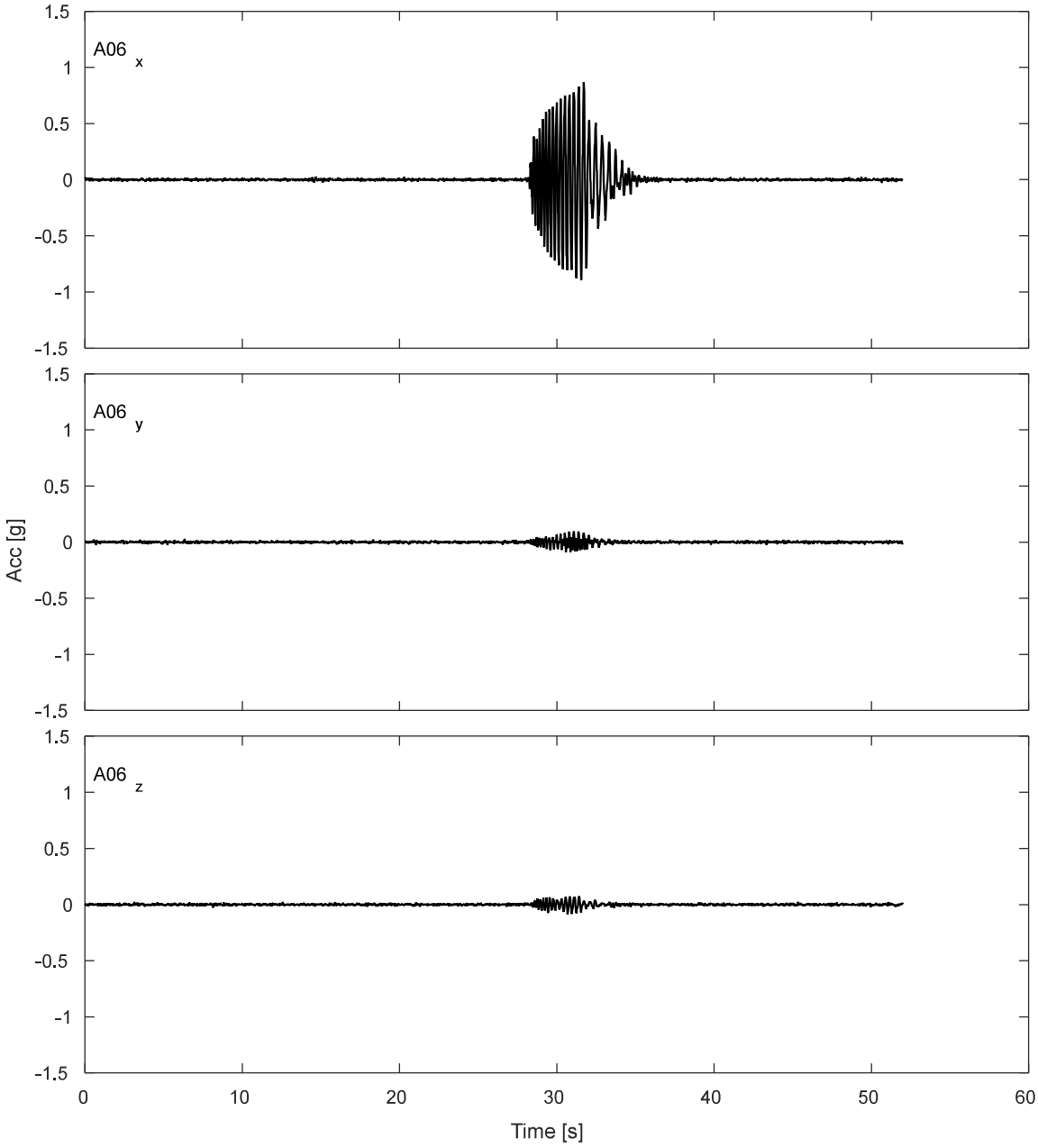

Figure I.3-5. Accelerations results for lumped mass of SDOF structure during DT01-SS300-F01F10 motion.

I.3.2 Potentiometers.

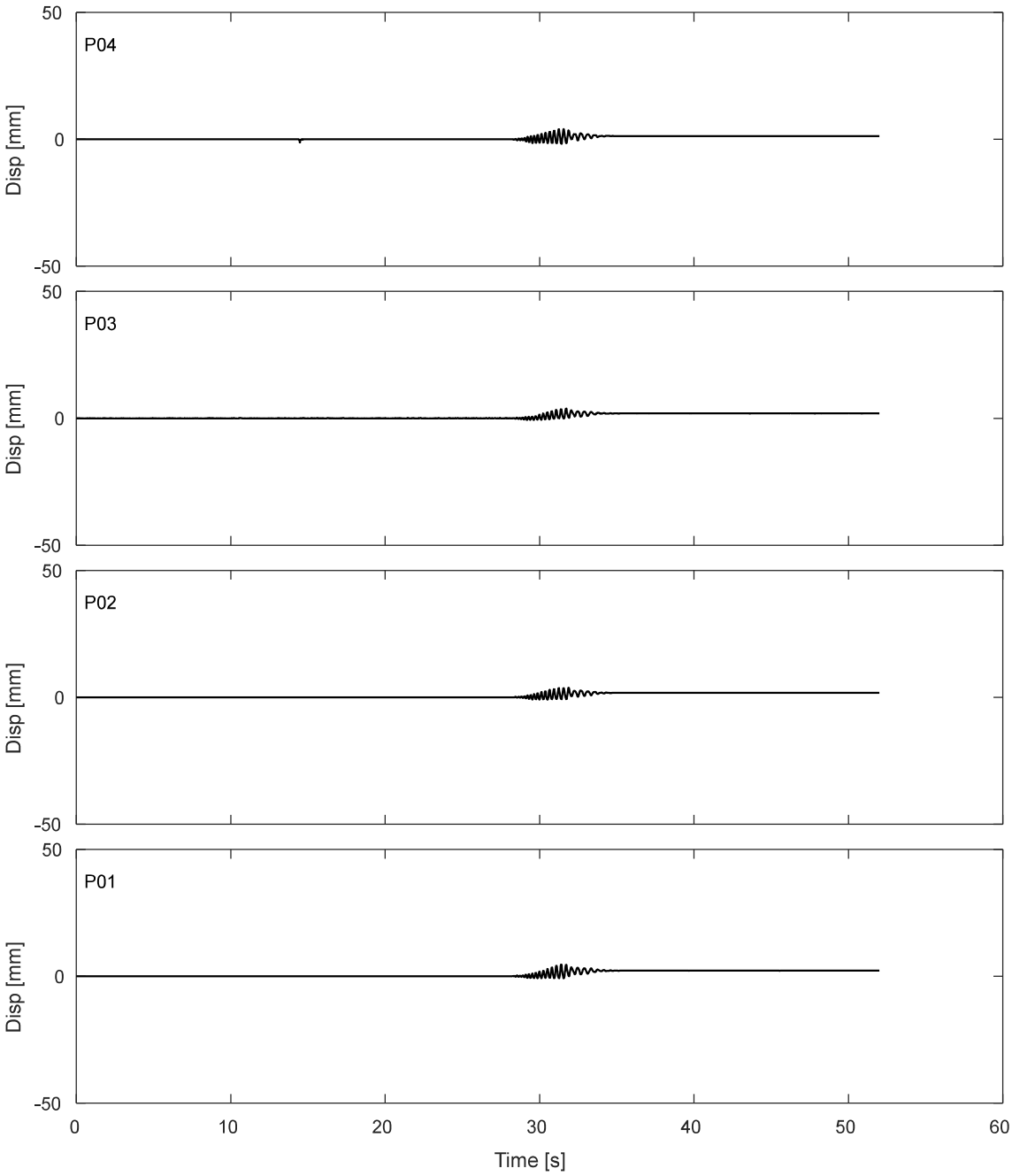

Figure I.3-6. Results of fully vertical potentiometers attached to corners of top of strip footing during DT01-SS300-F01F10 motion.

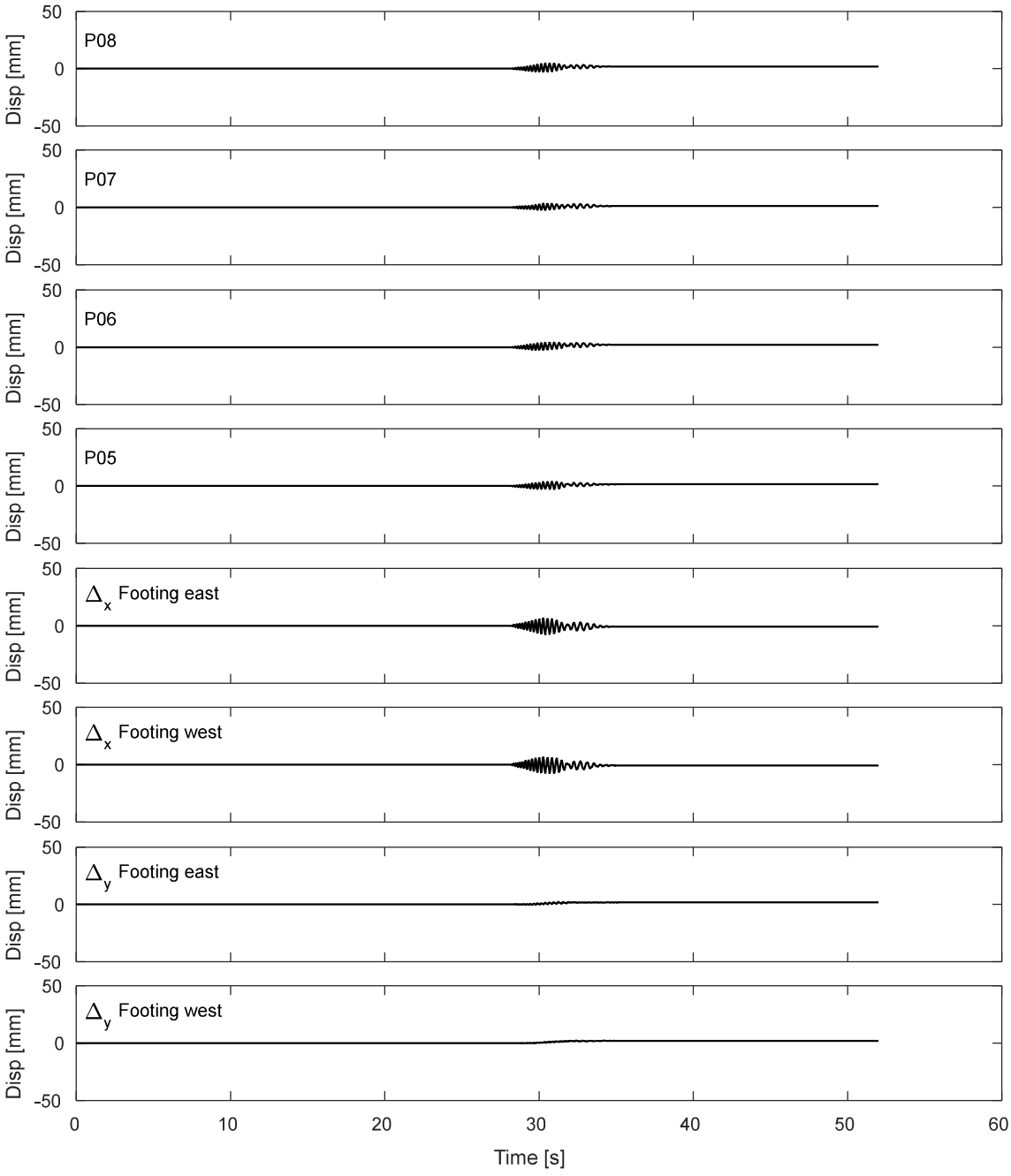

Figure I.3-7. Results of inclined potentiometers attached to top of strip footing during DT01-SS300-F01F10 motion.

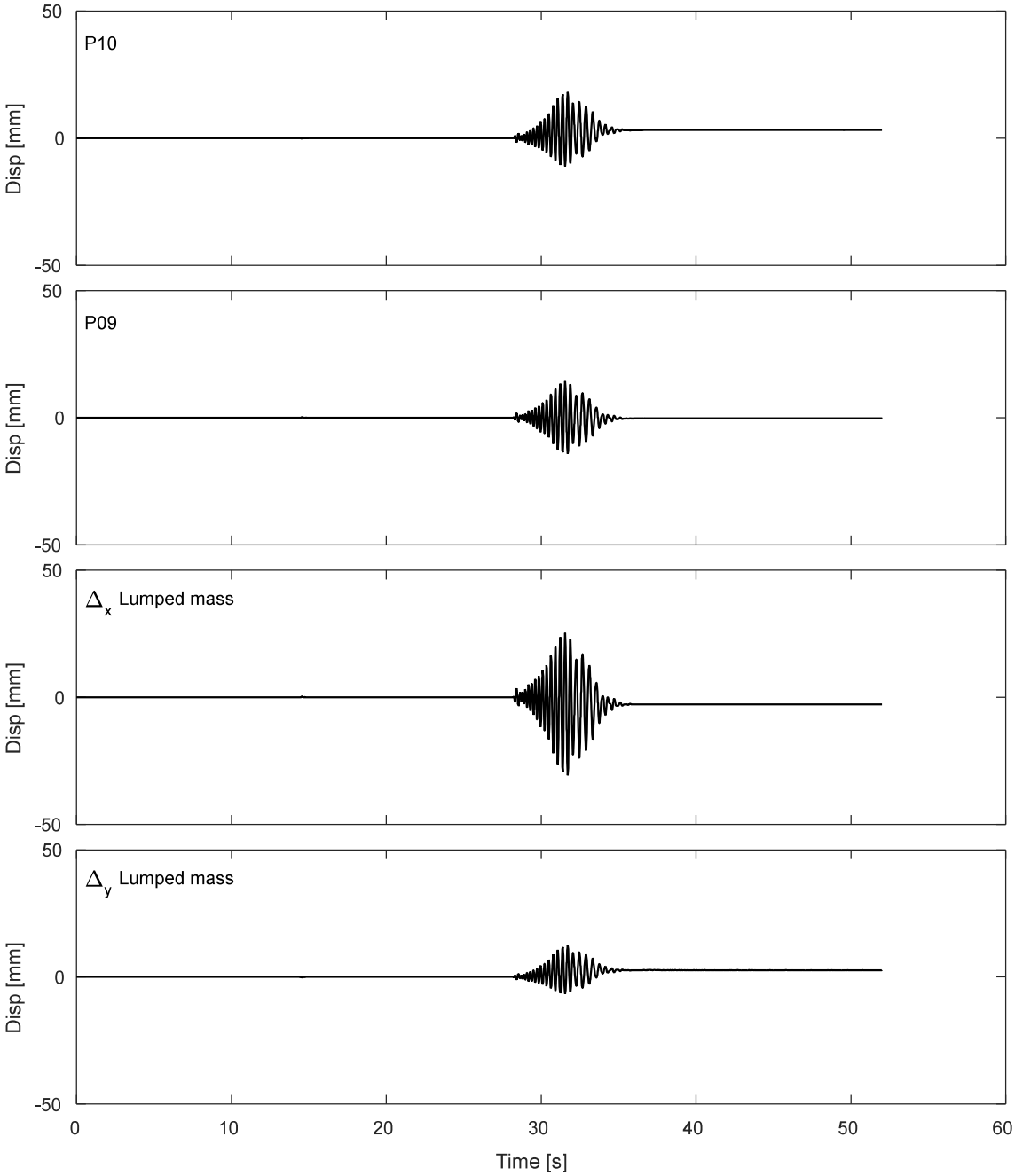

Figure I.3-8. Results of inclined potentiometers attached to lumped mass during DT01-SS300-F01F10 motion.

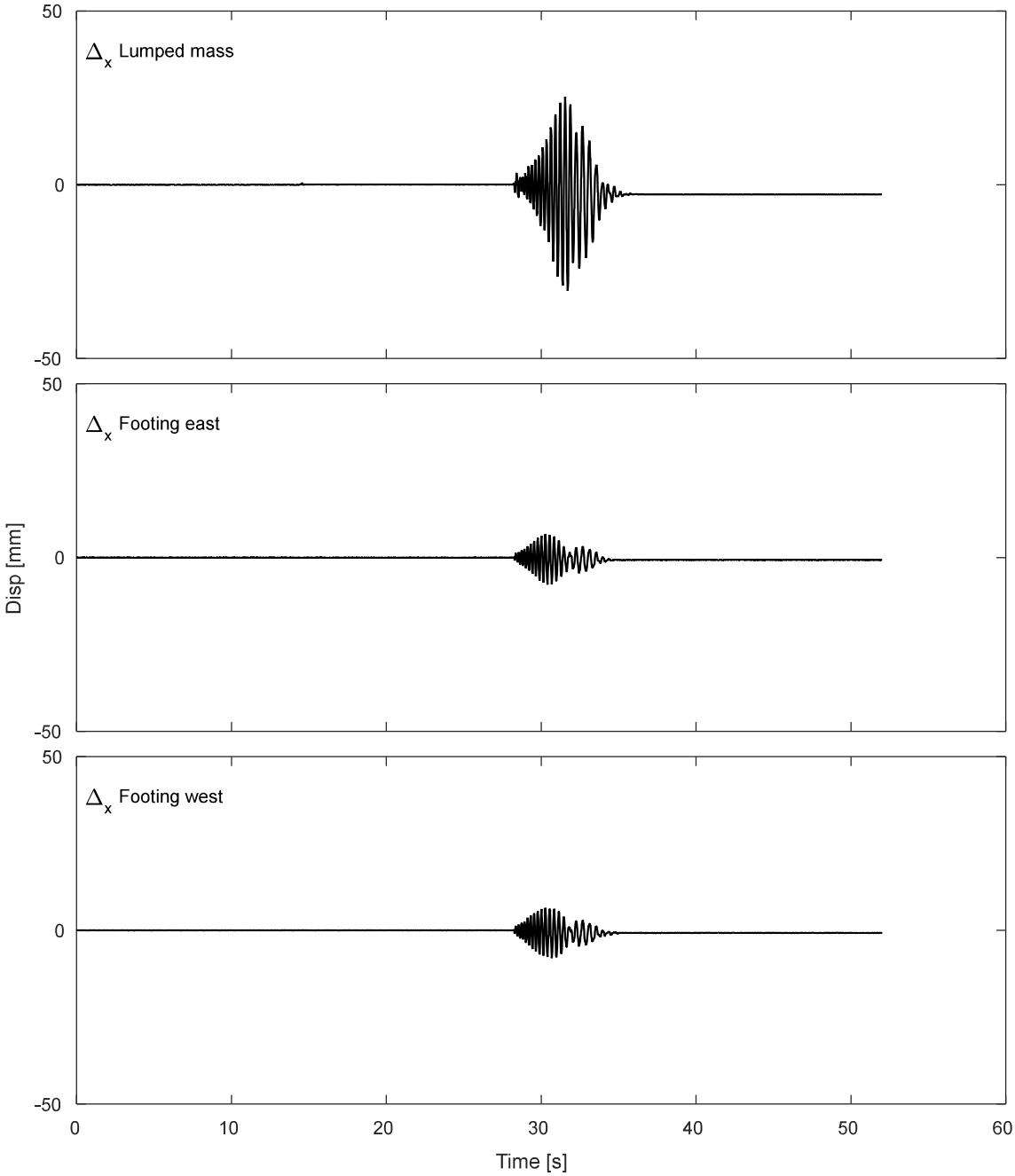

Figure I.3-9. Results of horizontal displacement of lumped mass and footing during DT01-SS300-F01F10 motion.

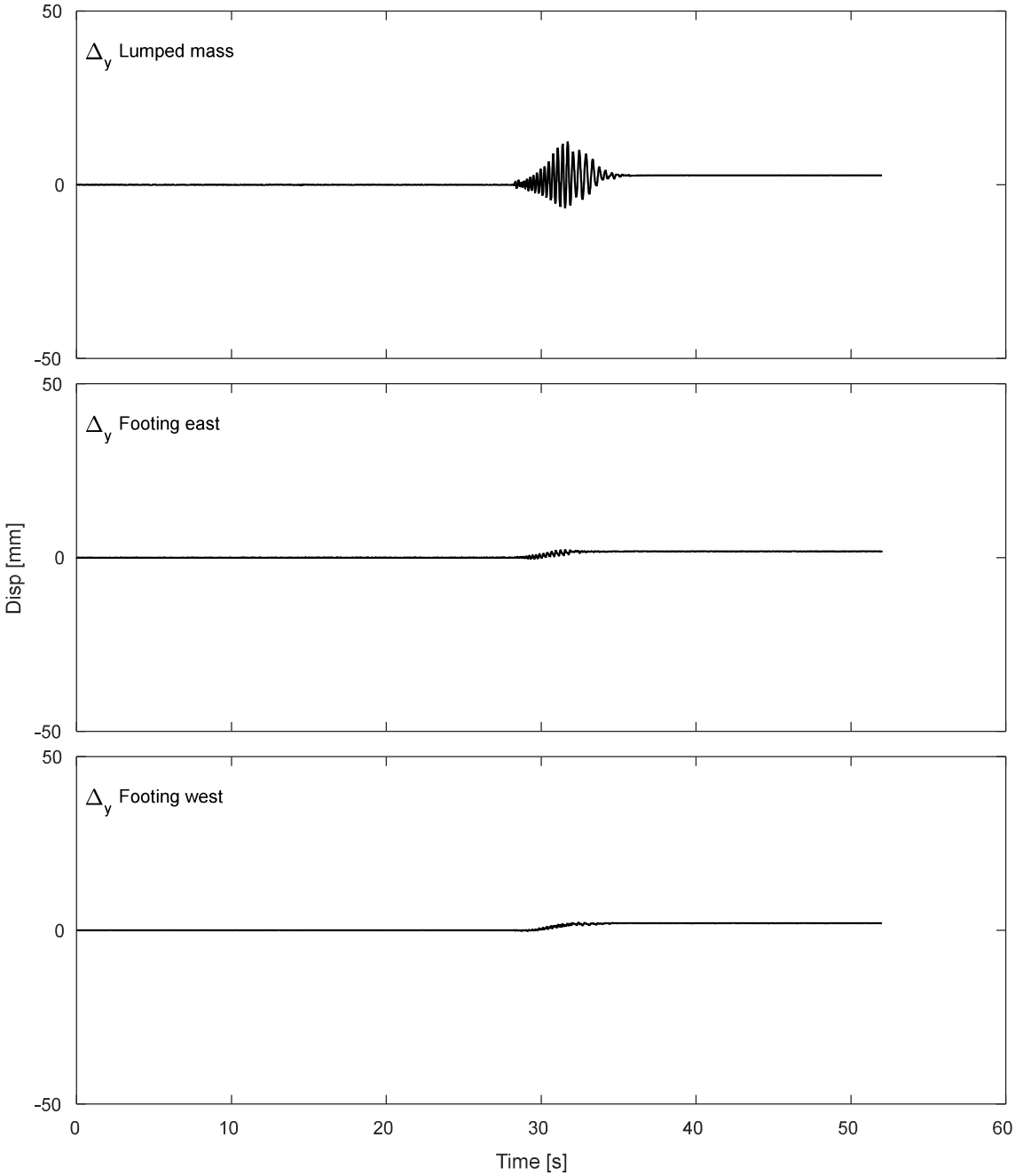

Figure I.3-10. Results of vertical displacement of lumped mass and footing during DT01-SS300-F01F10 motion.

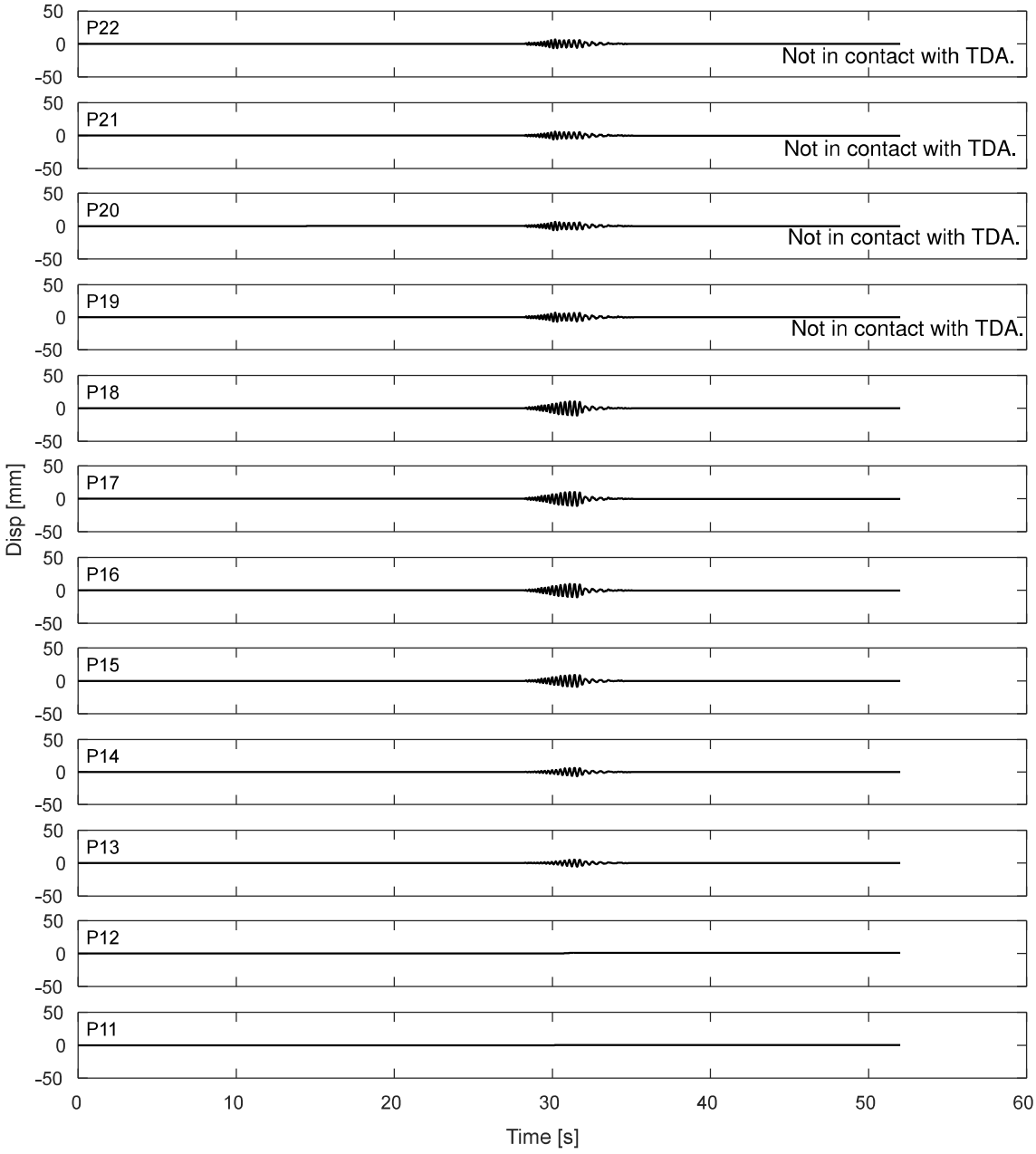

Figure I.3-11. Potentiometers results for the laminar box during DT01-SS300-F01F10 motion.

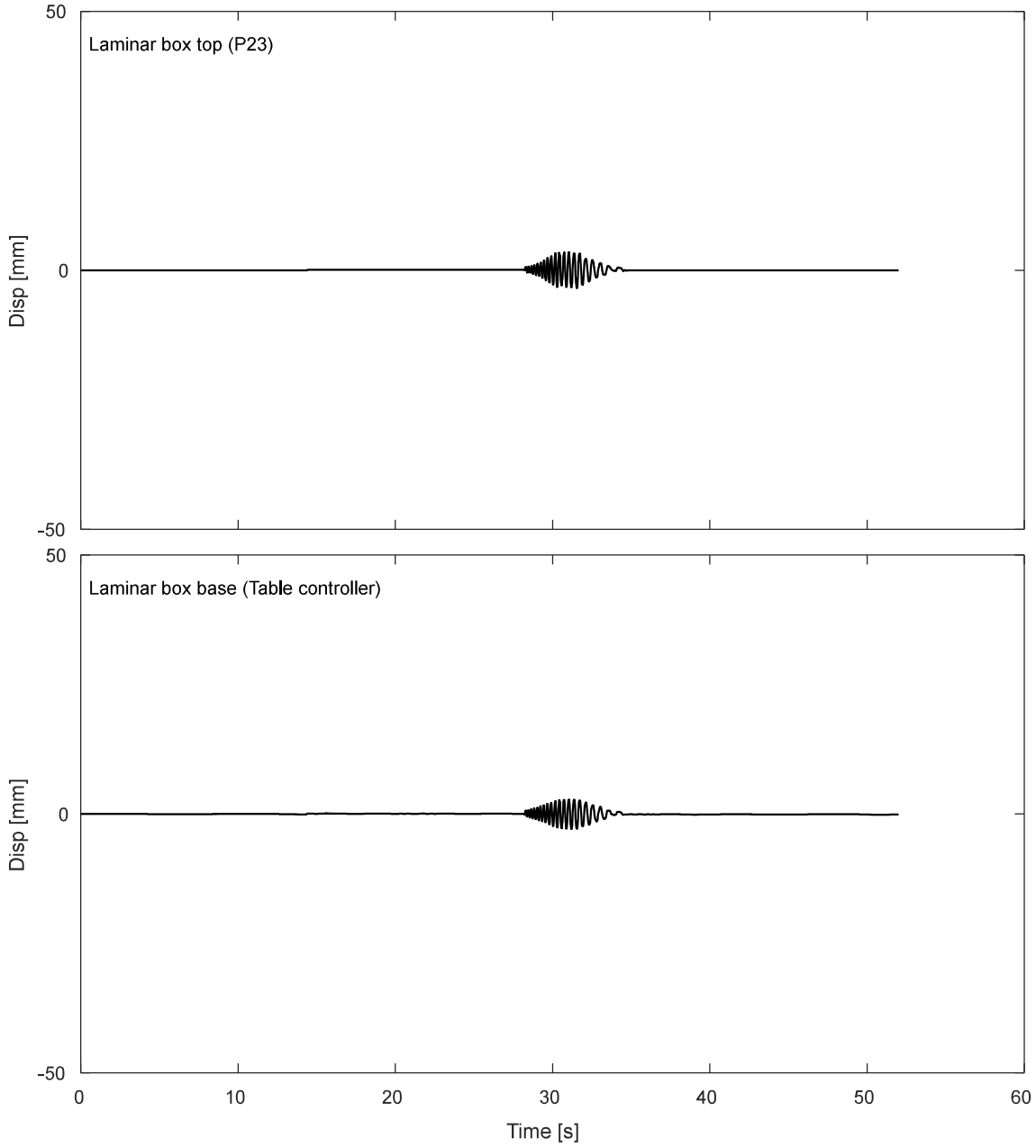

Figure I.3-12. Displacement response of top and base of laminar box during DT01-SS300-F01F10 motion.

I.3.3. Inclinometers.

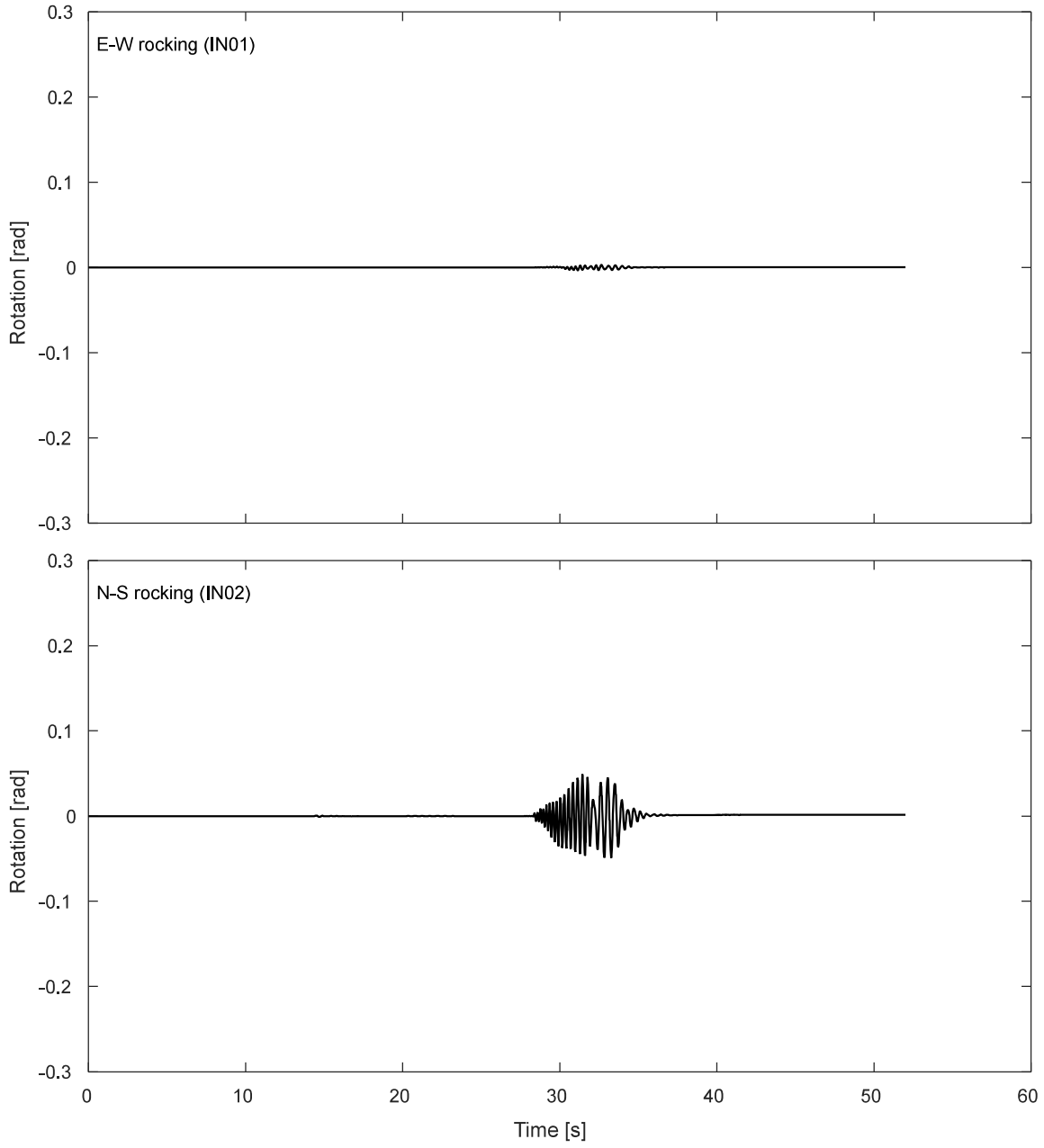

Figure I.3-13. Inclinometer results for the footing during DT01-SS300-F01F10 motion.

I.3.4. Pressure cells.

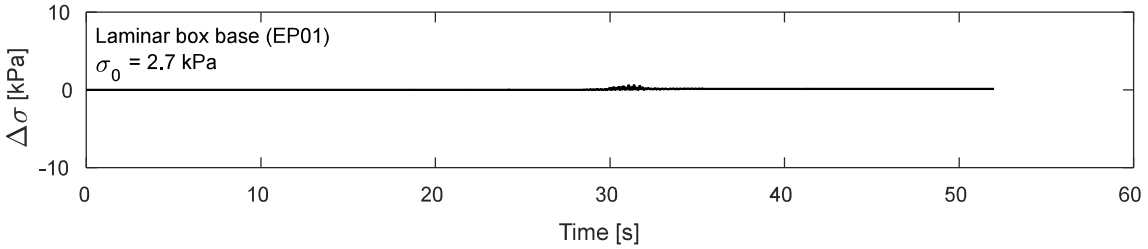

Figure I.3-14. Pressure cells results at laminar box base during DT01-SS300-F01F10 motion

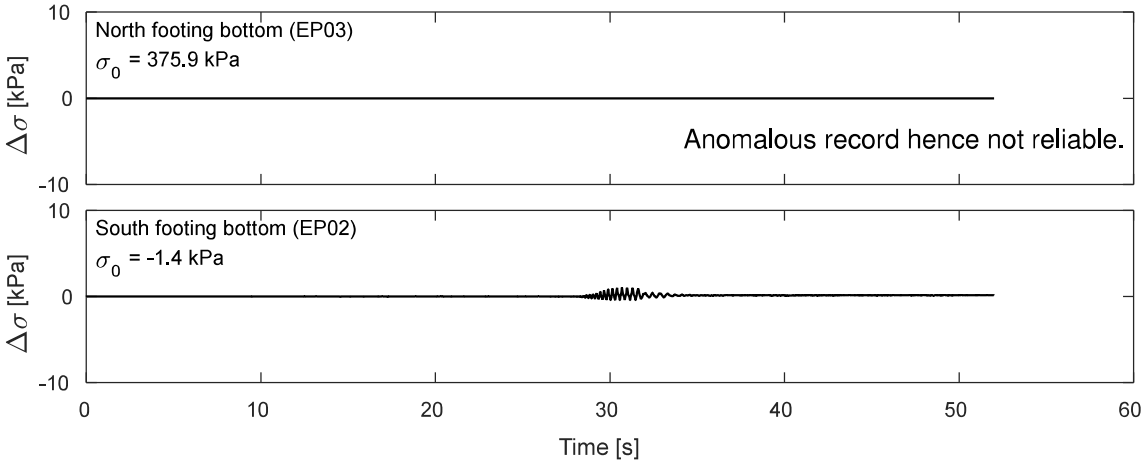

Figure I.3-15. Pressure cells results at footing bottom during DT01-SS300-F01F10 motion

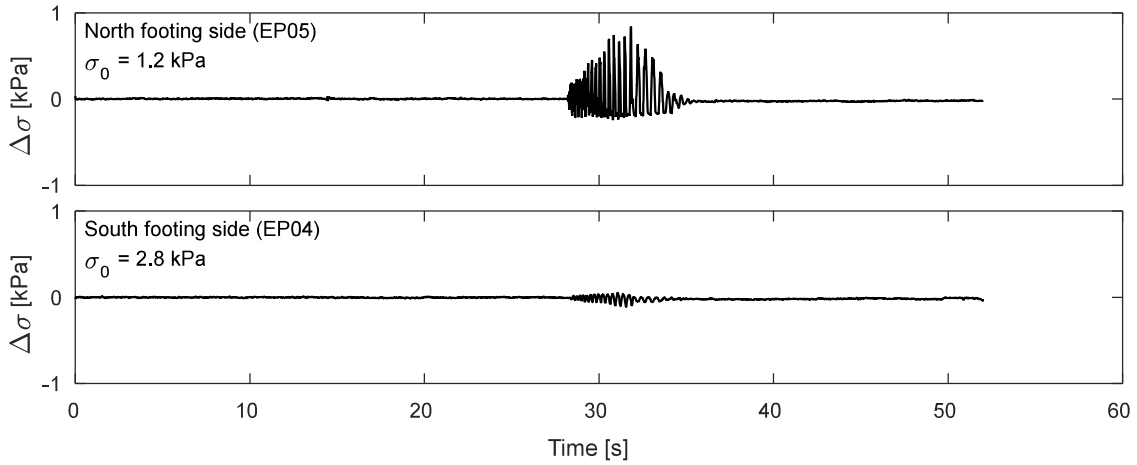

Figure I.3-16. Pressure cells results at footing sides during DT01-SS300-F01F10 motion

I.4. Time-history Records for DT01-SS450-F01F10 motion.

I.4.1 Input Motion

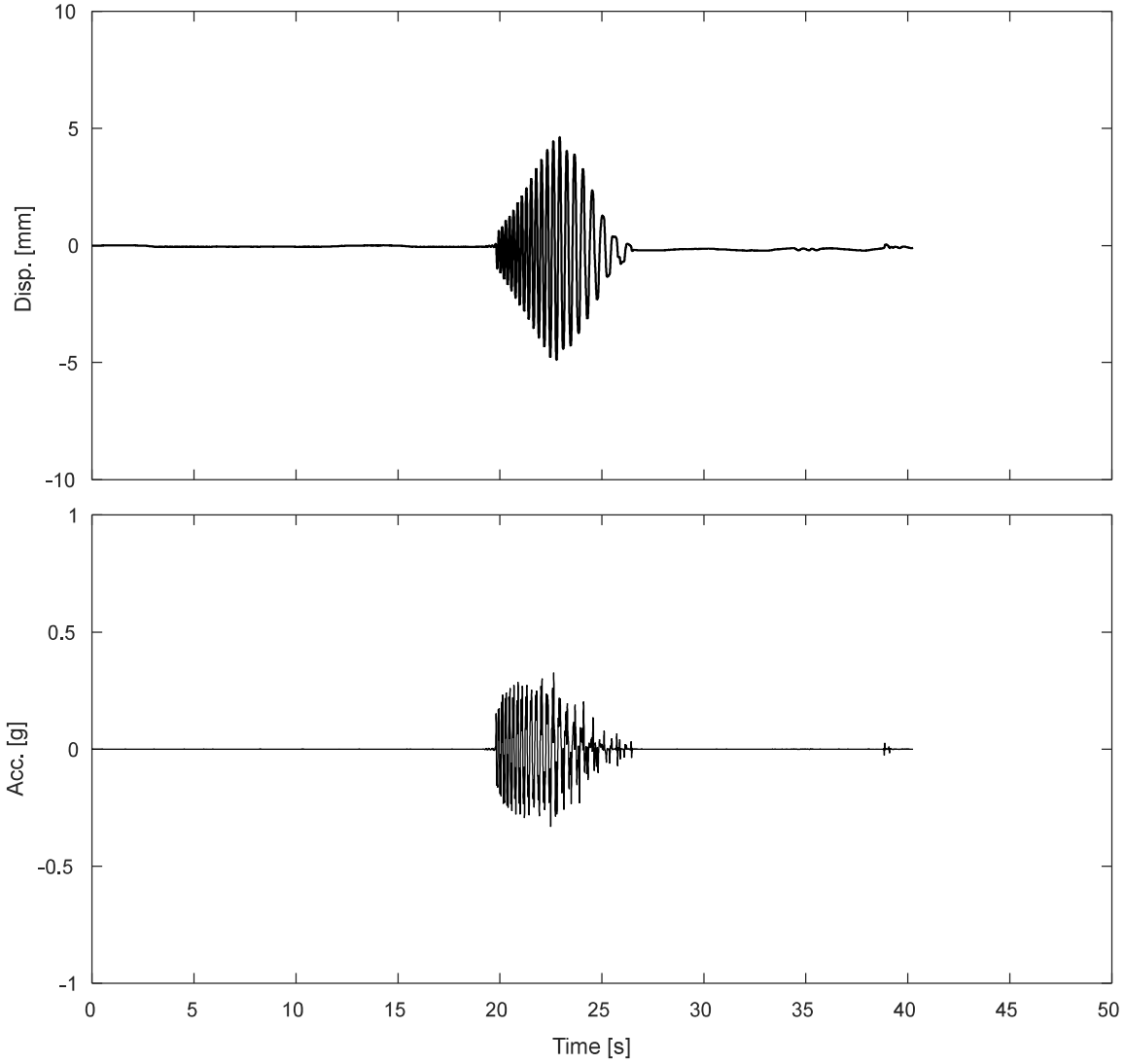

Figure I.4-1. Measured input displacement and acceleration at the base of the specimen during DT01-SS450-F01F10 motion

I.4.1 Accelerometers.

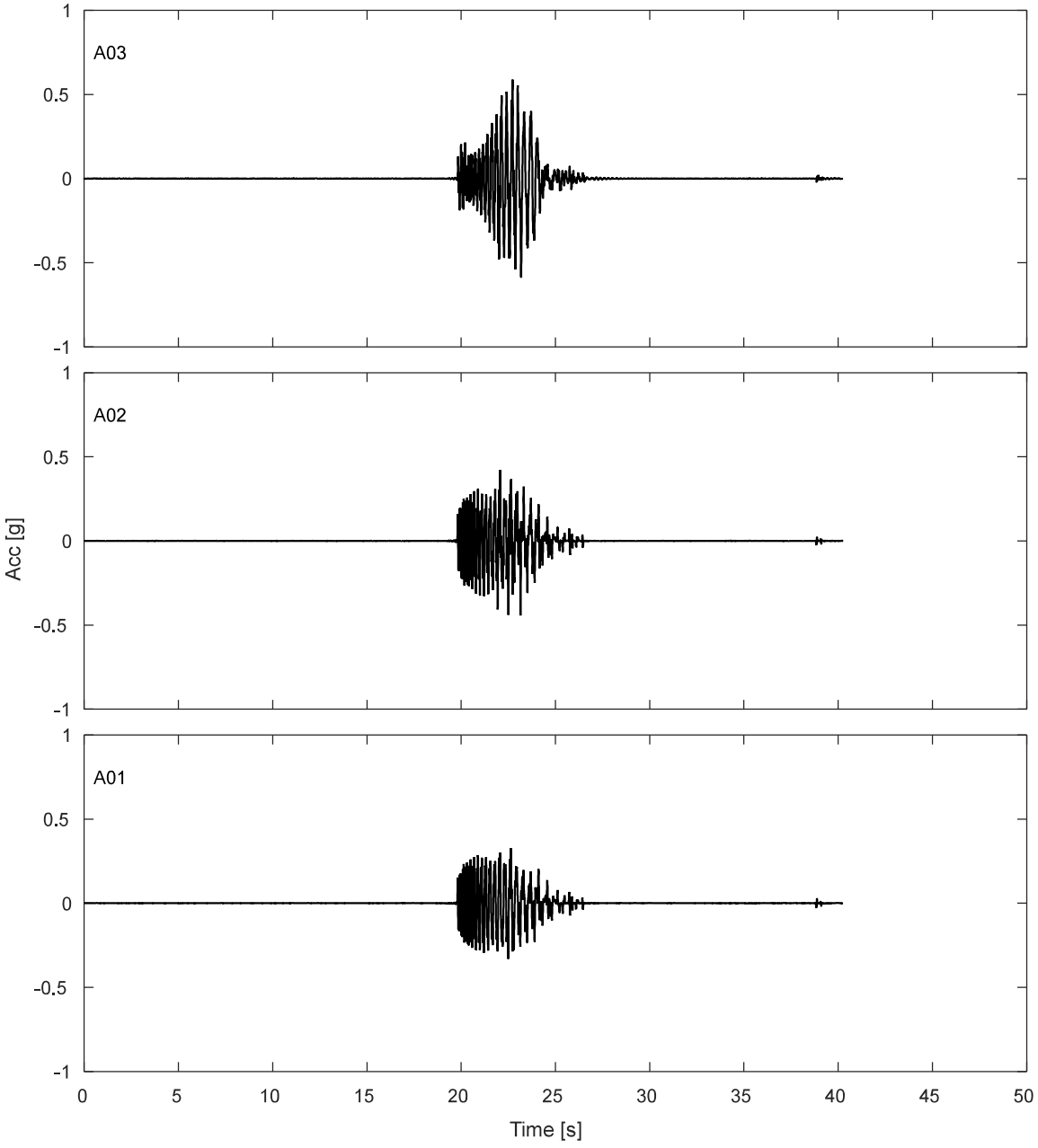

Figure I.4-2. Accelerations results along TDA during DT01-SS450-F01F10 motion.

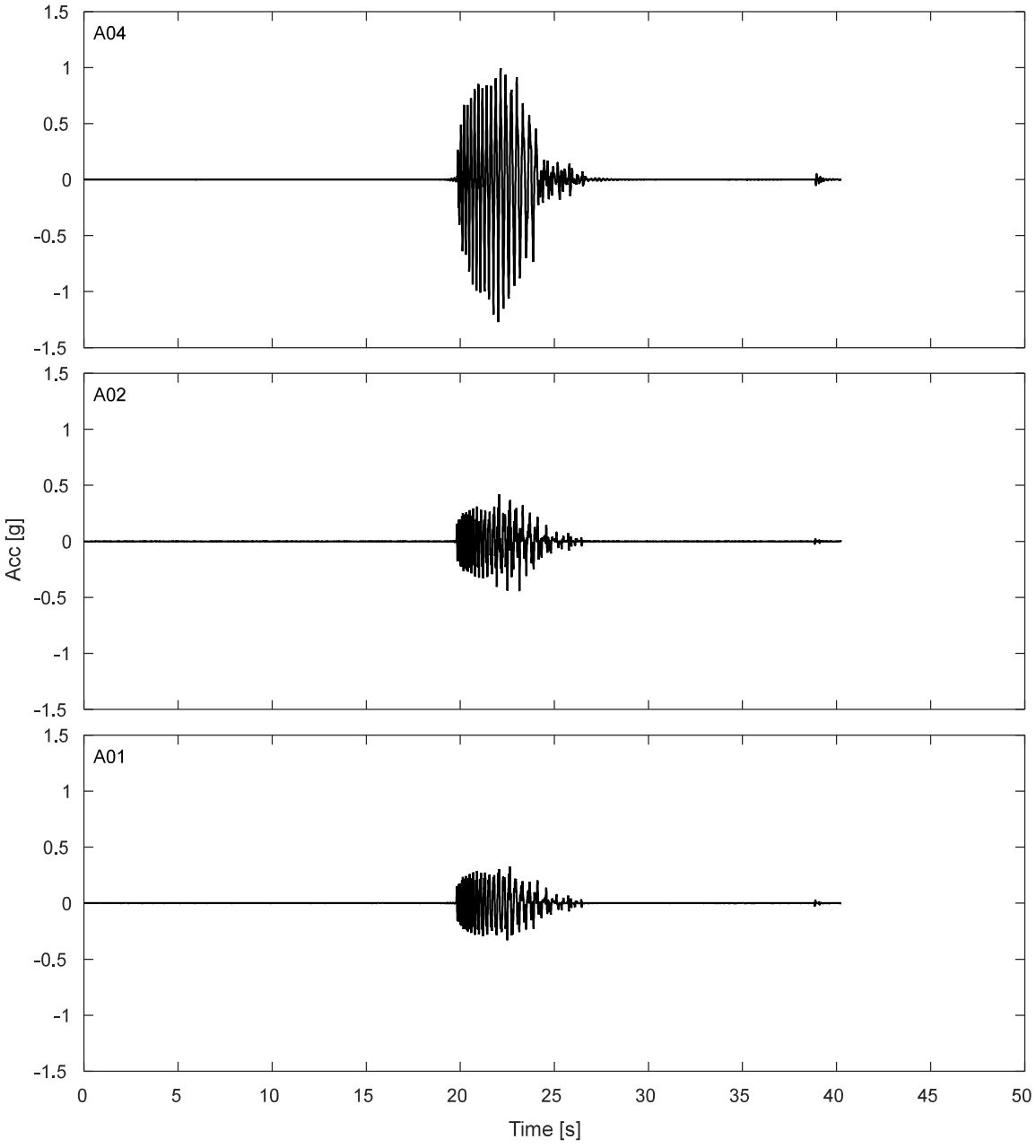

Figure I.4-3. Free field accelerations results for TDA during DT01-SS450-F01F10 motion.

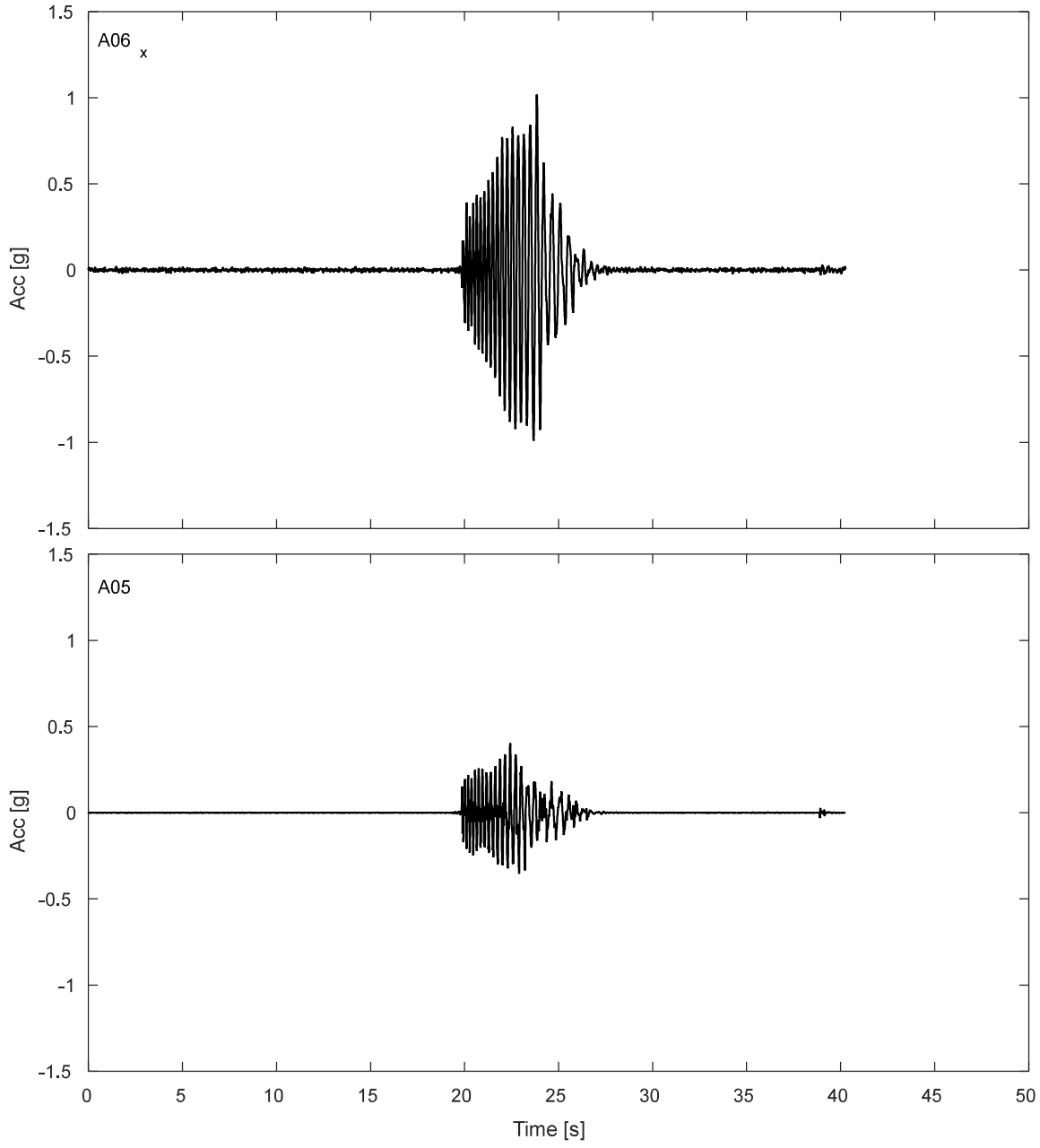

Figure I.4-4. Accelerations results SDOF structure during DT01-SS450-F01F10 motion.

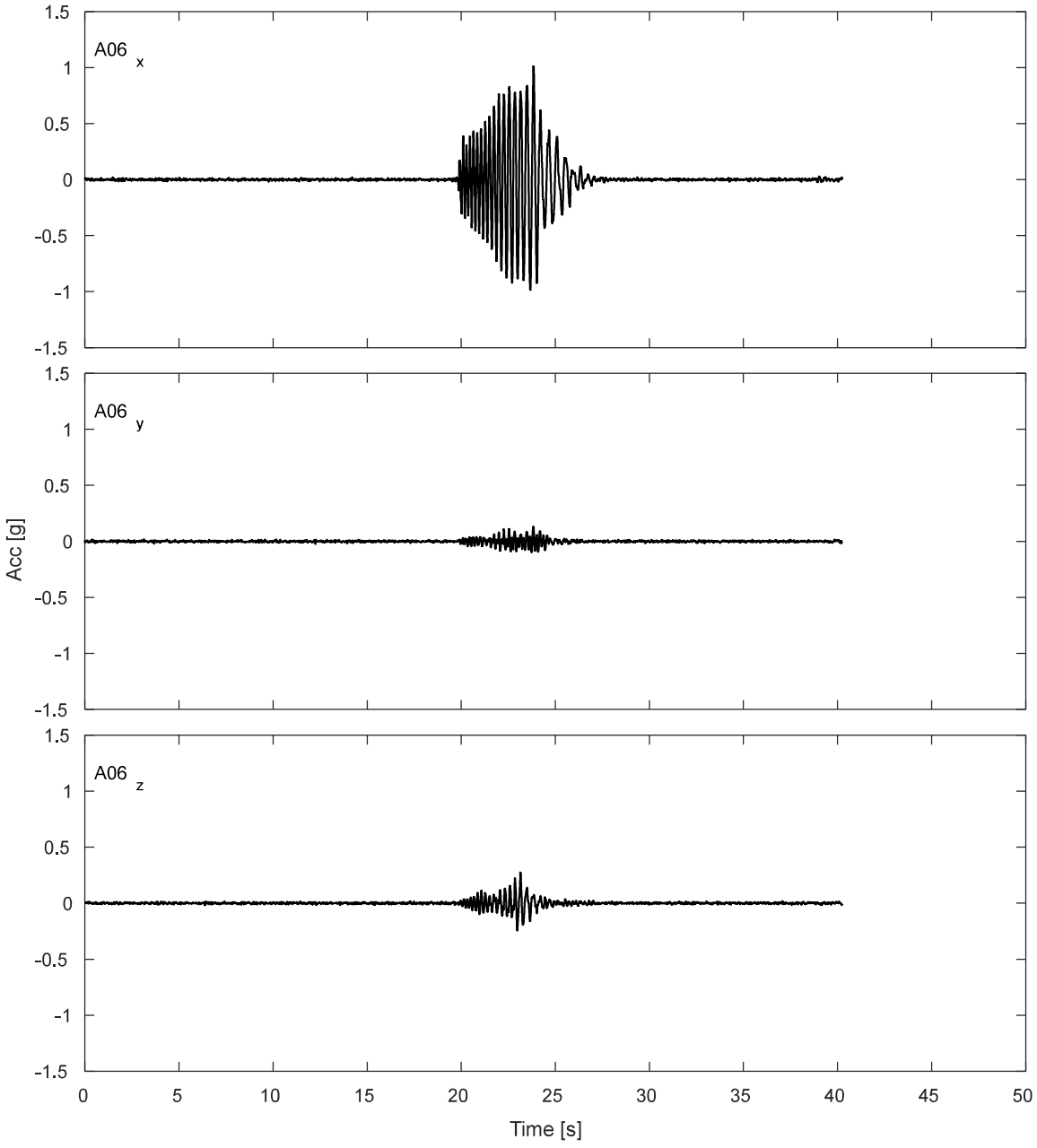

Figure I.4-5. Accelerations results for lumped mass of SDOF structure during DT01-SS450-F01F10 motion.

I.4.2 Potentiometers.

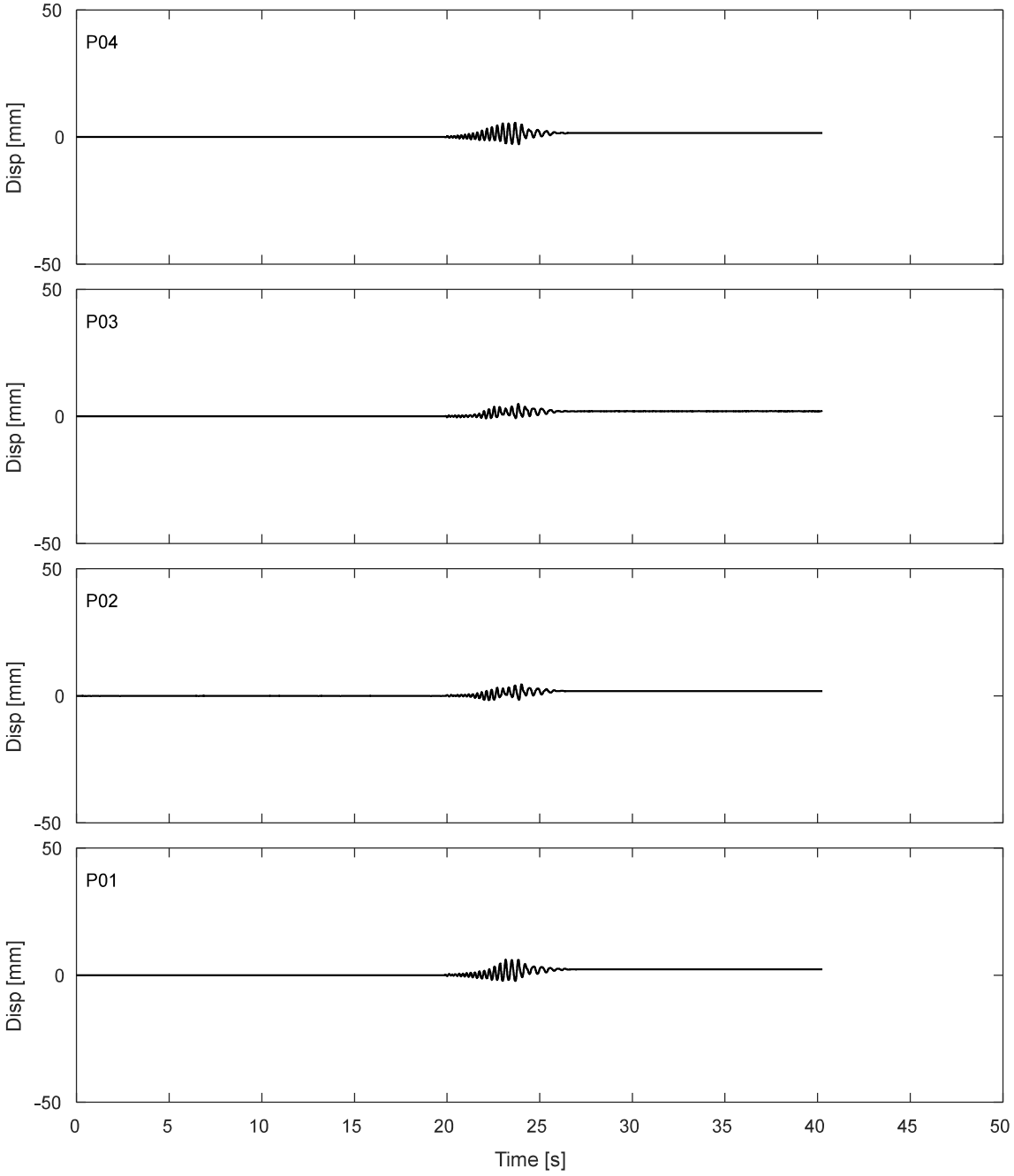

Figure I.4-6. Results of fully vertical potentiometers attached to corners of top of strip footing during DT01-SS450-F01F10 motion.

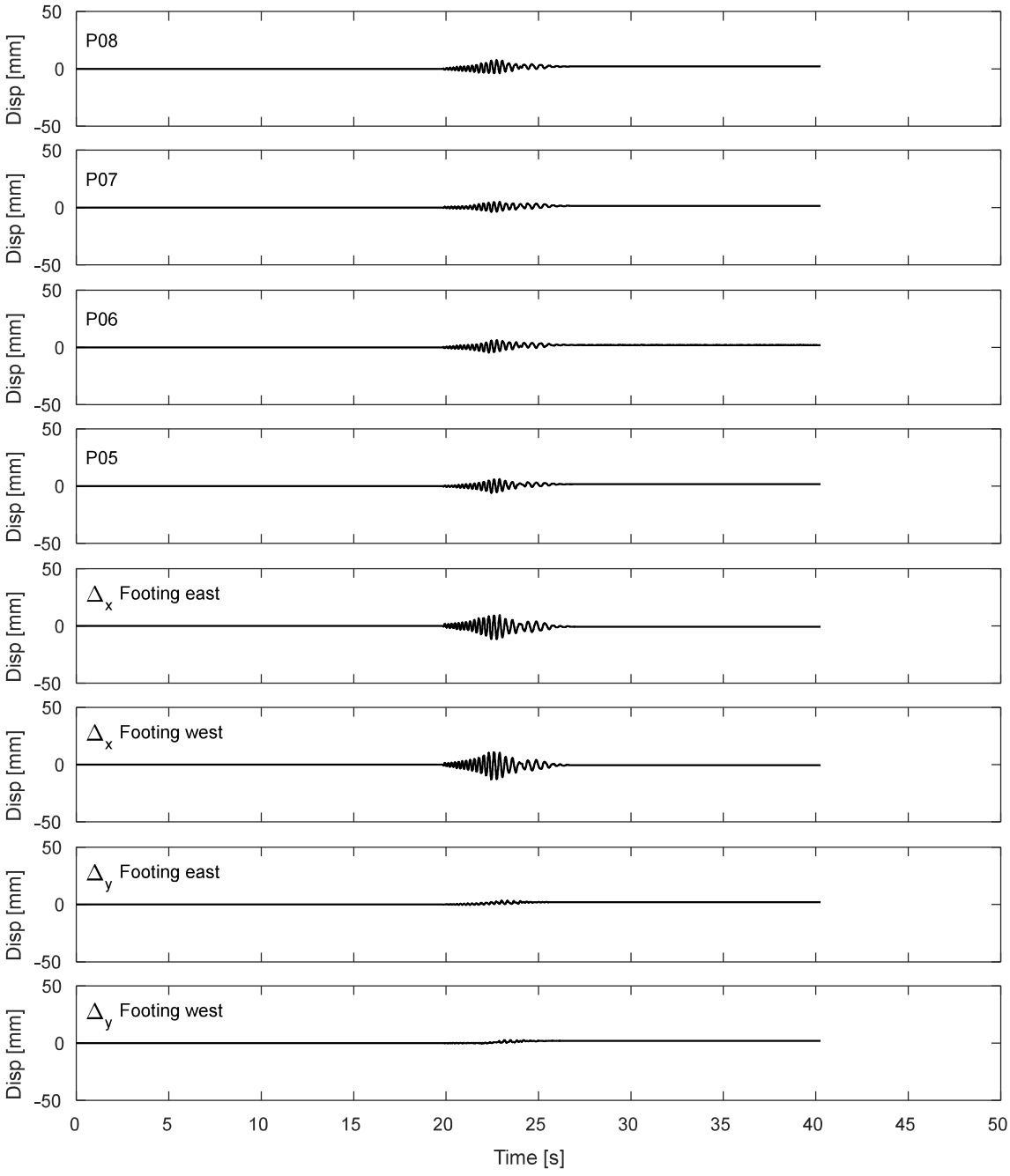

Figure I.4-7. Results of inclined potentiometers attached to top of strip footing during DT01-SS450-F01F10 motion.

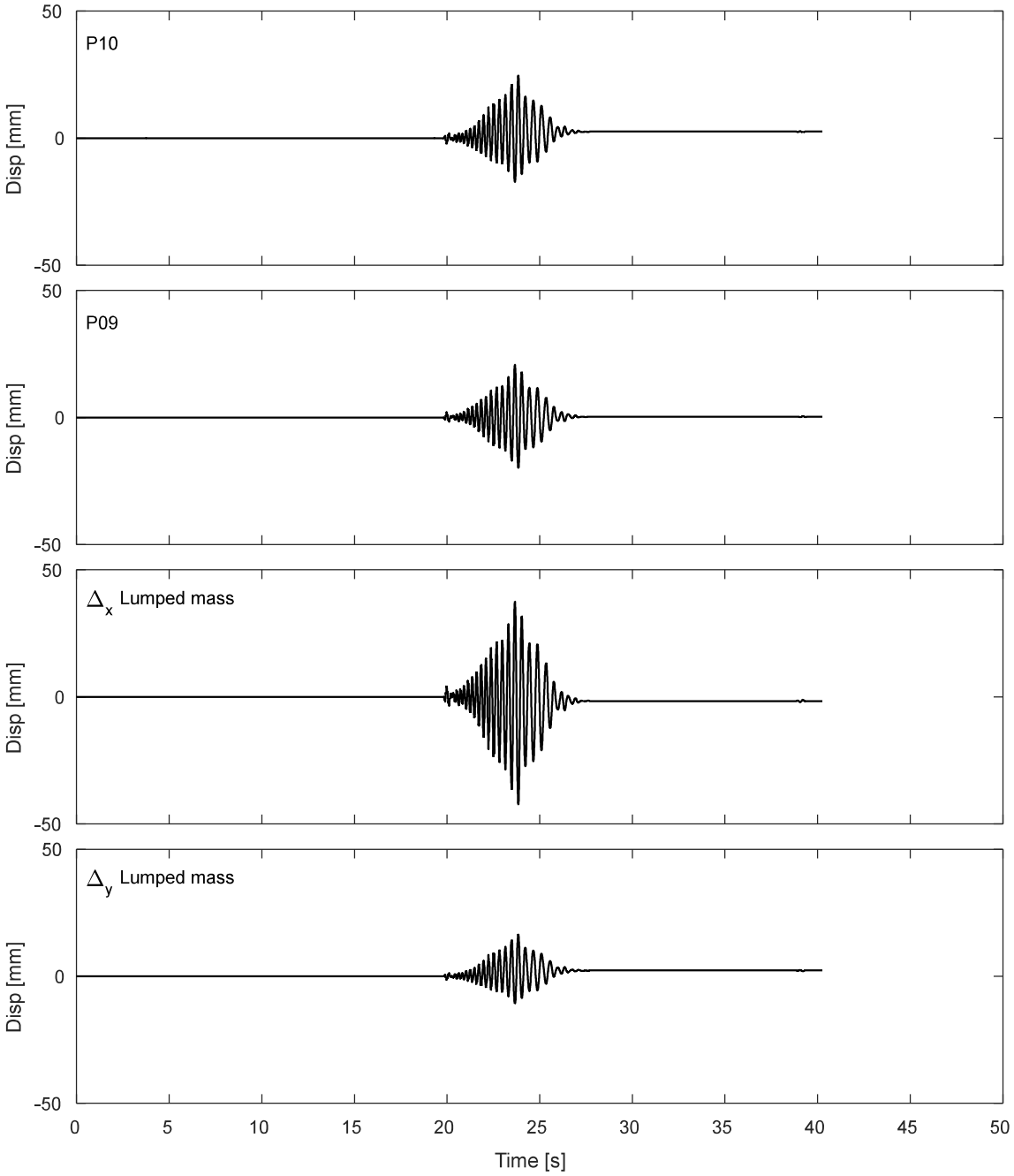

Figure I.4-8. Results of inclined potentiometers attached to lumped mass during DT01-SS450-F01F10 motion.

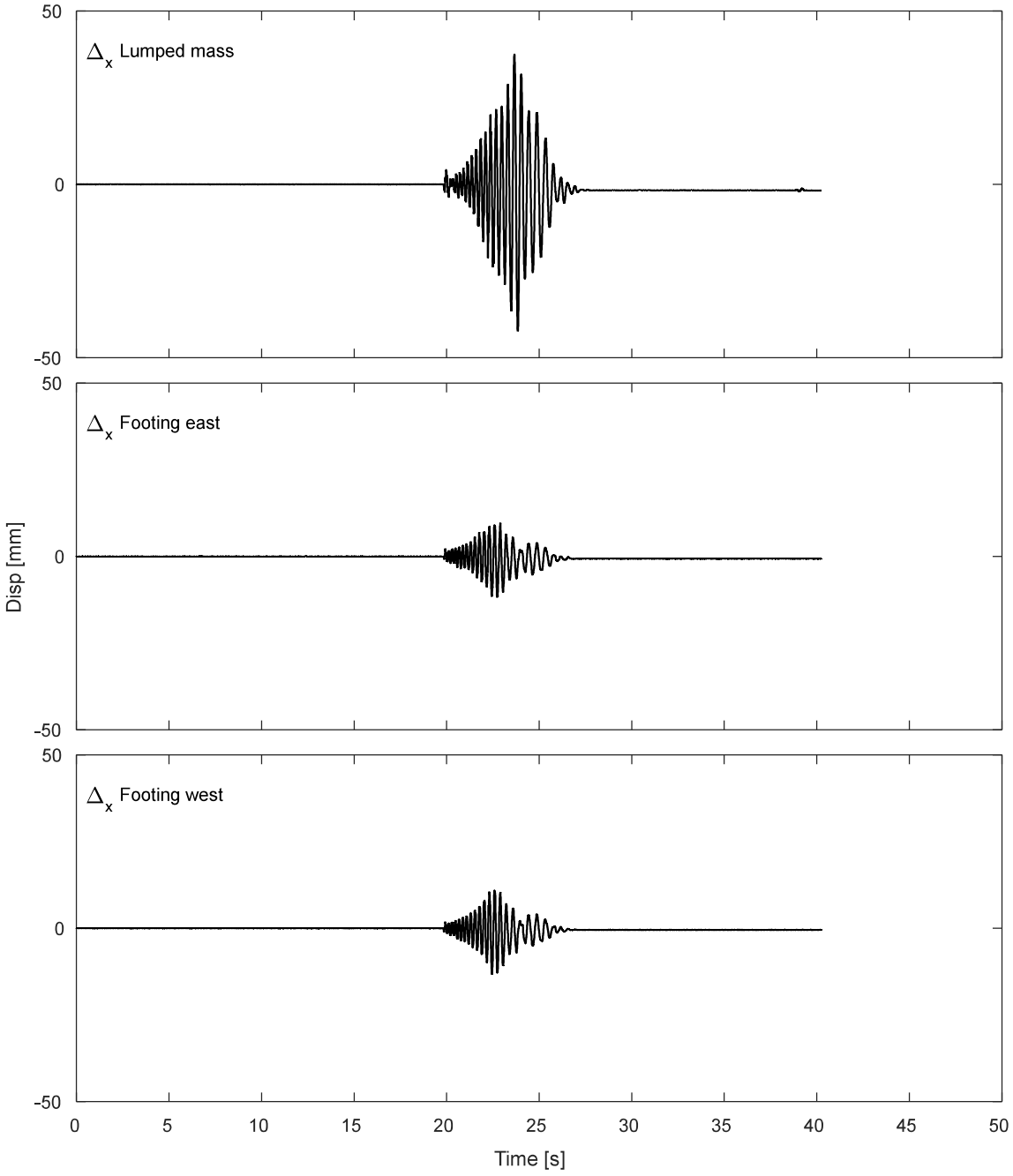

Figure I.4-9. Results of horizontal displacement of lumped mass and footing during DT01-SS450-F01F10 motion.

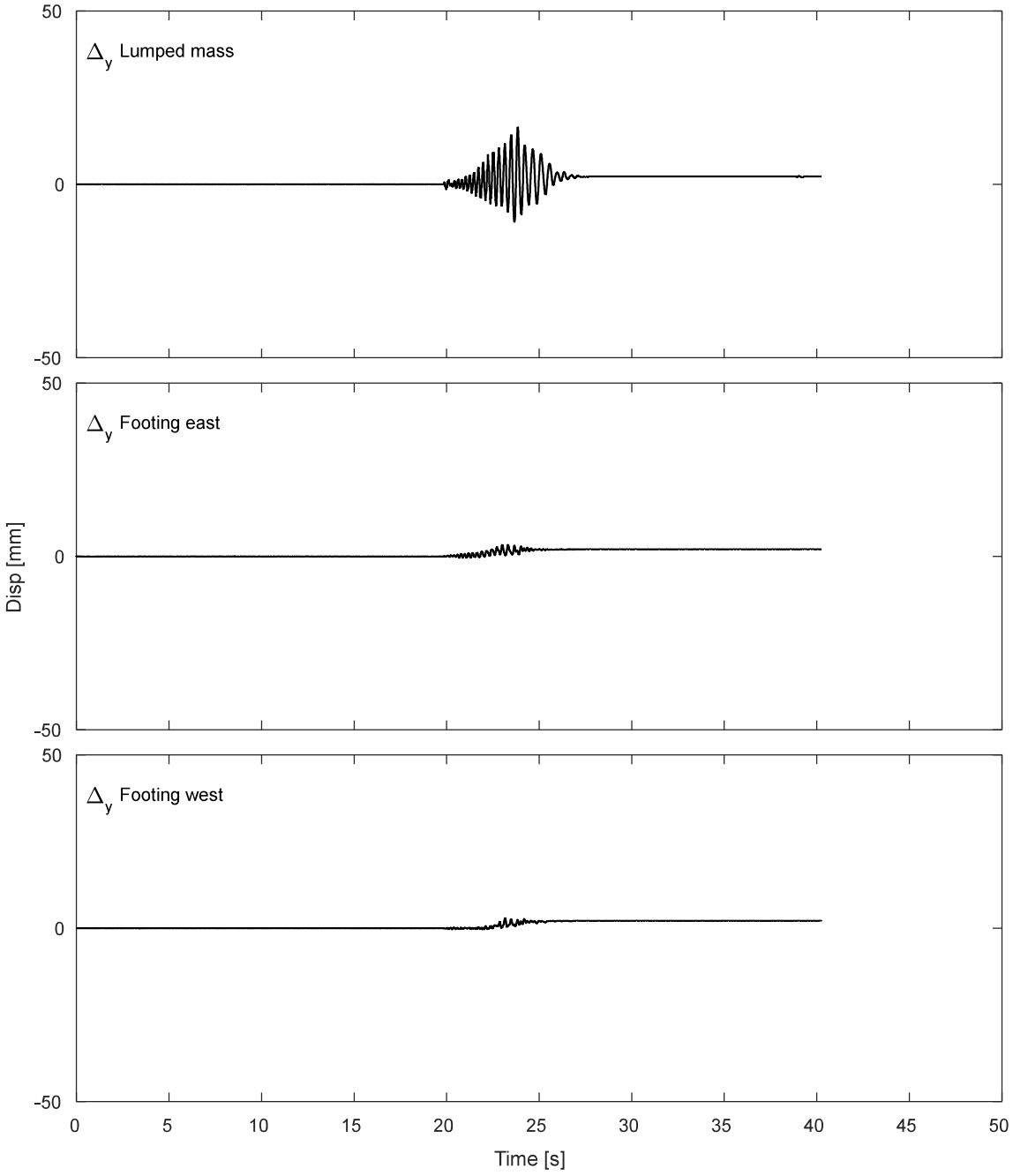

Figure I.4-10. Results of vertical displacement of lumped mass and footing during DT01-SS450-F01F10 motion.

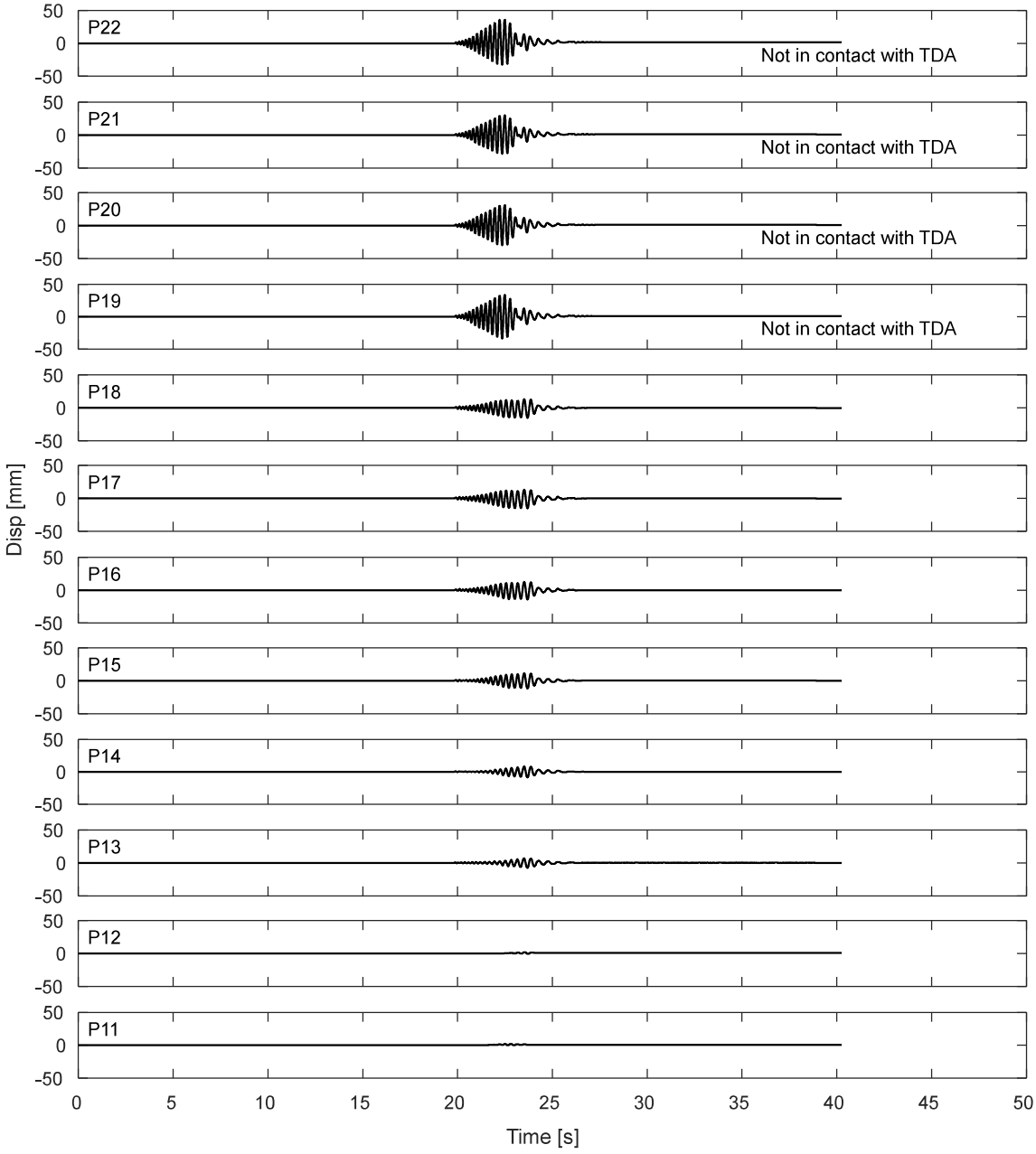

Figure I.4-11. Potentiometers results for the laminar box during DT01-SS450-F01F10 motion.

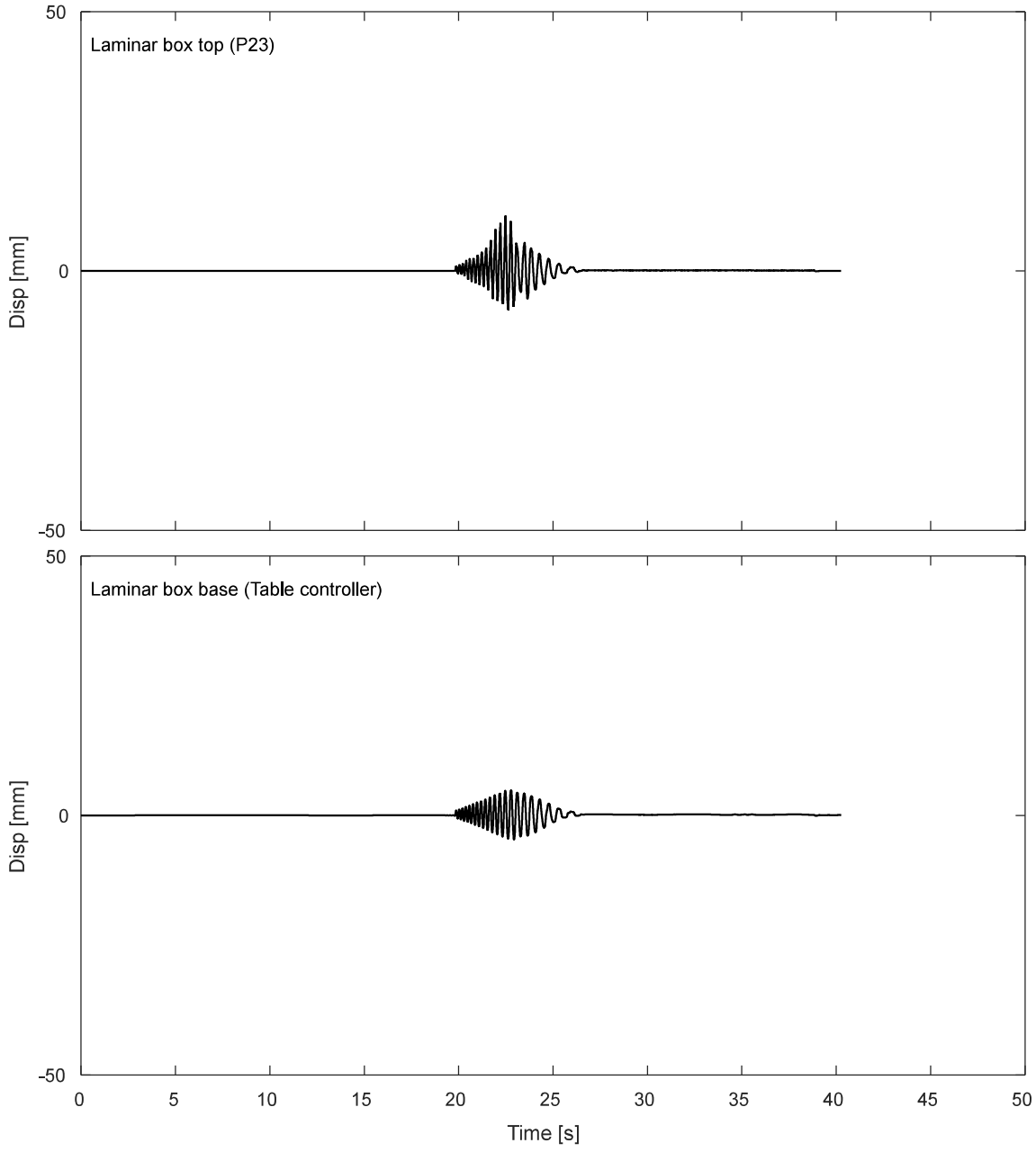

Figure I.4-12. Displacement response of top and base of laminar box during DT01-SS450-F01F10 motion.

I.4.3. Inclinometers.

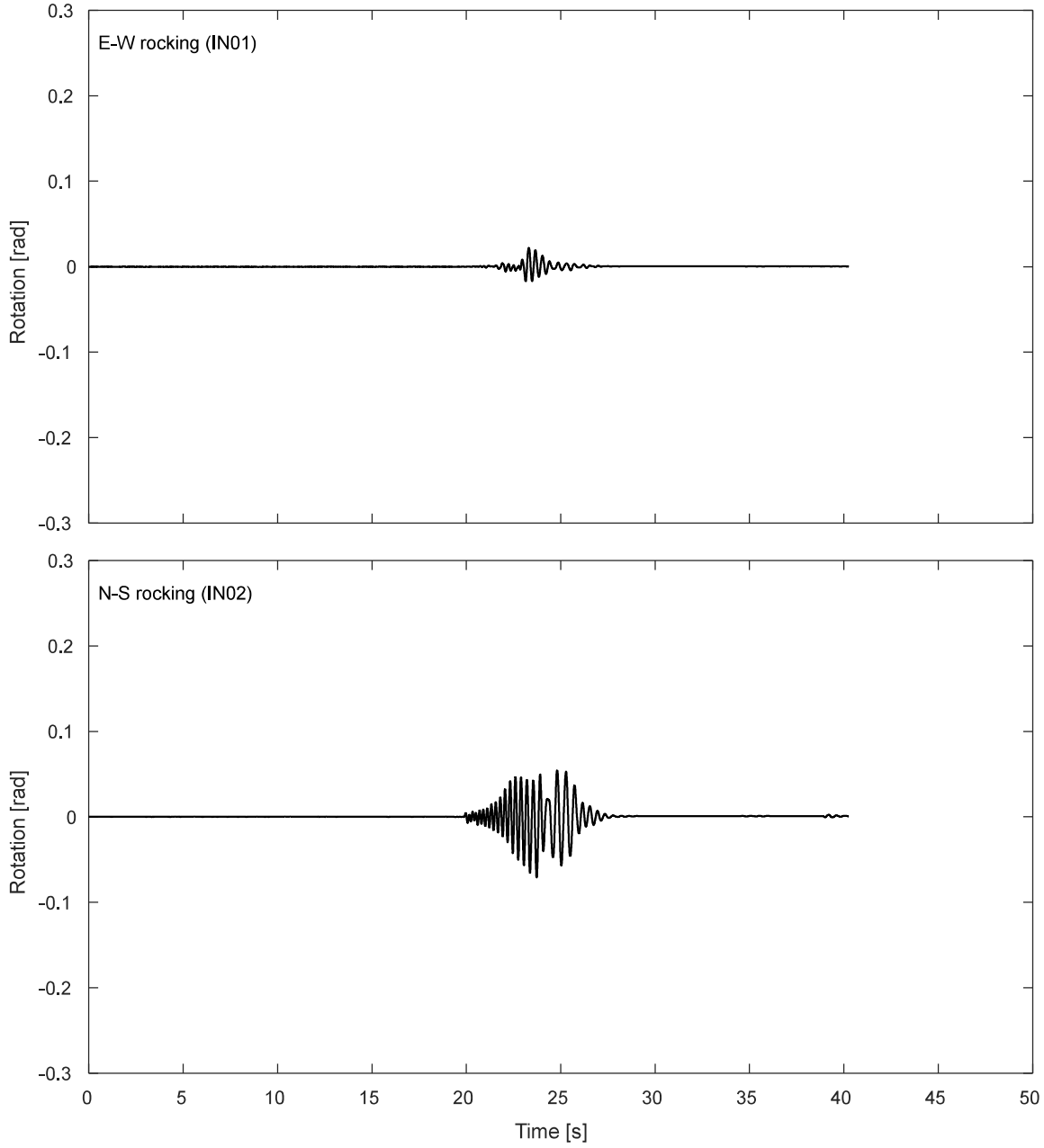

Figure I.4-13. Inclinometer results for the footing during DT01-SS450-F01F10 motion.

I.4.4. Pressure cells.

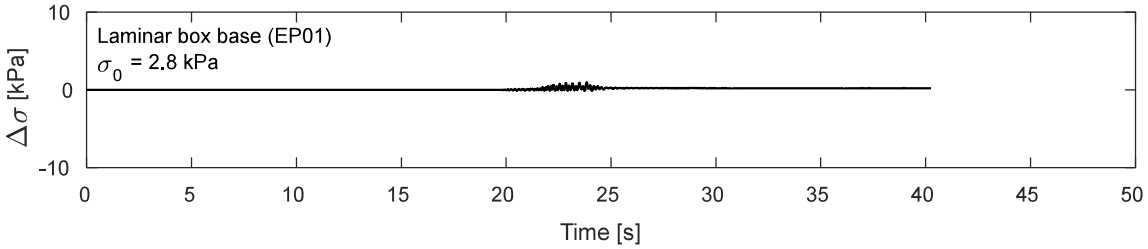

Figure I.4-14. Pressure cells results at laminar box base during DT01-SS450-F01F10 motion

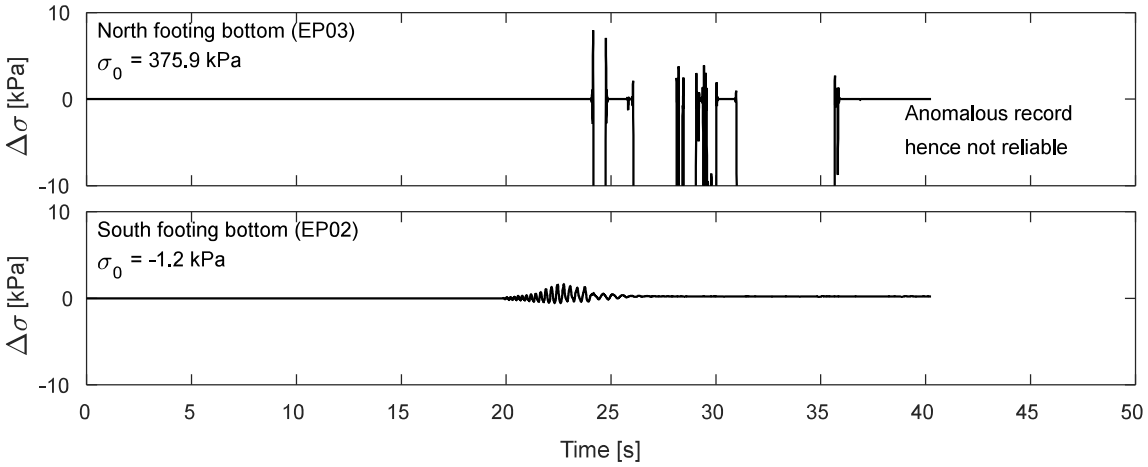

Figure I.4-15. Pressure cells results at footing bottom during DT01-SS450-F01F10 motion

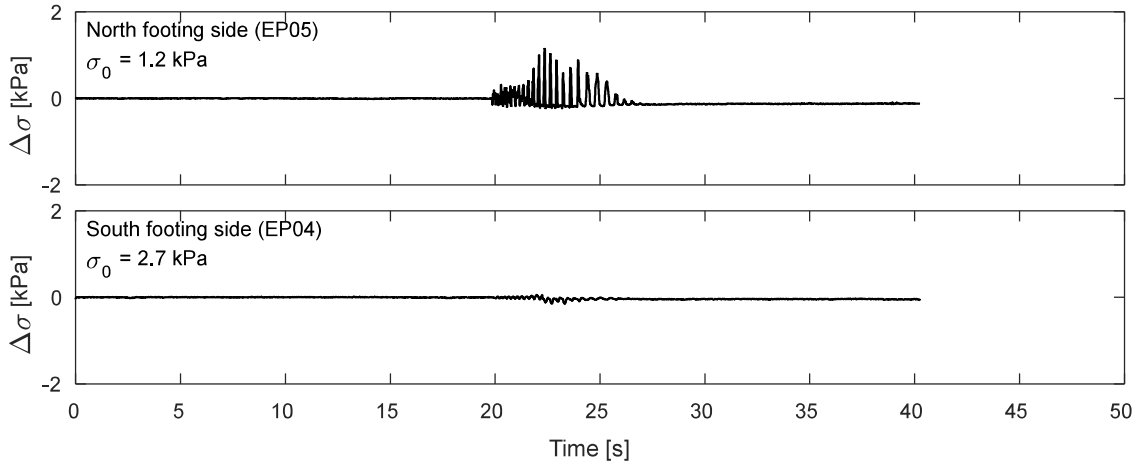

Figure I.4-16. Pressure cells results at footing sides during DT01-SS450-F01F10 motion

I.5. Time-history Records for DT01-SS525-F01F10 motion.

I.5.1 Input Motion

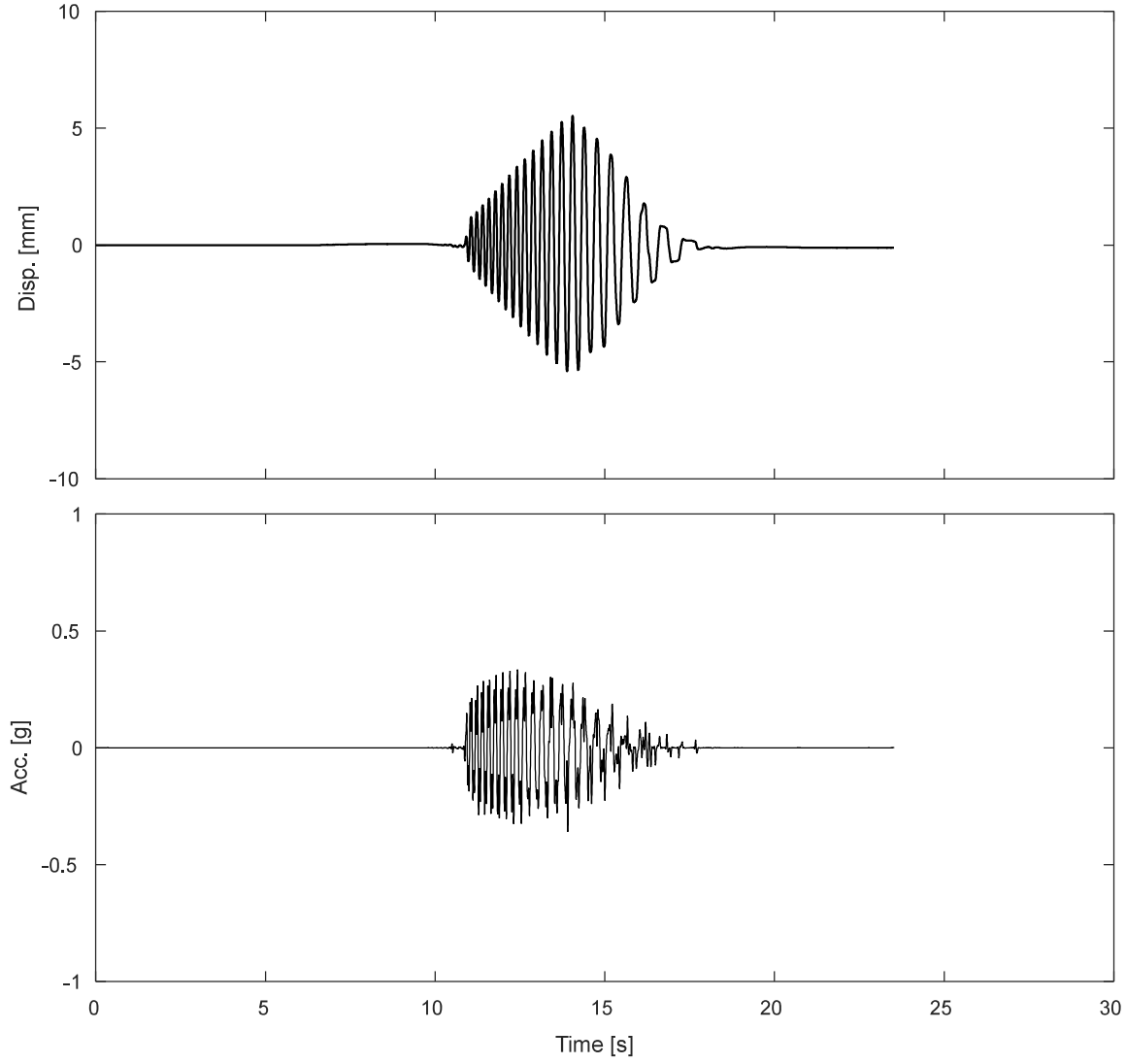

Figure I.5-1. Measured input displacement and acceleration at the base of the specimen during DT01-SS525-F01F10 motion

I.5.1 Accelerometers.

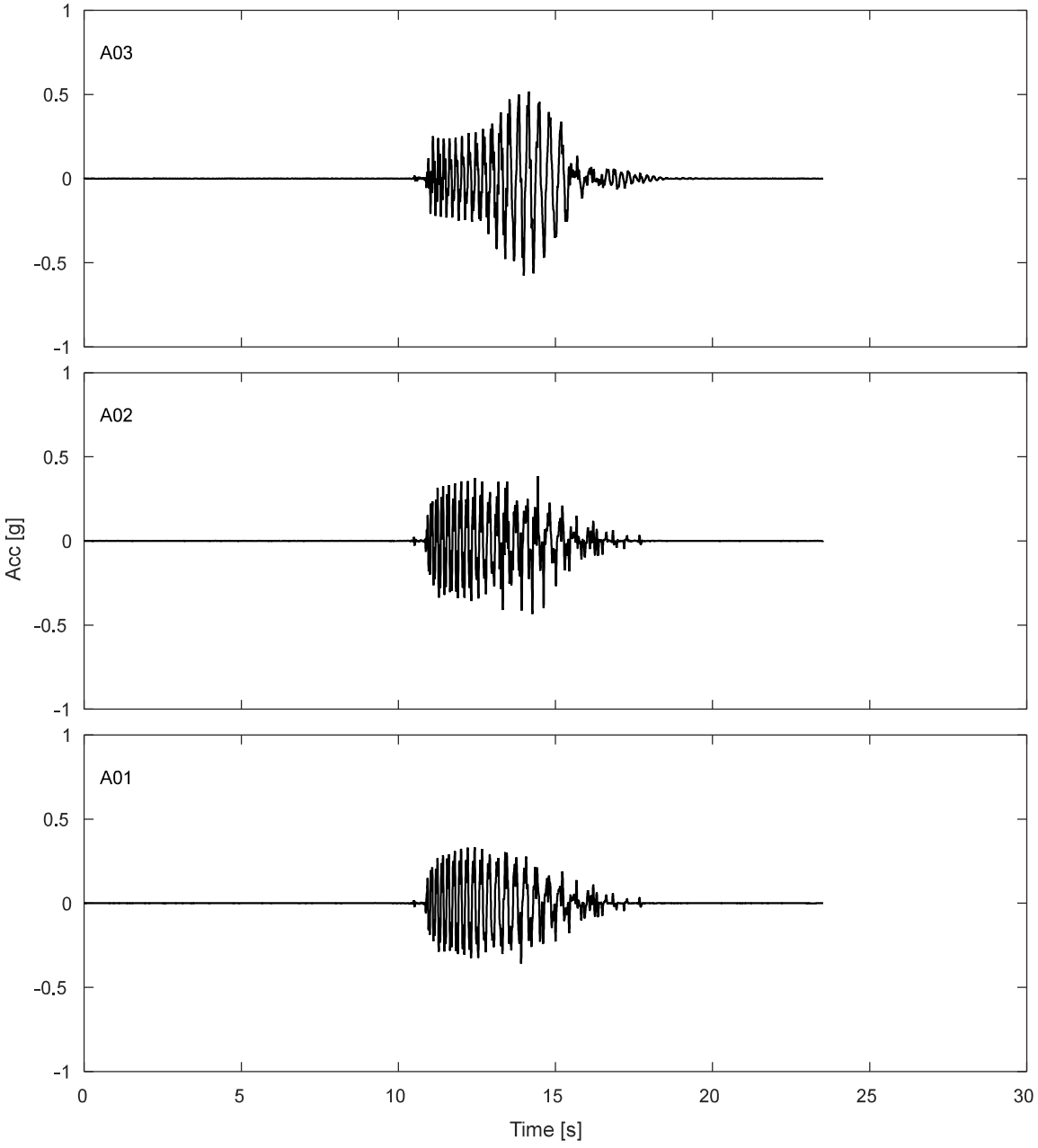

Figure I.5-2. Accelerations results along TDA during DT01-SS525-F01F10 motion.

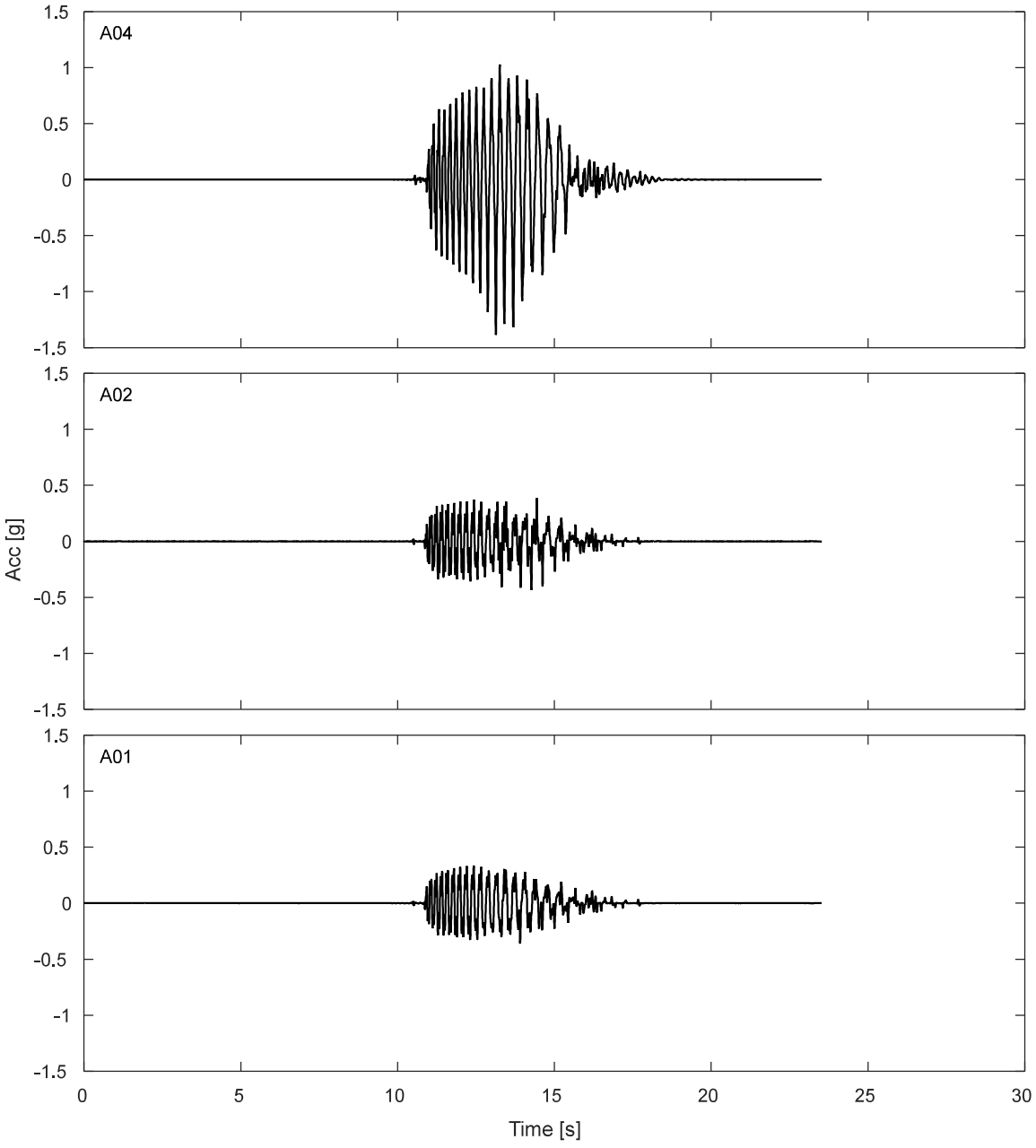

Figure I.5-3. Free field accelerations results for TDA during DT01-SS525-F01F10 motion.

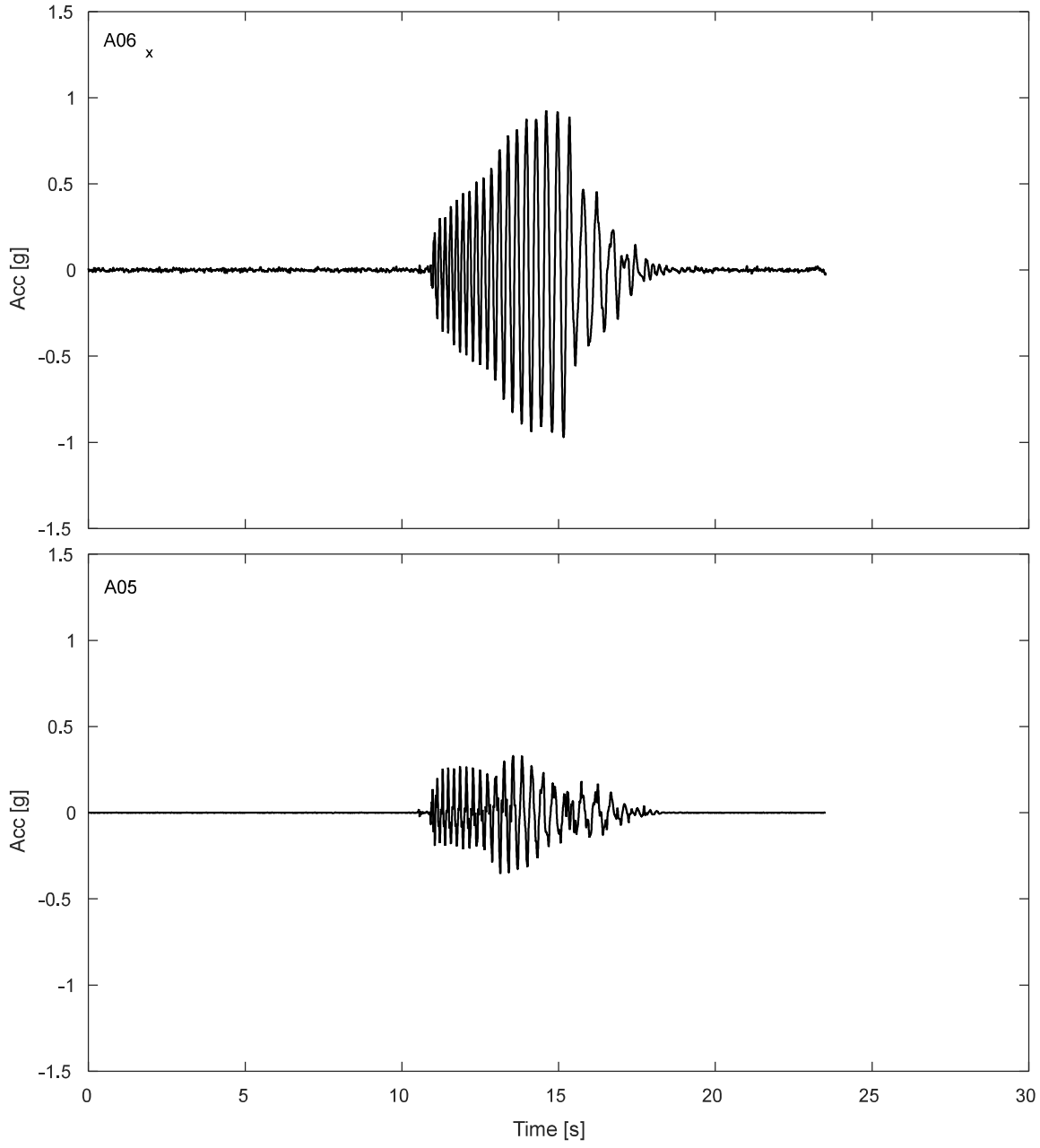

Figure I.5-4. Accelerations results SDOF structure during DT01-SS525-F01F10 motion.

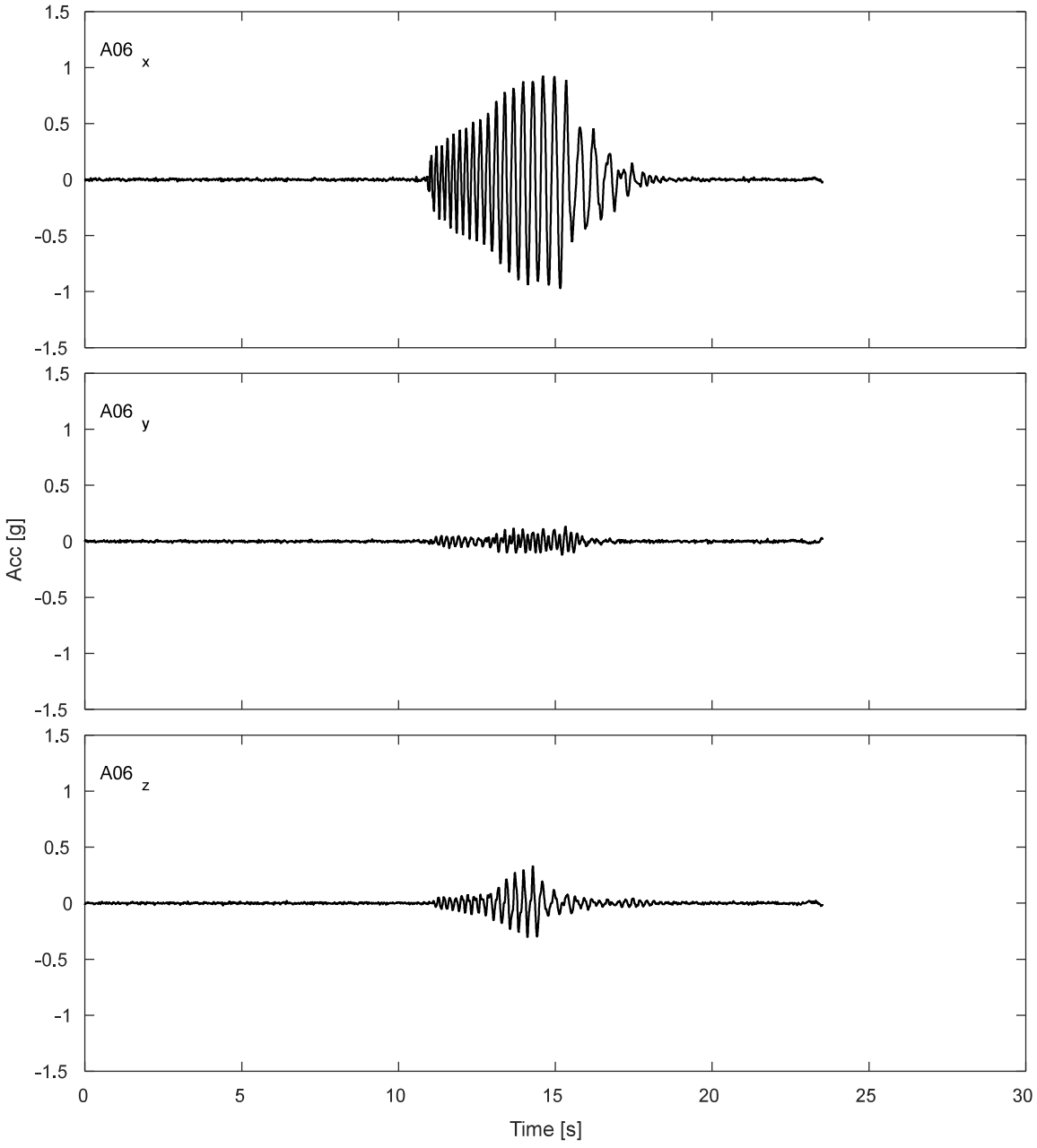

Figure I.5-5. Accelerations results for lumped mass of SDOF structure during DT01-SS525-F01F10 motion.

I.5.2 Potentiometers.

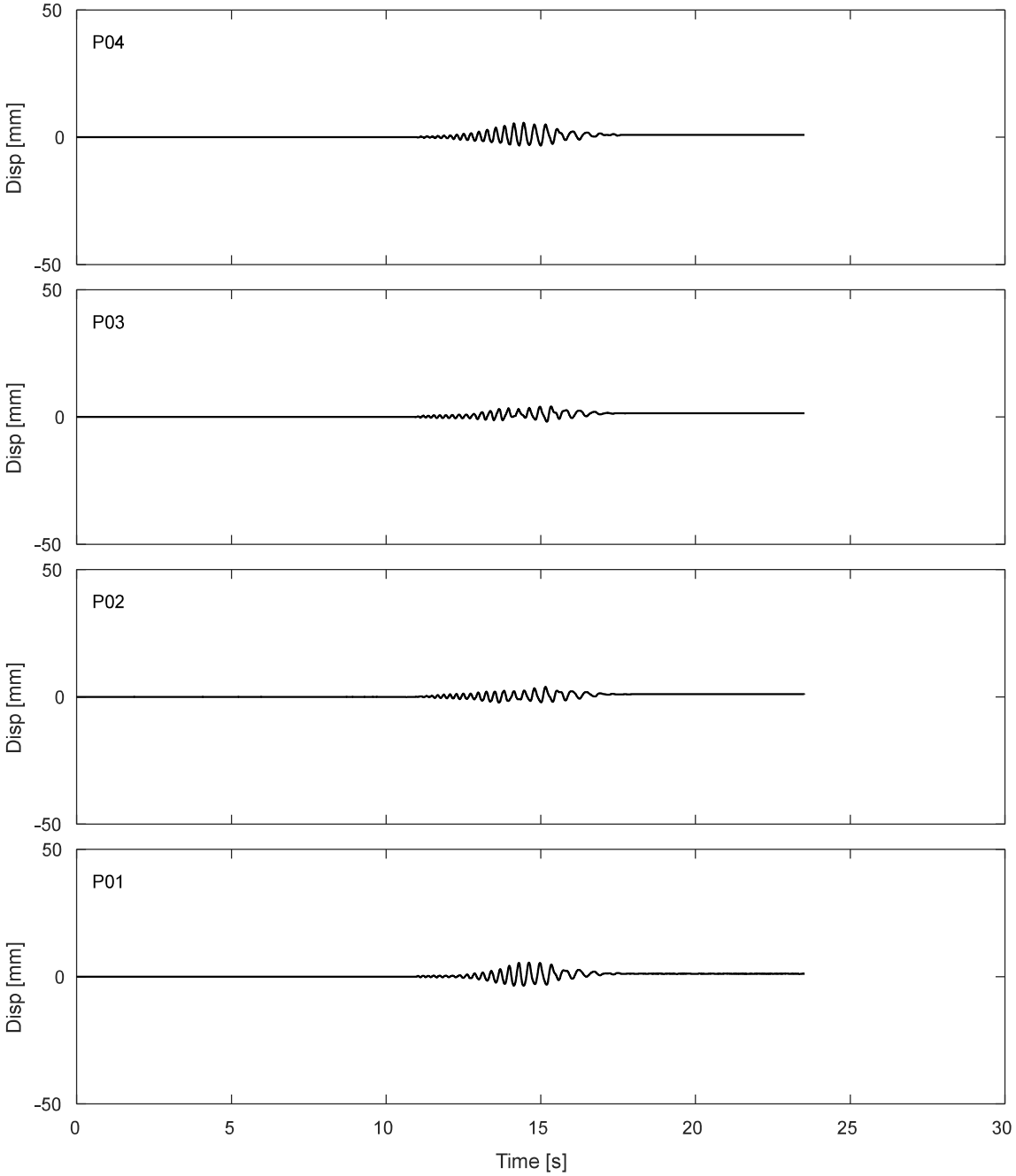

Figure I.5-6. Results of fully vertical potentiometers attached to corners of top of strip footing during DT01-SS525-F01F10 motion.

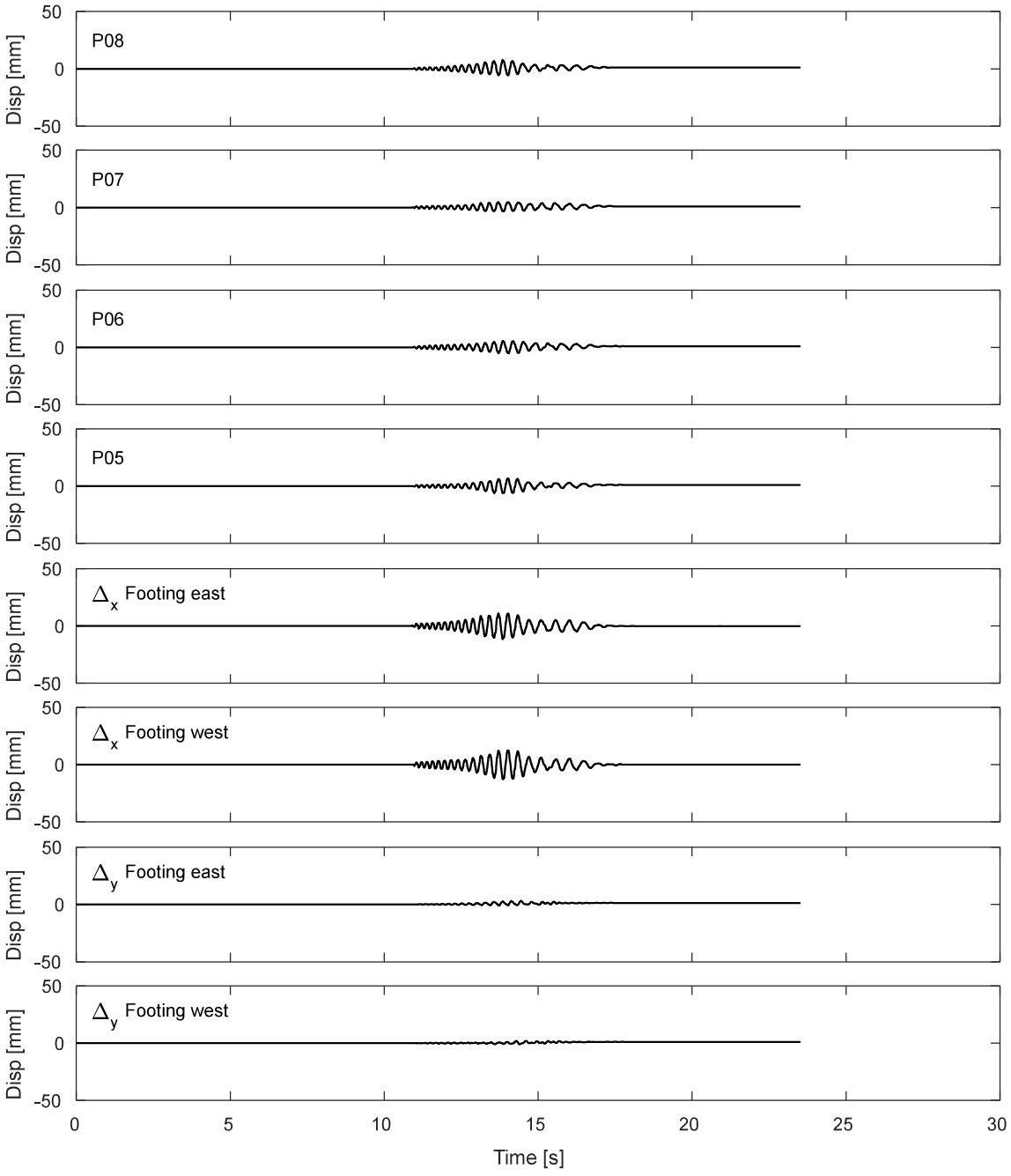

Figure I.5-7. Results of inclined potentiometers attached to top of strip footing during DT01-SS525-F01F10 motion.

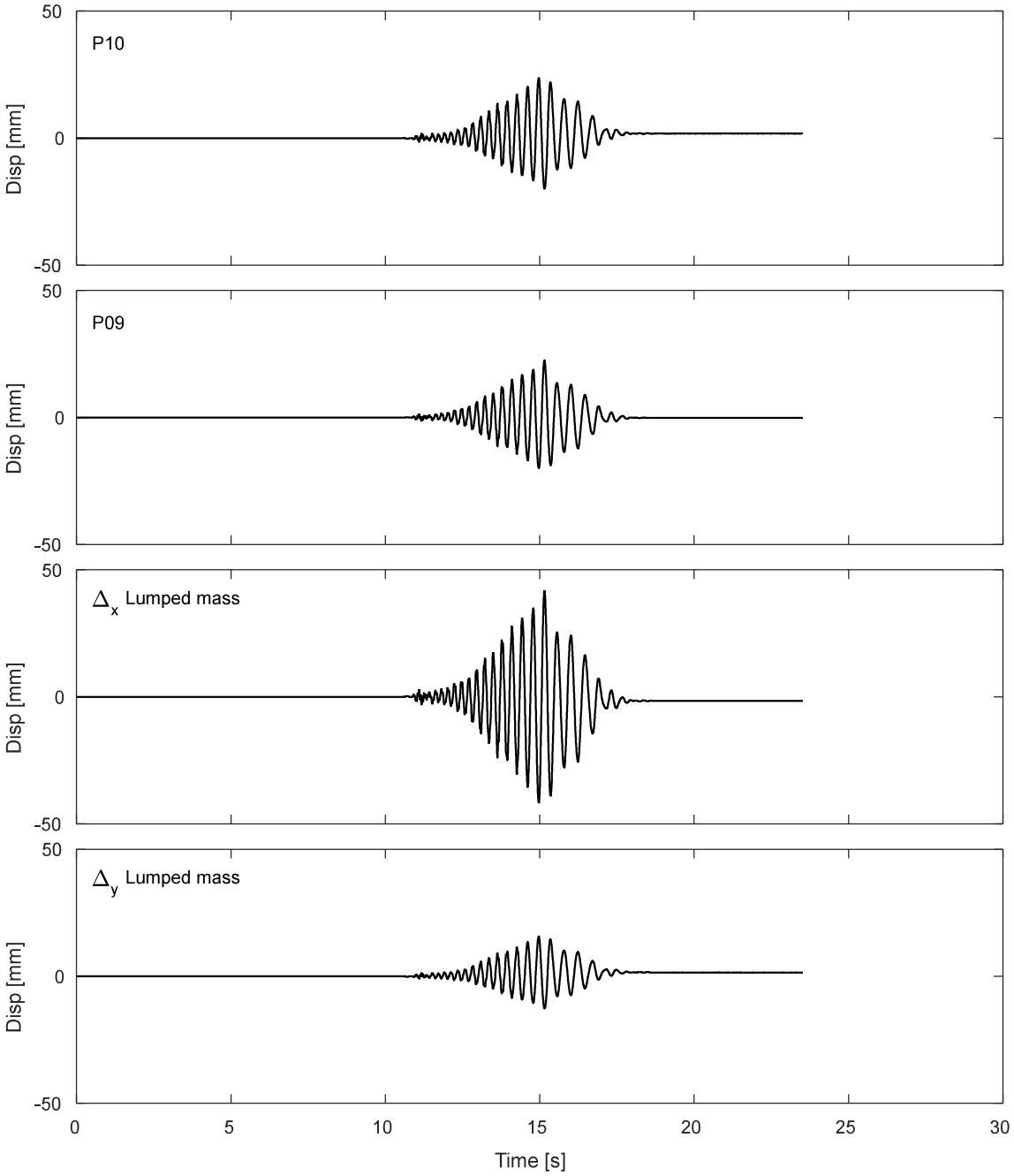

Figure I.5-8. Results of inclined potentiometers attached to lumped mass during DT01-SS525-F01F10 motion.

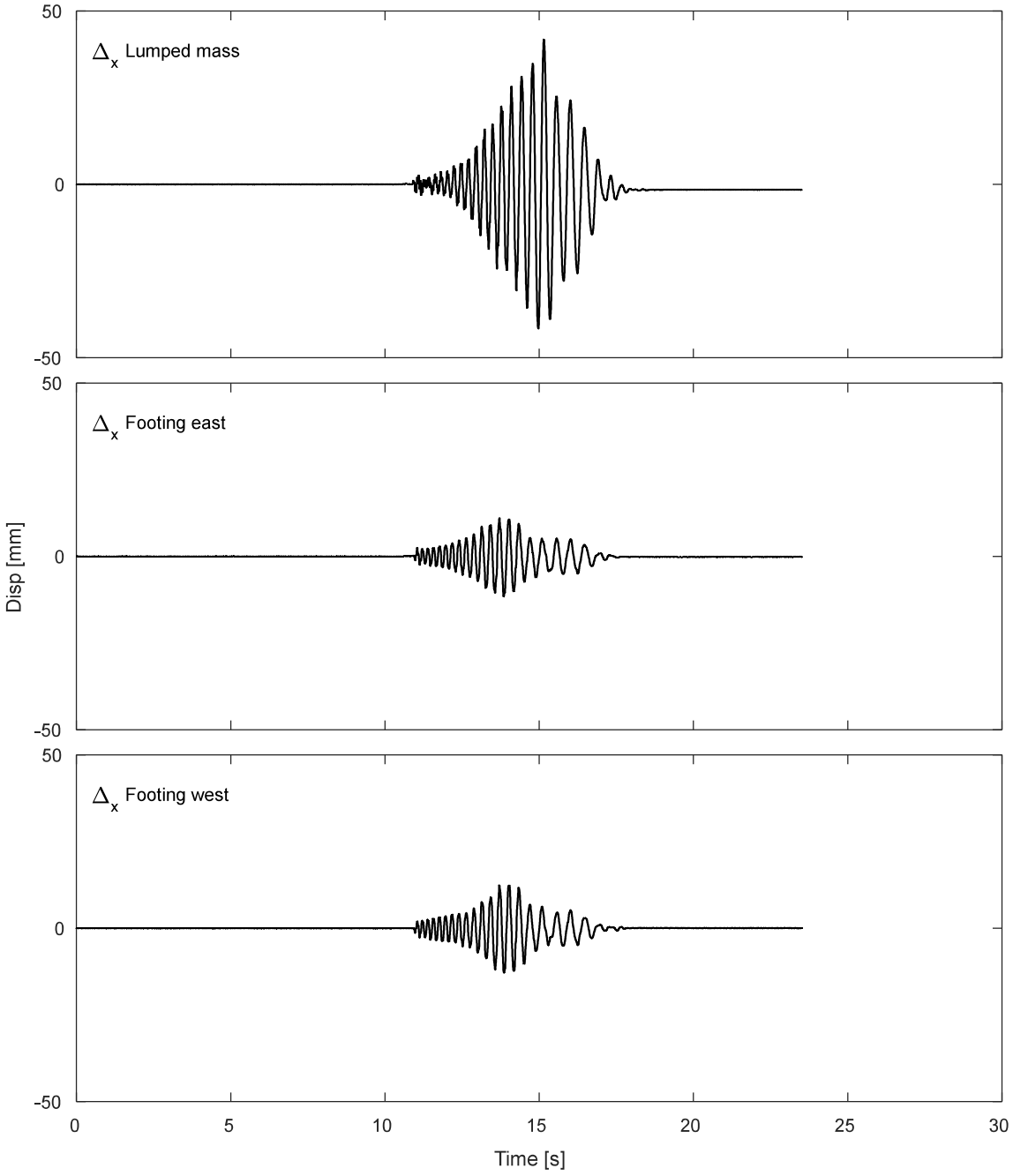

Figure I.5-9. Results of horizontal displacement of lumped mass and footing during DT01-SS525-F01F10 motion.

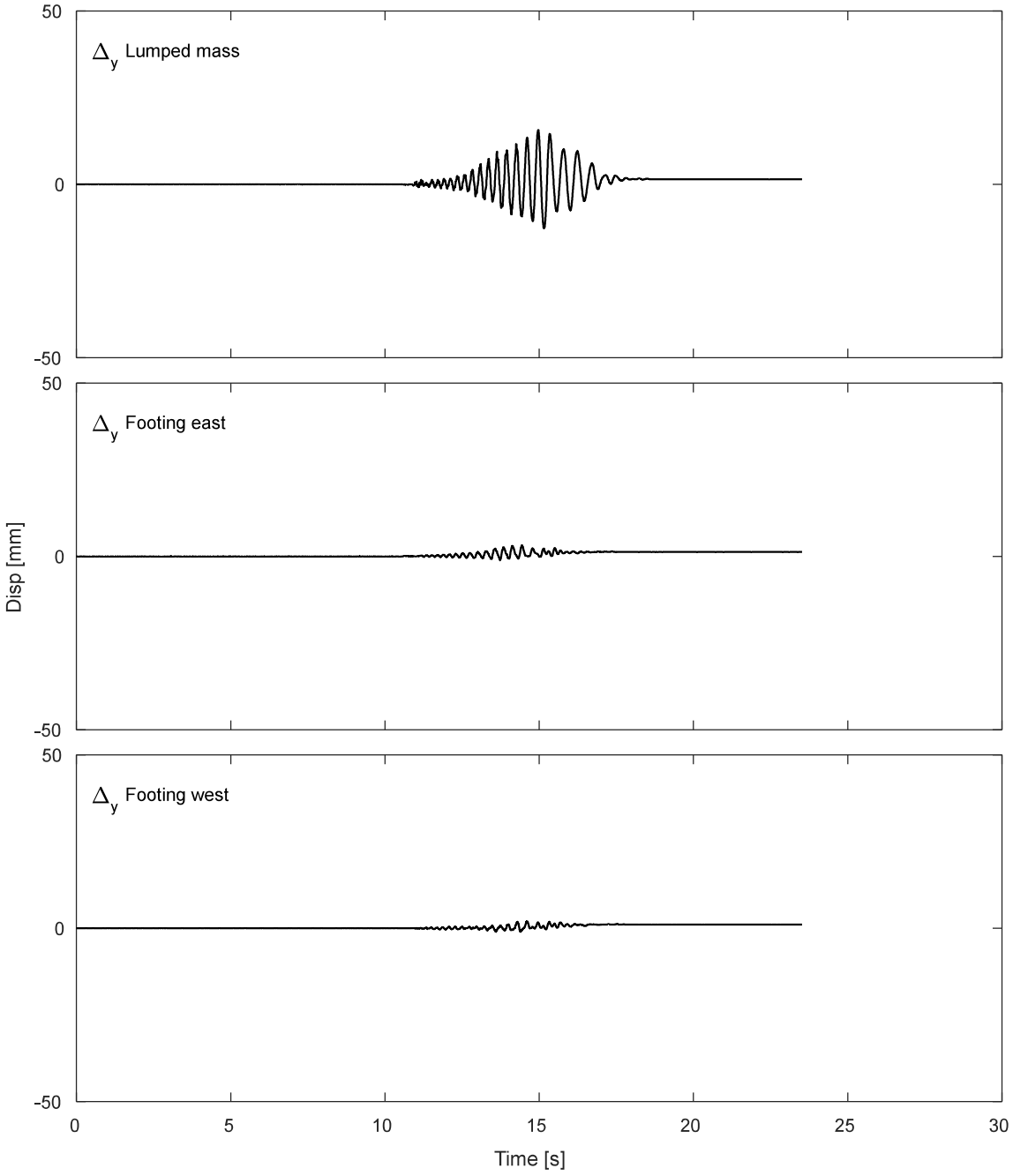

Figure I.5-10. Results of vertical displacement of lumped mass and footing during DT01-SS525-F01F10 motion.

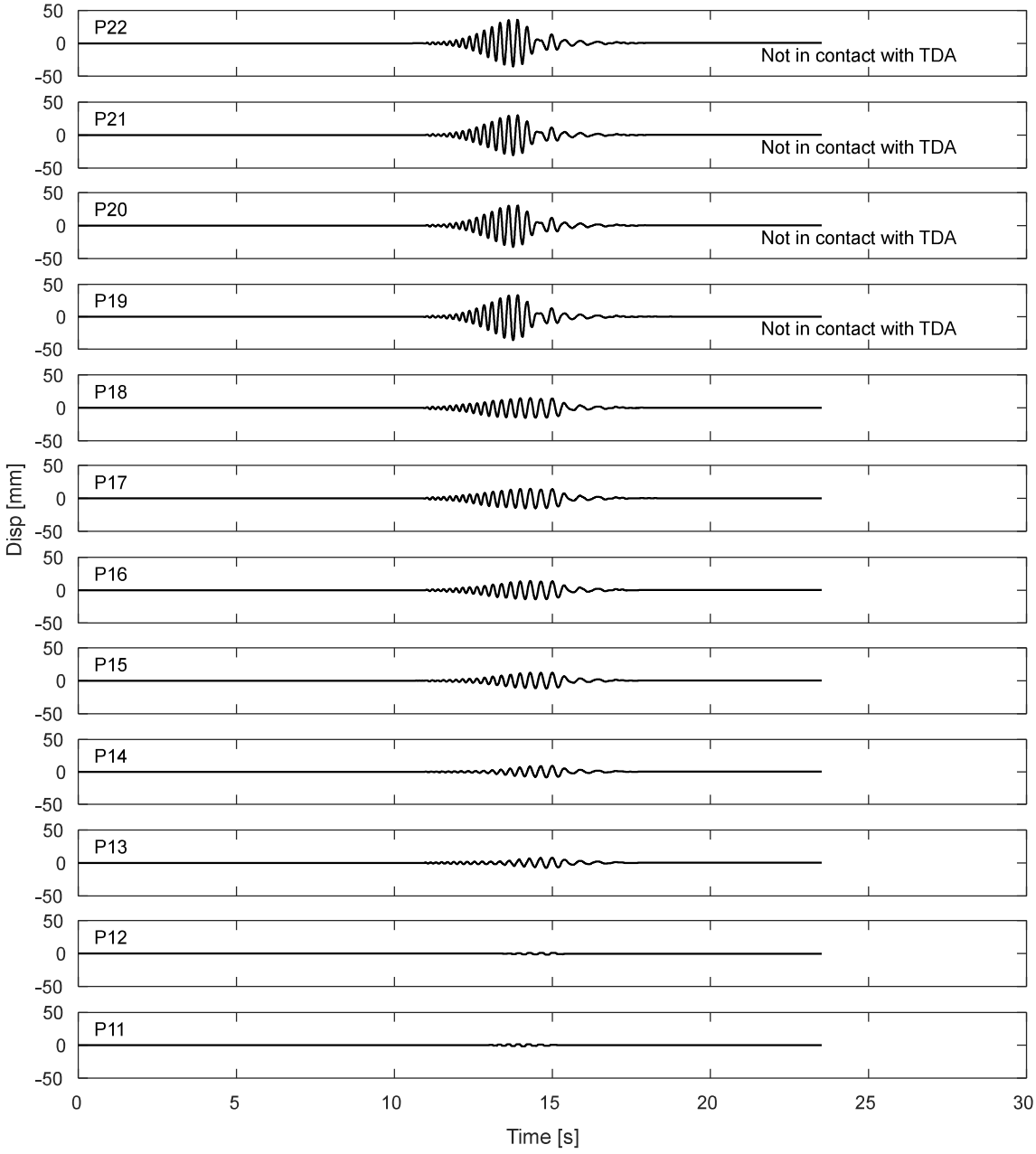

Figure I.5-11. Potentiometers results for the laminar box during DT01-SS525-F01F10 motion.

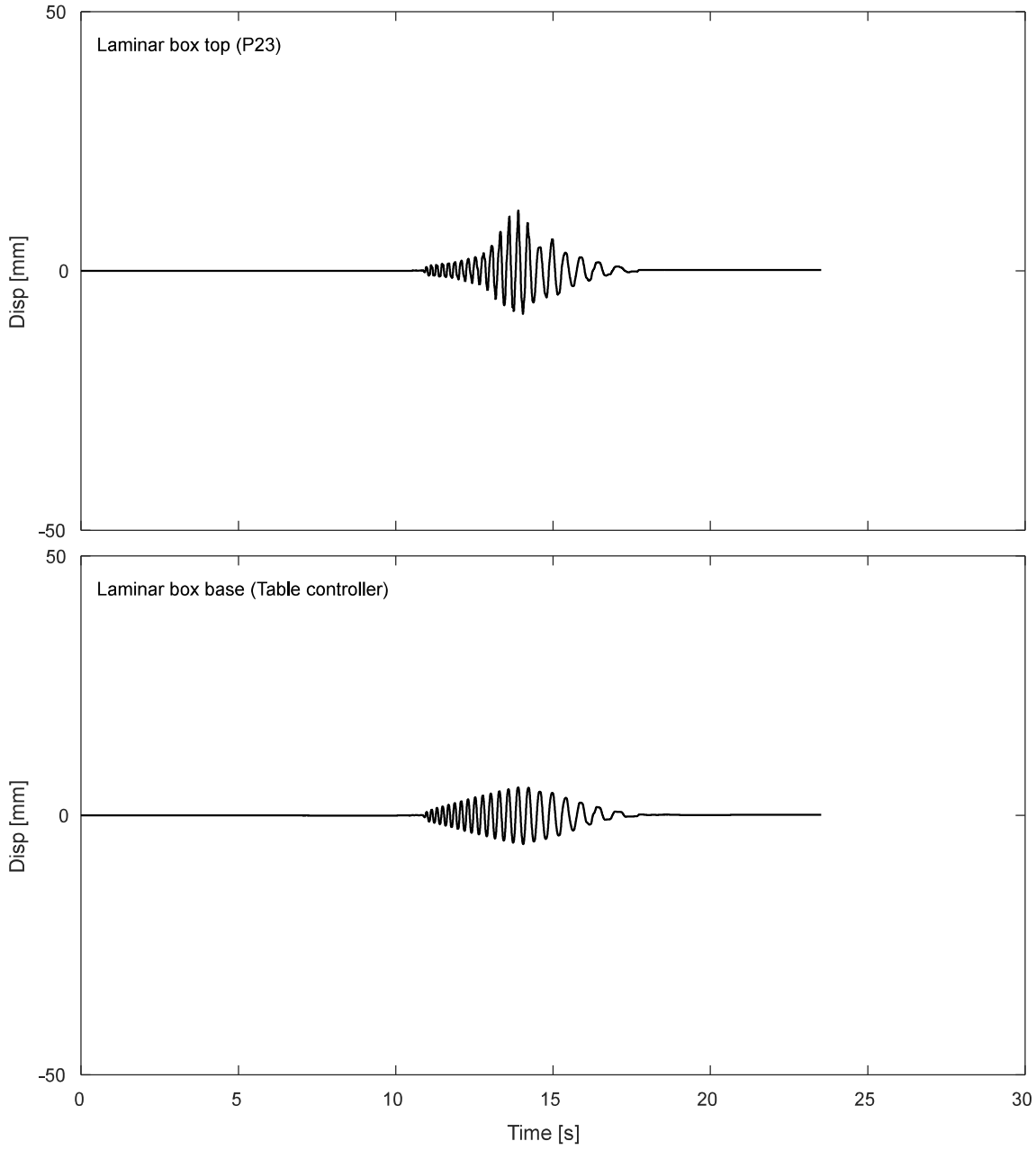

Figure I.5-12. Displacement response of top and base of laminar box during DT01-SS525-F01F10 motion.

I.5.3. Inclinometers.

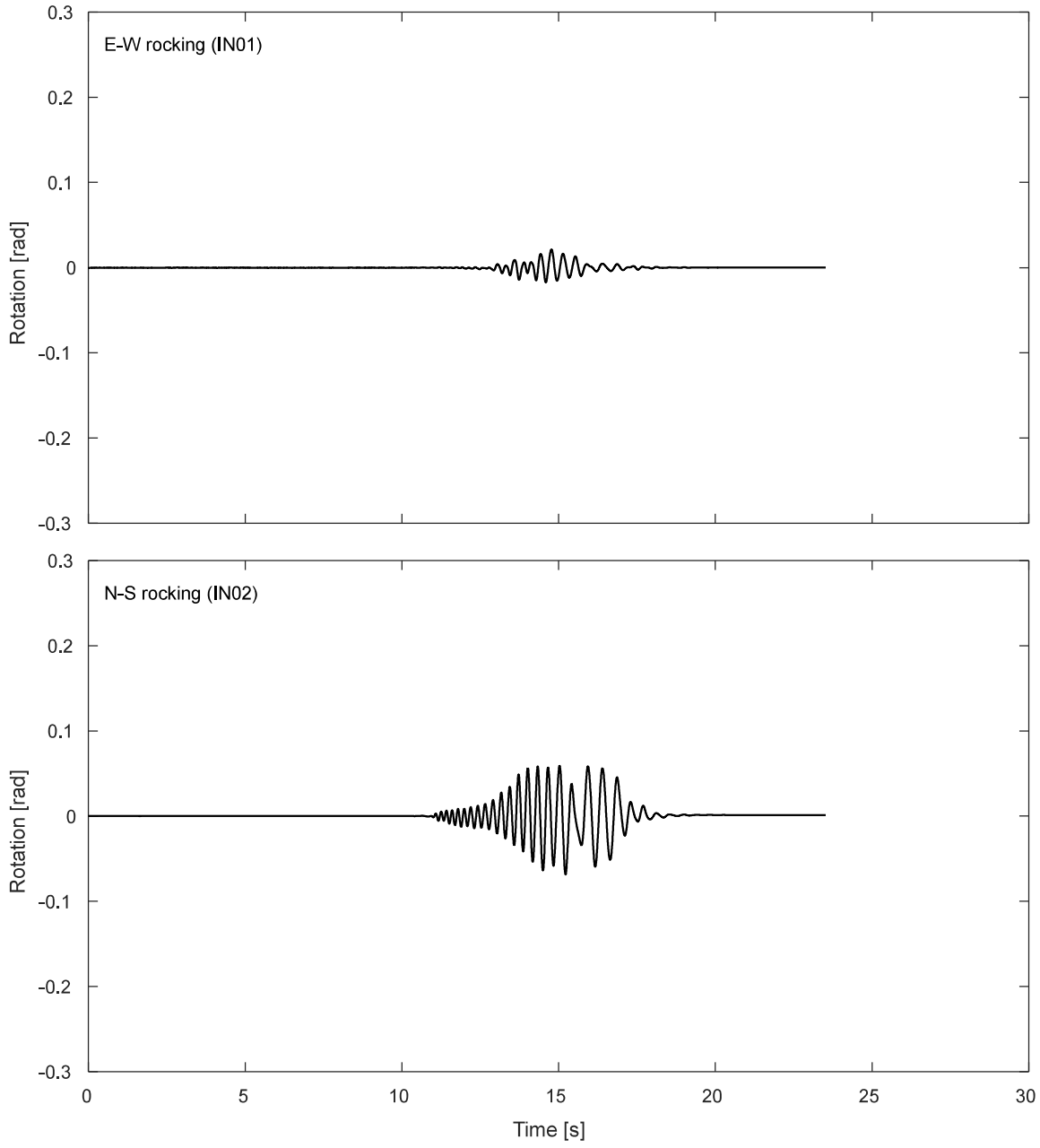

Figure I.5-13. Inclinometer results for the footing during DT01-SS525-F01F10 motion.

I.5.4. Pressure cells.

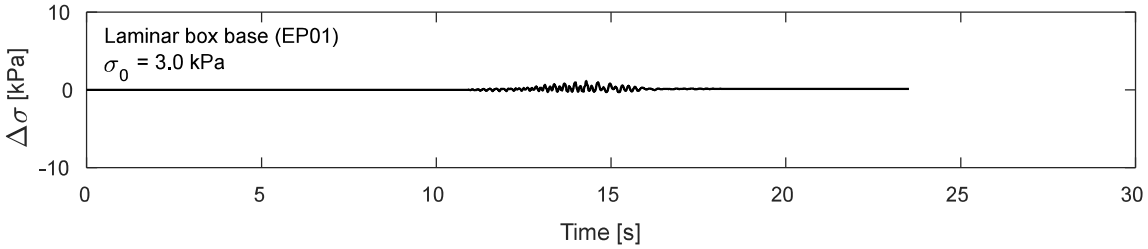

Figure I.5-14. Pressure cells results at laminar box base during DT01-SS525-F01F10 motion

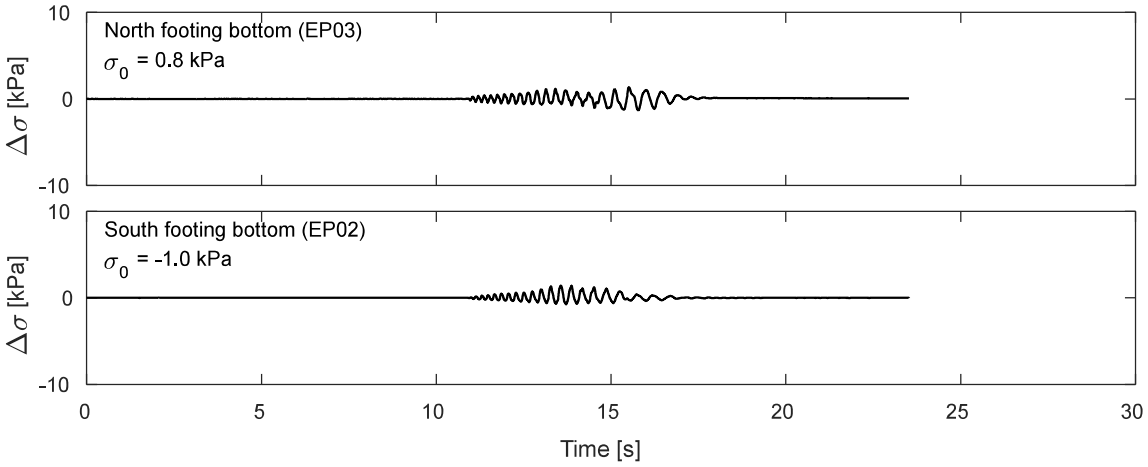

Figure I.5-15. Pressure cells results at footing bottom during DT01-SS525-F01F10 motion

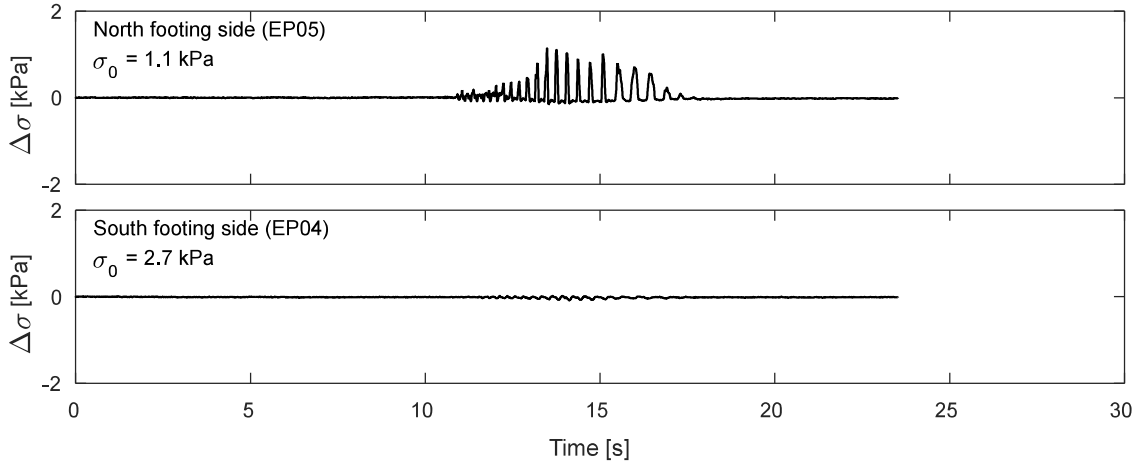

Figure I.5-16. Pressure cells results at footing sides during DT01-SS525-F01F10 motion

I.6. Time-history Records for DT01-NOR-050P motion.

I.6.1 Input Motion

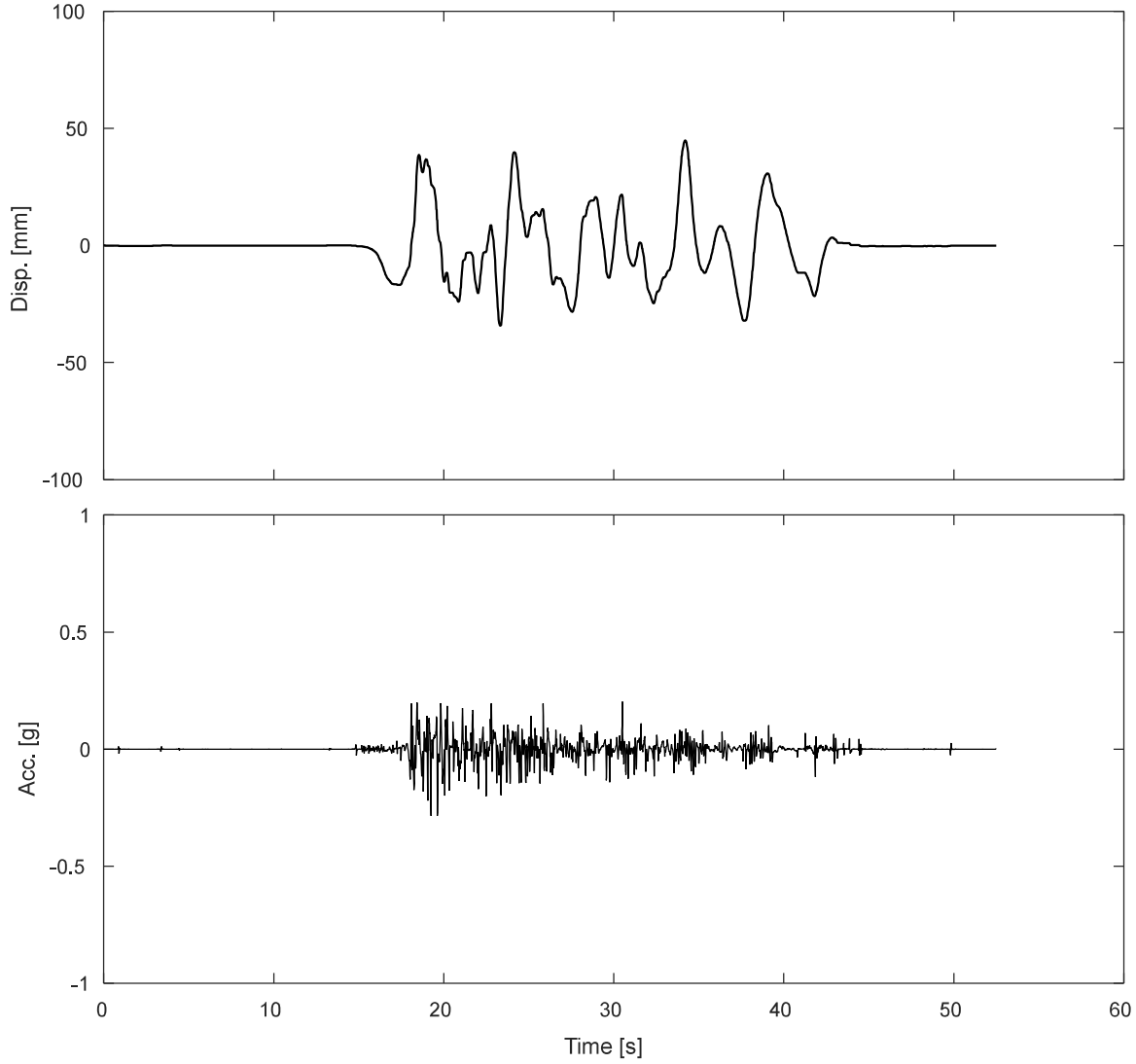

Figure I.6-1. Measured input displacement and acceleration at the base of the specimen during DT01-NOR-050P motion

I.6.1 Accelerometers.

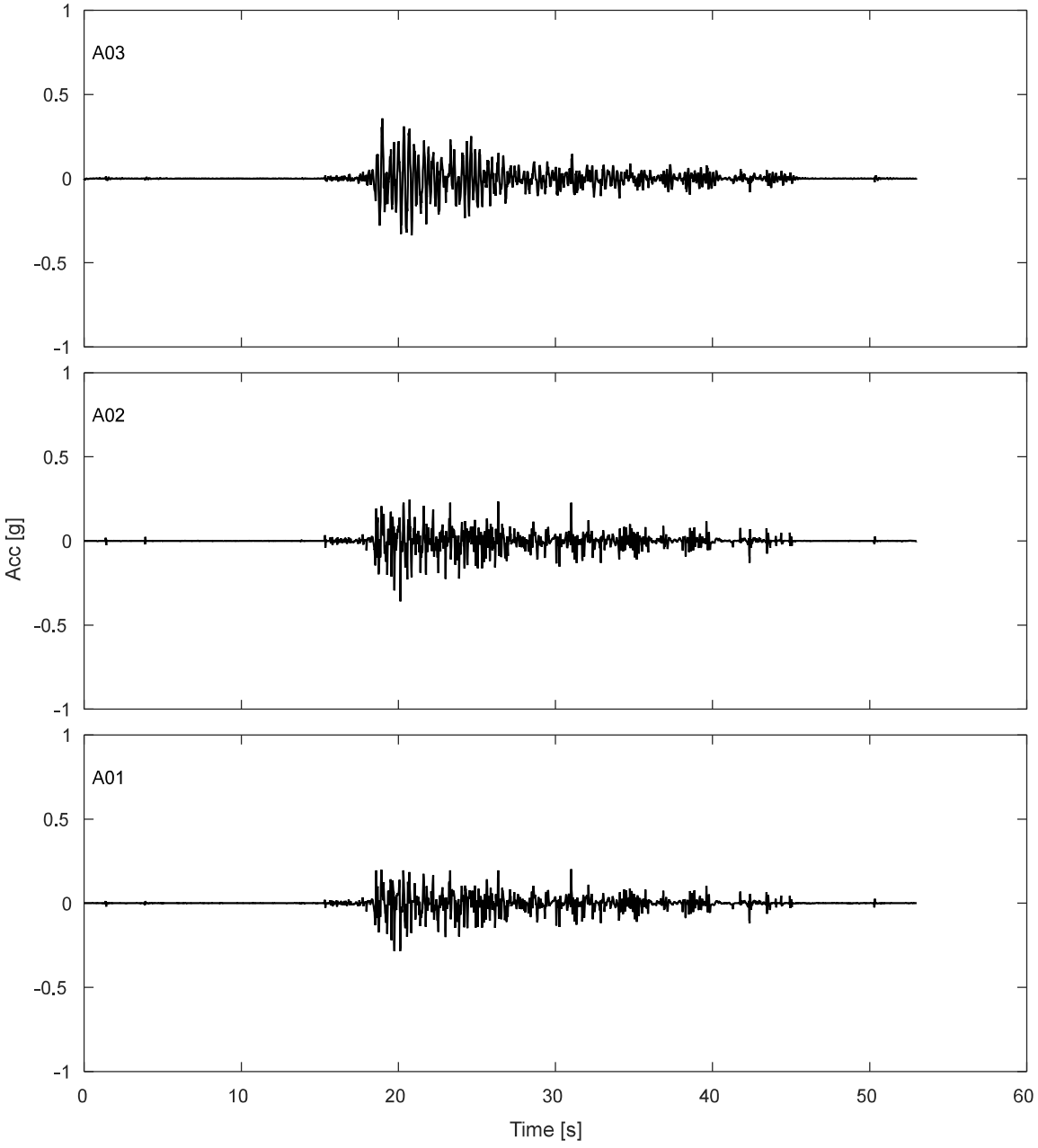

Figure I.6-2. Accelerations results along TDA during DT01-NOR-050P motion.

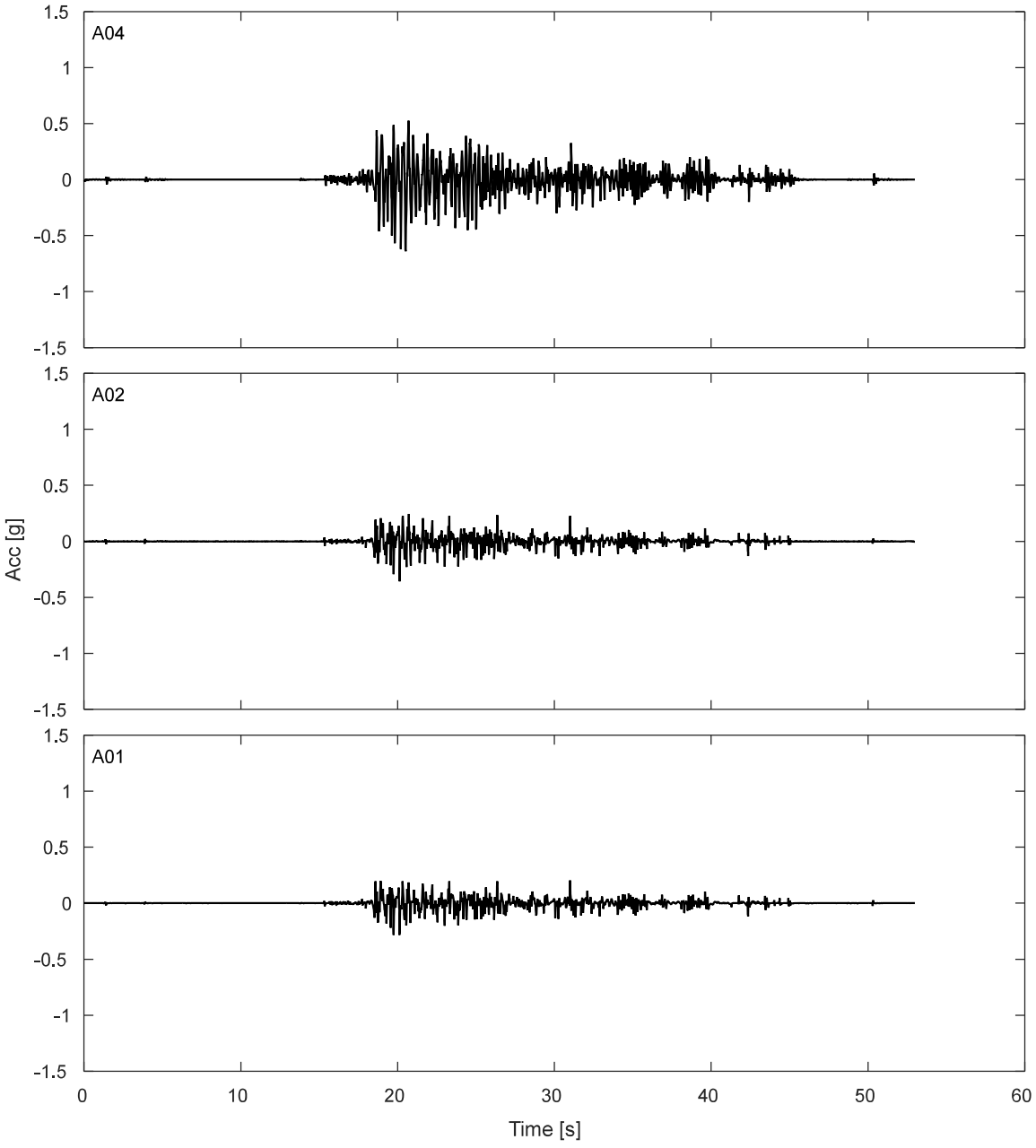

Figure I.6-3. Free field accelerations results for TDA during DT01-NOR-050P motion.

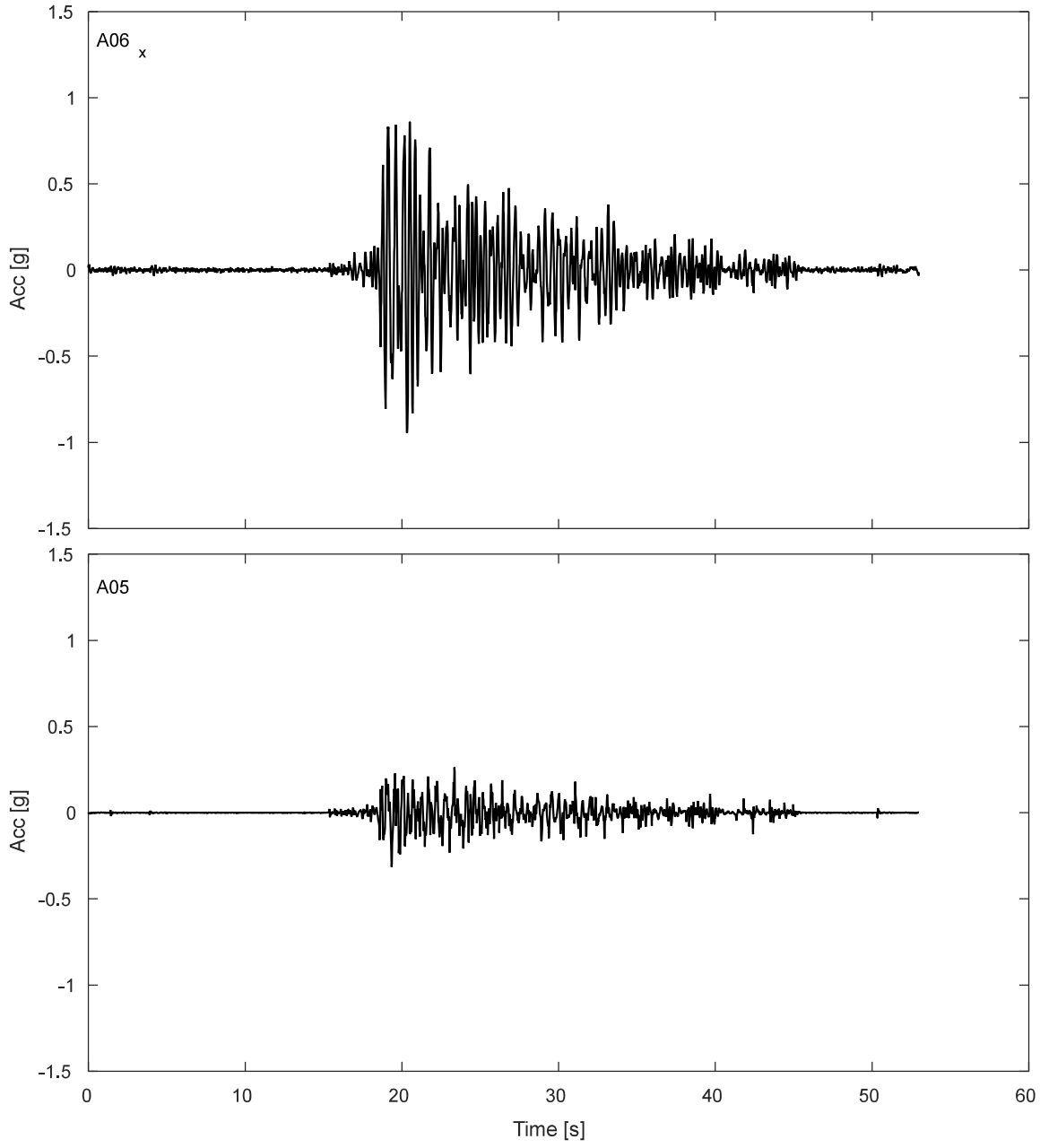

Figure I.6-4. Accelerations results SDOF structure during DT01-NOR-050P motion.

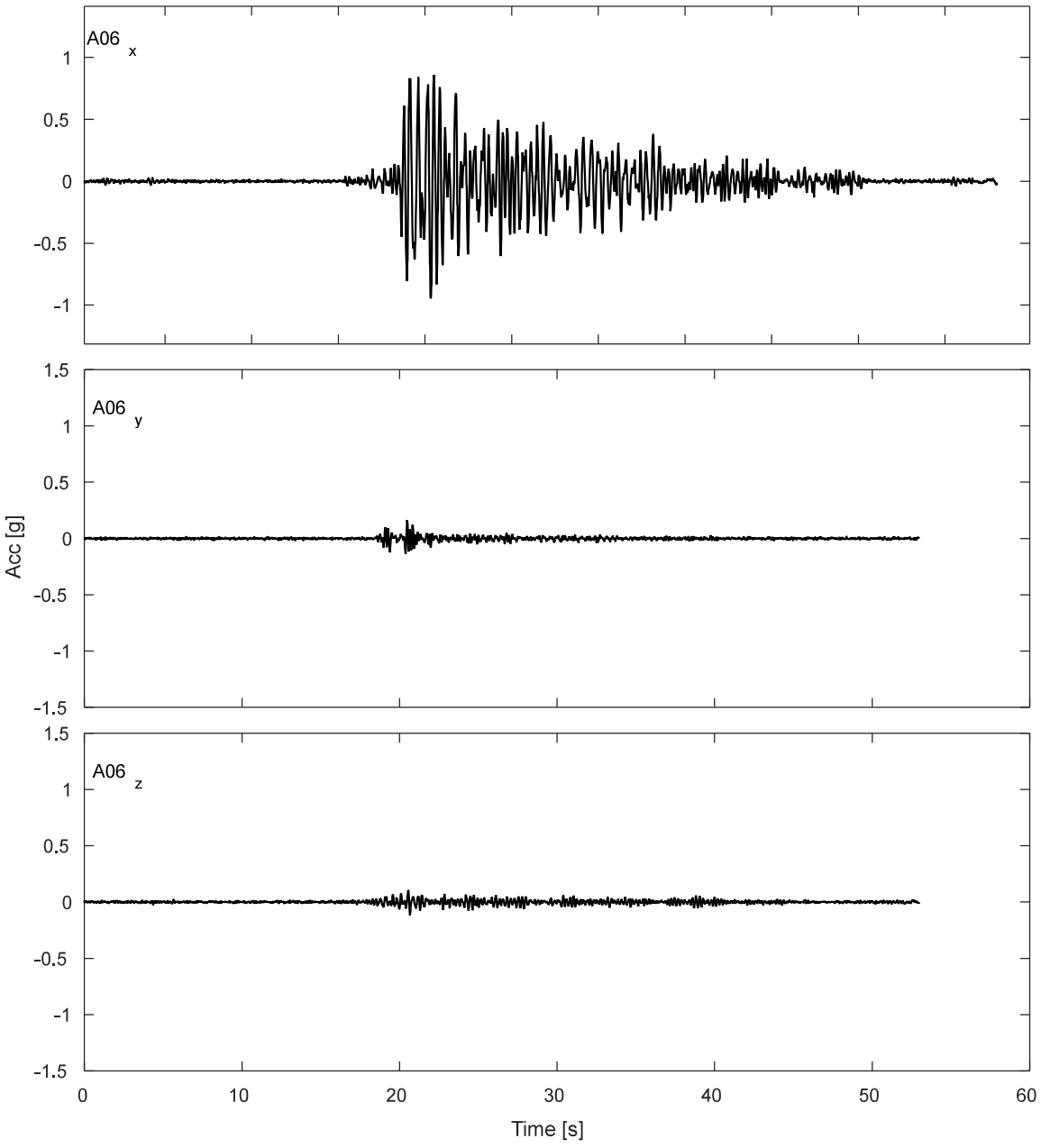

Figure I.6-5. Accelerations results for lumped mass of SDOF structure during DT01-NOR-050P motion.

I.6.2 Potentiometers.

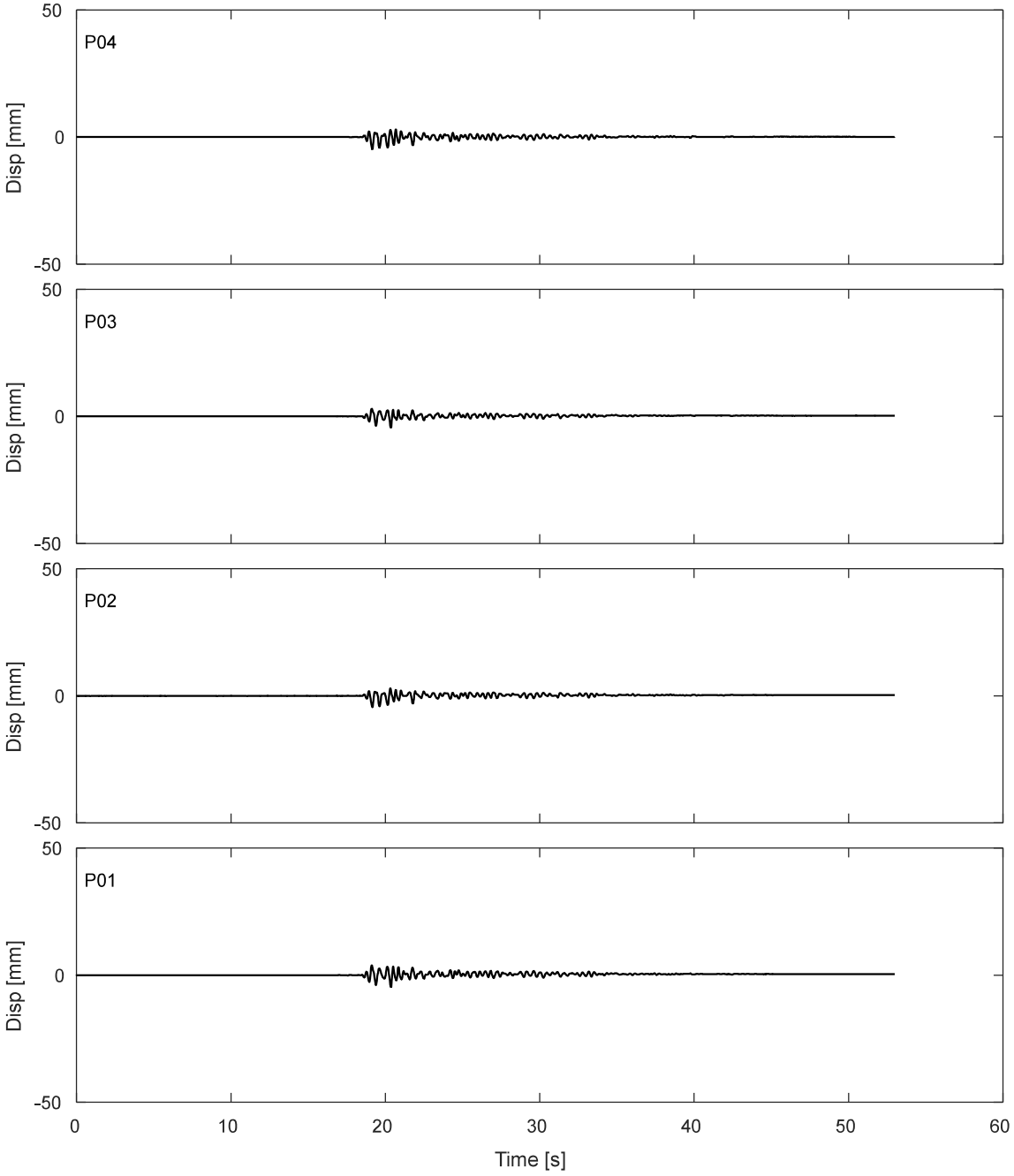

Figure I.6-6. Results of fully vertical potentiometers attached to corners of top of strip footing during DT01-NOR-050P motion.

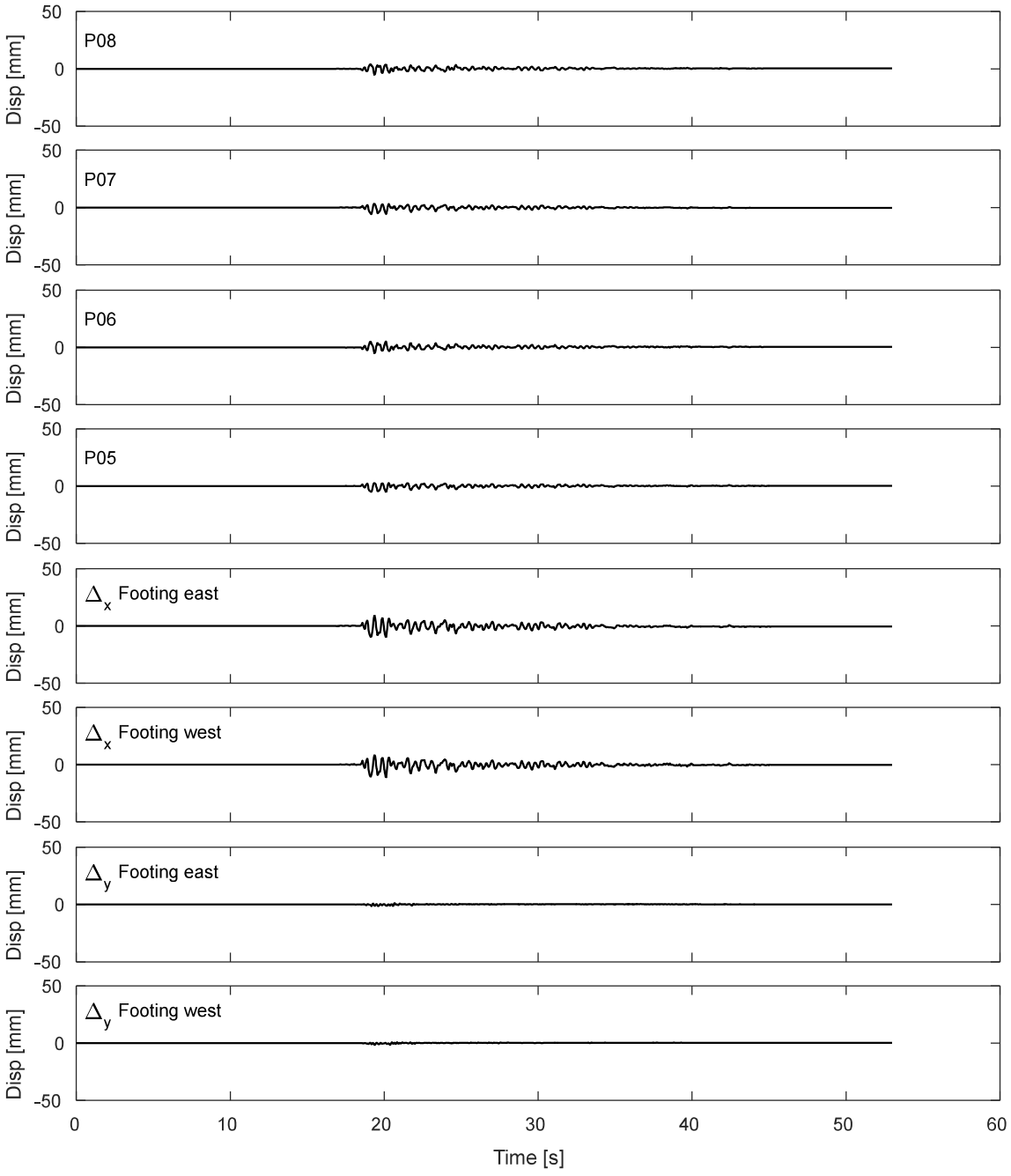

Figure I.6-7. Results of inclined potentiometers attached to top of strip footing during DT01-NOR-050P motion.

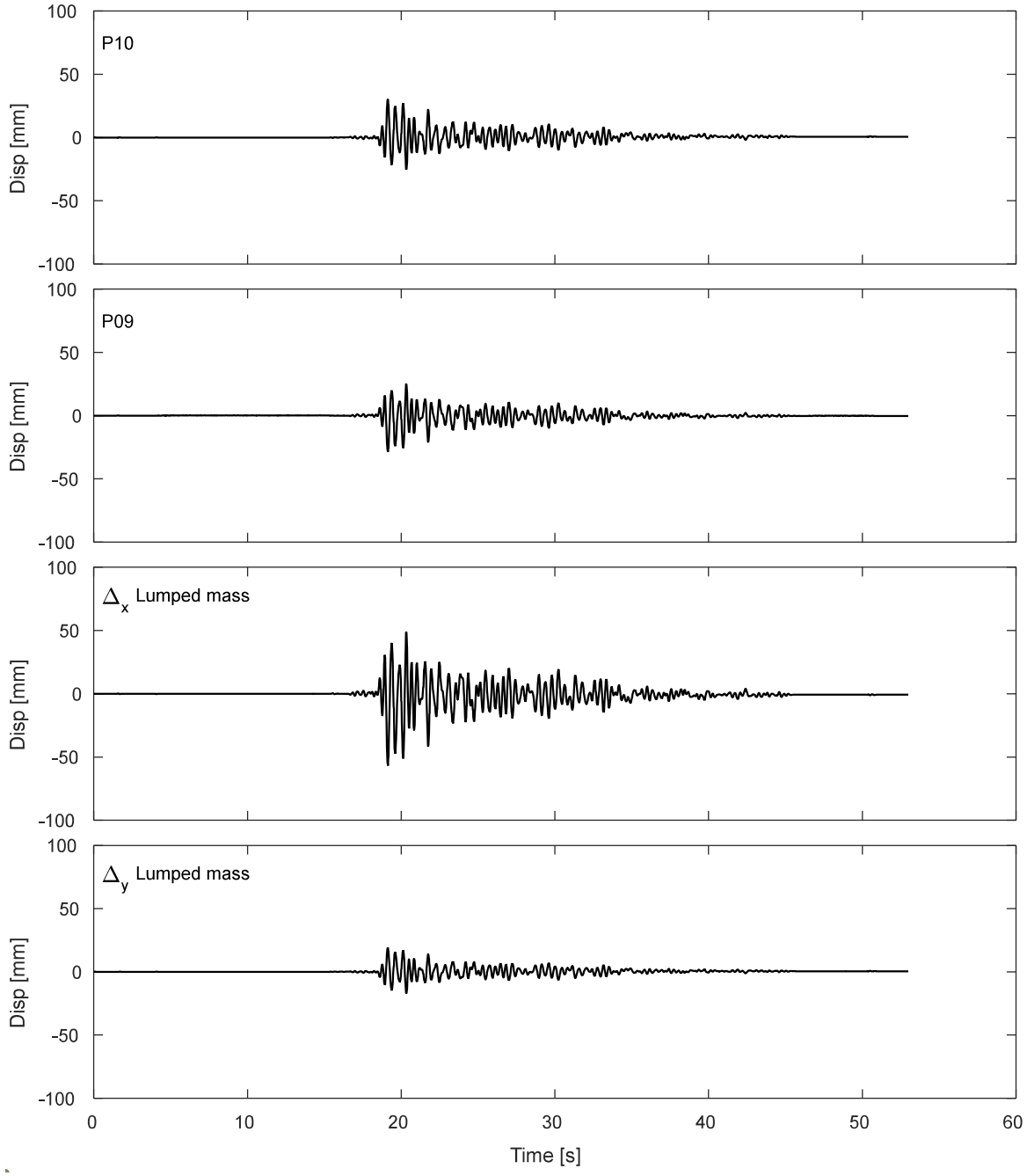

Figure I.6-8. Results of inclined potentiometers attached to lumped mass during DT01-NOR-050P motion.

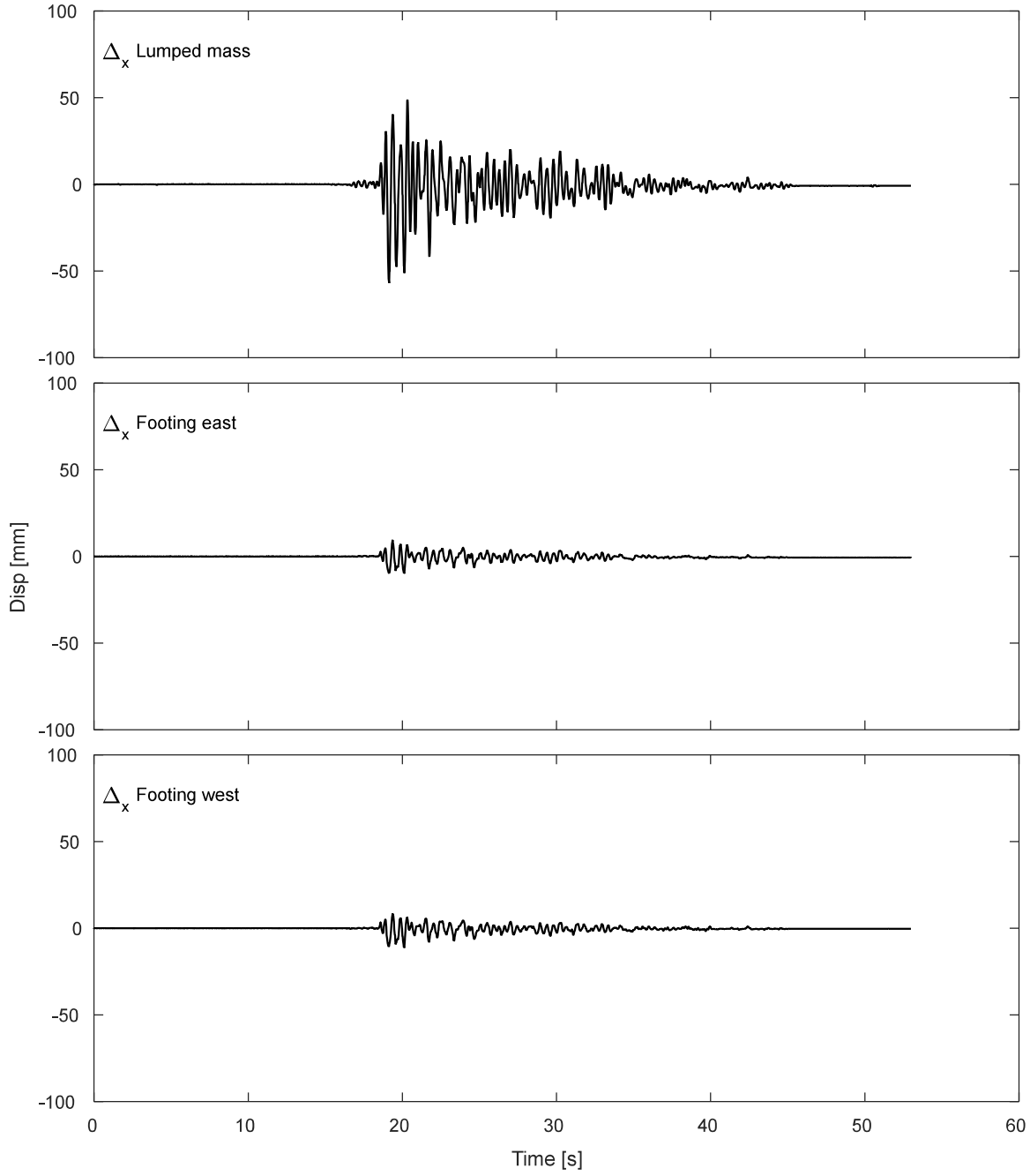

Figure I.6-9. Results of horizontal displacement of lumped mass and footing during DT01-NOR-050P motion.

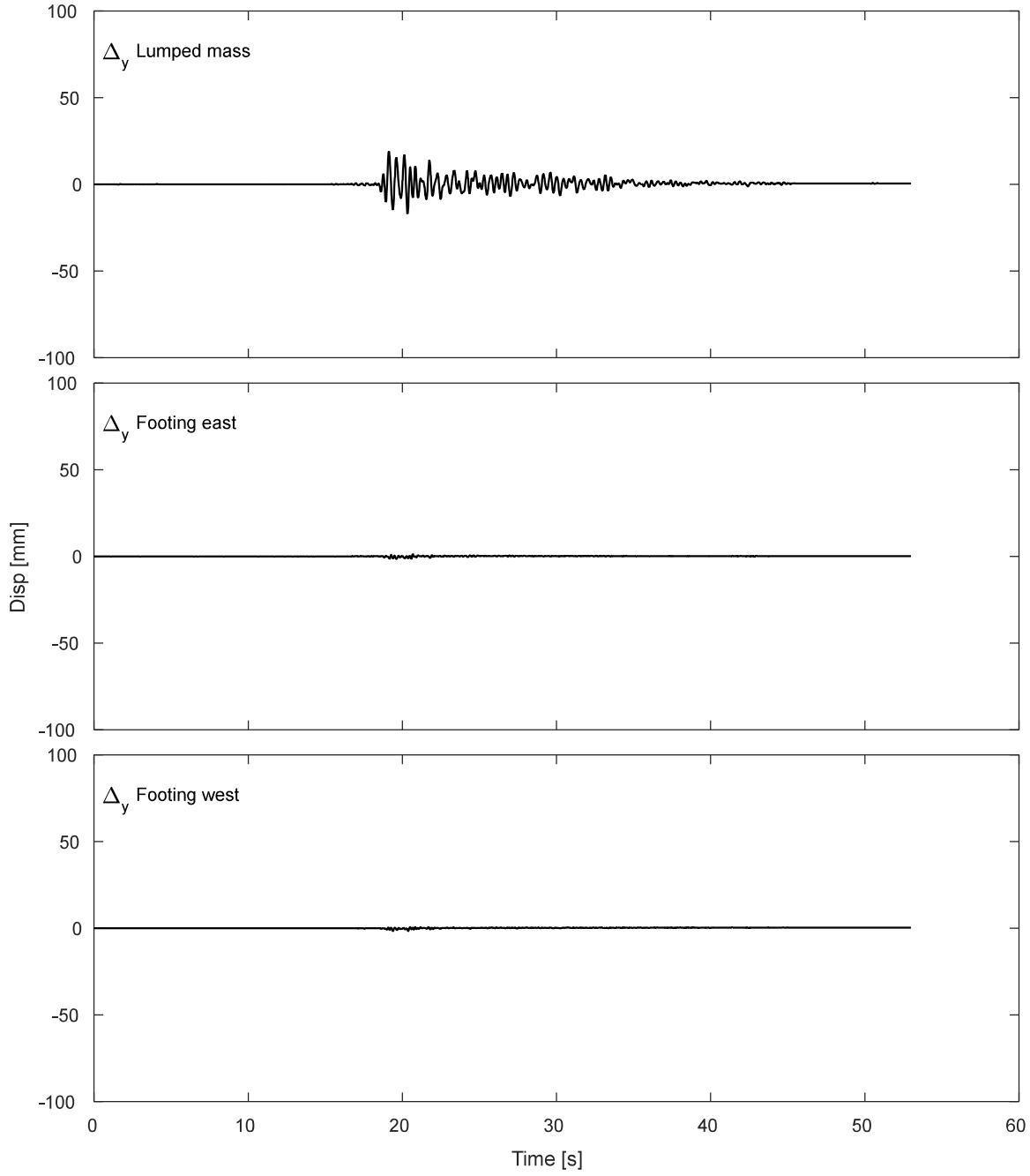

Figure I.6-10. Results of vertical displacement of lumped mass and footing during DT01-NOR-050P motion.

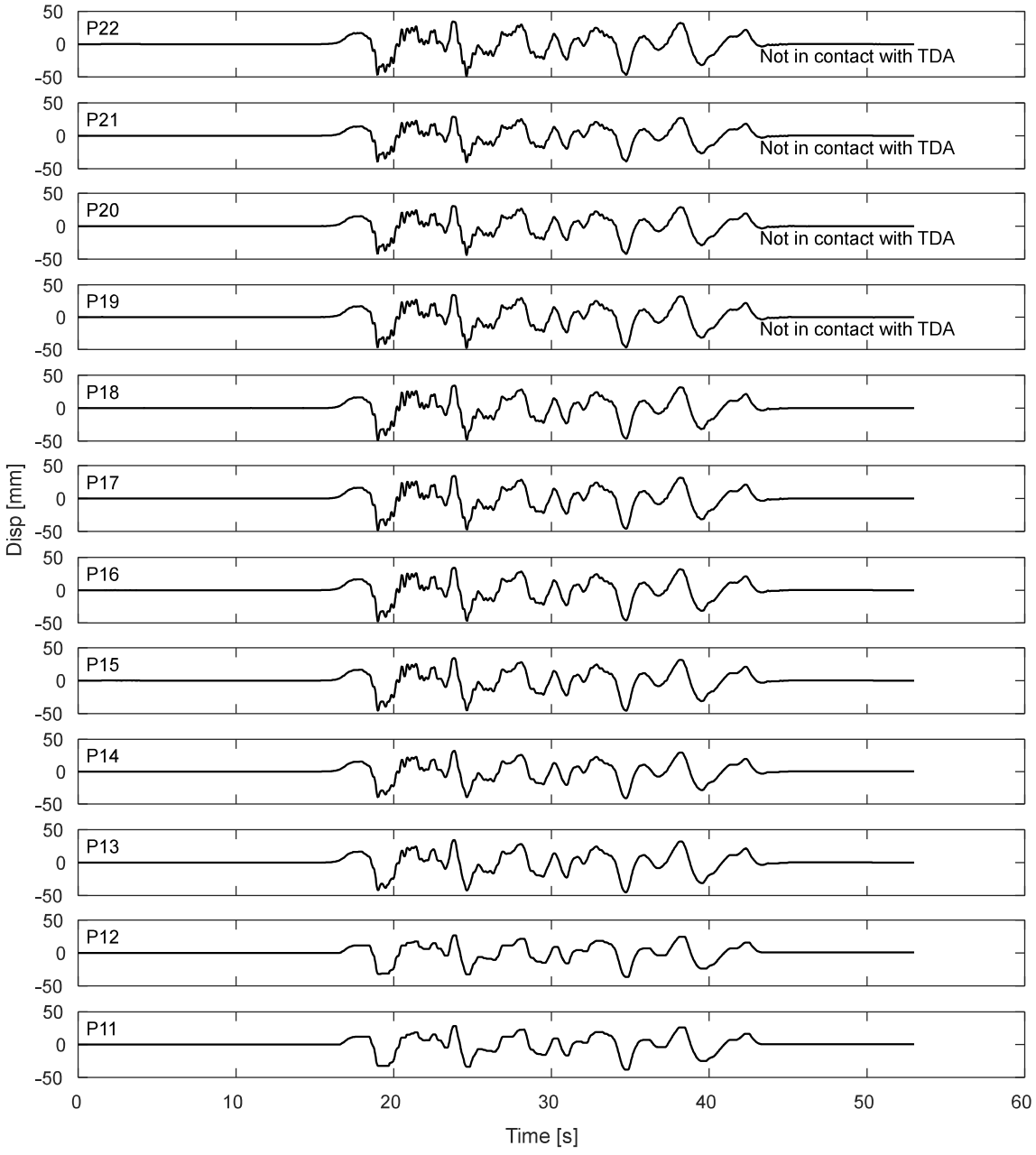

Figure I.6-11. Potentiometers results for the laminar box during DT01-NOR-050P motion.

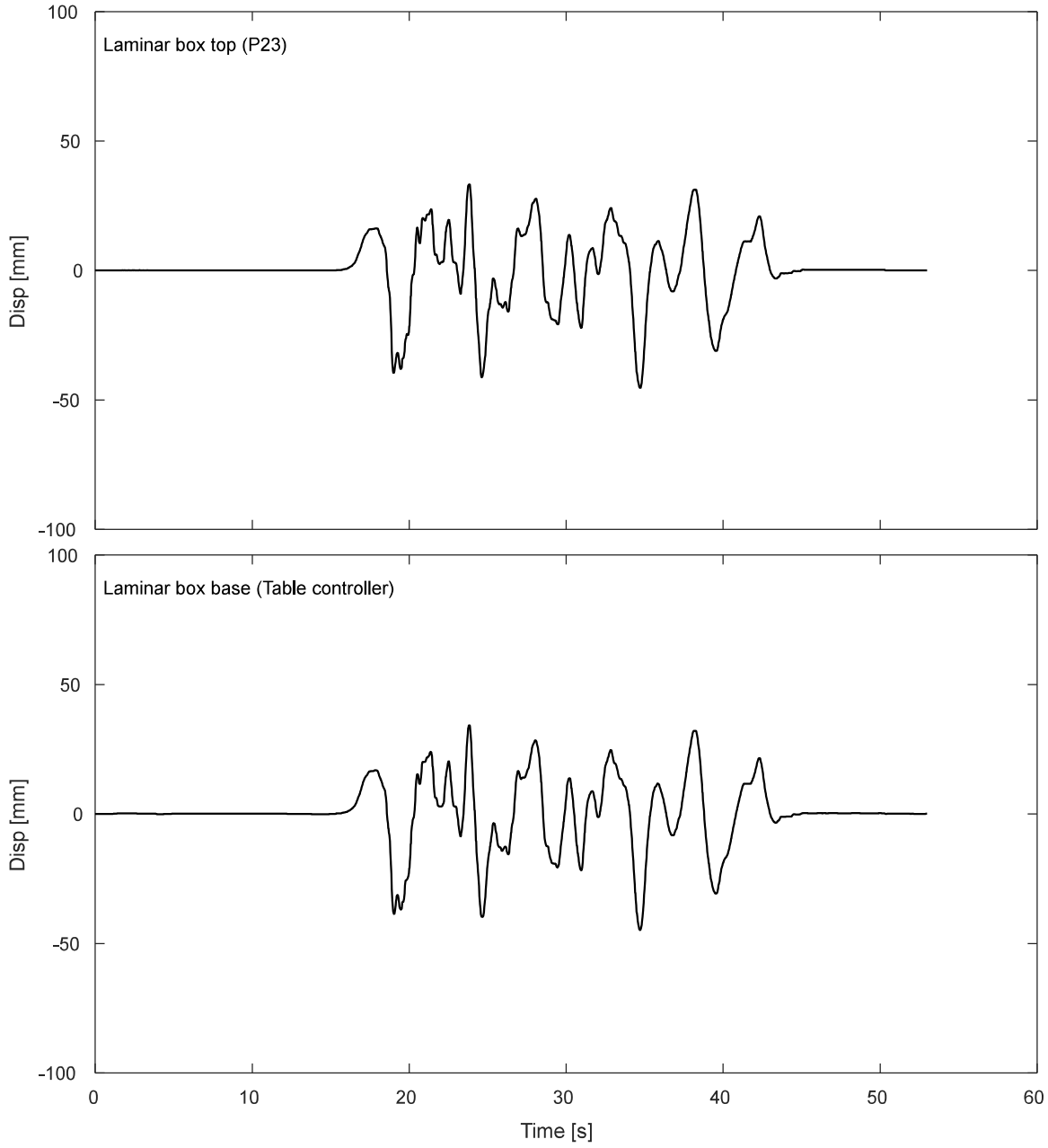

Figure I.6-12. Displacement response of top and base of laminar box during DT01-NOR-050P motion.

I.6.3. Inclinometers.

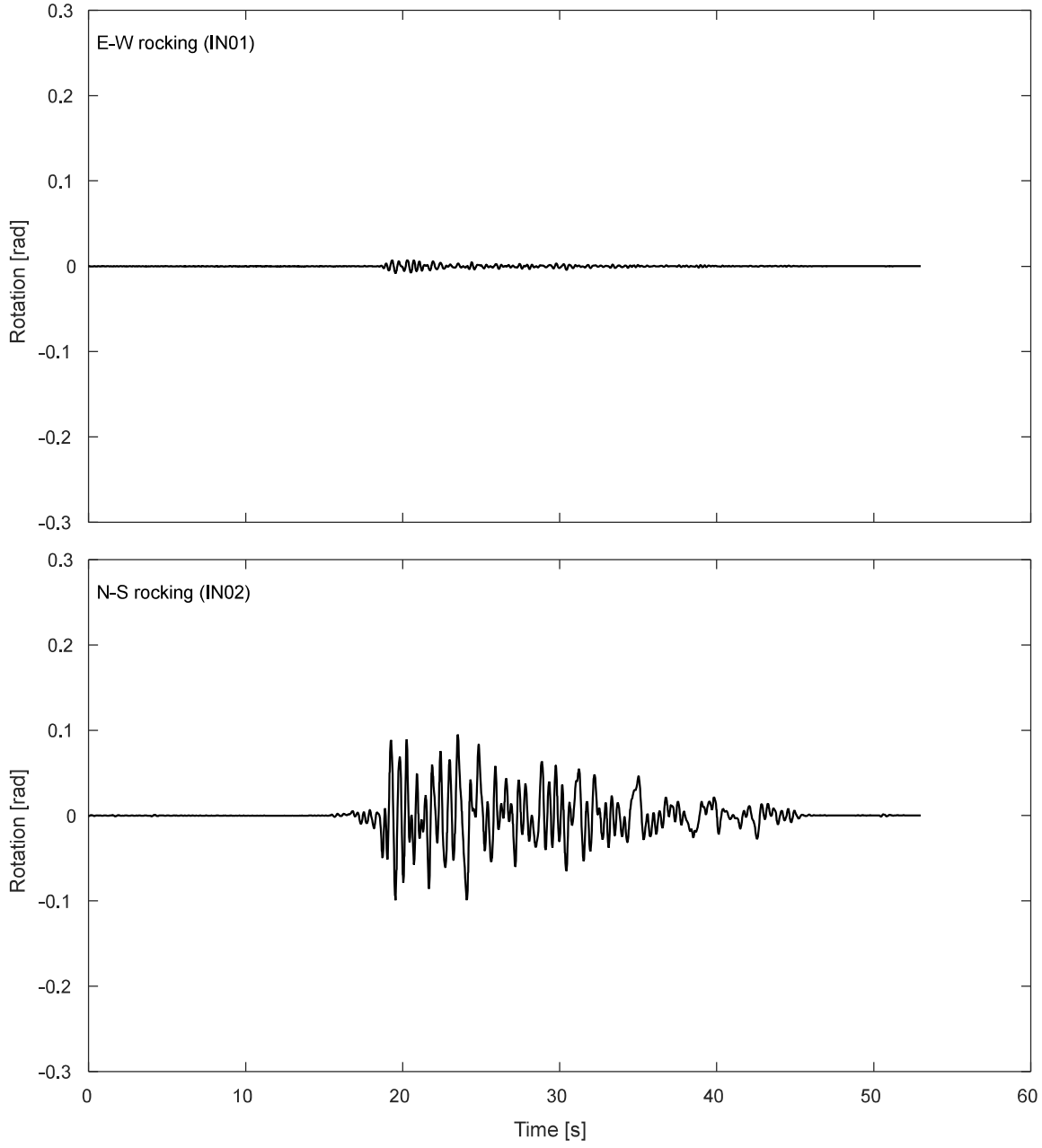

Figure I.6-13. Inclinometer results for the footing during DT01-NOR-050P motion.

I.6.4. Pressure cells.

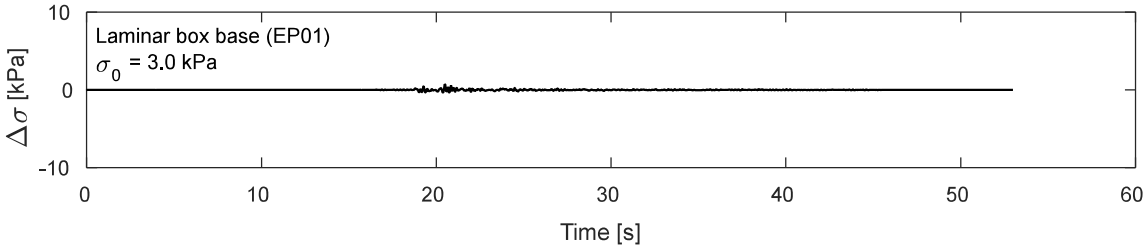

Figure I.6-14. Pressure cells results at laminar box base during DT01-NOR-050P motion.

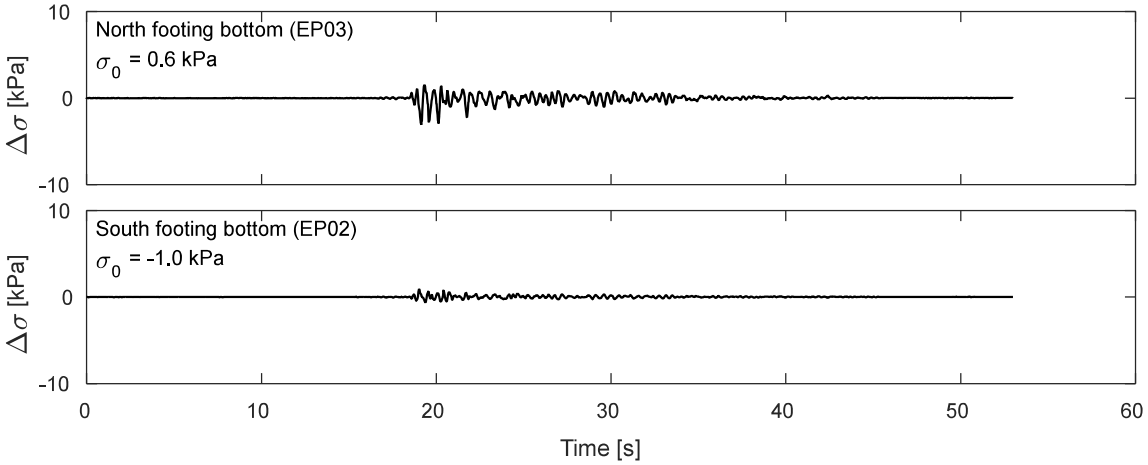

Figure I.6-15. Pressure cells results at footing bottom during DT01-NOR-050P motion.

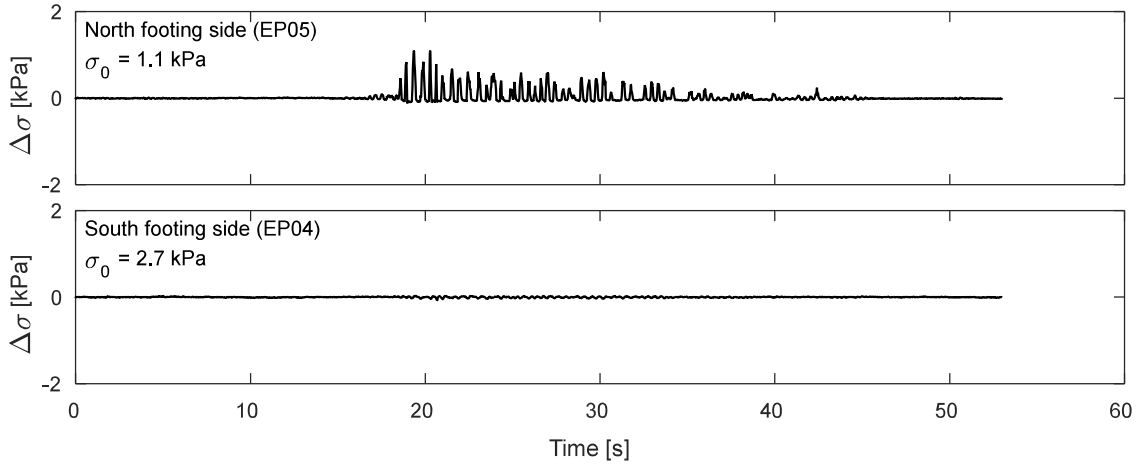

Figure I.6-16. Pressure cells results at footing sides during DT01-NOR-050P motion.

I.7. Time-history Records for DT01-NOR-075P motion.

I.7.1 Input Motion

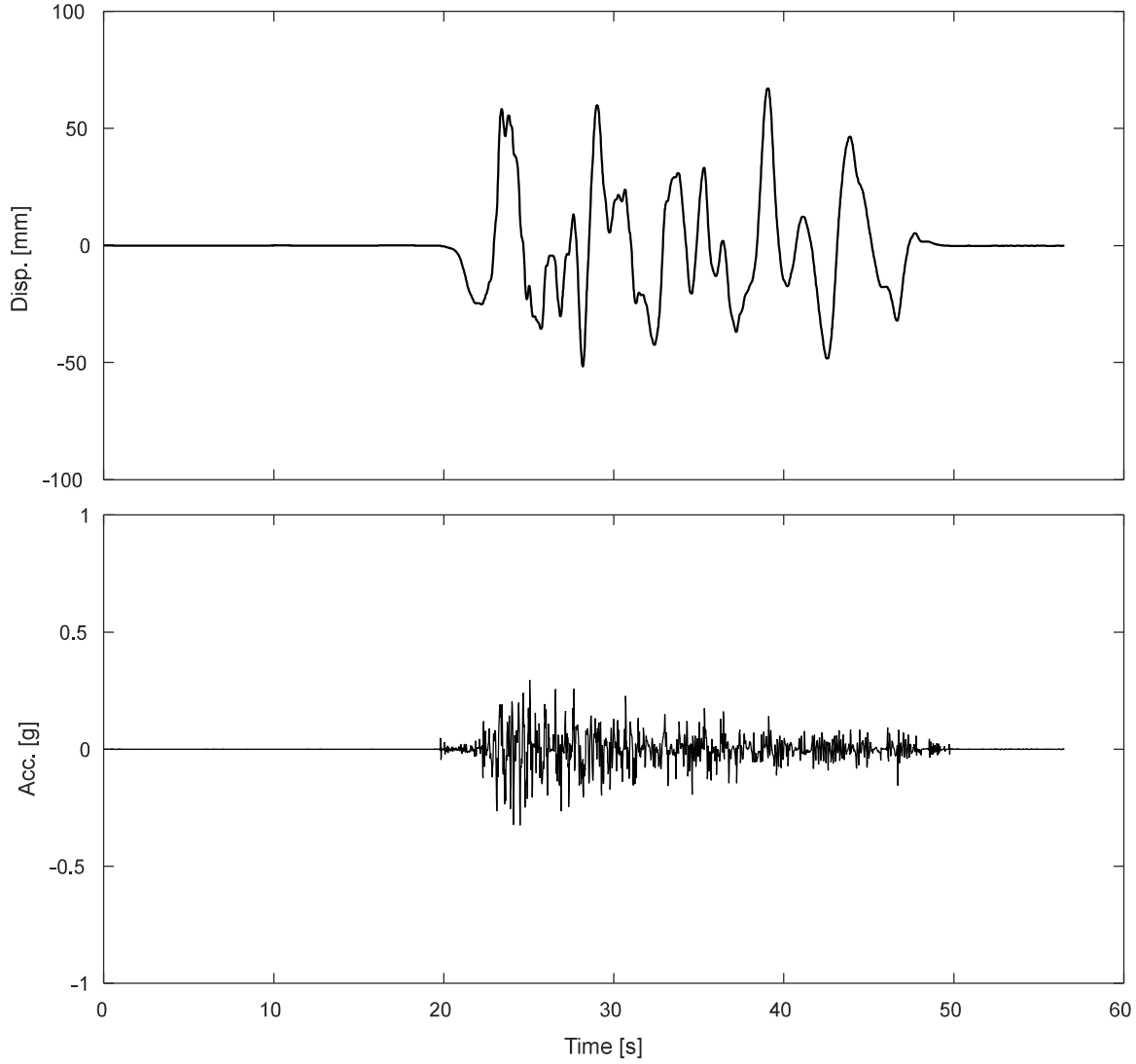

Figure I.7-1. Measured input displacement and acceleration at the base of the specimen during DT01-NOR-075P motion

I.7.1 Accelerometers.

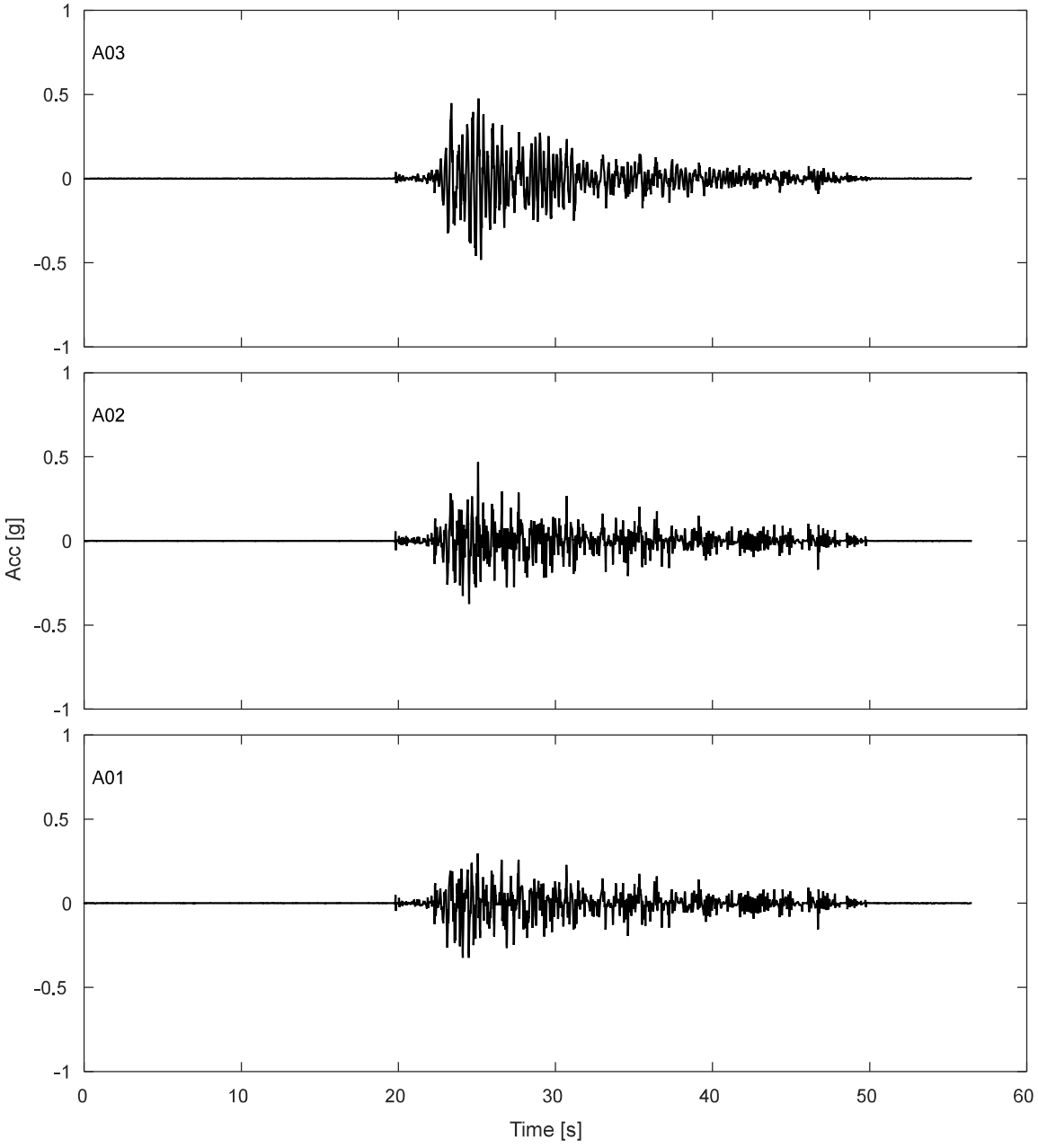

Figure I.7-2. Accelerations results along TDA during DT01-NOR-075P motion.

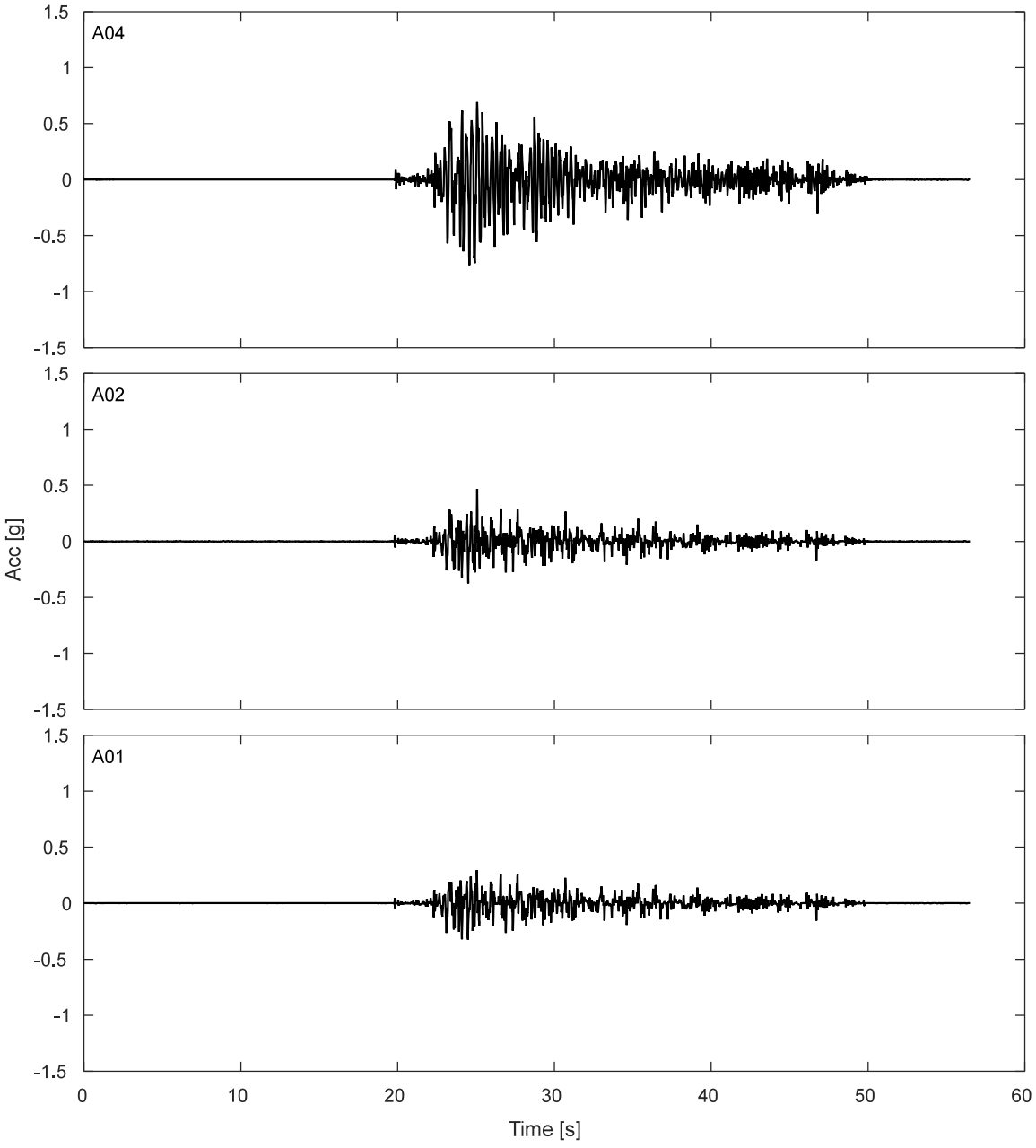

Figure I.7-3. Free field accelerations results for TDA during DT01-NOR-075P motion.

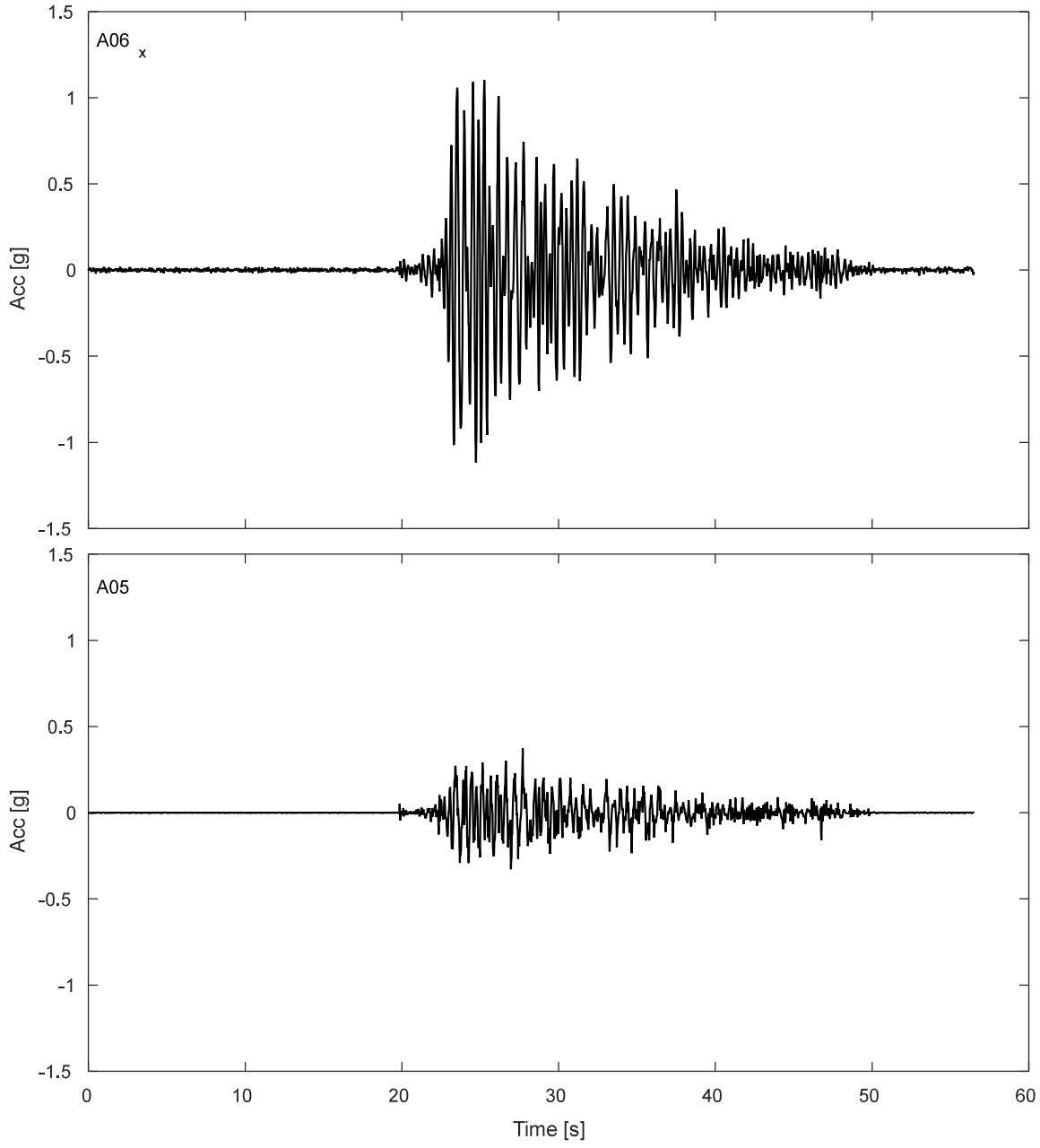

Figure I.7-4. Accelerations results SDOF structure during DT01-NOR-075P motion.

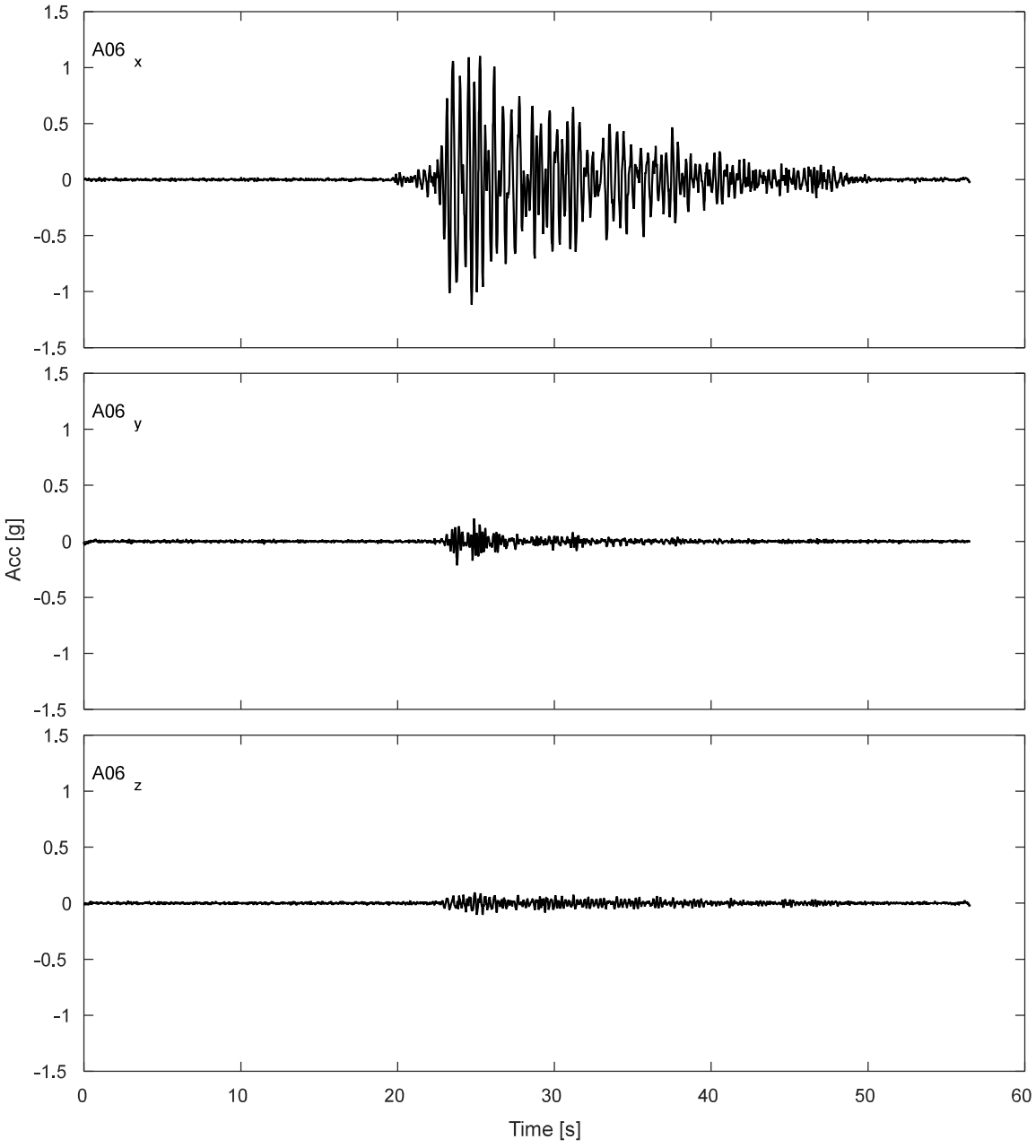

Figure I.7-5. Accelerations results for lumped mass of SDOF structure during DT01-NOR-075P motion.

I.7.2 Potentiometers.

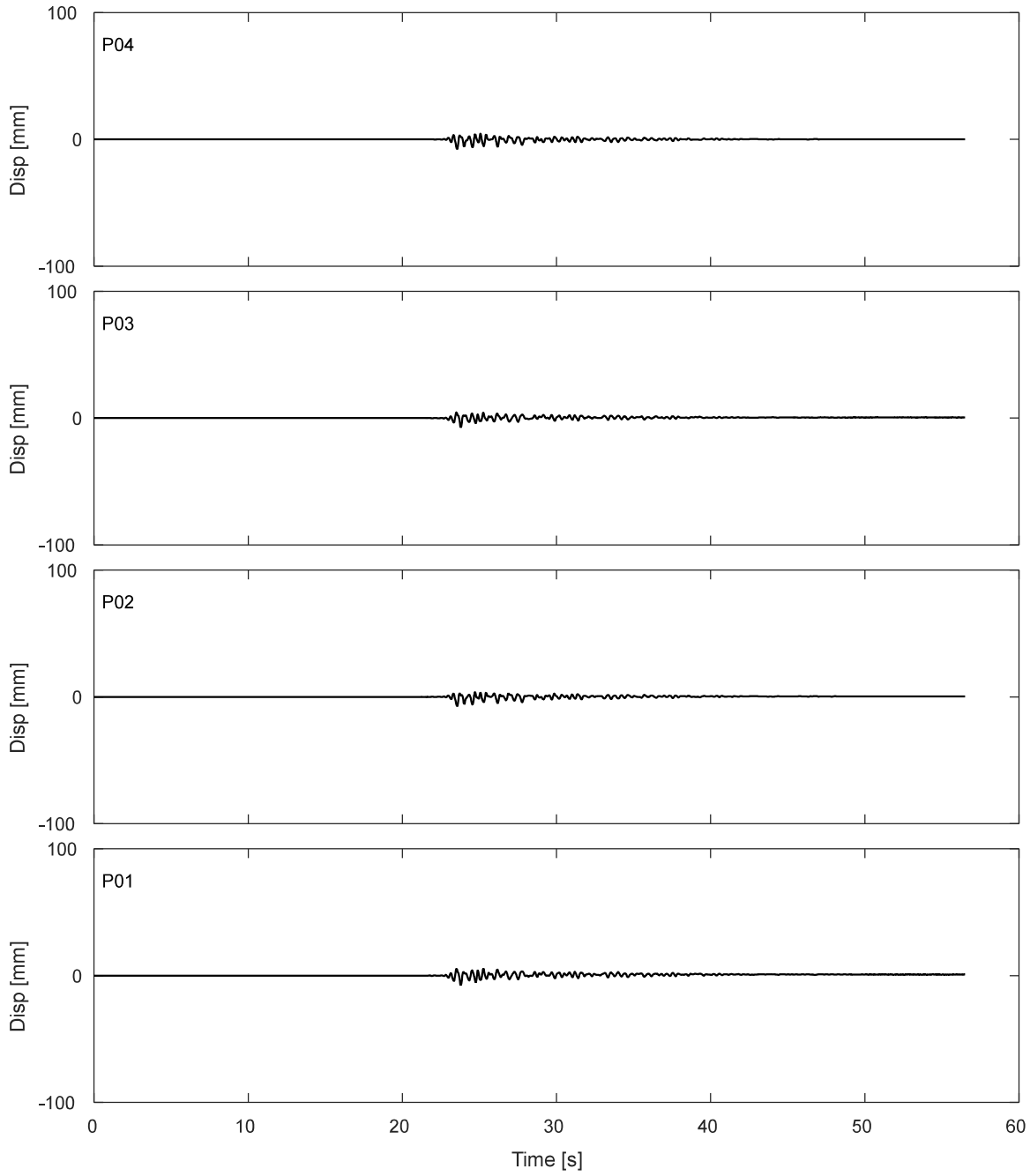

Figure I.7-6. Results of fully vertical potentiometers attached to corners of top of strip footing during DT01-NOR-075P motion.

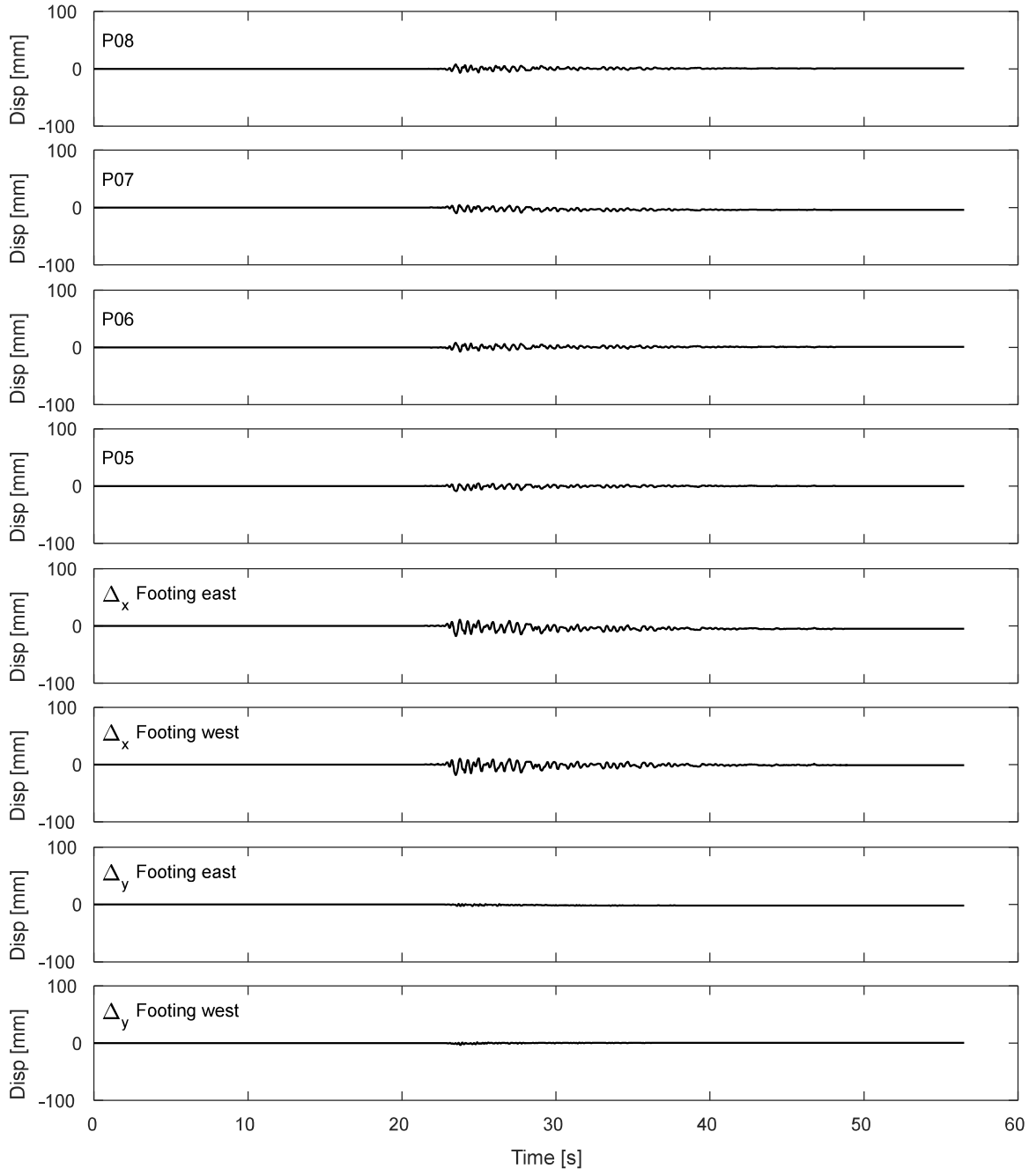

Figure I.7-7. Results of inclined potentiometers attached to top of strip footing during DT01-NOR-075P motion.

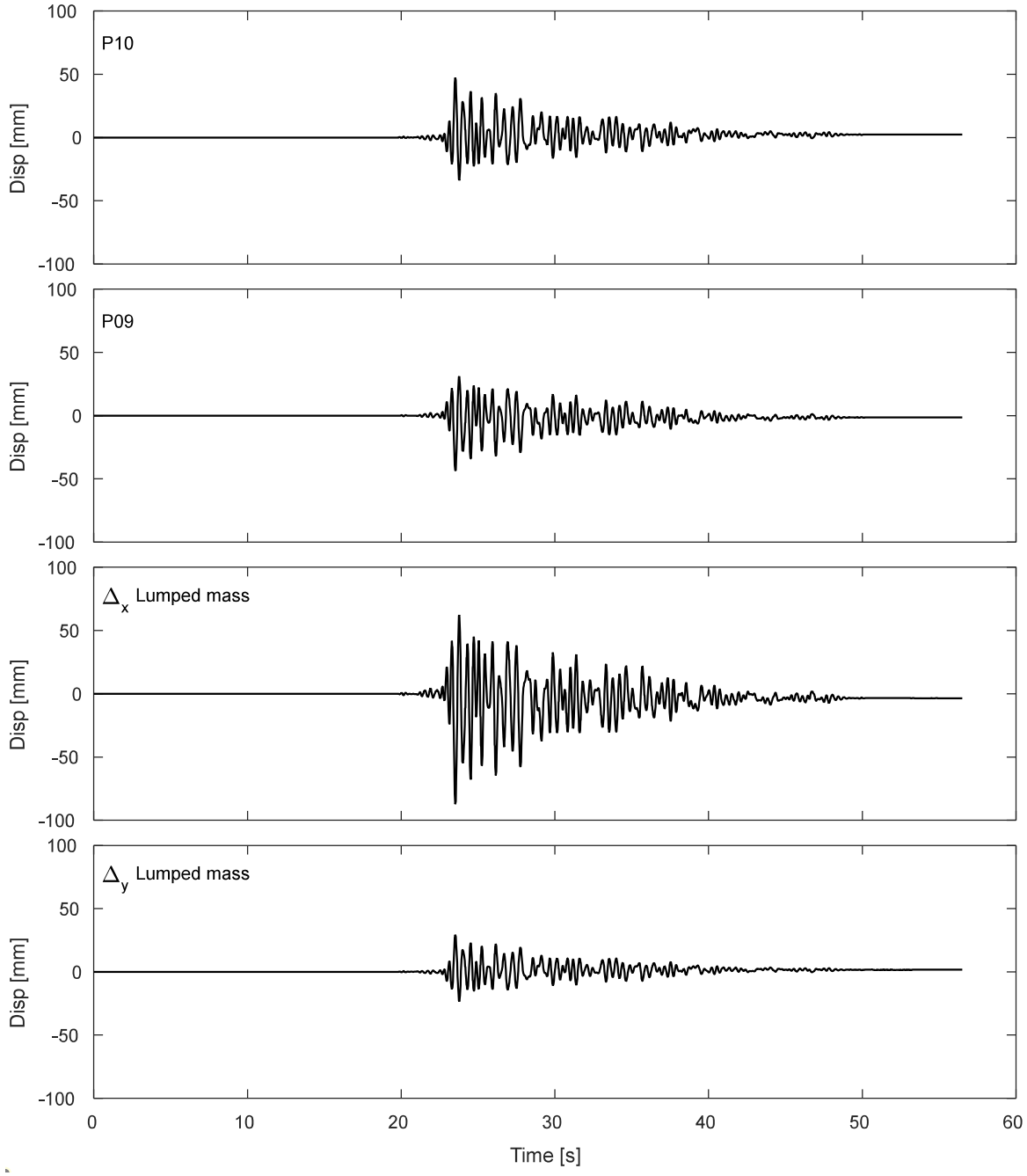

Figure I.7-8. Results of inclined potentiometers attached to lumped mass during DT01-NOR-075P motion.

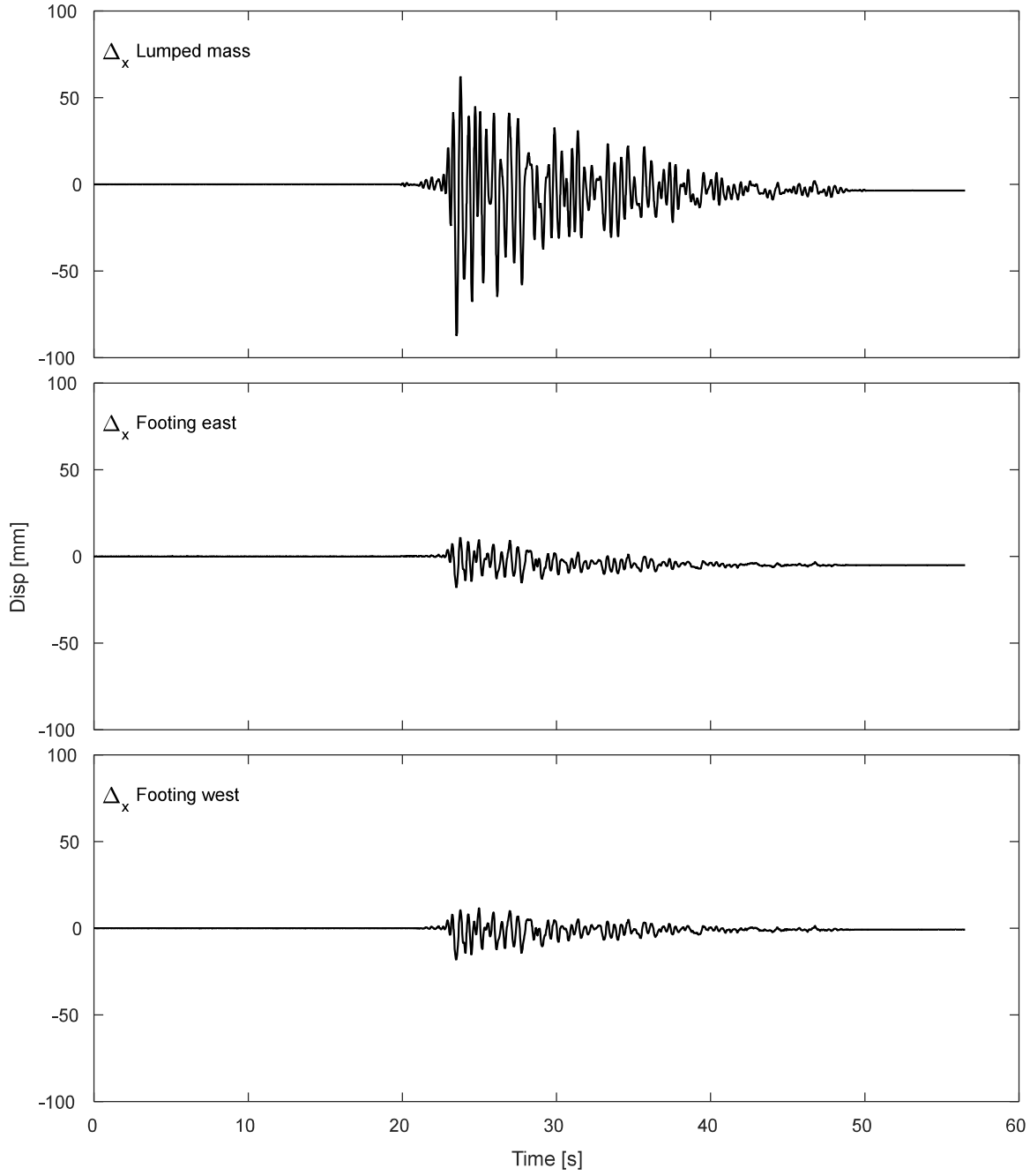

Figure I.7-9. Results of horizontal displacement of lumped mass and footing during DT01-NOR-075P motion.

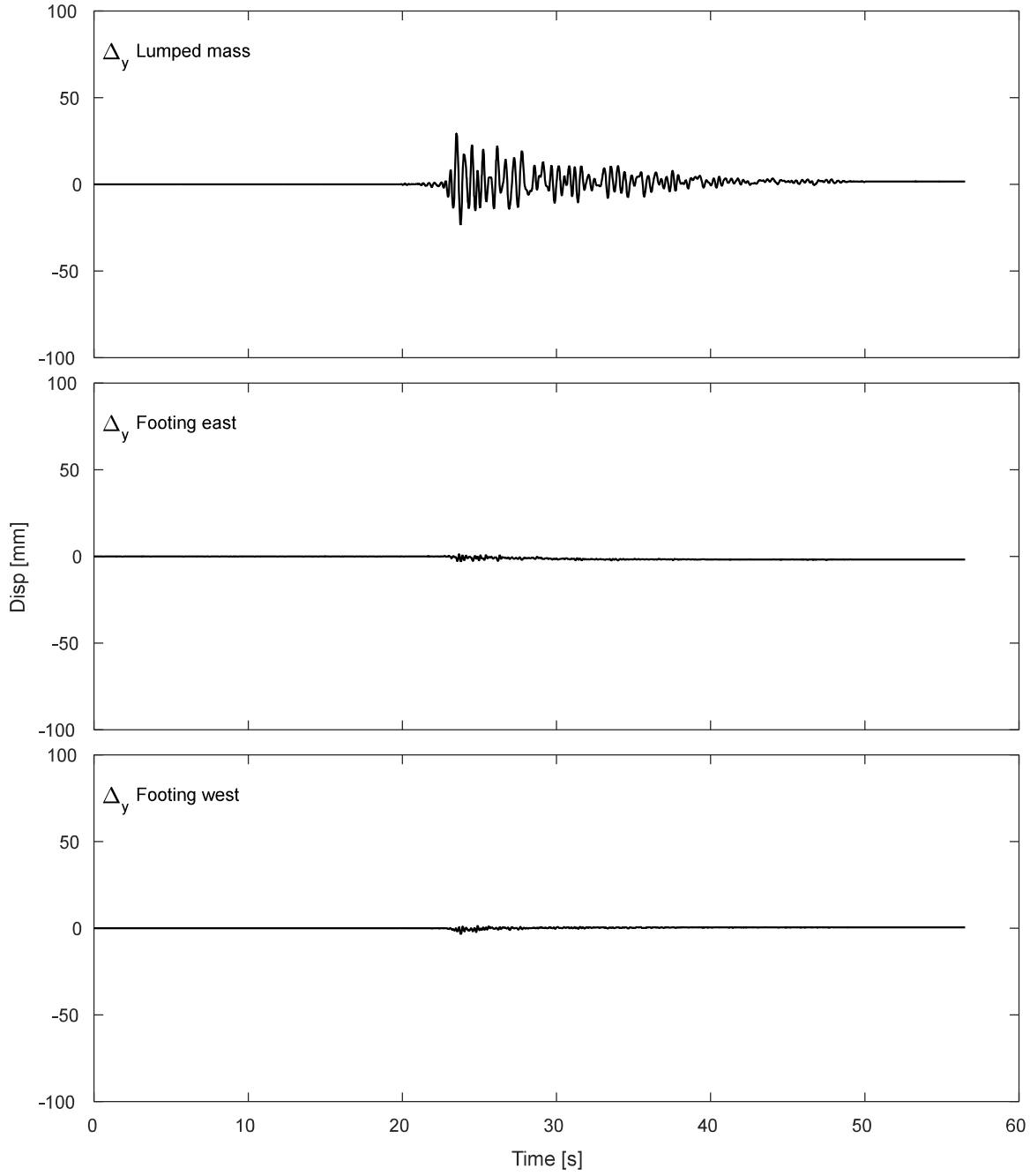

Figure I.7-10. Results of vertical displacement of lumped mass and footing during DT01-NOR-075P motion.

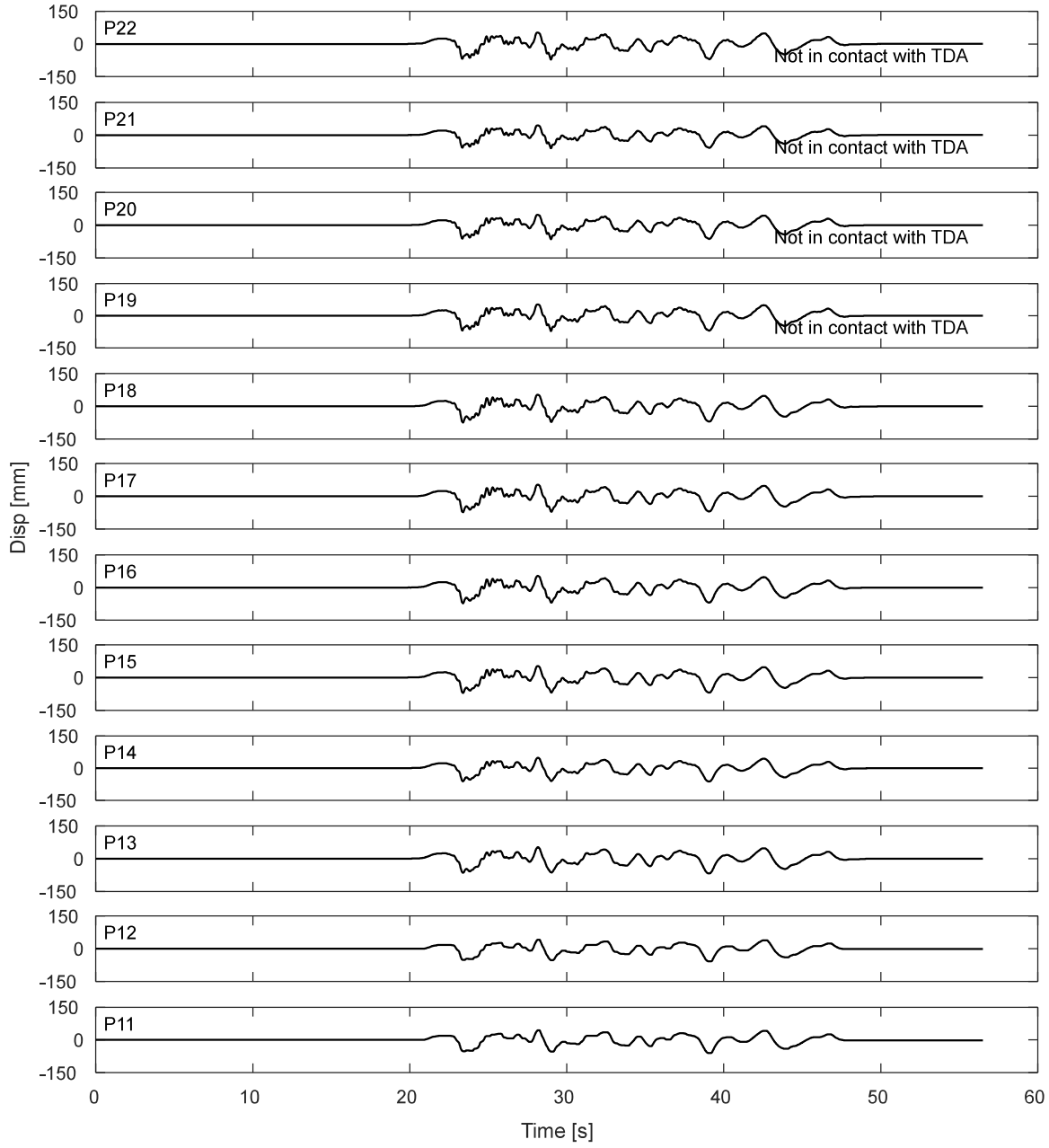

Figure I.7-11. Potentiometers results for the laminar box during DT01-NOR-075P motion.

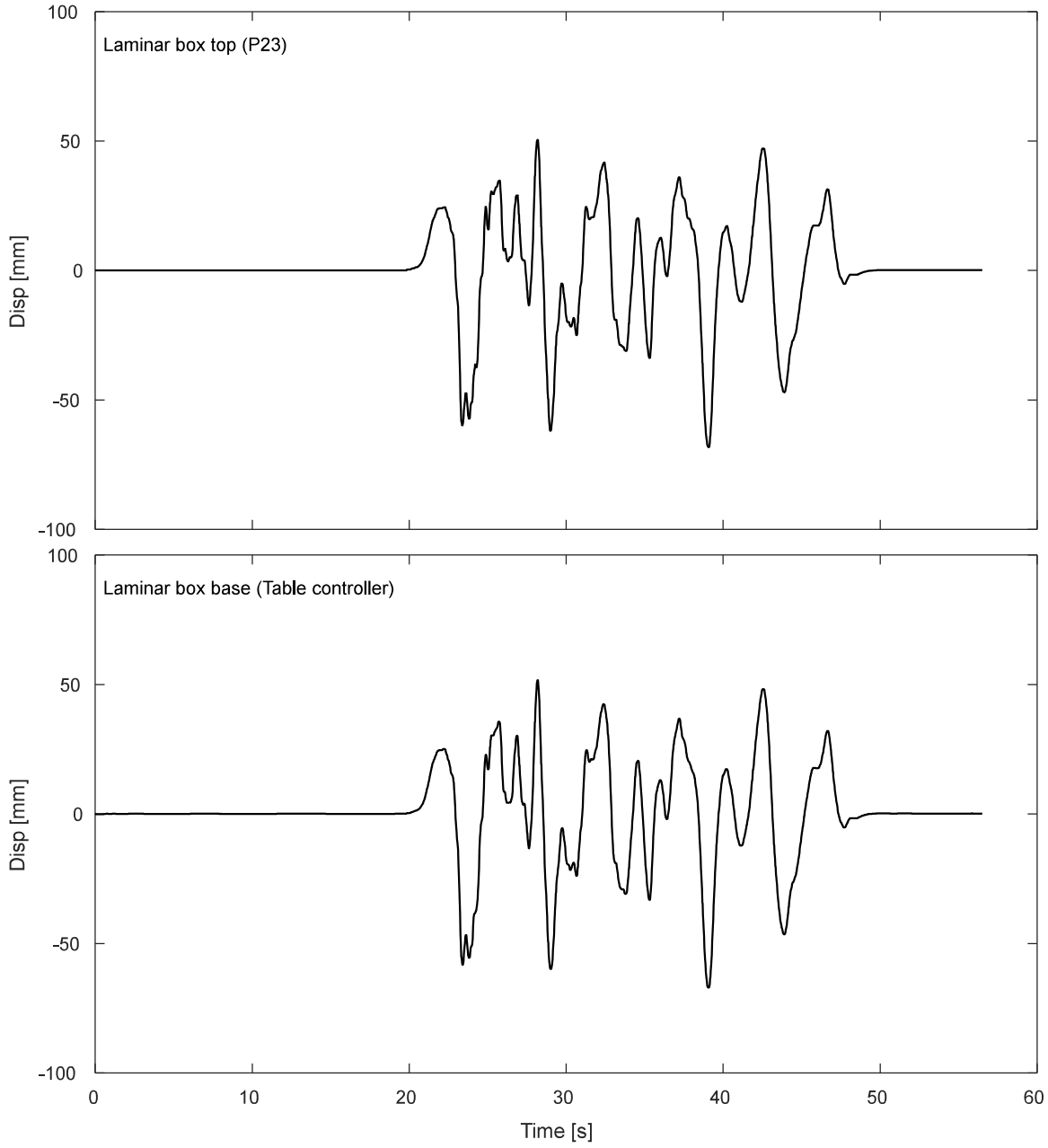

Figure I.7-12. Displacement response of top and base of laminar box during DT01-NOR-075P motion.

I.7.3. Inclinometers.

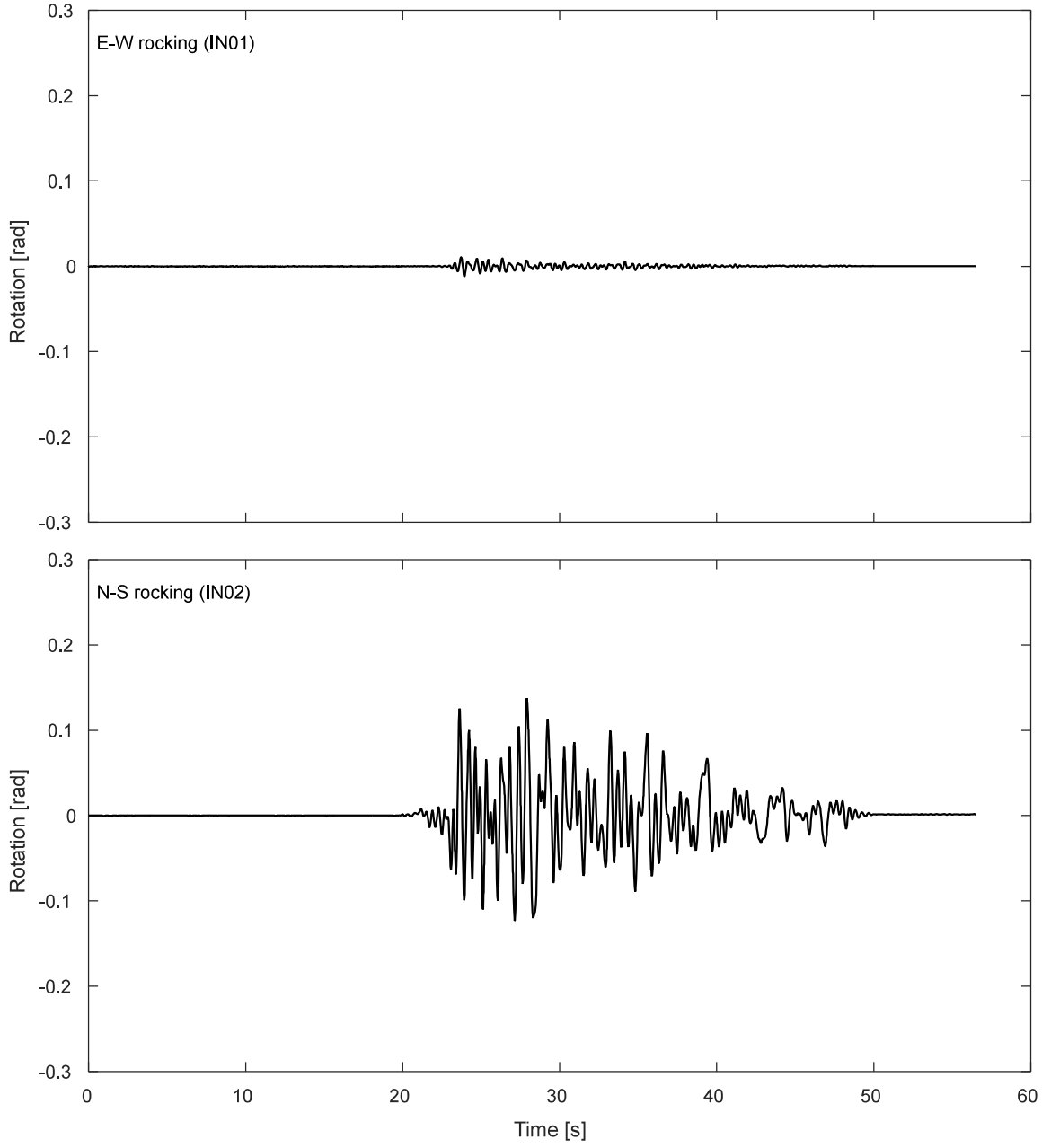

Figure I.7-13. Inclinometer results for the footing during DT01-NOR-075P motion.

I.7.4. Pressure cells.

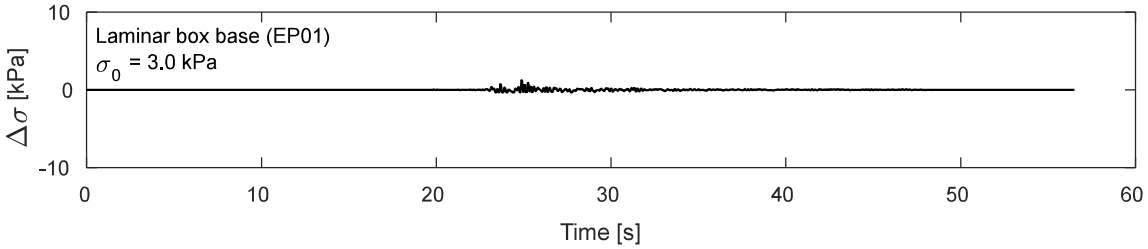

Figure I.7-14. Pressure cells results at laminar box base during DT01-NOR-075P motion.

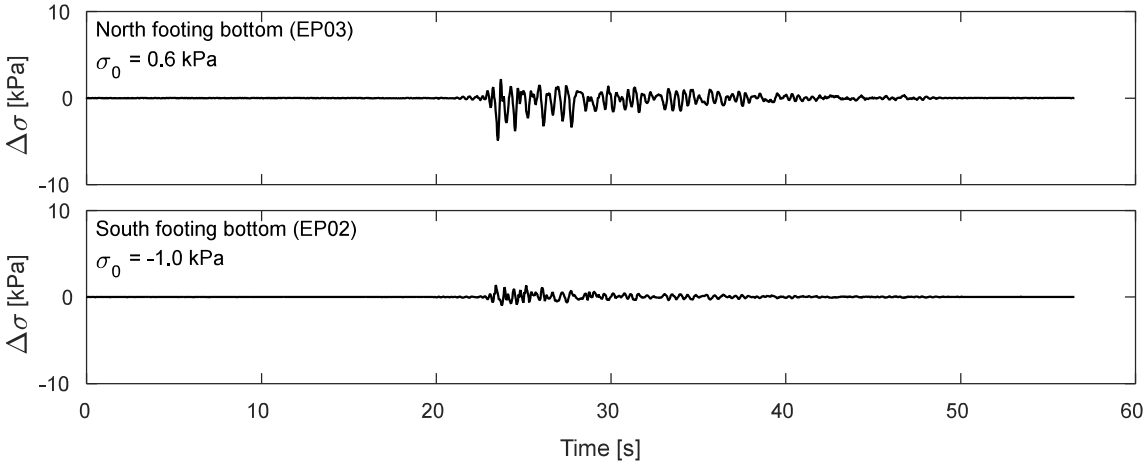

Figure I.7-15. Pressure cells results at footing bottom during DT01-NOR-075P motion.

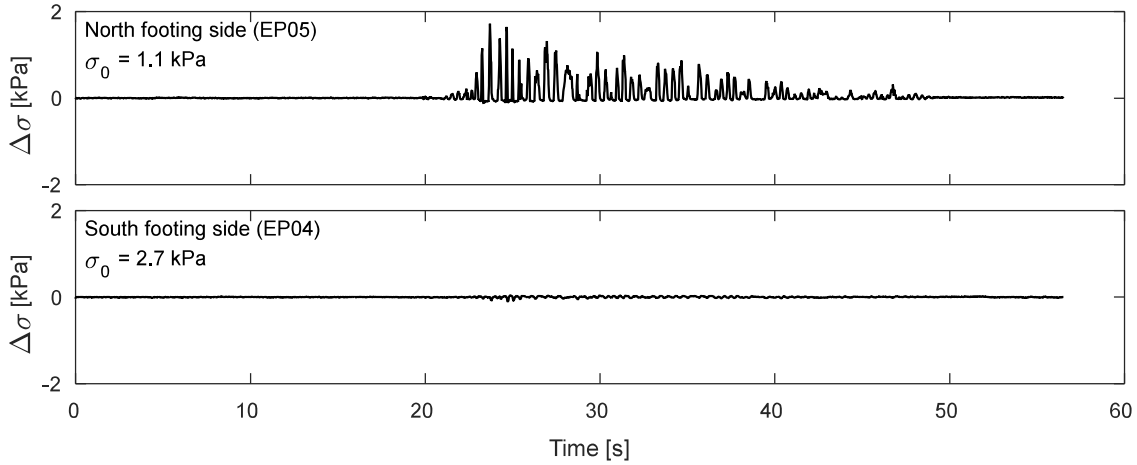

Figure I.7-16. Pressure cells results at footing sides during DT01-NOR-075P motion.

K.7. Time-history Records for DT03-NOR-050P motion.

K.7.1 Input Motion

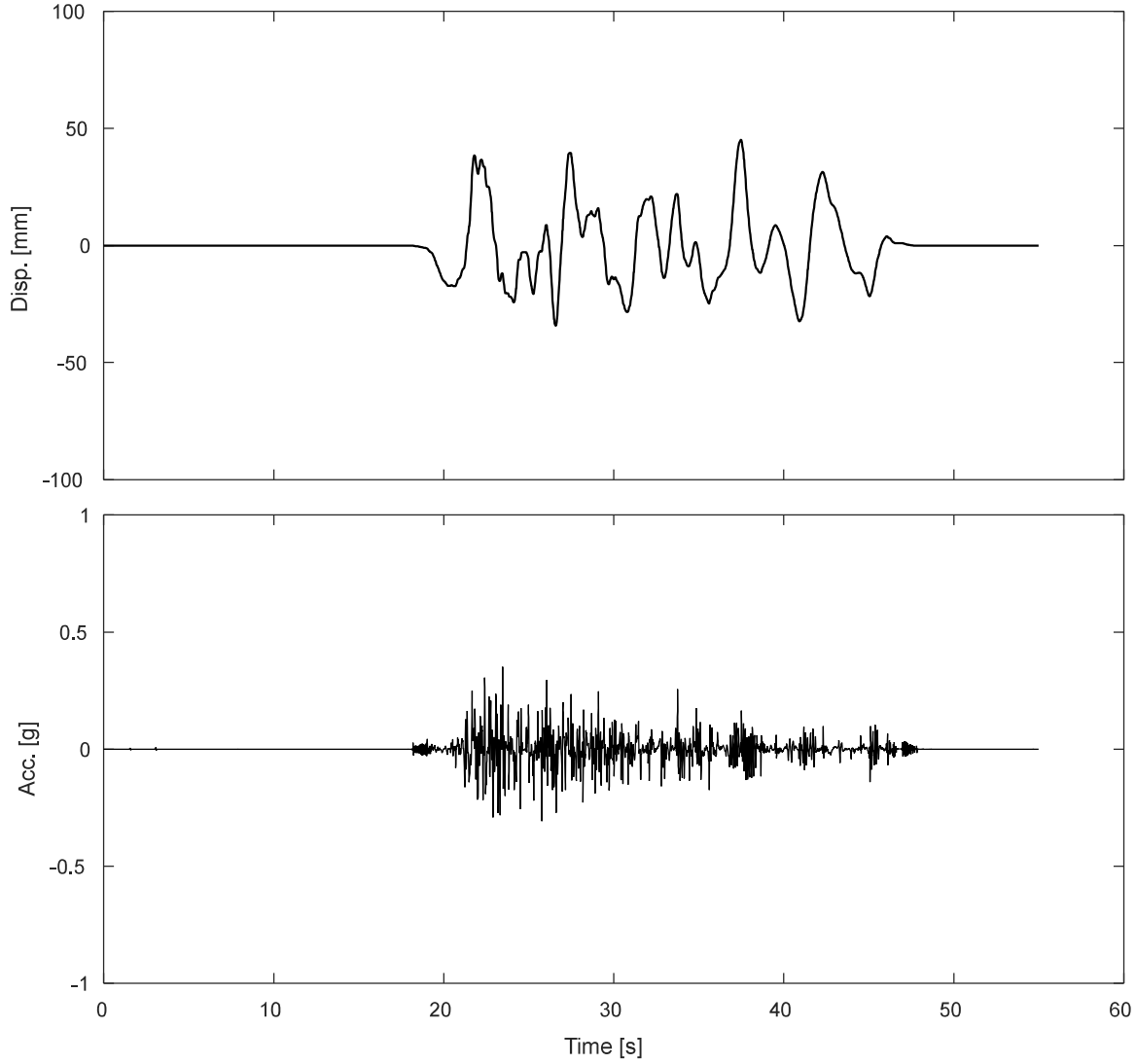

Figure K.7-1. Measured input displacement and acceleration at the base of the specimen during DT03-NOR-050P motion

K.7.1 Accelerometers.

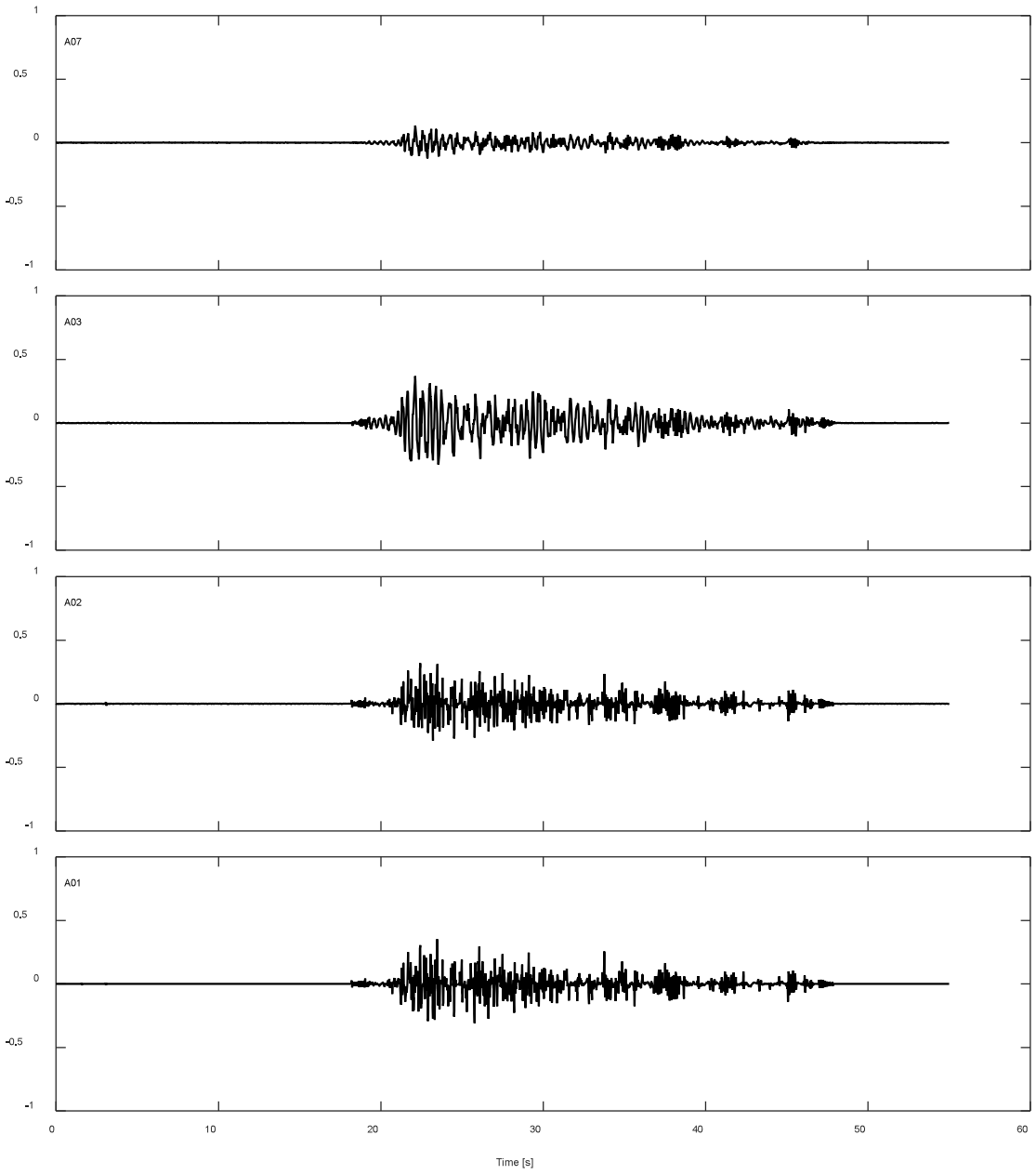

Figure K.7-2. Accelerations results along TDA during DT03-NOR-050P motion.

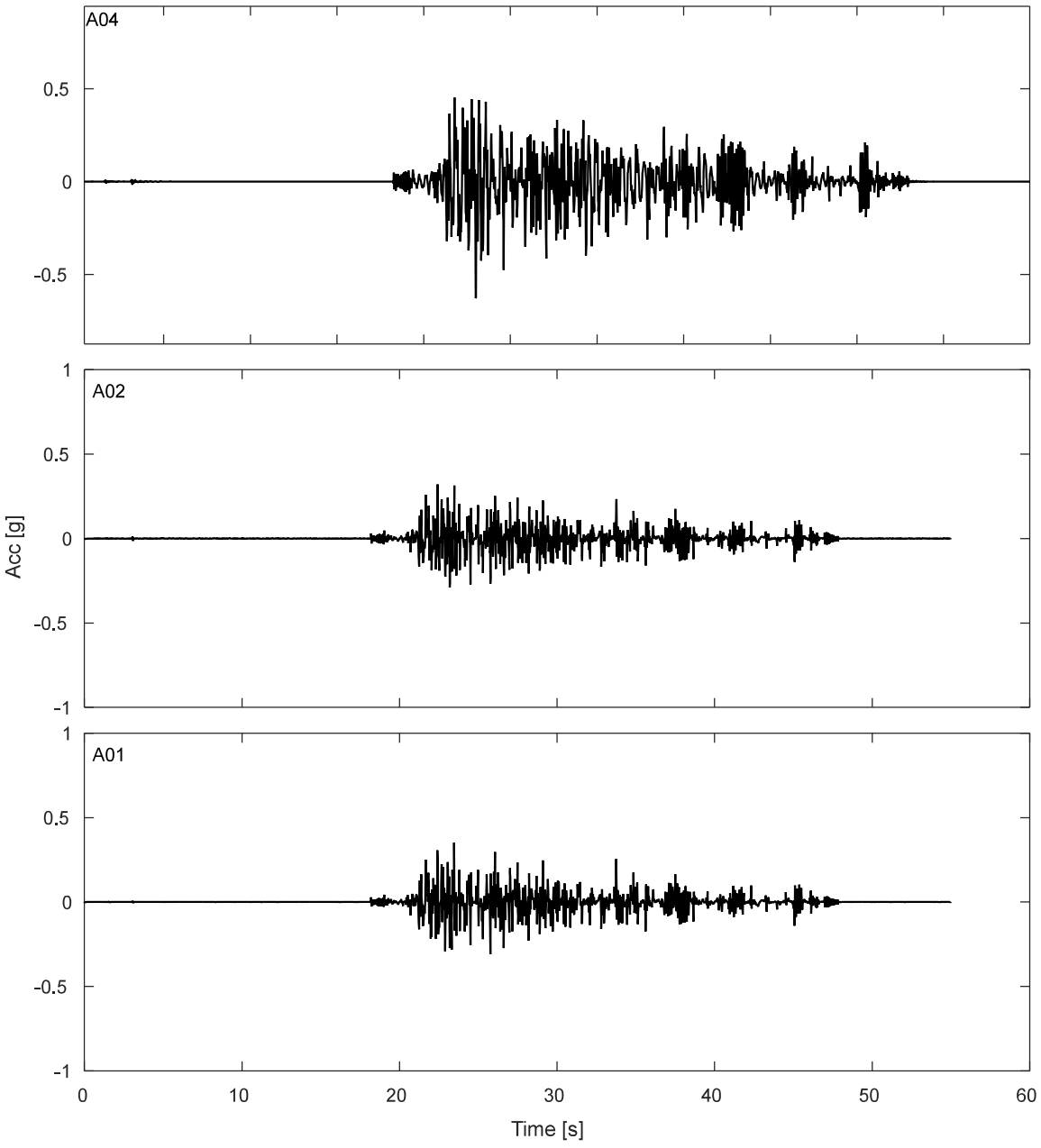

Figure K.7-3. Free field accelerations results for TDA during DT03-NOR-050P motion.

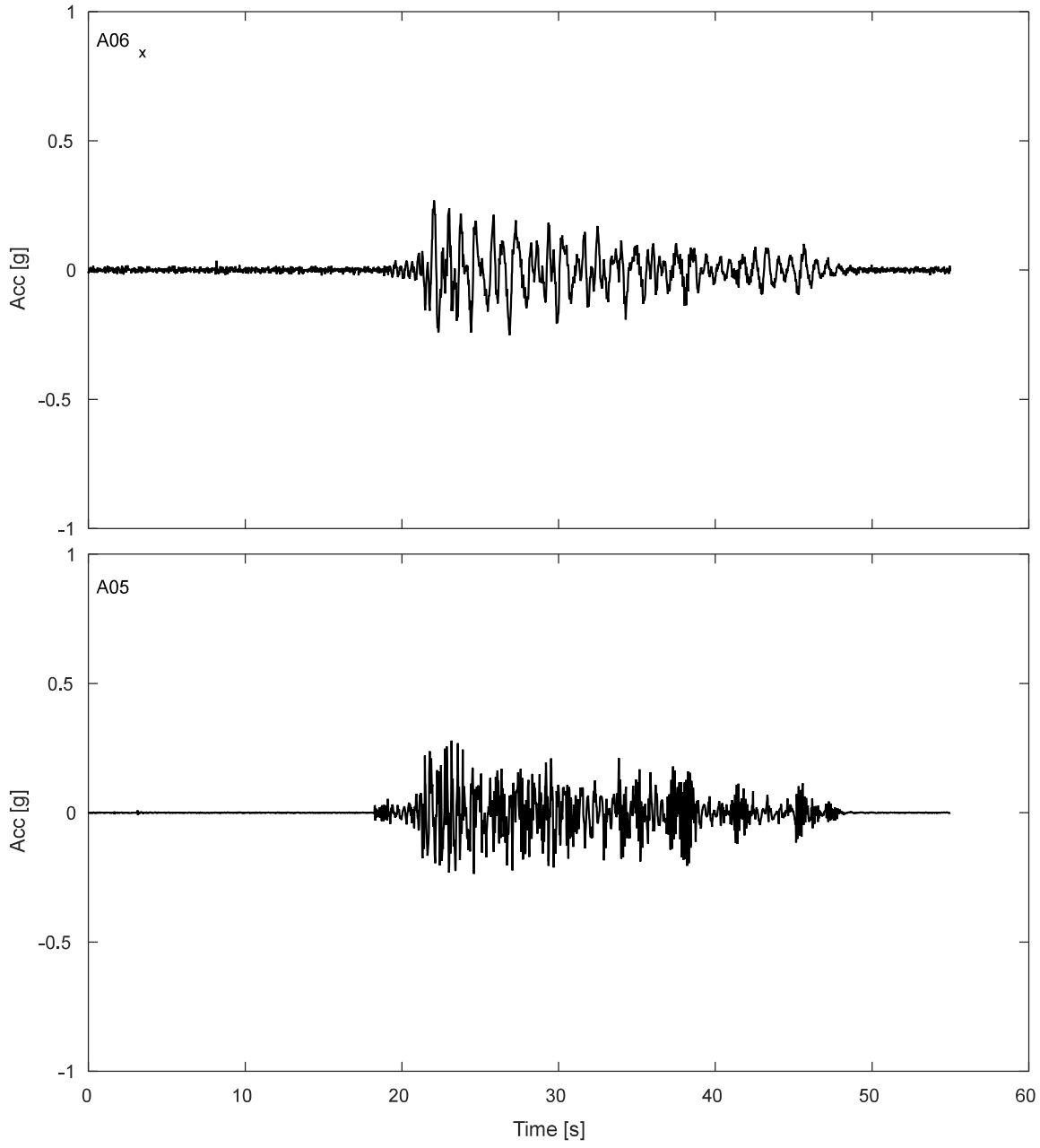

Figure K.7-4. Accelerations results SDOF structure during DT03-NOR-050P motion.

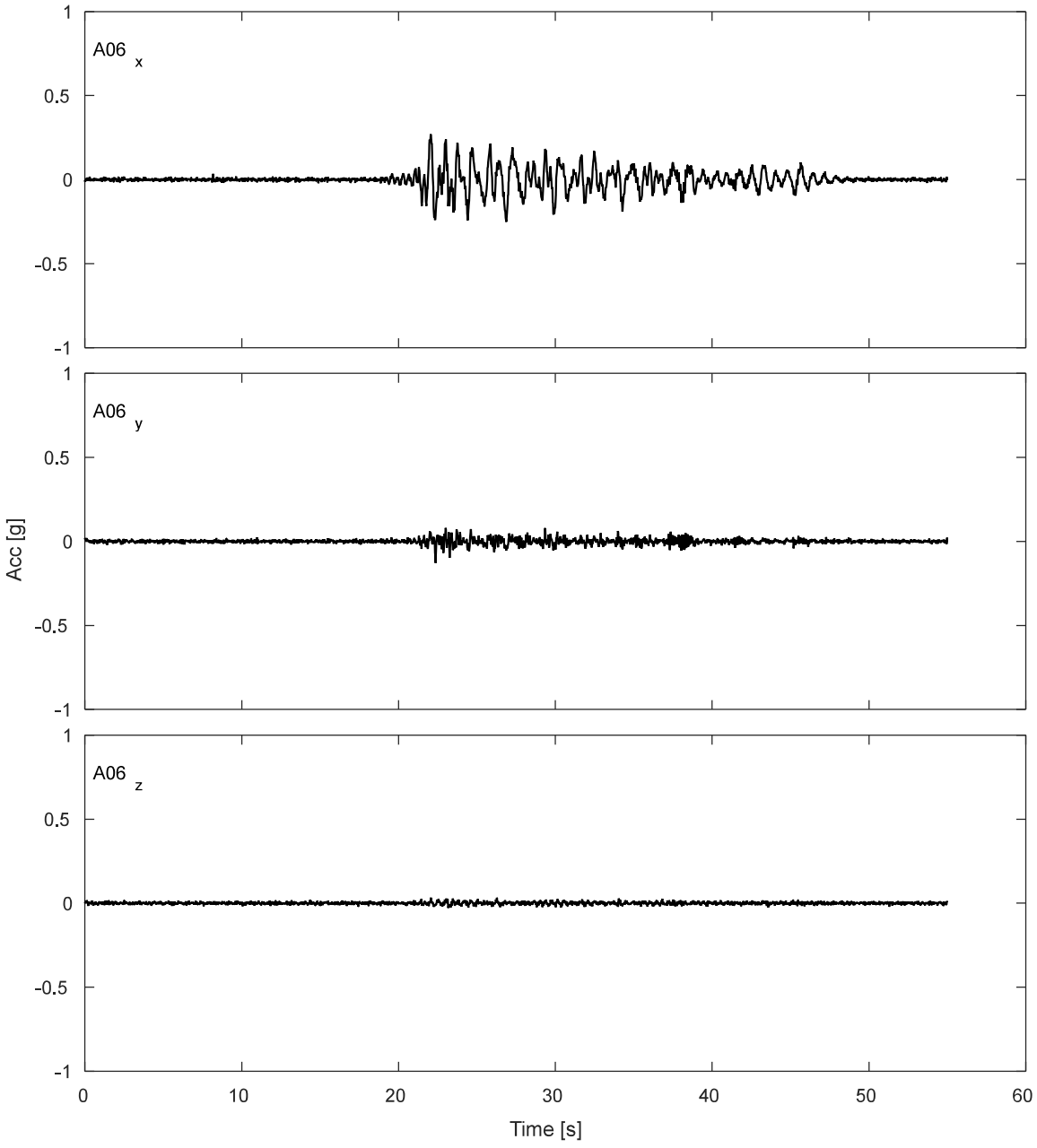

Figure K.7-5. Accelerations results for lumped mass of SDOF structure during DT03-NOR-050P motion.

K.7.2 Potentiometers.

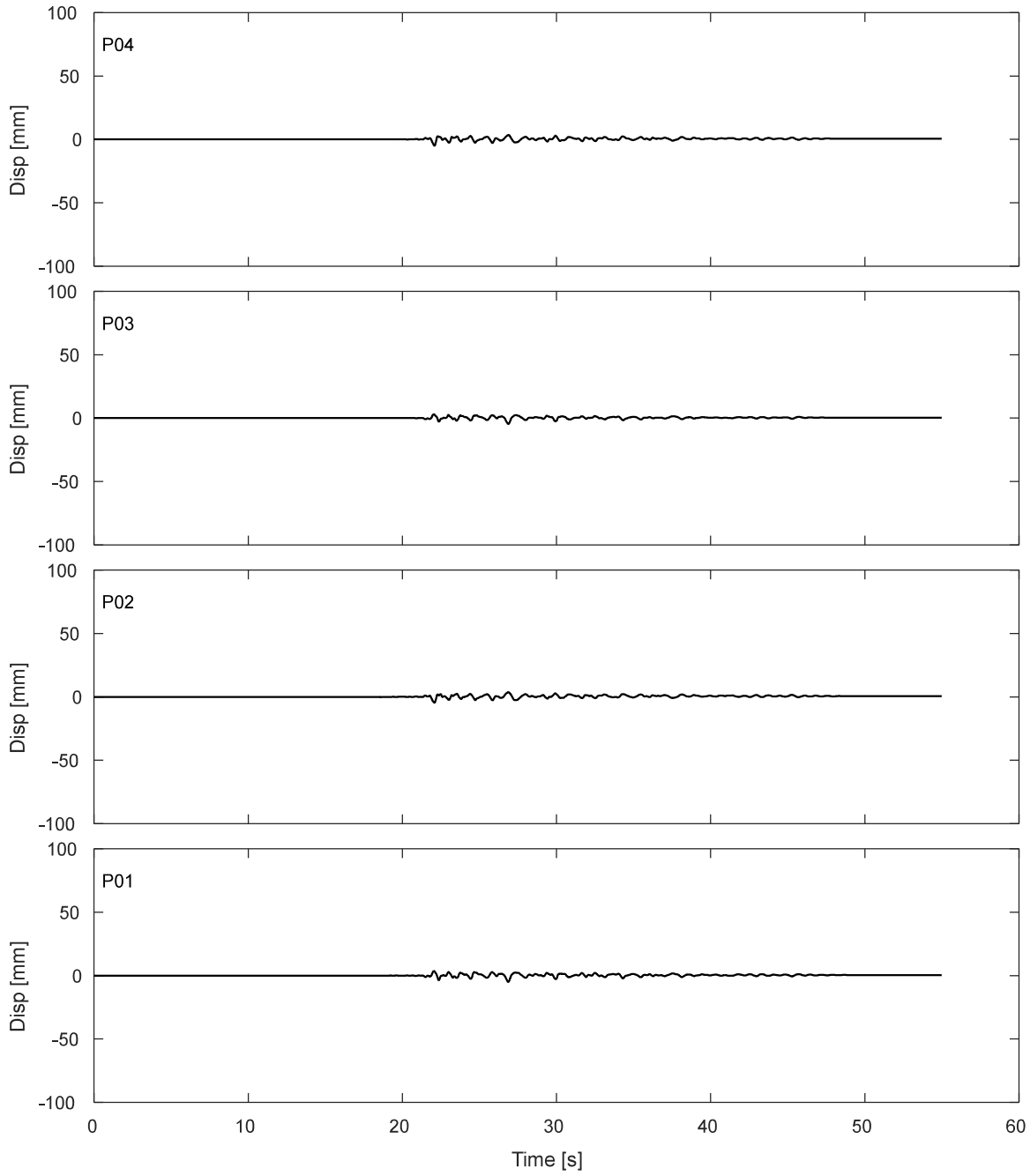

Figure K.7-6. Results of fully vertical potentiometers attached to corners of top of strip footing during DT03-NOR-050P motion.

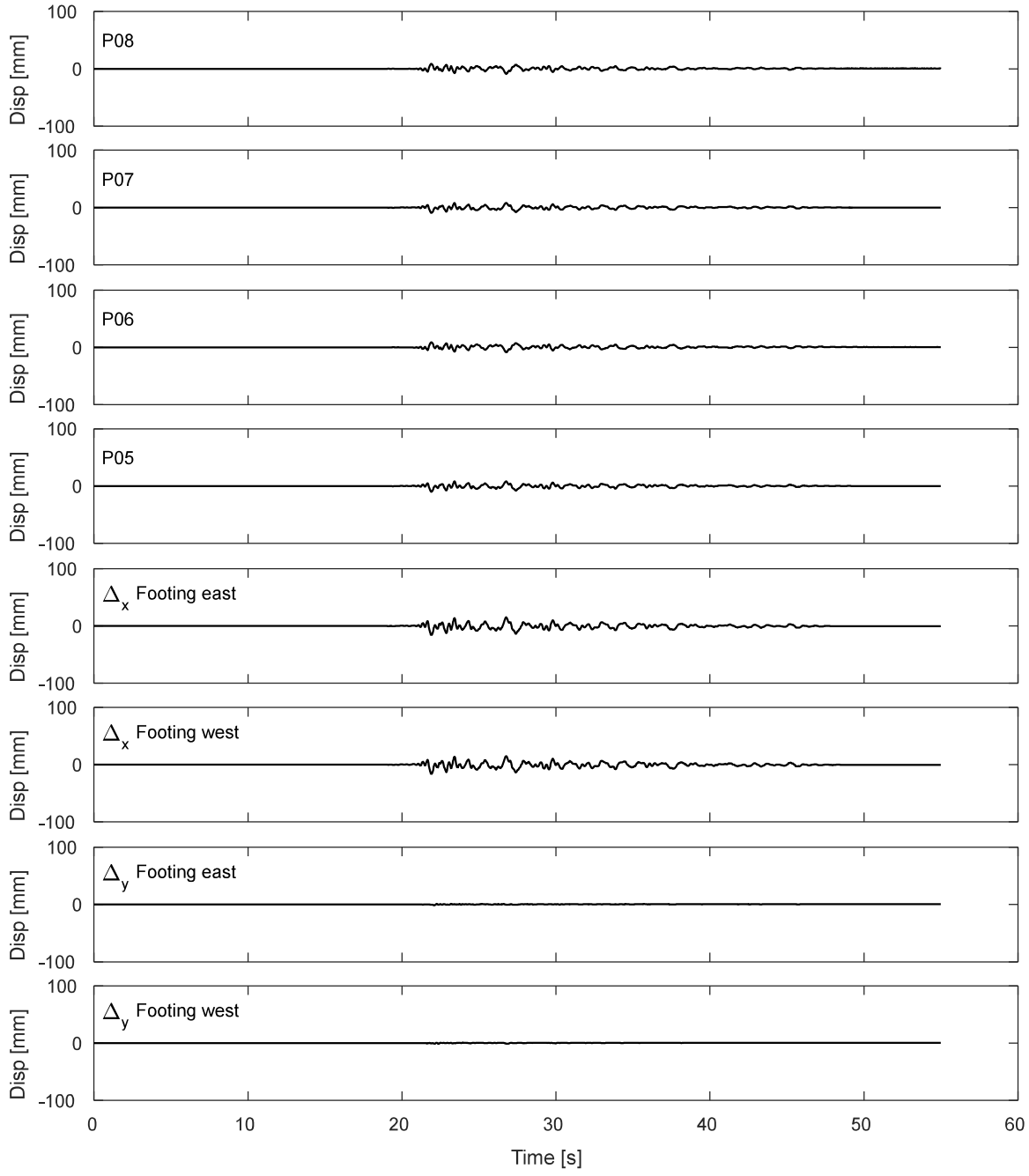

Figure K.7-7. Results of inclined potentiometers attached to top of strip footing during DT03-NOR-050P motion.

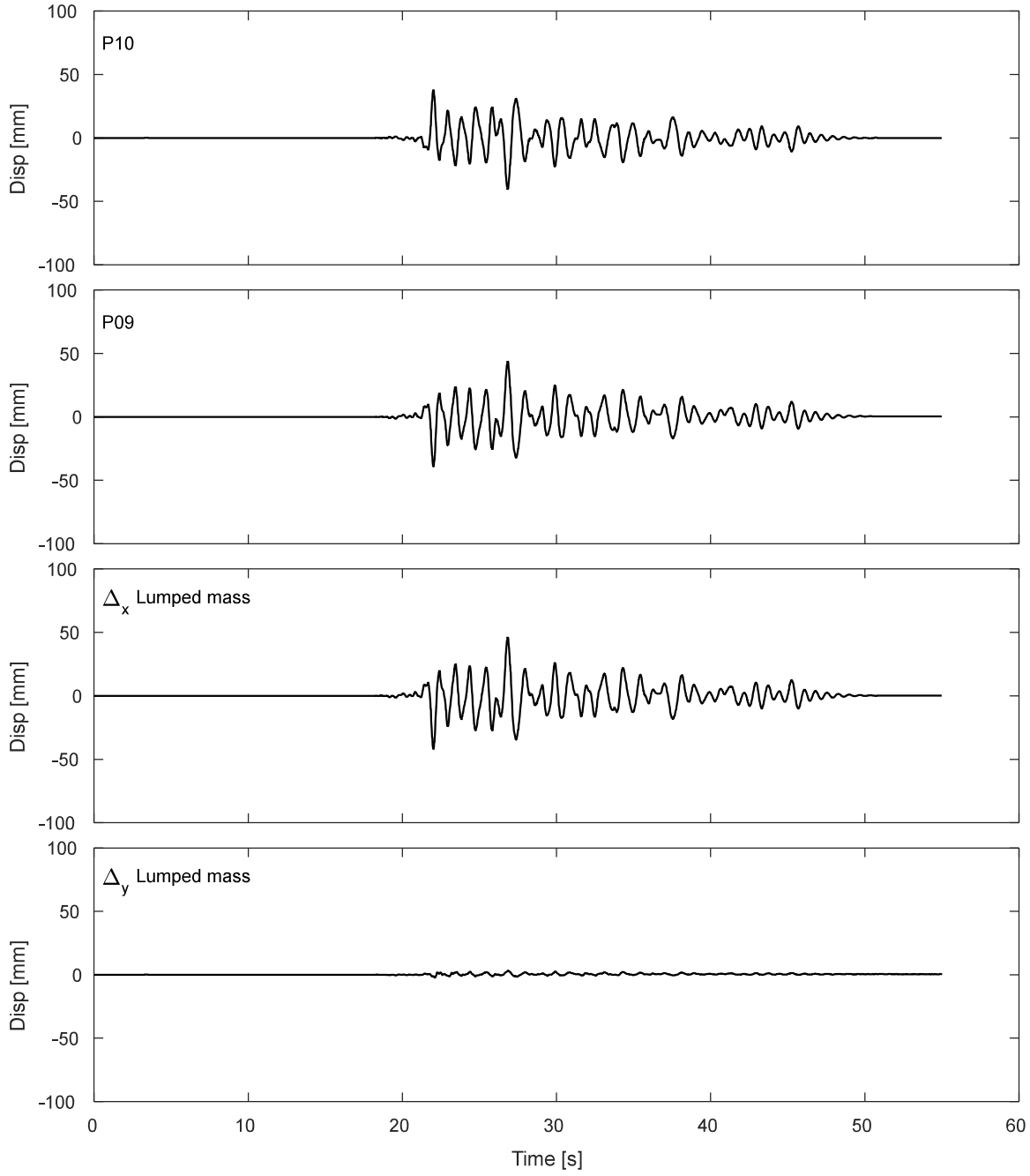

Figure K.7-8. Results of inclined potentiometers attached to lumped mass during DT03-NOR-050P motion.

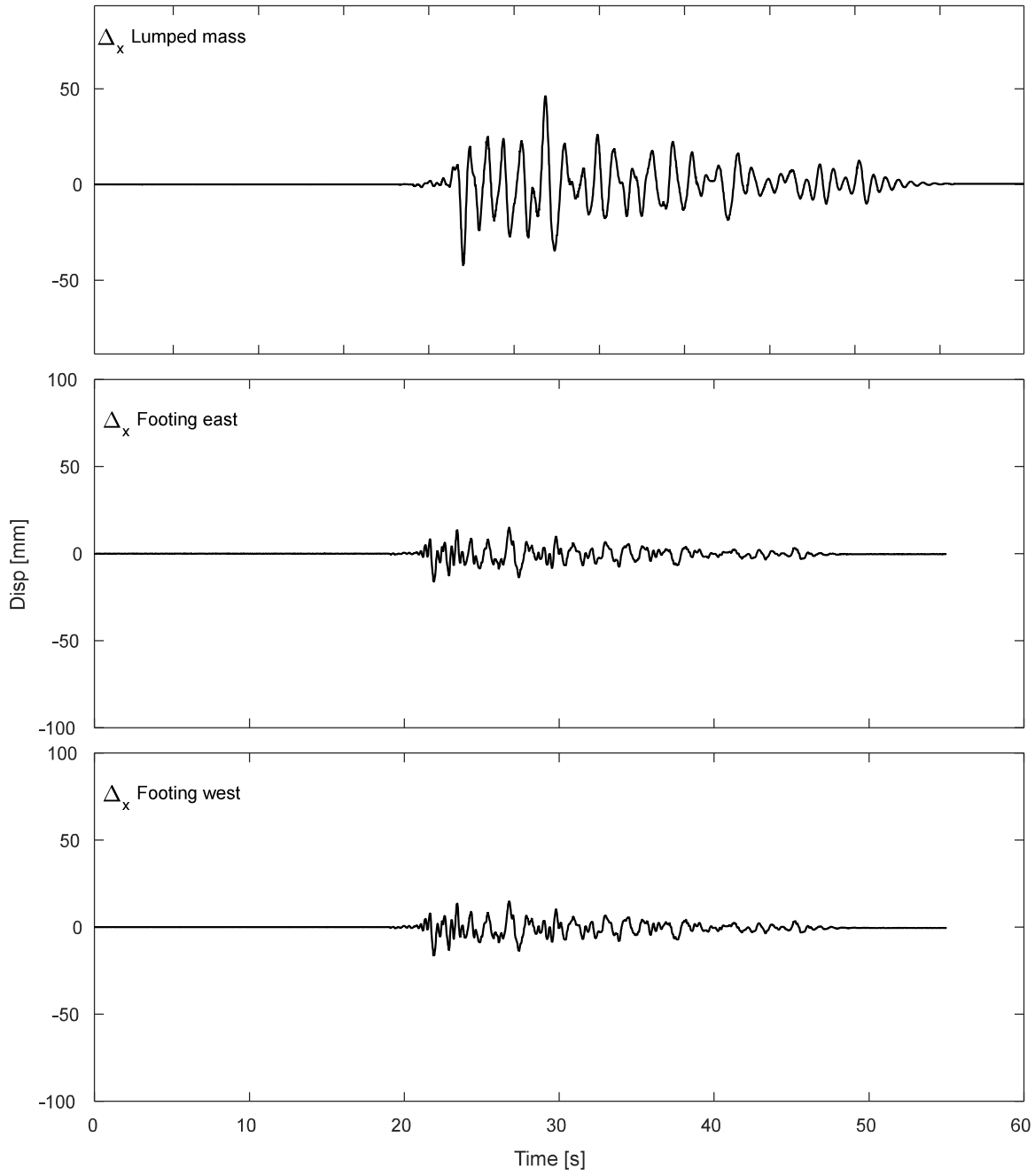

Figure K.7-9. Results of horizontal displacement of lumped mass and footing during DT03-NOR-050P motion.

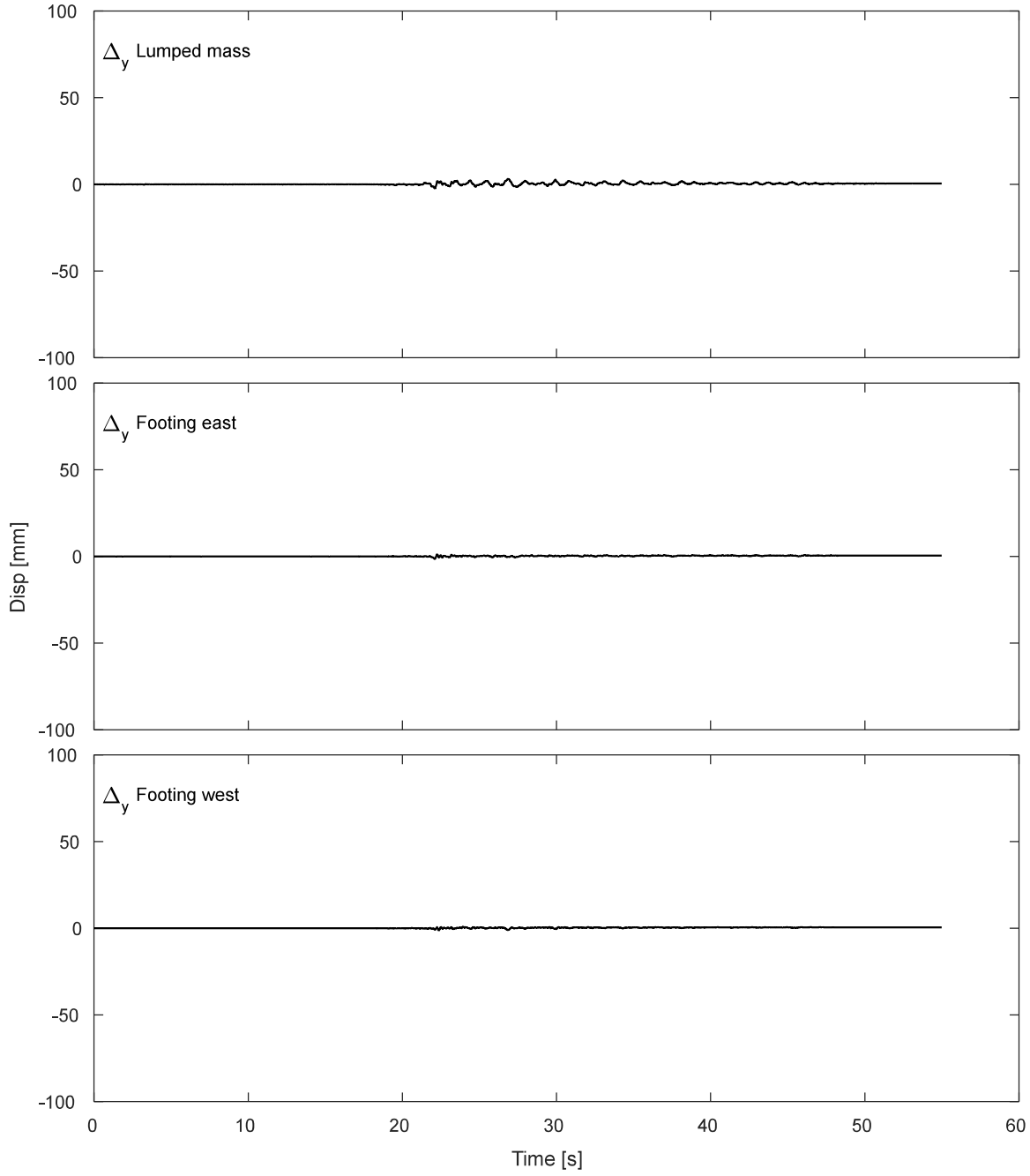

Figure K.7-10. Results of vertical displacement of lumped mass and footing during DT03-NOR-050P motion.

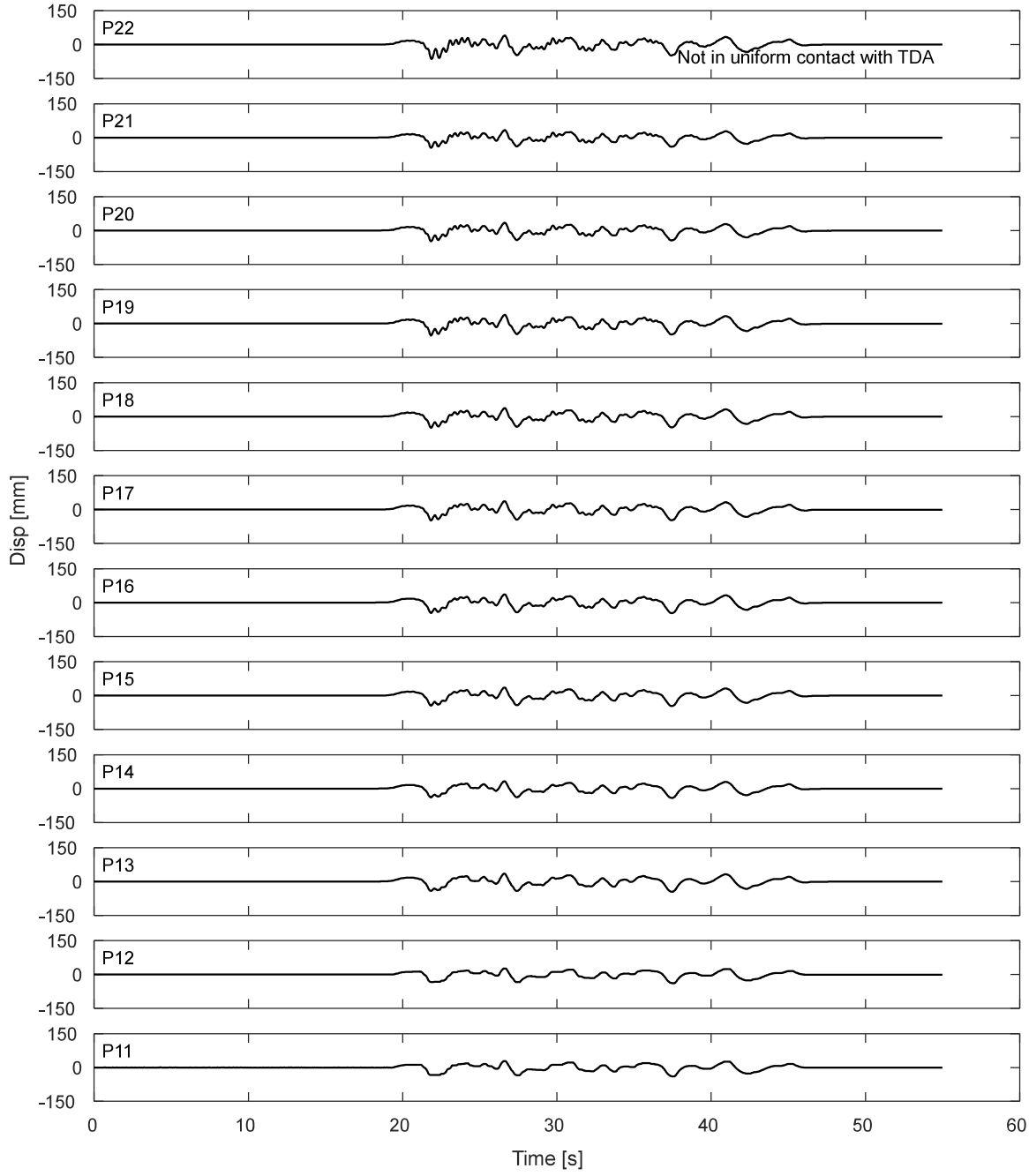

Figure K.7-11. Potentiometers results for the laminar box during DT03-NOR-050P motion.

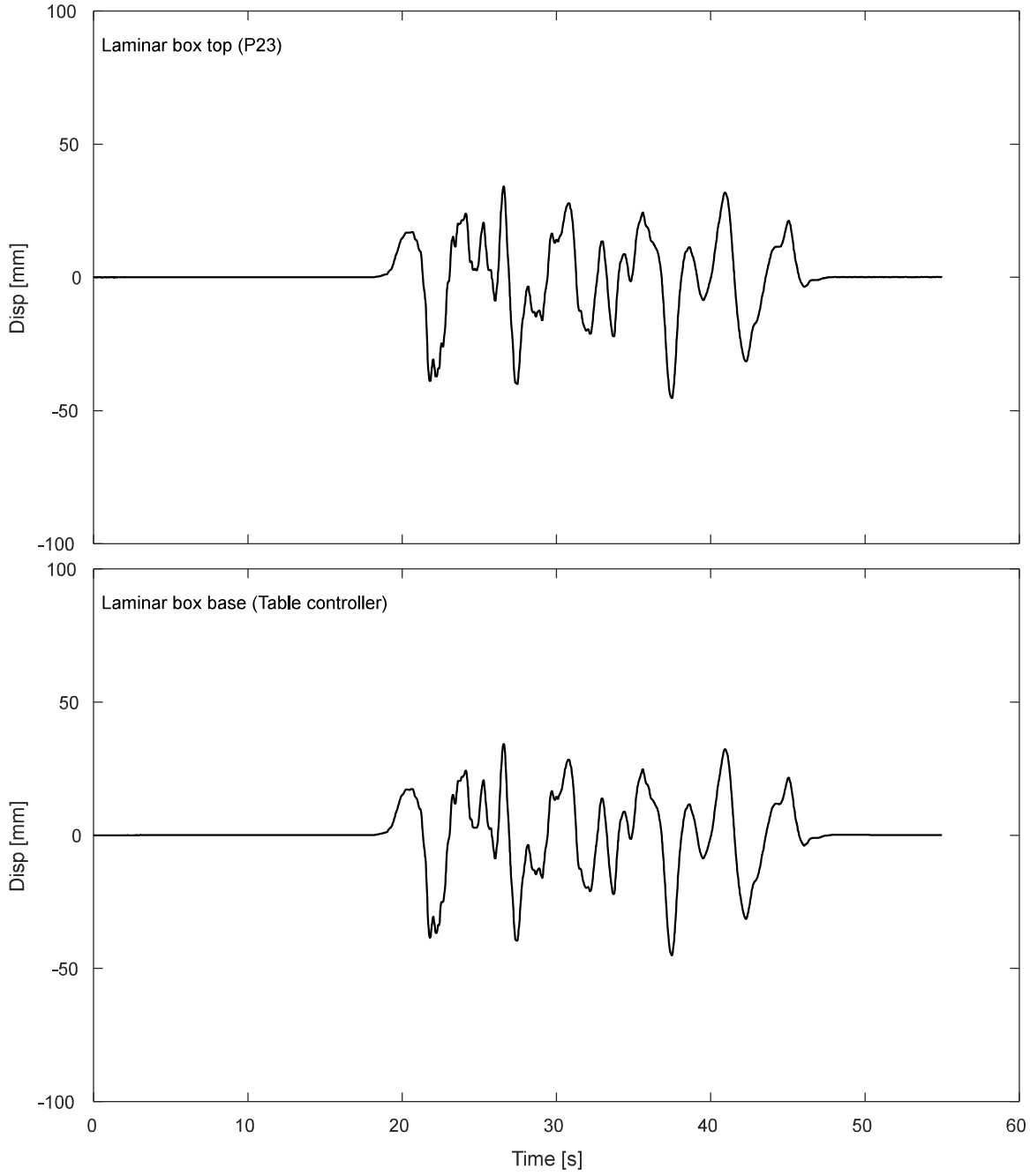

Figure K.7-12. Displacement response of top and base of laminar box during DT03-NOR-050P motion.

K.7.3. Inclinometers.

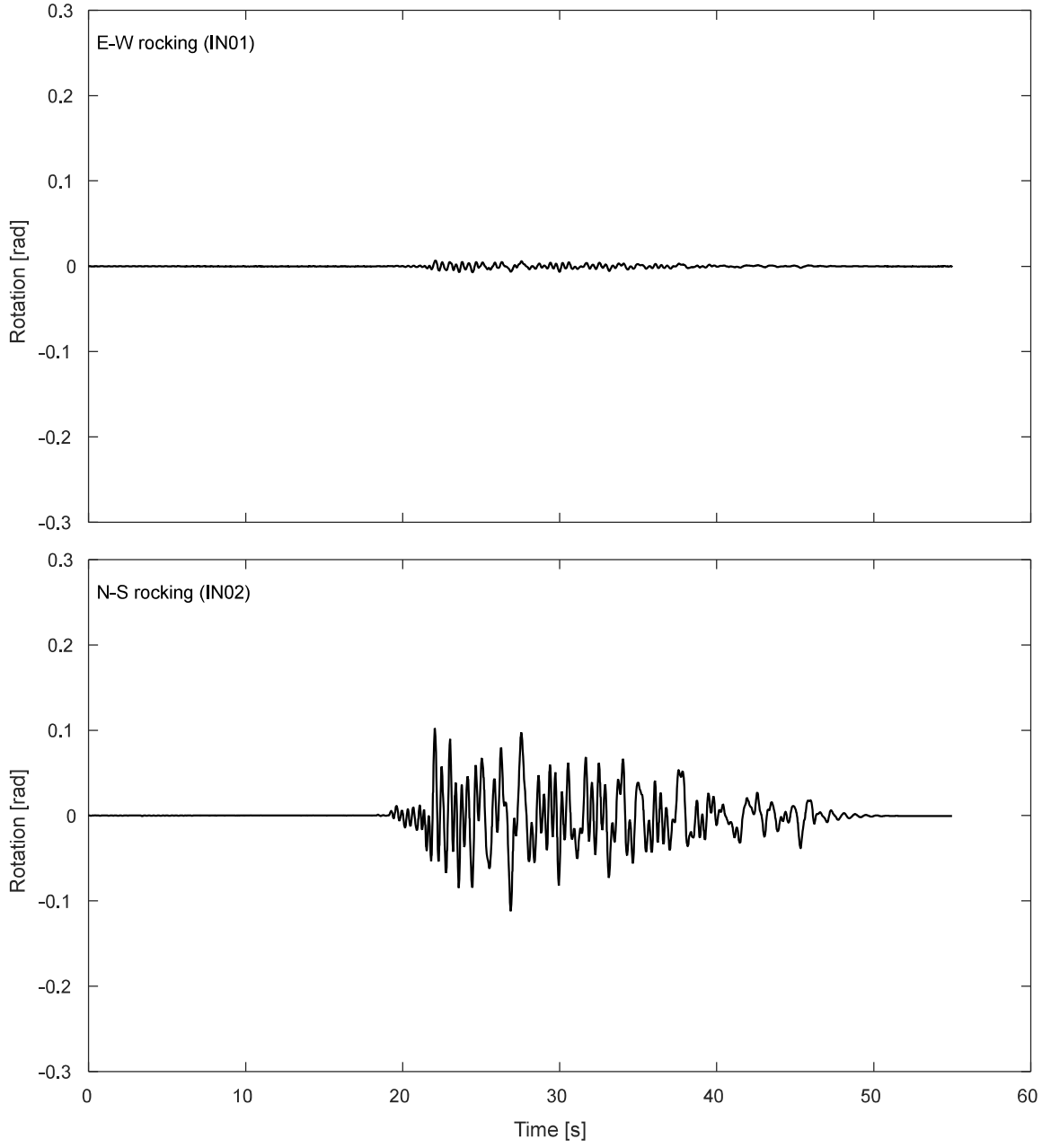

Figure K.7-13. Inclinometer results for the footing during DT03-NOR-050P motion.

K.7.4. Pressure cells.

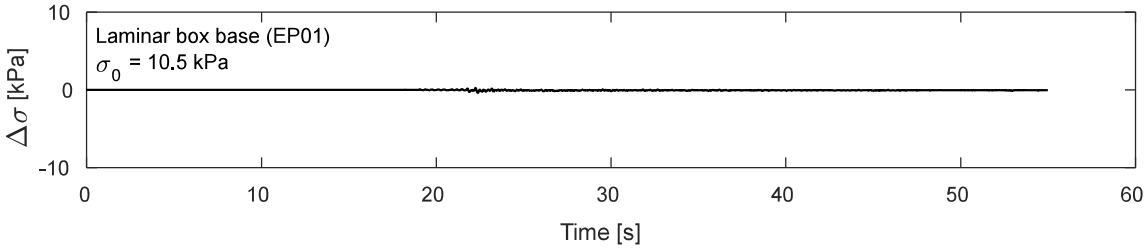

Figure K.7-14. Pressure cells results at laminar box base during DT03-NOR-050P motion.

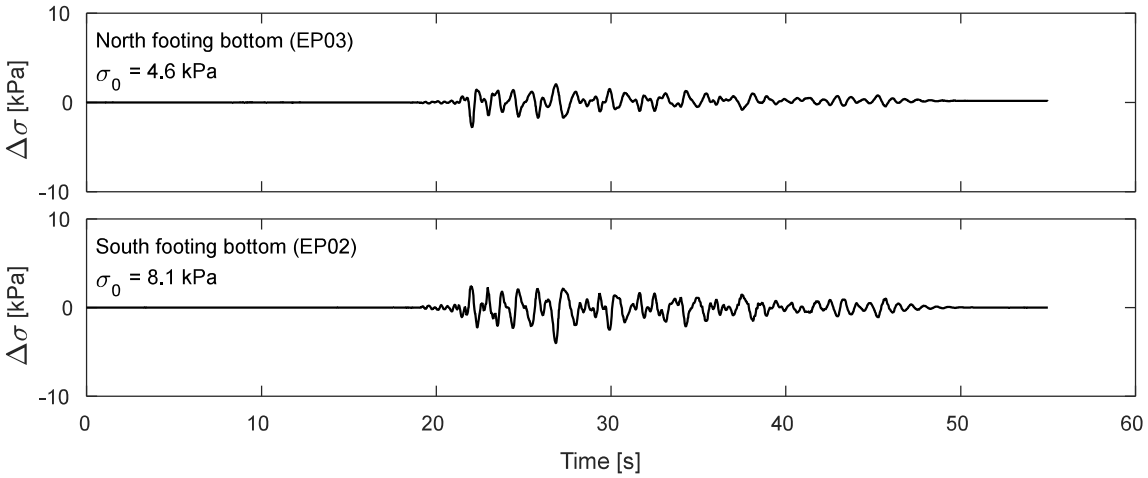

Figure K.7-15. Pressure cells results at footing bottom during DT03-NOR-050P motion.

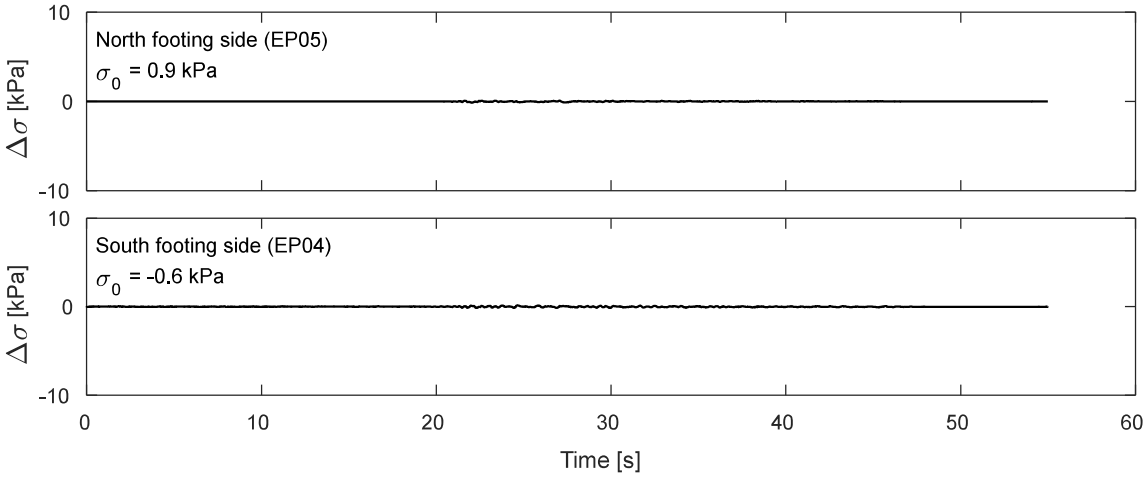

Figure K.7-16. Pressure cells results at footing sides during DT03-NOR-050P motion.

K.8. Time-history Records for DT03-NOR-075P motion.

K.8.1 Input Motion

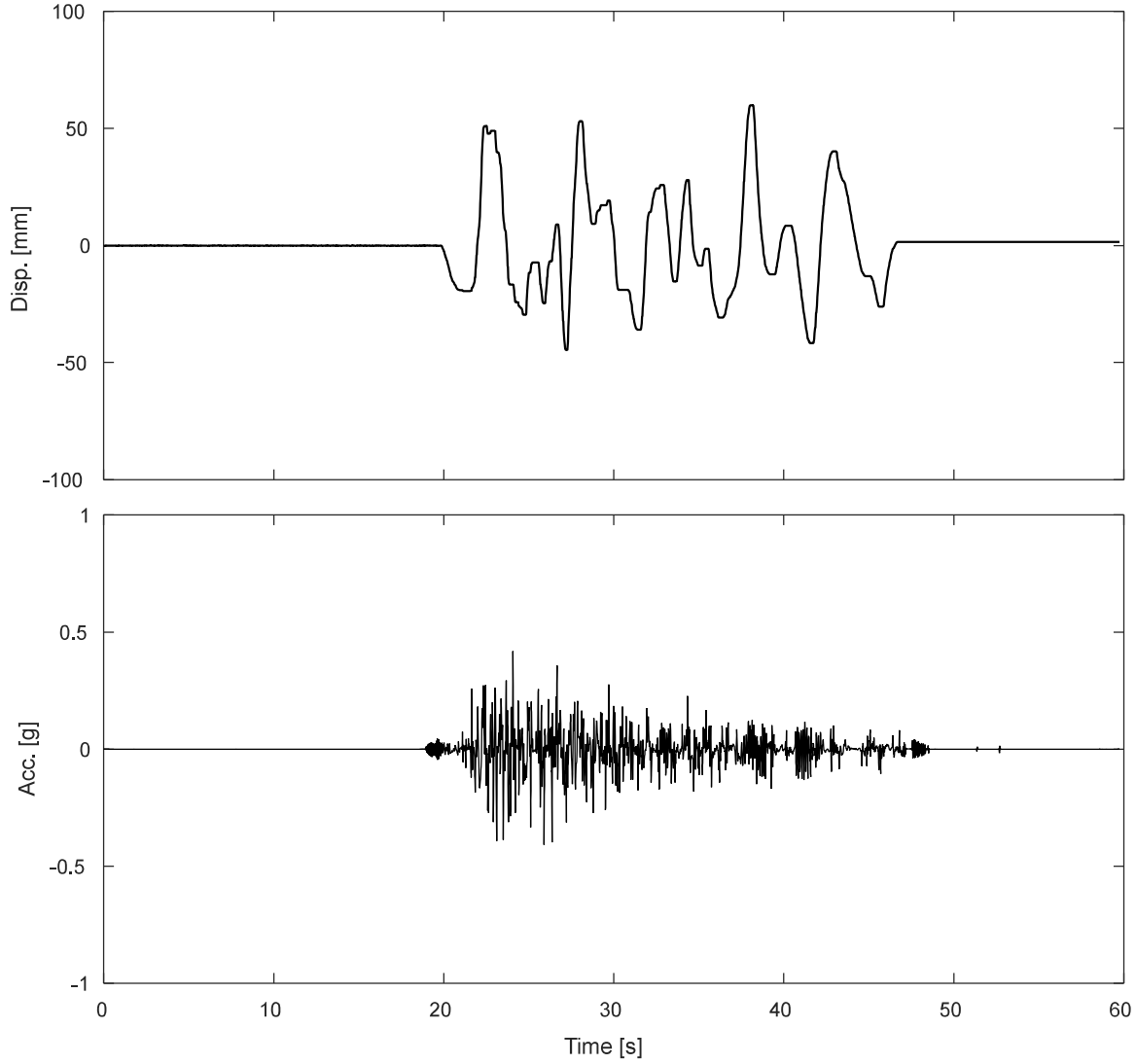

Figure K.8-1. Measured input displacement and acceleration at the base of the specimen during DT03-NOR-075P motion

K.8.1 Accelerometers.

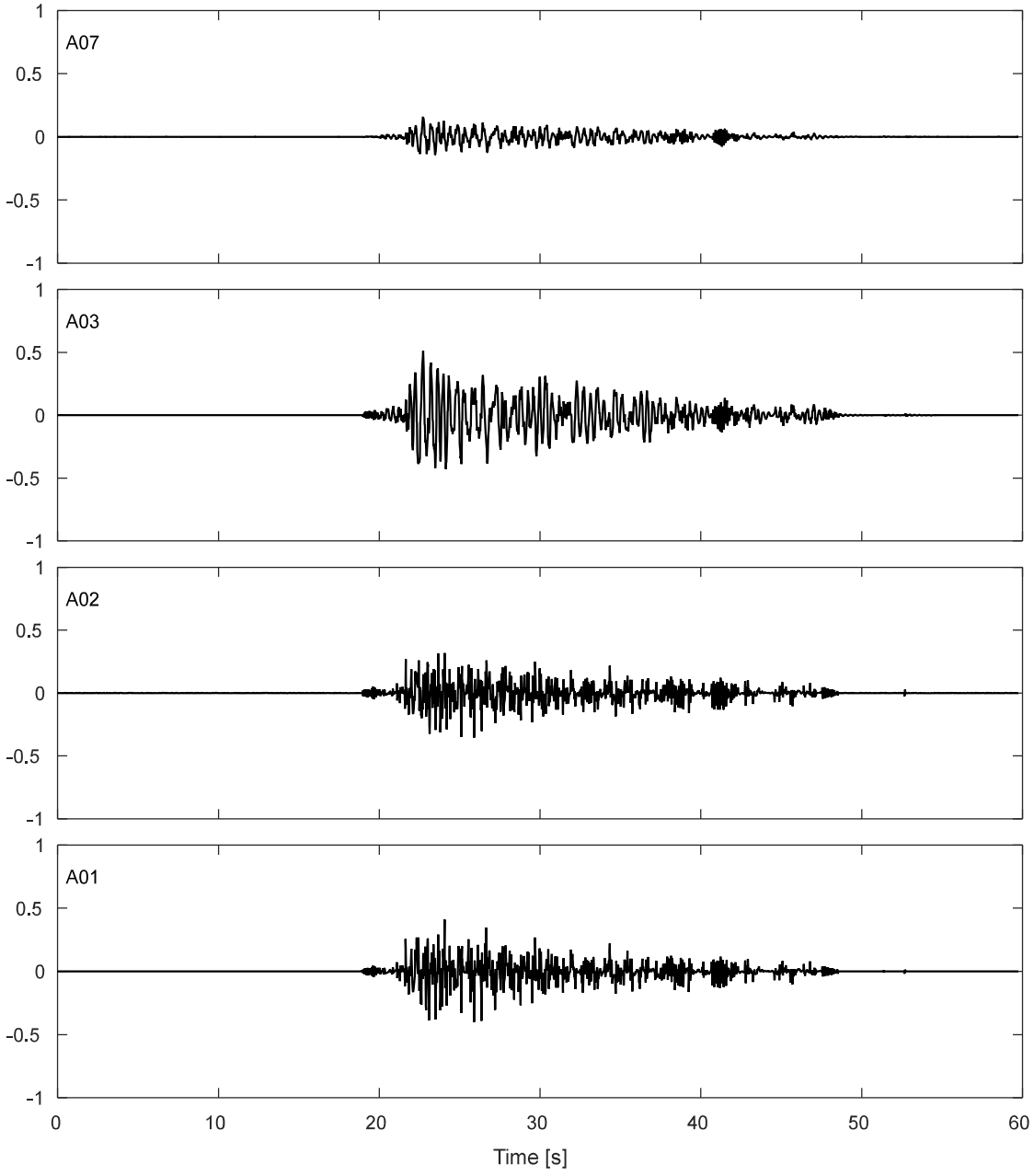

Figure K.8-2. Accelerations results along TDA during DT03-NOR-075P motion.

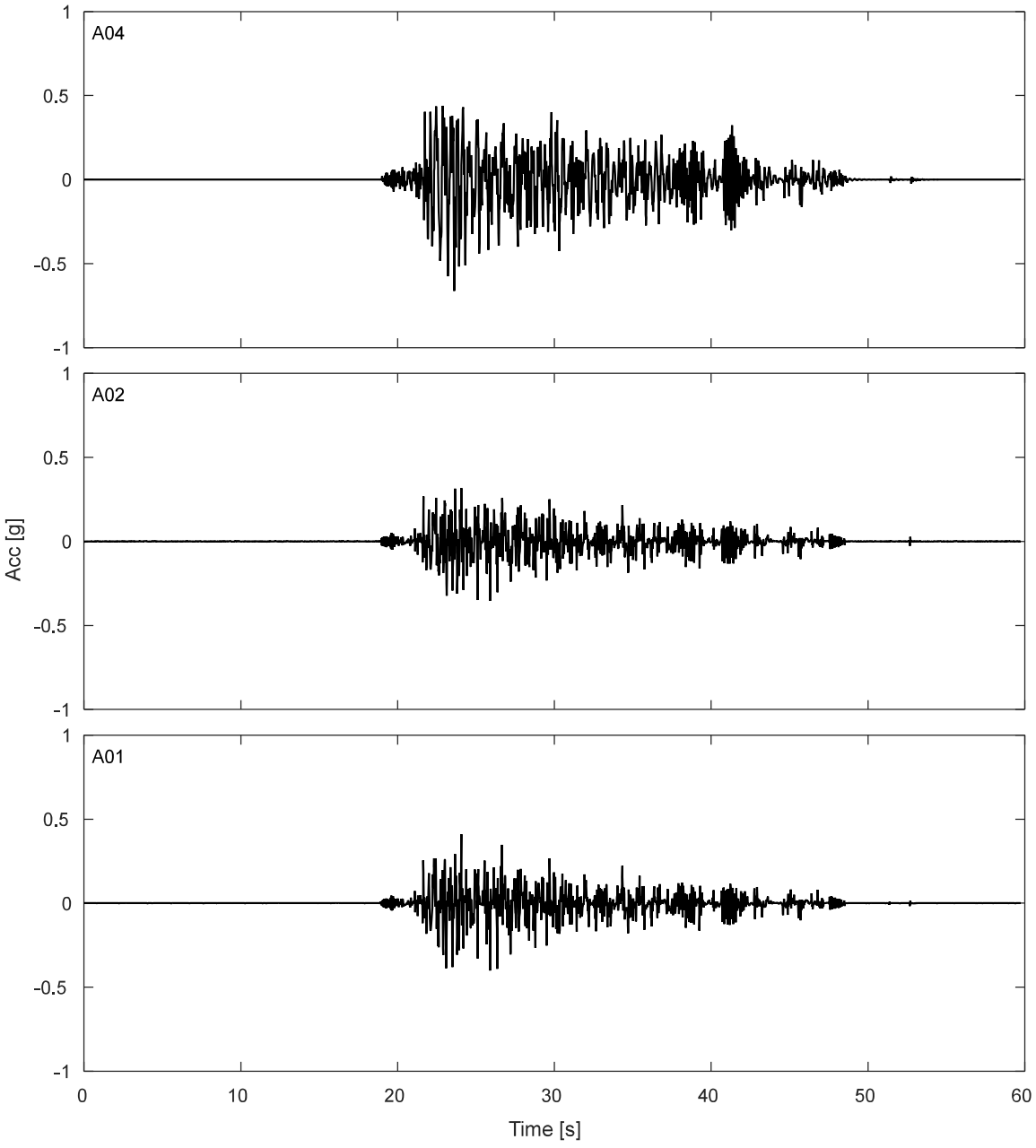

Figure K.8-3. Free field accelerations results for TDA during DT03-NOR-075P motion.

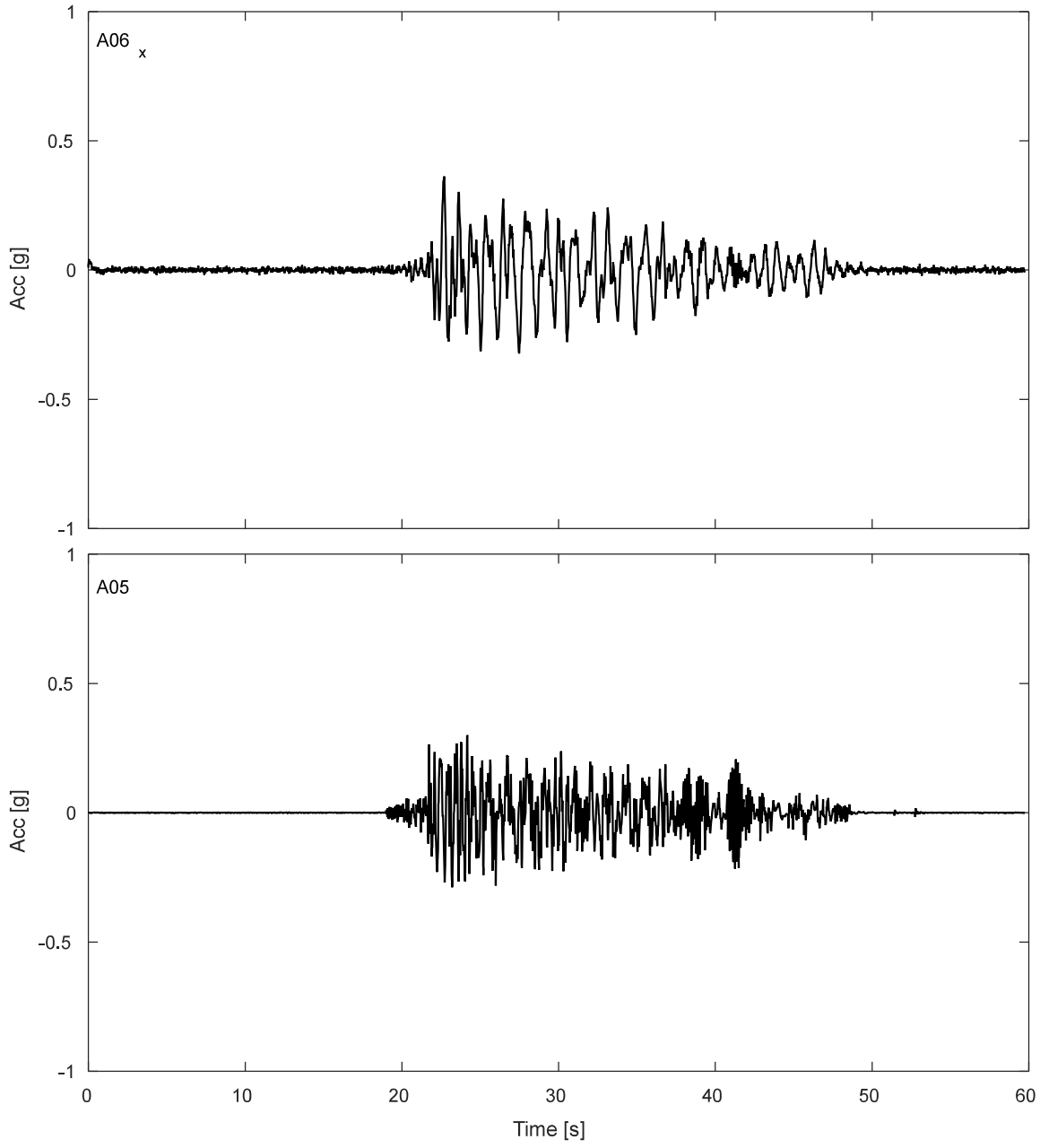

Figure K.8-4. Accelerations results SDOF structure during DT03-NOR-075P motion.

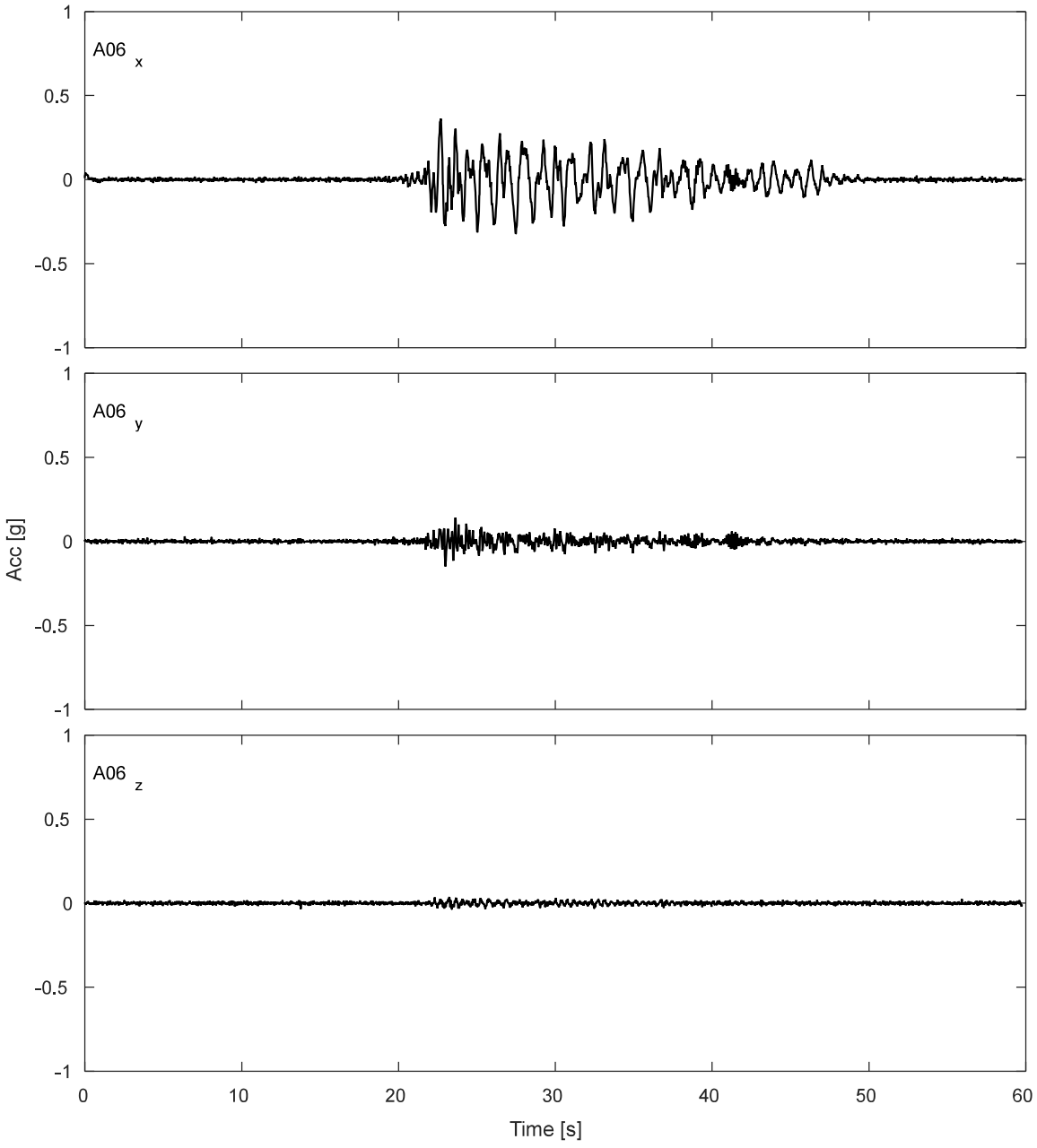

Figure K.8-5. Accelerations results for lumped mass of SDOF structure during DT03-NOR-075P motion.

K.8.2 Potentiometers.

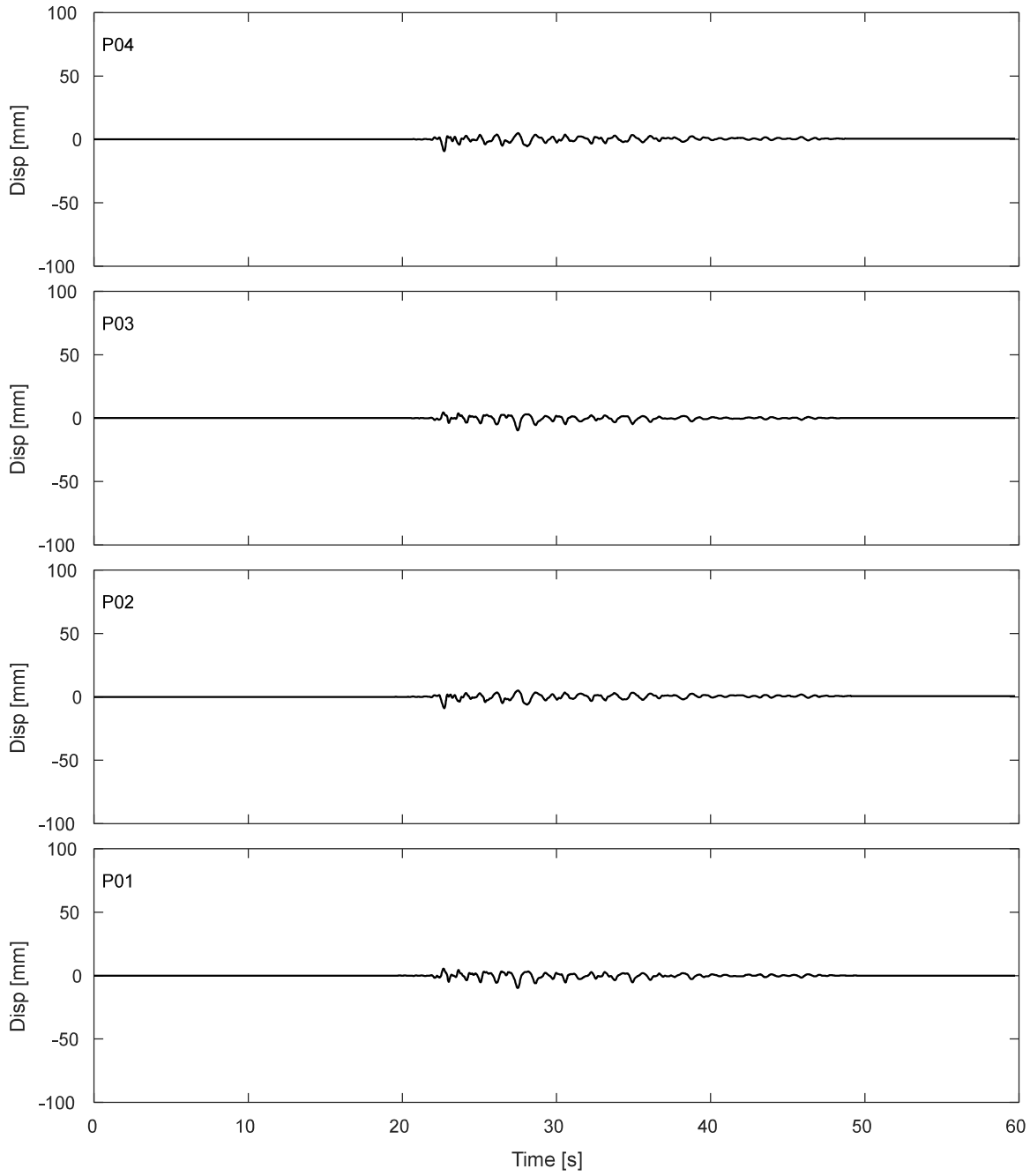

Figure K.8-6. Results of fully vertical potentiometers attached to corners of top of strip footing during DT03-NOR-075P motion.

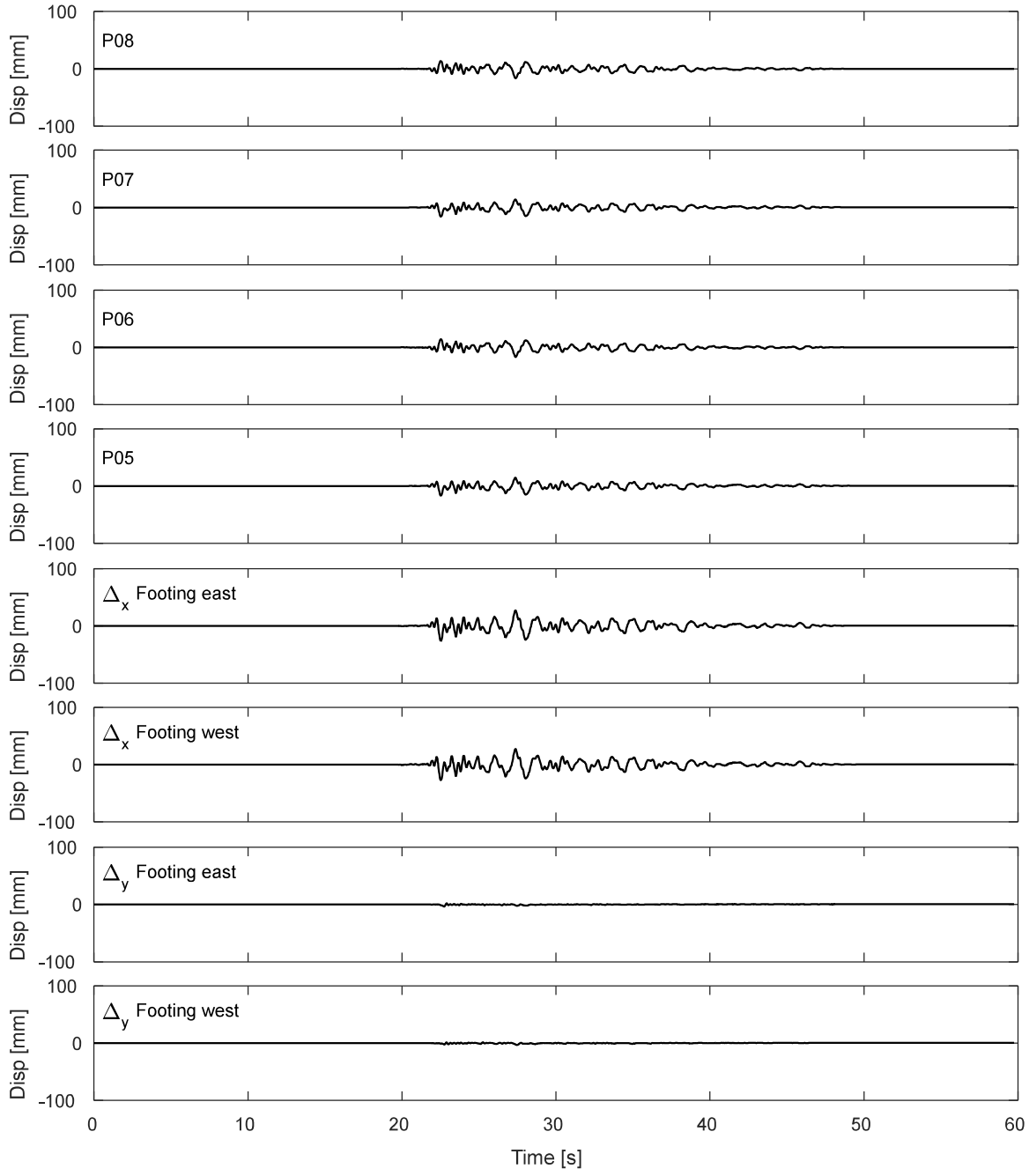

Figure K.8-7. Results of inclined potentiometers attached to top of strip footing during DT03-NOR-075P motion.

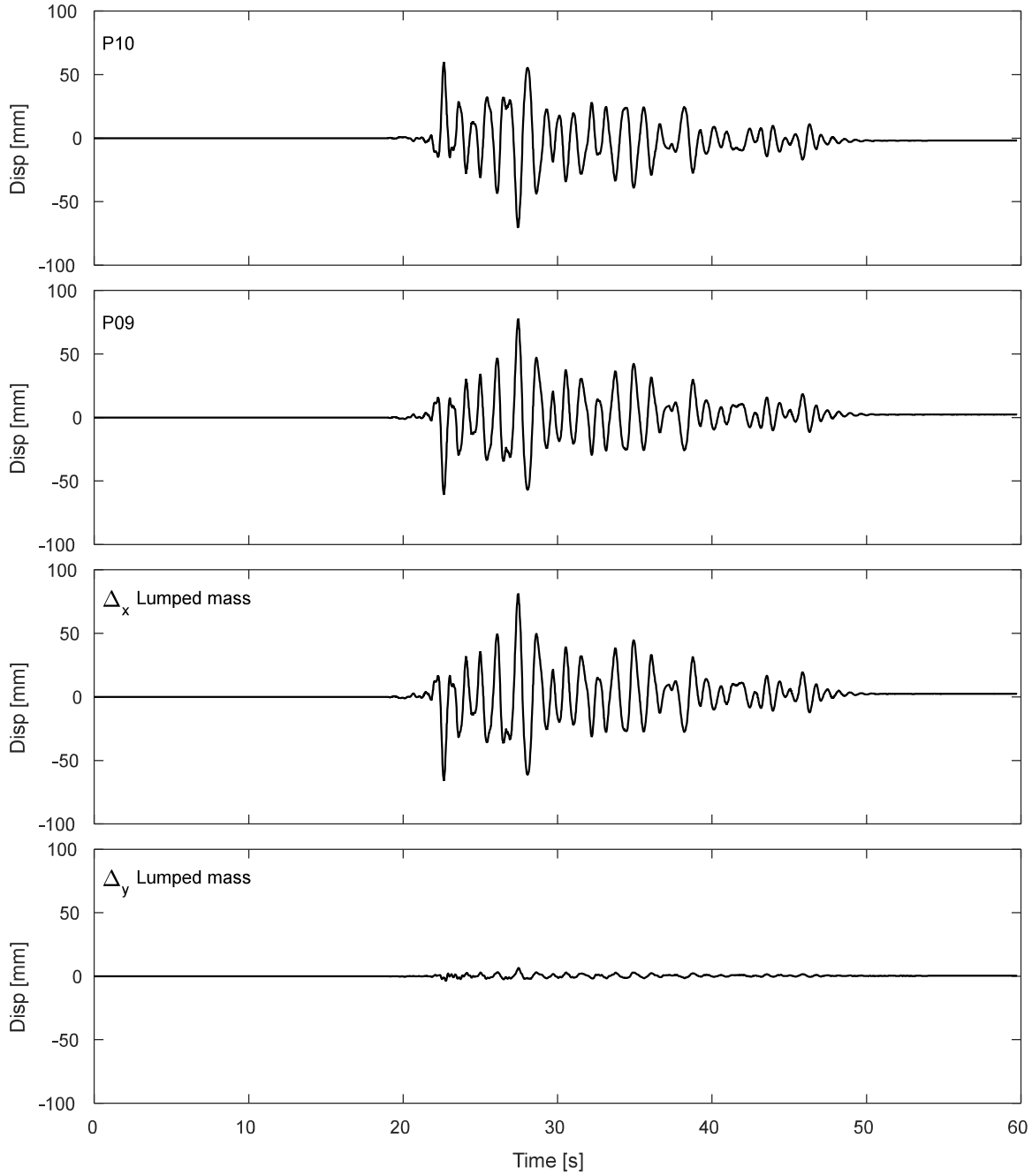

Figure K.8-8. Results of inclined potentiometers attached to lumped mass during DT03-NOR-075P motion.

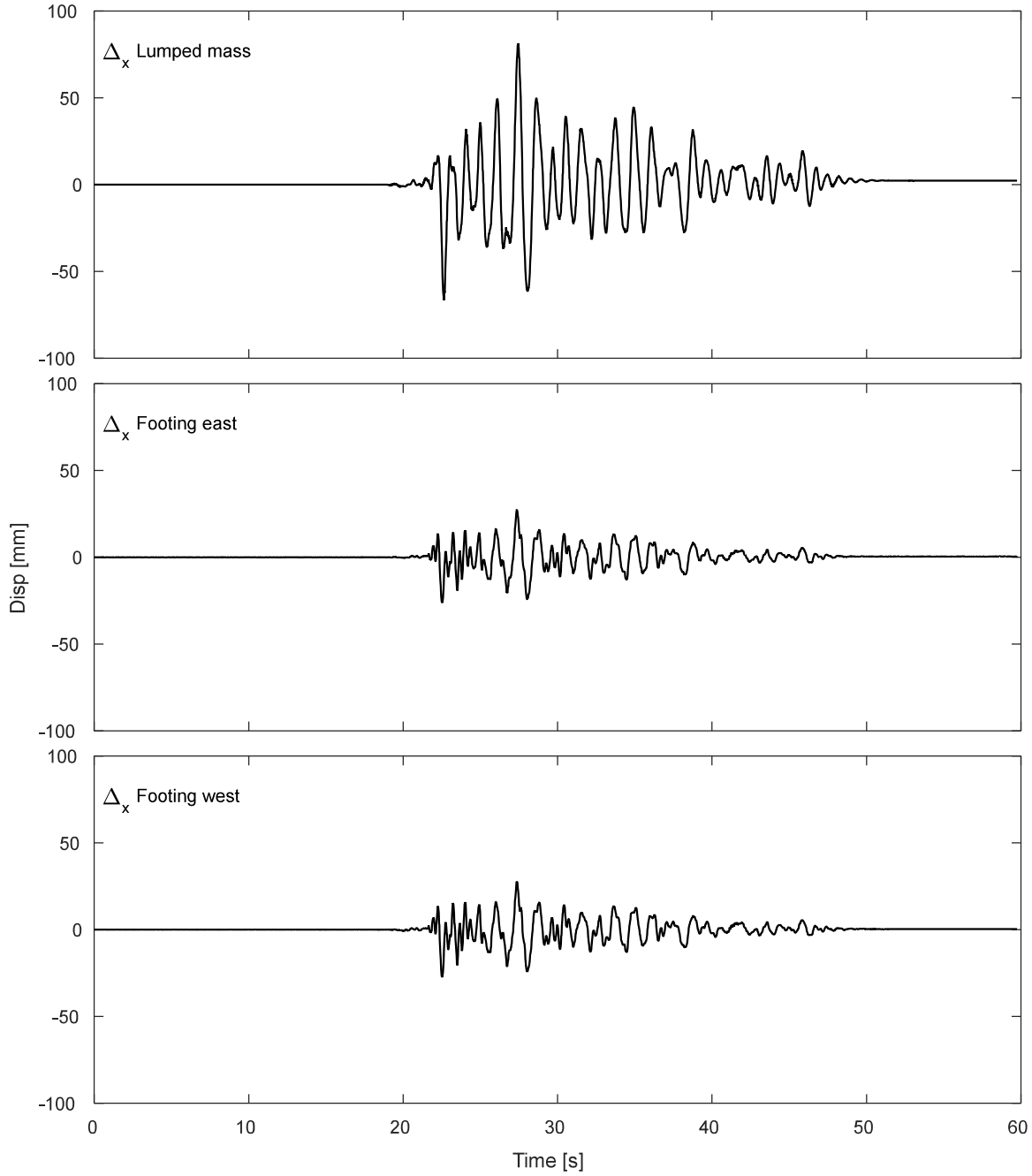

Figure K.8-9. Results of horizontal displacement of lumped mass and footing during DT03-NOR-075P motion.

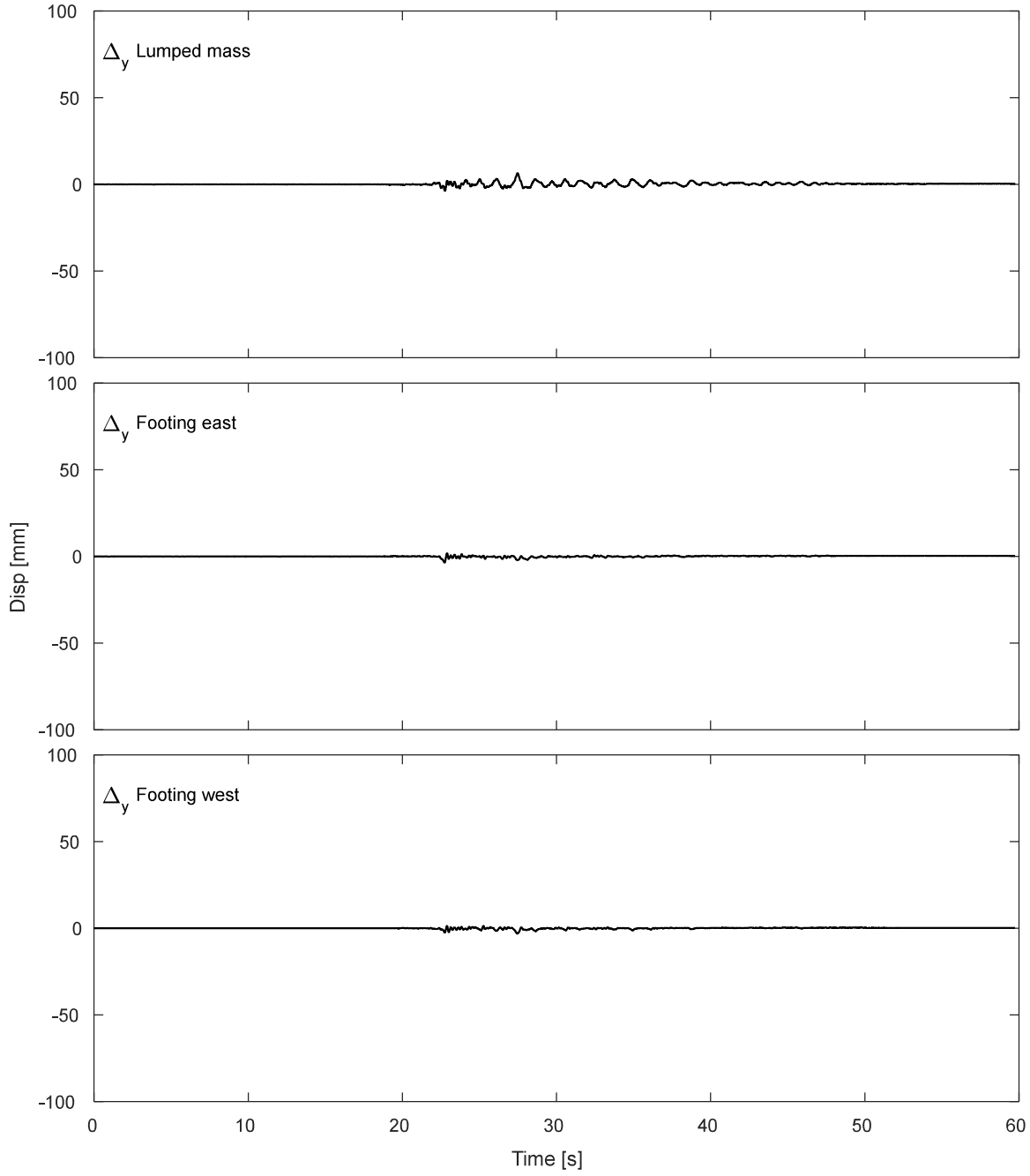

Figure K.8-10. Results of vertical displacement of lumped mass and footing during DT03-NOR-075P motion.

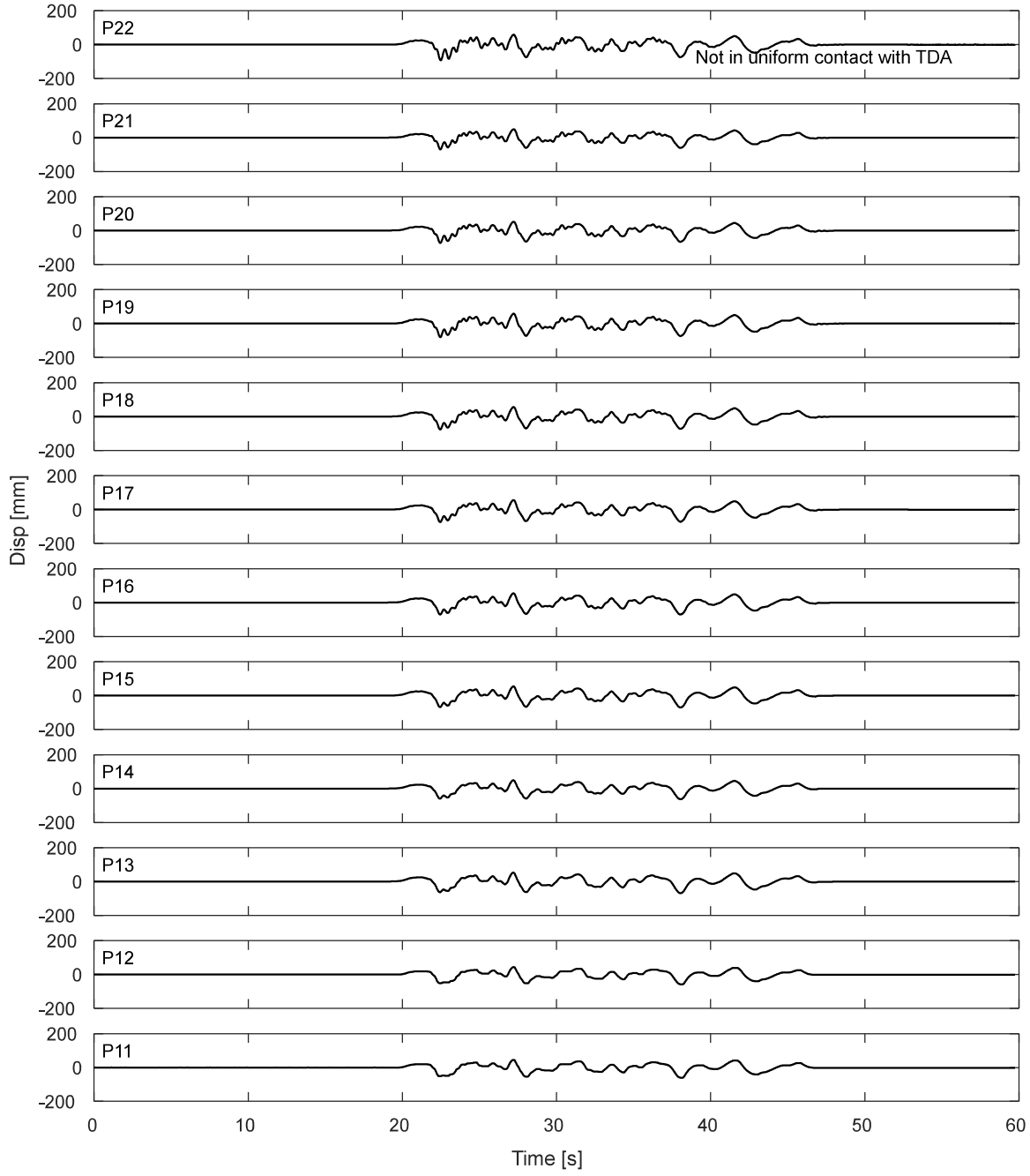

Figure K.8-11. Potentiometers results for the laminar box during DT03-NOR-075P motion.

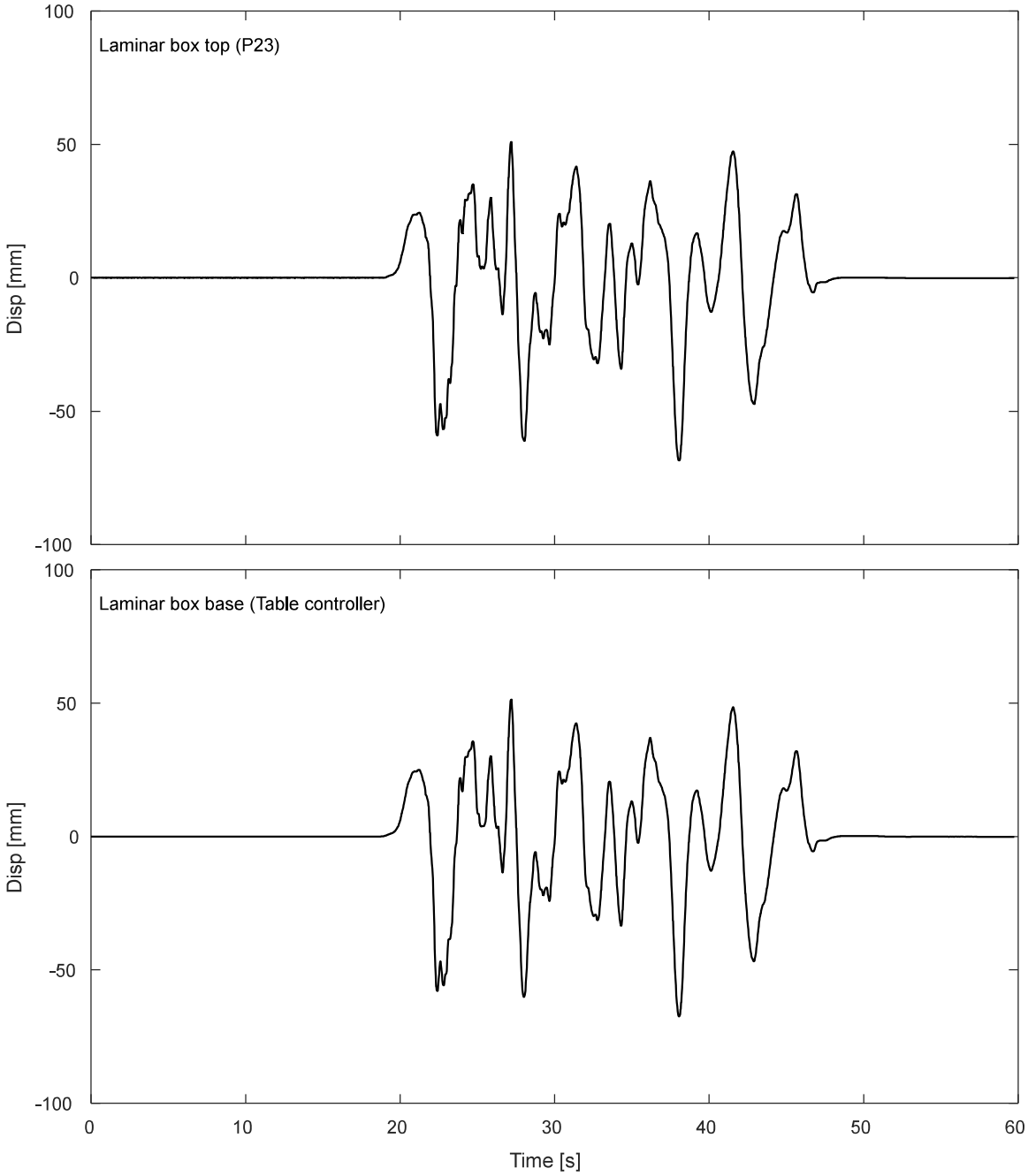

Figure K.8-12. Displacement response of top and base of laminar box during DT03-NOR-075P motion.

K.8.3. Inclinometers.

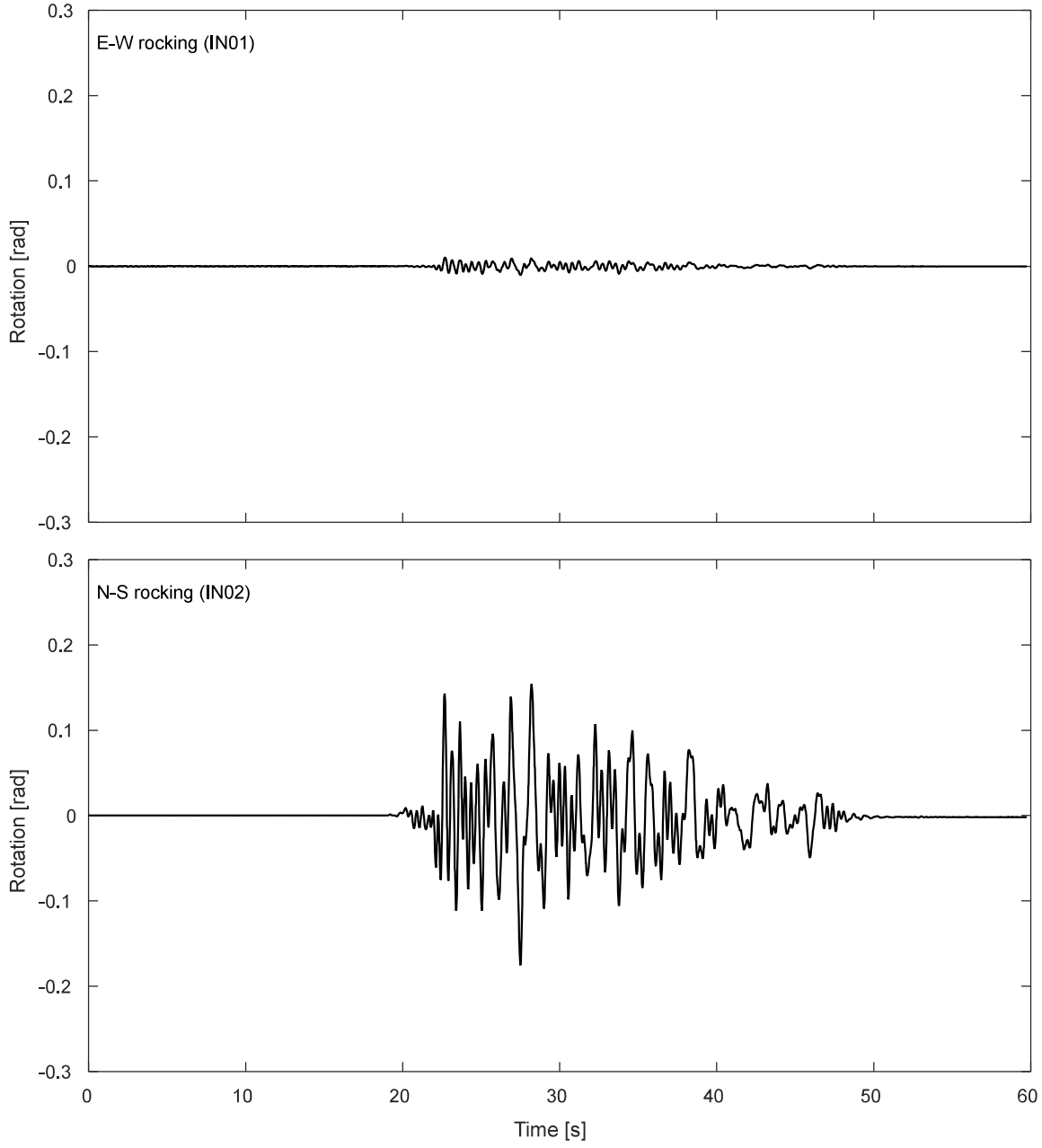

Figure K.8-13. Inclinometer results for the footing during DT03-NOR-075P motion.

K.8.4. Pressure cells.

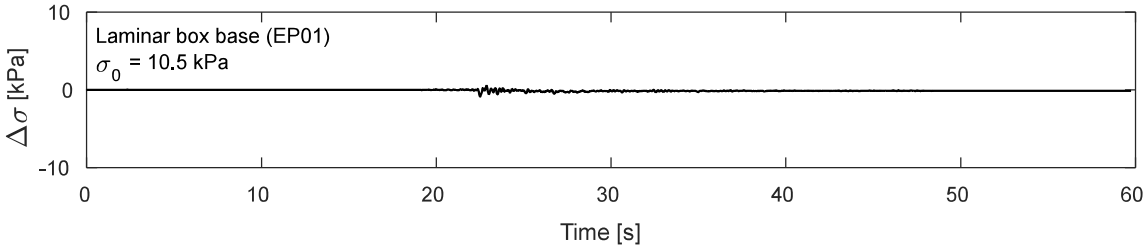

Figure K.8-14. Pressure cells results at laminar box base during DT03-NOR-075P motion.

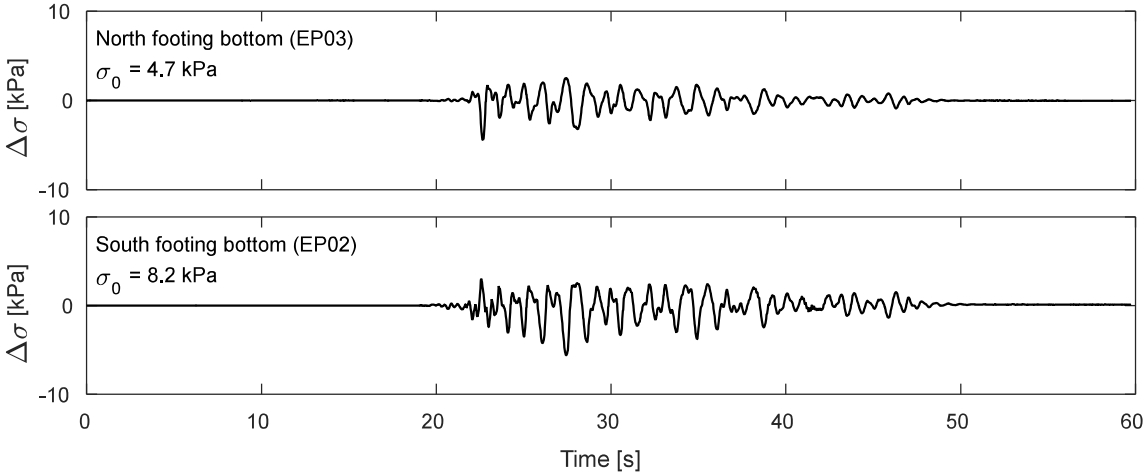

Figure K.8-15. Pressure cells results at footing bottom during DT03-NOR-075P motion.

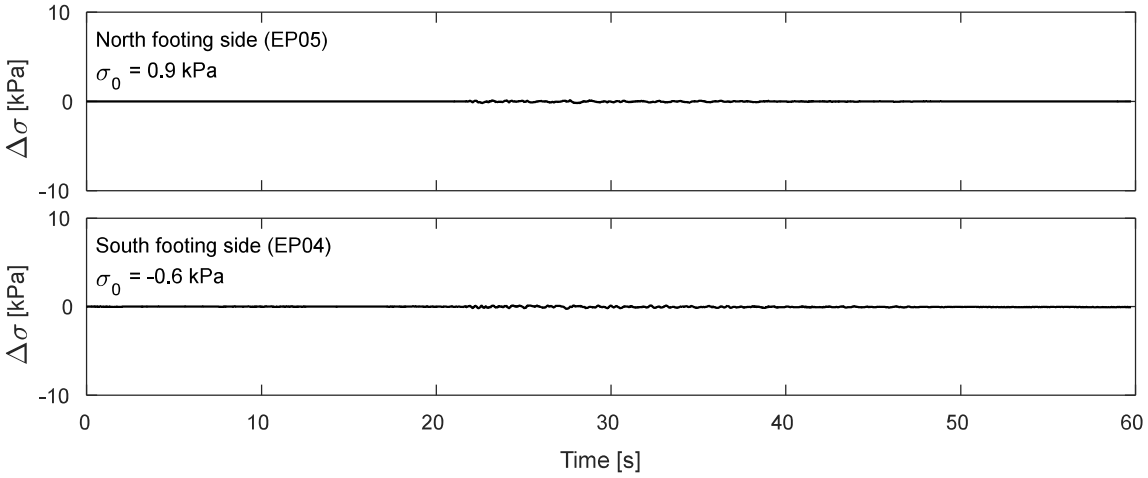

Figure K.8-16. Pressure cells results at footing sides during DT03-NOR-075P motion.

K.9. Time-history Records for DT03-NOR-100P motion.

K.9.1 Input Motion

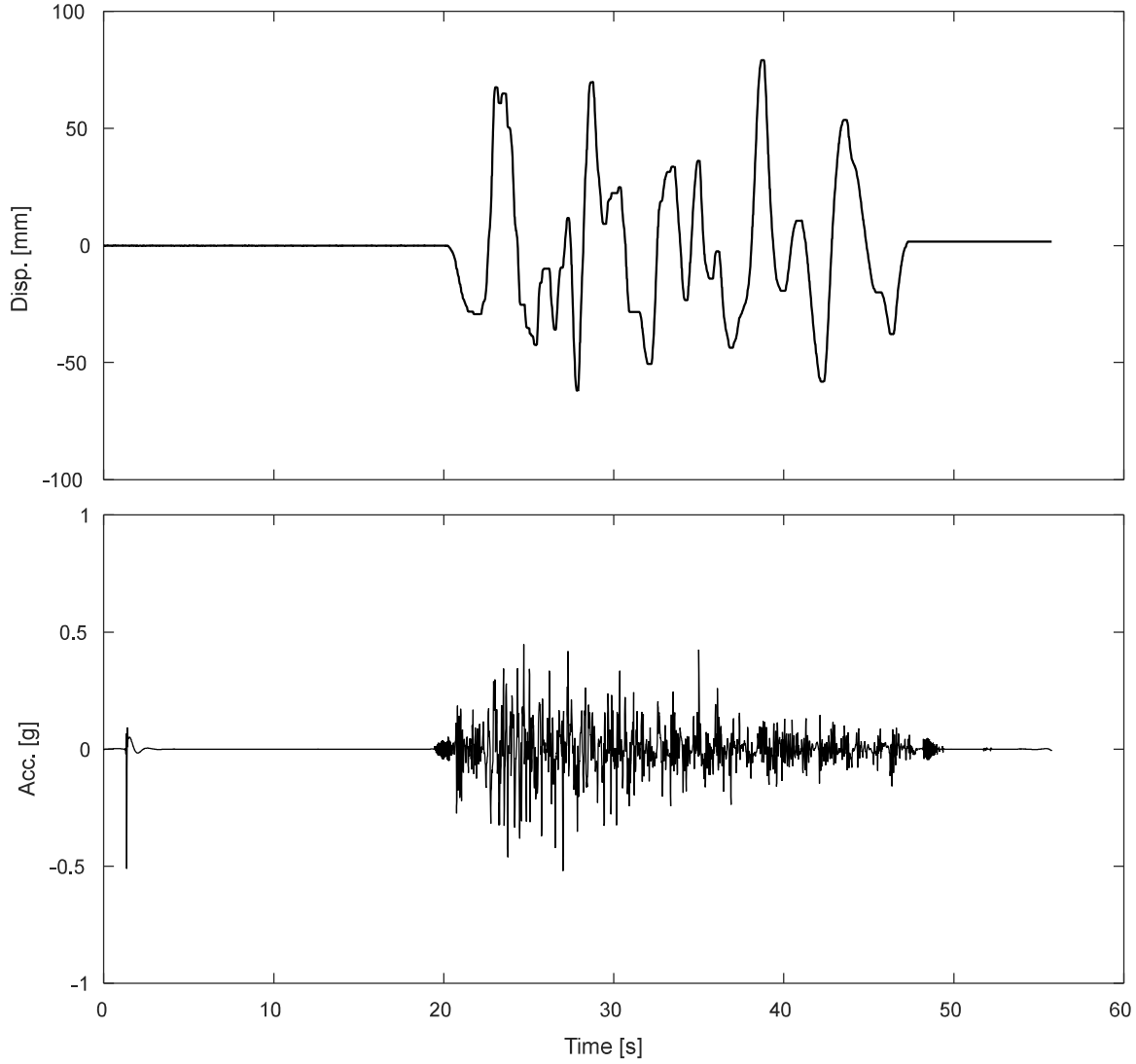

Figure K.9-1. Measured input displacement and acceleration at the base of the specimen during DT03-NOR-100P motion

K.9.1 Accelerometers.

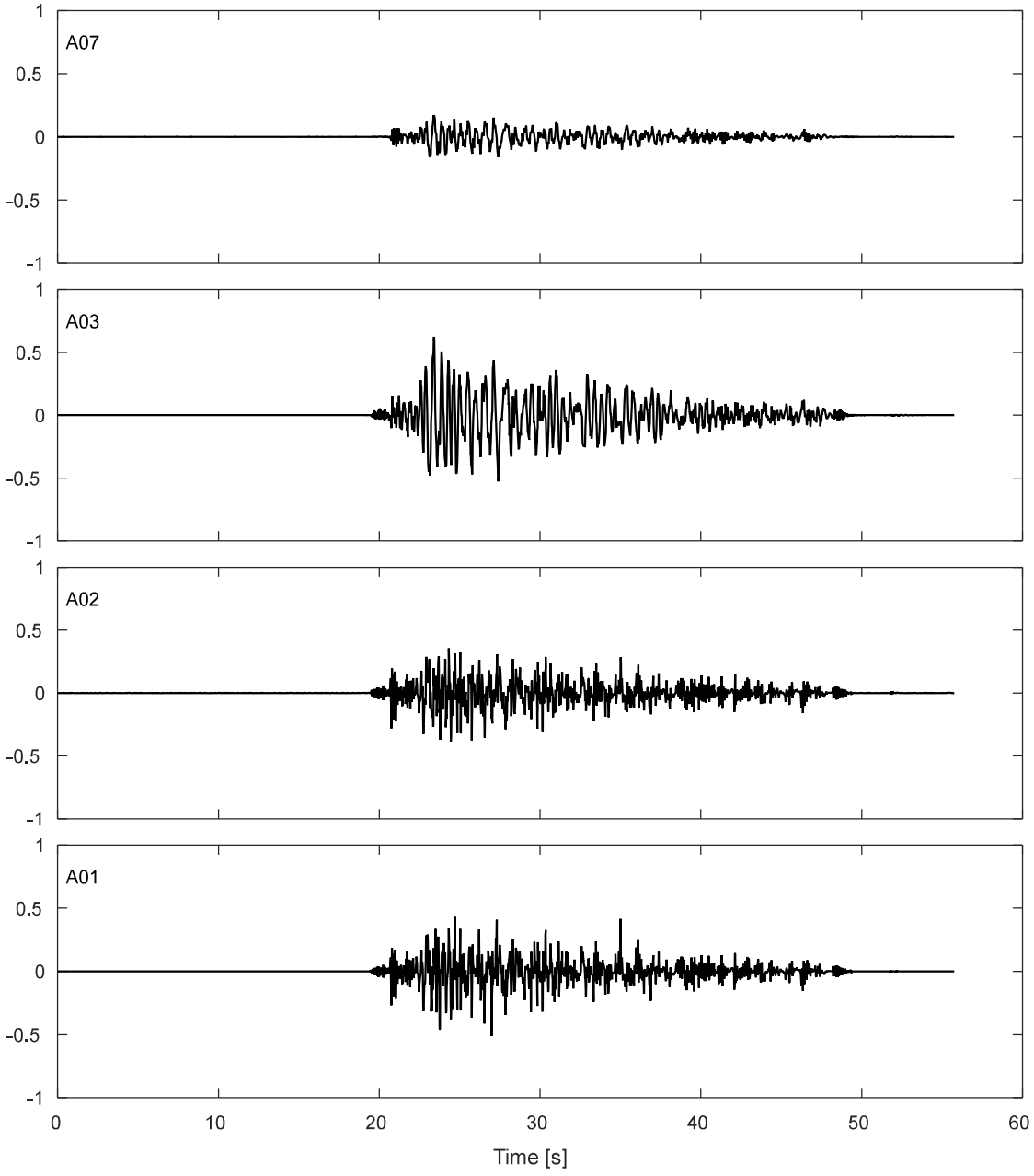

Figure K.9-2. Accelerations results along TDA during DT03-NOR-100P motion.

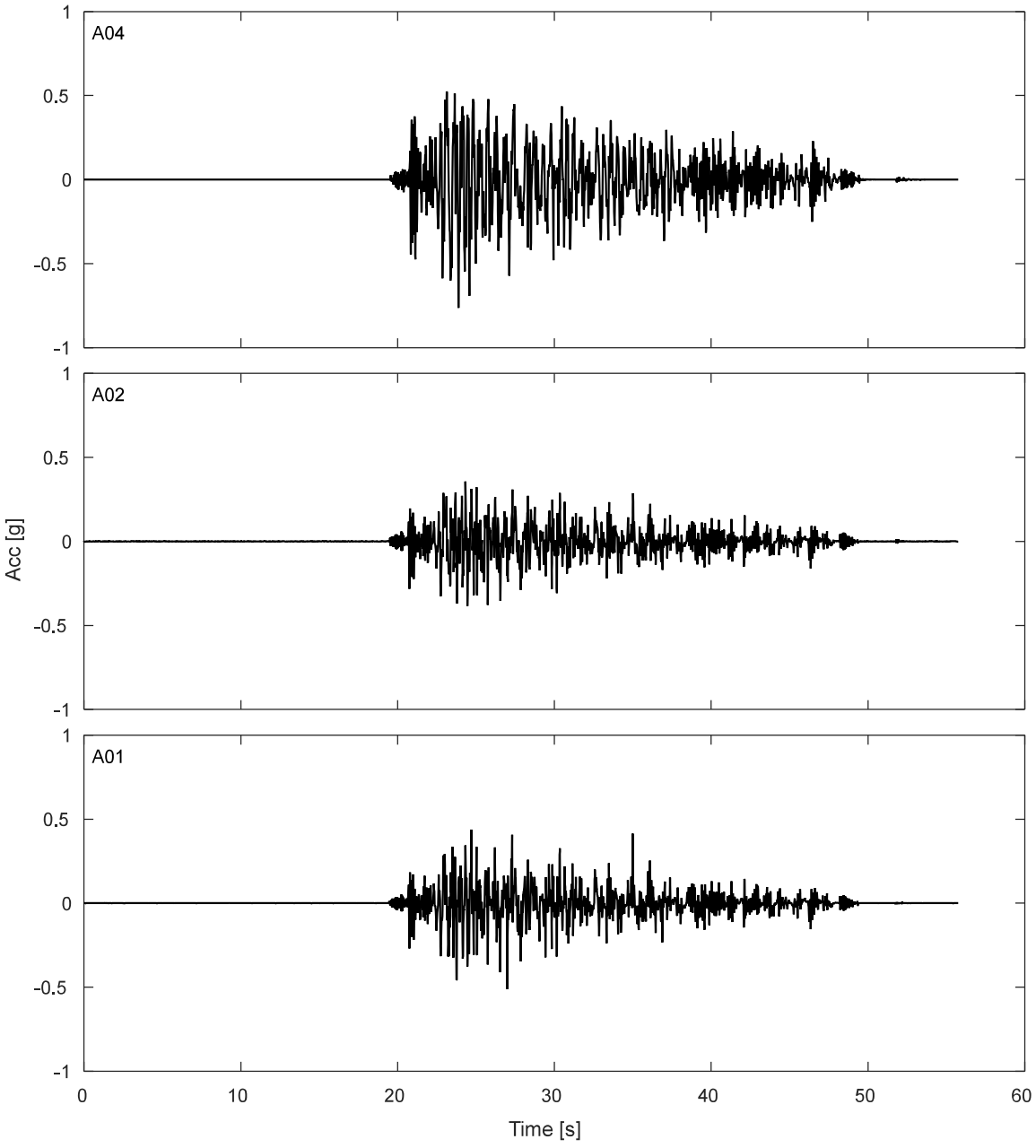

Figure K.9-3. Free field accelerations results for TDA during DT03-NOR-100P motion.

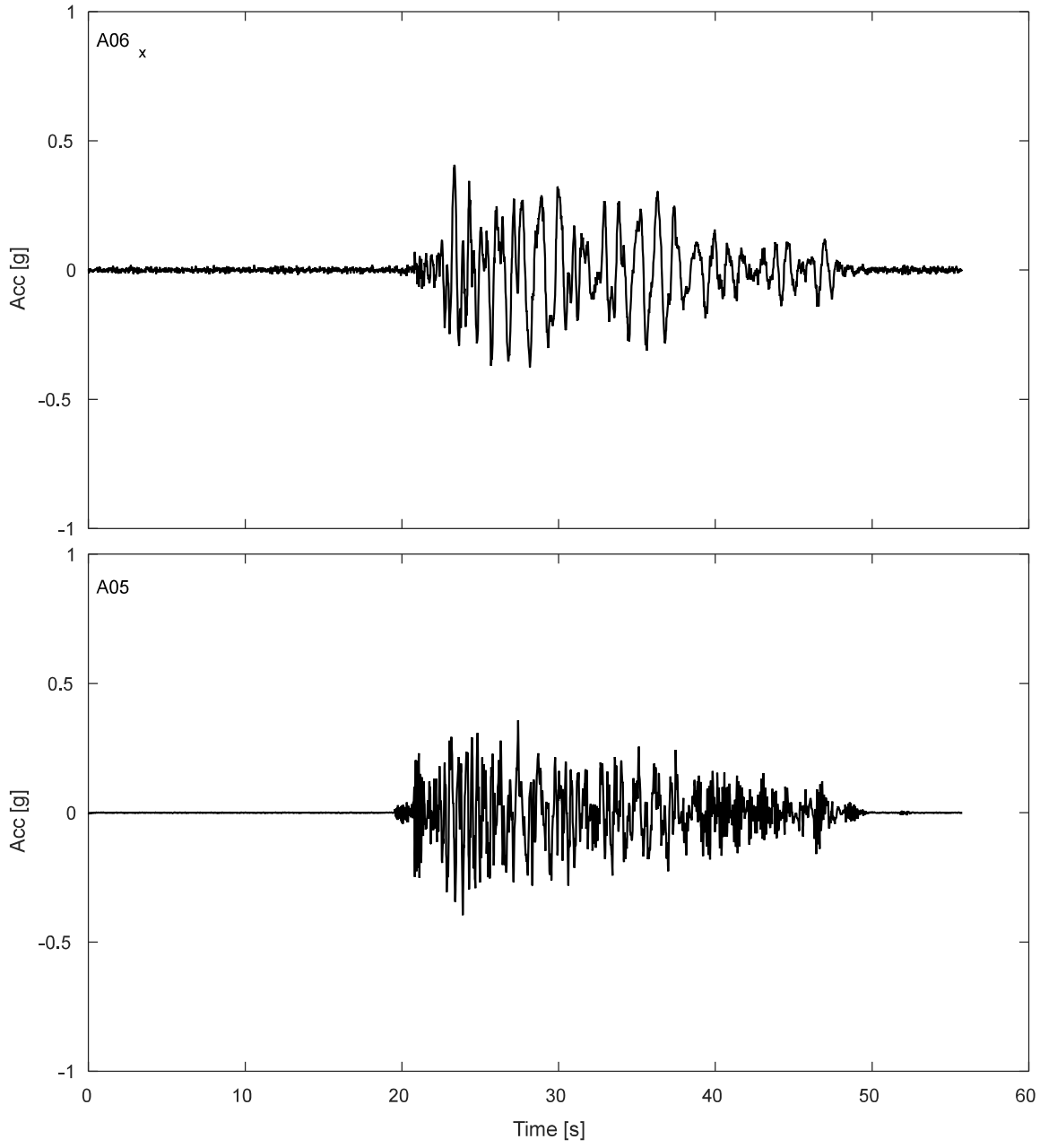

Figure K.9-4. Accelerations results SDOF structure during DT03-NOR-100P motion.

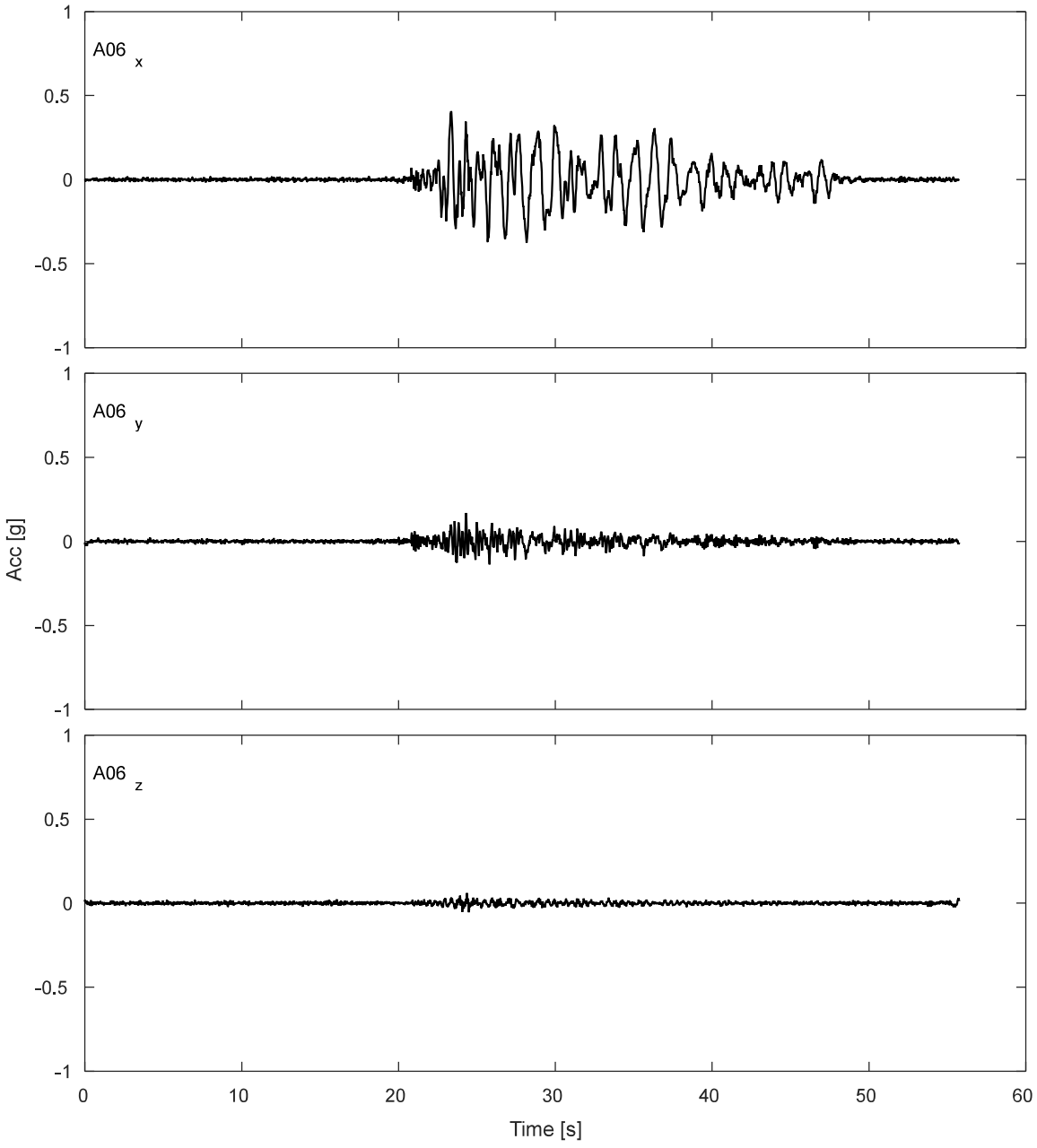

Figure K.9-5. Accelerations results for lumped mass of SDOF structure during DT03-NOR-100P motion.

K.9.2 Potentiometers.

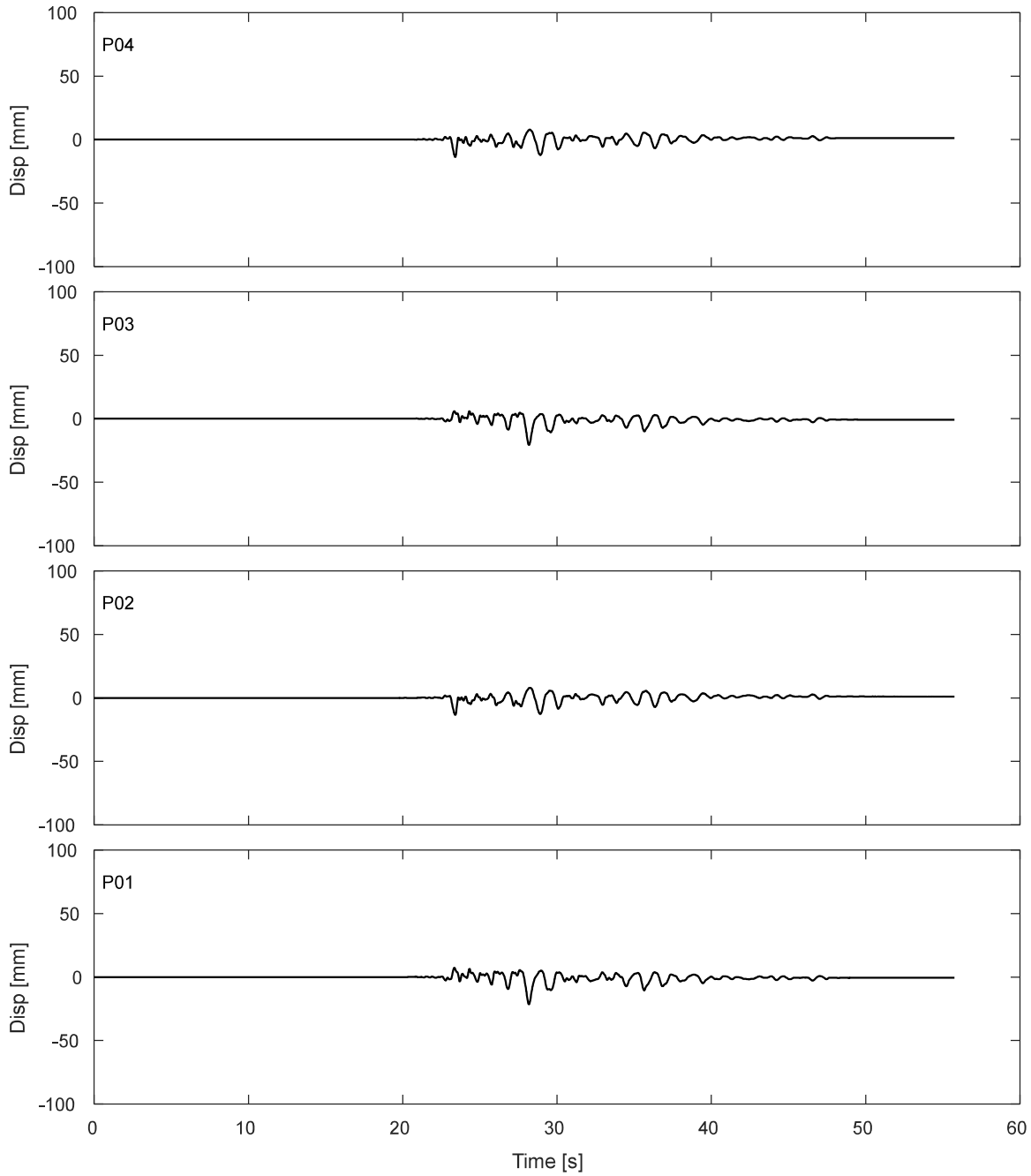

Figure K.9-6. Results of fully vertical potentiometers attached to corners of top of strip footing during DT03-NOR-100P motion.

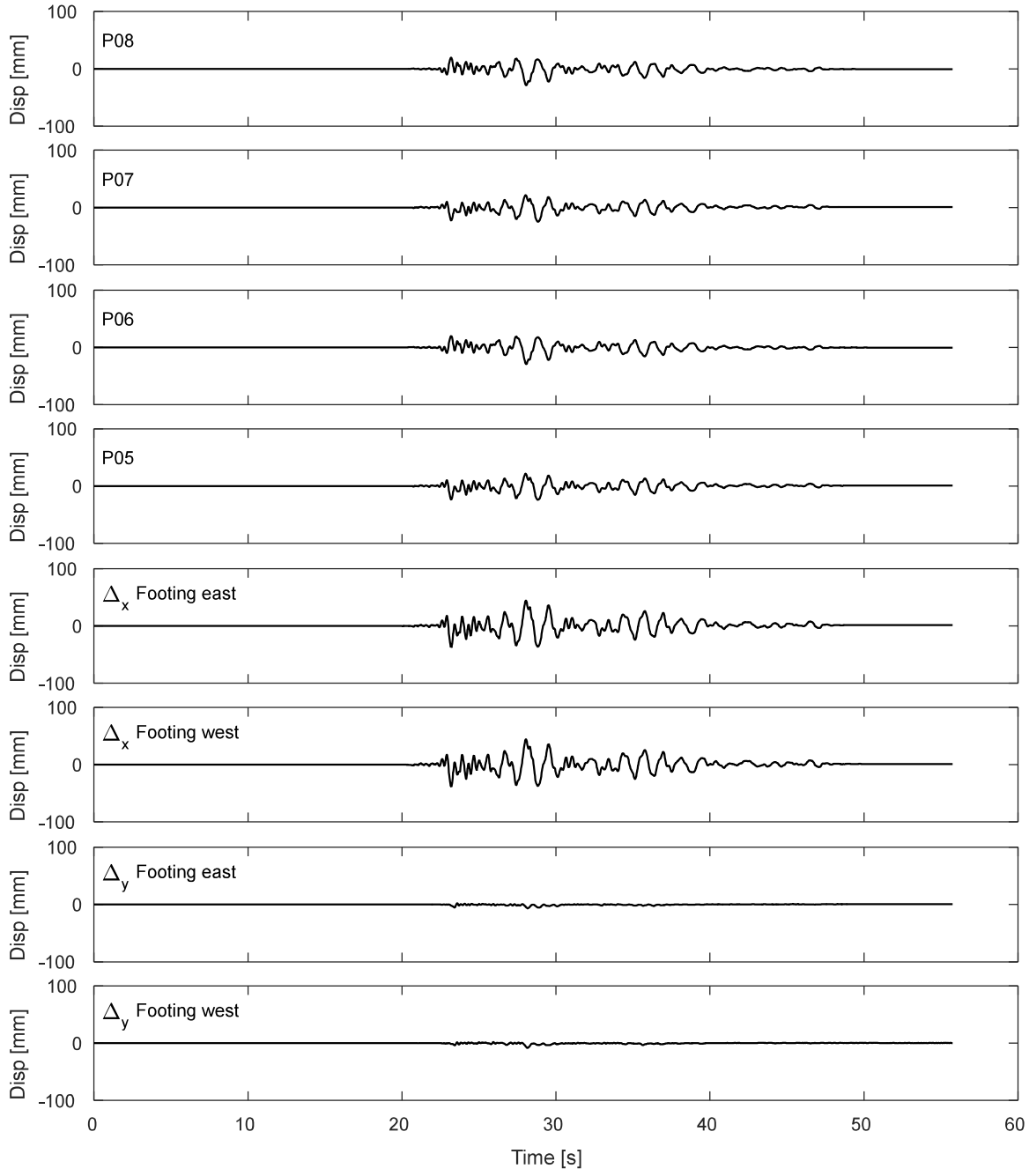

Figure K.9-7. Results of inclined potentiometers attached to top of strip footing during DT03-NOR-100P motion.

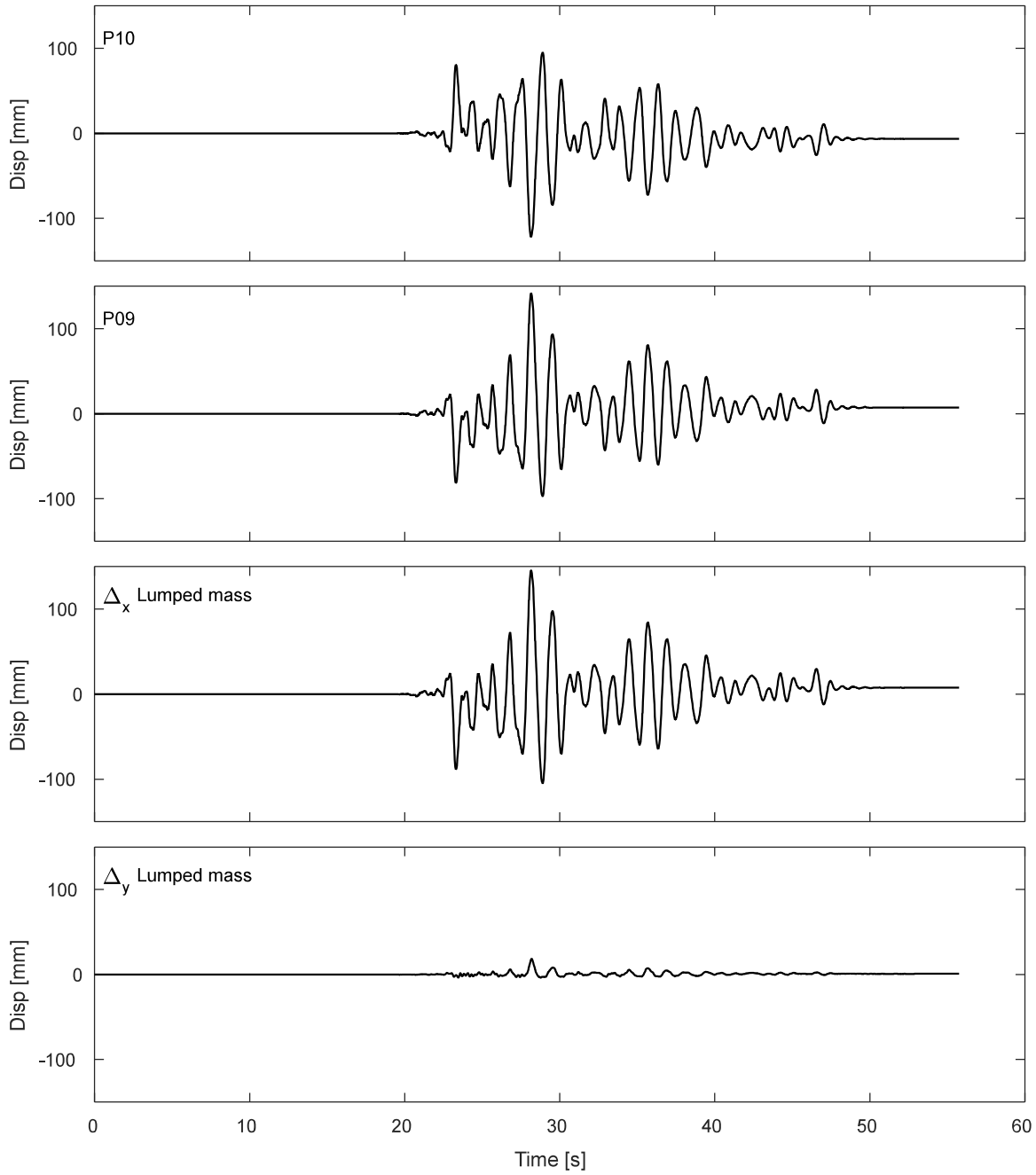

Figure K.9-8. Results of inclined potentiometers attached to lumped mass during DT03-NOR-100P motion.

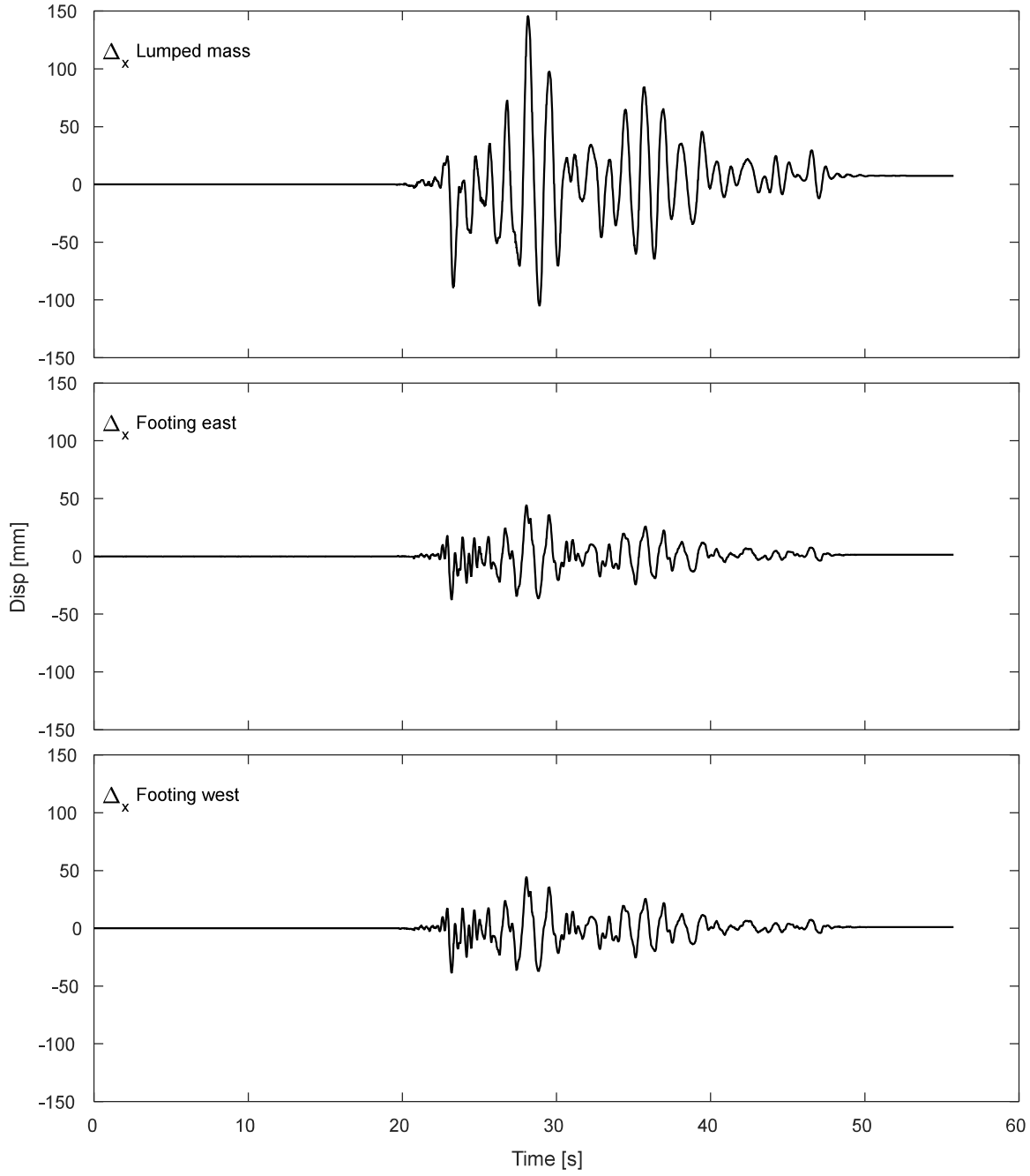

Figure K.9-9. Results of horizontal displacement of lumped mass and footing during DT03-NOR-100P motion.

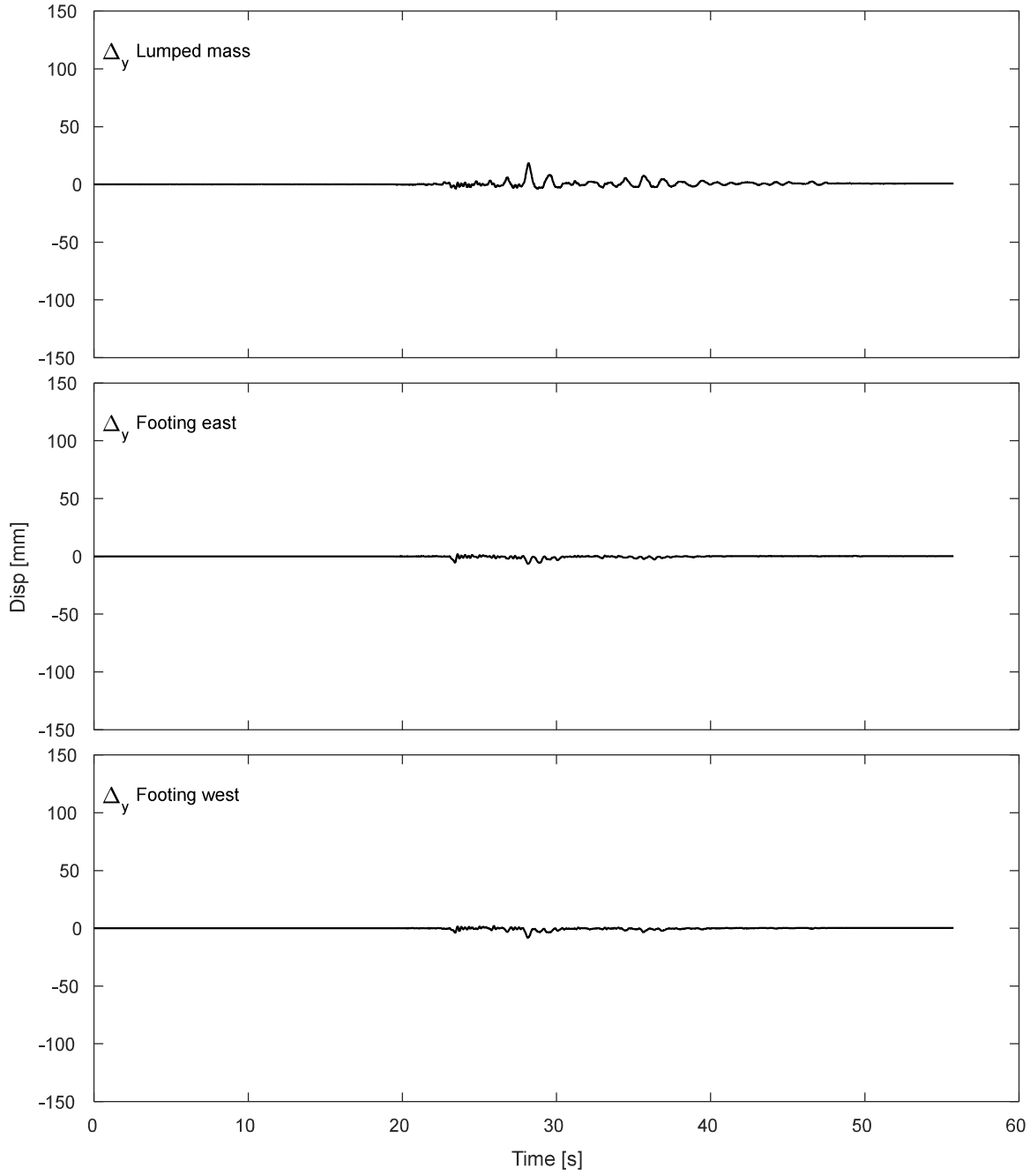

Figure K.9-10. Results of vertical displacement of lumped mass and footing during DT03-NOR-100P motion.

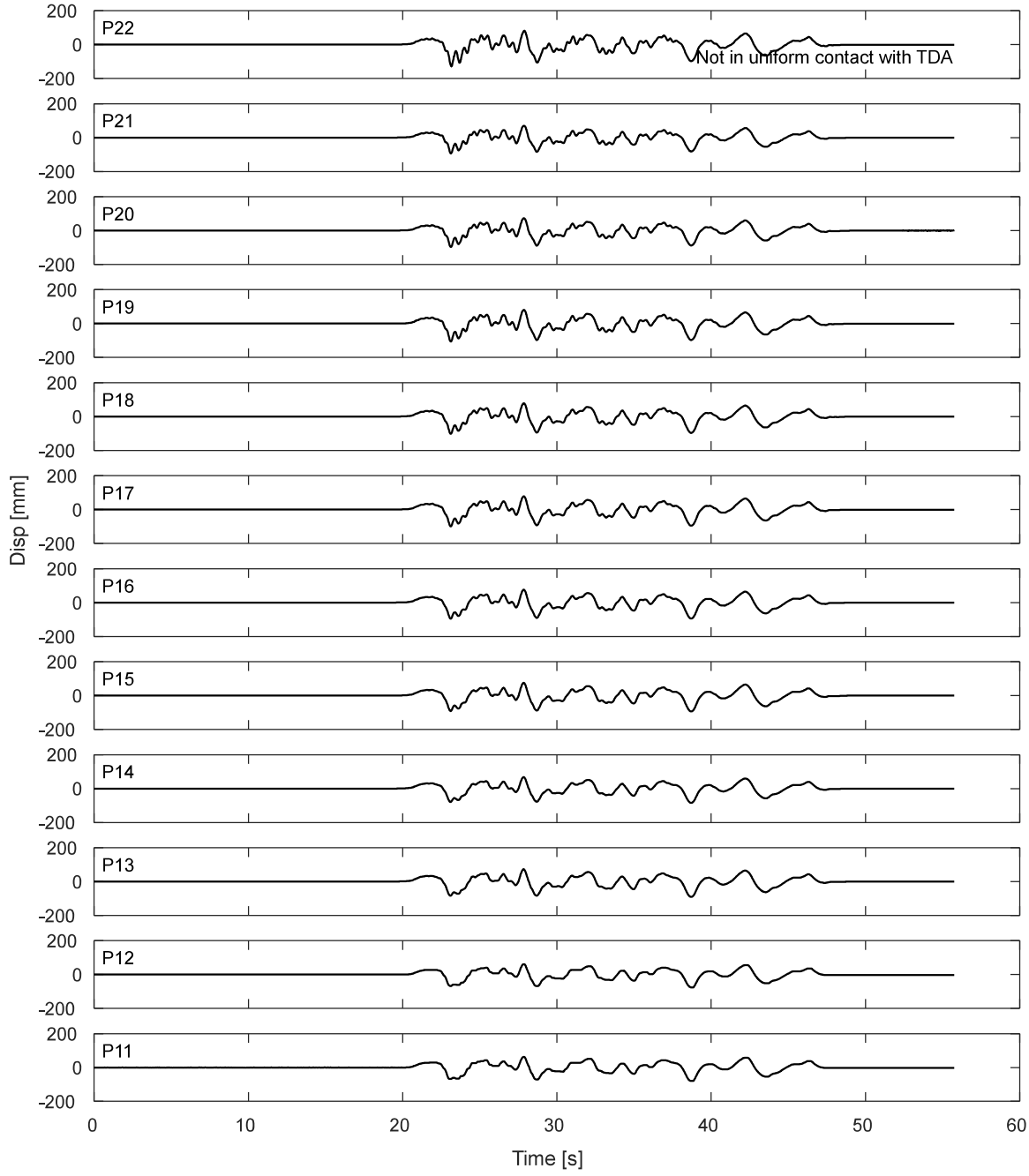

Figure K.9-11. Potentiometers results for the laminar box during DT03-NOR-100P motion.

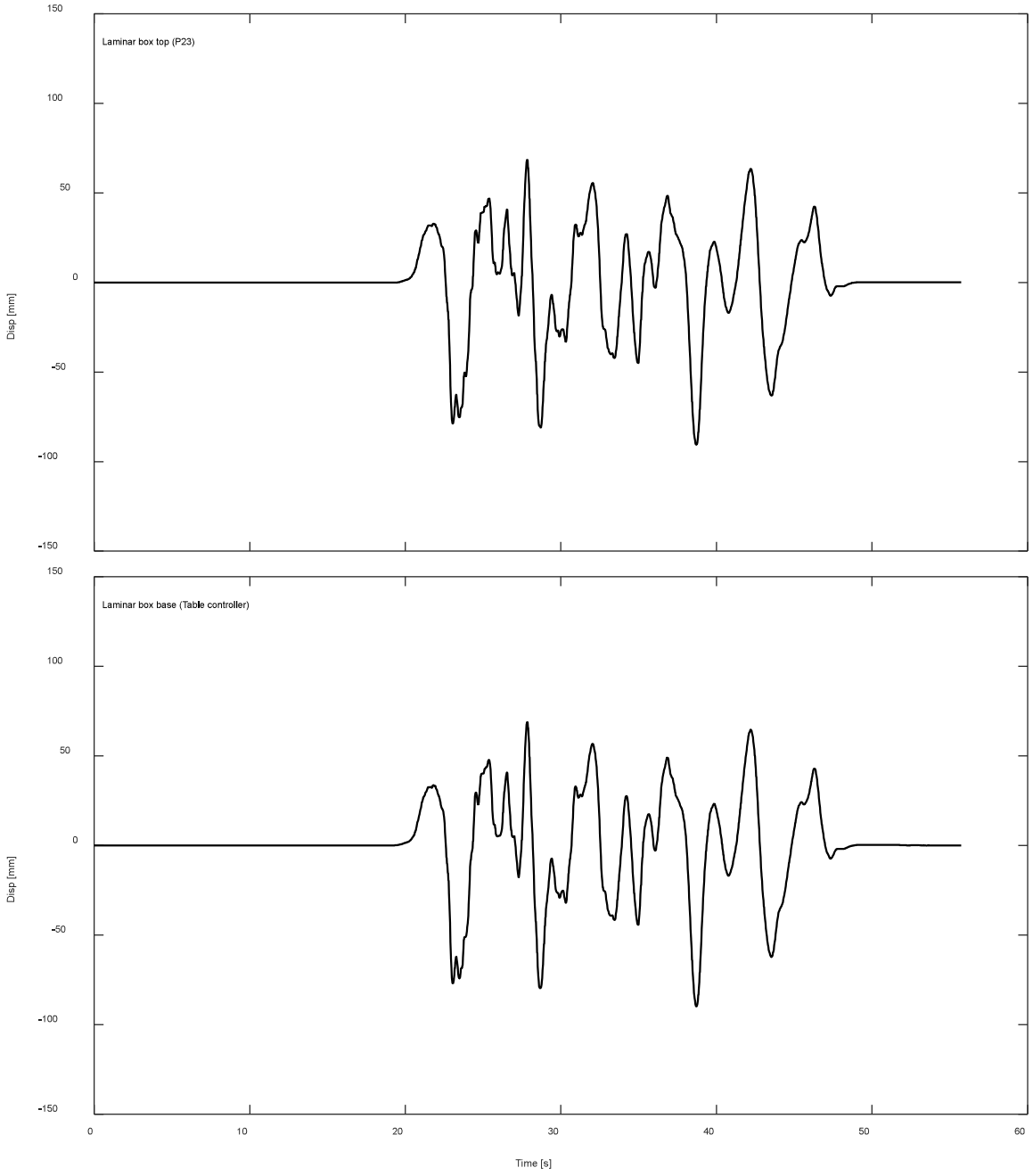

Figure K.9-12. Displacement response of top and base of laminar box during DT03-NOR-100P motion.

K.9.3. Inclinometers.

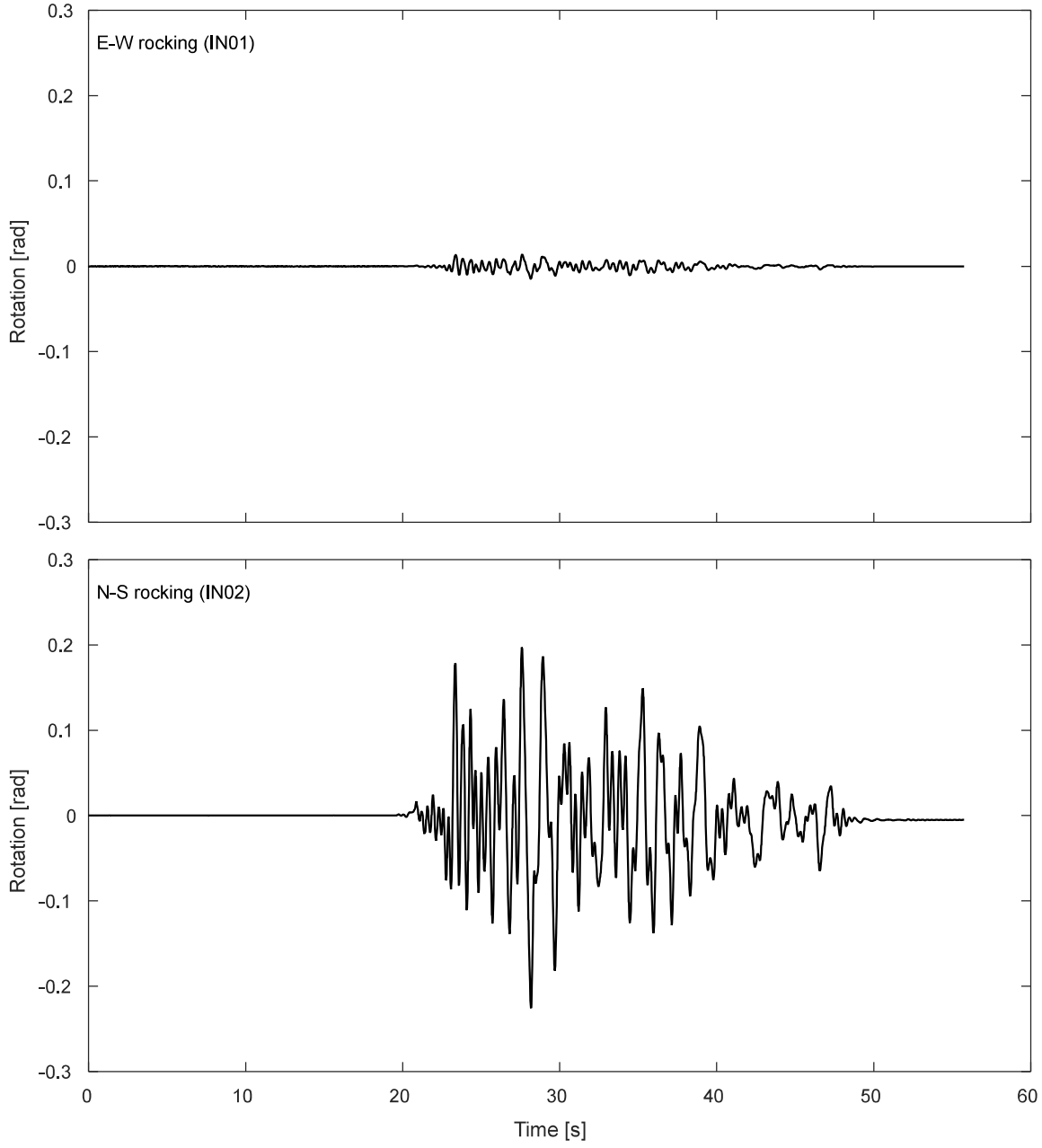

Figure K.9-13. Inclinometer results for the footing during DT03-NOR-100P motion.

K.9.4. Pressure cells.

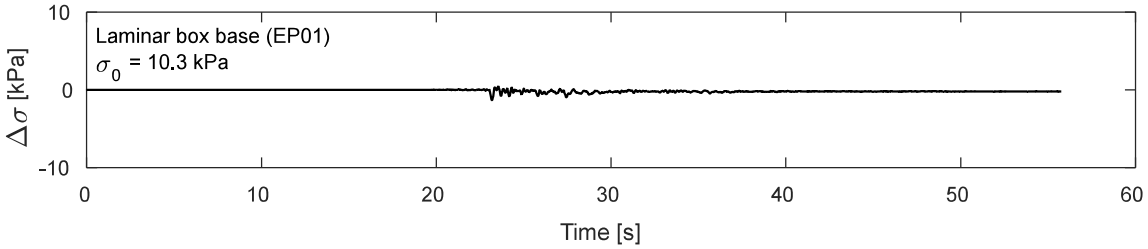

Figure K.9-14. Pressure cells results at laminar box base during DT03-NOR-100P motion.

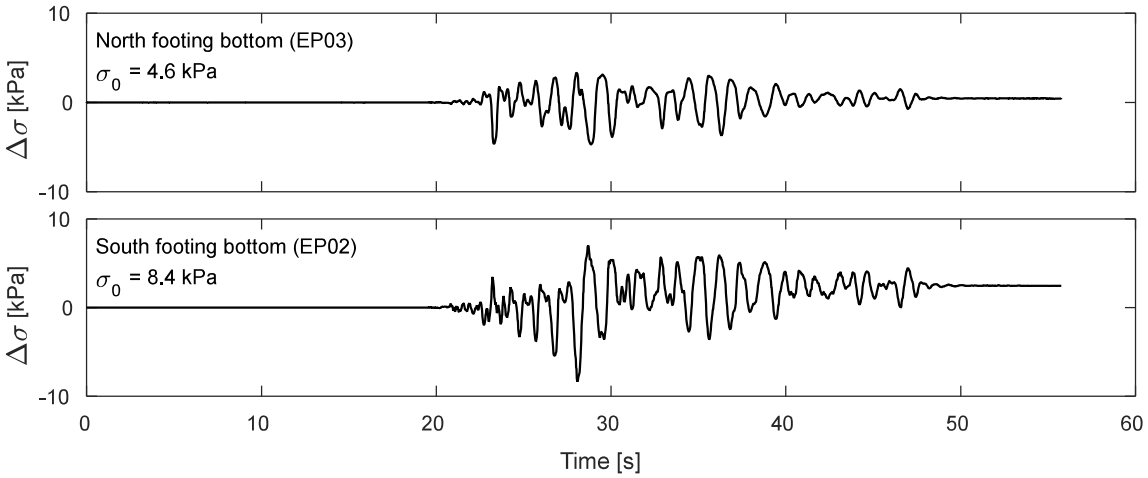

Figure K.9-15. Pressure cells results at footing bottom during DT03-NOR-100P motion.

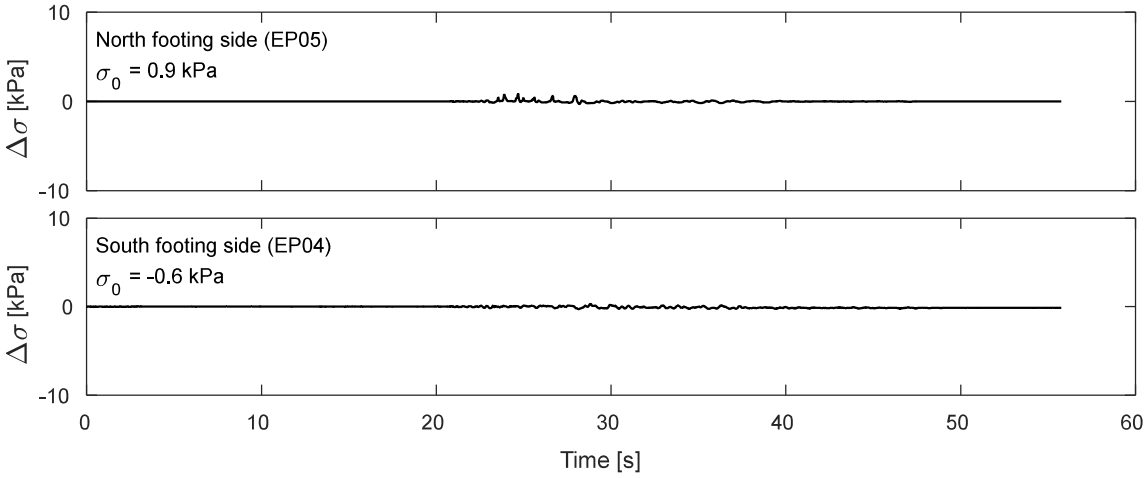

Figure K.9-16. Pressure cells results at footing sides during DT03-NOR-100P motion.

K.10. Time-history Records for DT03-MAU-100P motion.

K.10.1 Input Motion

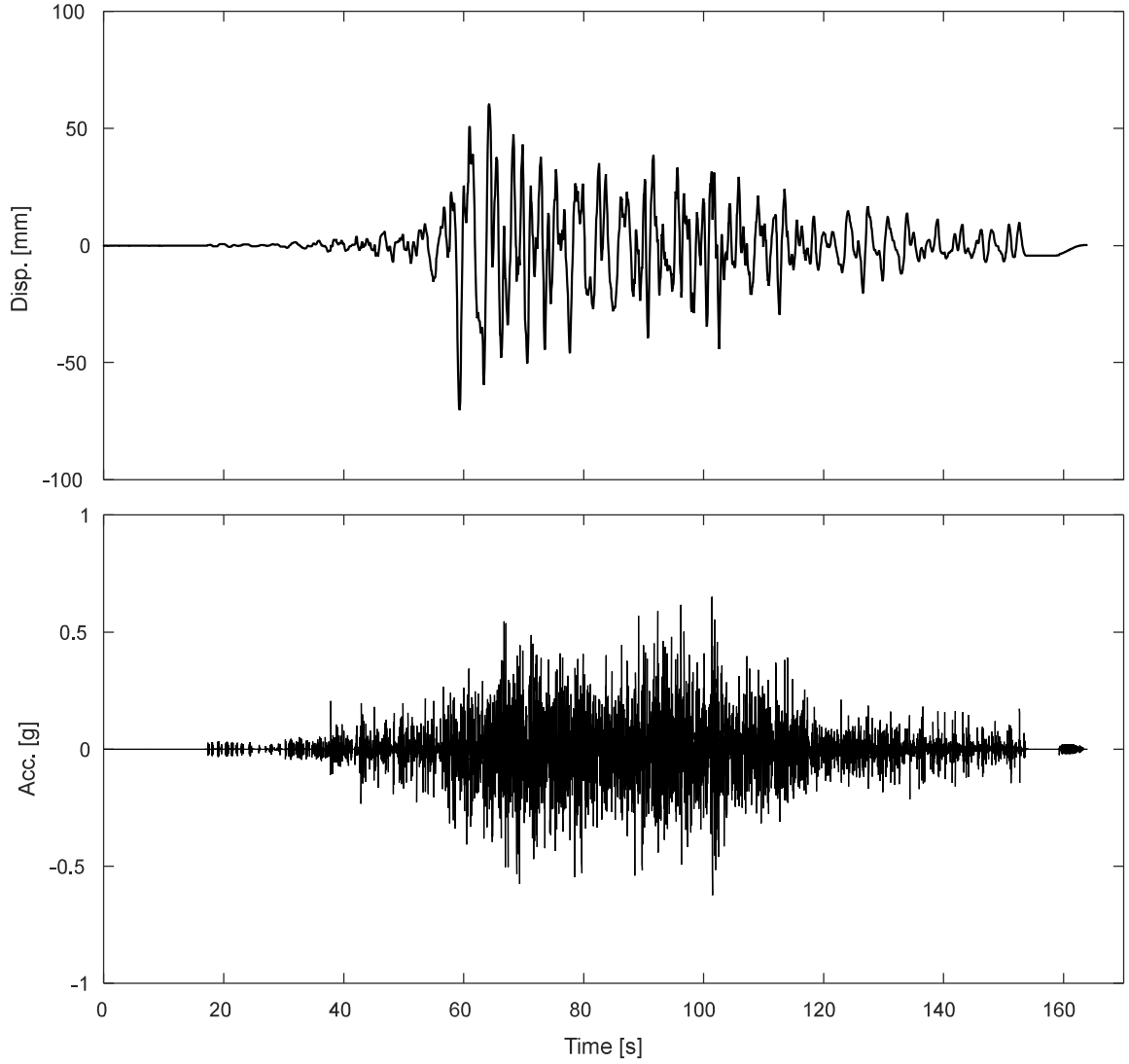

Figure K.10-1. Measured input displacement and acceleration at the base of the specimen during DT03-MAU-100P motion

K.10.1 Accelerometers.

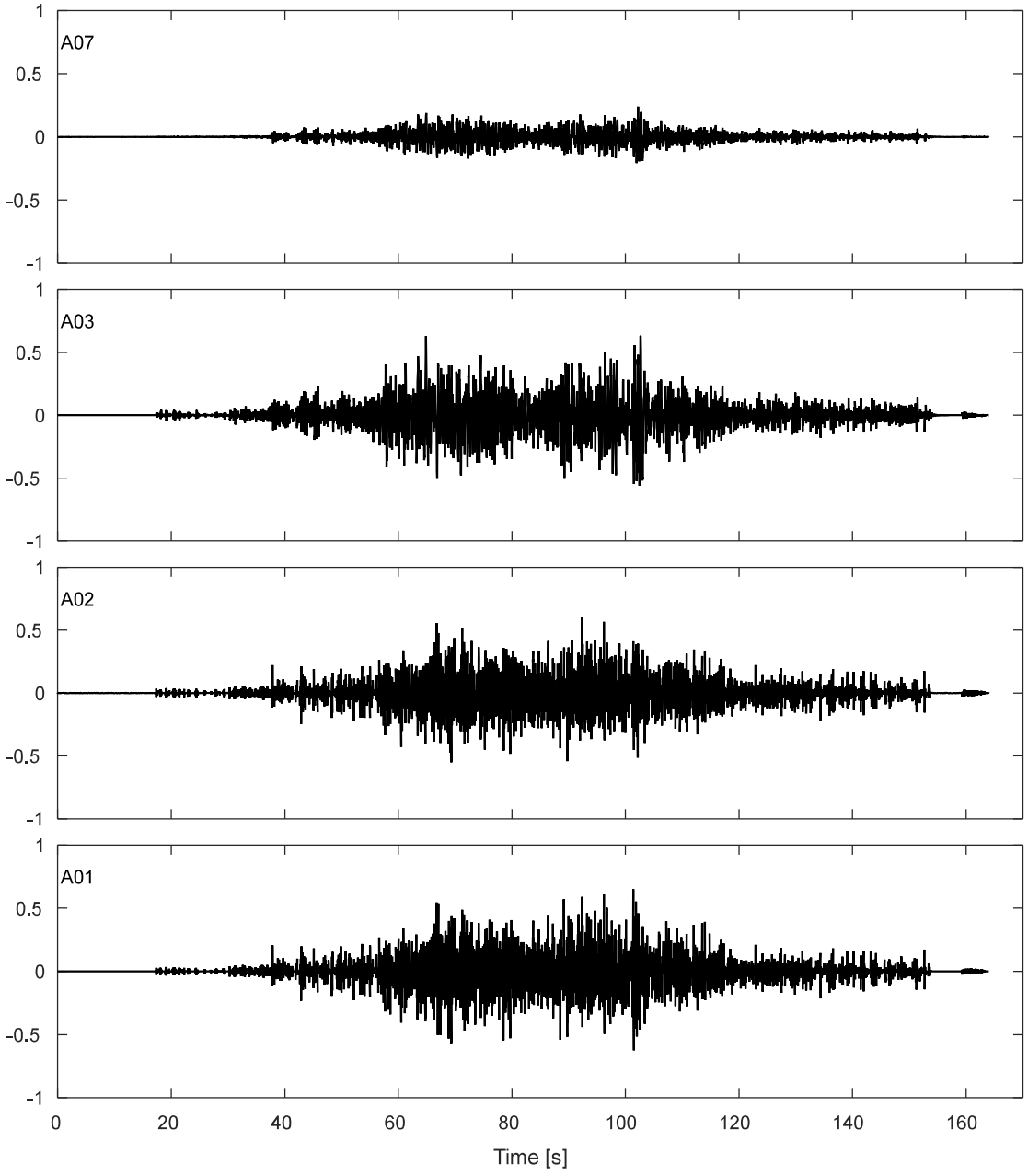

Figure K.10-2. Accelerations results along TDA during DT03-MAU-100P motion.

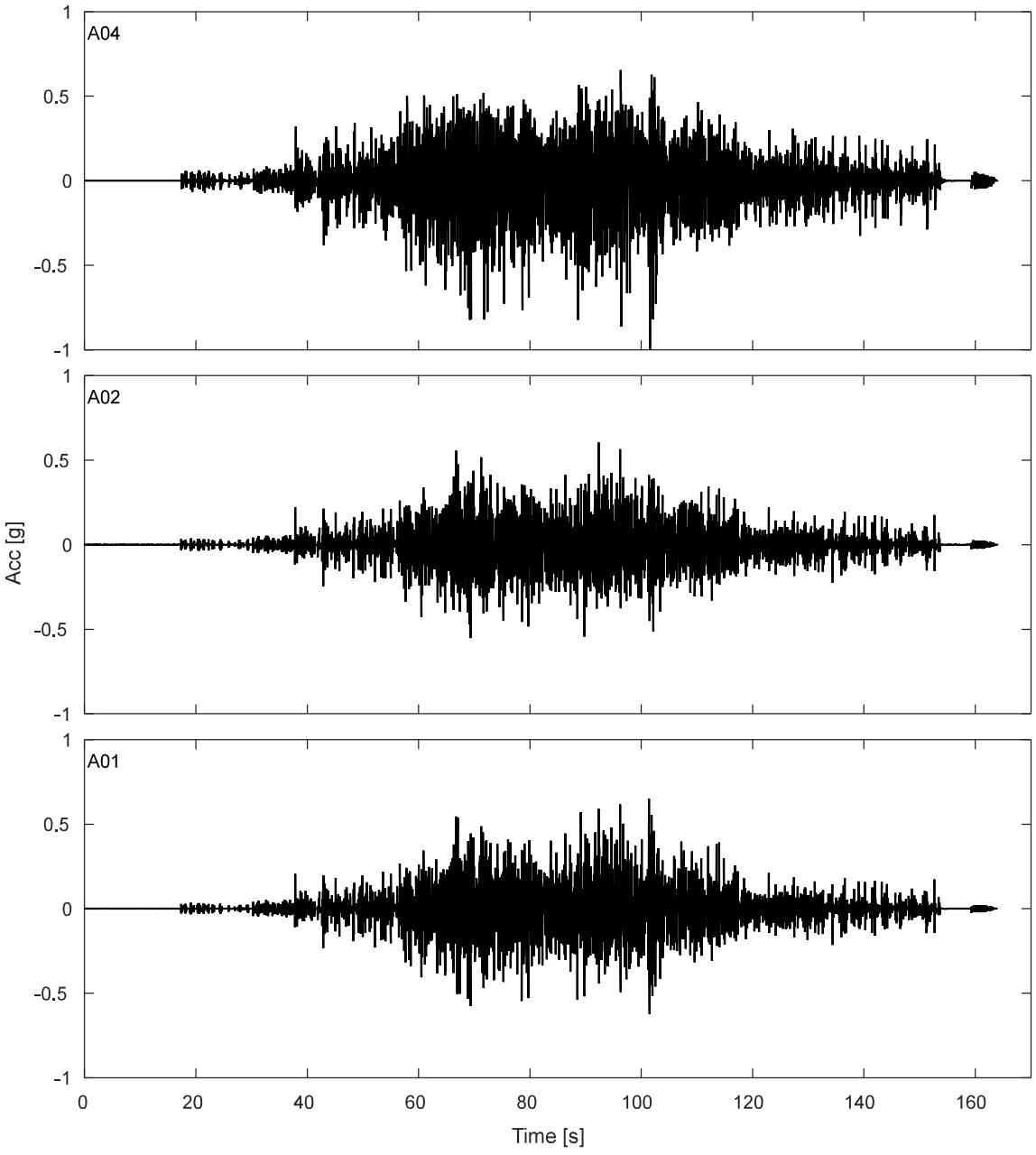

Figure K.10-3. Free field accelerations results for TDA during DT03-MAU-100P motion.

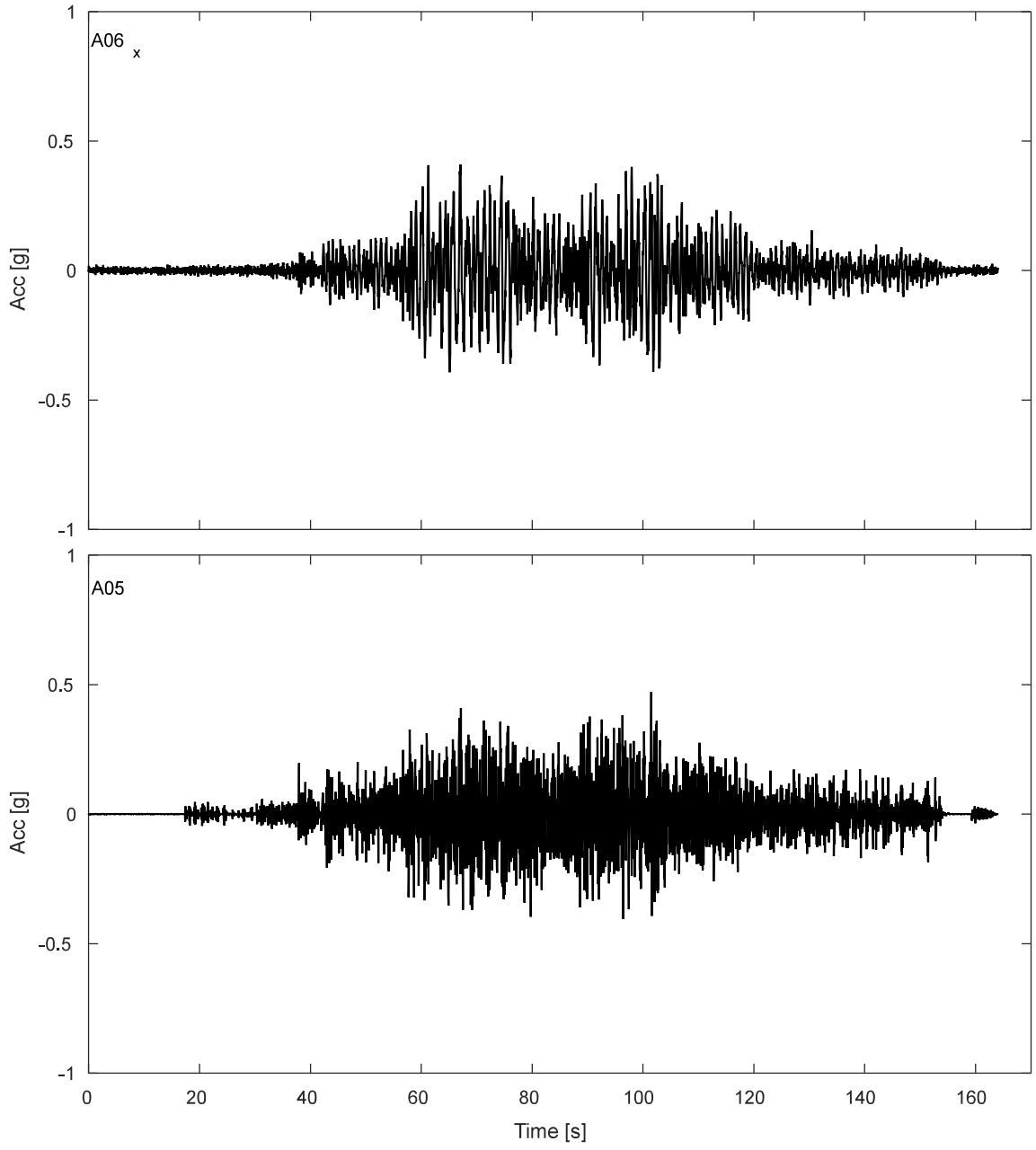

Figure K.10-4. Accelerations results SDOF structure during DT03-MAU-100P motion.

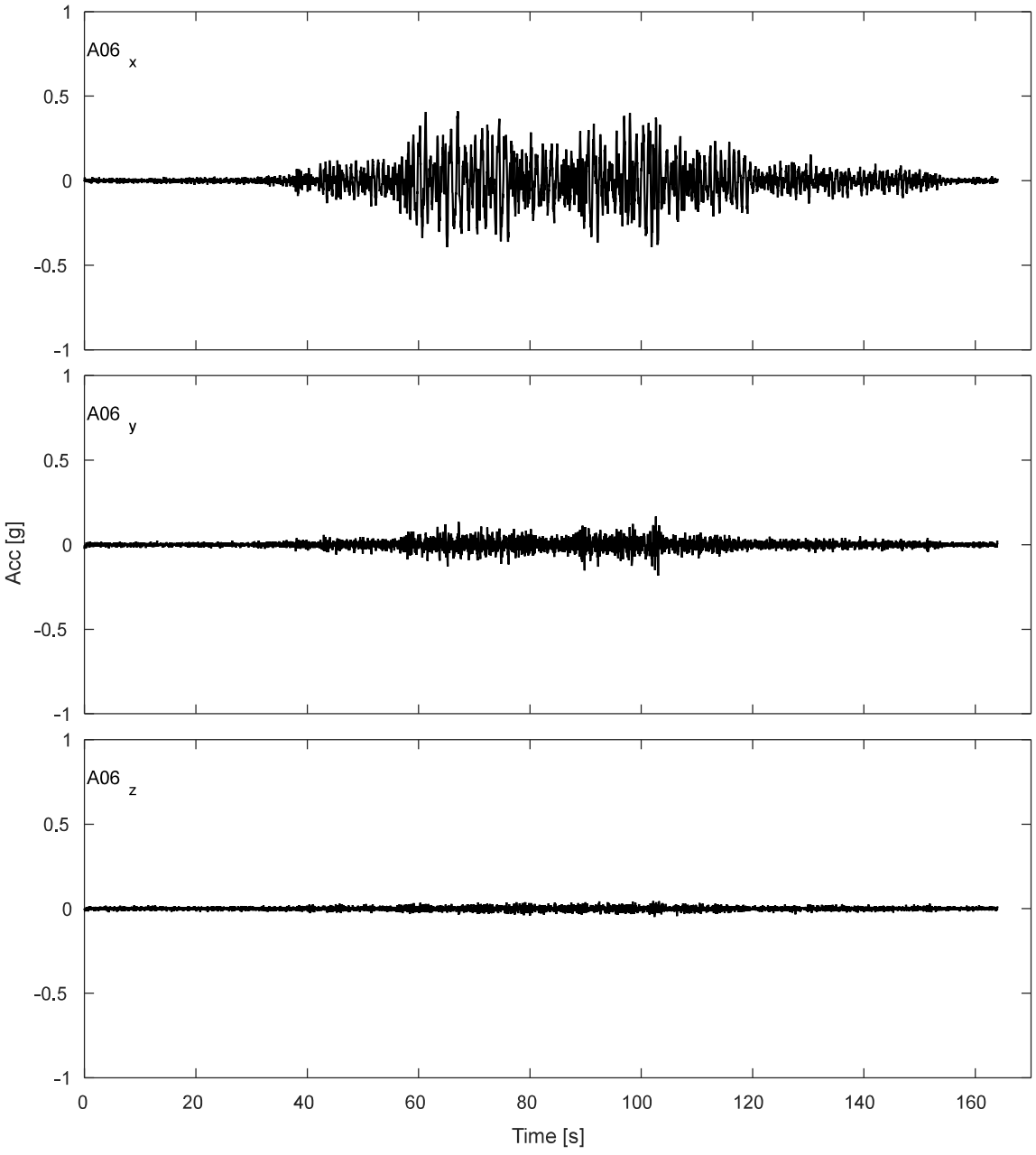

Figure K.10-5. Accelerations results for lumped mass of SDOF structure during DT03-MAU-100P motion.

K.10.2 Potentiometers.

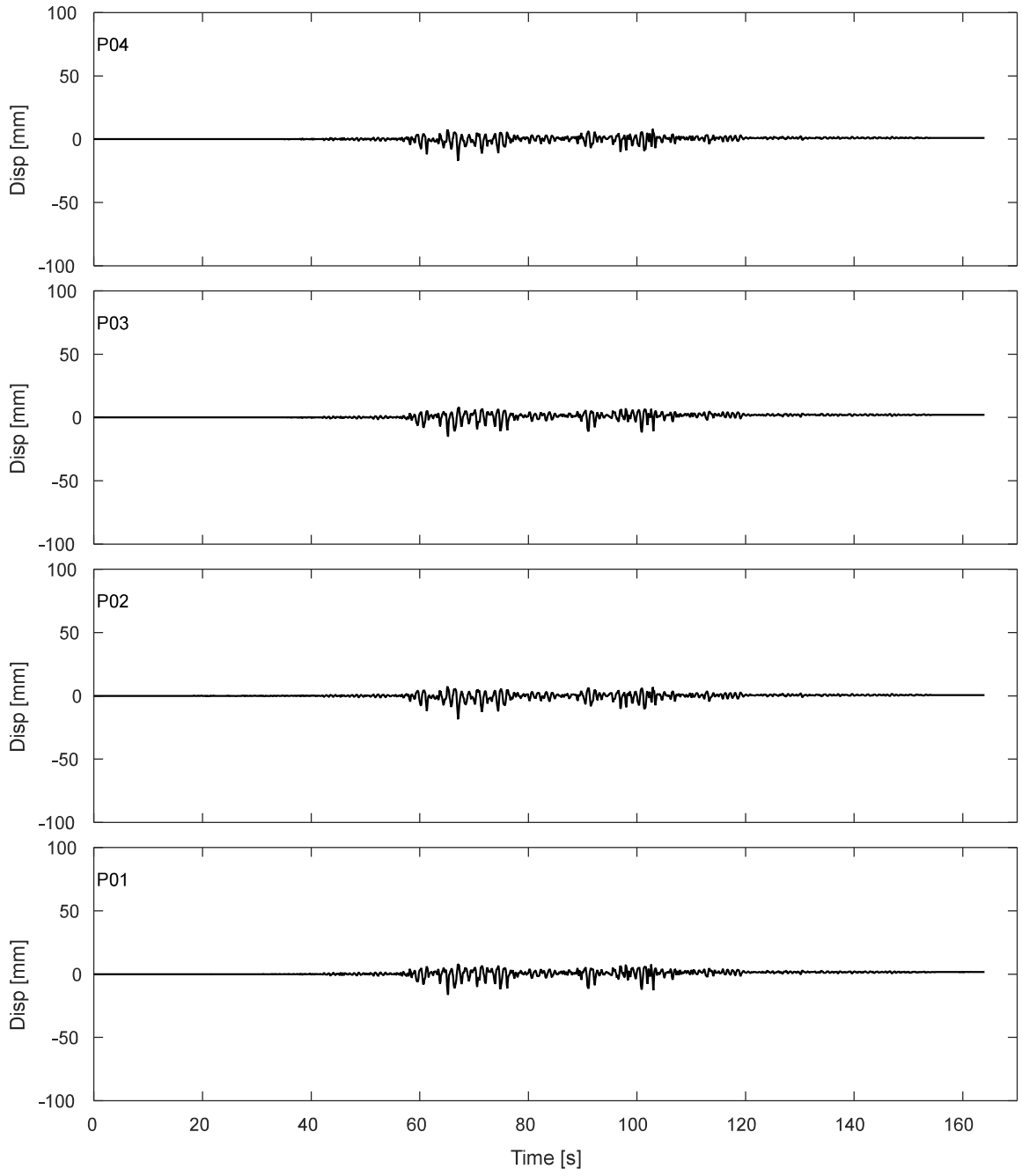

Figure K.10-6. Results of fully vertical potentiometers attached to corners of top of strip footing during DT03-MAU-100P motion.

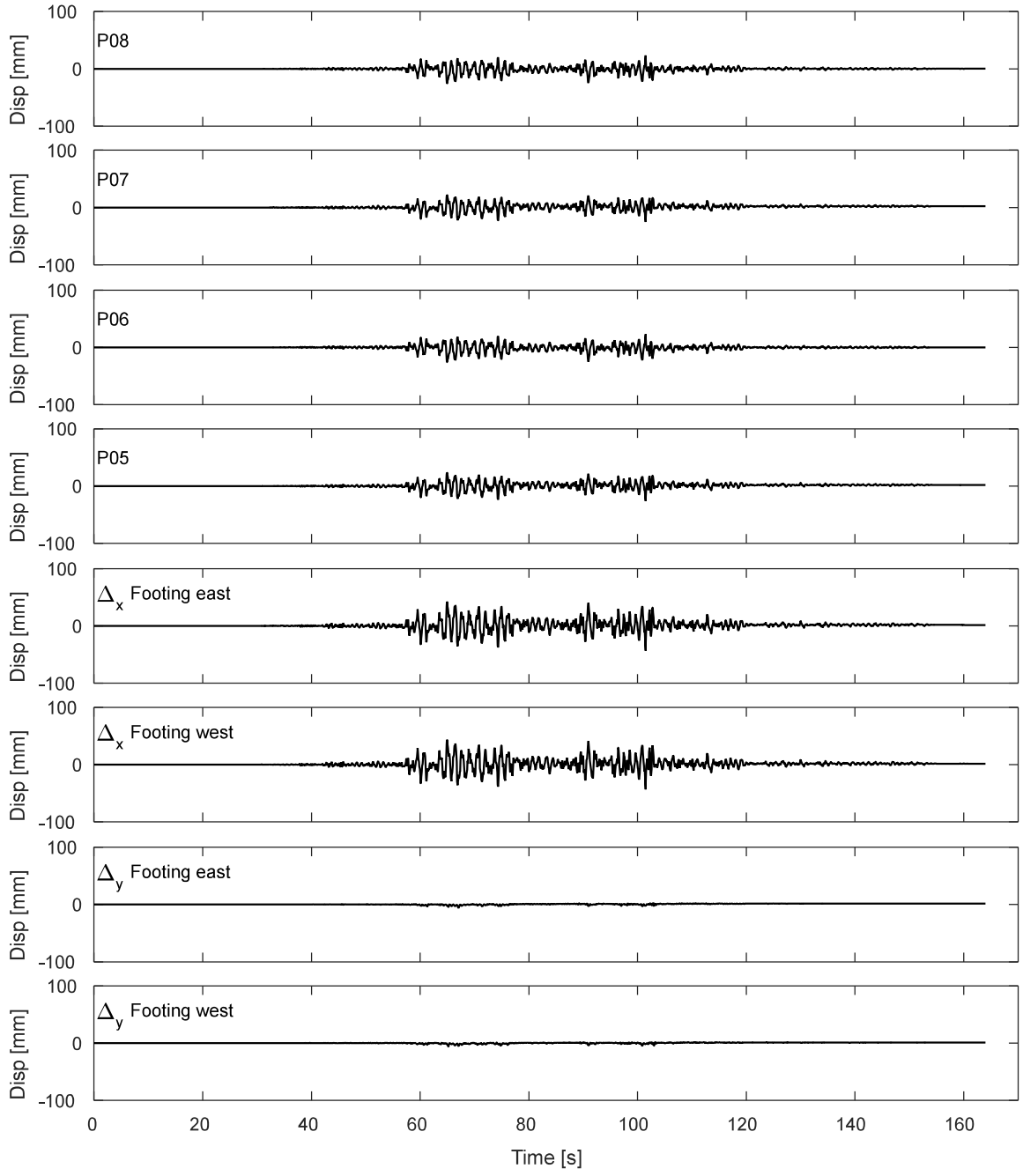

Figure K.10-7. Results of inclined potentiometers attached to top of strip footing during DT03-MAU-100P motion.

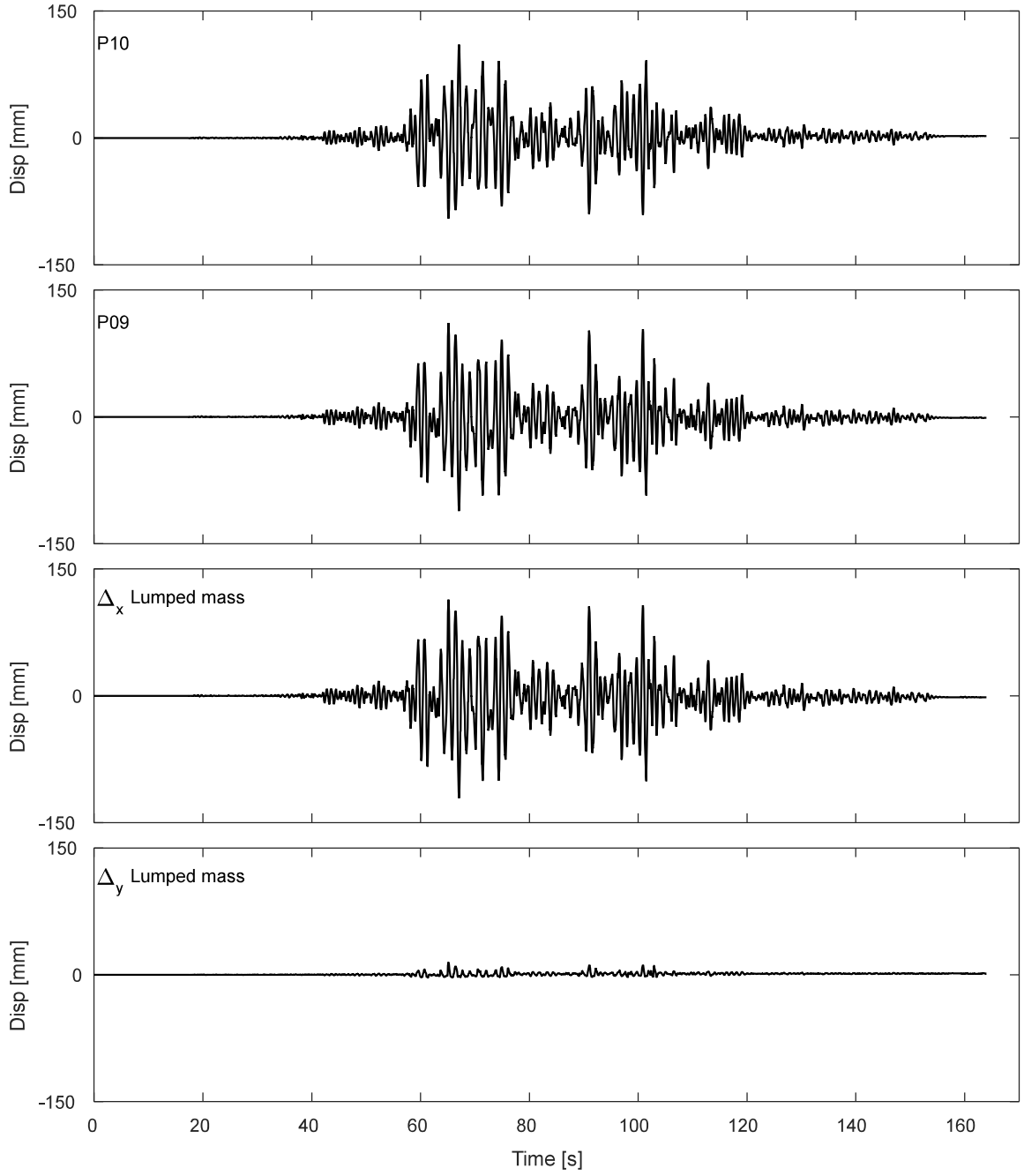

Figure K.10-8. Results of inclined potentiometers attached to lumped mass during DT03-MAU-100P motion.

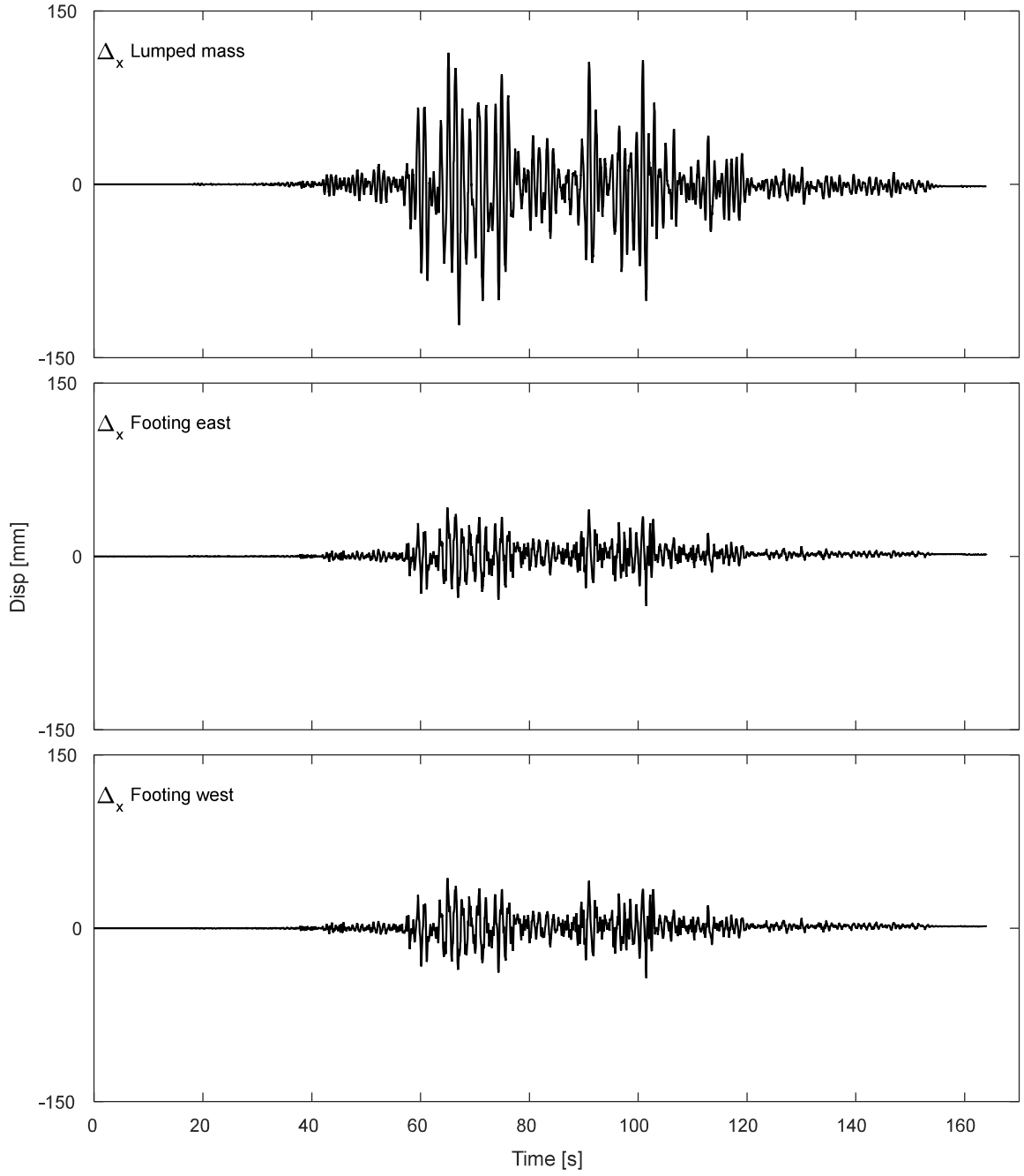

Figure K.10-9. Results of horizontal displacement of lumped mass and footing during DT03-MAU-100P motion.

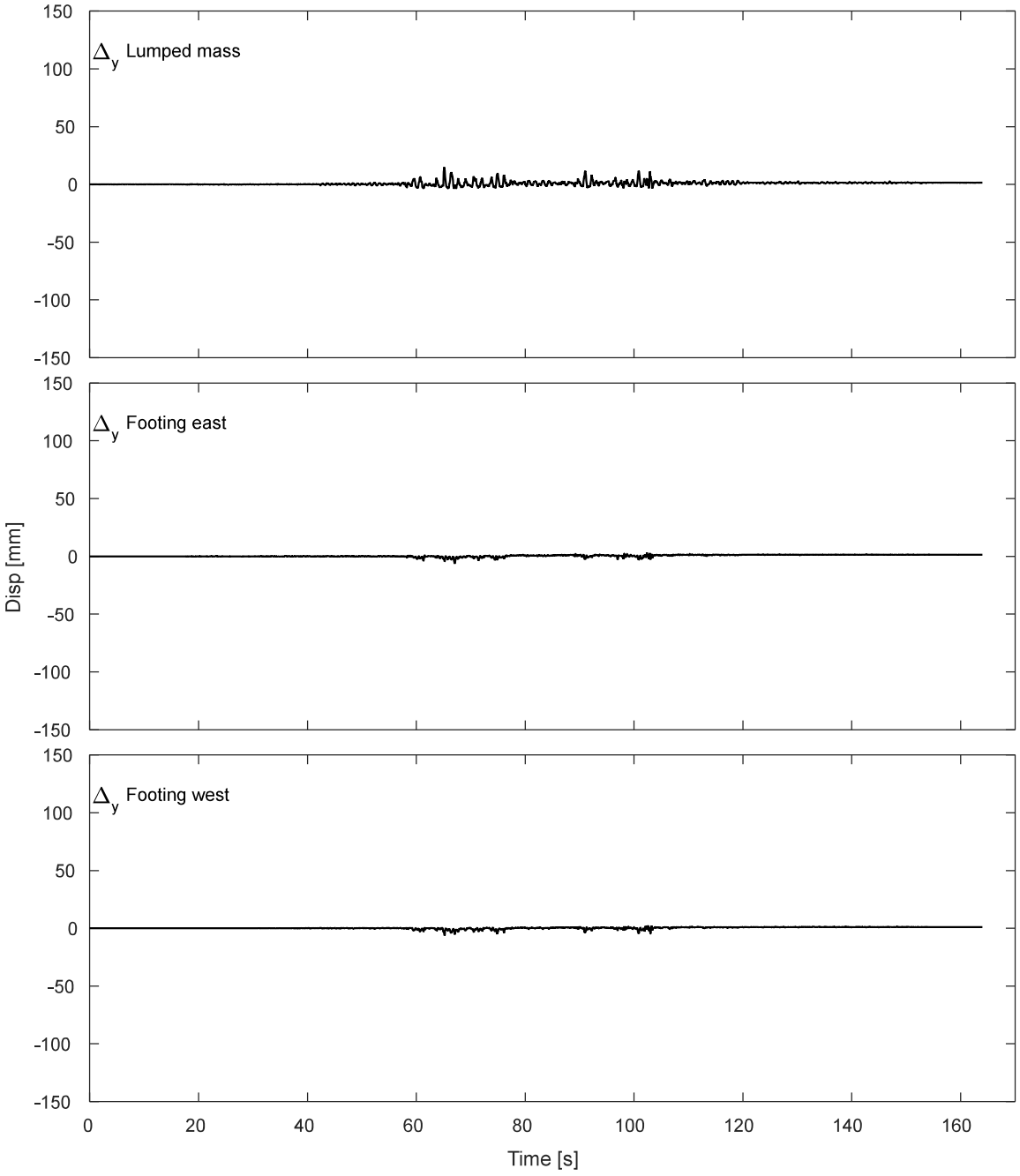

Figure K.10-10. Results of vertical displacement of lumped mass and footing during DT03-MAU-100P motion.

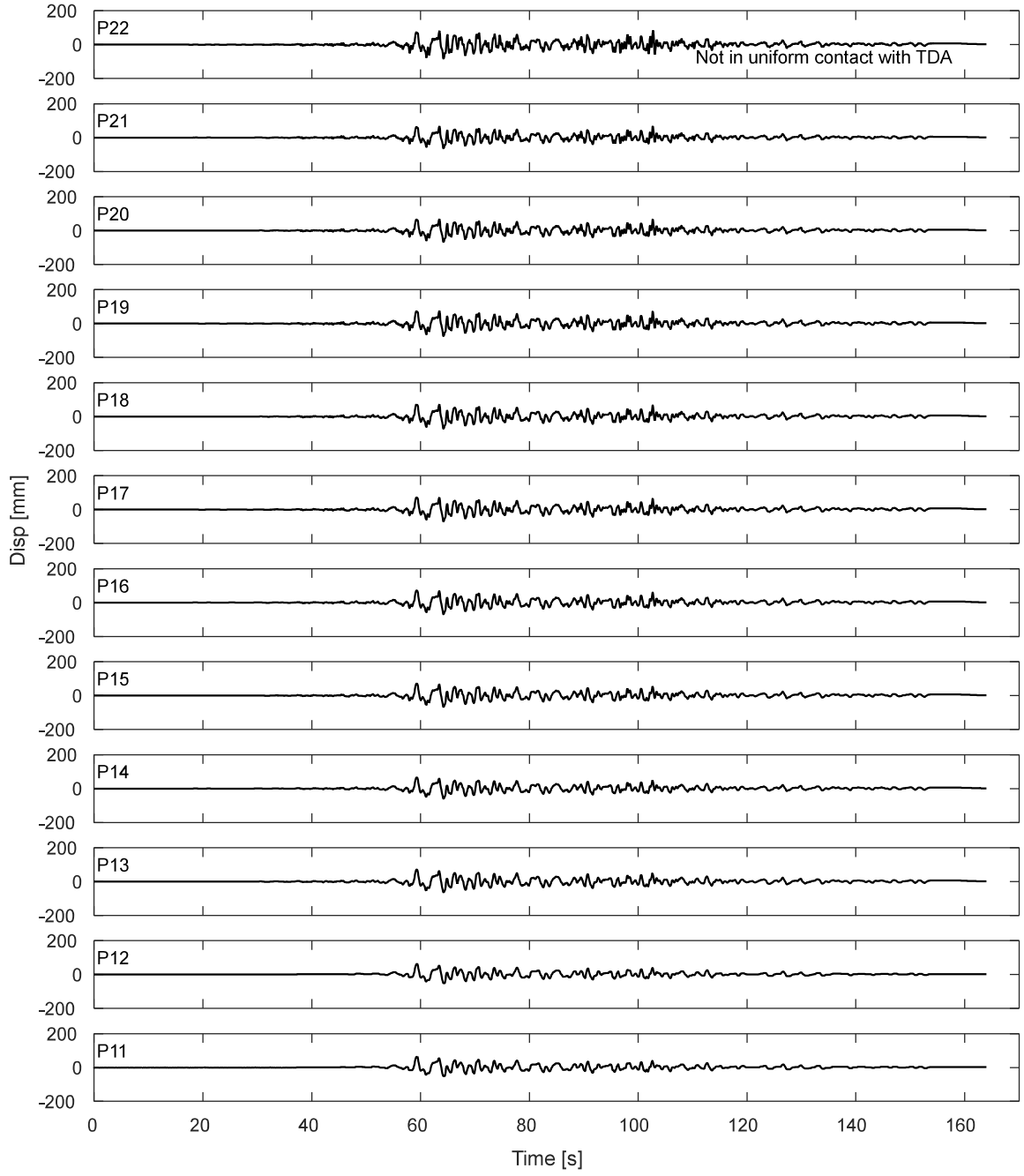

Figure K.10-11. Potentiometers results for the laminar box during DT03-MAU-100P motion.

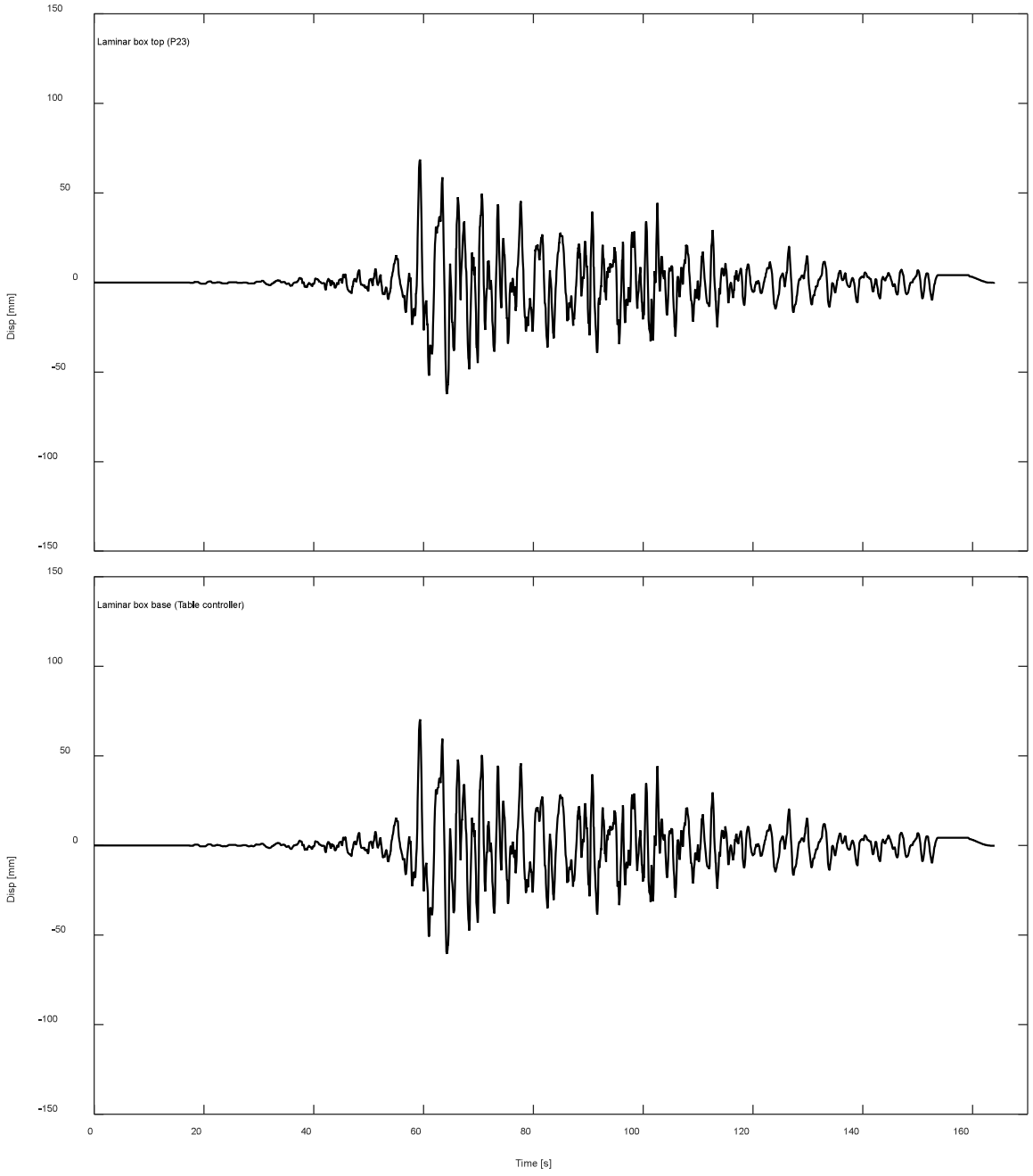

Figure K.10-12. Displacement response of top and base of laminar box during DT03-MAU-100P motion.

K.10.3. Inclinometers.

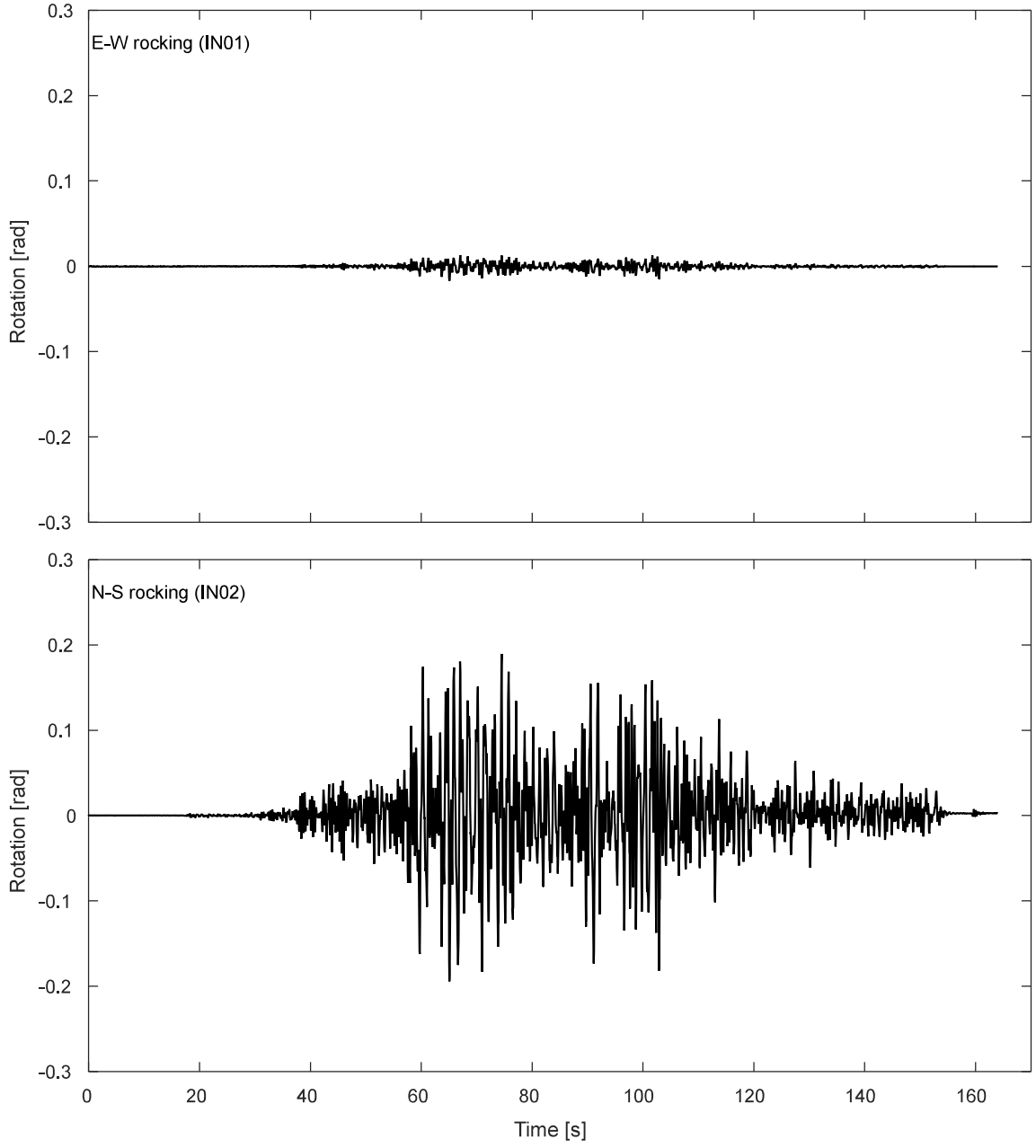

Figure K.10-13. Inclinometer results for the footing during DT03-MAU-100P motion.

K.10.4. Pressure cells.

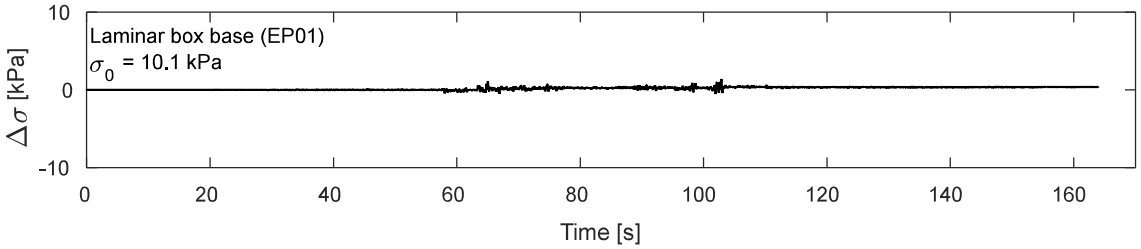

Figure K.10-14. Pressure cells results at laminar box base during DT03-MAU-100P motion.

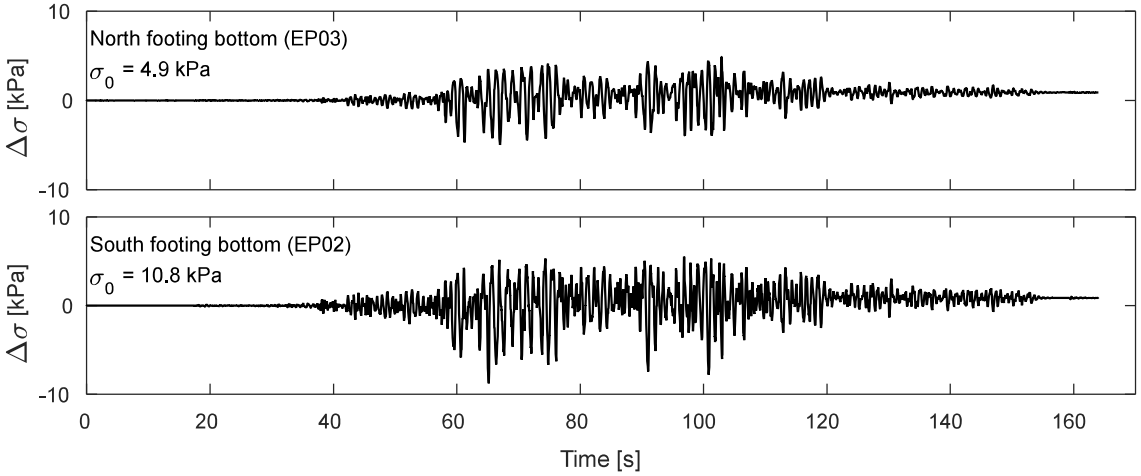

Figure K.10-15. Pressure cells results at footing bottom during DT03-MAU-100P motion.

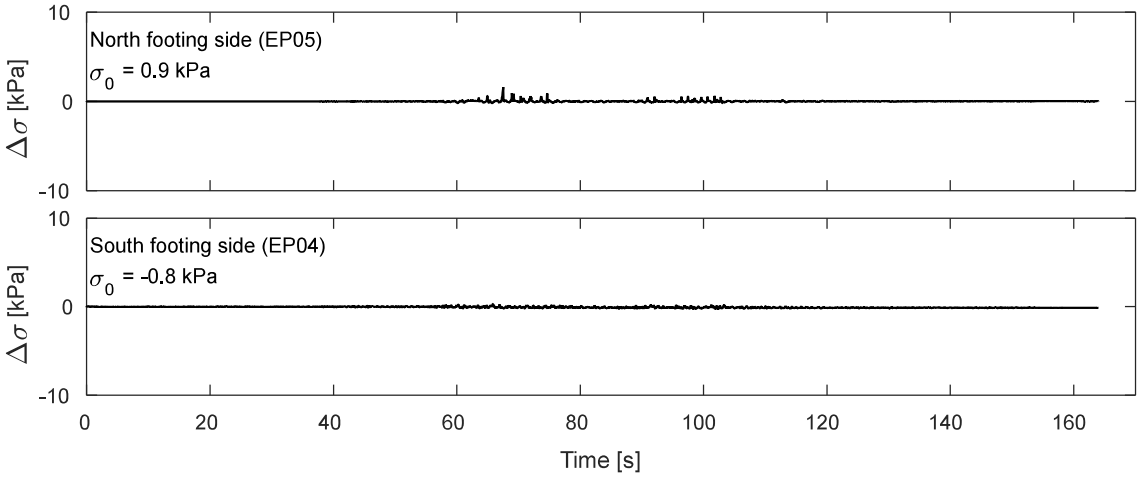

Figure K.10-16. Pressure cells results at footing sides during DT03-MAU-100P motion.

APPENDIX K – Dynamic testing specimen No 03 (DT03)

K.1 - Instrumentation Layout for Dynamic Test No 03.

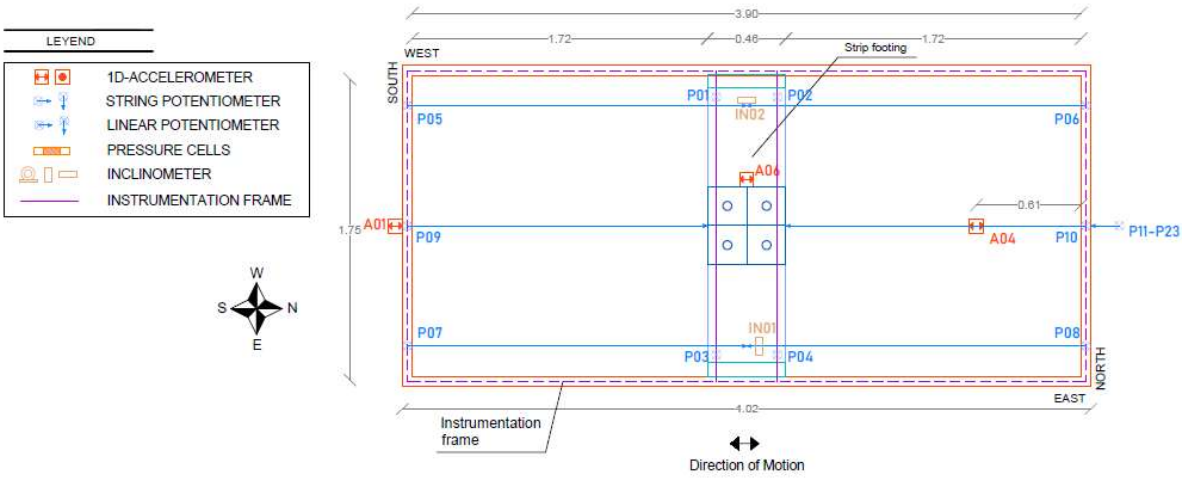

Figure K.1-1. Instrumentation Layout – Plan View.

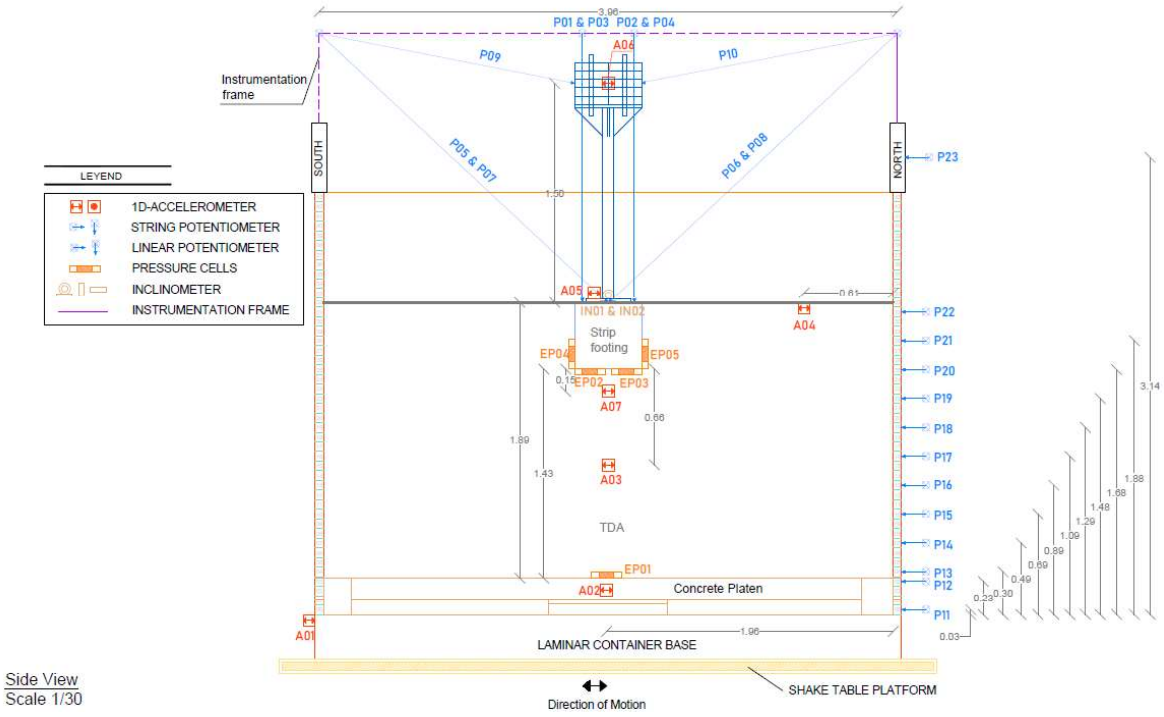

Figure K.1-2. Instrumentation Layout – Side View.

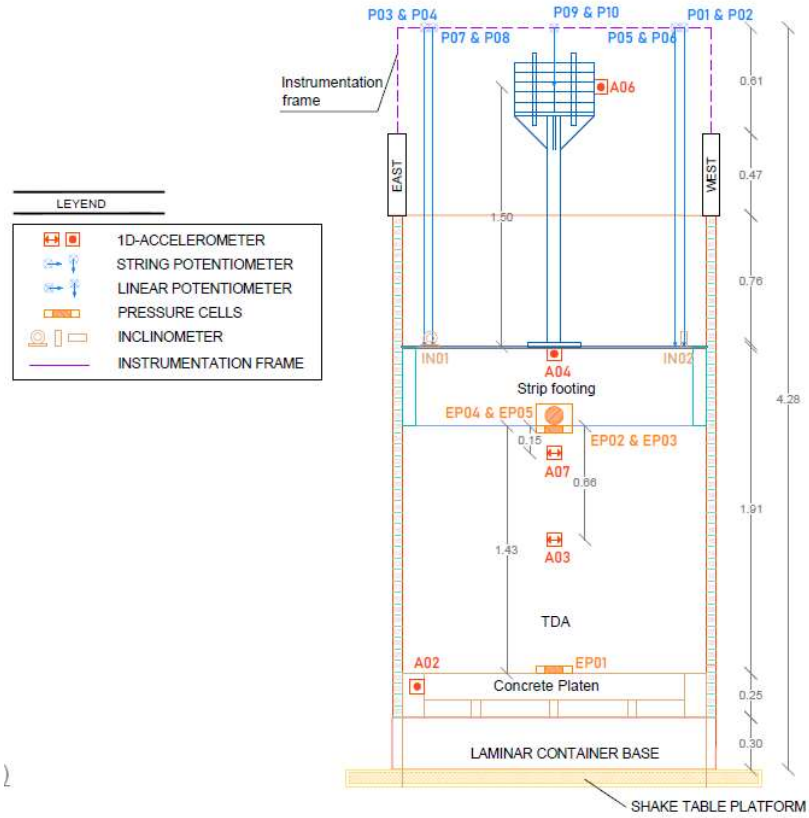

Figure K.1-3. Instrumentation Layout – Front View.

K.2. Time-history Records for DT03-SS08-F04F10 motion.

K.2.1 Input Motion

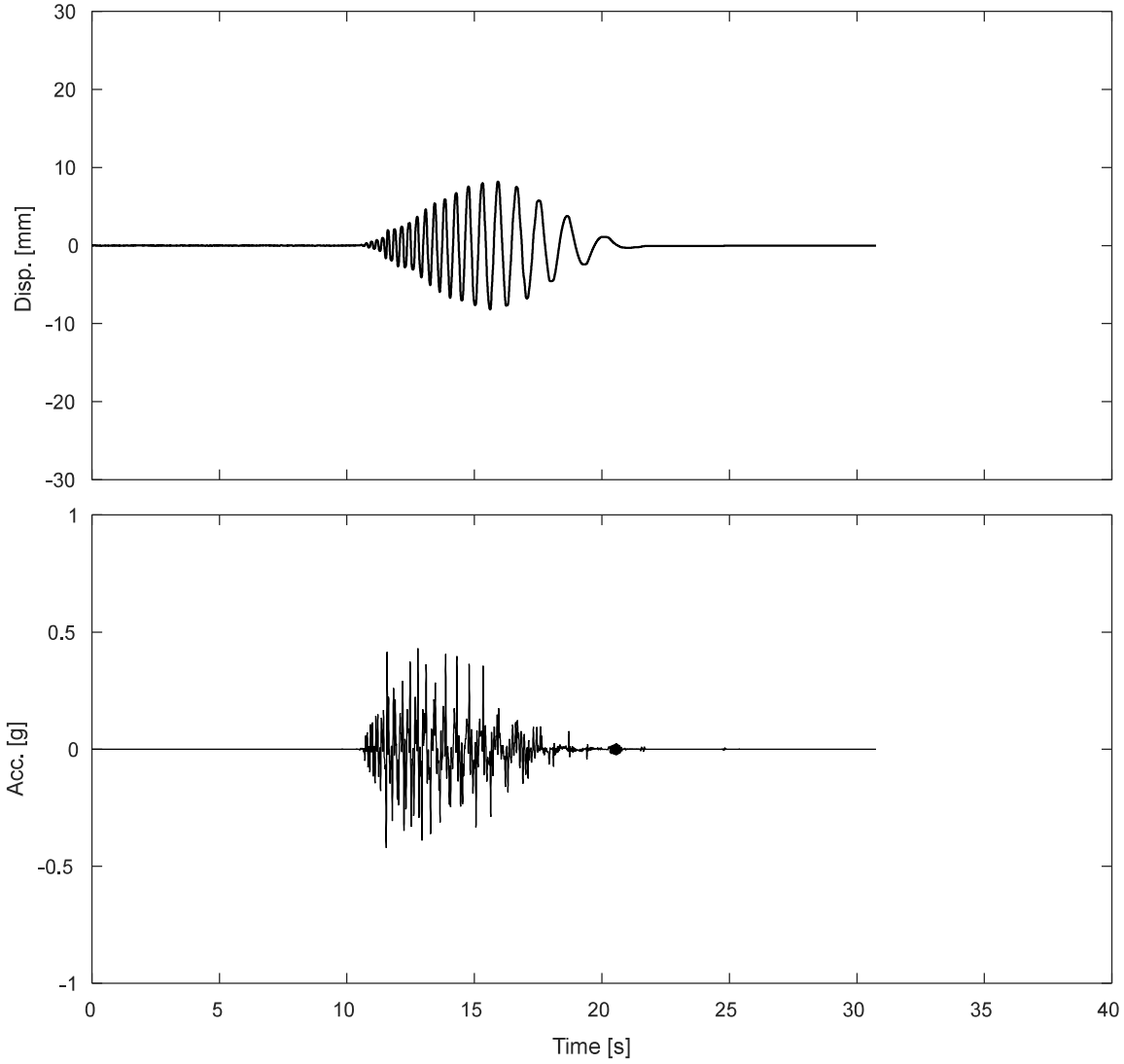

Figure K.2-1. Measured input displacement and acceleration at the base of the specimen during DT03-SS08-F04F10 motion

K.2.1 Accelerometers.

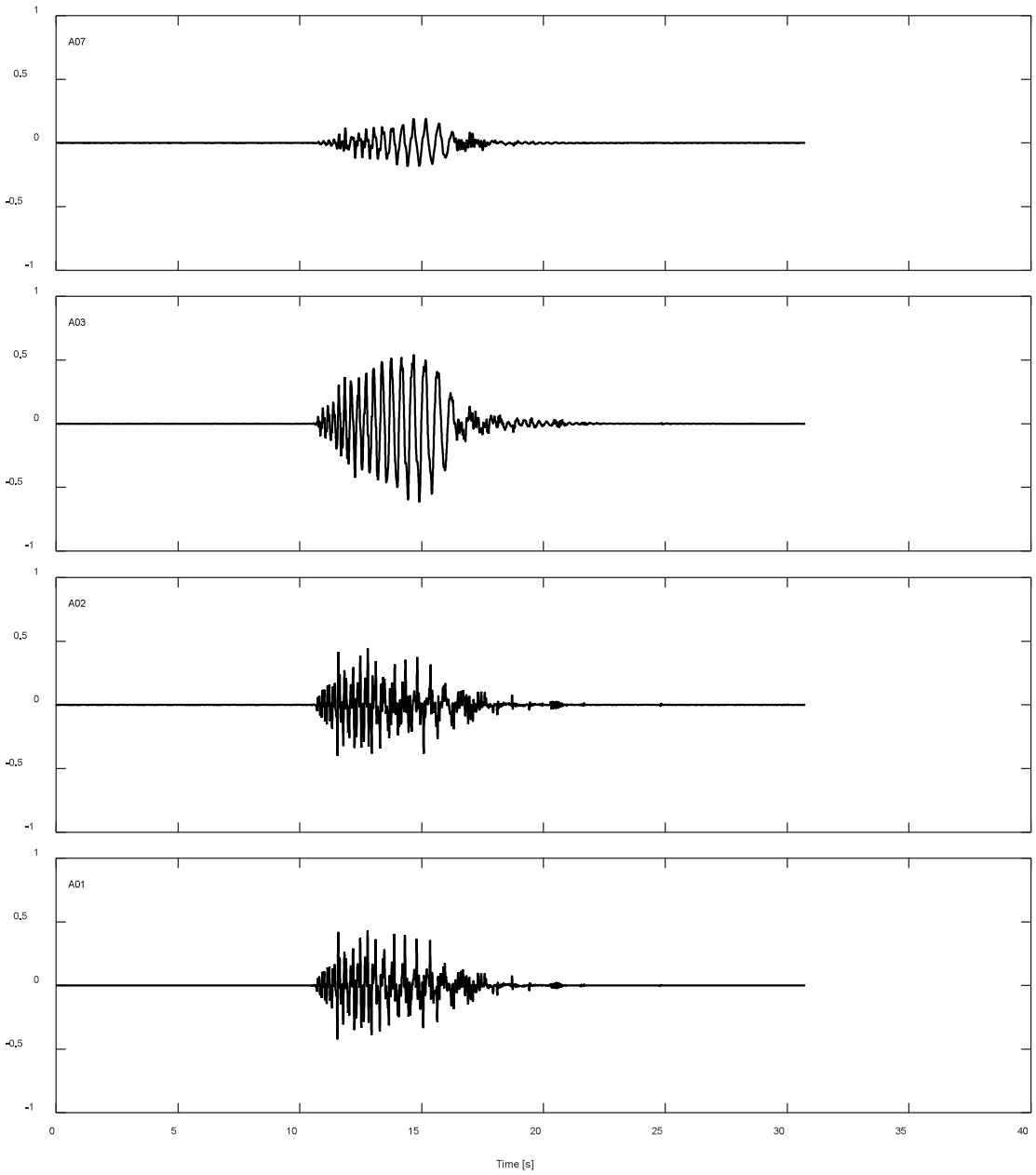

Figure K.2-2. Accelerations results along TDA during DT03-SS08-F04F10 motion.

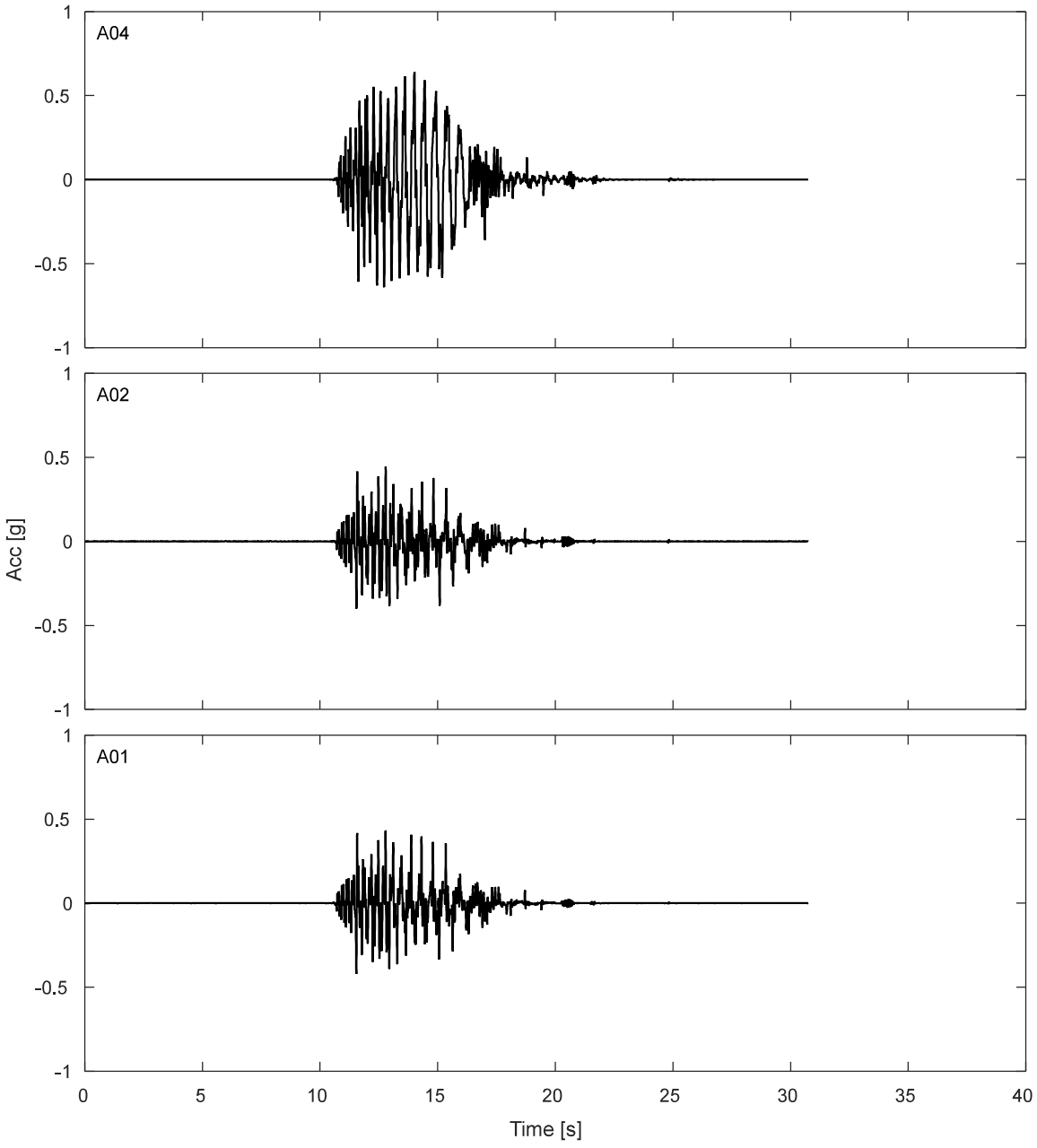

Figure K.2-3. Free field accelerations results for TDA during DT03-SS08-F04F10 motion.

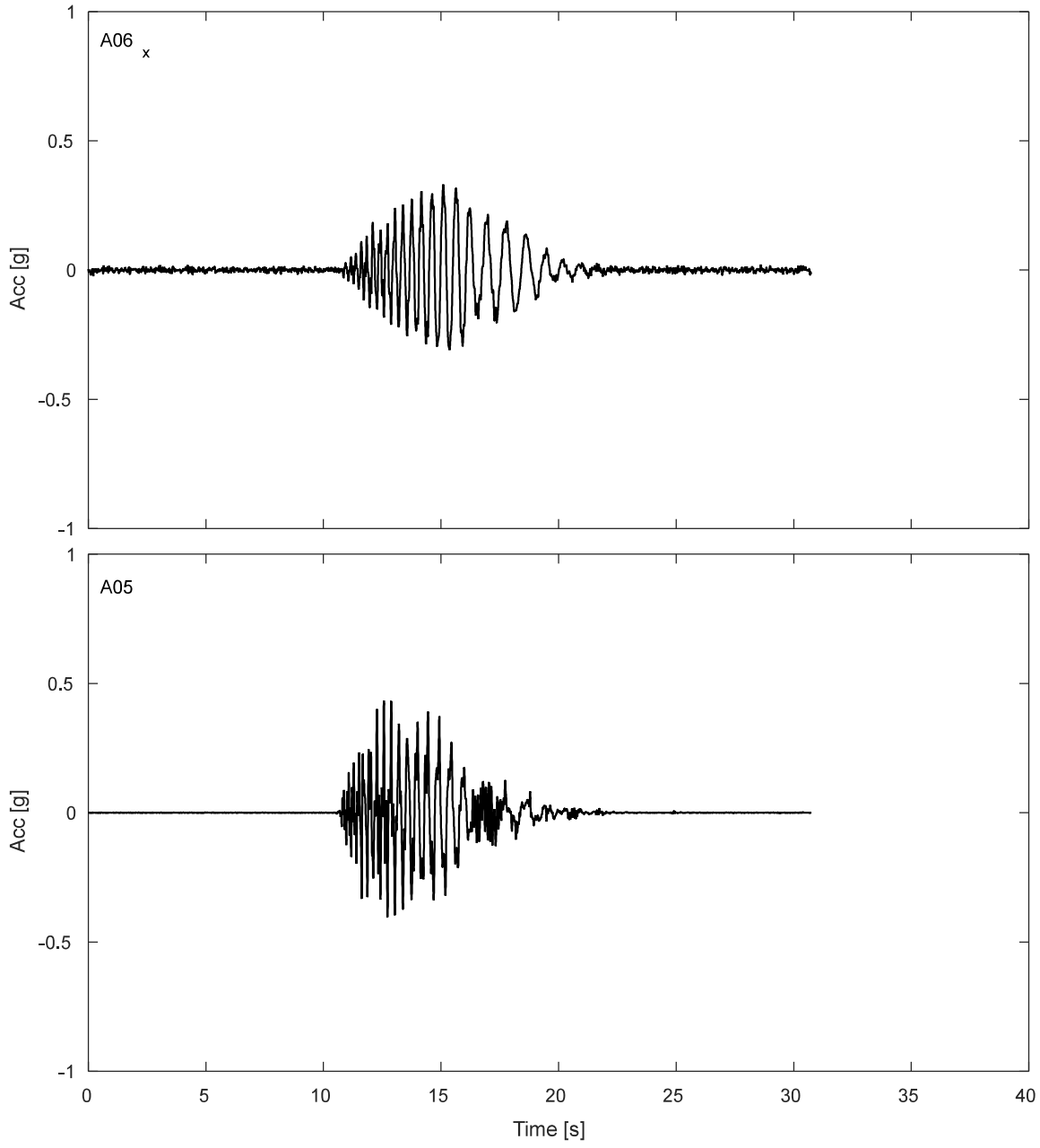

Figure K.2-4. Accelerations results SDOF structure during DT03-SS08-F04F10 motion.

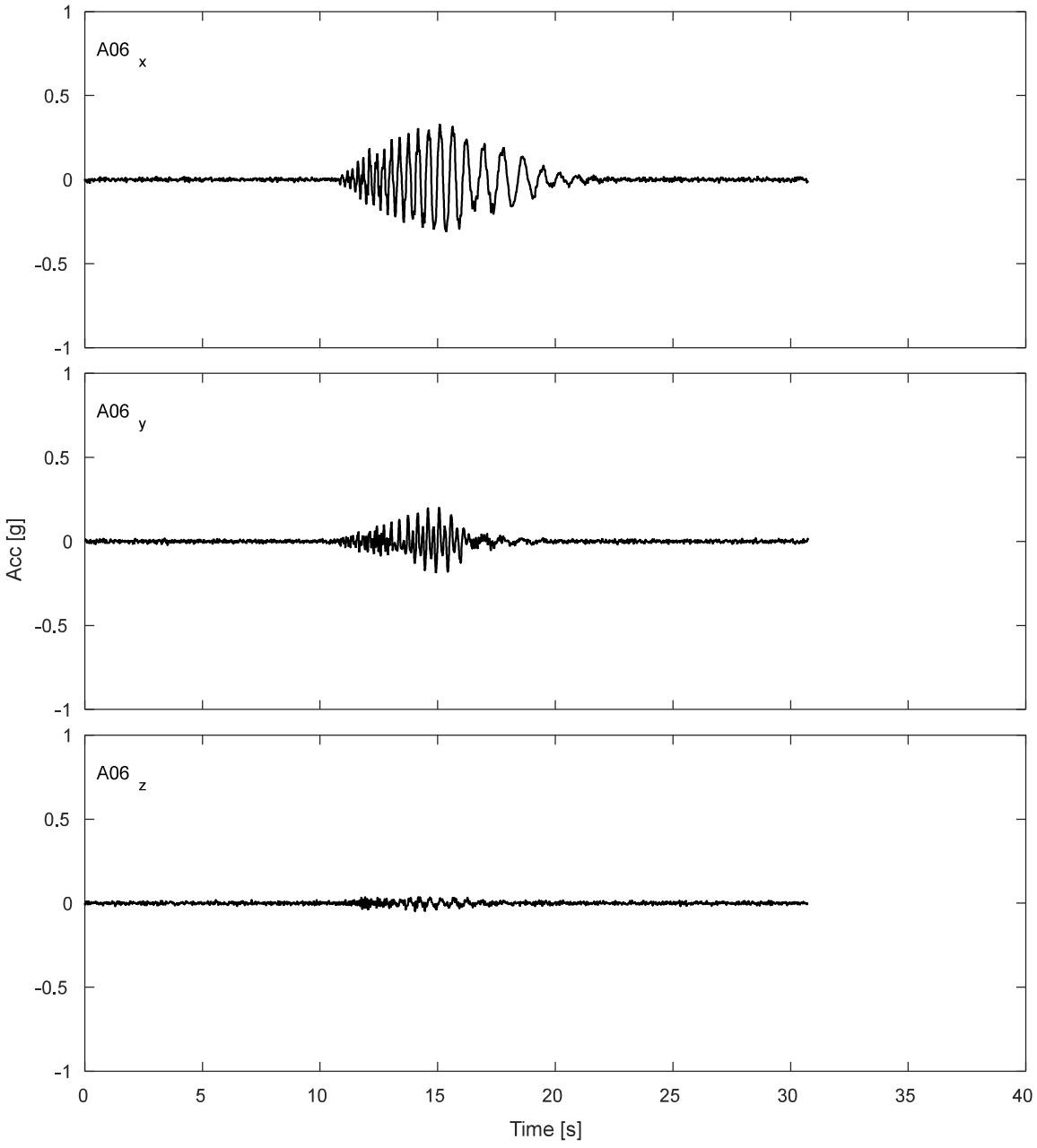

Figure K.2-5. Accelerations results for lumped mass of SDOF structure during DT03-SS08-F04F10 motion.

K.2.2 Potentiometers.

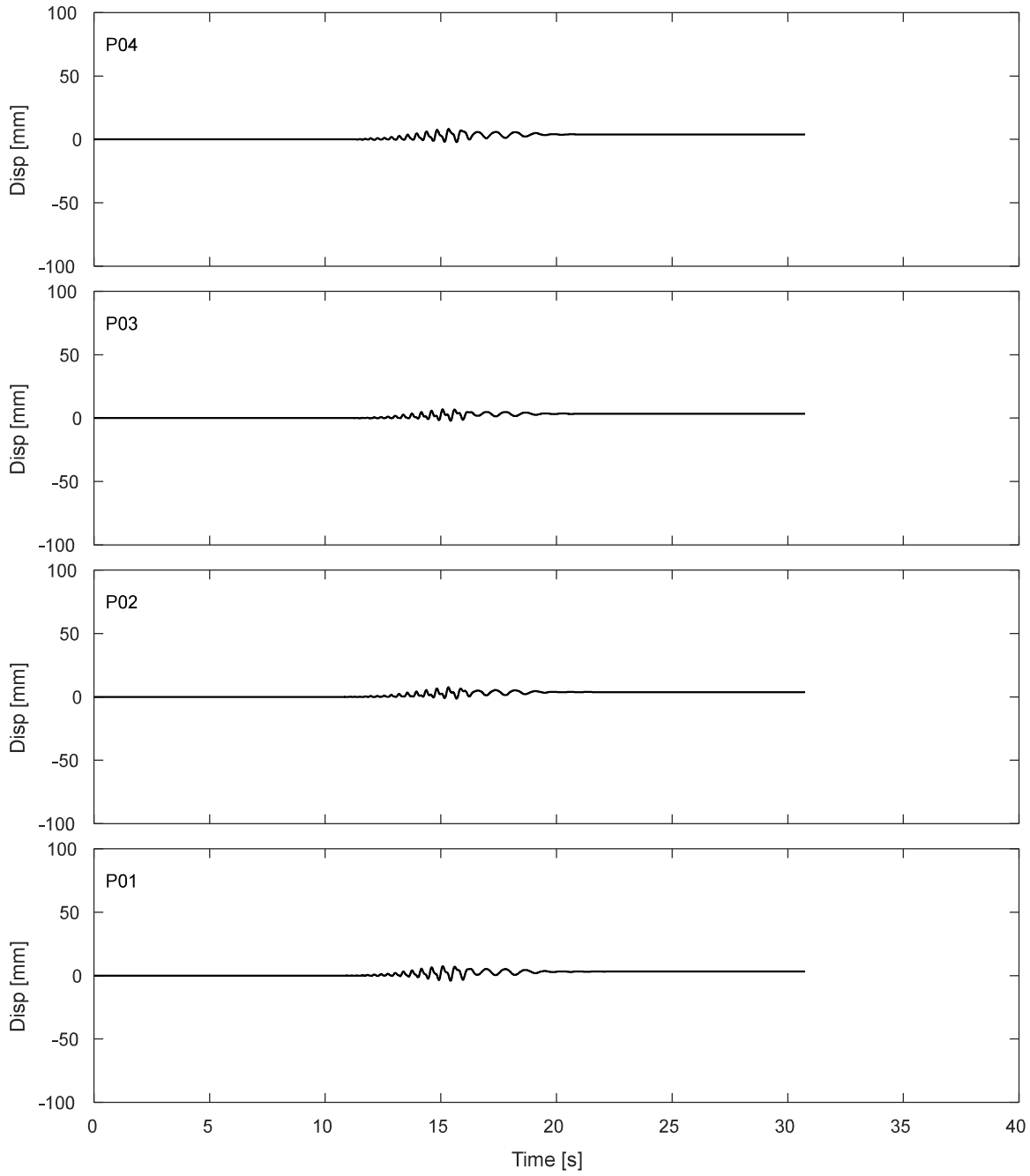

Figure K.2-6. Results of fully vertical potentiometers attached to Corners of top of strip footing during DT03-SS08-F04F10 motion.

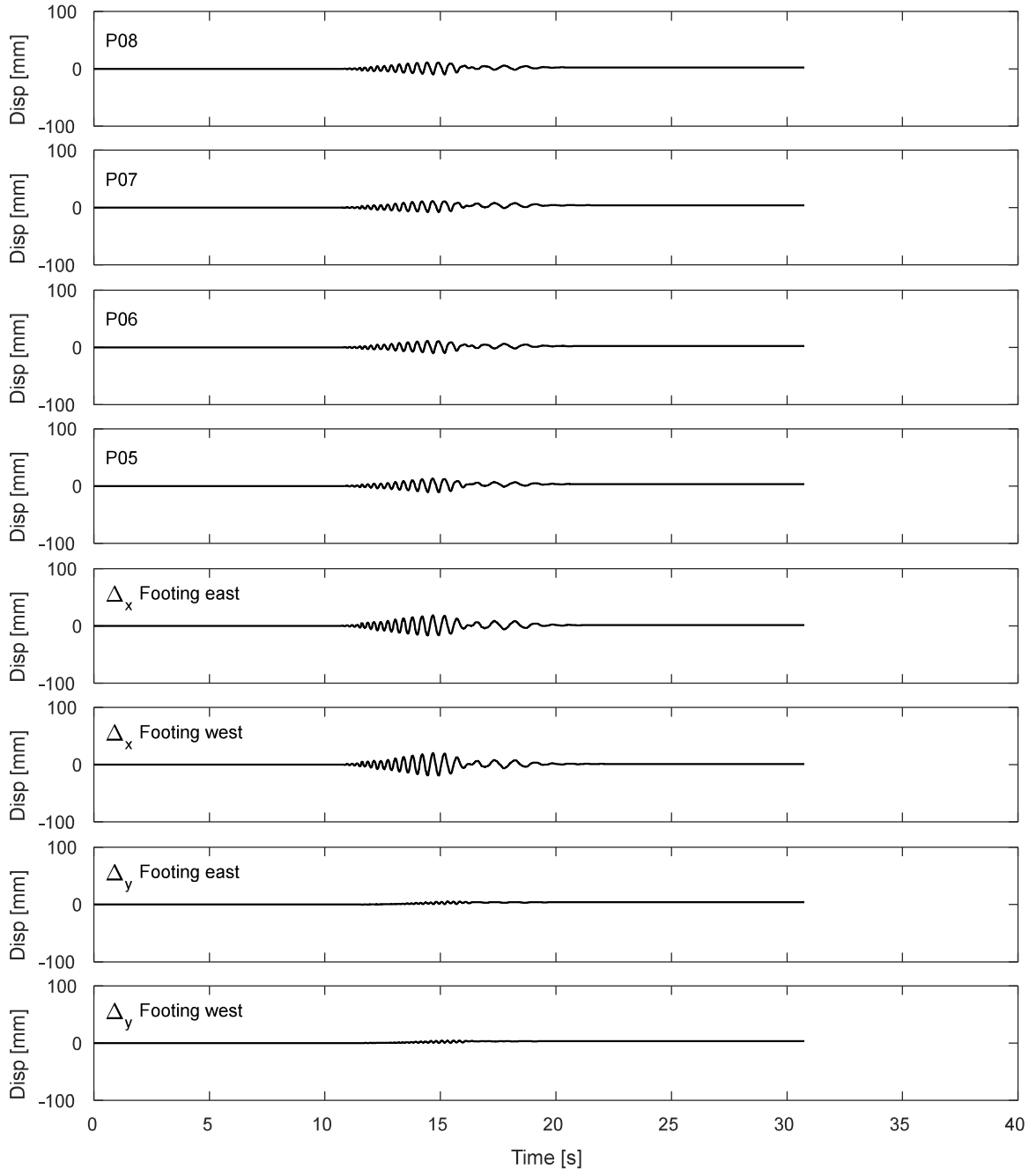

Figure K.2-7. Results of inclined potentiometers attached to top of strip footing during DT03-SS08-F04F10 motion.

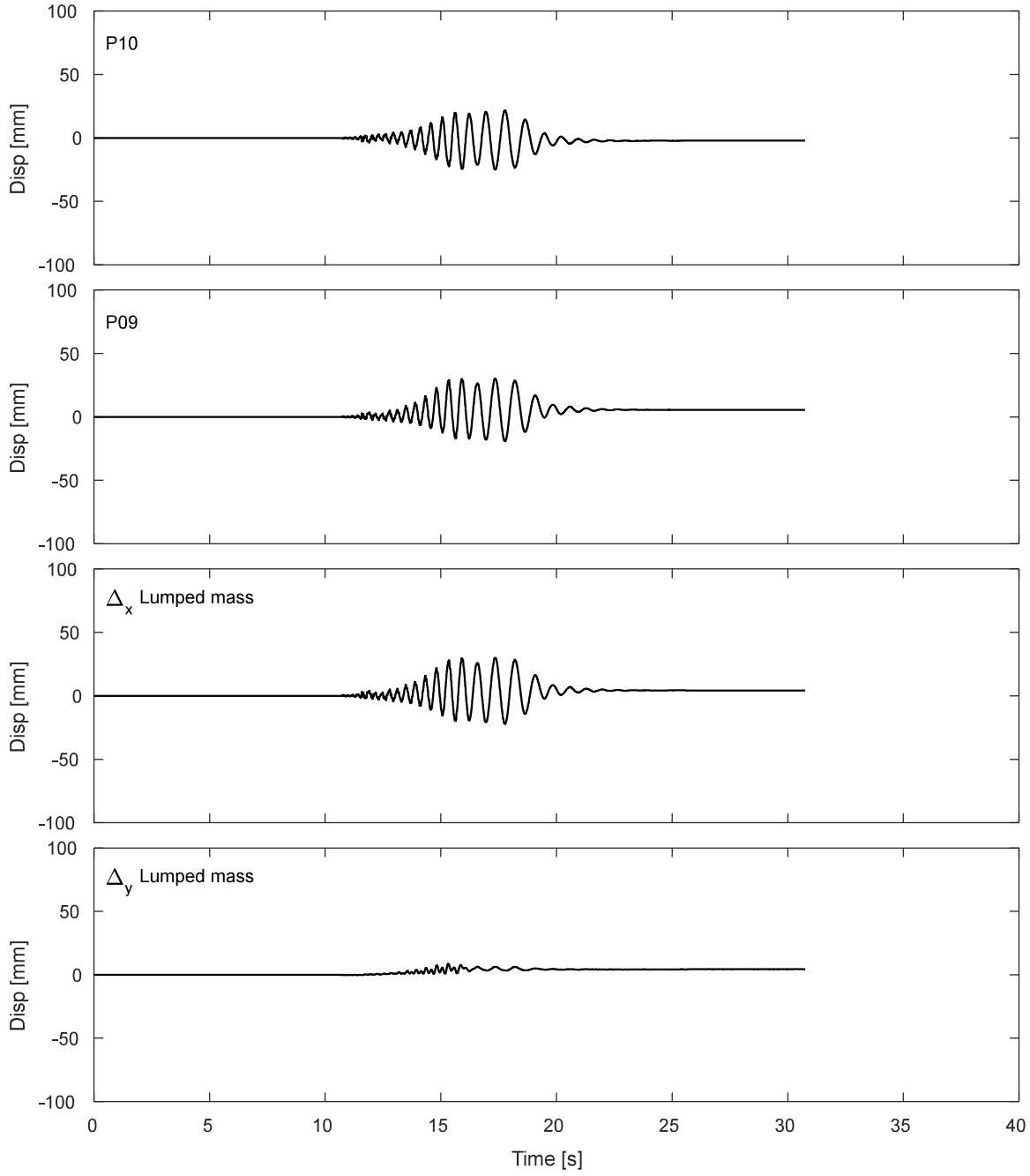

Figure K.2-8. Results of inclined potentiometers attached to lumped mass during DT03-SS08-F04F10 motion.

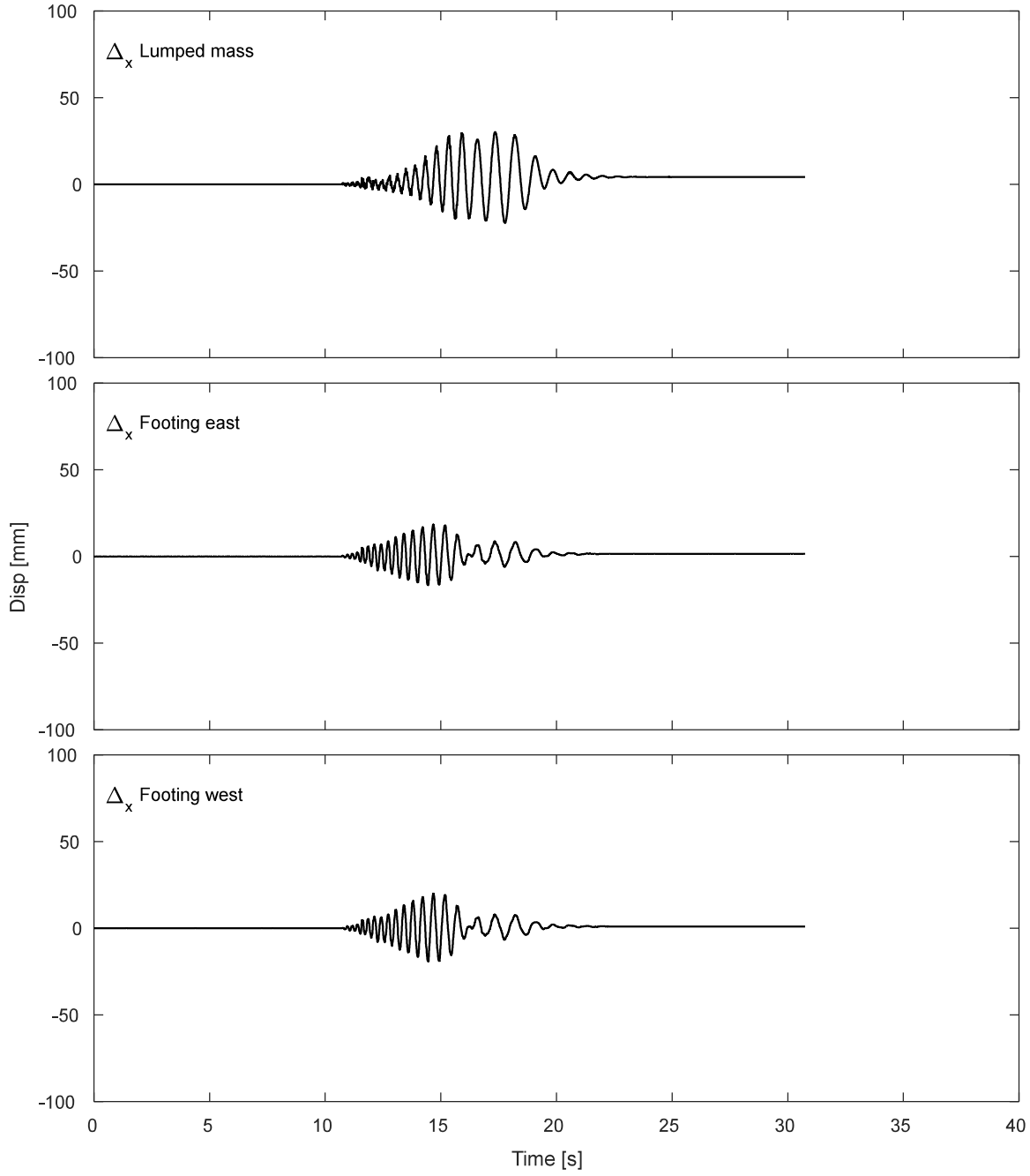

Figure K.2-9. Results of horizontal displacement of lumped mass and footing during DT03-SS08-F04F10 motion.

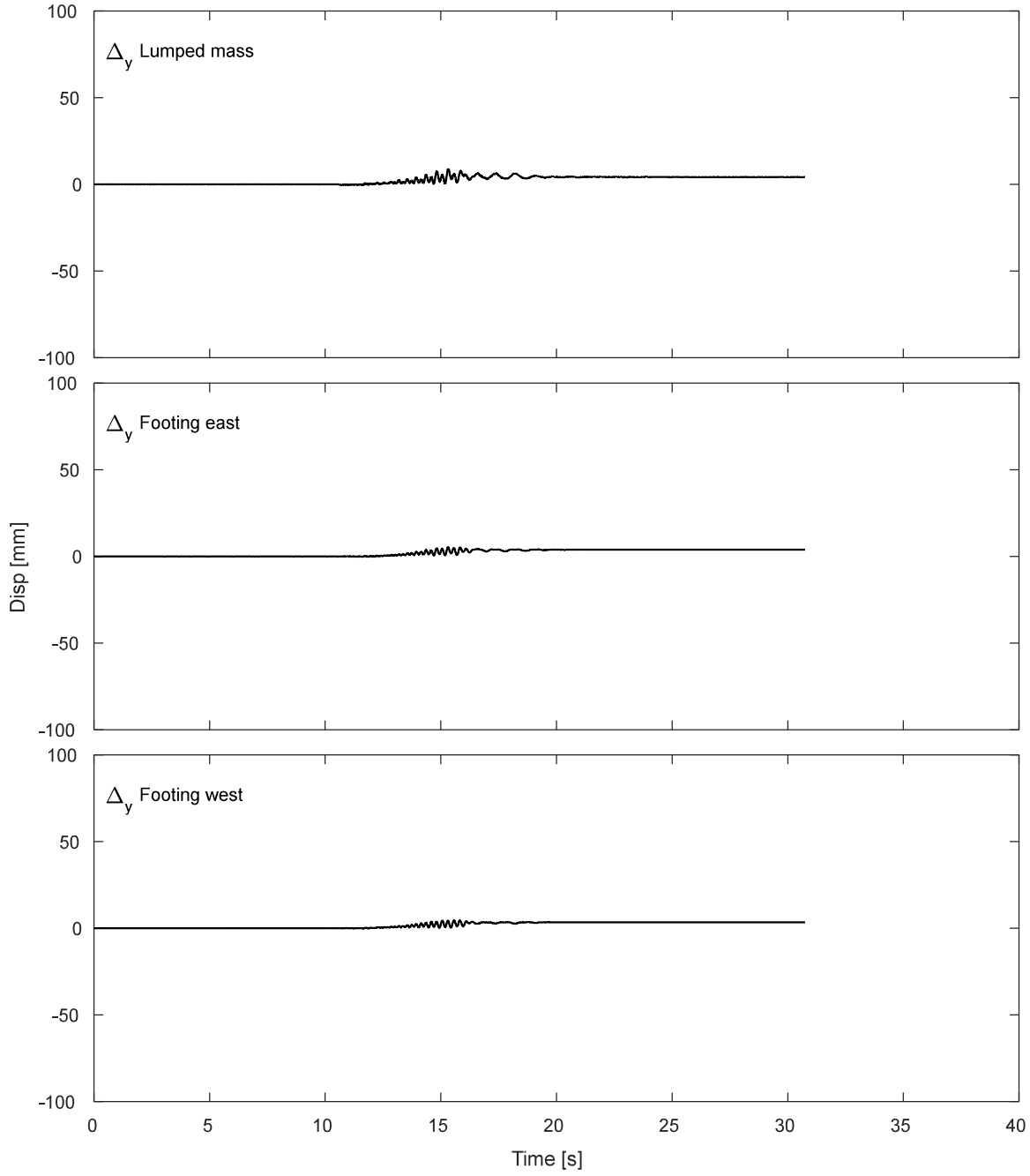

Figure K.2-10. Results of vertical displacement of lumped mass and footing during DT03-SS08-F04F10 motion.

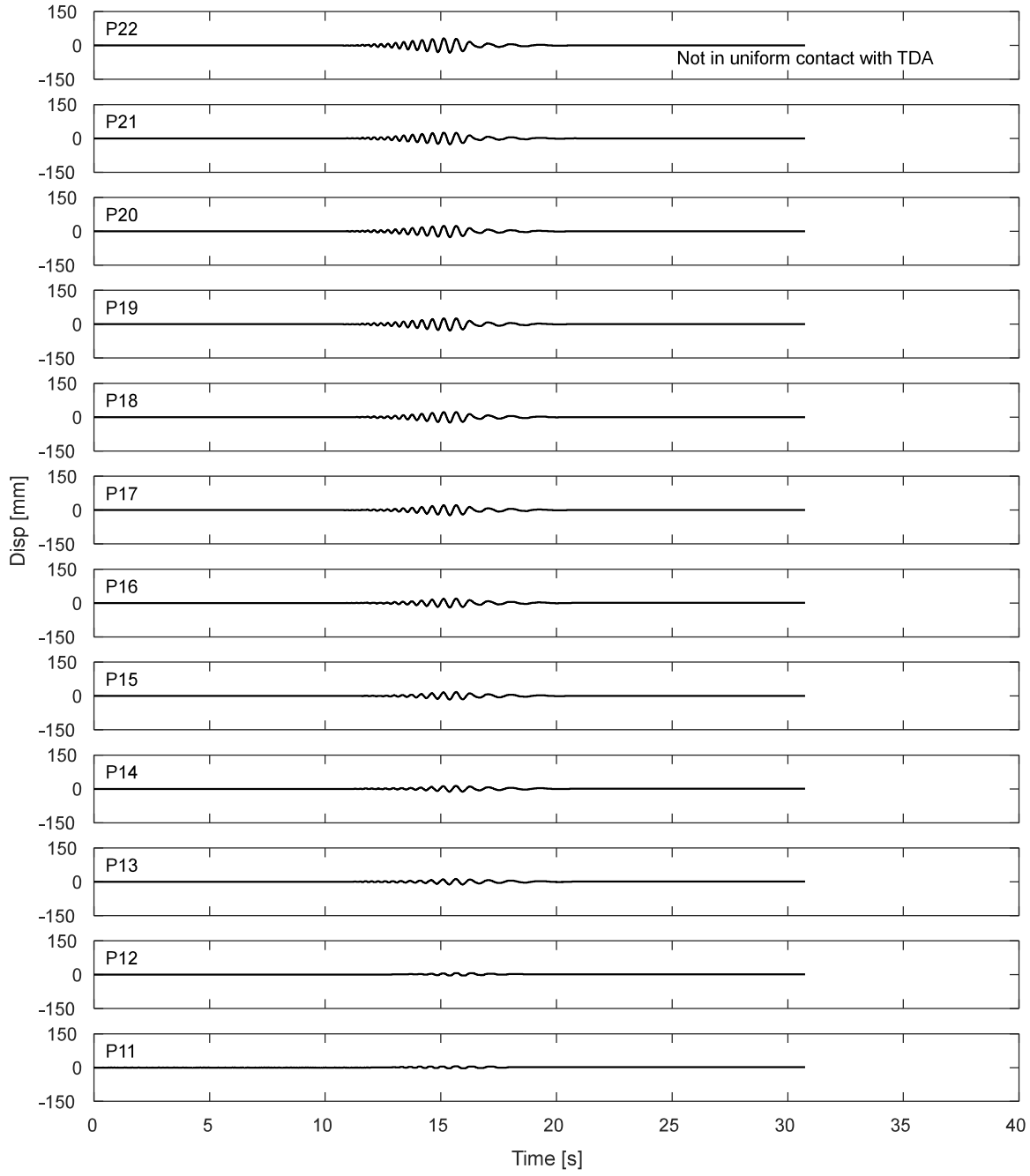

Figure K.2-11. Potentiometers results for the laminar box during DT03-SS08-F04F10 motion.

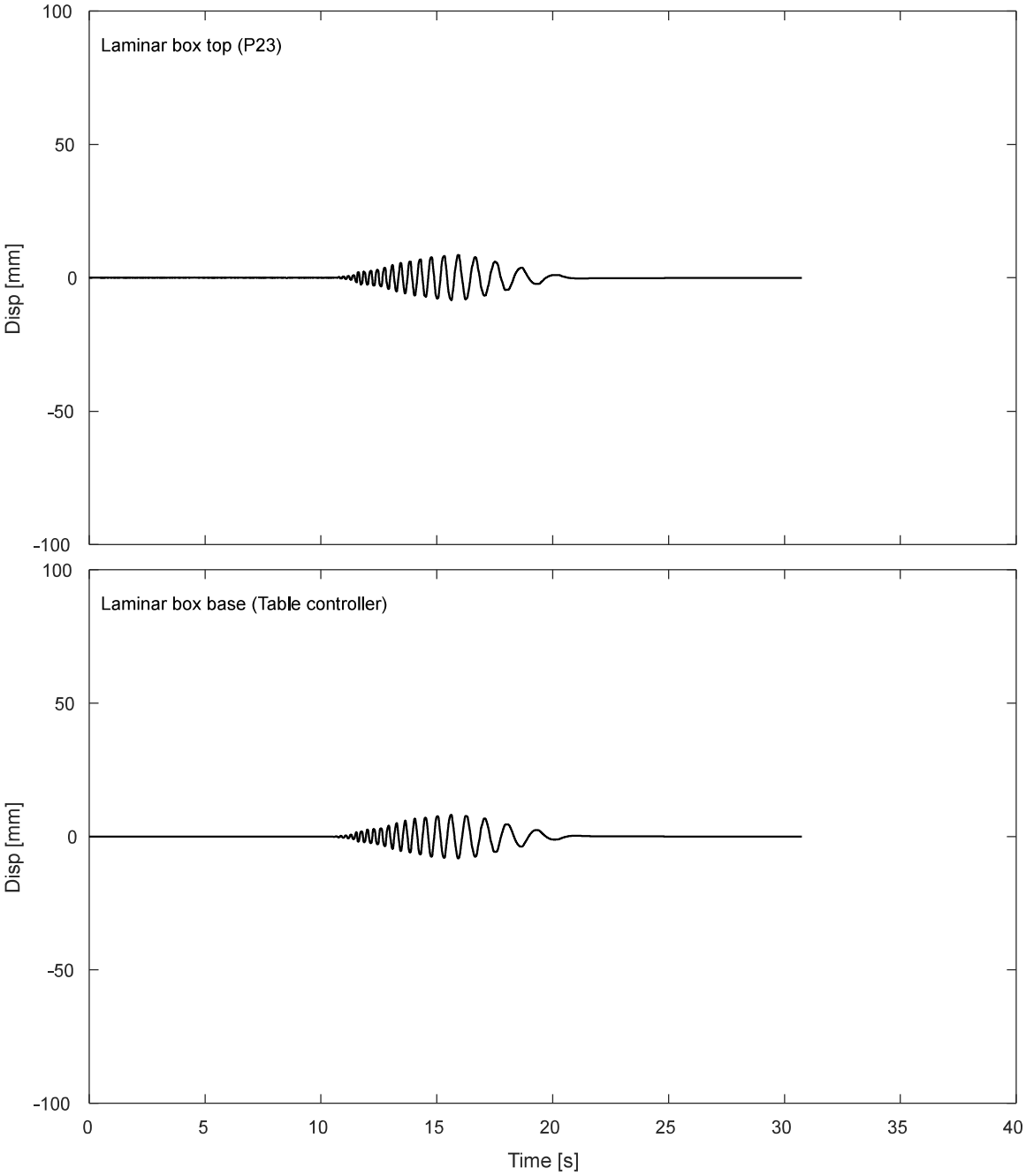

Figure K.2-12. Displacement response of top and base of laminar box during DT03-SS08-F04F10 motion.

K.2.3. Inclinometers.

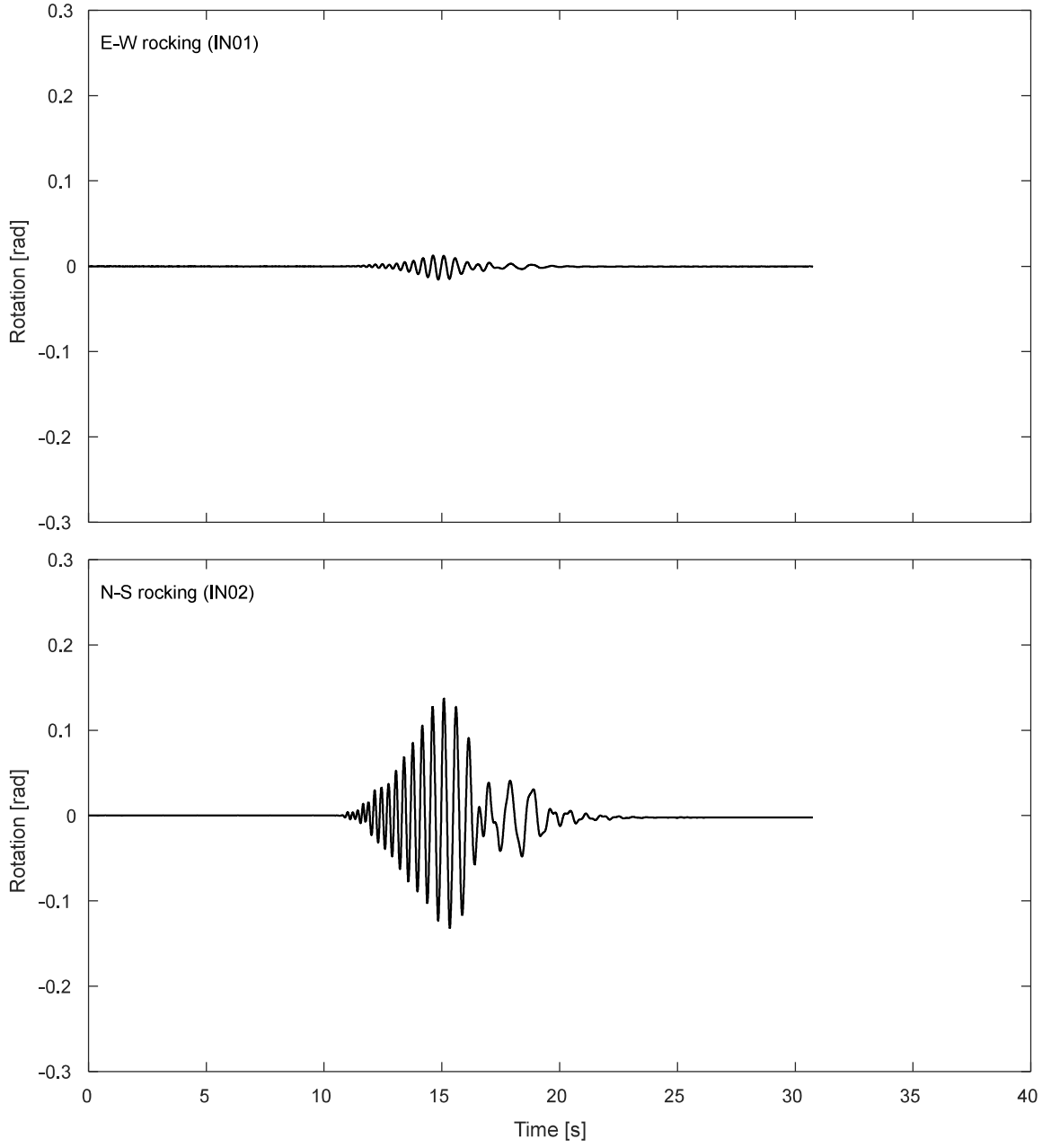

Figure K.2-13. Inclinometer results for the footing during DT03-SS08-F04F10 motion.

K.2.4. Pressure cells.

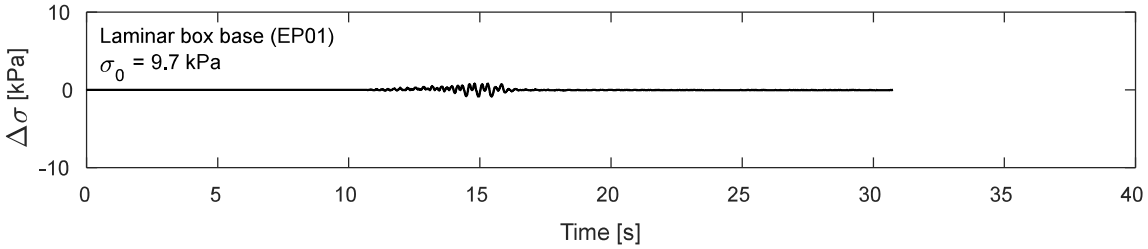

Figure K.2-14. Pressure cells results at laminar box base during DT03-SS08-F04F10 motion.

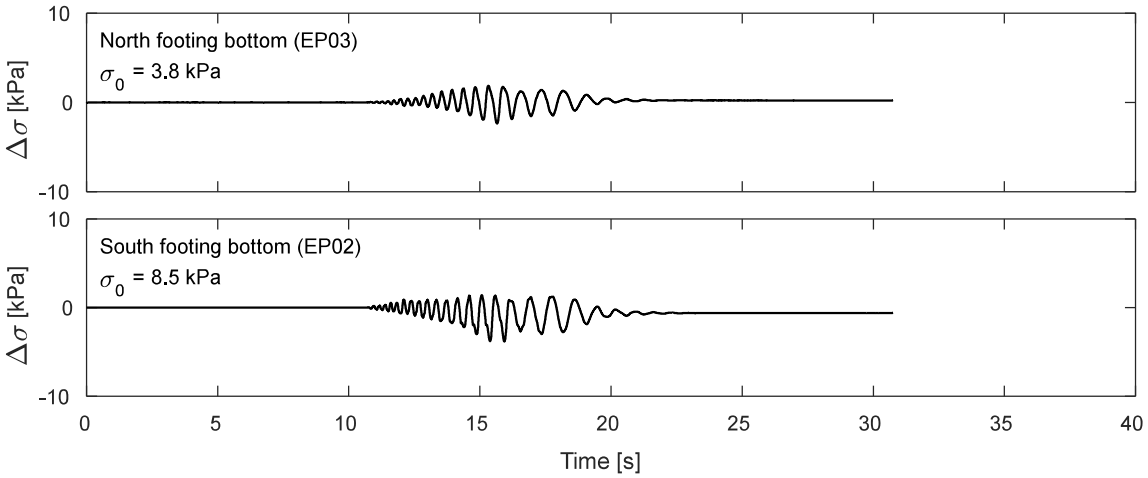

Figure K.2-15. Pressure cells results at footing bottom during DT03-SS08-F04F10 motion

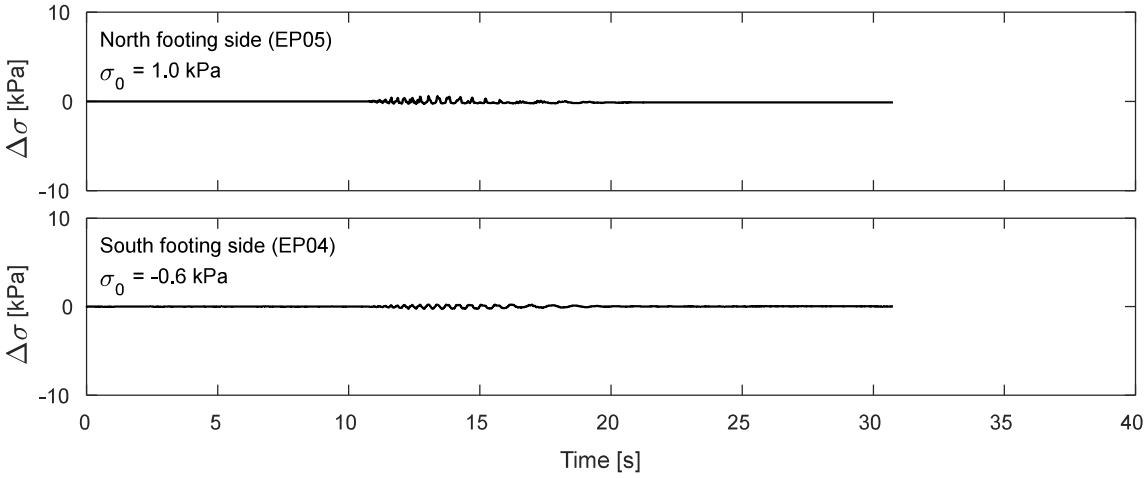

Figure K.2-16. Pressure cells results at footing sides during DT03-SS08-F04F10 motion.

K.3. Time-history Records for DT03-SS12-F04F10 motion.

K.3.1 Input Motion

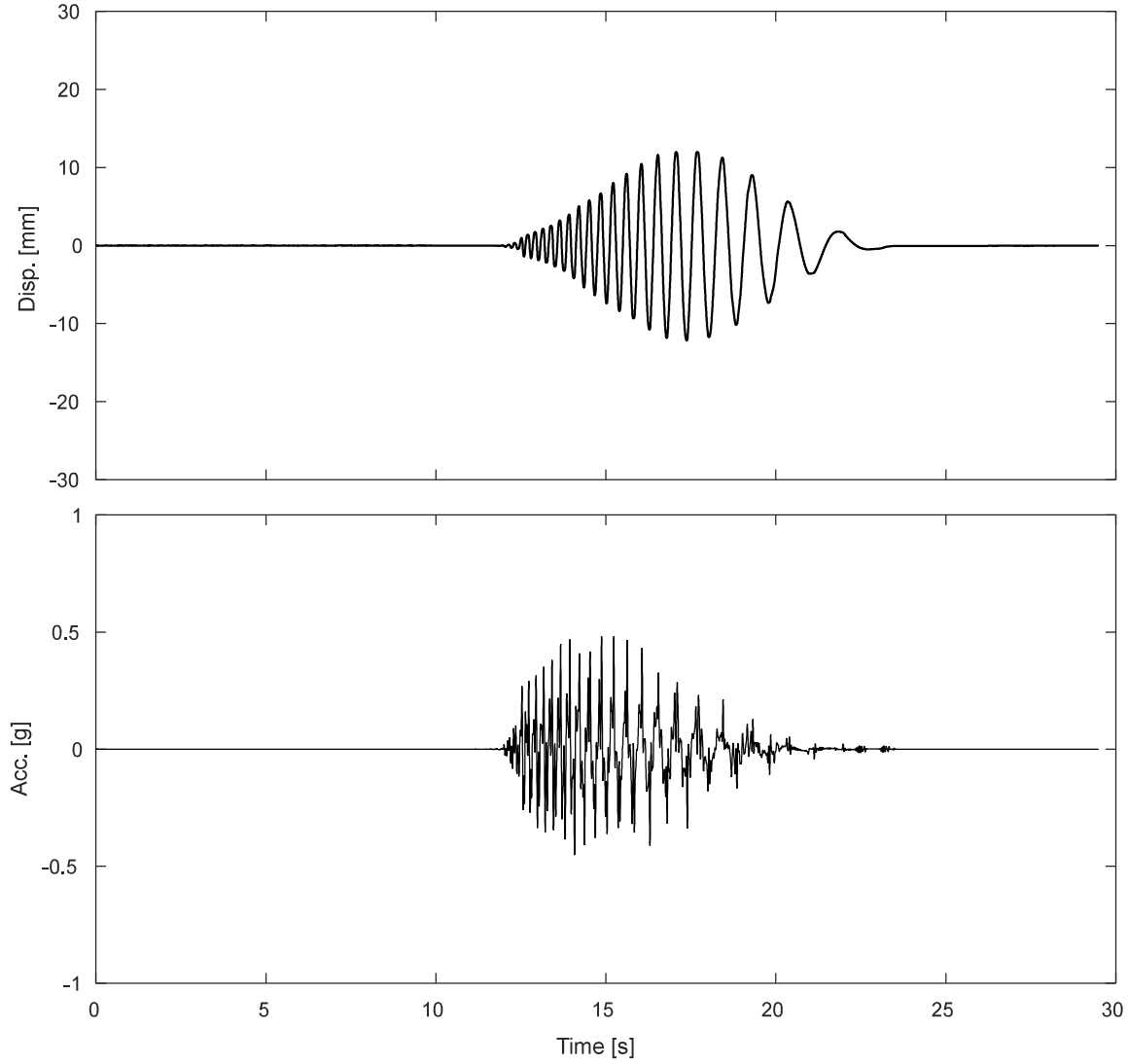

Figure K.3-1. Measured input displacement and acceleration at the base of the specimen during DT03-SS12-F04F10 motion

K.3.1 Accelerometers.

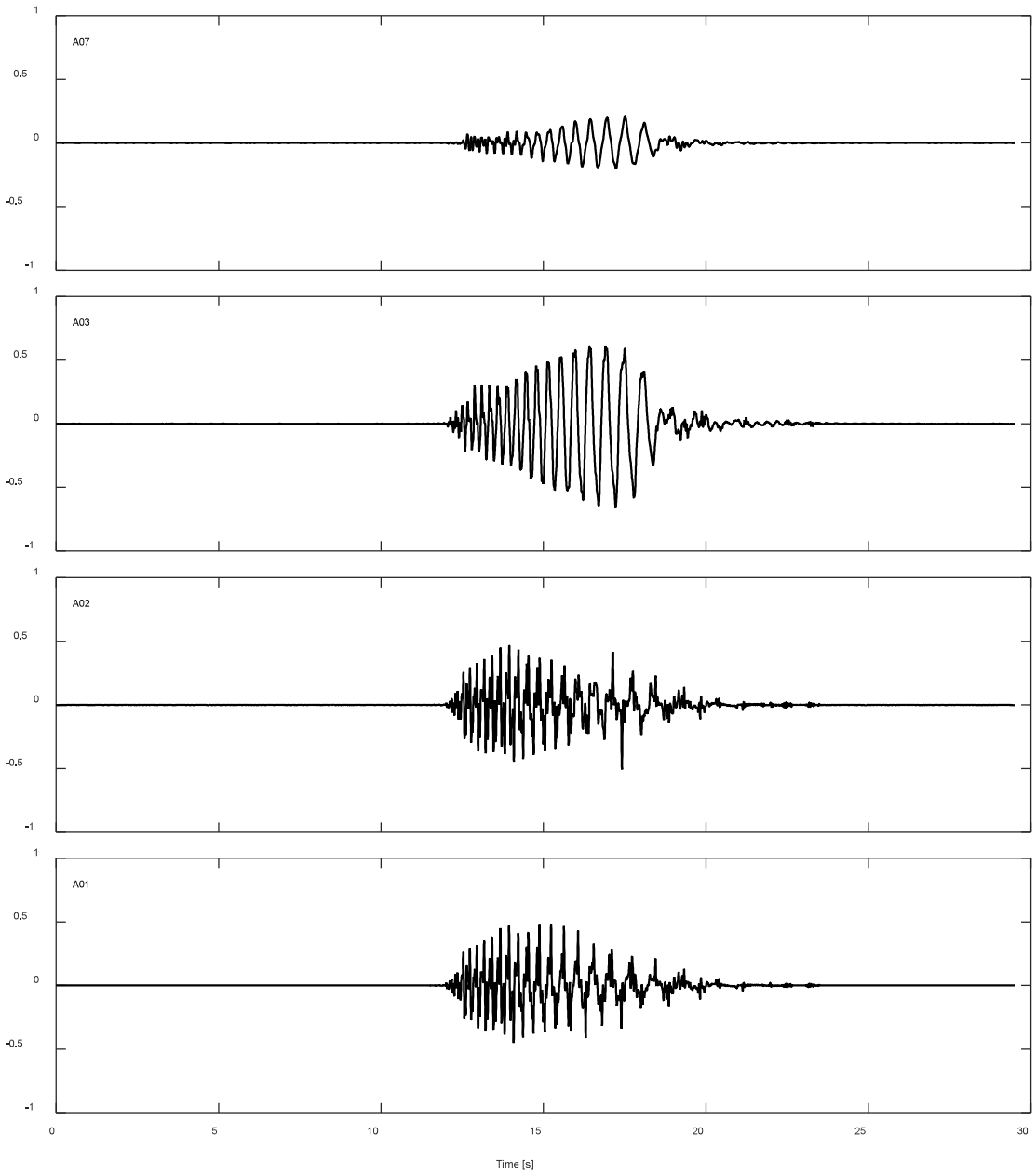

Figure K.3-2. Accelerations results along TDA during DT03-SS12-F04F10 motion.

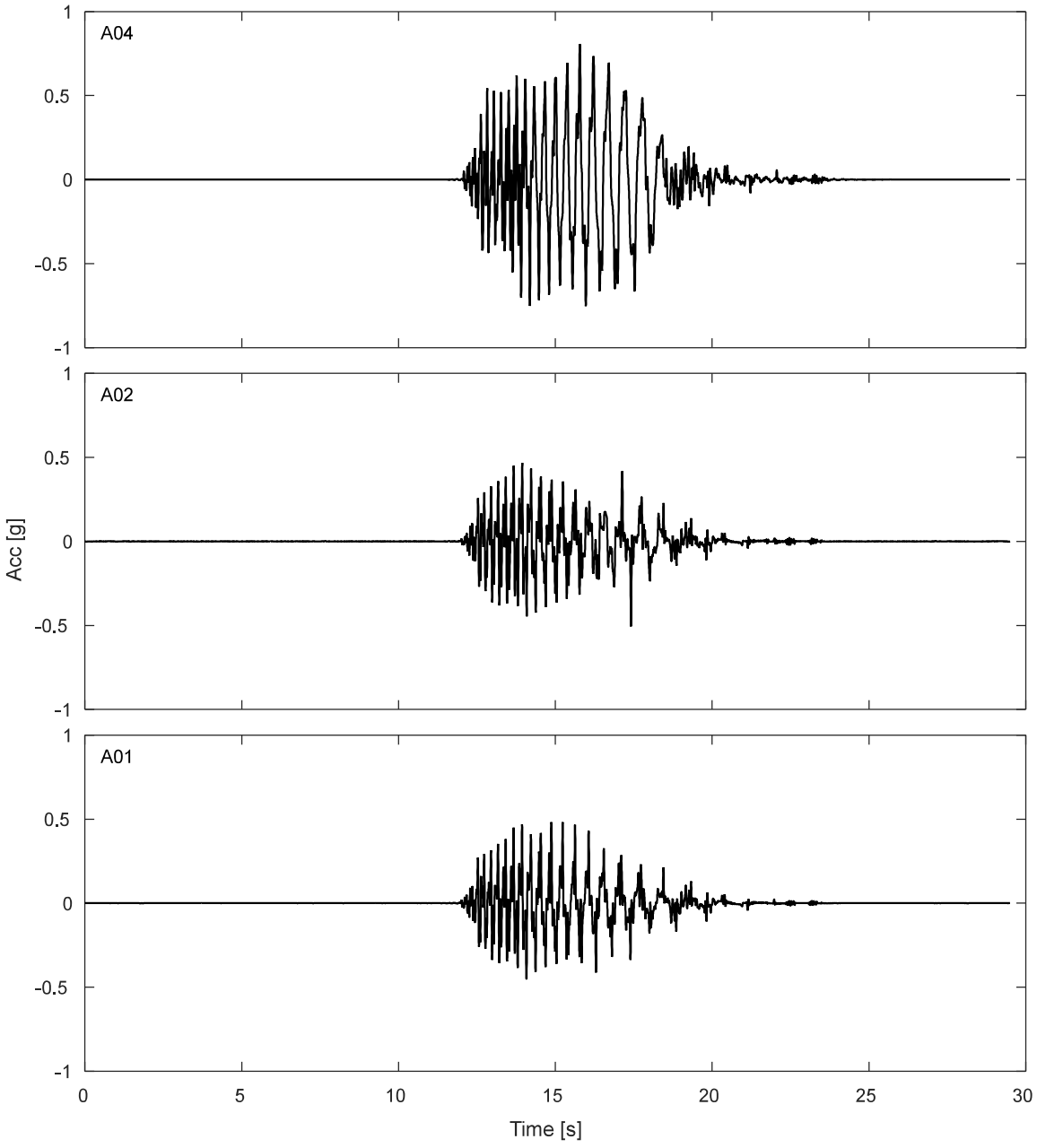

Figure K.3-3. Free field accelerations results for TDA during DT03-SS12-F04F10 motion.

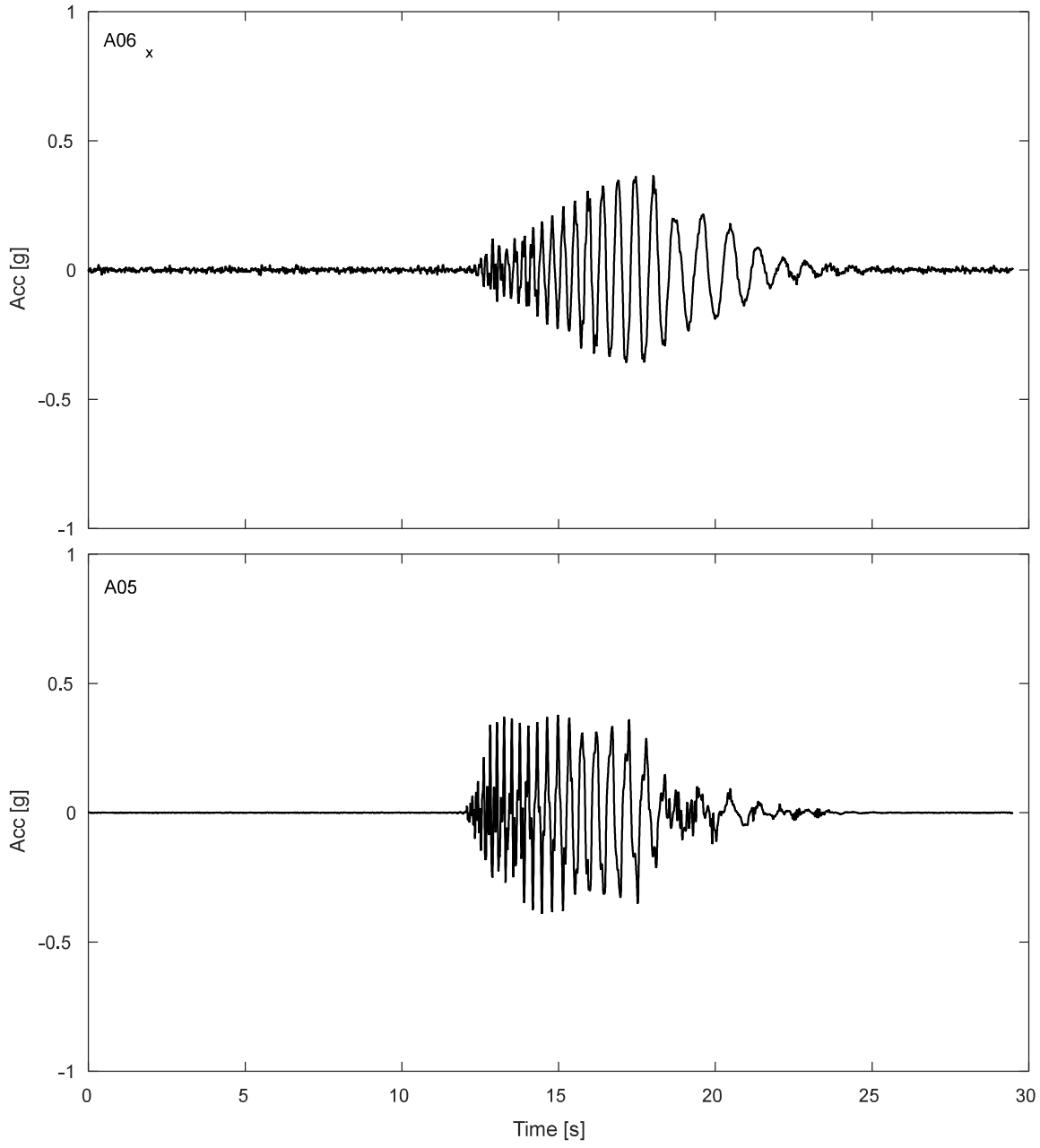

Figure K.3-4. Accelerations results SDOF structure during DT03-SS12-F04F10 motion.

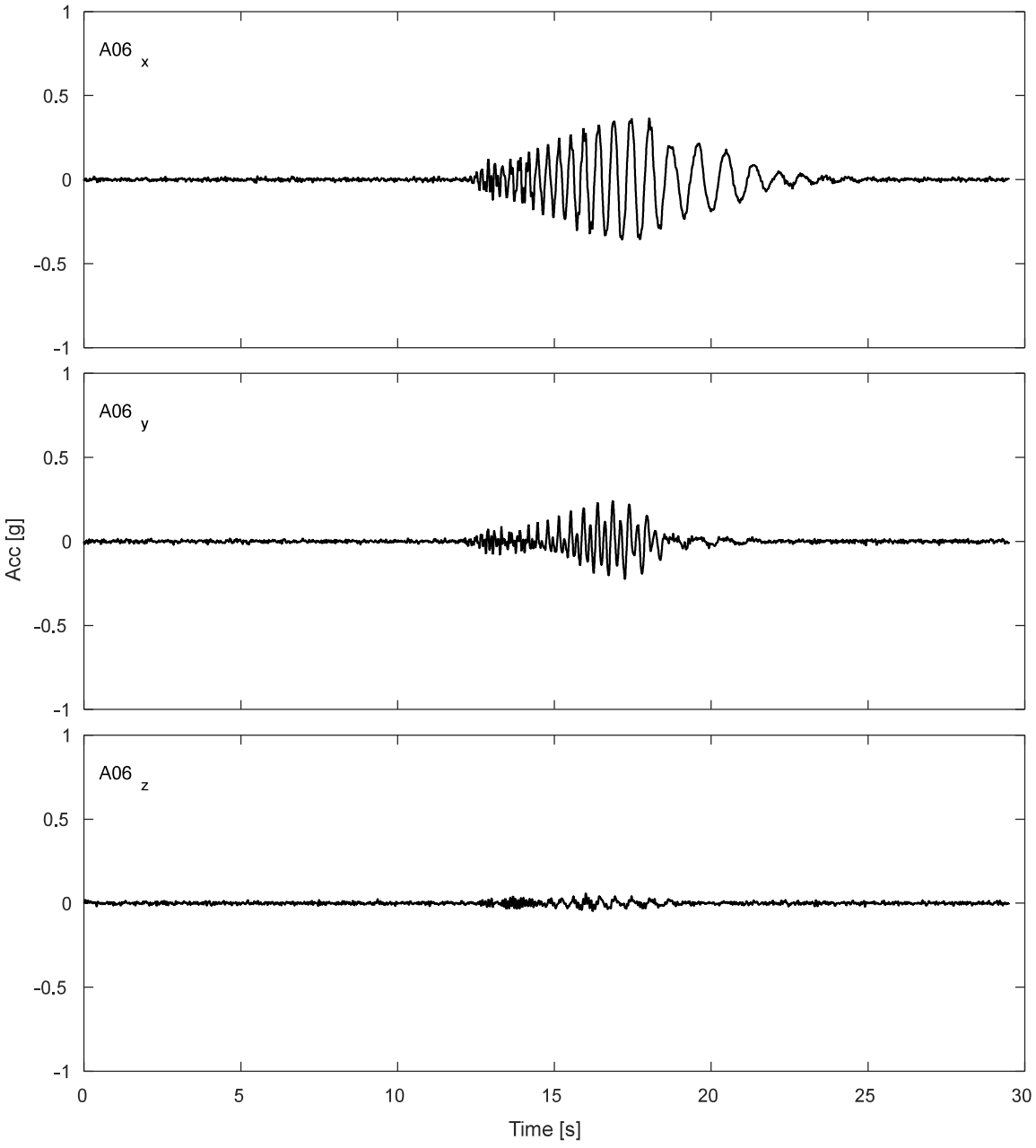

Figure K.3-5. Accelerations results for lumped mass of SDOF structure during DT03-SS12-F04F10 motion.

K.3.2 Potentiometers.

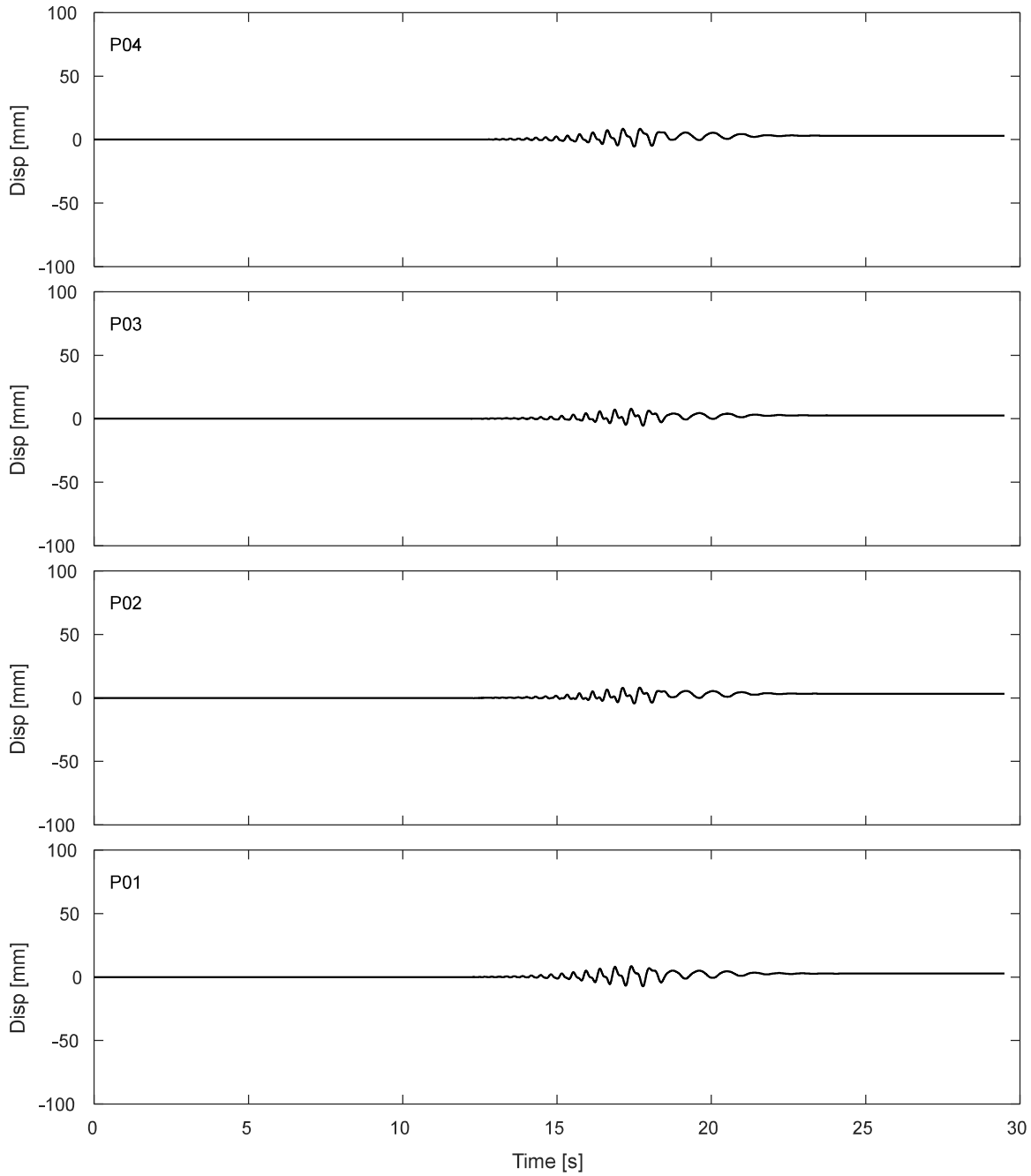

Figure K.3-6. Results of fully vertical potentiometers attached to corners of top of strip footing during DT03-SS12-F04F10 motion.

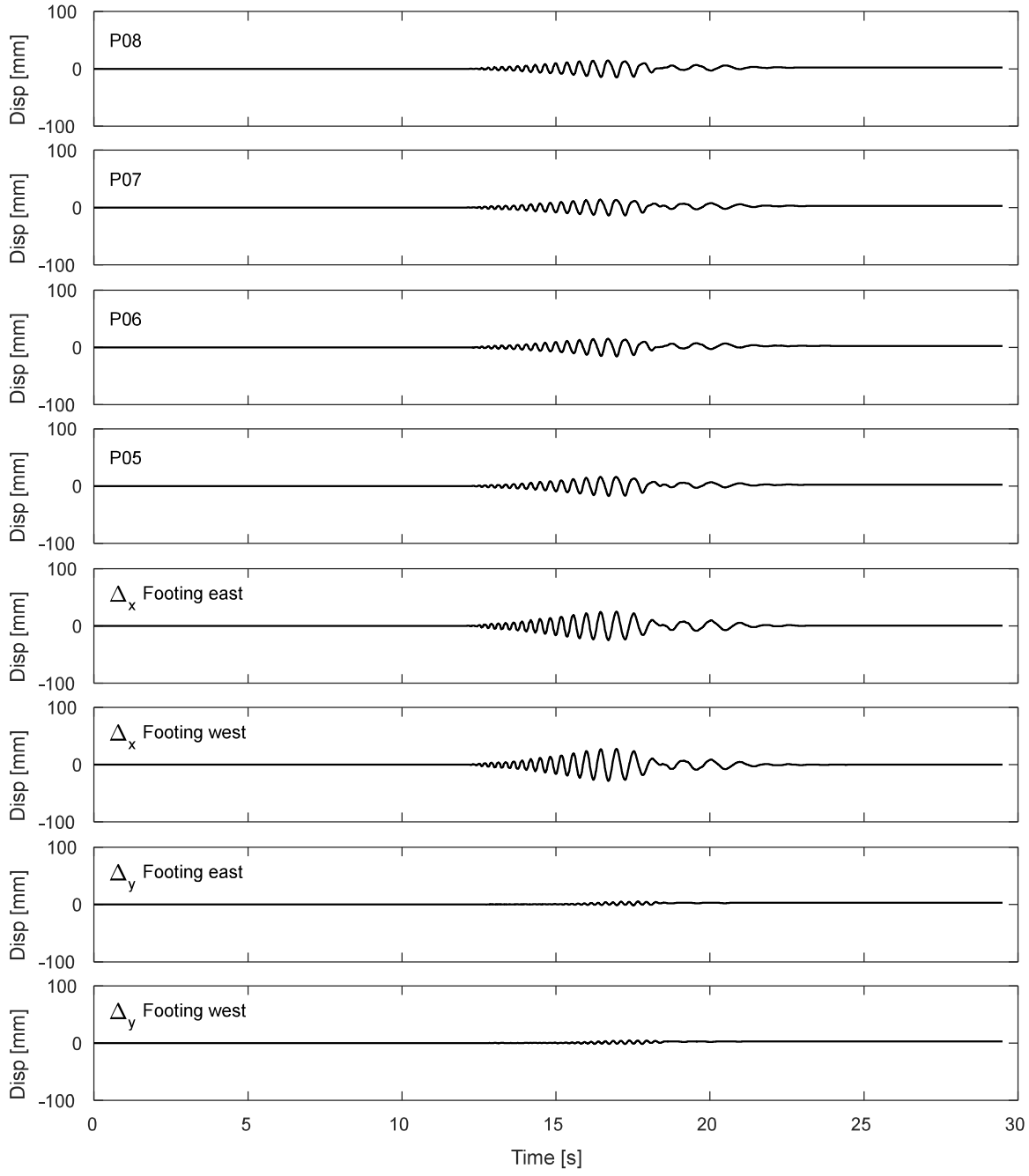

Figure K.3-7. Results of inclined potentiometers attached to top of strip footing during DT03-SS12-F04F10 motion.

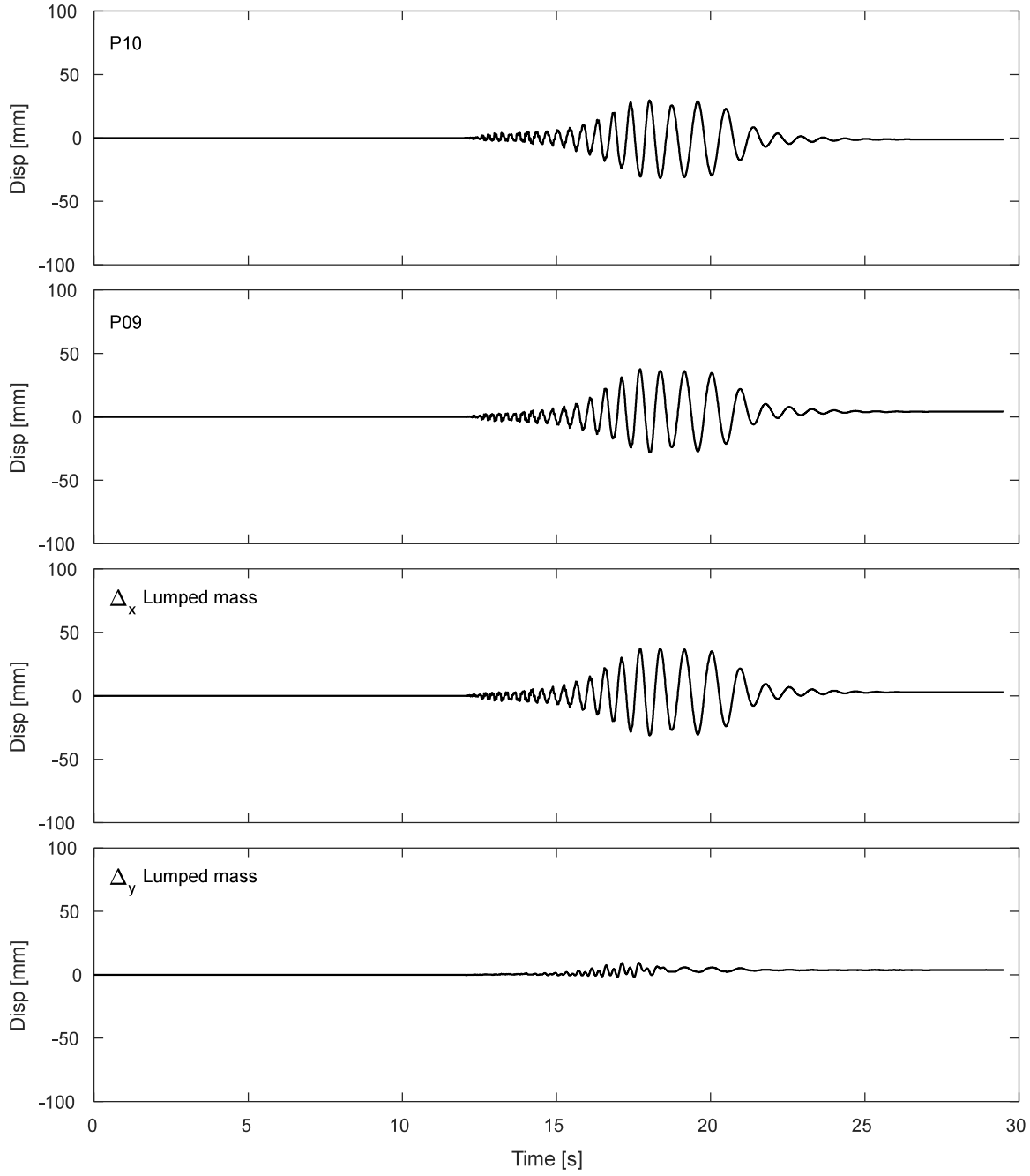

Figure K.3-8. Results of inclined potentiometers attached to lumped mass during DT03-SS12-F04F10 motion.

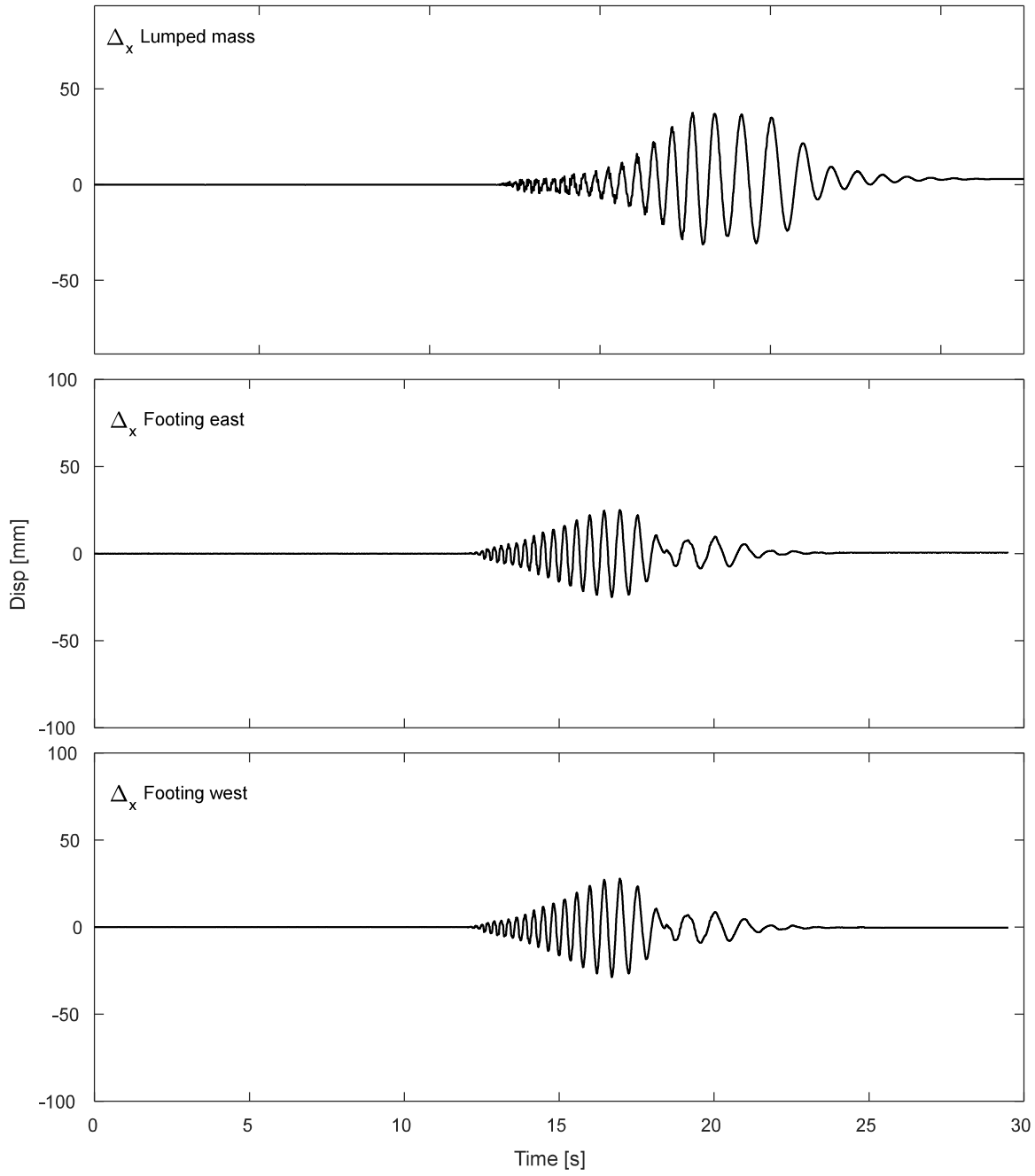

Figure K.3-9. Results of horizontal displacement of lumped mass and footing during DT03-SS12-F04F10 motion.

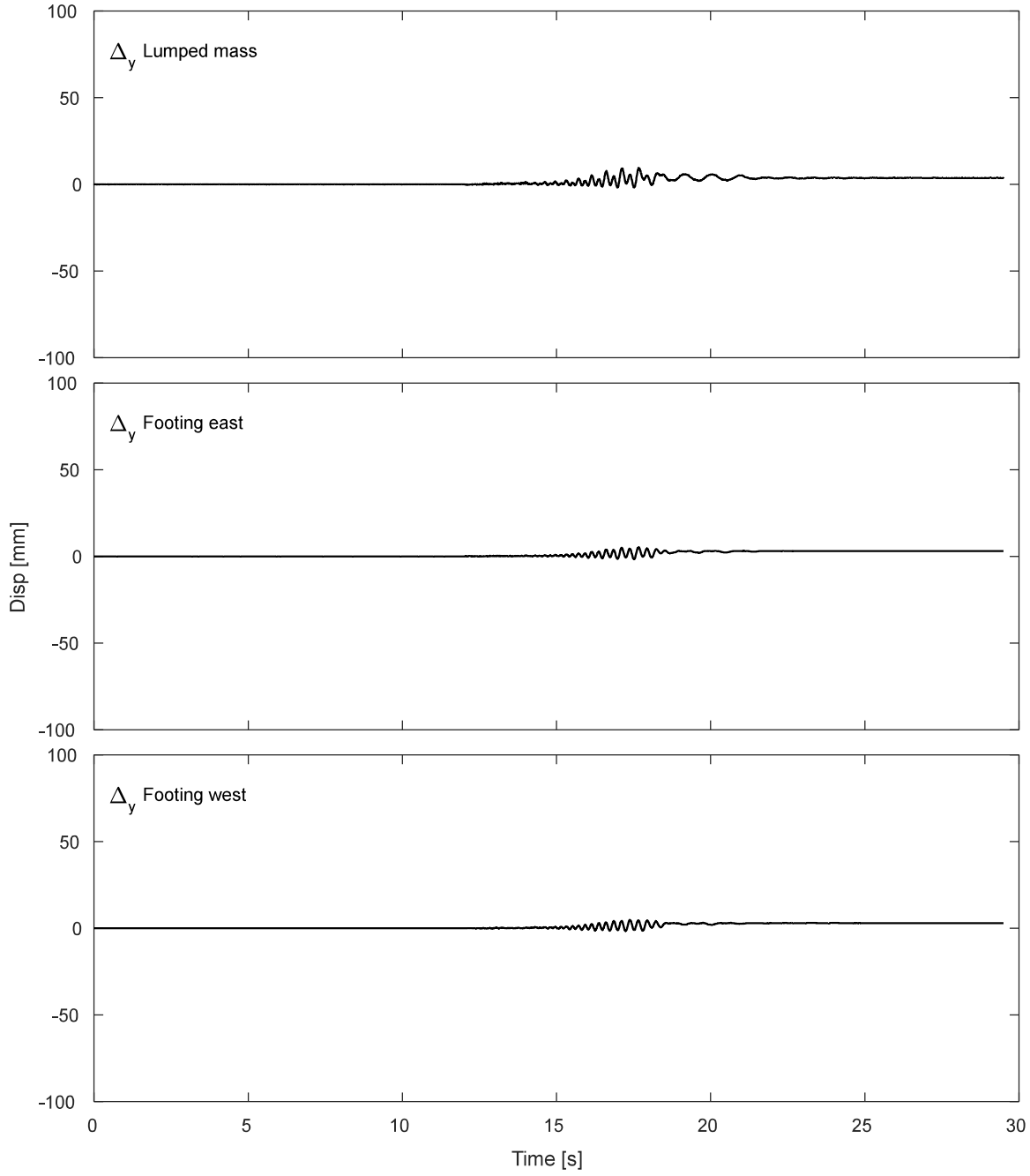

Figure K.3-10. Results of vertical displacement of lumped mass and footing during DT03-SS12-F04F10 motion.

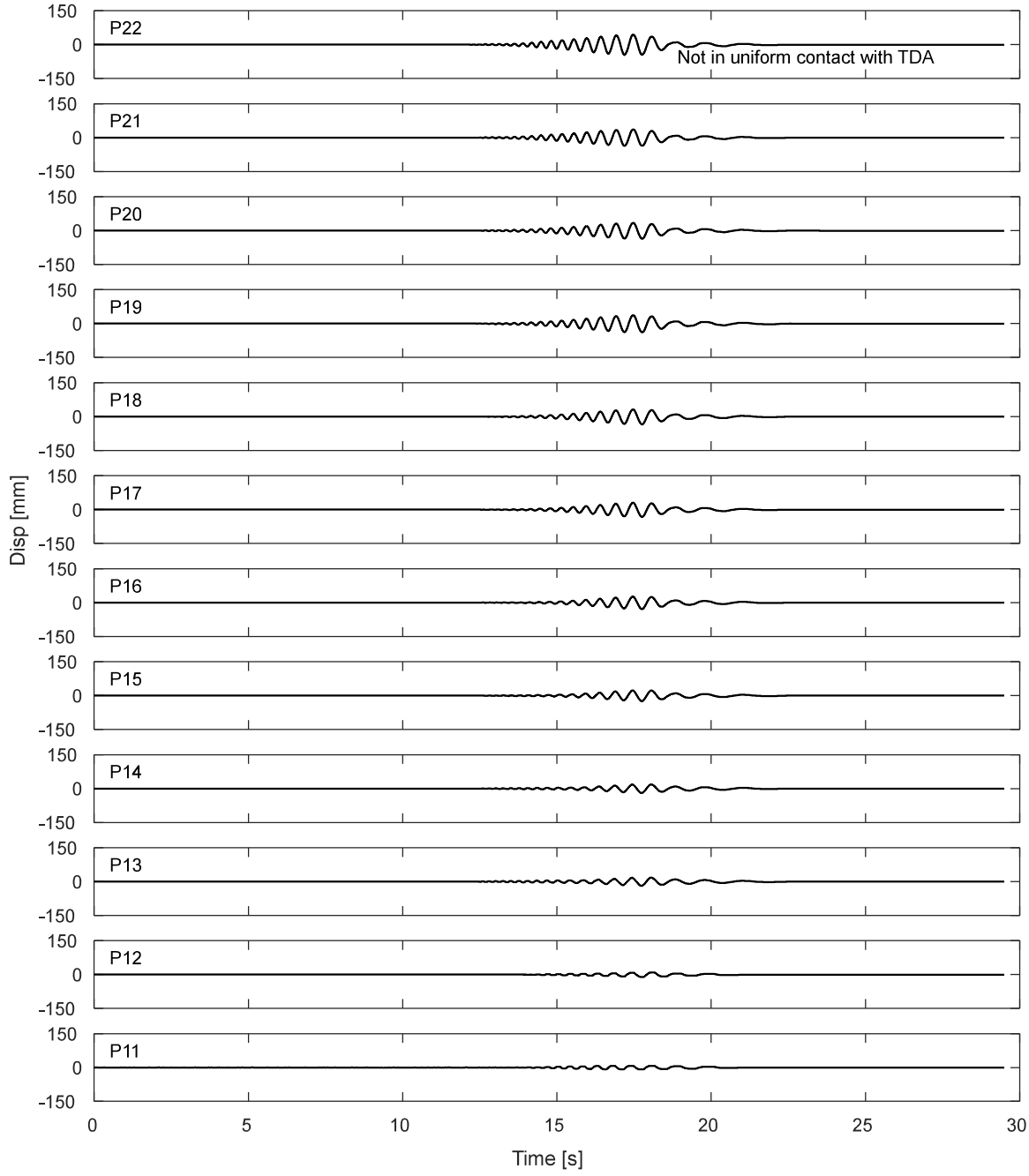

Figure K.3-11. Potentiometers results for the laminar box during DT03-SS12-F04F10 motion.

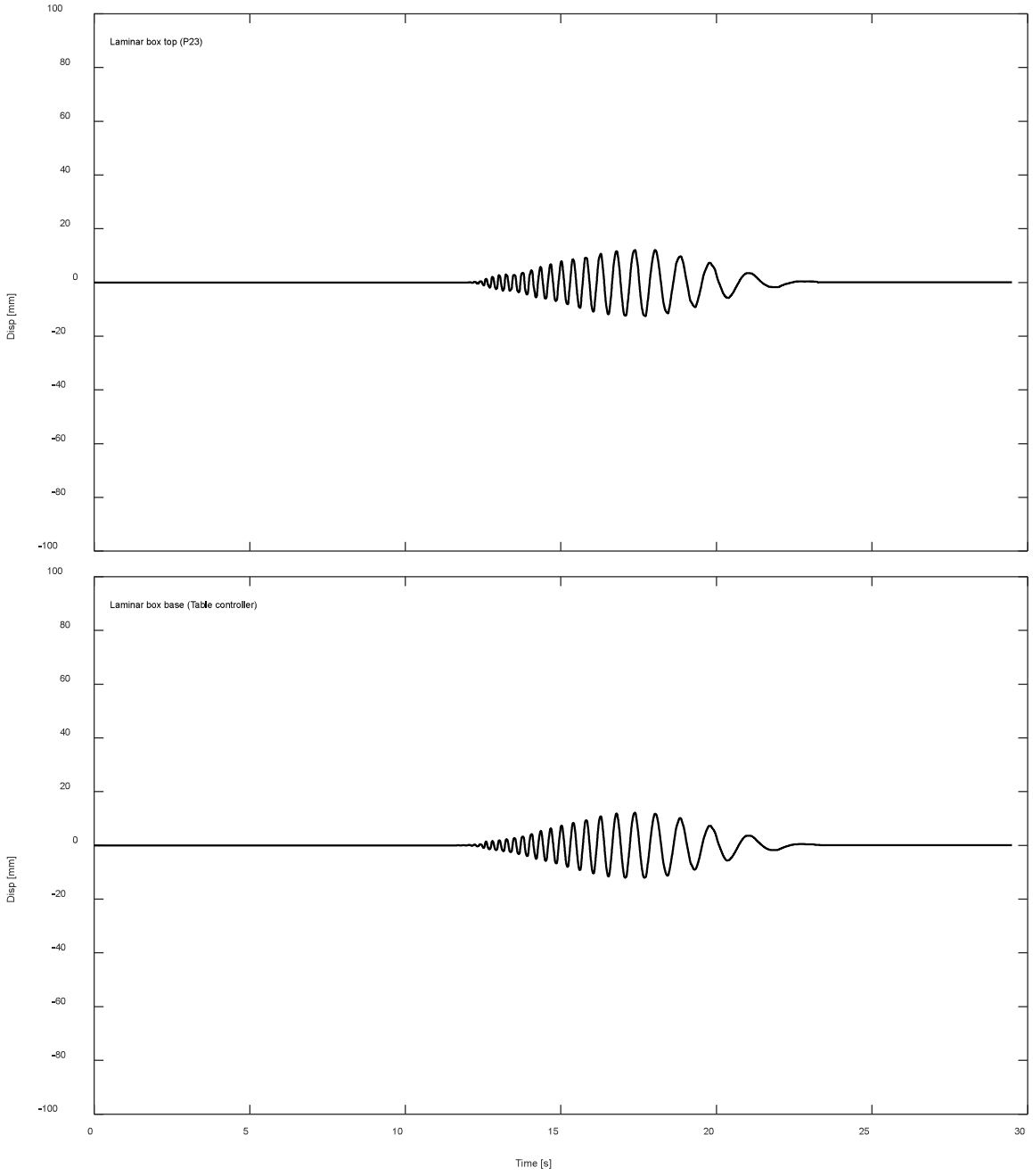

Figure K.3-12. Displacement response of top and base of laminar box during DT03-SS12-F04F10 motion.

K.3.3. Inclinometers.

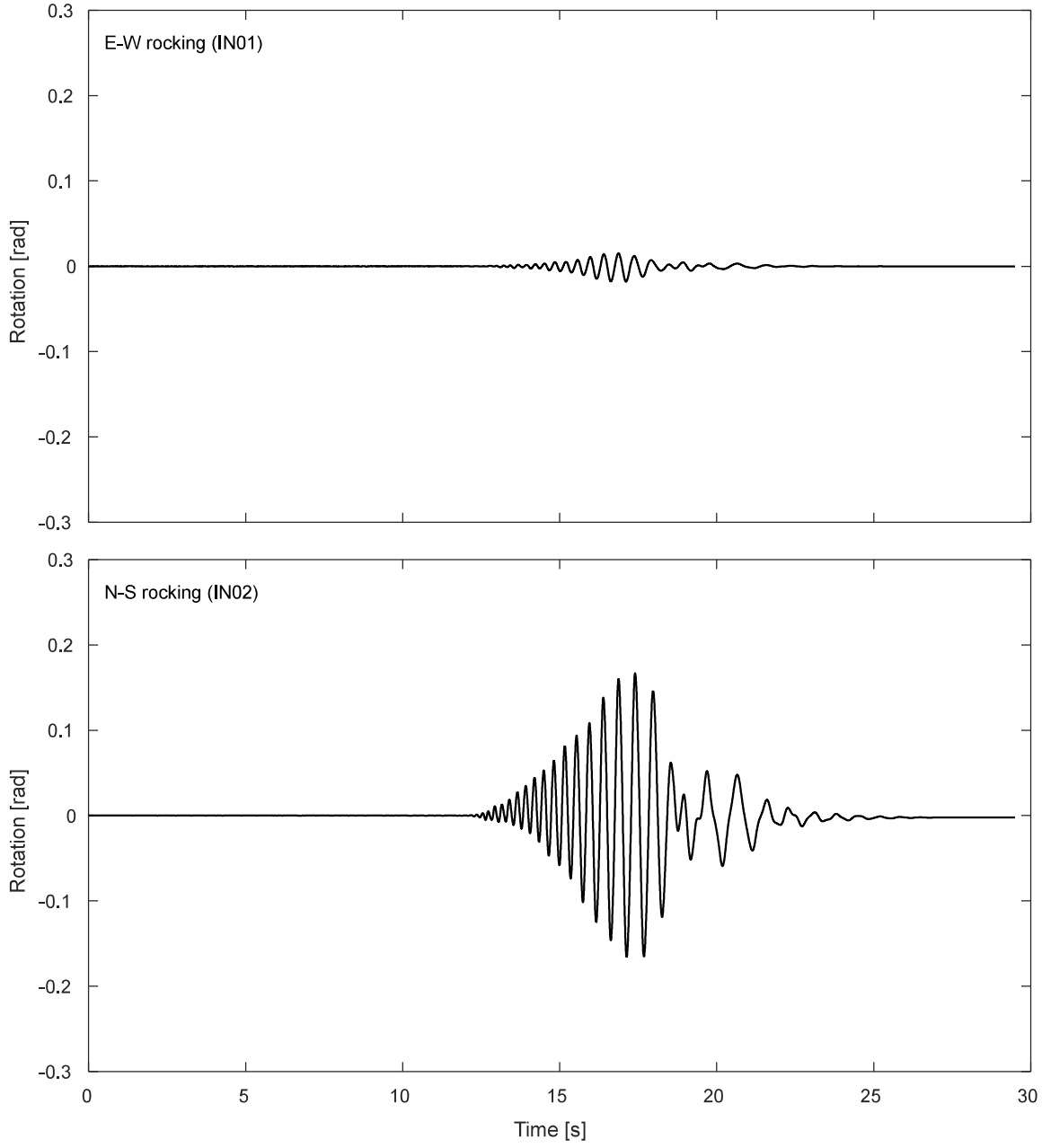

Figure K.3-13. Inclinometer results for the footing during DT03-SS12-F04F10 motion.

K.3.4. Pressure cells.

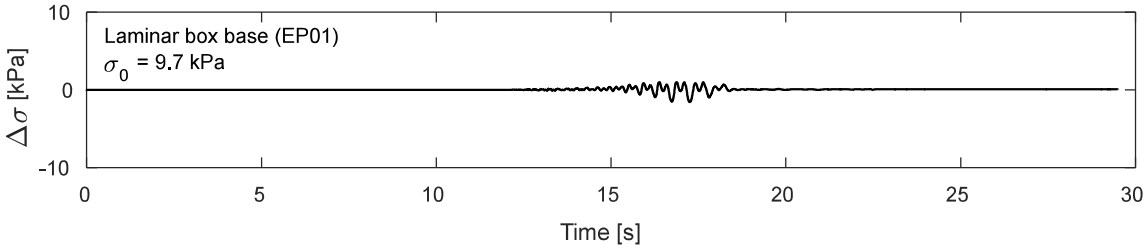

Figure K.3-14. Pressure cells results at laminar box base during DT03-SS12-F04F10 motion

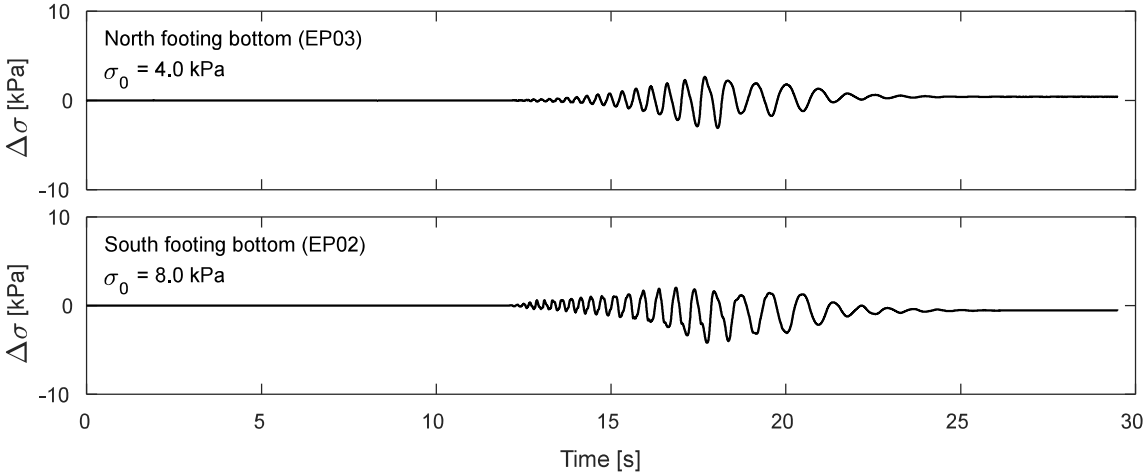

Figure K.3-15. Pressure cells results at footing bottom during DT03-SS12-F04F10 motion

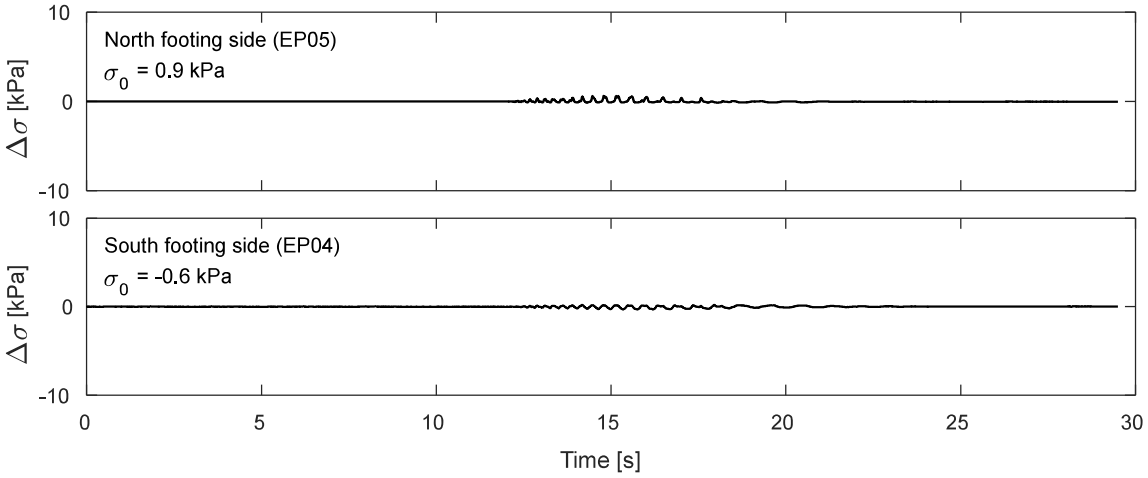

Figure K.3-16. Pressure cells results at footing sides during DT03-SS12-F04F10 motion

K.4. Time-history Records for DT03-SS16-F04F10 motion.

K.4.1 Input Motion

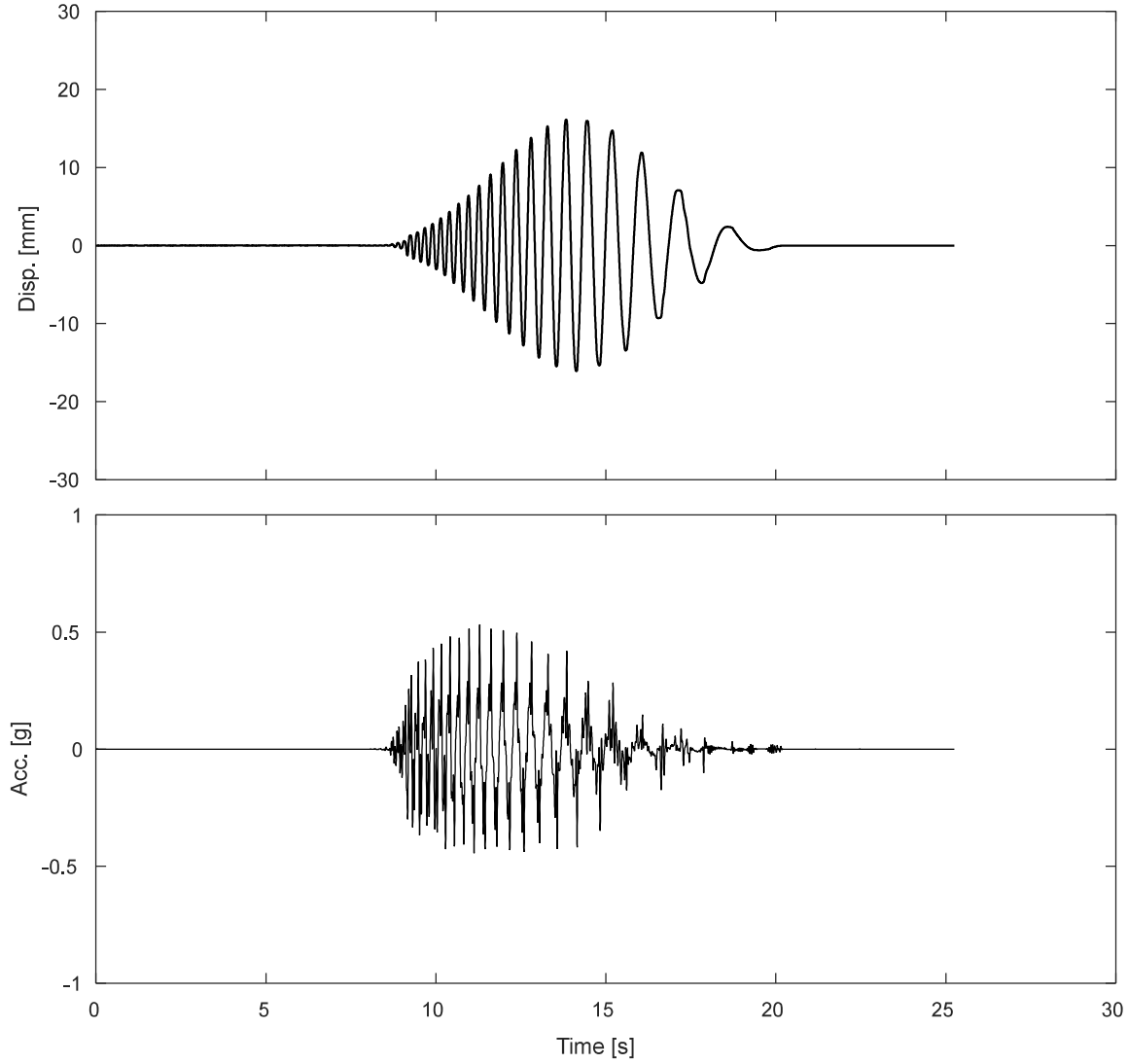

Figure K.4-1. Measured input displacement and acceleration at the base of the specimen during DT03-SS16-F04F10 motion

K.4.1 Accelerometers.

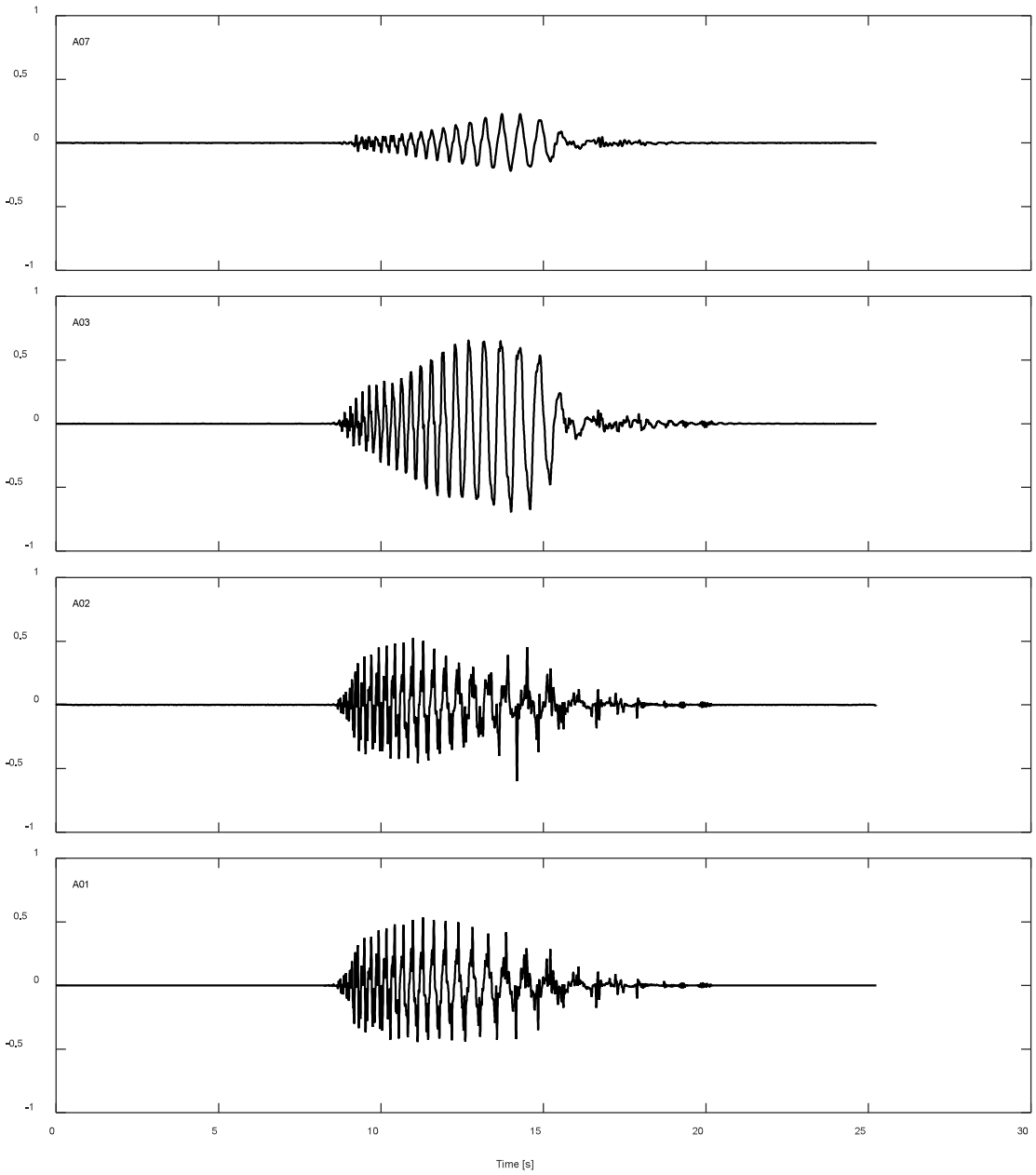

Figure K.4-2. Accelerations results along TDA during DT03-SS16-F04F10 motion.

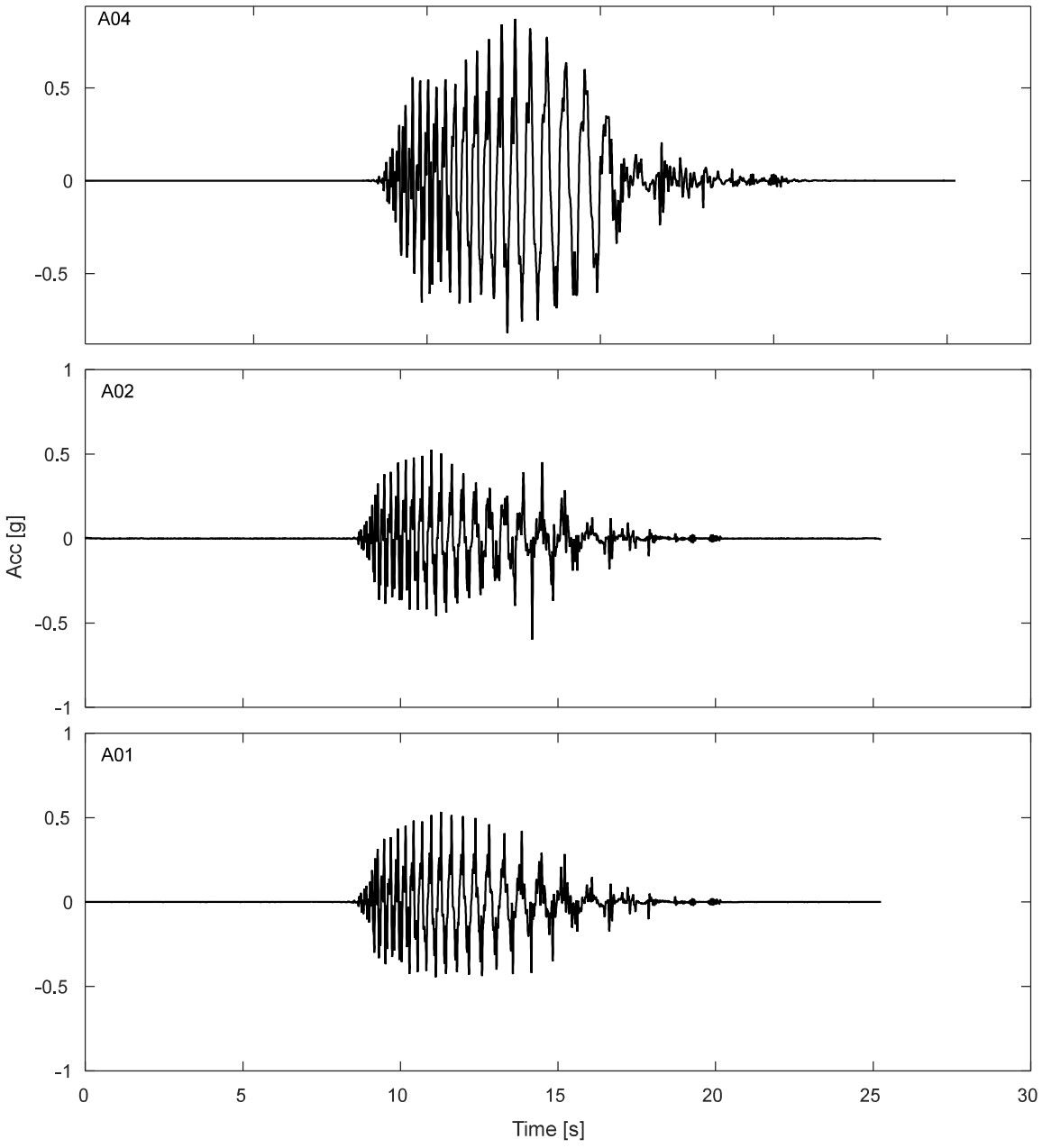

Figure K.4-3. Free field accelerations results for TDA during DT03-SS16-F04F10 motion.

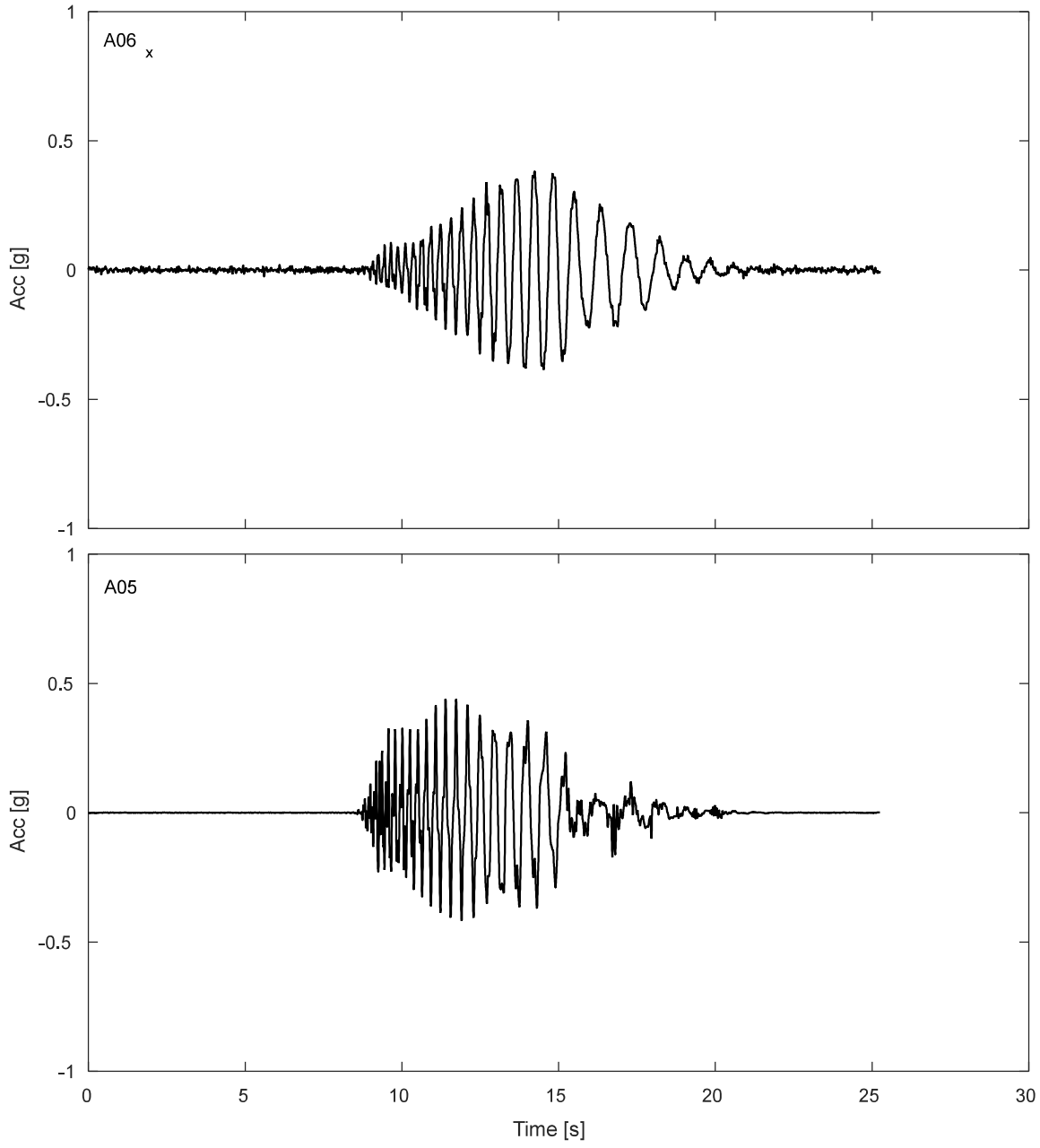

Figure K.4-4. Accelerations results SDOF structure during DT03-SS16-F04F10 motion.

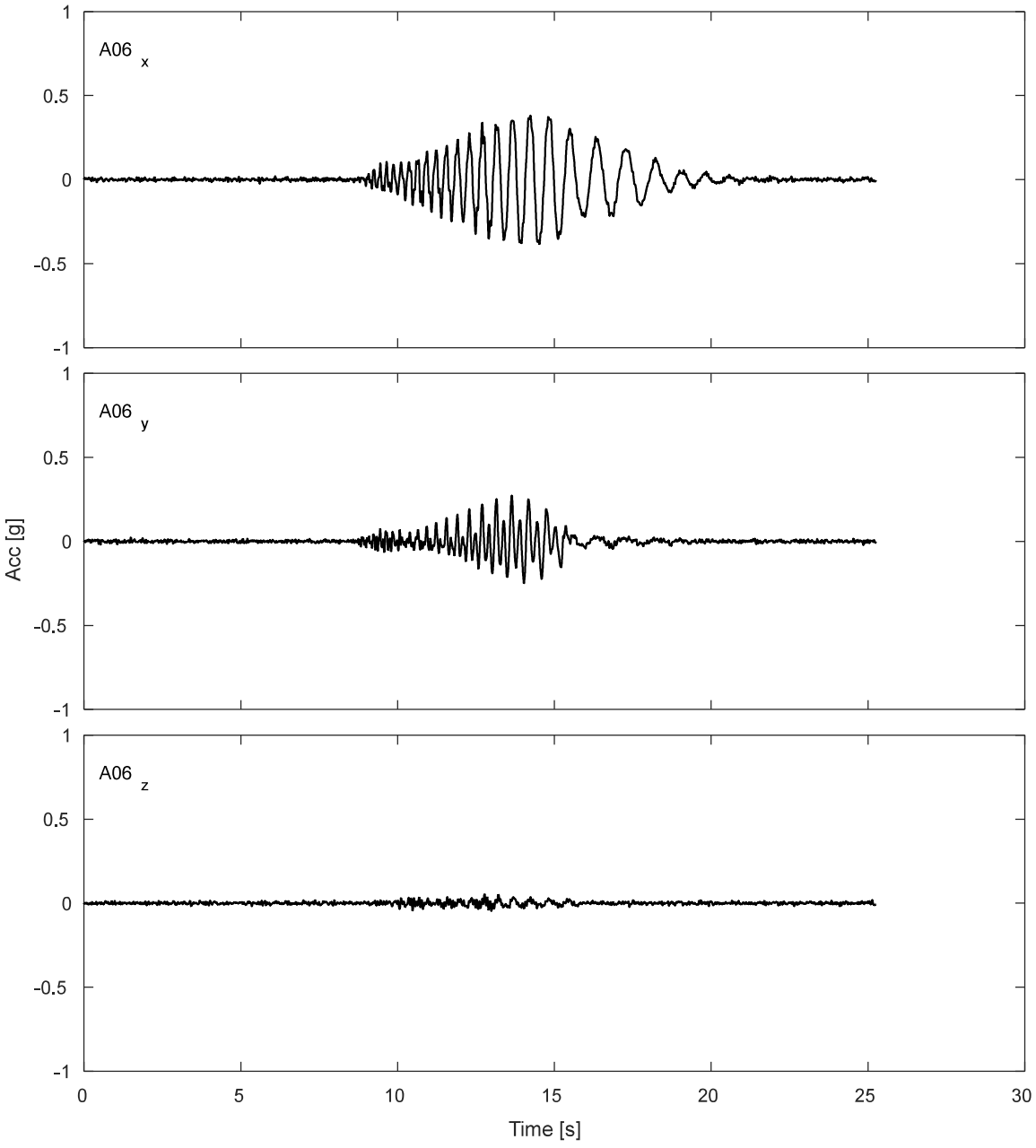

Figure K.4-5. Accelerations results for lumped mass of SDOF structure during DT03-SS16-F04F10 motion.

K.4.2 Potentiometers.

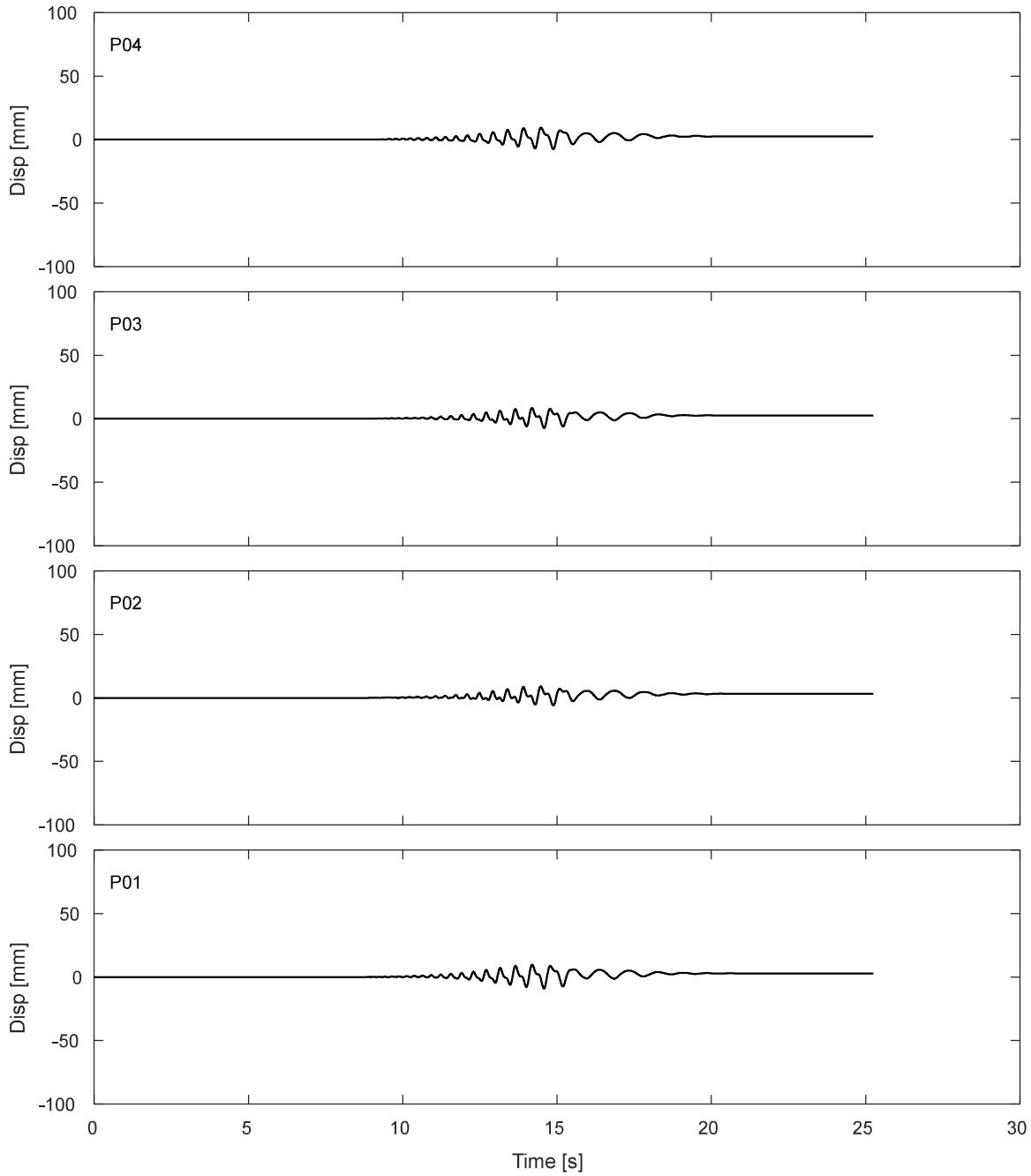

Figure K.4-6. Results of fully vertical potentiometers attached to corners of top of strip footing during DT03-SS16-F04F10 motion.

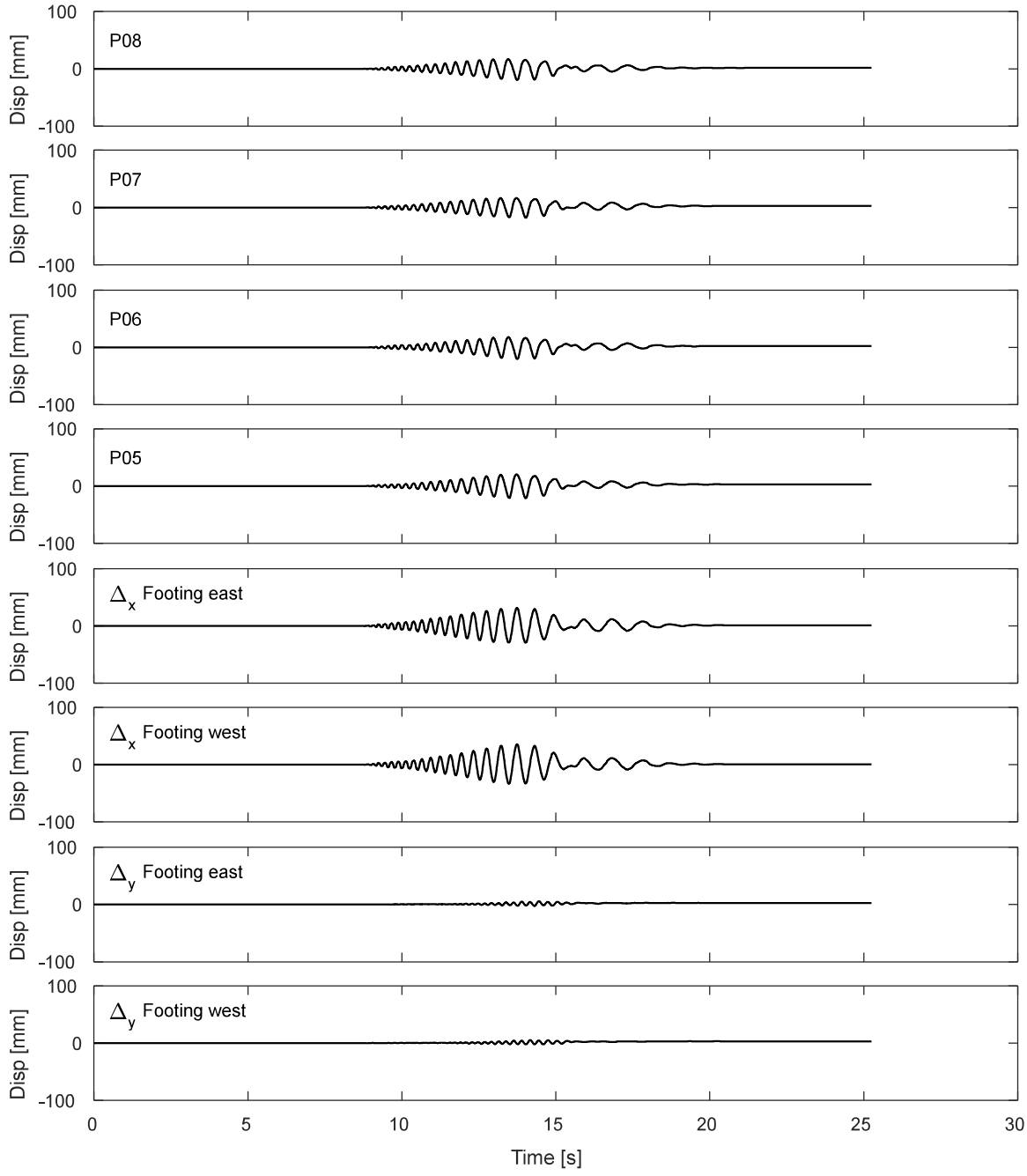

Figure K.4-7. Results of inclined potentiometers attached to top of strip footing during DT03-SS16-F04F10 motion.

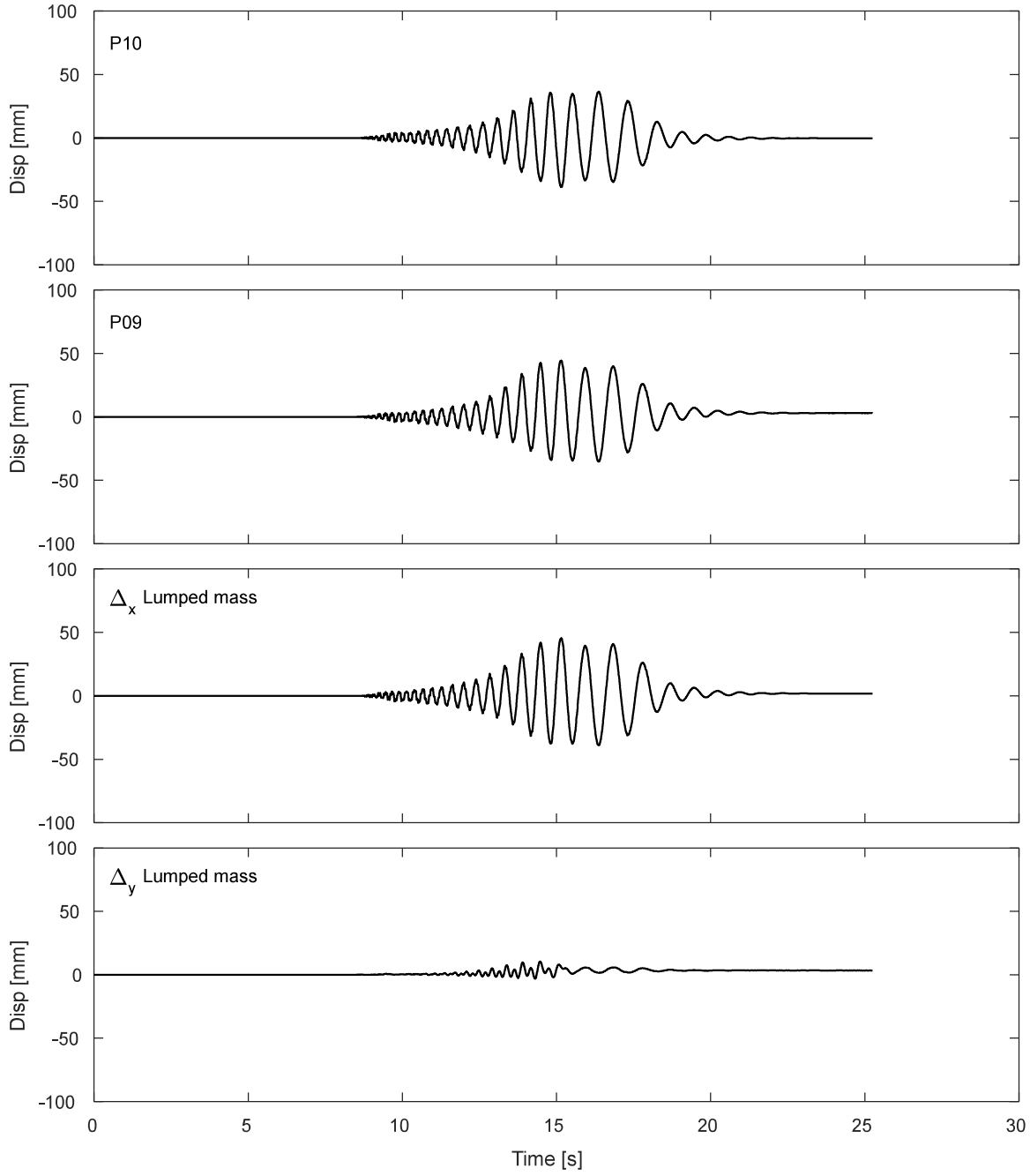

Figure K.4-8. Results of inclined potentiometers attached to lumped mass during DT03-SS16-F04F10 motion.

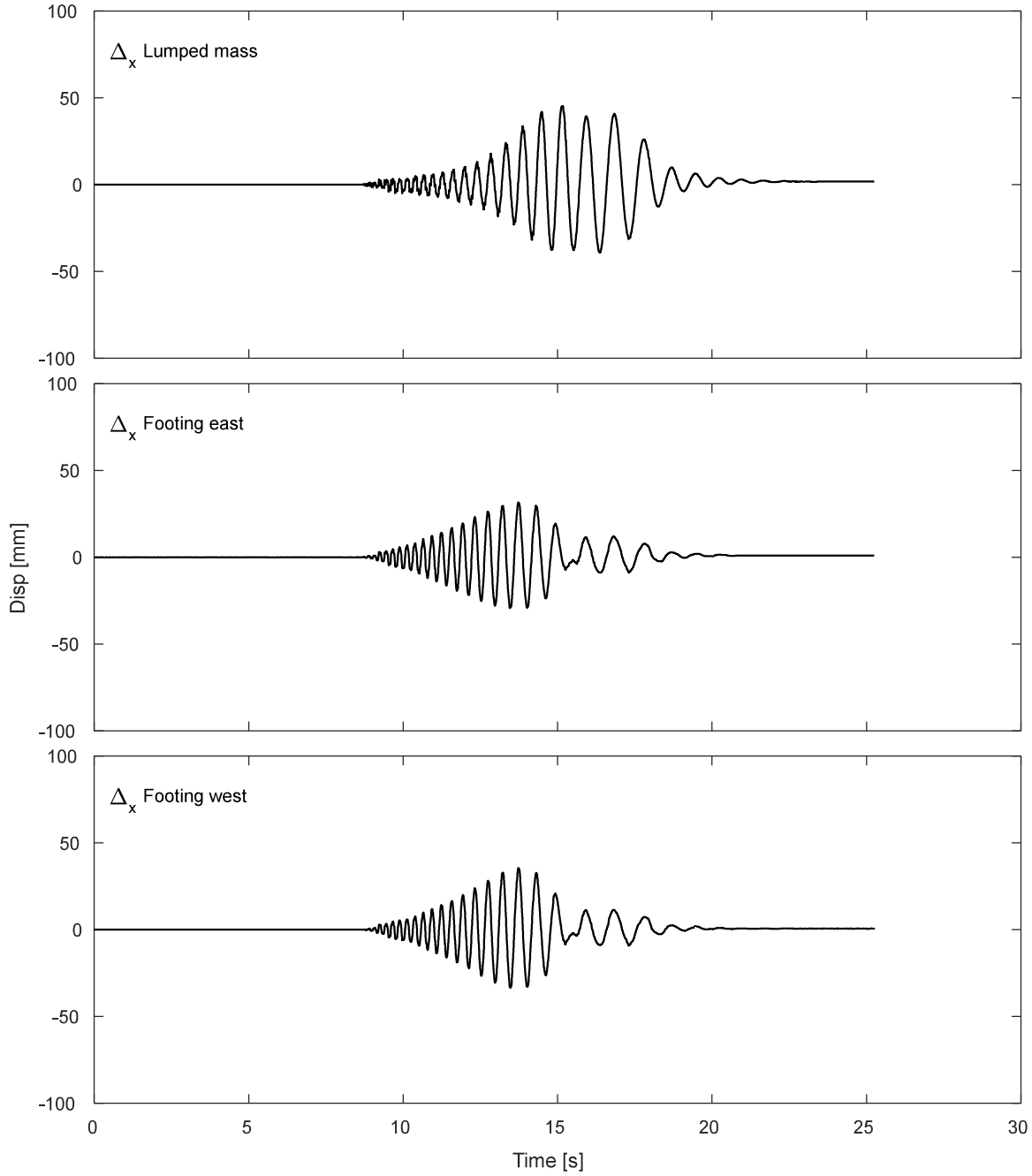

Figure K.4-9. Results of horizontal displacement of lumped mass and footing during DT03-SS16-F04F10 motion.

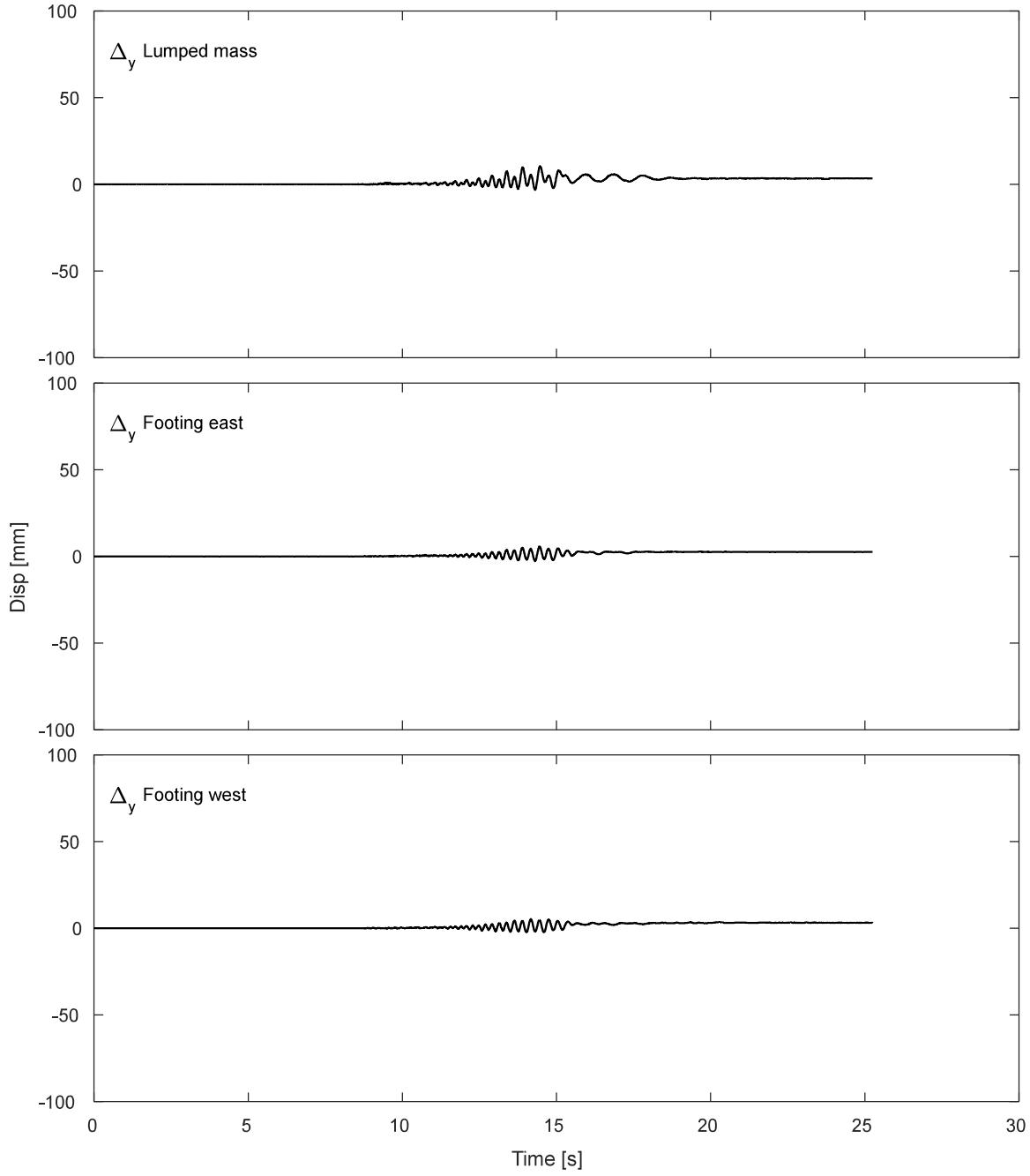

Figure K.4-10. Results of vertical displacement of lumped mass and footing during DT03-SS16-F04F10 motion.

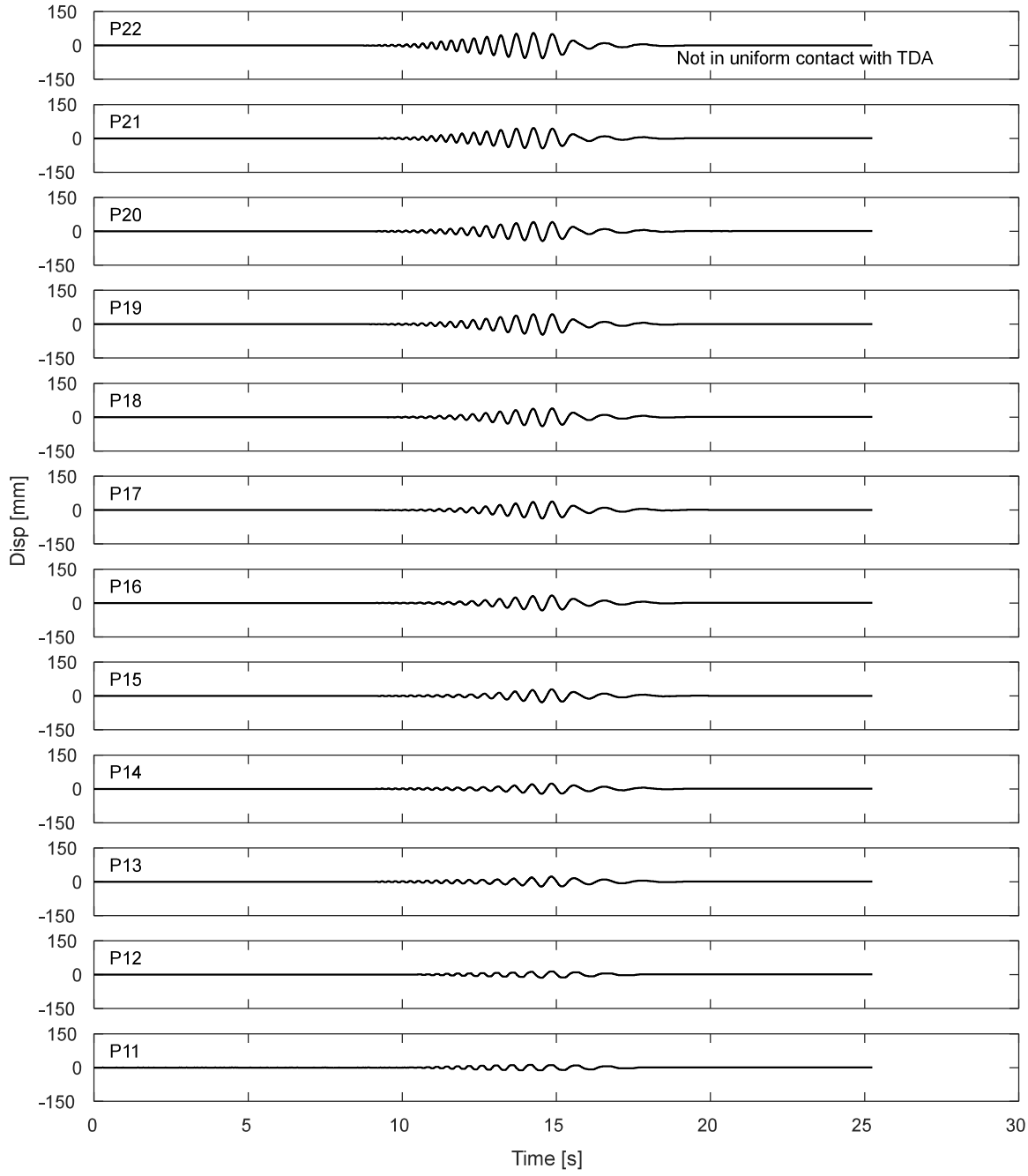

Figure K.4-11. Potentiometers results for the laminar box during DT03-SS16-F04F10 motion.

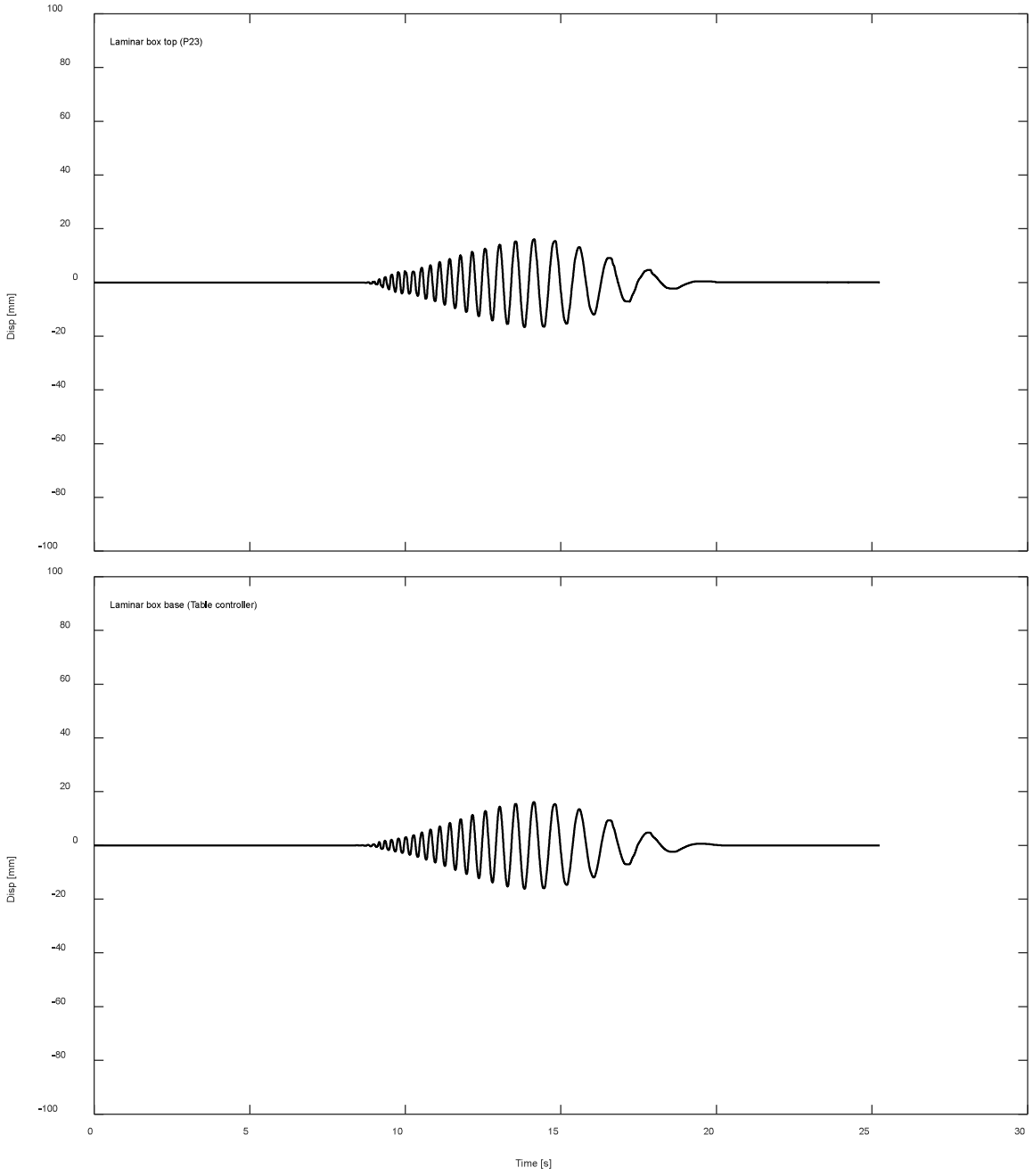

Figure K.4-12. Displacement response of top and base of laminar box during DT03-SS16-F04F10 motion.

K.4.3. Inclinometers.

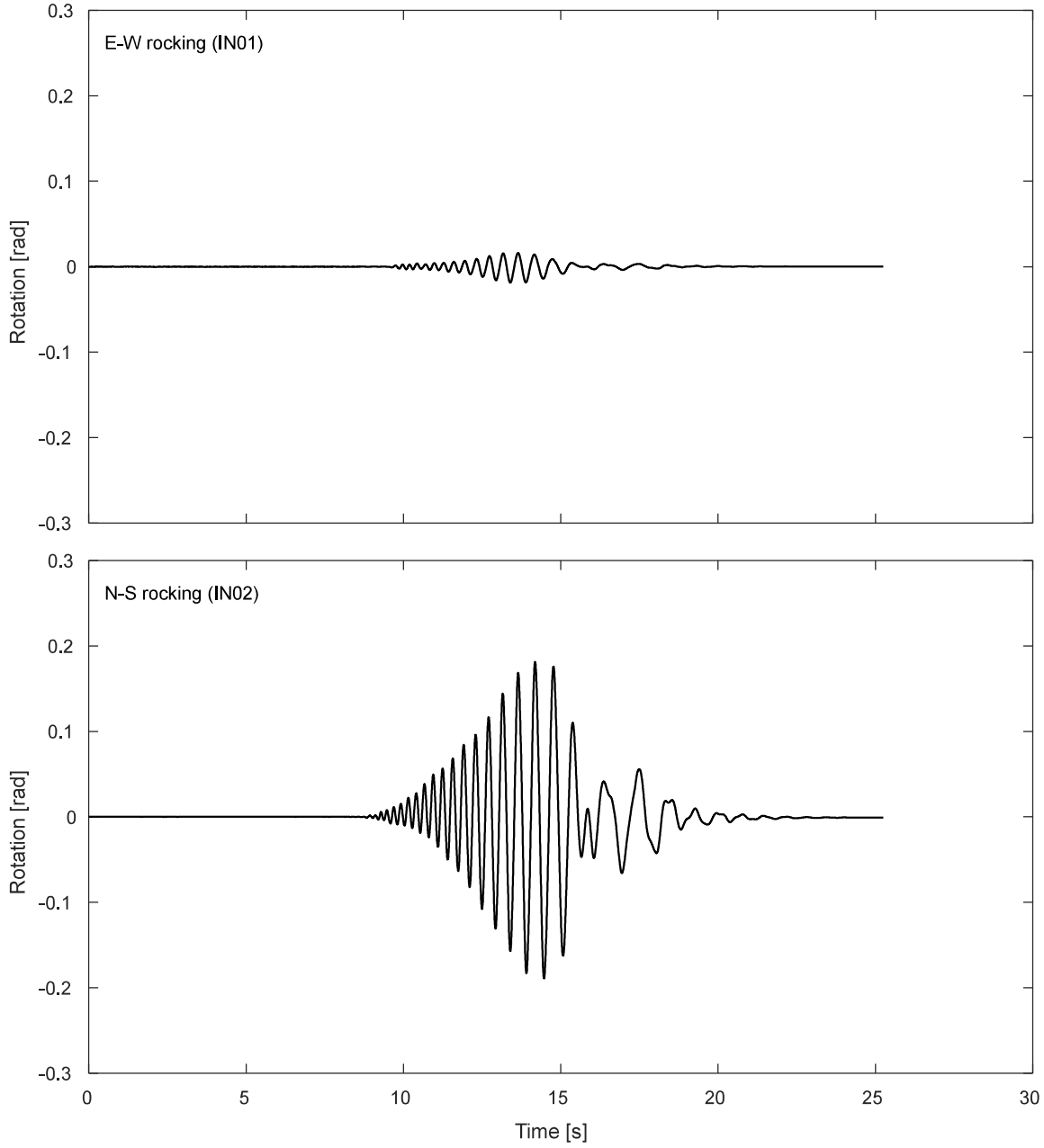

Figure K.4-13. Inclinometer results for the footing during DT03-SS16-F04F10 motion.

K.4.4. Pressure cells.

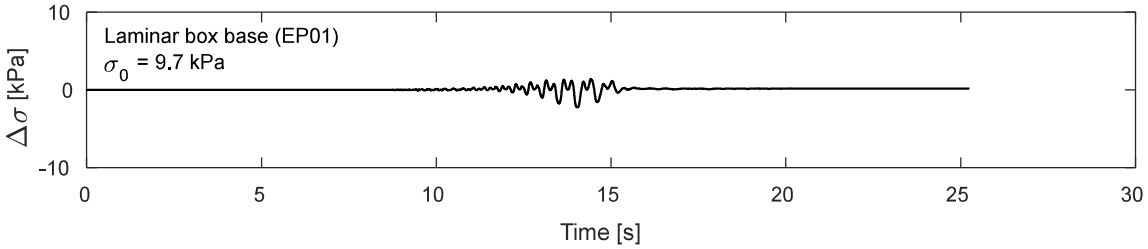

Figure K.4-14. Pressure cells results at laminar box base during DT03-SS16-F04F10 motion

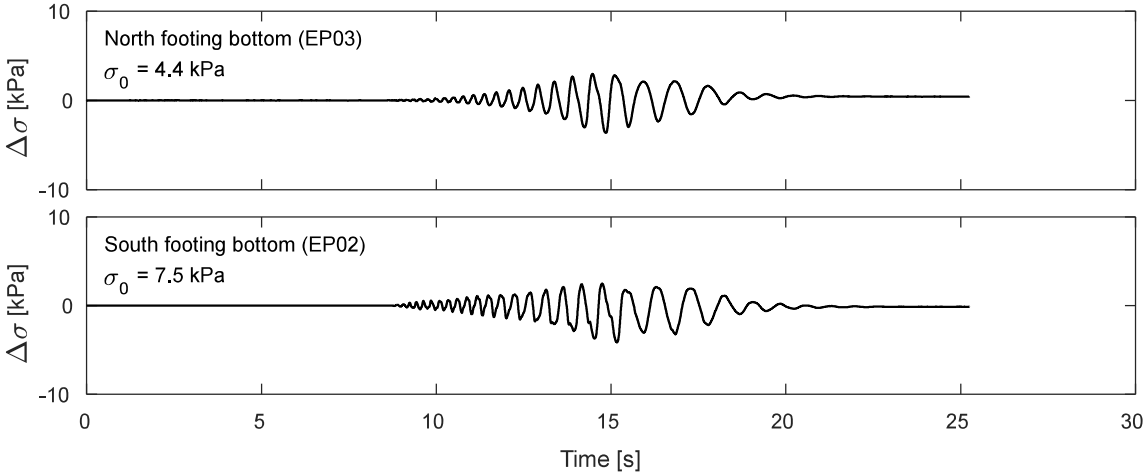

Figure K.4-15. Pressure cells results at footing bottom during DT03-SS16-F04F10 motion

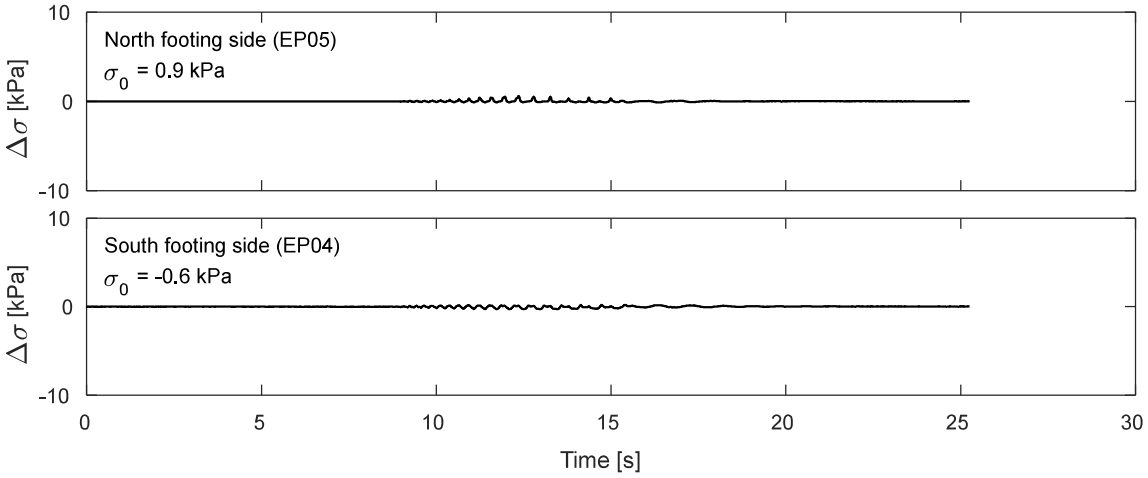

Figure K.4-16. Pressure cells results at footing sides during DT03-SS16-F04F10 motion

K.5. Time-history Records for DT03-SS20-F04F10 motion.

K.5.1 Input Motion

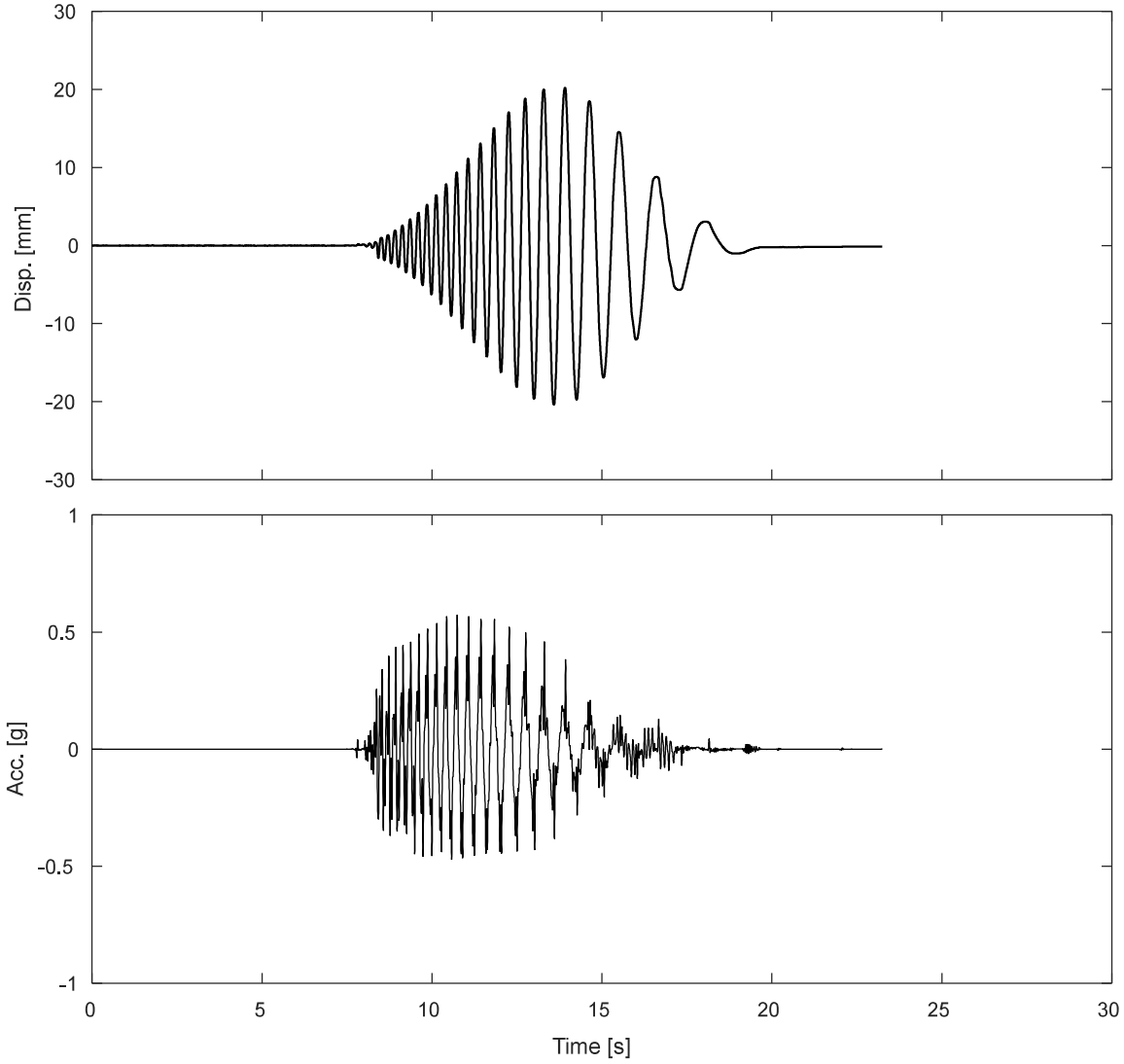

Figure K.5-1. Measured input displacement and acceleration at the base of the specimen during DT03-SS20-F04F10 motion

K.5.1 Accelerometers.

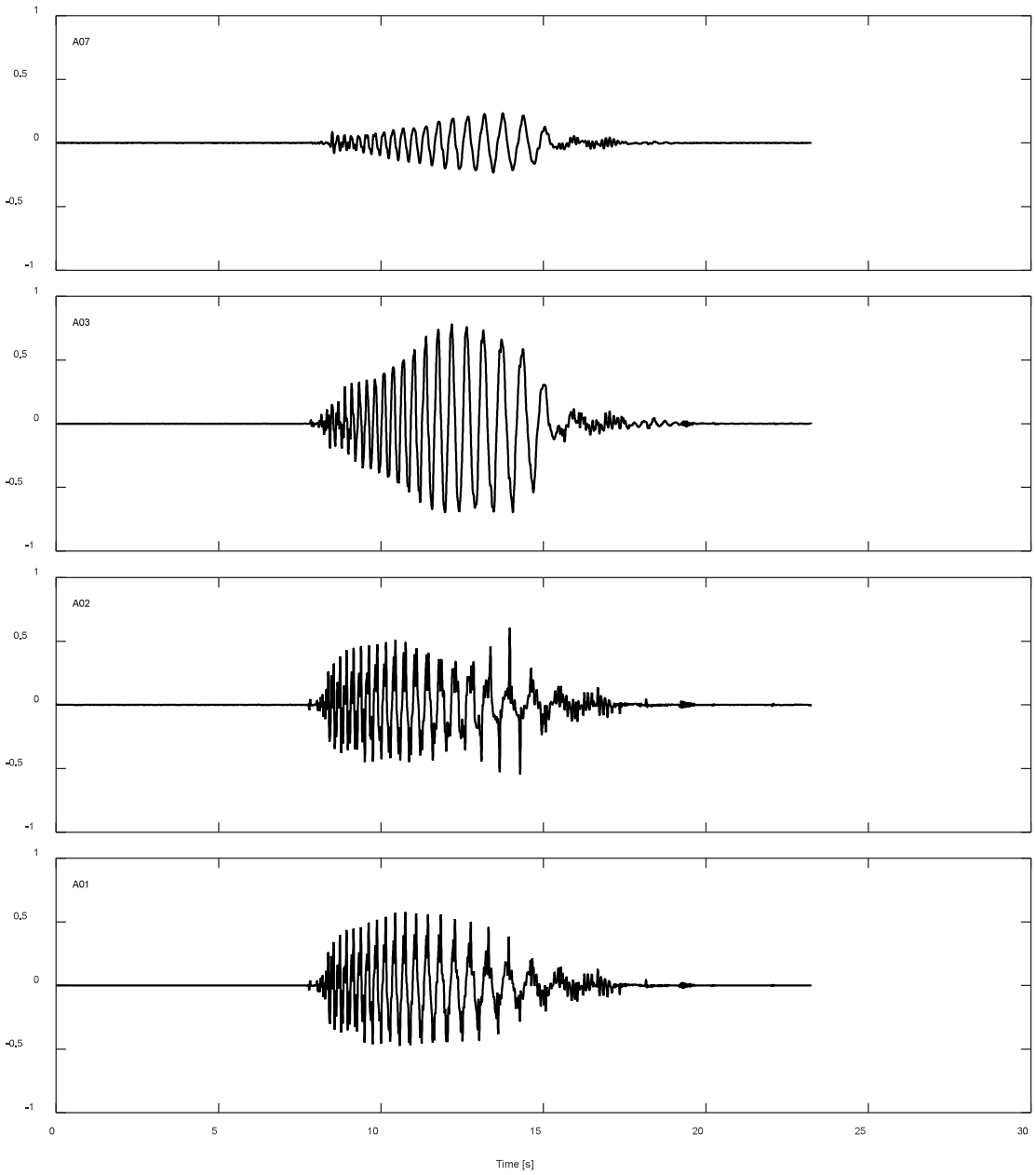

Figure K.5-2. Accelerations results along TDA during DT03-SS20-F04F10 motion.

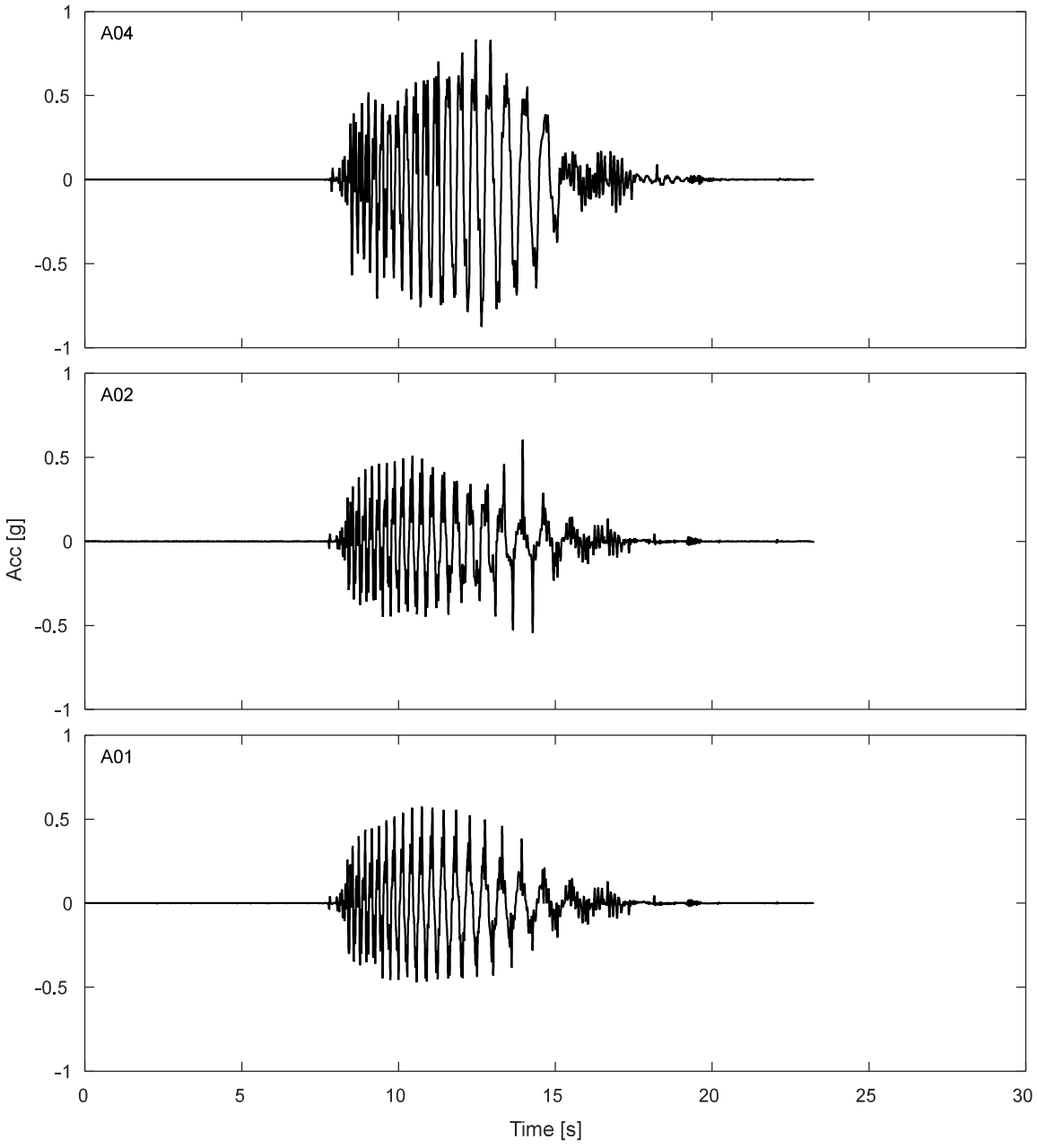

Figure K.5-3. Free field accelerations results for TDA during DT03-SS20-F04F10 motion.

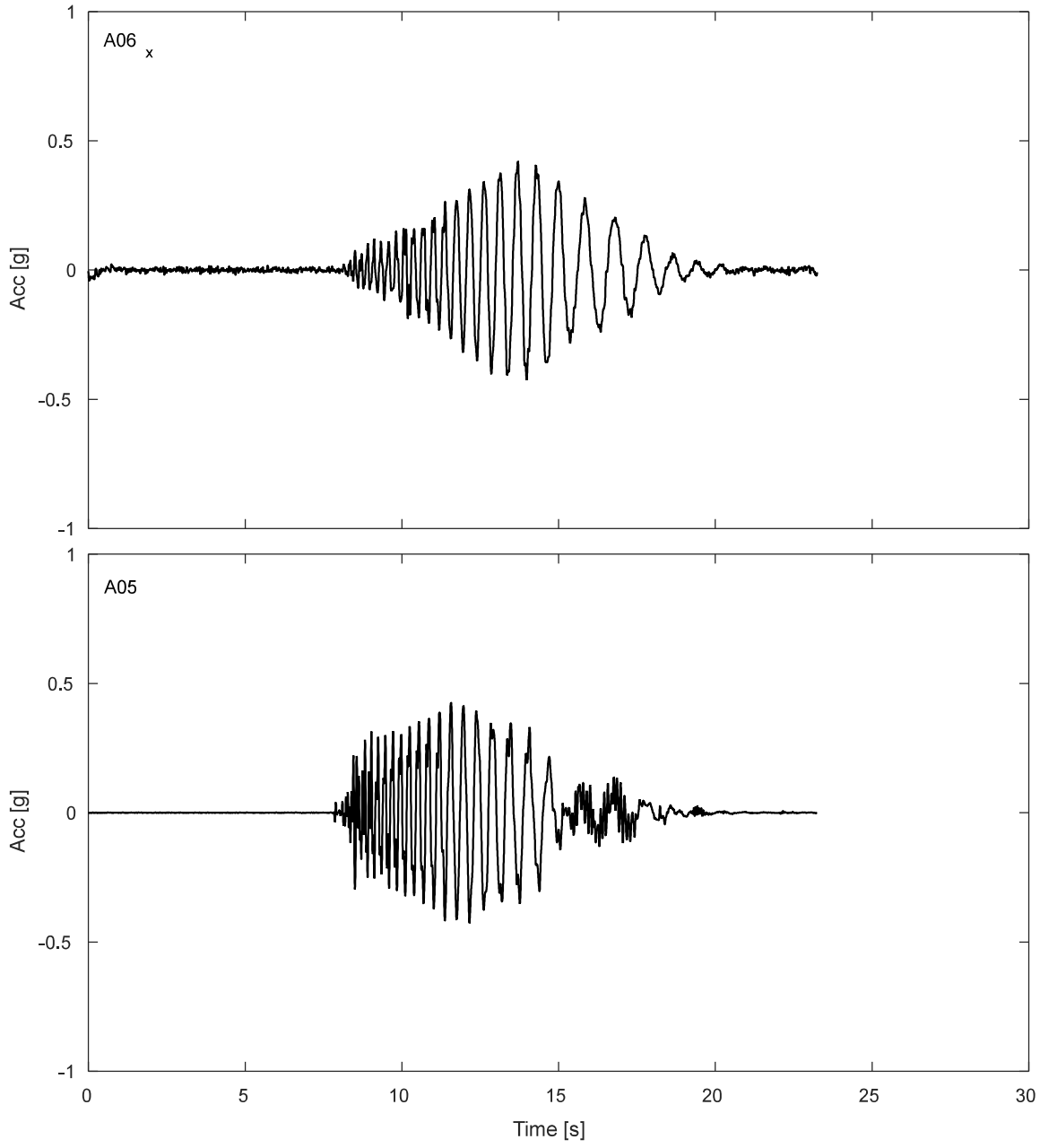

Figure K.5-4. Accelerations results SDOF structure during DT03-SS20-F04F10 motion.

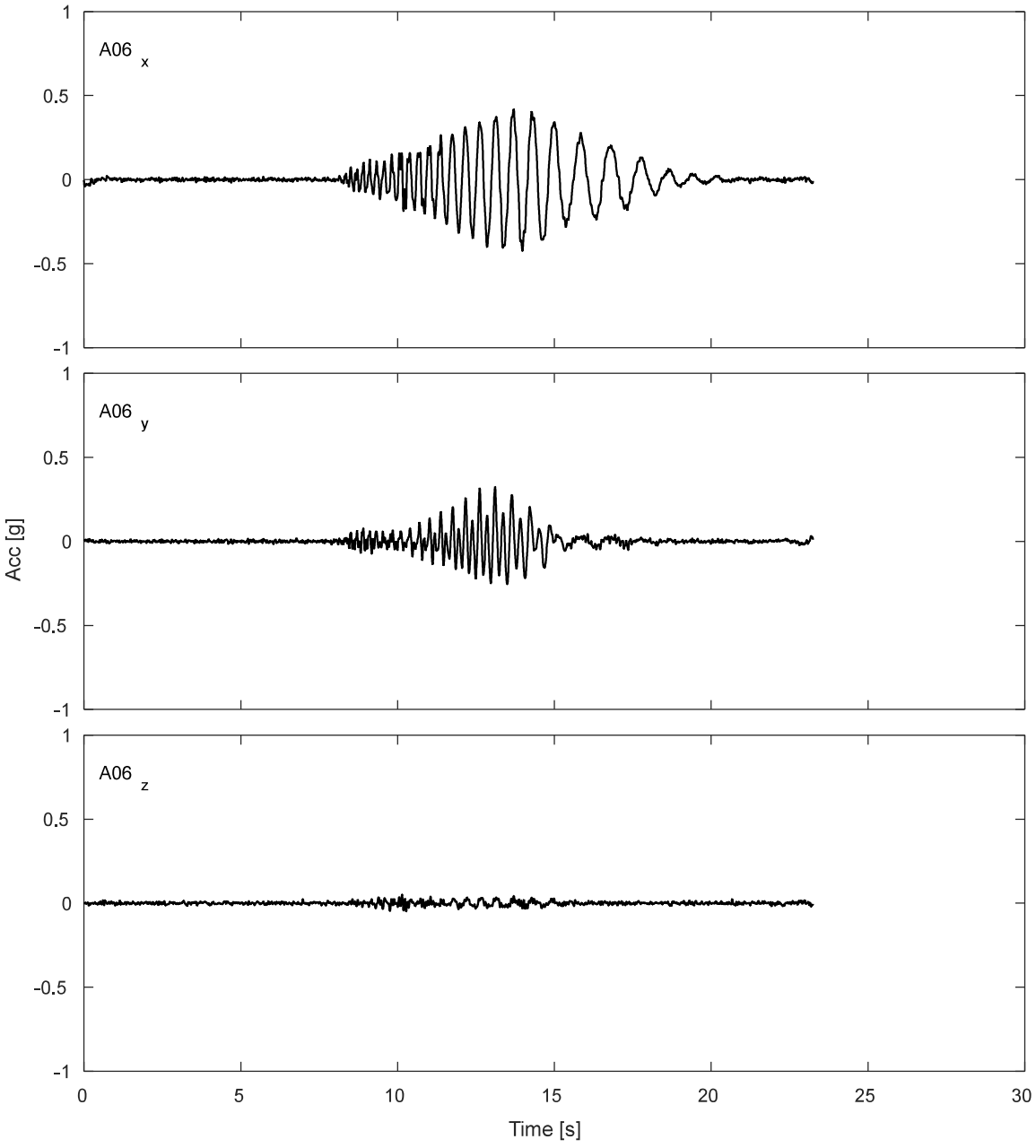

Figure K.5-5. Accelerations results for lumped mass of SDOF structure during DT03-SS20-F04F10 motion.

K.5.2 Potentiometers.

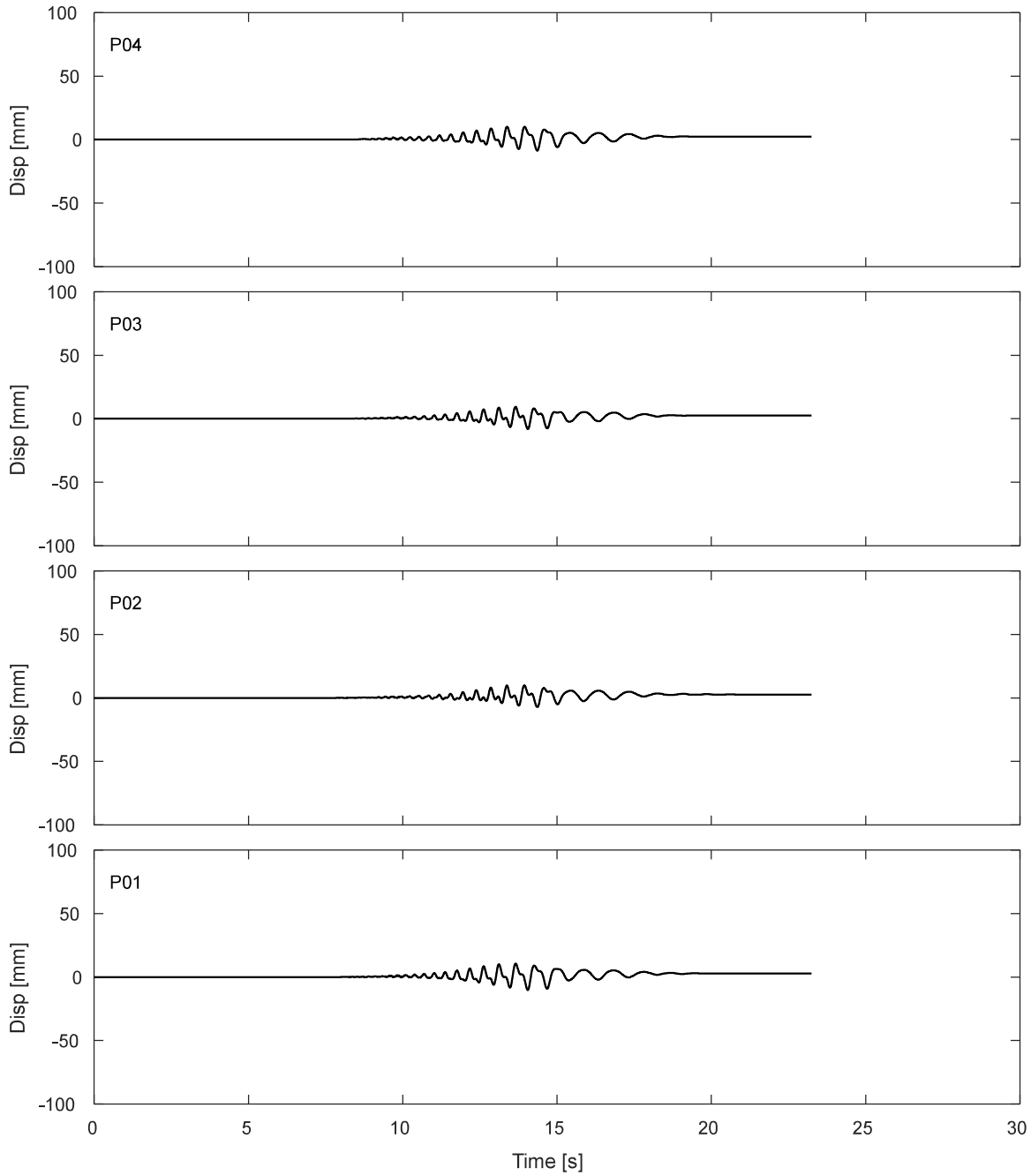

Figure K.5-6. Results of fully vertical potentiometers attached to corners of top of strip footing during DT03-SS20-F04F10 motion.

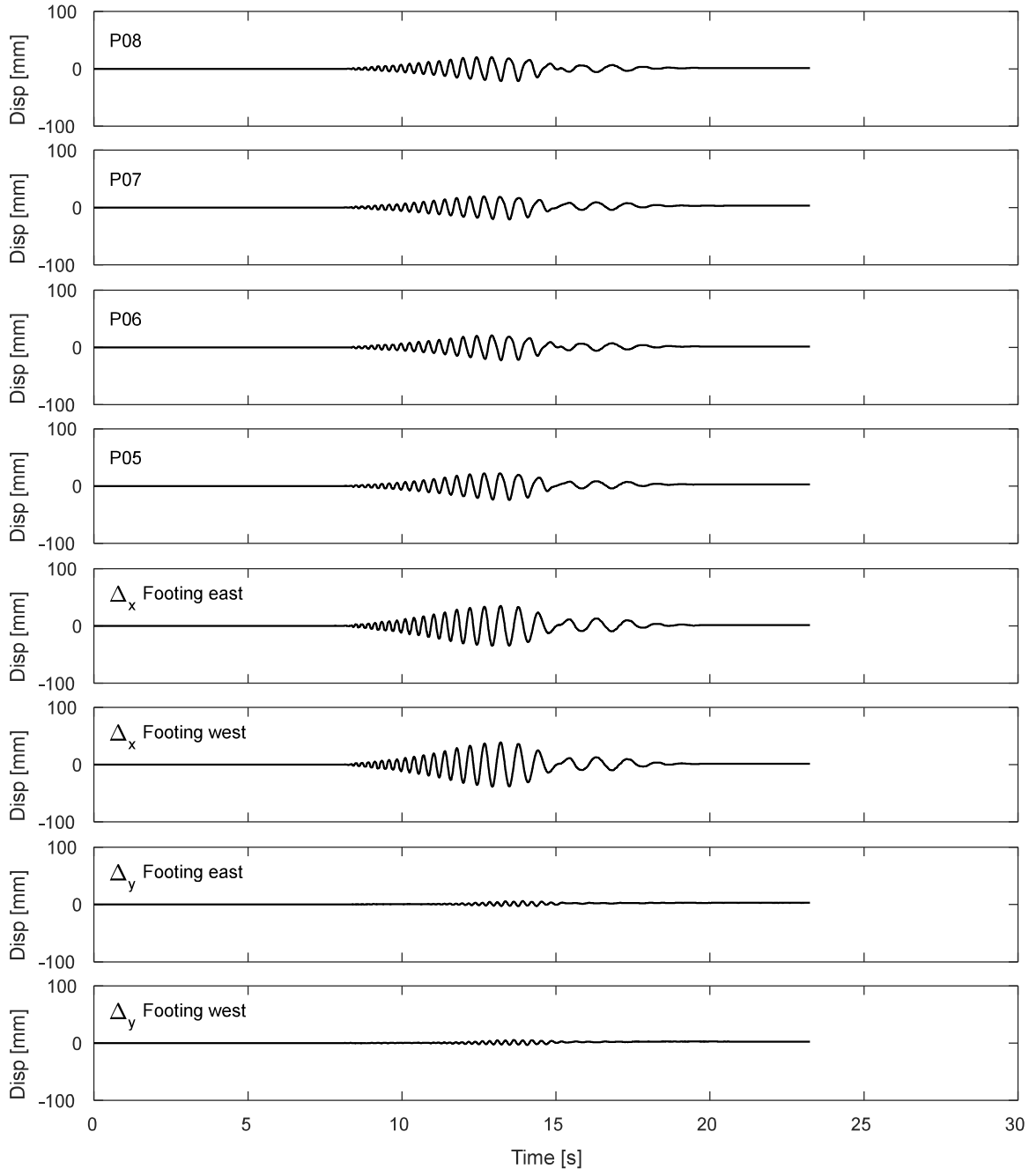

Figure K.5-7. Results of inclined potentiometers attached to top of strip footing during DT03-SS20-F04F10 motion.

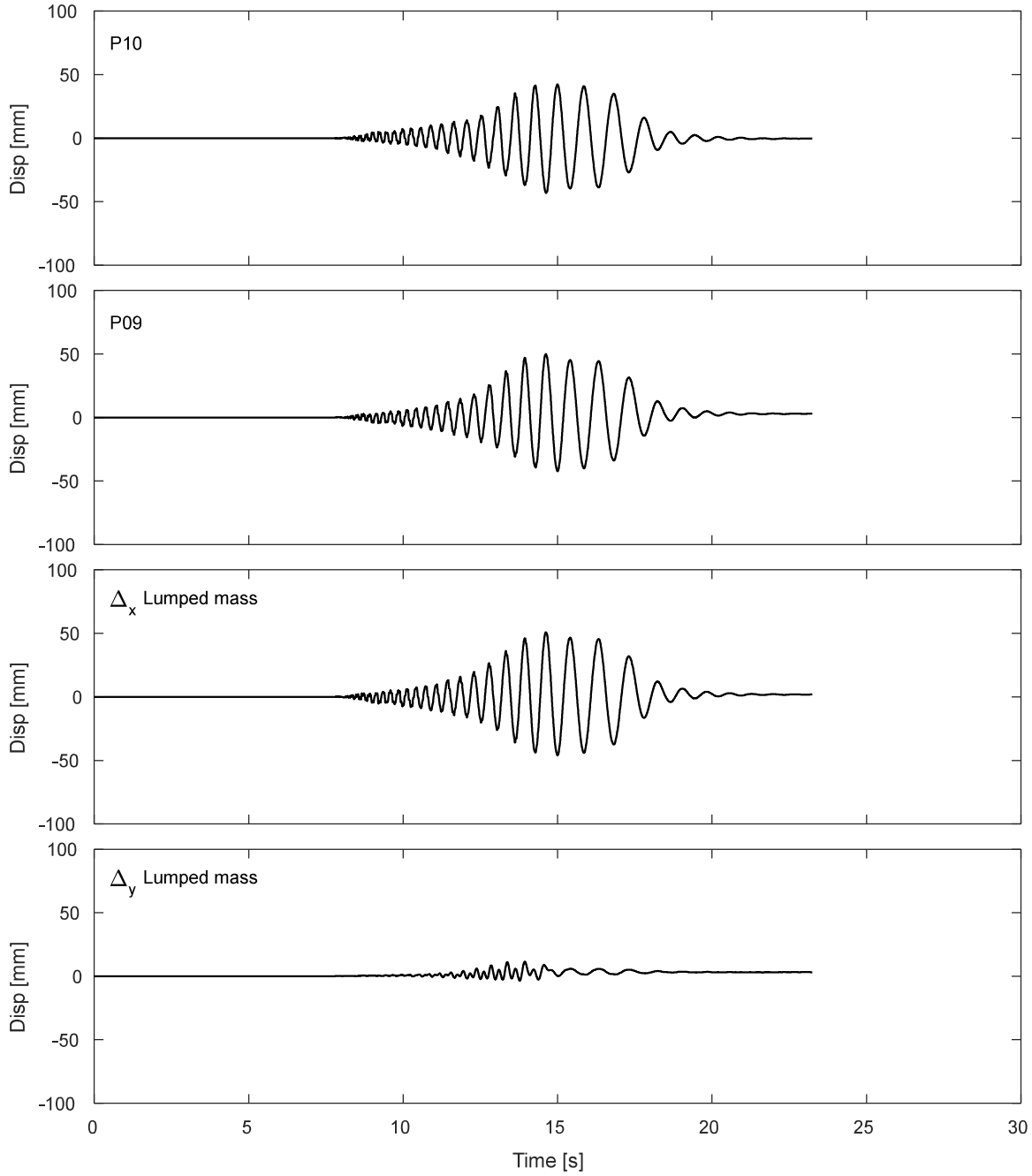

Figure K.5-8. Results of inclined potentiometers attached to lumped mass during DT03-SS20-F04F10 motion.

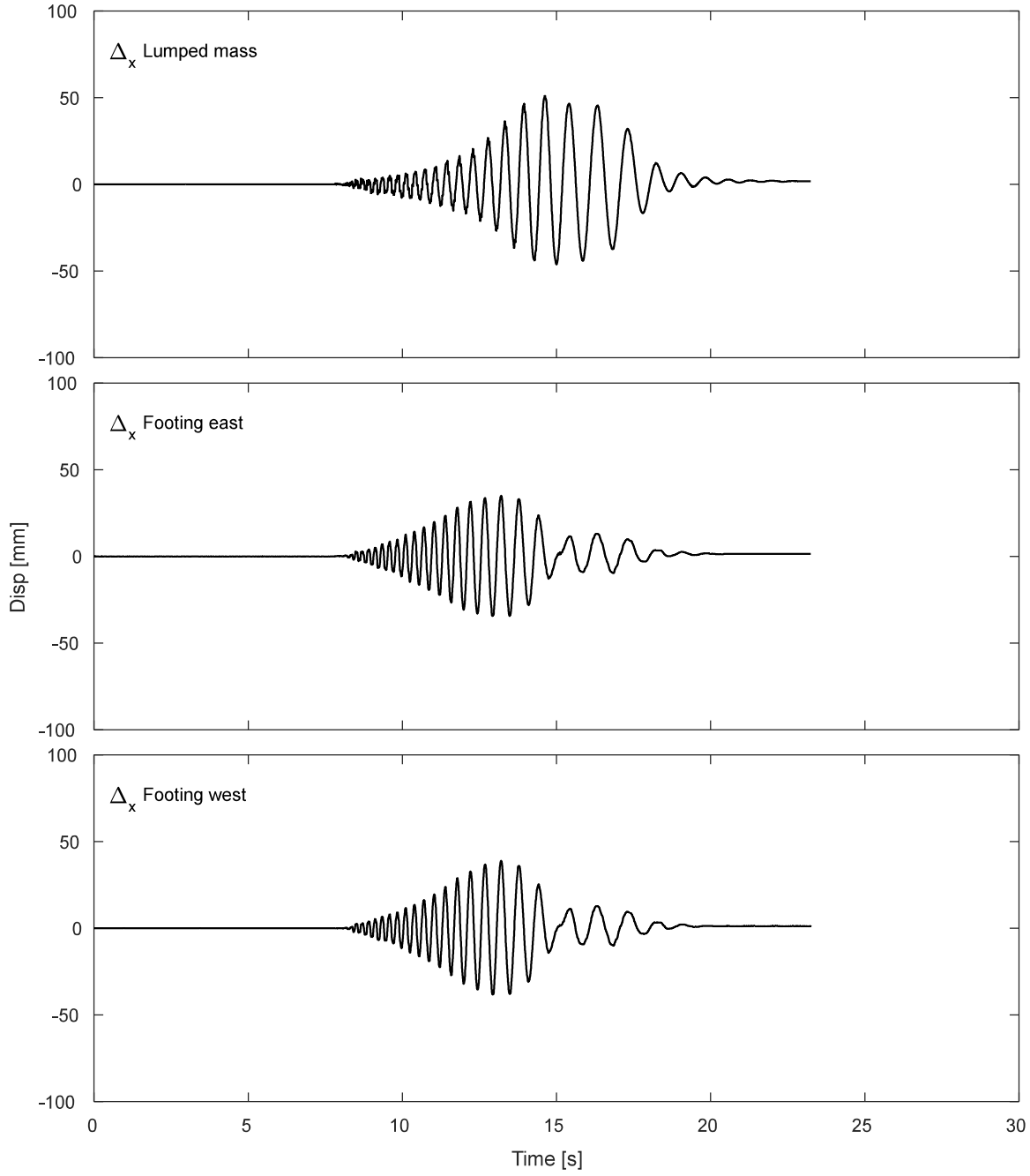

Figure K.5-9. Results of horizontal displacement of lumped mass and footing during DT03-SS20-F04F10 motion.

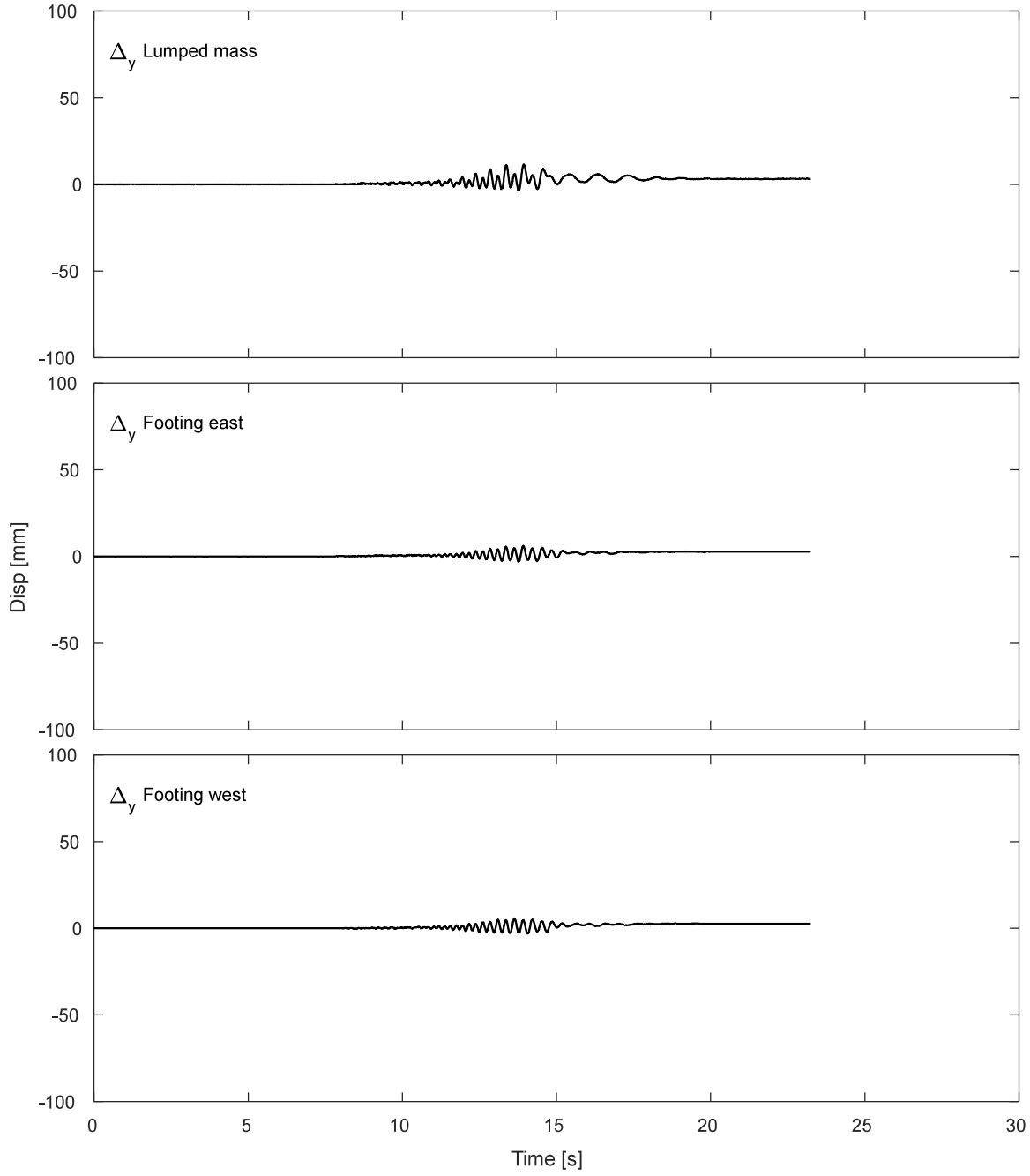

Figure K.5-10. Results of vertical displacement of lumped mass and footing during DT03-SS20-F04F10 motion.

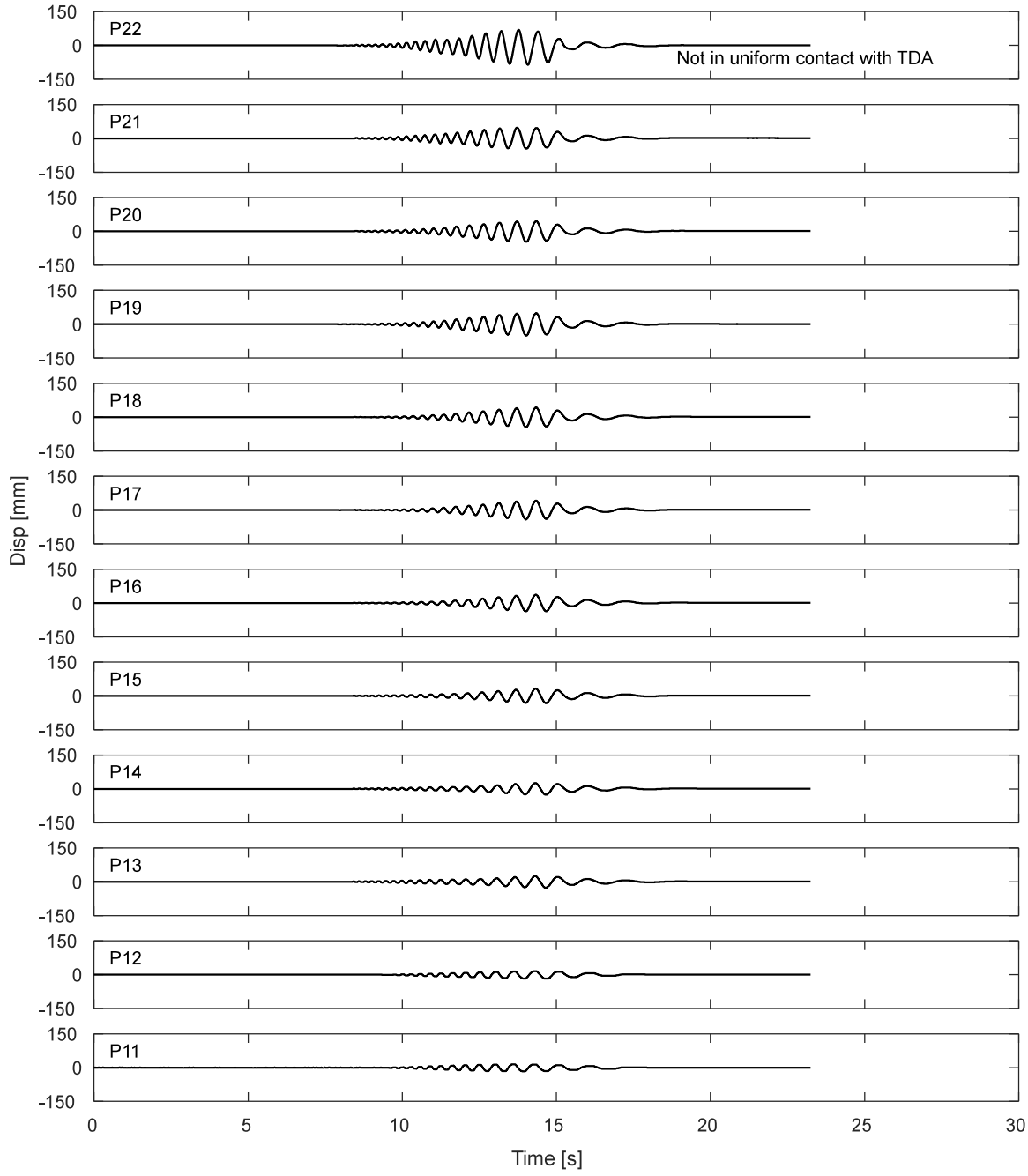

Figure K.5-11. Potentiometers results for the laminar box during DT03-SS20-F04F10 motion.

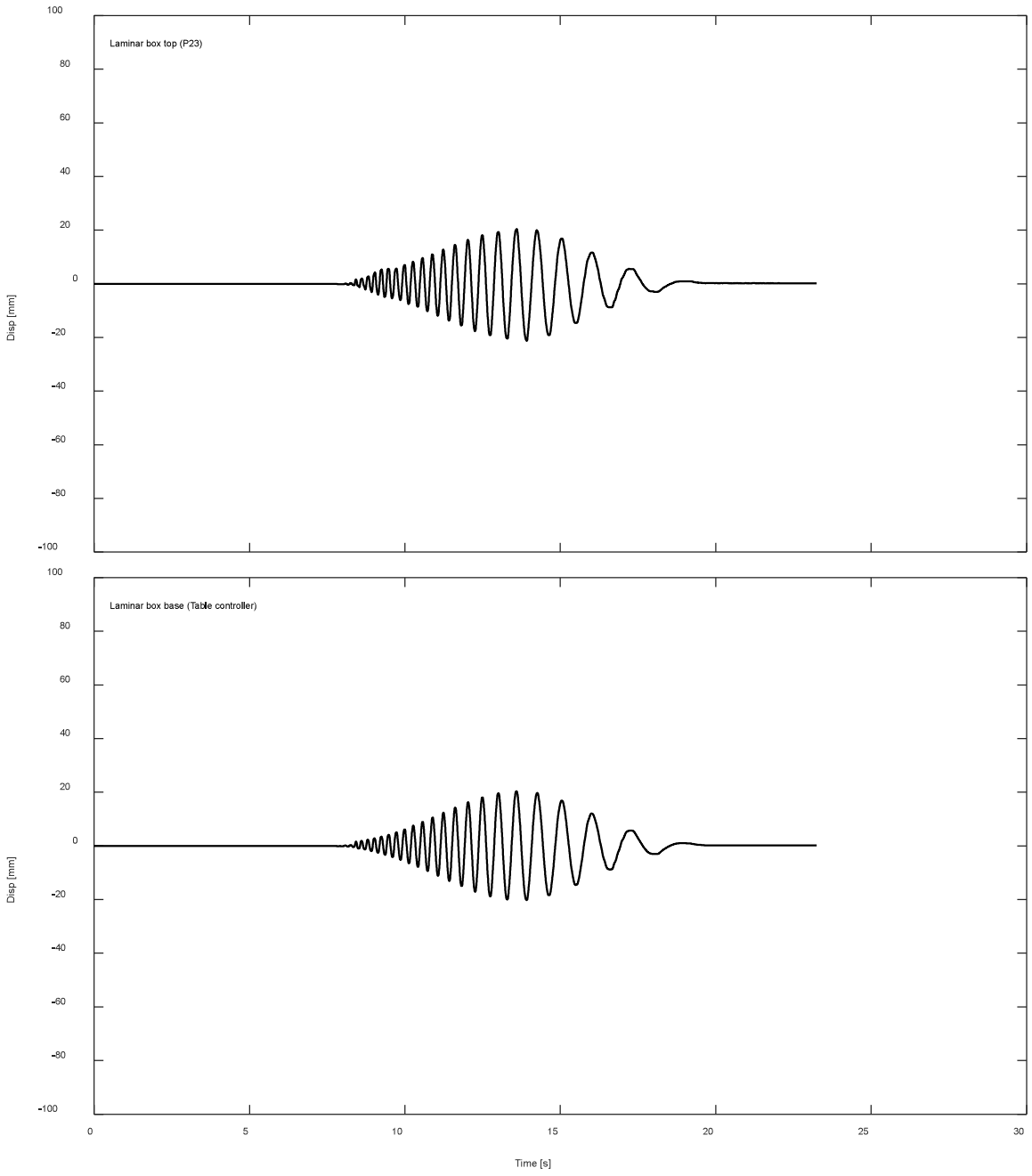

Figure K.5-12. Displacement response of top and base of laminar box during DT03-SS20-F04F10 motion.

K.5.3. Inclinometers.

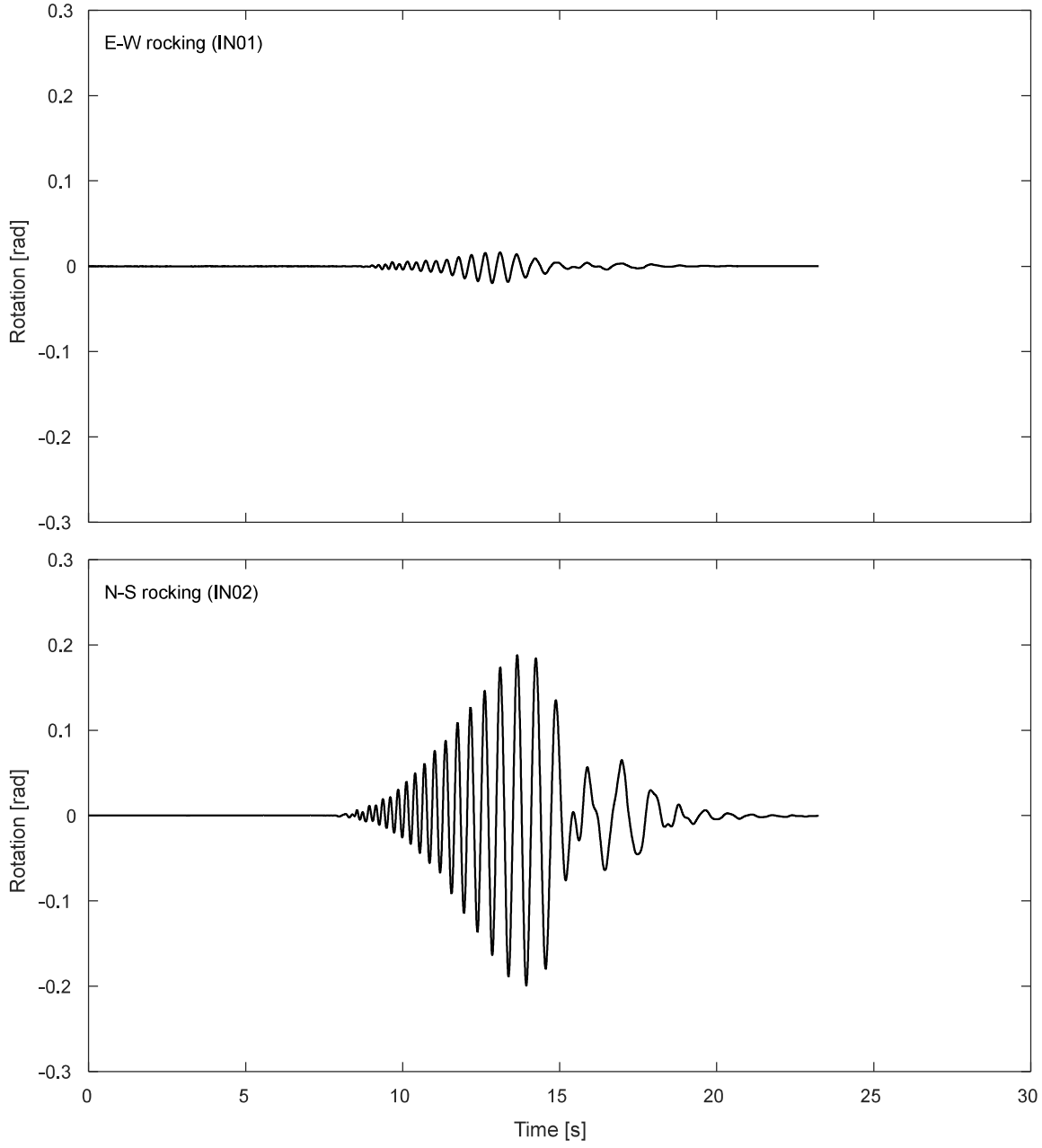

Figure K.5-13. Inclinometer results for the footing during DT03-SS20-F04F10 motion.

K.5.4. Pressure cells.

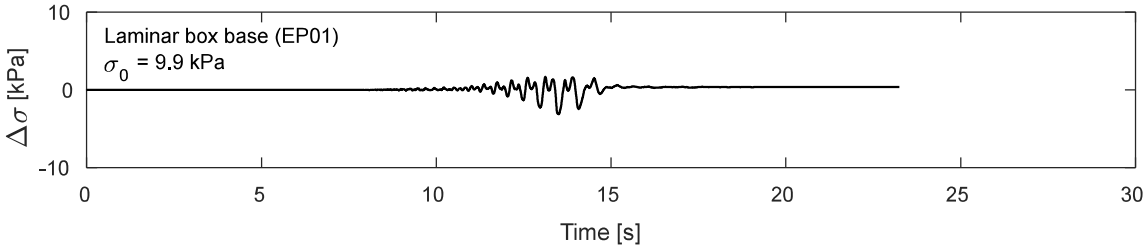

Figure K.5-14. Pressure cells results at laminar box base during DT03-SS20-F04F10 motion

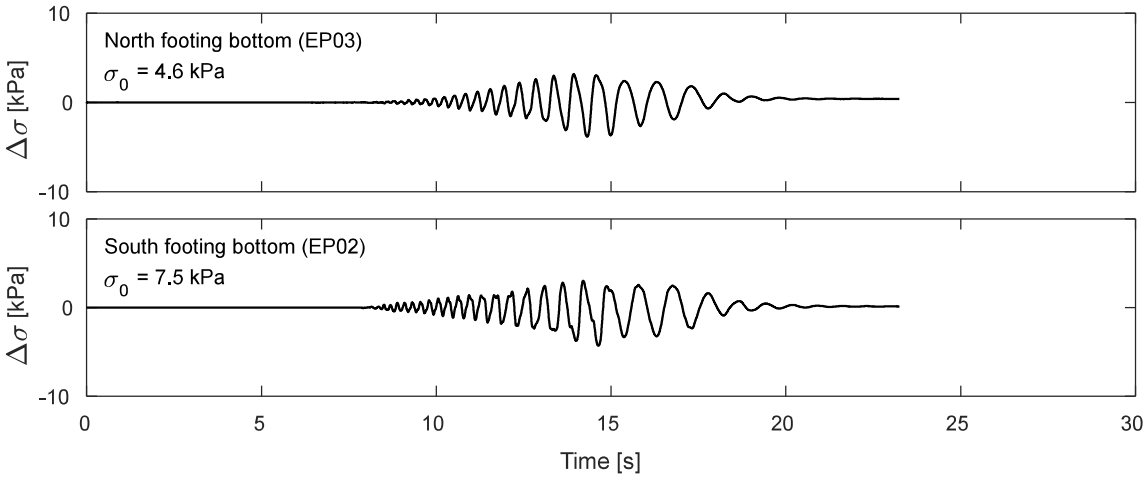

Figure K.5-15. Pressure cells results at footing bottom during DT03-SS20-F04F10 motion

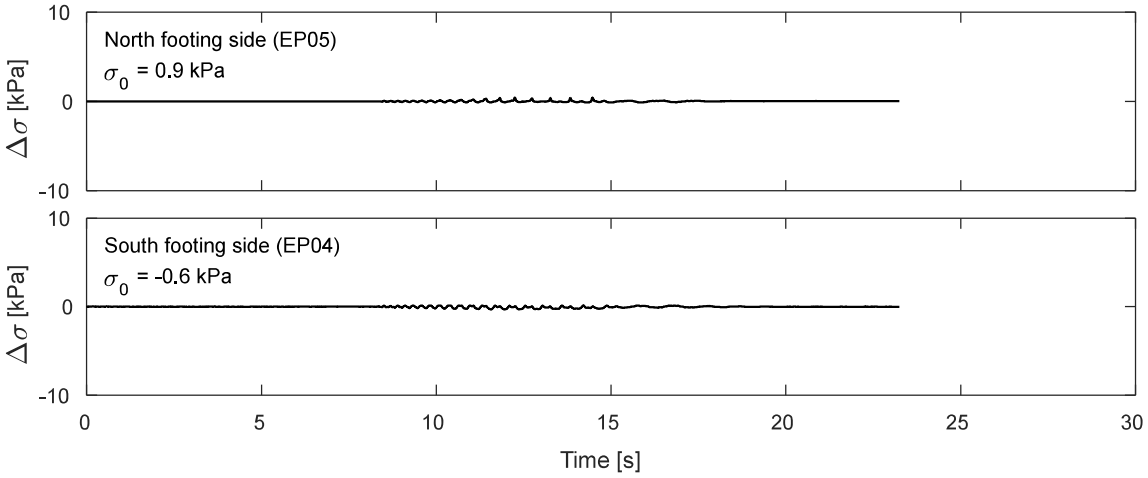

Figure K.5-16. Pressure cells results at footing sides during DT03-SS20-F04F10 motion

K.6. Time-history Records for DT03-SS24-F04F10 motion.

K.6.1 Input Motion

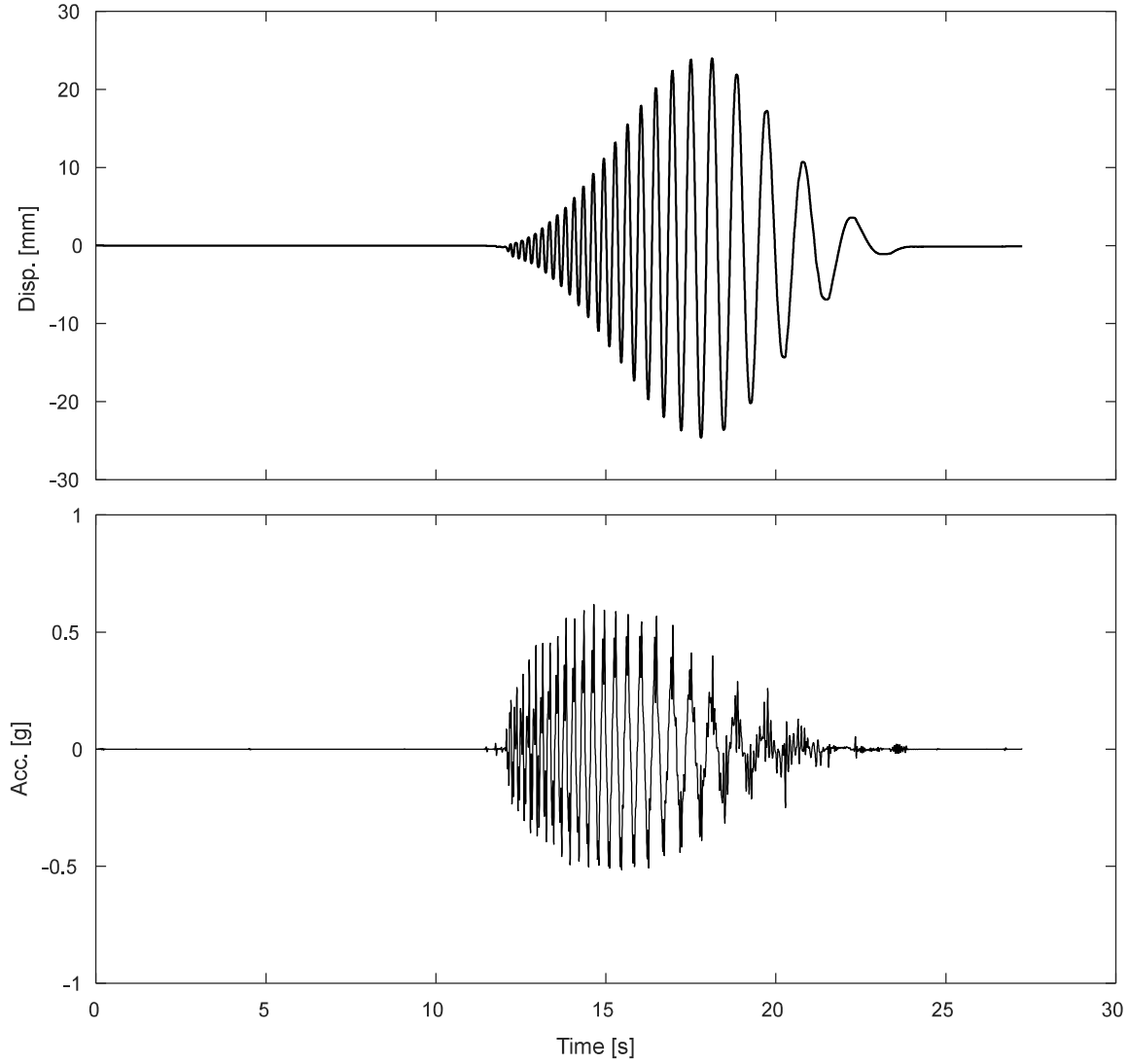

Figure K.6-1. Measured input displacement and acceleration at the base of the specimen during DT03-SS24-F04F10 motion

K.6.1 Accelerometers.

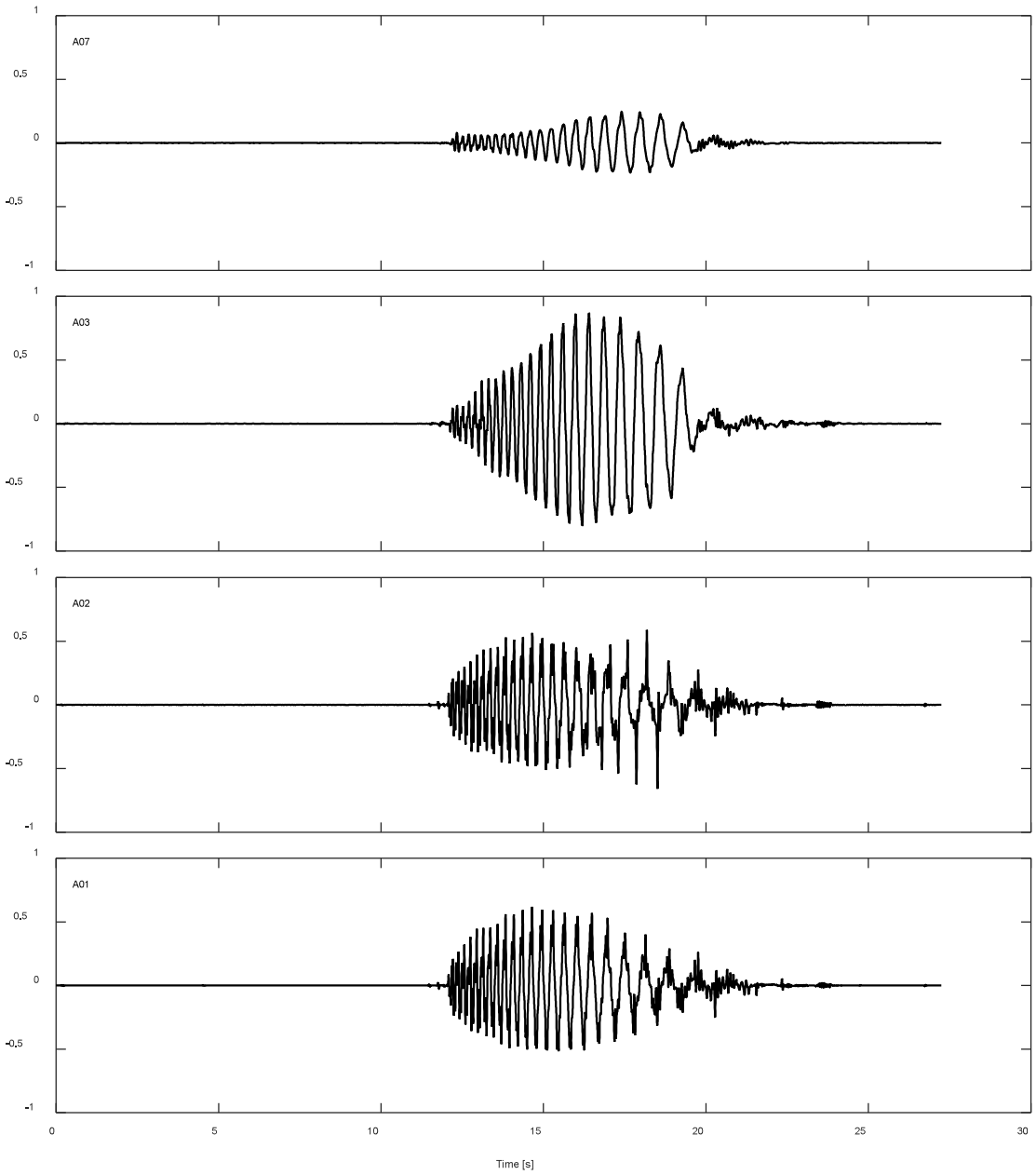

Figure K.6-2. Accelerations results along TDA during DT03-SS24-F04F10 motion.

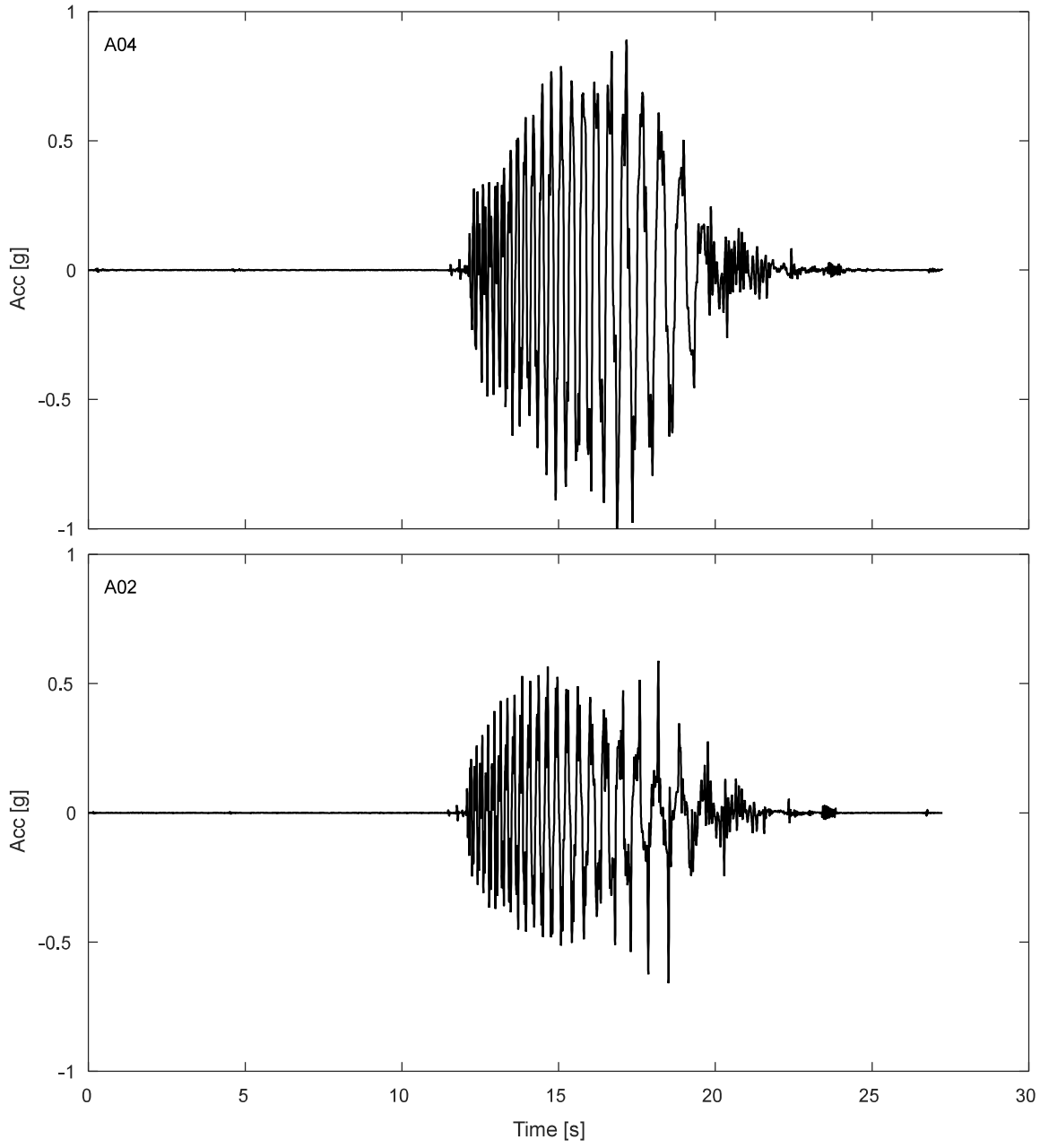

Figure K.6-3. Free field accelerations results for TDA during DT03-SS24-F04F10 motion.

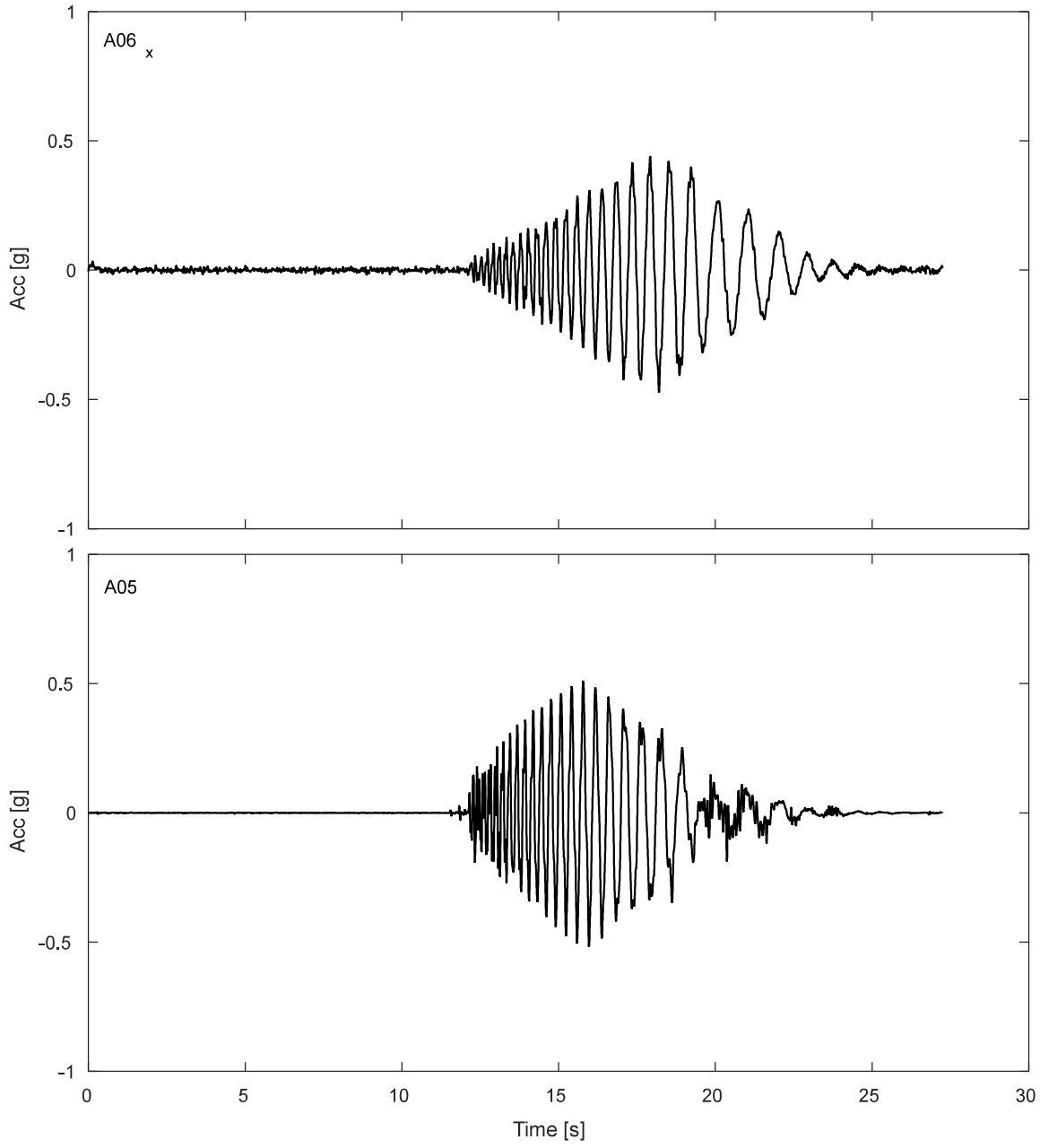

Figure K.6-4. Accelerations results SDOF structure during DT03-SS24-F04F10 motion.

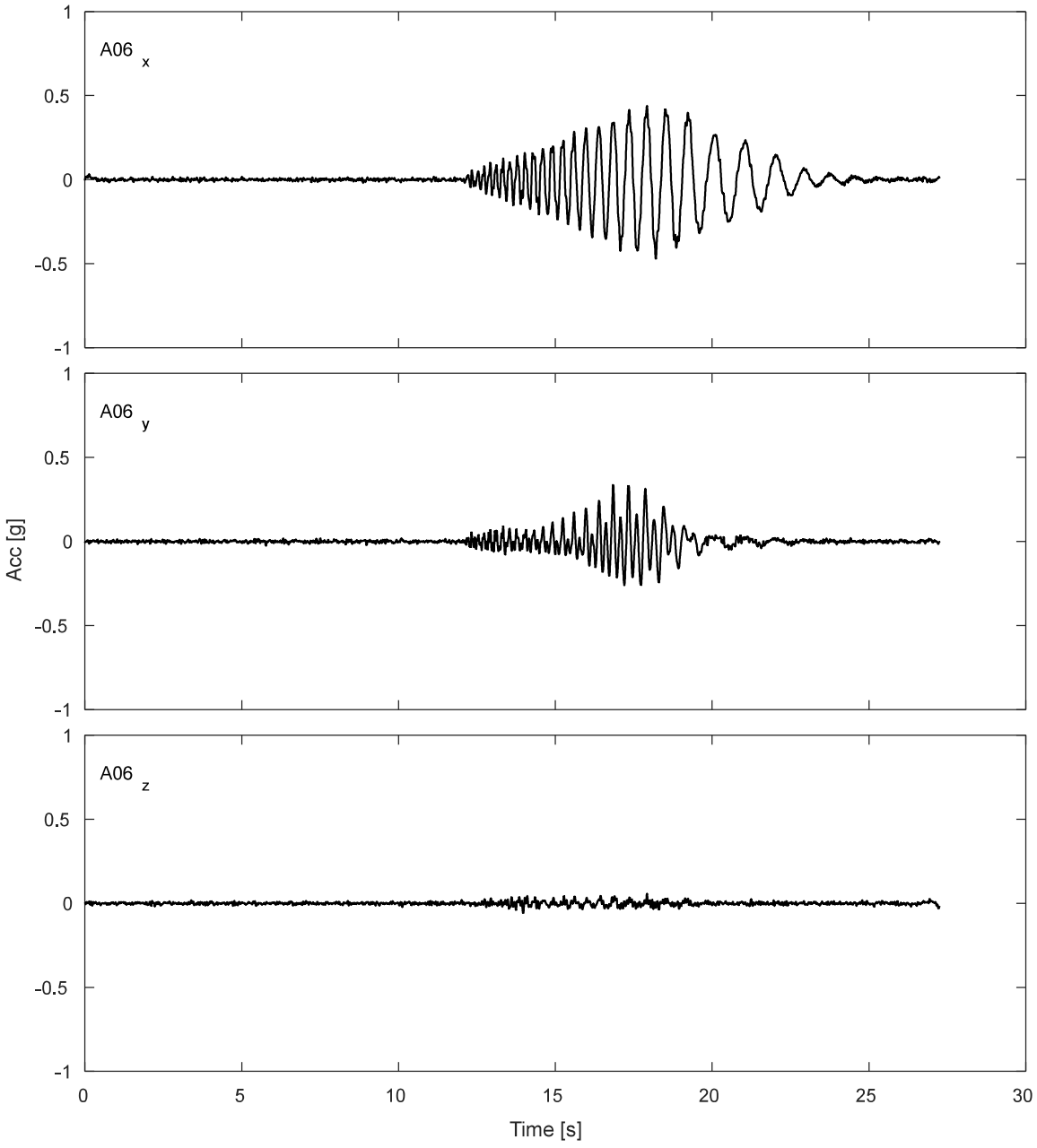

Figure K.6-5. Accelerations results for lumped mass of SDOF structure during DT03-SS24-F04F10 motion.

K.6.2 Potentiometers.

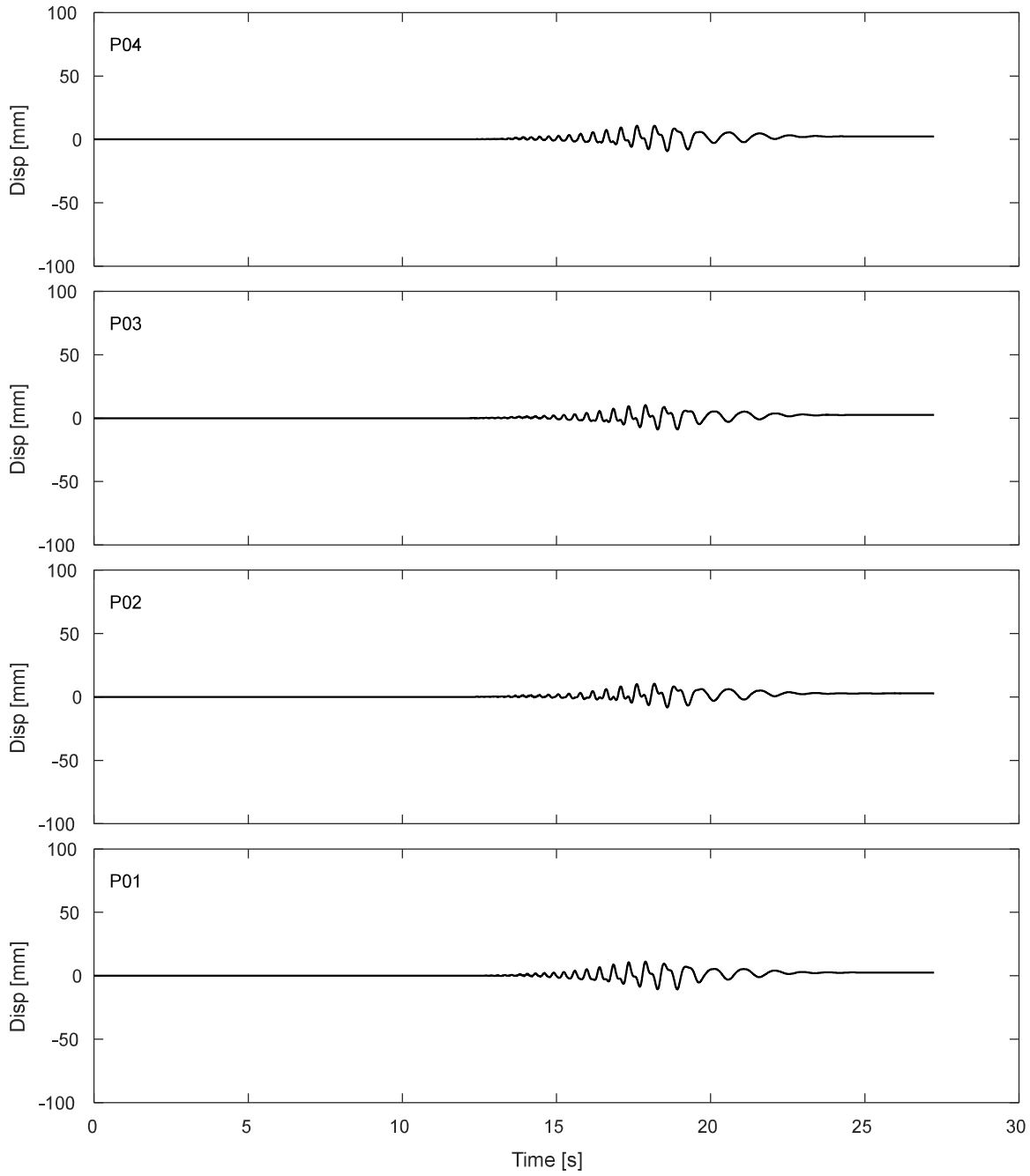

Figure K.6-6. Results of fully vertical potentiometers attached to Korners of top of strip footing during DT03-SS24-F04F10 motion.

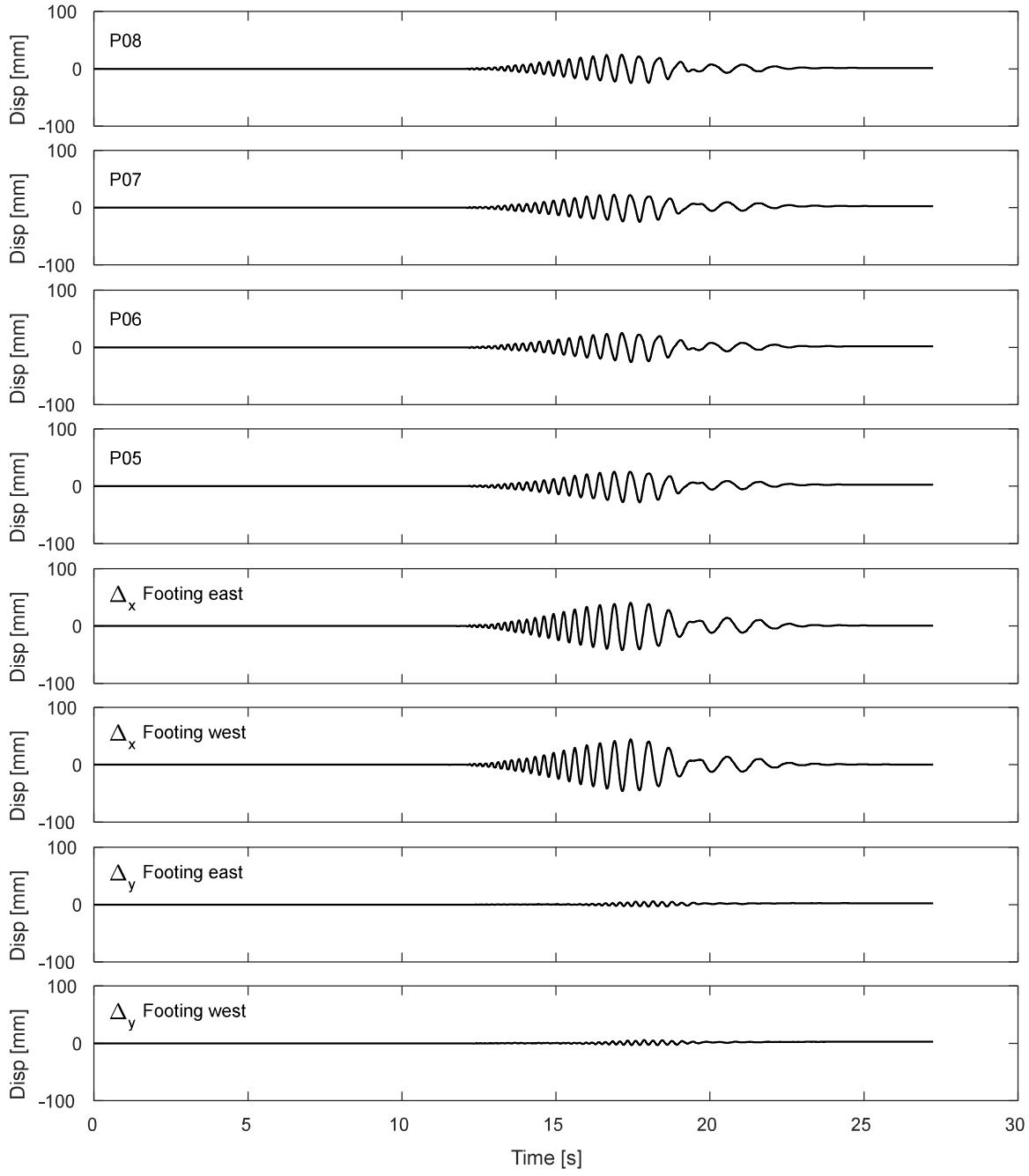

Figure K.6-7. Results of inclined potentiometers attached to top of strip footing during DT03-SS24-F04F10 motion.

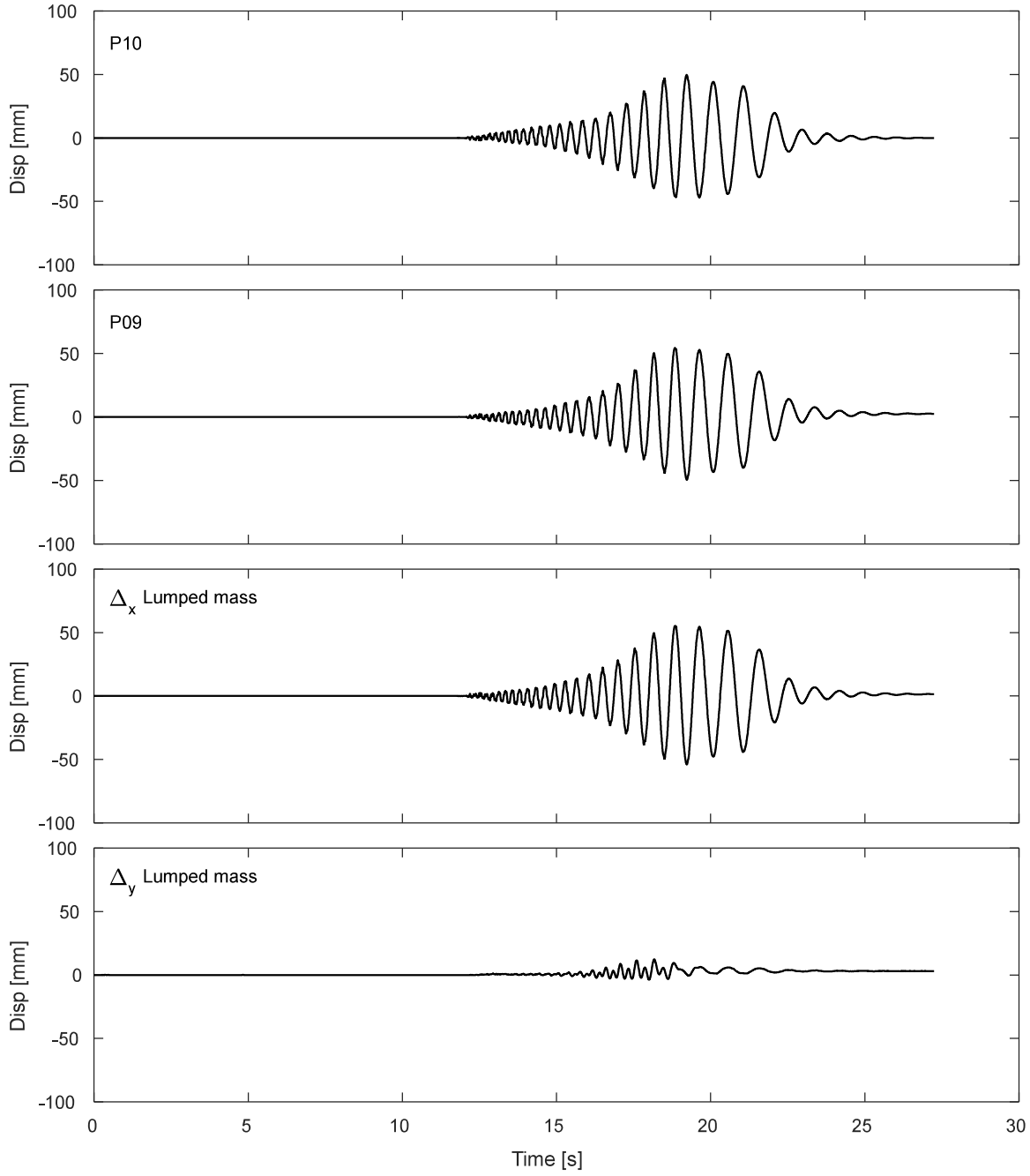

Figure K.6-8. Results of inclined potentiometers attached to lumped mass during DT03-SS24-F04F10 motion.

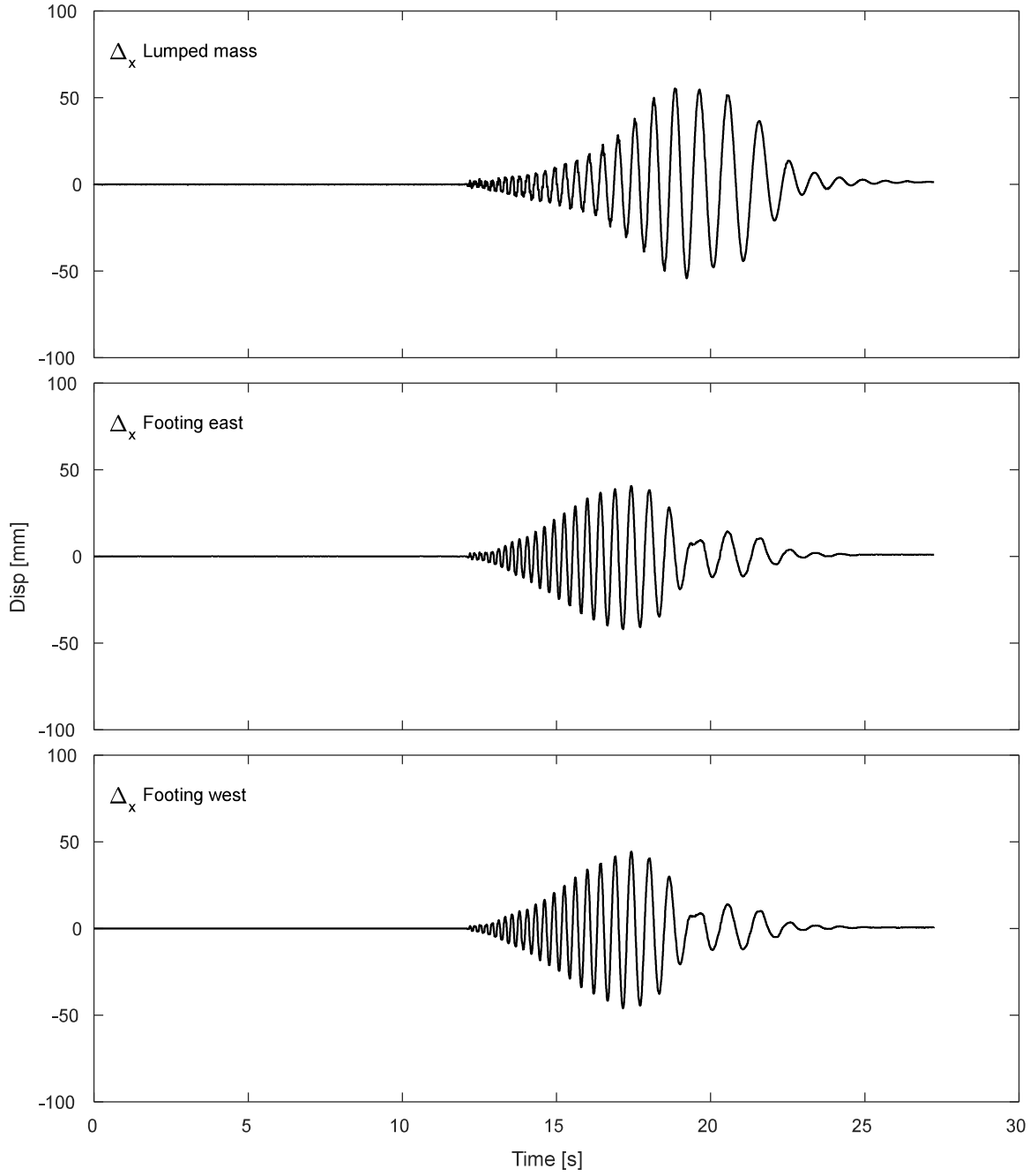

Figure K.6-9. Results of horizontal displacement of lumped mass and footing during DT03-SS24-F04F10 motion.

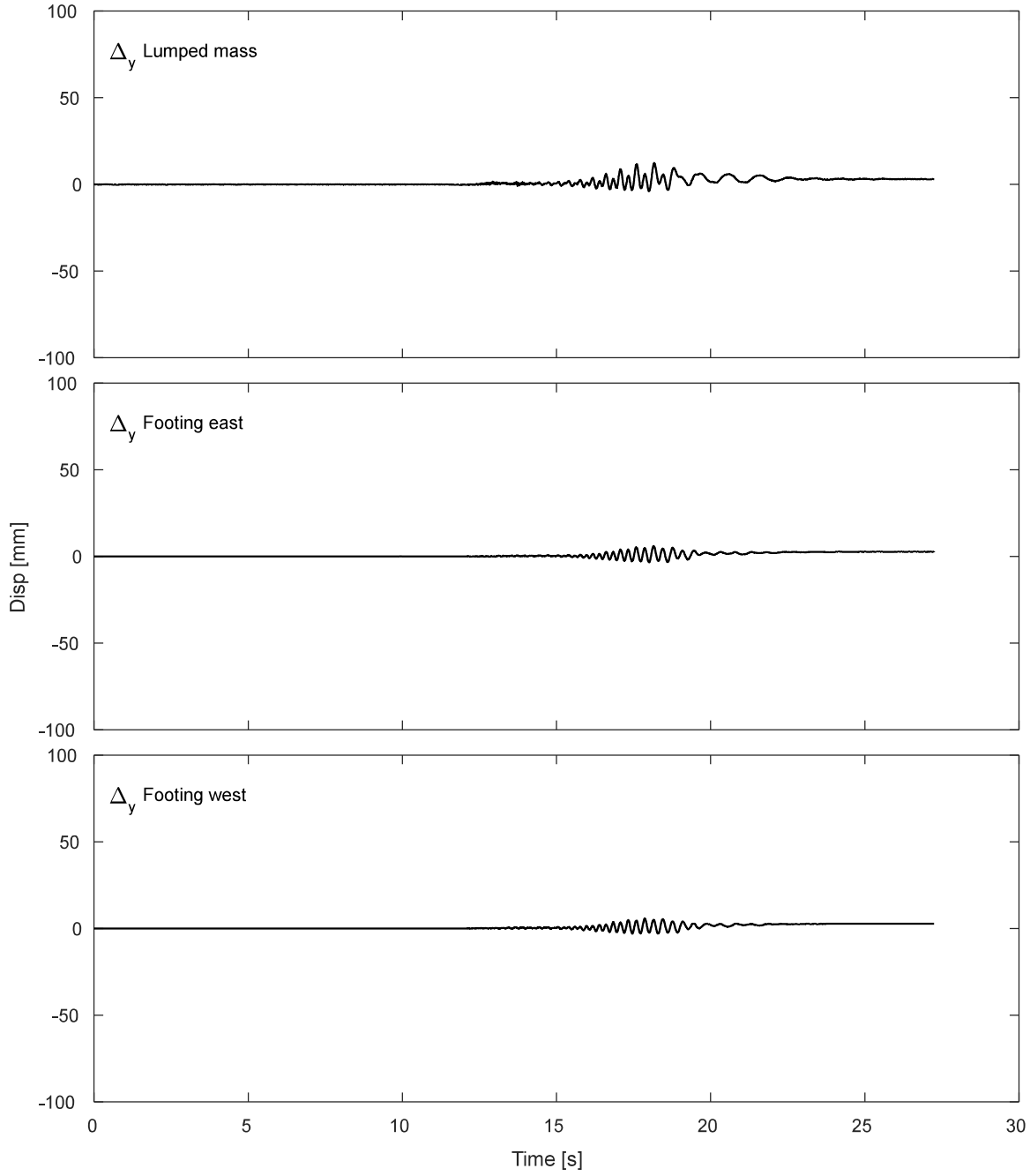

Figure K.6-10. Results of vertical displacement of lumped mass and footing during DT03-SS24-F04F10 motion.

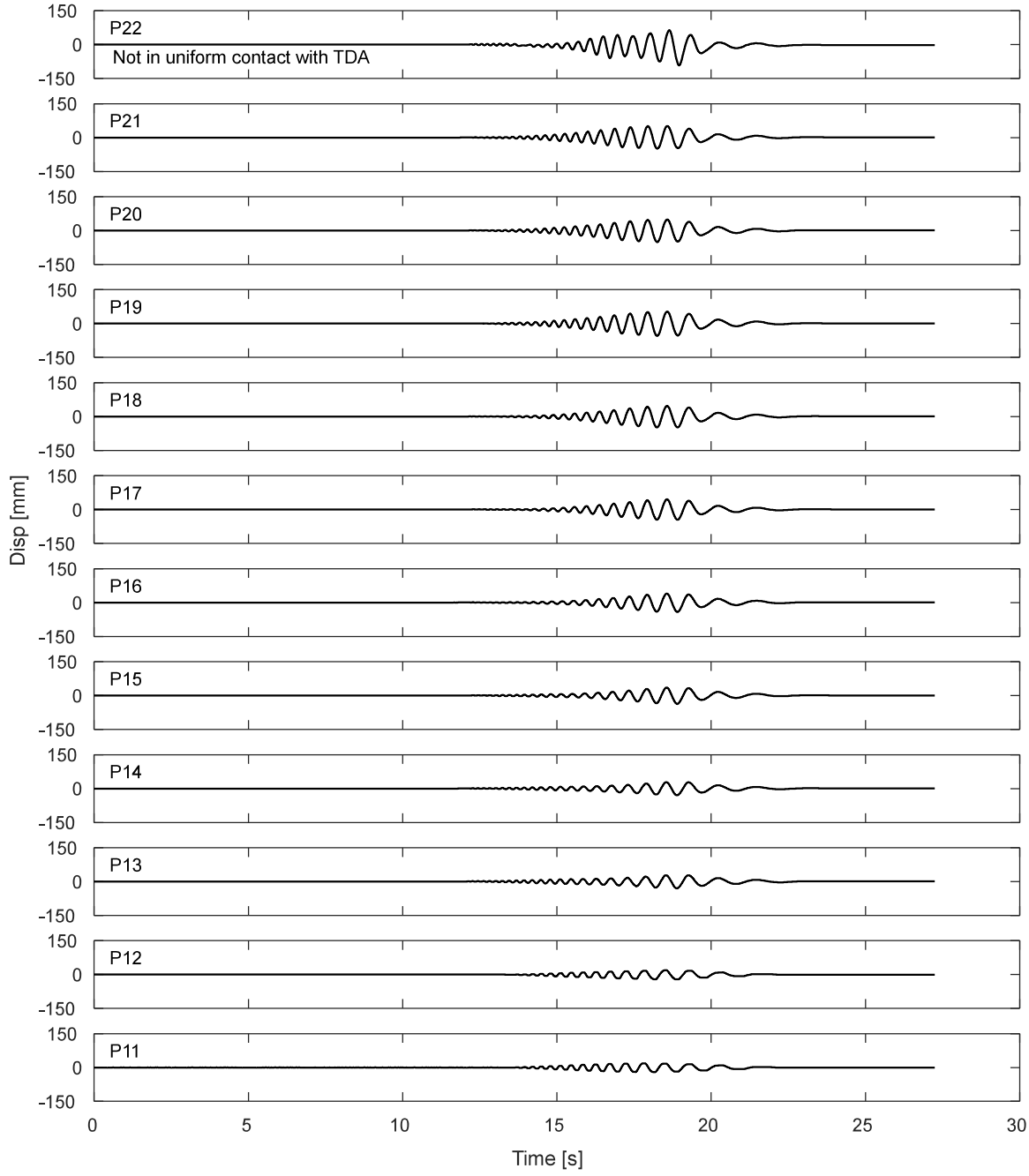

Figure K.6-11. Potentiometers results for the laminar box during DT03-SS24-F04F10 motion.

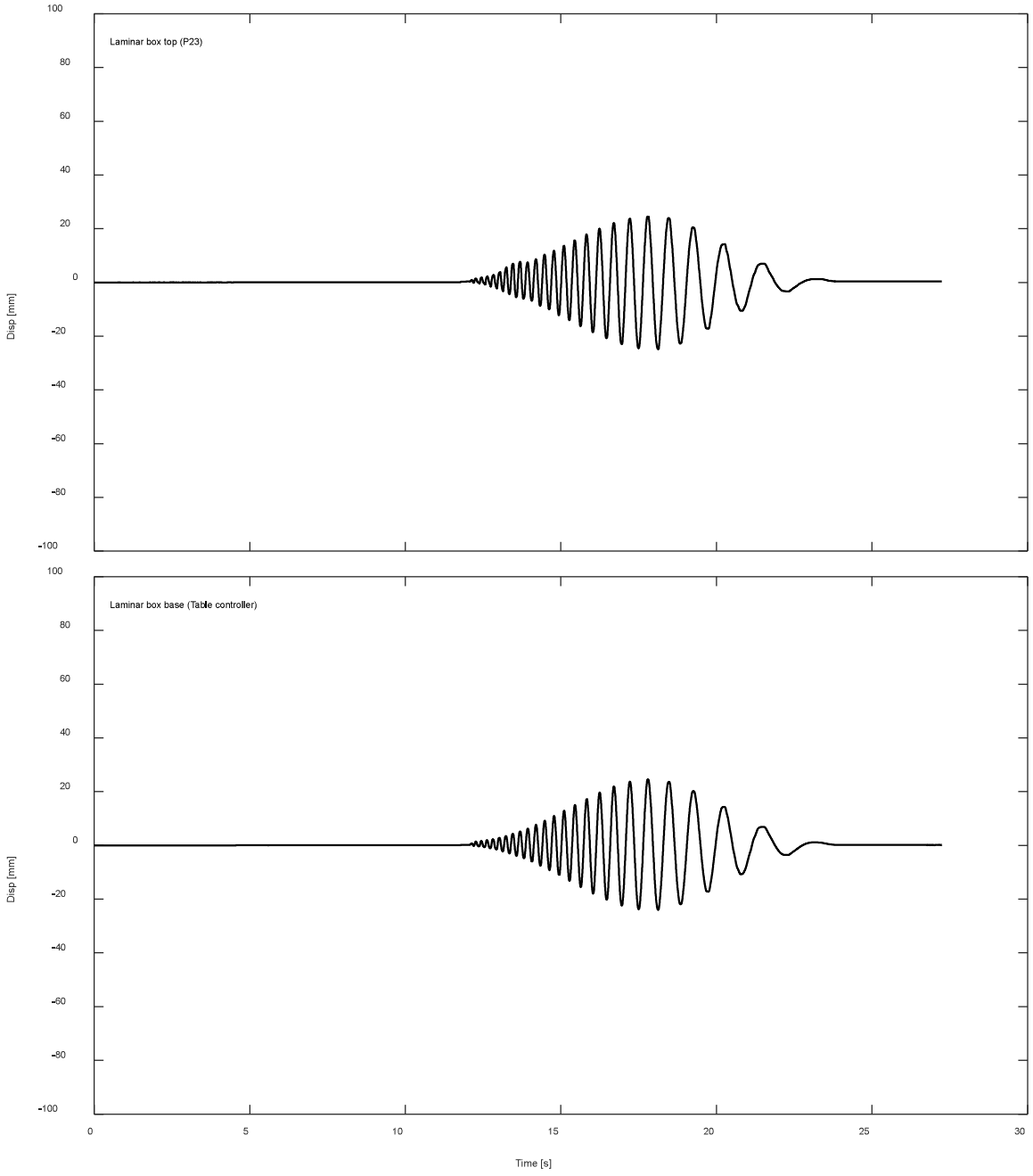

Figure K.6-12. Displacement response of top and base of laminar box during DT03-SS24-F04F10 motion.

K.6.3. Inclinometers.

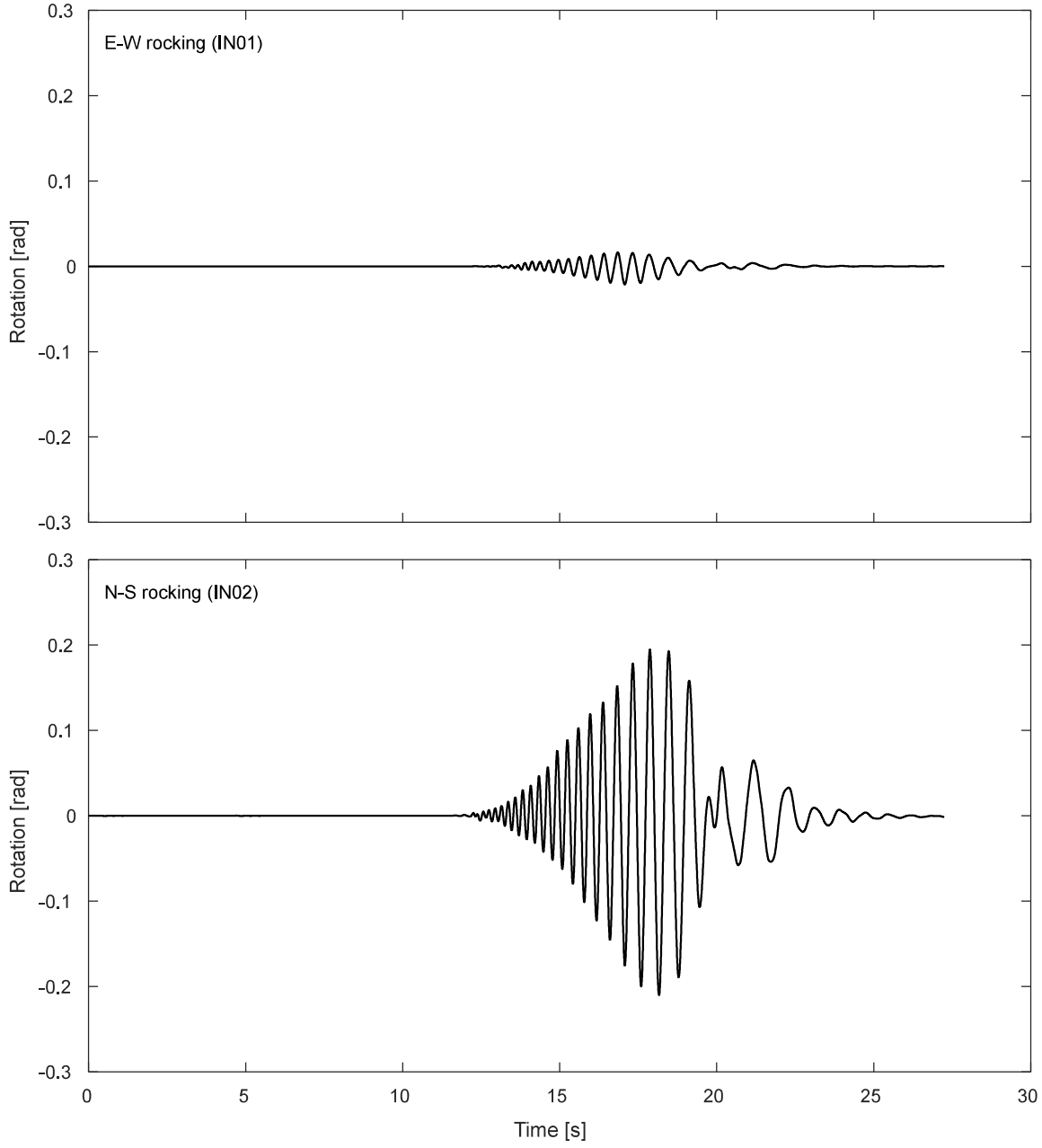

Figure K.6-13. Inclinometer results for the footing during DT03-SS24-F04F10 motion.

K.6.4. Pressure cells.

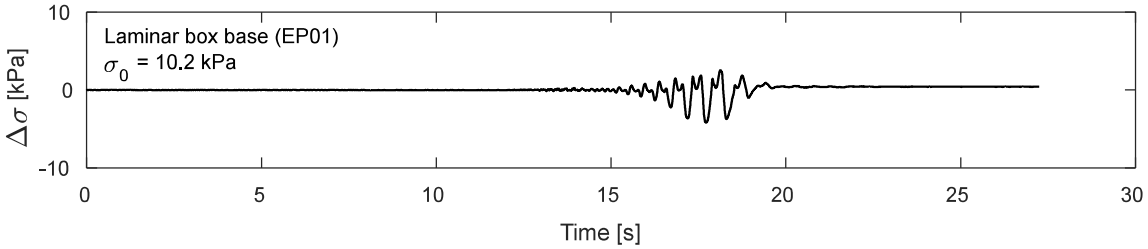

Figure K.6-14. Pressure cells results at laminar box base during DT03-SS24-F04F10 motion

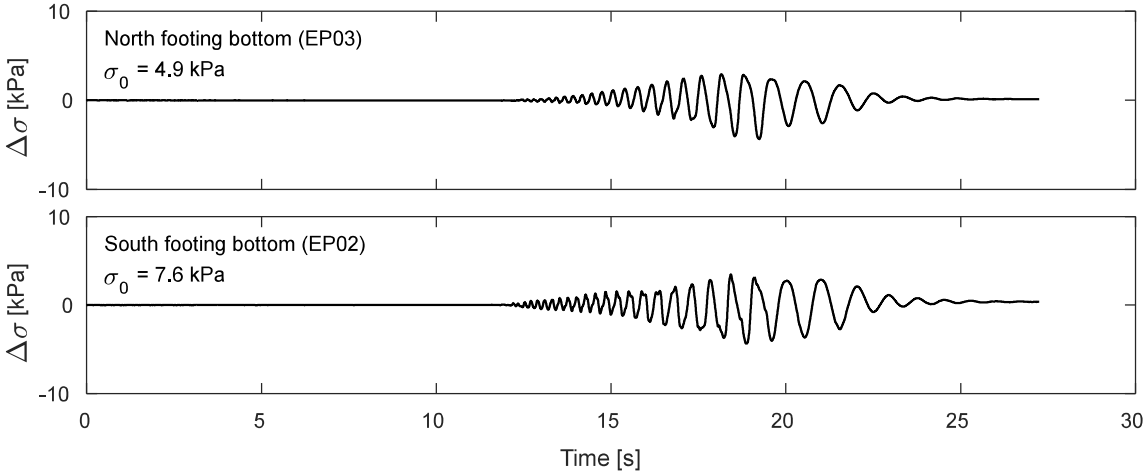

Figure K.6-15. Pressure cells results at footing bottom during DT03-SS24-F04F10 motion

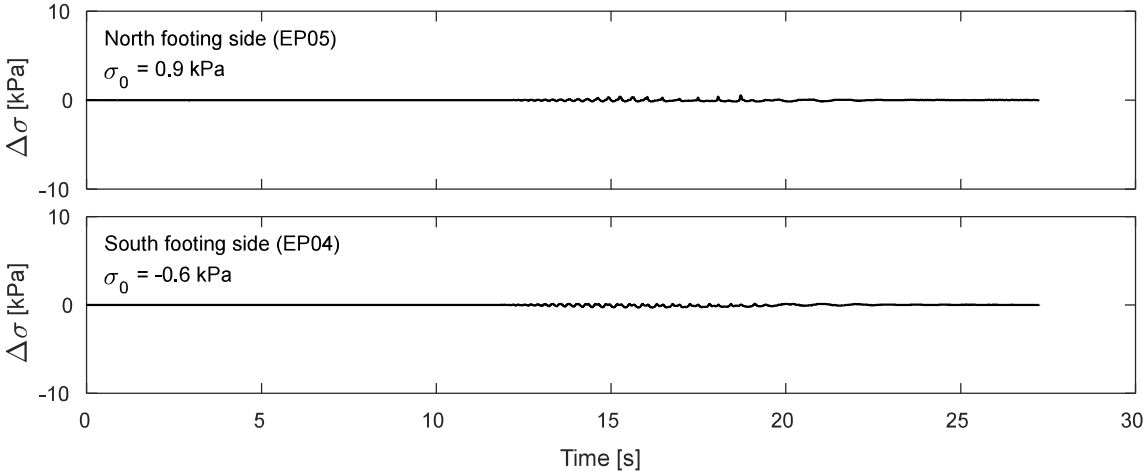

Figure K.6-16. Pressure cells results at footing sides during DT03-SS24-F04F10 motion